

Bragg Grating Solitons in Semilinear Couplers with Dispersive Reflectivity

S. A. M. S. Chowdhury and Javid Atai

School of Electrical and Information Engineering, The University of Sydney, NSW 2006, Australia

Abstract— The existence and stability of quiescent Bragg grating solitons in a semilinear dual core system (one core is nonlinear and carries a Bragg grating and the other is linear) with dispersive reflectivity are investigated. It is found that presence of dispersive reflectivity has a stabilizing effect on the solitons.

1. INTRODUCTION

It is well known that the coupling between the counter propagating modes in a fiber Bragg grating (FBG) gives rise to strong effective dispersion and a gap in the system's linear spectrum. The balance between the effective dispersion and nonlinearity results in soliton-like states which are generally termed Bragg-grating (BG) solitons.

The existence and stability of BG solitons in periodic media with Kerr nonlinearity have been the subject of much interest both theoretically and experimentally over the past two decades [1–6]. On the other hand, a main focus of experimental efforts in this area has been the generation of zero velocity BG solitons. Thus far, BG solitons with a velocity in excess of 23% of the speed of light in the medium have been experimentally observed [6]. They have also been investigated in more sophisticated systems such as grating assisted couplers [7–9] and cubic-quintic nonlinearity [10–12].

It has previously been shown that, in the standard model of gap solitons (i.e., Bragg grating in Kerr nonlinear medium) the presence of dispersive reflectivity leads to the expansion of the stability region [13, 14]. In this paper, we investigate the existence and stability of quiescent BG solitons in a semilinear dual-core system with dispersive reflectivity.

2. THE MODEL AND ITS LINEAR SPECTRUM

Starting with the model of [8] and assuming that a Bragg grating is present only in the nonlinear core and following the approach outlined in [13, 14], one can arrive at the following system of equations:

$$iu_t + iu_x + \left[|v|^2 + \frac{1}{2}|u|^2 \right] u + v + \kappa\phi + mv_{xx} = 0 \quad (1)$$

$$iv_t - iv_x + \left[|u|^2 + \frac{1}{2}|v|^2 \right] v + u + \kappa\psi + mu_{xx} = 0 \quad (2)$$

$$i\phi_t + ic\phi_x + \kappa u = 0 \quad (3)$$

$$i\psi_t - ic\psi_x + \kappa v = 0 \quad (4)$$

where u and v denote the forward- and backward-propagating waves in the nonlinear core and ϕ and ψ are their counterparts in the linear core, respectively. Also, κ is the linear coupling between the two cores, m represents the strength of the dispersive reflectivity and c is the relative group velocity in the linear core (group velocity in the nonlinear core has been set to 1). As was pointed out in Ref. [13, 14], the values $m > 0.5$ may not be physically meaningful. Therefore, we limit our analysis to the range $0 \leq m \leq 0.5$. Substituting $u, v, \phi, \psi \sim \exp(ikx - i\omega t)$ into the linearized form of the Eqs. (1)–(4), we obtain the following dispersion relation:

$$\omega^4 - [1 + 2\kappa^2 + (1 + c^2 - 2m)k^2 + m^2k^4] \omega^2 + \kappa^4 + (c^2 - 2c\kappa^2)k^2 + c^2(1 - 2m)k^4 + c^2m^2k^6 = 0 \quad (5)$$

Analyzing Eq. (5), it is found that in the case of $c = 0$ and $0 \leq m \leq 0.5$, the spectrum always contains two disjoint bandgaps. The gaps reside in the upper and lower halves of the spectrum, respectively (see Fig. 1(a)). It should also be noted that the width of the gaps is independent of the value of the coupling coefficient κ and m . On the other hand, as is shown in Fig. 1(b), when $c \neq 0$, the shapes of the dispersion curves change significantly resulting in the formation of a central gap. The width of the central gap varies with m and it completely closes at $c = m\kappa^2$.

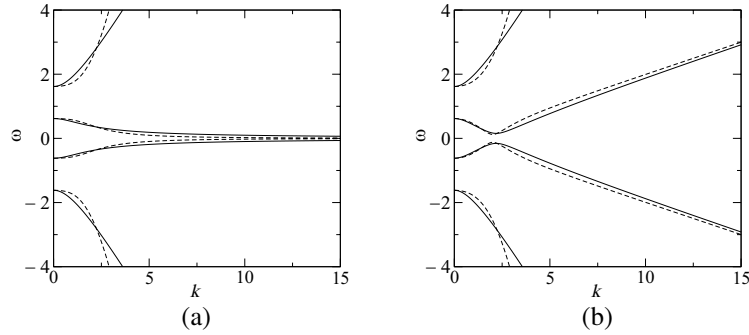


Figure 1: Dispersion diagrams obtained from (5) for (a) $\kappa = 1$, $c = 0$ and (b) $\kappa = 1$, $c = 0.2$. The solid and dashed lines correspond to $m = 0$ and $m = 0.4$, respectively.

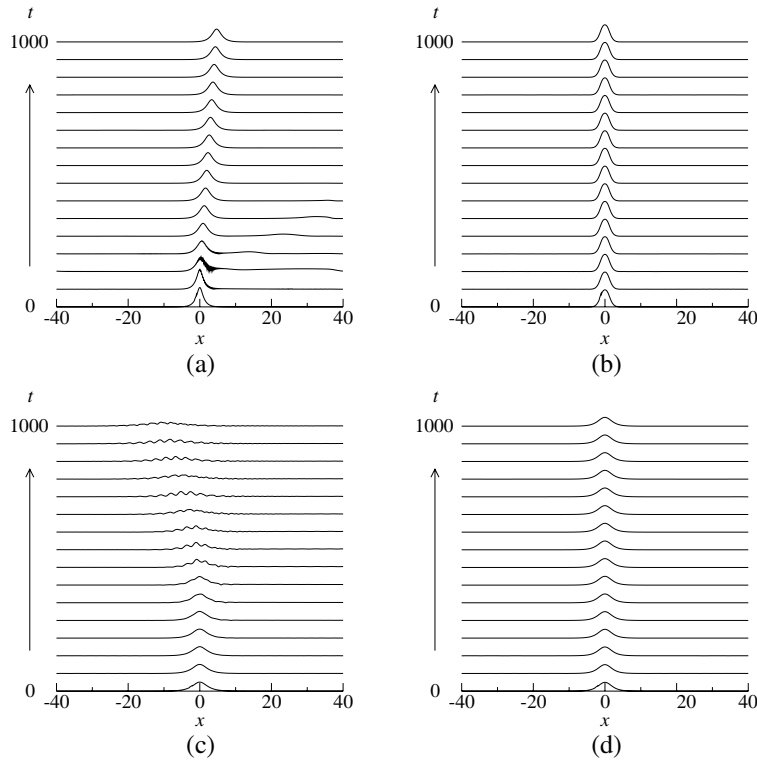


Figure 2: Evolution of asymmetrically perturbed soliton. (a) Unstable soliton with $\omega = 10.05$, $\kappa = 10.0$, $c = 0$, $m = 0$; (b) Stable soliton with $\omega = 10.05$, $\kappa = 10.0$, $c = 0$, $m = 0.30$; (c) Unstable soliton with $\omega = 1.48$, $\kappa = 1.0$, $c = 0.2$, $m = 0$; (d) Stable soliton with $\omega = 1.48$, $\kappa = 1.0$, $c = 0.2$, $m = 0.2$. Only the u -component is shown.

3. SOLITON SOLUTIONS AND STABILITY ANALYSIS

Since exact analytical solutions for Eqs. (1)–(4) are not available, the soliton solutions must be determined numerically. To this end, we sought for stationary solutions of Eqs. (1)–(4) as $\{u(x, t), v(x, t)\} = \{U(x), V(x)\}e^{-i\omega t}$ and $\{\phi(x, t), \psi(x, t)\} = \{\Phi(x), \Psi(x)\}e^{-i\omega t}$. Substituting these expressions into (1)–(4) results in a system of ordinary differential equations that can be solved using the relaxation algorithm. The analysis shows that for $c = 0$ solitons exist throughout the upper and lower gaps. In the case of $c \neq 0$, no solitons were found in the central gap. On the other hand, solitons exist in the upper and lower gaps. It should be noted that when $c \neq 0$ the upper and lower gaps are immersed into one branch of the continuous spectrum. Another noteworthy feature of the soliton solutions is that above a certain value of m , they develop sidelobes. A key finding is that the appearance of the sidelobes is also dependent on the value of c and above a certain value of c the sidelobes do not form.

We tested the stability of the solitons by numerically solving Eqs. (1)–(4). In all the simulations,

to seed any inherent instability, the stationary solutions obtained from the relaxation algorithm were initially perturbed asymmetrically. It is found that the presence of dispersive reflectivity has a stabilizing effect on solitons (see Fig. 2). In particular, when $c = 0$, the stabilization of solitons due to dispersive reflectivity is more pronounced for larger values of κ .

As for instability development, highly unstable solitons are destroyed whereas unstable solitons in the proximity of the stability border shed some energy in the form of radiation and subsequently evolve to robust quiescent or moving breathers.

REFERENCES

1. Aceves, A. B. and S. Wabnitz, *Phys. Lett. A*, Vol. 141, 37, 1989.
2. Christodoulides, D. N. and R. I. Joseph, *Phys. Rev. Lett.*, Vol. 62, 1746, 1989.
3. De Sterke, C. M. and J. E. Sipe, *Prog. Opt.*, Vol. 33, 203, 1994.
4. Eggleton, B. J., R. E. Slusher, C. M. de Sterke, P. A. Krug, and J. E. Sipe, *Phys. Rev. Lett.*, Vol. 76, 1627, 1996.
5. Eggleton, B. J., C. M. de Sterke, and R. E. Slusher, *J. Opt. Soc. Am. B*, Vol. 14, 2980, 1997.
6. Mok, J. T., C. M. de Sterke, I. C. M. Littler, and B. J. Eggleton, *Nature Phys.*, Vol. 2, 775, 2006.
7. Mak, W. C. K., B. A. Malomed, and P. L. Chu, *J. Opt. Soc. Am. B*, Vol. 15, 1685, 1998.
8. Atai, J. and B. A. Malomed, *Phys. Rev. E*, Vol. 62, 8713, 2000.
9. Atai, J. and B. A. Malomed, *Phys. Rev. E*, Vol. 64, 066617, 2001.
10. Atai, J. and B. A. Malomed, *Phys. Lett. A*, Vol. 284, 247, 2001.
11. Atai, J., *J. Opt. B: Quantum Semiclass. Opt.*, Vol. 6, S177, 2004.
12. Dasanayaka, S. and J. Atai, *Phys. Lett. A*, Vol. 375, 225, 2010.
13. Atai, J. and B. A. Malomed, *Phys. Lett. A*, Vol. 342, 404, 2005.
14. Neill, D. R., J. Atai, and B. A. Malomed, *J. Opt. A: Pure Appl. Opt.*, Vol. 10, 085105, 2008.

Dynamic Frequency Response of Charged Chiral Rods

K. Kang and J. K. G. Dhont

Forschungszentrum Juelich, ICS-3 (Soft Condensed Matter), Juelich, Germany

Abstract— Various phases and dynamical states are induced by an external AC electric field in concentrated suspensions of charged, fibrous viruses (fd). The observed phases and dynamical states are the result of chiral rod-rod interactions between polarized electric double layers, polarized layers of condensed ions and electro-osmotic flow.

1. INTRODUCTION

Various phases and dynamical states are induced by an external AC electric field in concentrated suspensions of charged, fibrous viruses (fd), which are model systems for very long and thin, stiff colloidal rods [1, 2]. The observed phases and dynamical states are the result of chiral rod-rod interactions between polarized electric double layers, polarized layers of condensed ions and electro-osmotic flow. We use various experimental methods, not only for the characterization of the field-induced phases/states, but also for the determination of the divergence of a length- and time-scale on approach of a non-equilibrium critical point [3–5]. Theory is developed for the frequency-dependent charge distribution and electrokinetic potential for both the diffusive double layer of very weakly charged rods, and condensed ions in case of highly charged rods [6, 7].

2. ELECTRODE POLARIZATION

Due to the finite diffusivity of salt ions, the double layer at the electrodes will not be the same as the true bulk field, as an applied field amplitude. Thus screening of the electrode double layer (at the surface of the ITO glasses) has to be taken into account to measure true bulk field amplitude. We estimate both attenuation factor and the bulk-induced polarization by followings:

For the Brownian force describing the diffusive motion by the concentration gradients,

$$\vec{F}_{\pm}(z, t) = -k_B T \frac{\partial}{\partial z} \ln \{\rho_{\pm}(z, t)\} \mp e \frac{\partial}{\partial z} \Phi(z, t) \quad (1)$$

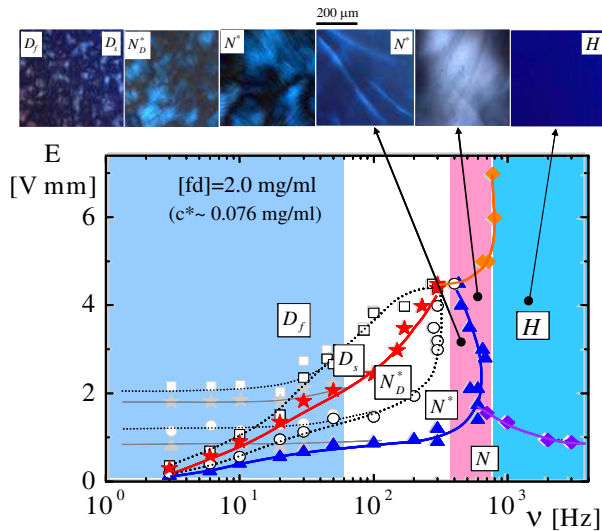


Figure 1: Bulk electric phase/state diagram of charged fd-rods: N^* , N_D^* -Chiral-nematic phases, D_S , D_f -dynamical states, and H -homeotropic phase. Electrode polarization is corrected in the low frequency range.

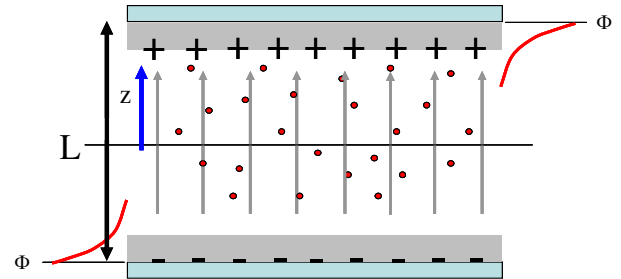


Figure 2: A simple feature of using the standard electrokinetic's model for the penetration depth, from the surface of ITO glass to the true bulk field in salt solution.

leads to, within the conservation law of the concentration, the equation of motion as

$$\frac{\partial \rho_{\pm}(z, t)}{\partial t} = D \frac{\partial^2}{\partial z^2} \rho_{\pm} \pm D \beta e \frac{\partial}{\partial z} \left[\rho_{\pm} \frac{\partial \Phi}{\partial z} \right] \quad (2)$$

Within the Debye-Hueckel limit, the linearization of above Eq. (2) gives to

$$\frac{\partial \Delta \rho_{\pm}}{\partial t} = D \frac{\partial^2}{\partial z^2} \Delta \rho_{\pm} \mp D \left(\frac{\kappa^2}{2} \right) [\Delta \rho_{+} - \Delta \rho_{-}], \quad \kappa \equiv \sqrt{\frac{2\beta e^2 \bar{\rho}}{\varepsilon}}, \quad (3)$$

where κ is the inverse Debye screening length.

The boundary condition for the potential is used as

$$\begin{aligned} \Delta \Phi(z, t) &\equiv \Phi \left(z = \frac{L}{2}, t \right) - \Phi \left(z = -\frac{L}{2}, t \right) = E_0 L \cos(\omega t) \\ \frac{\partial}{\partial z} [-\Delta \rho_{\pm}(z, t) \mp \varepsilon \kappa^2 \Phi(z, t)] &= 0 \quad \text{for } z = \pm \frac{L}{2} \quad \text{and } t > 0 \end{aligned} \quad (4)$$

Then we typically find the attenuation factor and the phase shift as

$$\begin{aligned} \gamma &= \sqrt{(P'_{bulk})^2 + (P''_{bulk})^2} = \Omega / \sqrt{4 + \Omega^2}, \\ \varphi &= \tan^{-1} (|P''_{bulk} / P'_{bulk}|) = \tan^{-1} (2/\Omega), \end{aligned} \quad (5)$$

where the dimensionless frequency is defined as $\Omega = \omega L / D \kappa$. Fig. 3 has shown the induced bulk polarization in-phase (P'_{bulk}) and out-of-phase (P''_{bulk}), the attenuation factor (γ) and the phase shift (φ).

Therefore we get the true bulk field amplitude is as

$$E_0 = E_{tr}^{bulk} / \gamma = E_{tr}^{bulk} \sqrt{4 + \Omega^2} / \Omega \quad (6)$$

Two sharp phase transitions at low frequency are checked with the variation of cell gap widths (in Fig. 4(a)) and the applied frequency (in Fig. 4(b)), for the electrode polarization.

3. BULK ELECTRIC PHASE/STATE DIAGRAM OF CHARGED CHIRAL FD-RODS

The electric phase/state diagram is given for a fd-virus concentration of 2.0 mg/ml (which is about 26 times the overlap concentration (of 0.076 mg/ml), and an analytical buffer concentration of 0.16 mM, in the electric field amplitude versus frequency plane in Fig. 1. The various transitions are due to the electric response of many interacting charged fibrous virus particles, which are chiral macromolecules.

The initial N -phase, without an applied field and at sufficiently low amplitudes, corresponds to a state where nematic domains are in coexistence with an isotropic phase. Above the threshold field amplitude of about ~ 1 V/mm (at low frequencies), a chiral-nematic N^* -phase (or the striped

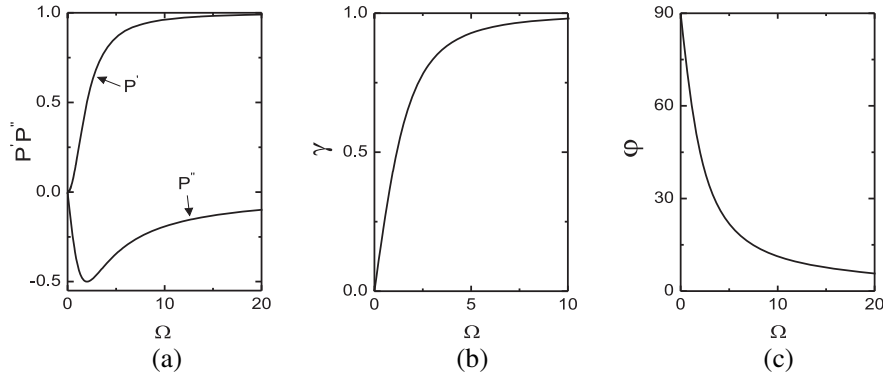


Figure 3: Induced polarization in-phase (P') and out of-phase (P''), (b) the attenuation factor, and (c) the tangent angle (phase angle shift) as a function of the dimensionless frequency $\Omega = \omega L / D \kappa$.

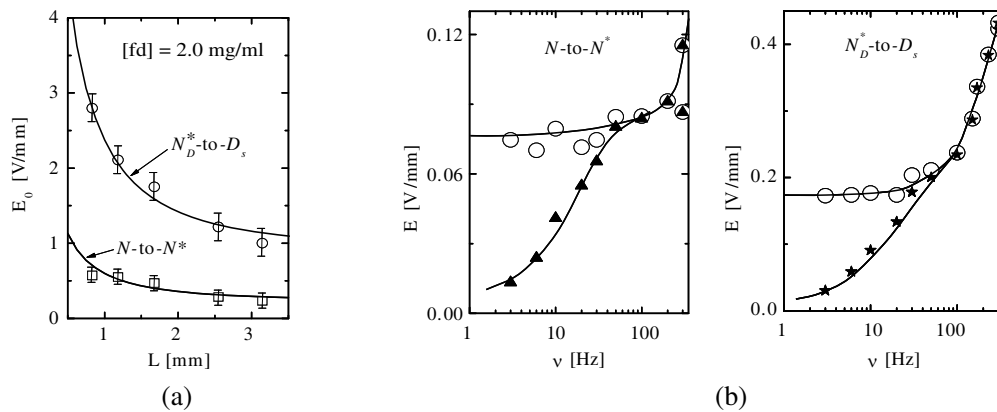


Figure 4: Two sharp phase transitions at low frequency as a function of (a) cell gap width, and (b) the applied frequency. Strong deviations of the true bulk electric field amplitude are present due to the electrode polarization, at low frequency, for both phase transitions.

“fingerprint” texture) is induced. On further increasing the field amplitude above 2.0 V/mm, chiral texture gradually disconnects from each other and become significantly smaller within a field-amplitude range. This phase is here referred to as the N_D^* -phase, where the subscript “D” stands for disconnected N^* -phase. There is a second sharp transition: the striped texture disappears at field amplitude of 3.3 V/mm, and at the same time the smaller N -domains melt and reform, without any indication of macroscopic flow. This dynamical state is denoted as the D_s -state, where the subscript “s” refers to “slow” (melting and forming occurs on a time scale of about 20s). On increasing the field amplitude further (again at low frequencies), the dynamics of melting and formation becomes faster (and levels off to 2s), which state is denoted as the D_f -state, where the subscript “f” stands for “fast”. The dynamics of melting and reformation is quantified by means of image-time correlation functions in Ref. [3]. At high frequencies, above a critical frequency (a few kHz), a uniform depolarized morphology is found (see the most right image in Fig. 1). The charged fd-rods are on average aligned along the direction of the electric field [4, 5]. This phase is referred to as the homeotropic, H -phase. On decreasing the frequency for a given field amplitude of 4 V/mm, the N^* -phase is formed, where the pitch is very large (about 50–100 μm). The pitch decreases on subsequently decreasing the frequency, toward the left-side image of the N^* -phase. The N_D^* -phase is formed on further lowering the frequency. The field-induced bulk phase/states are not influenced by the electrode polarization, which is typically important for the frequency range, below 60–100 Hz.

REFERENCES

1. Kang, K. and J. K. G. Dhont, “Double-layer polarization induced transitions in suspensions of colloidal rods,” *Eur. Phys. Lett.*, Vol. 84, 14005, 2008.
2. Kang, K. and J. K. G. Dhont, “Electric-field induced transitions in suspensions of charged colloidal rods,” *Soft Matter*, Vol. 6, 273, 2010.
3. Kang, K. and J. K. G. Dhont, “Criticality in a non-equilibrium, driven system: Charged colloidal rods (fd-viruses) in electric fields,” *Eur. Phys. J. E*, Vol. 30, 333, 2009.
4. Kang, K., “Charged fibrous viruses (fd) in external electric fields: dynamics and orientational order,” *New J. of Phys.*, Vol. 12, 063017, 2010.
5. Kang, K., “Diffusivity in an electric-field-induced homeotropic phase of charged colloidal rods,” *Europhys. Lett.*, Vol. 92, 18002, 2010.
6. Dhont, J. K. G. and K. Kang, “Electric-field-induced polarization and interactions of uncharged colloids in salt solutions,” *Eur. Phys. J. E*, Vol. 33, 51–68, 2010.
7. Dhont, J. K. G. and K. Kang, “Electric-field induced polarization of the layer of condensed ions on cylindrical colloids,” *Eur. Phys. J. E*, Vol. 34, 40, 2011.

Segmentation of OPG Images in Studying Jawbone Diseases

J. Mikulka

Department of Theoretical and Experimental Electrical Engineering
Brno University of Technology, Kolejní 4, Brno 612 00, Czech Republic

Abstract— Image processing in biomedical applications is strongly developing issue. Many methods and approaches for image preprocessing, segmentation and visualization were described. This paper describes OPG image processing. The aim of processing is to segment regions of jawbone cysts and evaluate their local descriptors. It is necessary to choose suitable segmentation method because of adverse parameters of regions. The regions of the cysts are of low contrast and the pixel intensity distribution is not homogenous. The level set, the watershed and the live-wire segmentation method were chosen to testing. The results are compared. The second step of processing is to evaluate local descriptors of segmented regions which correspond to cysts. Several parameters were chosen to describe these regions — region area, mean gray value of intensities, modal gray value of intensities, standard deviation of intensities, minimal and maximal gray value of intensities, integrated intensity, median of intensities and shape descriptors of region (perimeter, circularity, aspect ratio, roundness and solidity). Values of these parameters will be used in following development of semiautomatic processing method with regard to current assessment of cysts by doctors. The algorithm for classification of the type of cyst is presented.

1. INTRODUCTION

A cyst is defined as a pathological cavity having its own capsule, epithelium, and liquid or semi-solid contents. The wall of a cyst is formed by fibrous tissue; this wall behaves as a semi-permeable membrane, namely as a membrane unidirectionally permeable for the surrounding liquid. As a result of this behaviour, the cyst gradually enlarges; in principle, expansive growth is a main characteristic of cysts.

Follicular cysts (Fig. 1) develop from the epithelium of a tooth bud and grow either between the exposed crown and the joined inner and outer epithelium of enamel or between both layers of the epithelium. The cysts may appear in consequence of primary defects in tooth bud development, and they may occur as individual or multiple objects. In most cases, follicular cysts affect the mandibular region; large cysts often cause face-deforming bulges.

Radicular cysts (Fig. 2) are referred to as jaw bone cysts exhibiting the highest occurrence rates. It is assumed that they appear due to inflammatory irritation of the epithelial cell rests of Malassez in the periodontal crevice; this irritation is caused by infected content of the radicular duct of a transverse tooth. The cysts are bound to pulpless teeth and may occur in patients of all age categories (most frequently between 30 and 40 years of age). In terms of elementary gender division of the patients, it is necessary to note that men tend to be affected rather more than women. The radicular cyst sac usually exhibits a round or oval shape.

The imaging of damaged jaws is very often realized by means of X-ray examination utilizing an orthopantomograph (OPG), which enables us to acquire panoramic images of entire jaw bones.

However, the imaging procedure can also be performed using other methods such as nuclear magnetic resonance (NMR). Even though this concrete technique is primarily intended for the imaging of soft tissues, its combination with current imaging sequences allows us to represent changes occurring in hard tissues too. This application nevertheless exhibits a disadvantage consisting in image artefacts generated by changes in the susceptibility of the environment (factors such as implants or fillings) [1, 2].

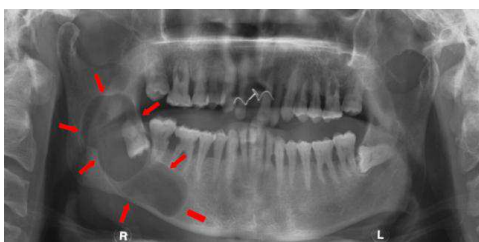


Figure 1: An OPG image of a follicular cyst.

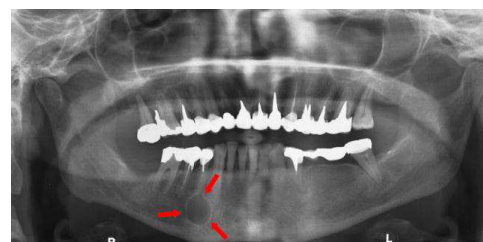


Figure 2: An OPG image of a radicular cyst.

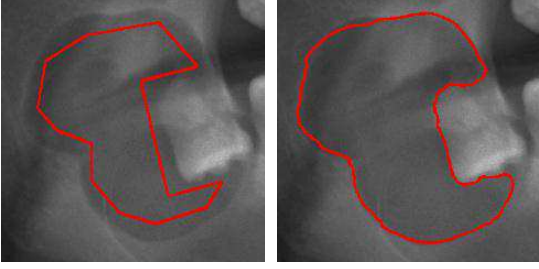


Figure 3: Segmentation of a follicular cyst via the LS method.

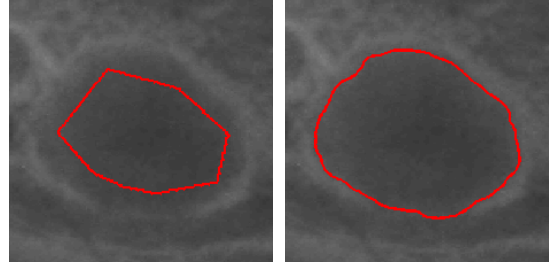


Figure 4: Segmentation of a radicular cyst via the LS method.

2. IMAGE SEGMENTATION

Considering the aspects characteristic of the areas that represent jaw bone cysts and assuming the necessity to ensure correct demarcation of the given area before the actual acquisition of corresponding local descriptors, we cannot disregard the fact that the selection of a convenient segmentation method constitutes a vital step. In this context, it is necessary to note that OPG images are not very contrastive; simultaneously, cystic areas are characterized by blurred edges and inhomogeneous distribution of the pixel intensities. Thus, the use of traditional segmentation methods becomes rather problematic. Techniques based on global thresholding of the image are handicapped by adverse matching of the segmented area and the environment; moreover, these techniques may produce only partial segmentation. In view of the above-mentioned characteristics of OPG images, the analysis of area edges is also very prone to failures.

In order to attain the highest possible degree of automatization for the image classification system, we analyzed the results provided by several segmentation methods (thresholding, watershed, the Canny and Sobel edge detection, the region-based and edge-based level set methods). The aim of the analysis consisted in seeking a compromise between the rapidity of segmentation and the minimum necessary interaction of the expert.

Good results can be obtained via the method of active contours utilizing the level set (LS) approach [3]. The technique is based on the solution of the partial differential equation describing the curve which, in the initial phase of the segmentation process, is selected by the user as a simple piecewise linear curve located inside the area of interest. Through the subsequent solution of the equation toward the steady-state condition, there occurs a change of the curve shape or topology in order to facilitate the minimization of energy functional of the given segmentation problem. The most widely applied approaches to segmentation can be identified in the edge-based and the region-based methods. In the first of these techniques, the steady-state curve approximates the edges of the area of interest; in the second approach, the curve constitutes the boundary between two or more thresholds that divides the different mean values of the area intensities. For the purposes of our research, the edge-based segmentation approach is more convenient, mainly because the distribution of intensity within the cystic areas may be described as not very homogeneous. The edge-based level set segmentation method is formulated by the following partial differential equation:

$$\frac{d\phi}{dt} = g(|\nabla I|) \operatorname{div} \left(\frac{\nabla \phi}{|\nabla \phi|} \right) + \alpha g(|\nabla I|) |\nabla \phi| + \nabla g \cdot \nabla \phi, \quad (1)$$

where I is the input image, α is the stabilizing constant ensuring convergence of the solution, and g is the function terminating the development of the level function at the location where the curve reaches the edge in the image. The function g is given by the relation:

$$g = \frac{1}{1 + |\nabla G_{\sigma} * I|^2}. \quad (2)$$

The expression in the denominator of the function is the convolution of the input image with the Gaussian filter; therefore, a smoothed image is assumed. The result of segmentation in two selected cysts is shown in Figs. 3 and 4.

While the left sections of both above-shown images indicate the initial curve, the right sections exhibit the shape of the curve in the steady state of the formula (1) solution.

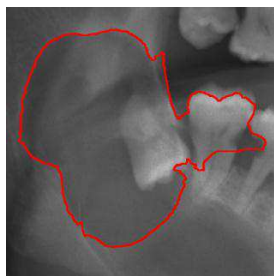


Figure 5: Segmentation via the watershed method with the opening initialization realized via marking the segmented objects.



Figure 6: Semi-automatic segmentation realized via the live-wire method — delimitation of a single area.

Segmentation realized via the LS methods requires the user to execute the initialization via manually selecting the shape of the curve and locating it inside the cystic area. Even with the manual selection, the time period necessary for the execution of segmentation in the Matlab environment on a PC (Intel Core 2 Quad 2.66 GHz, 4 GB RAM, Windows 7) did not exceed several tens of seconds. In order to stabilize the solution of the partial differential equation, the user is required to set convenient parameters for the segmentation; this fact may become rather problematic in practical applications of the system.

The remaining segmentation methods tested did not provide very good results, mainly owing to both the above-mentioned adverse characteristics of OPG images and the low contrast of the cystic area. In this context, the results obtained from segmentation via the watershed method could be used as an example, Fig. 5. The aim of the processing was to carry out segmentation of the upper section of the follicular cyst from the OPG image shown in Fig. 1. The segment curve largely delimits the cyst exactly along its boundary; the result, however, would require further processing. In other cysts, which did not exhibit a contrast in the OPG images similar to the presented example, the watershed method utterly failed to satisfy the requirements.

3. IMAGE CLASSIFICATION

The aim of further processing of the segmented images consists in acquiring local descriptors [4] of the areas representing jaw bone cysts [5, 6]. In relation to the cystic areas, both the statistical evaluation of the distribution of pixel intensities and the determination of shape parameters were carried out via the ImageJ program. Within this phase of the research, we selected parameters to be evaluated in the presented set of images. These parameters were as follows: surface, mean value of the area intensity, standard deviation of the area pixel intensities, median of the area pixel intensities, modal value of the area pixel intensities, minimum and maximum values of the area pixel intensities, integral of the area pixel intensities, and shape characteristics of the segmented areas. In the last mentioned aspect, we defined the perimeter of the area, its circularity according to formula (3), the relation between the major and minor semi-axes of the fitted ellipse, the roundness according to relation (4), and the convexity according to relation (5):

$$C = 4 \cdot \pi \cdot \frac{S}{P^2}, \quad (3)$$

$$R = 4 \cdot \frac{S}{\pi \cdot a_{\text{major}}^2}, \quad (4)$$

$$X = \frac{S}{S_C}, \quad (5)$$

where C is the circularity of the area, S is the surface of the area, P is the perimeter of the area, R is the roundness of the area, a_{major} is the length of the major semi-axis of the ellipse fitted into the area delimited by the original boundary points, X is the convexity of the area, and S_C is the surface of the convex area corresponding to the examined area.

The values presented in Tables 1 and 2 clearly indicate the difference between the follicular and the radicular cysts referred to in the introductory part of this study. While the follicular cysts exhibit a rather oblong shape, the radicular cysts are almost invariably of a circular character. Based on this parameter, it is possible to classify the cysts into two main groups:

- Circularity of the follicular cysts: 0.807 ± 0.149 ,
- Circularity of the radicular cysts: 0.932 ± 0.086 .

Quality improvement in the classification of the cysts may be achieved via selecting several parameters whose probability distribution does not overlap in any of the two types of cyst. As an example of these parameters, we could apply the ratio between the lengths of the major and the minor semi-axes of the fitted ellipse:

- Ratio between the lengths of semi-axes in the follicular cysts: 1.975 ± 0.613 ,
- Ratio between the lengths of semi-axes in the radicular cysts: 1.514 ± 0.401 .

Through subjective assessment of the values, it is also possible to select roundness as a suitable parameter enabling the classification of the cysts. Then, the related data are as follows:

- Roundness of the follicular cysts: 0.533 ± 0.159 ,
- Roundness of the radicular cysts: 0.767 ± 0.023 .

The automated system can be complemented with general classification of the cysts according to their types. The images evaluated by medical specialists will be correlated with the mentioned values, and a model facilitating the classification will be designed and trained.

4. CONCLUSIONS

Fundamental research described in the paper concerns the area of processing OPG images of jawbones with the aim of classifying follicular and radicular cysts. The results of image processing indicated the possibility of using a combination of several parameters for a binary classification of cysts (circularity, ratio of half-axes of inscribed ellipse, and area of cystic region). Within the planned follow-up study and after the available image database is processed by medical specialists, the selection of the model and the related training process will be carried out using the RapidMiner system.

ACKNOWLEDGMENT

This paper was supported by the project CZ.1.07/2.3.00/30.0039 of Brno University of Technology.

REFERENCES

1. Bartusek, K., M. Cap, P. Marcon, and J. Mikulka, "Magnetic susceptibility modeling using ANSYS," *PIERS Proceedings*, 190–193, Marrakesh, Morocco, Mar. 20–23, 2011.
2. Marcon, P., K. Bartusek, R. Korinek, et al., "Correction of artifacts in diffusion-weighted MR images," *34th International Conference on Telecommunications and Signal Processing (TSP)*, 391–397, 2011.
3. Mikulka, J., E. Gescheidtova, and K. Bartusek, "Soft-tissues image processing: Comparison of traditional segmentation methods with 2D active contour methods," *Measurement Science & Review*, Vol. 12, No. 4, 153–161, 2012, ISSN 1335-8871.
4. Mikulka, J., E. Gescheidtova, P. Marcon, K. Bartusek, and A. Sprlakova, "Evaluation of tissue properties in MR images," *PIERS Proceedings*, 339–342, Moscow, Russia, Aug. 19–23, 2012.
5. Mikulka, J. and M. Kabrda, "X-ray image processing in studying jawbone tissues," *PIERS Proceedings*, 145–148, Moscow, Russia, Aug. 19–23, 2012.
6. Mikulka, J., M. Kabrda, E. Gescheidtova, and V. Perina, "Classification of jawbone cysts via orthopantomogram processing," *35th International Conference on Telecommunications and Signal Processing (TSP)*, 499–502, 2012.

An Improved Segmentation of Brain Tumor, Edema and Necrosis

J. Mikulka and E. Gescheidtová

Department of Theoretical and Experimental Electrical Engineering
Brno University of Technology, Kolejní 4, Brno 612 00, Czech Republic

Abstract— Image processing in biomedical applications is strongly developing issue. Many methods and approaches for image preprocessing, segmentation and visualization were described. This paper deals with image segmentation, concretely brain tumor segmentation. The main problem in medical practice is to recognize the type of brain or other tumor. There are many methods for tumor classification and one of them is perfusion imaging/analysis. Perfusion images are of very low contrast and they are devaluated by noise. The main idea is to identify the level of perfusion of contrast agent transported into the pathological tissue. The level of perfusion may decide on the type of tumor. The perfusion has to be monitored in tumor region, edema around the tumor region and in the interface between brain tumor and edema. The goal described in this paper is to propose a segmentation method to recognize brain tumor, edema and necrosis in structural magnetic resonance images (T1, T2) and create a binary mask that enables measurement in perfusion weighted images.

1. INTRODUCTION

Segmentation of brain tissues is in last few years very actual topic. It is very important to understand information obtained by tomographic techniques for diagnosis, monitoring of disorder development or effectiveness of treatment. This article describes design of methods for processing images obtained by magnetic resonance tomography (MR). MR can be used both in medicine [1] and other fields for example in agriculture or ecology [2] or in physics [3]. The goal of processing is to segment the brain tumor. The area of the brain tumor can be divided to the intrinsic tumor, necrotic tissue and surrounding edema. In Fig. 1, example of the brain tumor and its parts in one MR slice are shown in T2-weighted image with its thickness 5 mm. For this purpose Turbo Spin Echo (TSE) acquisition sequence was used.

In T2-weighted image a tumor exhibits sharp edges and higher intensity (1687.9 ± 207.7), but distribution of intensities is very inhomogeneous. The necrotic tissue exhibits the highest intensity (2193.8 ± 42.5) and sharp edge. Conversely the edema is of low intensity (1333.1 ± 83.7) and very smoothed edges in T2-weighted image. The same slice weighted by relaxation time T1 and by diffusion coefficient (DWI) is shown in Fig. 2.

In T1-weighted image the tumor is bounded by sharp edge. This fact could be used for segmentation by edge analysis. The edema has comparably the same T1 relaxation characteristic/mean intensity (565.8 ± 18.6) as the surrounding white matter (672.5 ± 14.2), so it is difficult to recognize them. The necrotic tissue is of very low intensity (357.4 ± 17.4), which is very close to inner parts of the tumor (482.6 ± 47.2). Considering these facts it follows that distinctiveness of individual parts of the tumor in T1-weighted image is almost impossible.

In diffusion-weighted images we can observe very similar characteristics of tissues as in the T2-weighted images, but DW images are of lower resolution and with higher noise level. The tumor

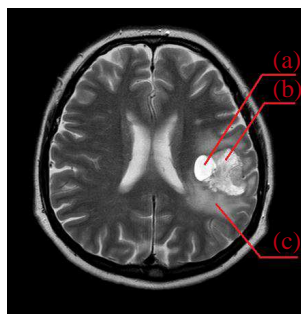


Figure 1: T2-weighted image showing the brain tumor. (a) Tumor. (b) Necrotic tissue. (c) Edema.

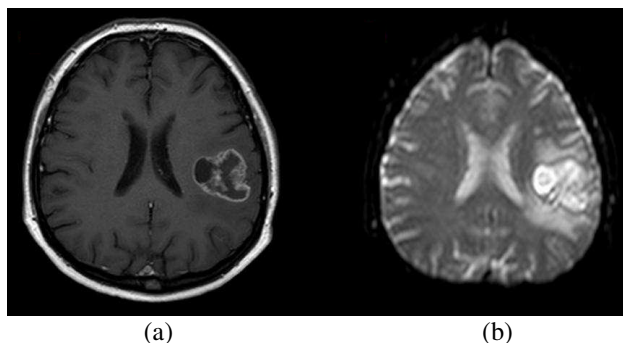


Figure 2: (a) T1-weighted image showing the brain tumor. (b) Diffusion-weighted image showing the brain tumor.

region has similar standard deviation as in T2-weighted image but it has slightly higher mean intensity (1841.3 ± 226.0). The necrotic tissue is due to “inner ring” more inhomogeneous but it has higher intensity (2102.4 ± 193.0) in diffusion-weighted image and it is clearly bounded. The characteristics of the edema region are very similar to corresponding region in T2-weighted images. Interface between the edema and the tumor region is clearer than in T2-weighted images and its intensity is the lowest (1624.9 ± 85.6) in the region of interest. With respect to these intensity distributions it is clear that the tissues segmentation in one image is practically impossible. The goal of described research is to design such segmentation method, which is able to differentiate automatically individual parts of pathological tissue. In our described case the three-dimensional information (T1-weighted, T2-weighted and diffusion-weighted image) in each pixel of pathological and healthy tissue can be used for image segmentation.

Multi-parametric image analysis is very actual topic. In fact we can build on traditional segmentation methods (thresholding, active contours), but the multi-parametric methods process information in more images concurrently. The second approach the image can be segmented by solving a problem of classification multi-parametric data. These algorithms are described for example in [4]. This work deals with segmentation of brain tissues into 15 classes. The model of each tissue approximates a distribution of their parameters by Gauss-Markov fields. For the segmentation the T1-weighted, T2-weighted, Gd+T1-weighted and perfusion images were used. Very similar issue is described in [5]. This research deals with segmentation with use of 7-dimensional information about brain tissues: B0-weighted, diffusion-weighted, fluid-attenuated inversion recovery images, T1-weighted, Gd+T1-weighted and two scalar maps calculated from images of diffusion tensor. Statistical model was designed from 14 patients with high-grade neoplasm. Research described in [6] the lesions in white matter segmentation by Support Vector Machine (SVM) is proposed. There were used 4 types of images: T1-weighted, T2-weighted, proton density and fluid attenuation inversion recovery. In [7], the histogram analysis is described. The healthy and ischemic tissues are recognized by the use of diffusion-weighted images, ADC maps and T1-weighted and T2-weighted images. At first the histogram analysis was performed and consequently the MR images for individual classes and following analysis (segmentation) were calculated. Healthy tissues are segmented using T1-weighted images and ischemic tissues using T2-weighted and diffusion-weighted images with ADC maps.

Segmentation of individual tissues can be used for their recognition/masking during the contrast agent perfusion monitoring. In past, some studies have been reported, where a relationship between the fluid perfusion into to pathological tissue and its character were proved. Differentiation between high-grade glioma and a solitary metastasis using the perfusion imaging demonstrate [8]. In this paper, the problem of two types of neoplasms recognition using conventional MR imaging is shown. The perfusion imaging is demonstrated. More extensive study in the field of tumor classification in described in [9]. There are described 8 types of pathological tissues in brain based on large database (105 patients) and for these types of tissues the Cerebral Blood Volume (CBV) values are given. The mean values and their standard deviations gives an evidence about high degree of distinctiveness of pathological tissues using perfusion imaging.

2. TUMOR TISSUE MODELING

Trainable segmentation technique was implemented in RapidMiner environment to segment individual parts of the tumor. The whole chain of processing is shown in Fig. 3.

The segmentation operator is realized by Support Vector Machine (SVM) classification model. The main process of segmentation consists of two main stages: training and testing. During the training stage some pixels inside and outside of region of interest are manually marked. This set of intensities in processed images (T1-weighted, T2-weighted and diffusion-weighted) are entering into the model as training data. The same images could be used as a testing data.

3. SEGMENTATION RESULTS

Results of segmentation are shown in Fig. 4. (a) the red contour bounds searched edge of brain tumor; (b) the searched edge of surrounding edema is added to contour of the tumor; (c) the result of necrotic tissue segmentation is shown. All the red contours bound the regions of interest.

In Fig. 5, the result of brain tumor segmentation in one image by SVM is shown. (a) is the result of T2-weighted image segmentation and (b) of the result of T1-weighted image segmentation. It is clear that the process of segmentation in one image fails. In T2-weighted image the curve interferes to edema region, which has very similar intensity as tumor neighborhood. In T1-weighted image

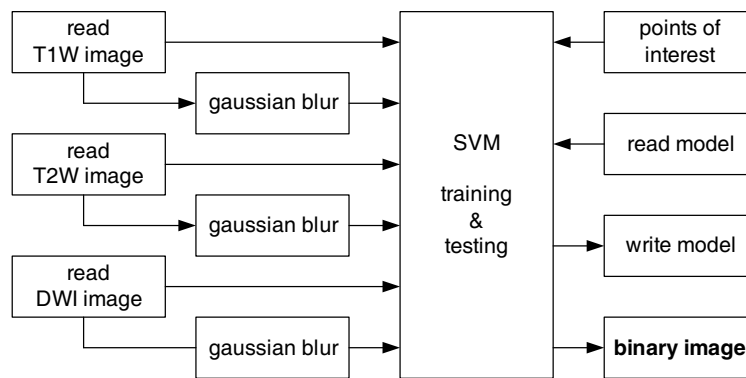


Figure 3: The proposed chain of multi-parametric image processing.

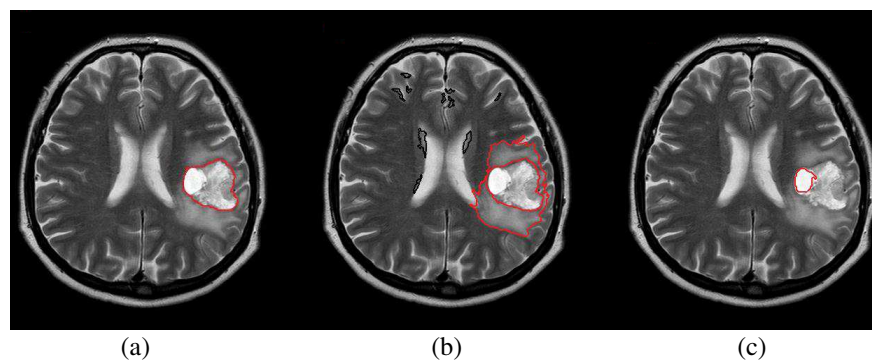


Figure 4: The result of segmentation. (a) Brain tumor. (b) Edema. (c) Necrotic tissue. Red curve bounds the region of interest.

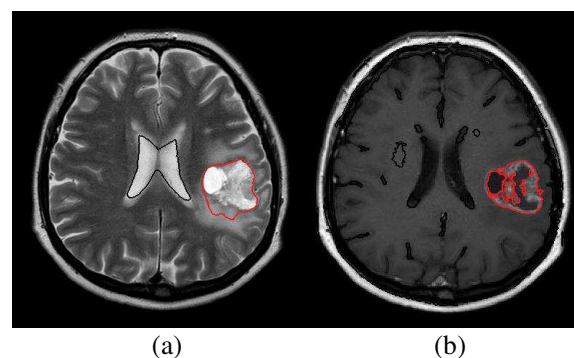


Figure 5: The result of wrong segmentation of brain tumor with use of the same SVM classification method but with use only one image at the input ((a) T2W, (b) T1W).

the edema region is not so visible but the segmentation fails due to inhomogeneity inside tumor region.

4. CONCLUSIONS

This article presented utilization of classification methods for MR image segmentation. The goal of the design of segmentation method is to have a tool for differentiation individual parts of the pathological tissue. It consists of the tumor, surrounding edema and the necrotic tissue. Segmentation of pathological tissue parts is needful for the further processing. For example the mask of the surrounding edema can be used for accurate monitoring of contrast agent perfusion [10]. Level and course of the agent perfusion indicates the type of tumor (malignant, benign). Currently the process of perfusion is evaluated in inaccurately bounded region. Very often it is the rectangular region, which contains in addition to edema and tumor also the surrounding healthy tissue. Determined perfusion parameters are then weighted by high errors.

ACKNOWLEDGMENT

This work was supported in part by the Grant 102/12/1104 and project FEKT-S-11-5/1012.

REFERENCES

1. Mikulka, J., E. Gescheidtová, and K. Bartusek, “Soft-tissues image processing: Comparison of traditional segmentation methods with 2D active contour methods,” *Measurement Science Review*, Vol. 12, 153–161, 2012, ISSN 1335-8871.
2. Mikulka, J., E. Gescheidtová, and K. Bartusek, “Perimeter measurement of spruce needles profile using MRI,” *PIERS Proceedings*, 1128–1131, Beijing, China, Mar. 23–27, 2009.
3. Marcon, P., K. Bartusek, M. Burdkova, et al., “Magnetic susceptibility measurement using 2D magnetic resonance imaging,” *Measurement Science & Technology*, Vol. 22, No. 10, 2011.
4. Zavaljevski, A., A. P. Dhawan, M. Gaskil, et al., “Multi-level adaptive segmentation of multi-parameter MR brain images,” *Computerized Medical Imaging and Graphics*, Vol. 2, 87–98, 2000.
5. Verma, R., E. I. Zacharaki, Y. Ou, et al., “Multiparametric tissue characterization of brain neoplasms and their recurrence using pattern classification of MR images,” *Academic Radiology*, Vol. 8, 966–977, 2008.
6. Lao, Z. Q., D. G. Shen, D. F. Liu, et al., “Computer-assisted segmentation of white matter lesions in 3D MR images using support vector machine,” *Academic Radiology*, Vol. 3, 303–313, 2008.
7. Bernarding, J., J. Braun, J. Hohmann, et al., “Histogram-based characterization of healthy and ischemic brain tissues using multiparametric MR imaging including apparent diffusion coefficient maps and relaxometry,” *Magnetic Resonance in Medicine*, Vol. 1, 52–61, 2000.
8. Law, M., C. Soonmee, A. K. Edmond, et al., “High-grade Gliomas and solitary metastases: Differentiation by using perfusion and proton spectroscopic MR imaging,” *Neuroradiology*, Vol. 3, 715–721, 2002.
9. Hakyemez, B., C. Erdogan, N. Bolca, et al., “Evaluation of different cerebral mass lesions by perfusion-weighted MR imaging,” *Journal of Magnetic Resonance Imaging*, Vol. 4, 817–824, 2006.
10. Cap, M., E. Gescheidtova, P. Marcon, K. Bartusek, and A. Sprlakova, “Fusion of the T1, T2 weighted and perfusion weighted images for peritumoral region evaluation,” *PIERS Proceedings*, 103–105, Suzhou, China, Sep. 12–16, 2011.

Bone Marrow Analysis in Multi-contrast MR Images

P. Marcon¹ and K. Bartusek²

¹Department of Theoretical and Experimental Electrical Engineering
Brno University of Technology, Czech Republic

²Institute of Scientific Instruments of the ASCR
v.v.i, Kralovopolska 147, Brno 61264, Czech Republic

Abstract— In the article, a magnetic resonance multi-contrast data collection and analysis are described. MRI imaging of small bones is problematic, because the measured are loaded with susceptibility artifacts and low signal to noise ratio. Therefore, we focus on the comparison between commonly used MRI contrast (Proton Density-PD, relaxation time T_1 , relaxation time T_2 and Susceptibility Weighted Imaging — SWI) and multi-contrast weighted imaging (T_1/T_2 , SWI/ T_1 , SWI/PD). Acquired images are classified in terms of signal to noise ratio, intensity difference and steepness of edges.

1. INTRODUCTION

The research of pathology of bone marrow is very interesting at present. MRI measurement is very interesting method of bone marrow imaging because this technique provides images with excellent soft tissue contrast. In adults the bone marrow is in general composed of fatty tissue, which appears hyperintense on T_1 and T_2 weighted images and occurs hypointense on MR-sequences with fat-saturation. In case of trauma, tumor or infection infiltration, replacement and depletion of fatty bone marrow takes place resulting in intermediate to hypointense signals on T_1 -weighted images and T_2 weighted images with fat-saturation [1, 2]. These changes obscure the distinct appearance of fatty bone marrow and serve as early indicators of pathology, which makes this imaging technique a very sensitive diagnostic tool [3].

MRI imaging of small bones is problematic, because the measured are loaded with susceptibility artifacts and low signal to noise ratio [4, 5]. In this paper, we also focus on the calculation SWI images. These images allow us to see better difference in the intensity of the magnetic field, particularly where one tissue turns into other tissue. For the images calculation we used two methods. The first one is based on classical measurement gradient echo sequence and the second one is based on measuring of asymmetrical spin echo [6, 7].

The experiment was accomplished on a MR tomograph with static field flux density $B_0 = 4.7$ T. Method of measurement and processing was tested on the chicken wing, especially bone: ulna and radius.

2. MEASUREMENT METHODS

One of the main advantages of MRI compared with other imaging modalities is the excellent soft tissue discrimination in resulting image [8]. The most commonly used contrasts in MRI are: proton density, relaxation time T_1 and relaxation time T_2 . The basic method for measurement these parameters is the conventional spin echo (see Fig. 1(a)). This pulse sequence uses a 90° excitation pulse followed by one or more 180° rephasing pulses to generate a spin echo on time called T_E . If only one echo is generated, a T_1 weighted image can be obtained using a short echo time T_E and short repetition time between individual spin echo sequences — T_R . For proton density and T_2 weighting a two RF rephasing pulses generating two spin echoes are applied. The first echo has a short T_E and a long T_R to achieve proton density weighting, and the second has a long T_E and a long T_R to achieve T_2 weighting. For more information about sequences and coding see studies reported in [7].

For SWI images, we used the Gradient echo (GE) method, see Fig. 1(b). This method is very sensitive to inhomogeneities of the static magnetic field and this can be useful for susceptibility measurement [9]. Because the reaction field is generated proportionally to material susceptibility, it is possible to use the GE method for its measurement [10–12].

The MR image obtained using the GE technique is phase-modulated by the magnetic induction change and, on condition of proper experiment arrangement we can obtain the image of magnetic

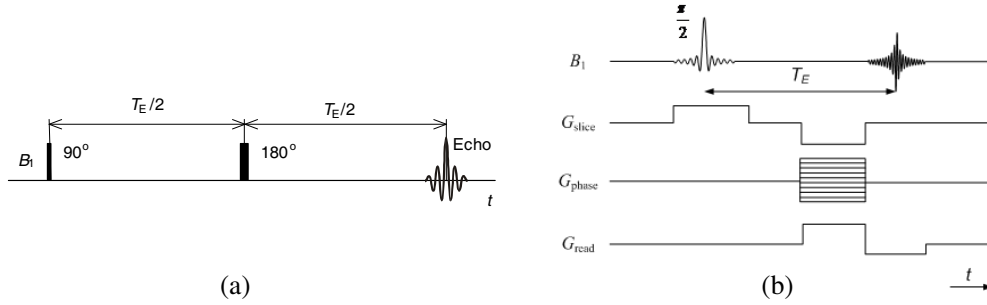


Figure 1: (a) Diagram of the spin echo sequence. (b) Diagram of the gradient echo sequence.

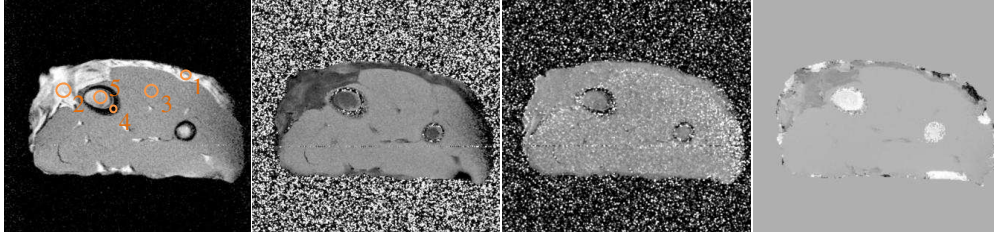


Figure 2: One-contrast image chicken wing: PD weighted with region of interest (ROI), T_1 weighted image, T_2 weighted image and SWI weighted image.

field distribution in the specimen vicinity. For the calculation of the reaction field ΔB we can give the following relation:

$$\Delta B = B - B_0. \quad (1)$$

The equation between reaction field and phase is described in:

$$\Delta B = \frac{\Delta\varphi}{\gamma \cdot T_E} \quad (2)$$

where γ is the gyromagnetic ratio of reference substance, $\Delta\varphi$ is the phase image, and T_E is the echo time of the GE measuring sequence.

Evaluation of various tissues such as skin, fat, muscle, bone and bone marrow can help us to diagnose various pathologies. The images were evaluated mean values and standard deviation (s.d.). Collected parameters we can continue to serve for multiparametric analysis and segmentation of tissues [13, 14].

3. EXPERIMENT

Experiment was accomplished on a MR tomograph at the Institute of Scientific Instruments, Academy of Sciences of the Czech Republic (ISI ASCR). The MR tomograph dispose of static field flux density $B_0 = 4.7$ T, ^1H nuclei resonance frequency is 200 MHz. Method was tested on the chicken wing, especially bone: ulna and radius. Similar multiparametric data collection could be used also for human tissue.

On the Fig. 2, you can see these weighted images: proton density (PD), relaxation time T_1 (T_{1W}), relaxation time T_2 (T_{2W}) and susceptibility weighted (SWI). The images have 128×128 pixel resolution and size: 30×30 mm. For the measurement PD image was used SE sequence with these parameters: $T_E = 16$ ms, $T_R = 1$ ms. In this image are shown the areas from which the parameters of tissues were evaluated (Region of interest — ROI, 1 — skin, 2 — fat, 3 — muscle, 4 — bone, 5 — bone marrow).

For the measurement T_{1W} image was used inversion recovery SE sequence with parameters: $T_E = 16$ ms, $T_R = 1$ s, $T_I = 16 \div 2500$ ms).

For the measurement T_{2W} image was used SE sequence with parameters: $T_E = 15, 16, 17$ ms and $T_R = 1$ s.

For the measurement SWI image was used GE sequence with parameters: (GE, $T_E = 6$ ms). The SWI weighted image is calculated using (1) and (2).

The evaluated parameters are shown in Table 1.

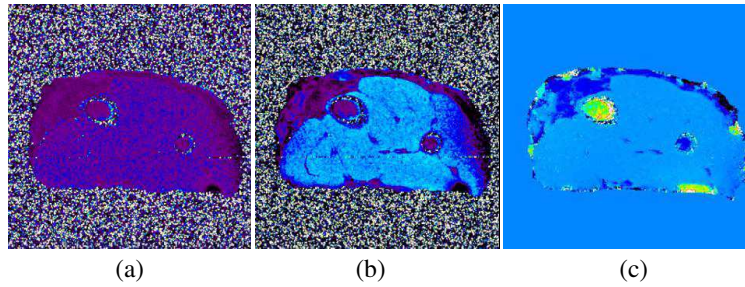
Figure 3: Multi-contrast image of chicken wing: T_1/T_2 , $SWI*T_1$, $SWI*T_2$.

Table 1: The evaluate parameters from one-contrast images.

$N.$	Tissue	PD_{Mean}	$PD_{s.d.}$	$T_{1W}Mean$ [ms]	$T_{1W}s.d.$ [ms]	$T_{2W}Mean$ [ms]	$T_{2W}s.d.$ [ms]	SWI_{Mean} [$\times 10^{-6}$]	$SWI_{s.d.}$ [$\times 10^{-6}$]
1	Skin	102479	28057	353	32	47	8	-9.67	2.96
2	Fat	112615	22149	301	36	47	9	6.65	2.59
3	Muscle	66039	7599	650	55	50	19	2.05	0.54
4	Bone	16020	7419	453	327	27	62	32.98	5.17
5	Bone marrow	82564	14103	344	48	40	11	1.83	12.5

Table 2: The evaluate parameters from multi-contrast images.

$N.$	Tissue	T_1/T_2 mean	T_1/T_2 s.d.	$SWI*T_1$ mean	$SWI*T_1$ s.d.	$SWI*T_2$ mean	$SWI*T_2$ s.d.
1	Skin	6.126	1.267	348.1	32.23	-0.018	0.016
2	Fat	6.838	1.751	296.68	39.65	-0.037	0.008
3	Muscle	14.368	4.565	651.4	48.33	0.0068	0.0024
4	Bone	54.789	94.71	372.1	416.5	-0.052	0.294
5	Bone marrow	8.817	2.878	345.74	43.67	0.141	0.041

To improve tissues classification we also evaluated the multi-contrast images. The images have 128×128 pixel resolution and size: 30×30 mm. On the Fig. 3(a) you can see T_1/T_2 weighted image. There is T_{1W} image divided by T_{2W} image. In this image are the evaluated mean and s.d. values not better then one-contrast T_{1W} image and T_{2W} image. On the Fig. 3(b) you can see very interesting $SWI*T_{1W}$ weighted image. There is the SWI image multiplied by T_{1W} image. In this case, the values of signal to noise ratio are sufficient and differences between tissues are very good. On the Fig. 3(c), there is $SWI*T_{2W}$ image. The evaluated tissues results of mean and s.d. are not sufficient for tissue classification in this case.

The evaluated parameters of the tissues from multi-contrast images are shown in Table 2.

4. CONCLUSIONS

This work is focused on the measurement of several parameters soft tissues. To measure three types of MR data spin-echo method was used and to measure of SWI data the gradient echo was used. We evaluated parameters of different soft tissues by one-contrast and multi-contrast images.

To the classification and segmentation of tissues are very interesting obtained data from PD image (one-contrast image) and $SWI*T_1$ image (multi-contrast image). Proton density weighted images and $SWI*T_1$ images shows good contrast and very good signal to noise ratio in all examined tissues. The PD images are easily measurable and feasible for consequent image processing. This kind of weighting appears to be the best for image segmentation. T_2 weighted images show worst contrast and small signal to noise ratio. Image segmentation and tissue differentiation will be difficult in this type of image. We also examined the data achieved by measurement of gradient echo and calculated SWI weighted image. The signal processing is more difficult in this case, but

the information obtained about bone marrow is very interesting.

Future work will be focused on analyzing of the multi-parametric data of the tissues, which were mentioned in this paper. The values in tables are very important for selection of segmentation methods such as thresholding, edge analysis by Sobel mask, watershed and very interesting method based on region-based level set approach or active contour [15, 16]. The segmentation can play an important role in determining pathology in animal tissues even in human tissues.

ACKNOWLEDGMENT

This work was supported within GACR 102/11/0318 and GA102/12/1104 and GA FEKT-S-11-5/1012.

REFERENCES

1. Mouloupoulos, L. A., et al., "MR prediction of benign and malignant vertebral compression fractures," *Journal of Magnetic Resonance Imaging*, Vol. 6, 668–674, 1996.
2. Johnson, G., D. H. Miller, D. MacManus, P. S. Tofts, D. Barnes, E. Boulay, and W. McDonald, "Primary title: STIR sequences in NMR imaging of the optic nerve," *Neuroradiology*, Vol. 29, 238–245, Springer, Berlin, Heidelberg, 2004.
3. Rupp, R. E., N. A. Ebraheim, and R. J. Coombs, "Magnetic resonance imaging differentiation of compression spine fractures or vertebral lesions caused by osteoporosis or tumore," *Spine*, Vol. 20, 2499–2503, 1995.
4. Marcon, P., K. Bartusek, E. Gescheidtova, and Z. Dokoupil, "Diffusion MRI: Magnetic field inhomogeneities mitigation," *Measurement Science Review*, Vol. 12, No. 5, 205–212, 2012.
5. Marcon, P. and K. Bartusek. "Errors in diffusion coefficients measurement," *PIERS Proceedings*, 1035–1039, Cambridge, USA, Jul. 5–8, 2010.
6. Andris, P. and I. Frollo, "Measurement of magnetic field with background using a low-field NMR scanner," *Measurement Science and Technology*, Vol. 23, No. 6, 2012.
7. Vladingerbroek, M. T. and J. A. Den Boer, *Magnetic Resonance Imaging*, Springer-Verlag, Heidelberg, Germany, 1999, ISBN 3-540-64877-1.
8. Mikulka, J., E. Gescheidtova, and K. Bartusek, "Soft-tissues image processing: Comparison of traditional segmentation methods with 2D active contour methods," *Measurement Science Review*, Vol. 12, No. 4, 153–161, 2012.
9. Marcon, P., K. Bartusek, M. Burdkova, and Z. Dokoupil, "Magnetic susceptibility measurement using 2D magnetic resonance imaging," *Measurement Science and Technology*, Vol. 22, No. 10, 2011.
10. Andris, P. and I. Frollo, "Measurement of magnetic field with background using a low-field NMR scanner," *Measurement Science and Technology*, Vol. 23, No. 6, 2012.
11. Frollo, I., P. Andris, J. Pribil, L. Vojtisek, T. Dermek, and L. Valkovic, "Measurement and Imaging of planar electromagnetic phantoms based on NMR imaging methods," *Measurement Science Review*, Vol. 10, No. 3, 97–101, 2010.
12. Bartusek, K., R. Kubasek, and P. Fiala, "Determination of pre-emphasis constants for eddy current reduction," *Measurement Science and Technology*, Vol. 21, No. 10, 2010.
13. Bartusek, K., E. Gescheidtova, and J. Mikulka, "Data processing in studying biological tissues, using MR imaging techniques," *33rd International Conference on Telecommunications and Signal Processing*, 171–175, Asszisztenda Szervezo, Budapest, 2010.
14. Gescheidtova, E., R. Kubasek, Z. Smekal, and K. Bartusek, "Digital filter banks in MR measurement of gradient magnetic fields," *Applied Magnetic Resonance*, Vol. 33, No. 4, 399–417, 2008.
15. Mikulka, J., E. Gescheidtova, and K. Bartusek, "Perimeter measurement of spruce needles profile using MRI," *PIERS Proceedings*, 1128–1131, Beijing, China, Mar. 23–27, 2009.
16. Mikulka, J., E. Gescheidtova, and K. Bartusek, "Processing of MR slices of human liver for volumetry," *PIERS Proceedings*, 202–204, Xi'an, China, Mar. 22–26, 2010.

Stochastic Models of Electrodynamics and Numerical Models

R. Urban, P. Fiala, M. Hanzelka, and J. Mikulka

Department of Theoretical and Experimental Electrical Engineering
Brno University of Technology, Czech Republic

Abstract— The article presents the transient task numerical modelling of the electrodynamic process in gas with a pulsed electric field and its application to a test device. Within the numerical model, non-linear electric properties of gas are respected and, by the help of a non-deterministic stochastic model, the possibility of an electric charge generation is analyzed. The authors examine the problem of electric charge probability evaluation; on the basis of testing the tip-tip disposition, a comparison of individual instances of the probability function evaluation is provided.

1. INTRODUCTION

The origins of research in the field of single-shot processes modelling date back deep into the past century. Then, the related problems were solved through the use of experimental methods as applied by Nikola Tesla, the late doyen of electrical engineering [1, 2]. For the solution of the pulse process in an electromagnetic field, models based on the conversion of a physical model into a mathematical one can be classified as stochastic. From the perspective of a macroscopic physical model, the concerned tasks mostly involve a high number of relations of the system elements, with the possibility of description comprising only several external parameters and functions of the system. The models can be further solved as stochastic [3] or deterministic. For numerical models based on finite methods, it is easier to utilize the stochastic approach [4] in the first approximation. This article utilizes the example of a 2-D and 3-D model to present the algorithm and parameters of a stochastic model of discharge generation in an air spark gap [3], Figure 1. The related experiments on a test circuit are indicated in Figure 2.

2. STOCHASTISATION OF THE MODEL: THE STOCHASTIC/DETERMINISTIC APPROACHES

One of the many techniques of “stochastisation” is focused on the change of input parameters of a deterministic model consisting of the stochastic (probabilistic) processes. The solution of the final model has a random process character (stochastic approach). A simple differential equation can be written in the form

$$\frac{dx}{dt} = a(x, \dots, z, t). \quad (1)$$

Stochastic form of the equation with the member added to the right-hand side can be written as $b(t, X(t), \dots, Z(t))\xi(t)$

$$\frac{d}{dt}X(t) = a(X(t), \dots, Z(t), t) + b(X(t), \dots, Z(t), t)\xi(t), \quad (2)$$

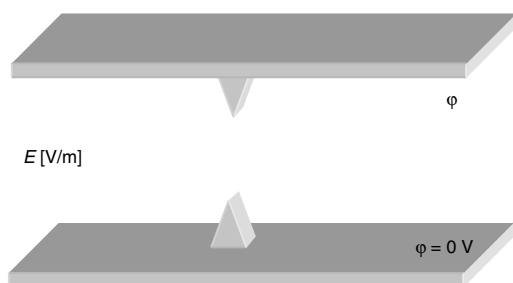


Figure 1: A simple electrical spark gap, 3D.

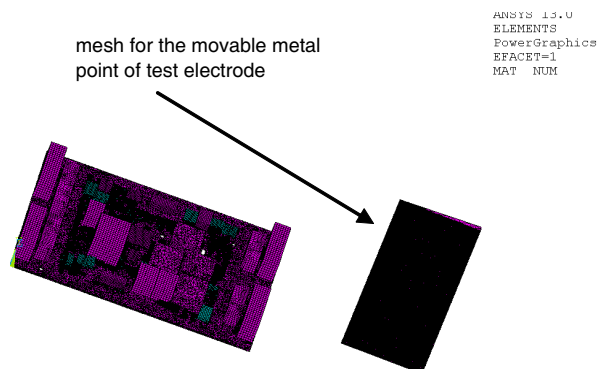


Figure 2: A test PCB circuit for an electrodynamic test, 3D analysis.

where the symbol $x(t)$ describes the stochastic process of the main function change. The solution of this equation will include the stochastic process $X(t)$. Another stochastisation technique is based on deterministic solution of the relation (2) for the non-trivial function with discontinuities in the time domain. Modification of the model (2) is performed by changing

$$dX(t) = a(X(t), \dots, Z(t), t) dt + b(X(t), \dots, Z(t), t) \xi(t) dt, \quad (3)$$

and after that, the part $\xi(t) dt$

$$dW(t) = \xi(t) dt, \quad (4)$$

where $dW(t)$ is known as the Wiener process $W(t)$ incrementation. The function can be explained as Brown movement. Then the model changes the formula. Then the stochastic differential equation from relation (3) can be written as

$$dX(t) = a(X(t), \dots, Z(t), t) dt + b(X(t), \dots, Z(t), t) dW(t), \quad (5)$$

and the next step for the description of the time domain is in the form

$$X(t) = X_{T_0} + \int_{T_0}^T a(X(t), \dots, Z(t), t) dt + \int_{T_0}^T b(X(t), \dots, Z(t), t) dW_t \quad (6)$$

The above-stated model (6) can be further solved by means of well-known methods. One of the promising techniques is based on utilizing cognitive functions and system [1–9] in solving the stochastic system of partial differential equations. In the following sections of this study, the stochastic approach tested within article [3] will be analyzed.

3. THE NUMERICAL MODEL

As it was already discussed in study [3, 4], the model is formulated for a quasi-stationary electric field from reduced Maxwell's equations

$$\operatorname{div} \varepsilon \mathbf{E} = q, \quad \operatorname{div} \mathbf{J} = -\frac{\partial q}{\partial t}, \quad (7)$$

$$\operatorname{div} (\gamma \mathbf{E}) = -\frac{\partial q}{\partial t}, \quad (8)$$

where \mathbf{E} is the electric field intensity, \mathbf{J} is the current density vector, ε is the permittivity, γ the conductivity, and q the electric charge. After modification, the equations from (7) become

$$\operatorname{div} \left(\gamma \mathbf{E} + \frac{\partial (\varepsilon \mathbf{E})}{\partial t} \right) = 0. \quad (9)$$

If the formulation of electric intensity vector by the help of potential φ is respected,

$$\mathbf{E} = -\operatorname{grad} \varphi, \quad (10)$$

then the model according to expression (7) can be written as

$$\operatorname{div} \left(\gamma \operatorname{grad} \varphi + \frac{\partial (\varepsilon \operatorname{grad} \varphi)}{\partial t} \right) = 0. \quad (11)$$

In the expression (11), the partial derivative includes the formulation $\varepsilon \operatorname{grad} \varphi$. If we assume time independence of the environment macroscopic characteristic — permittivity ε , the form can be written in a manner consistent with paper [4]

$$\operatorname{div} \left(\gamma \operatorname{grad} \varphi + \varepsilon \operatorname{grad} \frac{\partial \varphi}{\partial t} \right) = 0. \quad (12)$$

This form, in the dynamical modelling of an electric field shock wave, does not include the effect of permittivity variation. Conversely, conductivity γ , or electrical resistivity ρ as its reversed value, is shown in Figure 3.

If we assume the dependence of electrical permittivity ε on time variation and the module of electric intensity \mathbf{E} , model (11) could be employed for more exact description of the processes related to an electric discharge. The time behaviour of electric potential variation was preset with parameters of 1.2/50 μs , Figure 4.

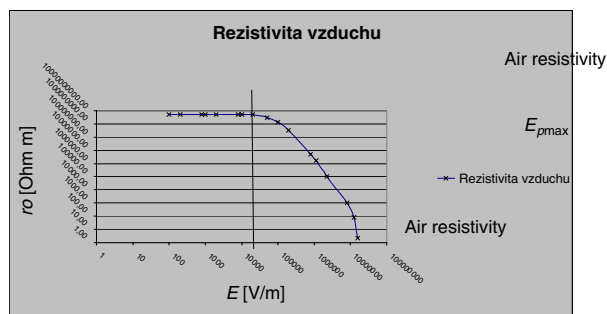


Figure 3: Characteristics of the electrical resistivity dependence on electric field intensity.

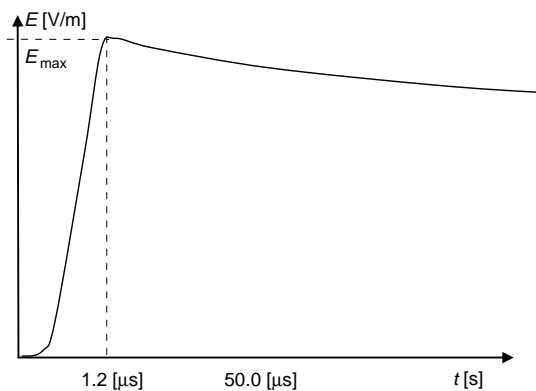


Figure 4: The electric potential time behaviour in model (11).

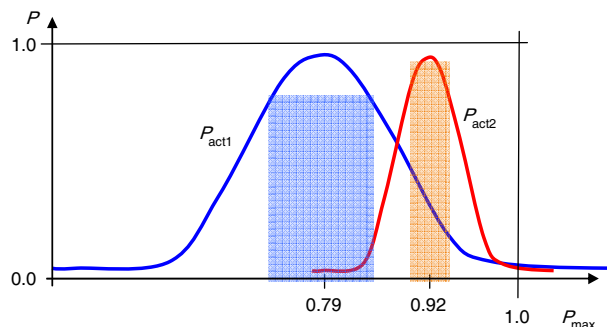


Figure 5: The applied probability function.

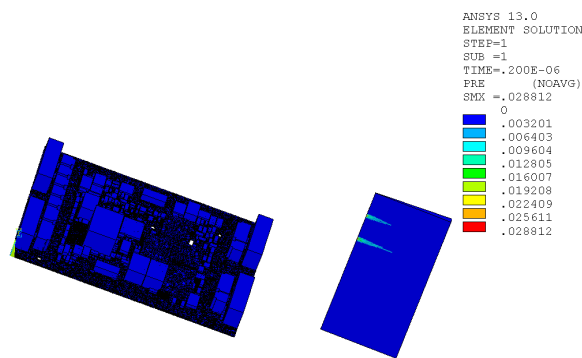


Figure 6: The distribution of probability P , $t = 0.2 \mu\text{s}$.

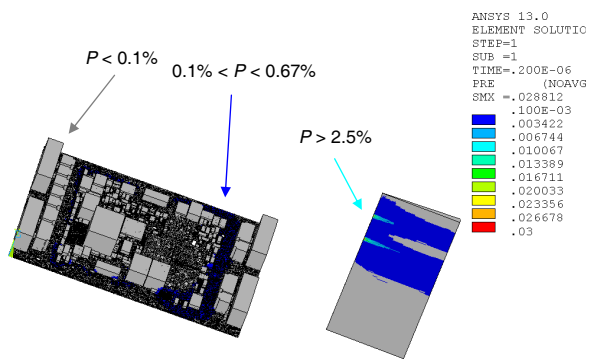


Figure 7: The distribution of the probability function P , $t = 0.2 \mu\text{s}$: the probability function P at the start of the electric discharge.

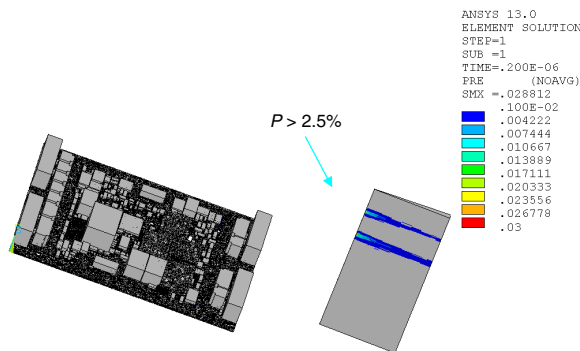


Figure 8: The distribution of the probability function P , $t = 0.2 \mu\text{s}$: the probability function P at the start of the electric discharge.

4. A 3D STOCHASTIC MODEL

If we apply the probability function according to reference [3] for the 2D/3D stochastic model based on relation (6), then

$$P_{i,j} = \left(\frac{E_{i,j}}{\sum_{i,j} E_{\max}} \right)^\eta, \quad (13)$$

where $E_{i,j}$ is the electric intensity module of the numerical model element solved by means of the finite element method (FEM), E_{\max} , is the maximal allowable electric intensity module (strength) in the air, η relates to the growth probability with the local electric field. The time behaviour

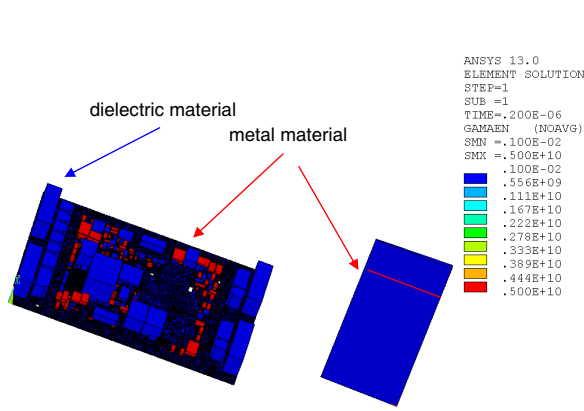


Figure 9: The distribution of conductivity γ , $t = 0.2 \mu\text{s}$.

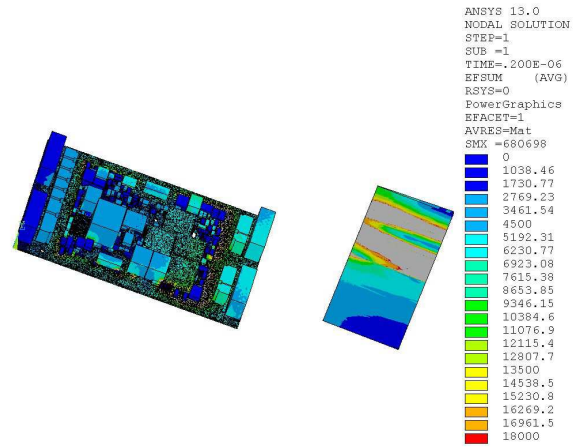


Figure 10: The distribution of electric field intensity, $t = 0.2 \mu\text{s}$, range from 1000 to 18000 V/m.

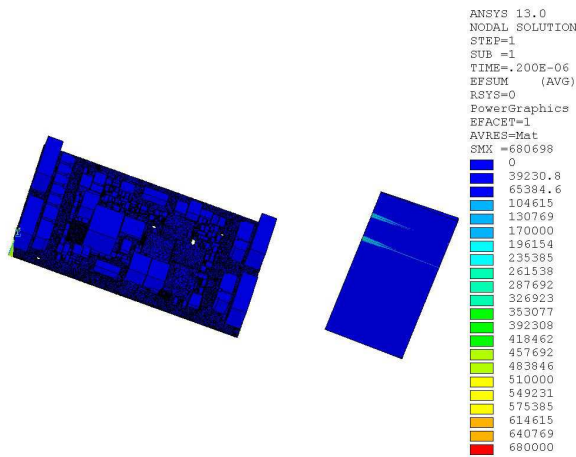


Figure 11: The distribution of electric field intensity, $t = 0.2 \mu\text{s}$, range from 1000 to 680000 V/m.

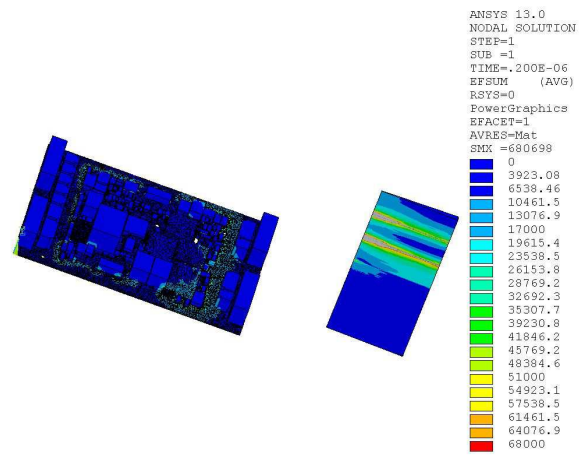


Figure 12: The distribution of electric field intensity, $t = 0.2 \mu\text{s}$, range from 1000 to 68000 V/m.

of electric potential φ is shown in Figure 4; we tested the model behaviour for $E_{\text{max}} = 3 \text{ kV/cm}$, $E_{\text{max}} = 100 \text{ kV/cm}$. The probability function (13) consists of two basic functions and is indicated in Figure 5.

For example, for entering the waveform of intensity of electric field E (electric potential φ) from the behaviour described in Figure 3 $E_{\text{max}} = 30 \text{ kV/cm}$, the distribution of electric field E for the non-uniform mesh of the 3D model elements is shown in Figure 2. However, for the process described in paper [3] and the evaluation of probability function (13), probability distribution P in the quasi-stationary 3D model (12) is indicated in Figure 6. Figure 7 presents the probability function P in scales that indicate locations to which the electric discharge is likely to jump; Figure 8 shows the location where the electric discharge will start; Figure 9 indicates the model complemented with a known value of specific conductivity γ . In Figures 10, 11, 12, the distribution of the electric field intensity modules in different scales is shown. All these data can be utilized by the designer for proper implementation of changes to the board design.

5. CONCLUSION

The tests conducted by the help of a 3D numerical model designed for the modelling of the electric discharge stochastic process proved that the quality of the assembled numerical model, uniform distribution, and boundary conditions setting are of fundamental importance to the modelling procedure. The stochastic model algorithm was tested on the design of a preliminary module having an architecture of intermediate complexity.

We selected one probability function and applied it to the tested model of the electronic module.

ACKNOWLEDGMENT

The funding of the project was supported by the Ministry of Industry and Trade of the CR (Diagnostics of superfast objects for safety testing, FR-TI1/368), Ministry of Education, Youth and Sports of the CR, and was supported by the project CZ.1.07/2.3.00/30.0005 of Brno University of Technology, state grant GA 102/09/0314.

REFERENCES

1. <http://www.rastko.rs/projekti/tesla/delo/10761>.
2. http://books.google.cz/books?id=QclcZw7I4yMC&pg=PA112&lpg=PA112&dq=Nikola+Tesla+discharge&source=bl&ots=s1VLwDeNNX&sig=bqNGiCHEwHagK4PnlOSgWgqn-bYg&hl=cs&ei=SEGoTd6TCoebOpW0scwJ&sa=X&oi=book_result&ct=result&resnum=2-&ved=0CCIQ6AEwAQ#v=onepage&q=Nikola%20Tesla%20discharge&f=false.
3. Enokizono, M. and H. Tsutsumi, “Finite element analysis for discharge phenomenon,” *IEEE Transactions on Magnetics*, Vol. 30, No. 5, 2936–2939, Sep. 1994.
4. Fiala, P., “Finite element method analysis of a magnetic field inside a microwave pulsed generator,” *2nd European Symposium on Non-Lethal Weapons*, Ettlingen, SRN, May 13–15, 2003.
5. Fiala, P. and P. Drexler, “Measurement methods of pulsed power generators,” *4th European Symposium on Non-Lethal Weapons*, Ettlingen, SRN, May 21–23, 2007.
6. Kikuchi, H., *Electrohydrodynamics in Dusty and Dirty Plasmas, Gravito-electrodynamics and EHD*, Kluwer Academic Publishers, Dordrecht/Boston/London, 2001.
7. Stratton, J. A., *Theory of Electromagnetic Field*, SNTL, Praha, Czech, 1961.
8. Fiala, P. and M. Friedl, “Stochastic models of electrodynamics,” *PIERS Proceedings*, 91–96, Suzhou, China, Sep. 12–16, 2011.
9. Drexler, P. and P. Fiala, “Methods for high-power EM pulse measurement,” *IEEE Sensors Journal*, Vol. 7, No. 7–8, 1006–1011, Jul.–Aug. 2007.

Stochastic Description of Wireless Channel for Cognitive Radio

R. Urban, P. Fiala, T. Kriz, and J. Mikulka

Department of Theoretical and Experimental Electrical Engineering
Brno University of Technology, Kolejní 2906/4, Brno 612 00, Czech Republic

Abstract— The common description of wireless propagation channel is frequency dependence of the attenuation, which is not appropriate parameter for modern communication systems using micro cells. It is more required to have information about utilization and interference in the particular channels, because there is no difficulty to set up link budget for small cell wireless transmission. This paper introduces innovative stochastic channel description mainly for cognitive radio application. Based on the localization of the primary users in the frequency spectrum at current location, cognitive system minimizes risk of the interference between primary and cognitive users using dynamic spectrum sharing. Hence we are presenting suitable model of spectrum occupancy for cognitive system based on stochastic analyses. According to the typical utilization of the wireless channel it is possible to classify typical radio transmission according to several criteria as following: utilization of the specific frequency band, bandwidth of the unused part of spectrum, duration of the spectral holes in the frequency band. These parameters should be used for wireless service planning rather than conventional one. Subsequently, we can reach more reliable results.

1. INTRODUCTION

Data communications have been changed during last few decades. Slow telephone line was replaced by optical cable transporting several Gbps. Similar progress can be observed in wireless systems as well. The best example is well-known WI-FI system, working in ISM band. The basic speed several Mbps in IEEE 802.11b was increased up to several hundred Mbps in IEEE 802.11n [1]. All of these improvements were connected with using similar or lower radiation power but using more complicated modulation schemes (64 QAM and more), which need sufficient SINR (signal to interferences and noise ratio) to secure reliable data demodulation. It became more complicated to plan wireless coverage using conventional models based on the radio wave attenuation [2] on significant frequency. New methods of the planning in micro and femto cells are necessary to ensure reliable results. Moreover, the problem of nowadays communication systems is also under utilization of the frequency spectrum. Conventional licensing schemes led to massive under utilization of the frequency bandwidth [3, 4]. Moreover, some shared parts of the spectrum (such as ISM band) are used by several services (WI-FI, Bluetooth etc.) at the same time and location. Therefore it is very difficult to reach sufficient transmitting/receiving conditions in these shared bands.

The possible solution of the problems mentioned above was recently opened and discussed in dynamic spectrum sharing [5]. Dynamic spectrum sharing is mostly taken into account as a part of cognitive radio system [6, 7], which is an intelligent, autonomous wireless system using its awareness ability of the other wireless environment (providers, users, etc.) to optimize its wireless traffic. The most important part of the cognitive radio is called cognitive engine and it is managing all data inputs and outputs. The main goal of the cognitive engine is to maximize SINR and minimize effect of the cognitive radio (secondary) users for the current (primary) users of the shared wireless domain. Dynamic spectrum sharing divides the spectrum (or users into two main groups). Firstly, the licensed (primary) users have their privilege to use the frequency band by a licensing operator. Secondly, the transmitting resources of the cognitive (secondary) users, are managed by cognitive engine [8]. Cognitive engine should allocate primary users band when privileged user is inactive for secondary users to increase capacity of their service or reallocate cognitive users to minimize interference.

It is obvious, that model of frequency spectrum and its changes in time are necessary for establishing cognitive system. Spectrum sensing, as an awareness feature of cognitive radio, should be improved by statistic data. In this paper we present preliminary results of the stochastic [9] wireless channel modelling. We are not focusing on the conventional frequency parameters such as attenuation and dispersion but we are establishing model on time evolution of the primary user's frequency spectrum utilization and spectrum holes durations.

This paper is divided as follows. After this introduction section, there are defined some prerequisites for wireless channel planning and cognitive radio phenomena. Secondly, parameters of the channel description are presented with results and finally, paper is concluded in the last section.

2. CHANNEL NETWORK MODEL

The situation in the frequency spectrum is quite chaotic. Some bands are allocated only for one service and the rest of them are shared by many providers. In both cases, some parts of the frequency spectrum are not used in current time and location as it is depicted in Figure 1. The main goal for dynamic spectrum sharing is to improve spectrum utilization by using spectrum holes by deploying another service or to increase capacity of the current service. The main problem of the dynamic sharing is to aware actual information about spectrum situation and distribution of the spectrum users in time, which is mainly represented by spectrum sensing. There are three main possibilities how to perform spectrum sensing. Firstly, matched filters are used for its sensitivity and speed, but we need to have information about the service. Secondly, cyclostacinary detection uses autocorrelation of the sensed signal and bank of partly known signals. It is robust and provides good results for low SNR, but information about sensing signal required. Finally, energy detection is used for its complexity. It is possible to detect completely unknown signals, but it is not working for low SNR (threshold level must be carefully set). Unfortunately, it is impossible to perform wideband real-time spectrum sensing. Using statistical model looks as good opportunity to provide useful additional information about wireless channel with satisfactory precision to improve sharing possibilities.

The measurements [3, 4] prove that average utilization of the large frequency band (0.7–2.7 GHz) is less than 5%. In [4] the location and consecutively number of people occupying that location are also taken into account. People using wireless services are increasing risk of interference at current location. Subsequently it is necessary to implement this feature to the channel describing model. To be more specific in this paper we deal with WI-FI system, which works in the ISM band.

WI-FI system is generally operating in 13 channels, each is 22 MHz wide. Channels are overlapping, because every other channel bandwidth begins only 5 MHz after the previous start. Channels #1, #6 and #11 are not overlapping each other and therefore most of the traffic is placed into these channels. Due to modern WI-FI devices using OFDM it is impossible to distinguish used channels only by energy detection. The possible situation in the WI-FI frequency band is depicted in Figure 2, where the top figure shows the time progress of spectrum utilization (spectrum utilization was determined according to [4]). The middle plot shows the average utilization in time and finally, bottom plot shows utilization of several channels in time. From Figure 2 it is obvious, that there is plenty of the spectrum sharing possibilities in all channels, including most utilized channel #1. Statistical information from this figure is also summarized in Table 1, where is calculated typical spectrum hole duration.

The analysis of the measurement results show [4], that there is real sharing possibility in each WI-FI channel. It clear, that in heavily used channels (such as channel #1 in Figure 2) it is only lack of sharing possibilities. On the other hand, the same location during the public holidays has totally different values (Table 1). The measurement contains a one hour sample of the spectrum situation at specific locations.

The typical spectrum gap duration is key factor of the sharing mechanism. Cognitive engine needs to predict duration of these spectrum gaps, because allocation new service into small gaps should decrease performance of the whole system.

3. STOCHASTIC CHANNEL DESCRIPTION

Generally, the conventional method of planning wireless system is by using signal attenuation model. This type of model does not take into account real situation at current location and it provides

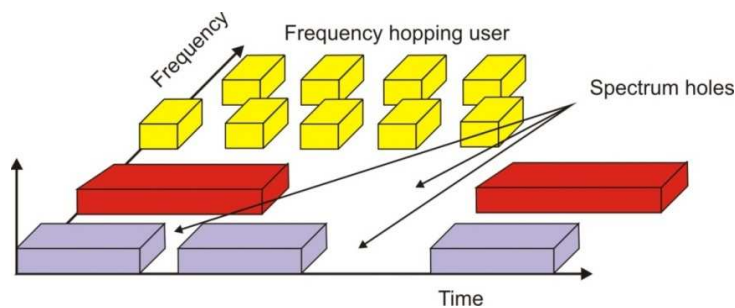


Figure 1: Frequency spectrum evolution in time.

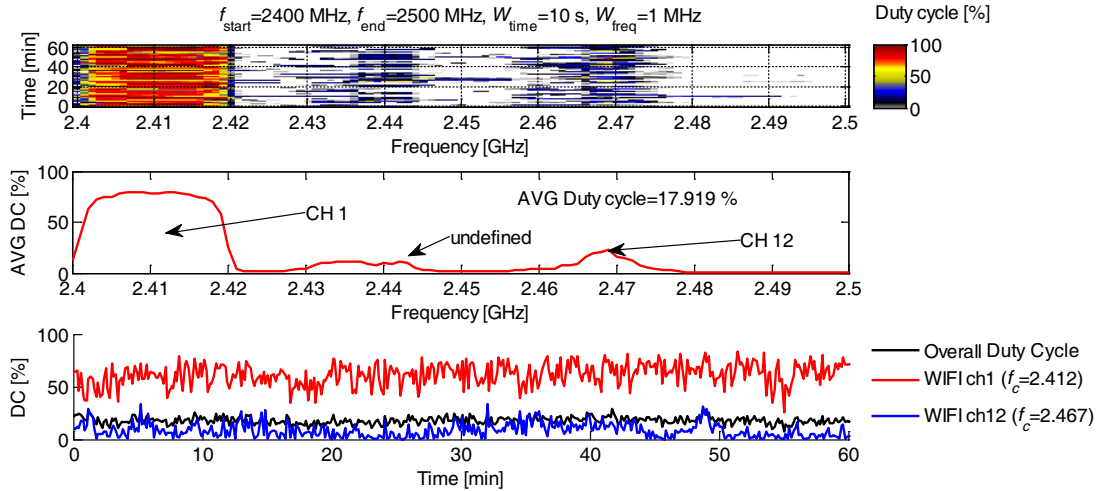


Figure 2: Overview on the spectrum situation.

Table 1: Example of spectrum holes duration from measurement at different locations.

	Channel #1	Channel #2	Channel #3	Channel #6
Indoor-occupied				
Spectrum hole duration, avg. [s]	2.35	2.41	36.24	20.3
Number of holes, [-]	366	363	99	170
Indoor-unoccupied				
Spectrum hole duration, avg. [s]	35.92	57.29	All time	124.51
Number of holes, [-]	97	62	1	29
Outdoor-rural				
Spectrum hole duration, avg. [s]	126.1	121.75	All time	All time
Number of holes, [-]	28	29	1	1

only “best situation” results. For putting it more in practice, we have to be concerned with many real-time variables, such as: moving users, providers, type of the service which is used by users and etc.. We found solution in stochastic model of wireless channel, which provides opportunity of prediction in time domain and it is also possible to solve cognitive radio problems via Game Theory [8].

Our proposed model is set according to several parameters and it is developed mainly for cognitive system applications. It defines probability of sharing possibilities P_{SP} (see flowchart of the calculations in Figure 3). Nonetheless to say, that we are not focusing on particular frequency. The attention is paid on particular channel or whole band of some service (in this case WI-FI). Firstly, we need to describe environment in which the whole process take place. Each type of the environment has its own “spectrum sharing” probability function in proposed model. The shape of the function is based on the type of the environment (indoor/outdoor) and on the service description as well. Some of these values were tuned by values obtained from measurements [4]. The result of this part is the probability of the spectral hole (P_{SH}) caused by environment. Secondly, the users and service providers are randomly generated into the environment. As we mentioned above, in this paper we present preliminary results limited for WI-FI band. This service is well described in the literature [1]. In our model we also take into account, that non-overlapping channels (#1, #6 and #11) are statistically more used than the other (by weighting coefficients). Also we classified several type of user. Users using WI-FI network for streaming TV broadcast demand stable connection and full bandwidth. Contrary, users using network only for web or e-mail have much lower requirements regarding to stability and quality and capacity of the connection. Behaviour of both user groups should be changed in time.

The results are calculated by “brutal-force” method, which has to be improved in further research. Finally, the outputs from the simulations are divided into two groups. Optimistic case in meaning of spectrum sharing is likely to be the best possible situation for cognitive radio. On the other hand, pessimistic case stands as the worst possible scenario. In this case we are able to

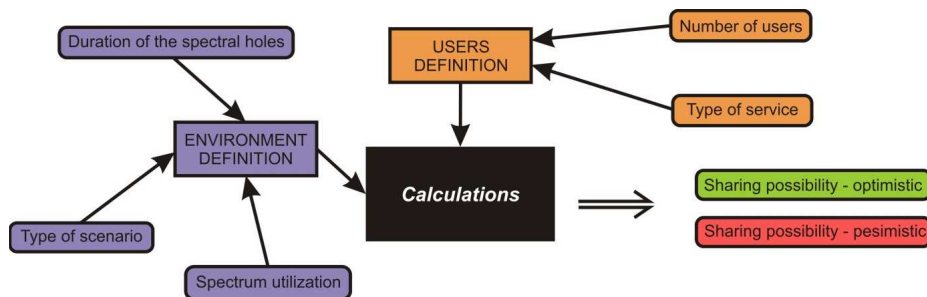


Figure 3: Flowchart of the calculations.

Table 2: Results of WI-FI channel description with comparison to measurements.

Scenario	Channel	Optimistic possibility of spectrum sharing [%]	Spectrum utilization by measurement [%]
Indoor	Overall		17.9
	#1	6	77.2
	#2	7	78.3
Occupied area	#6	4	9.8
	Overall		4.8
Unoccupied area	#1	80	2.96
	#2	81	0
	#6	79	1.3

guarantee no influence for primary users. Naturally, in this case the sharing performance is very limited. Typical observed values for channel description are summarized in Table 2.

4. CONCLUSION

This paper presents preliminary results of the innovative channel description tool, which improves cognitive engine efficiency in the dynamic spectrum sharing. It was proved that under utilization of the frequency spectrum should be used to increase system performance. Presented model of the wireless channels is based on statistical functions of channel utilization and spectrum holes duration instead of classical attenuation approach. The results from the simulation are mostly worse than the measurements, due to the type of measurements, as a snapshot at specific location for some part of time (approx. hours). Nevertheless, statistical model is a global model based on probability functions. Also utilization is calculated as a ratio of the “used” frequency points divided by total measured frequency points. It is obvious that not all spectral holes are suitable for spectrum sharing and they are not taken into account in our simulations. Right spectrum planning should improve SINR around 30 dB.

Cooperative games according to the game theory [8] and preparation of wideband results are the main areas we would like to deal with in further research. All of these values need to be calibrated by measurement values in order to reach maximal fidelity. It is likely to be demanding to go deeper inside WI-FI service to comprehend also with unused parts of each channel in order to achieve more complex measurements. OFDM allows us to use also unused parts of the spectrum in the channel. More coordination and intelligence is assumed from cognitive engine.

ACKNOWLEDGMENT

This work was supported by the project CZ.1.07/2.3.00/30.0005 of Brno University of Technology.

REFERENCES

1. IEEE, “Part 11: Wireless LAN Medium Access Control (MAC) and Physical Layer (PHY) specifications,” *Amendment 4: Further Higher Data Rate Extension in the 2.4 GHz Band*, Ed: The Institute of Electrical and Electronics Engineers, Inc., 2003.
2. Fontán, F. P. and P. M. Espiñeira, *Modelling the Wireless Propagation Channel: A Simulation Approach with Matlab*, Wiley, 2008.

3. *Shared Spectrum Company (SSC)*, Available 2011, <http://www.sharedspectrum.com/company-overview/>.
4. Urban, R., T. Korinek, and P. Pechac, “Broadband spectrum survey measurements for cognitive radio applications,” *Radioengineering*, accepted September 2012.
5. Hu, W., D. Willkomm, M. Abusubaih, J. Gross, G. Vlantis, M. Gerla, and A. Wolisz, “Cognitive radios for dynamic spectrum access — Dynamic frequency hopping communities for efficient IEEE 802.22 operation,” *IEEE Communications Magazine*, Vol. 45, 80–87, 2007.
6. Haykin, S., “Cognitive radio: brain-empowered wireless communications,” *IEEE Journal on Selected Areas in Communications*, Vol. 23, 201–220, 2005.
7. Mitola, J., “Cognitive radio architecture evolution,” *Proceedings of the IEEE*, Vol. 97, 626–641, 2009.
8. Wang, C.-W., Y.-P. Hsu, and K.-T. Feng, “Dynamic power management in cognitive radio networks based on constrained stochastic games,” *IEEE Global Telecommunications Conference, GLOBECOM*, 1–6, 2009.
9. Fiala, P. and M. Friedl, “Stochastic models of electrodynamics,” *PIERS Proceedings*, 91–94, Suzhou, China, September 12–16, 2011.

Statistical Evaluation of Diffusion-weighted Imaging of the Human Tissues

P. Marcon¹, J. Mikulka¹, E. Gescheidtova¹, K. Bartusek², and A. Sprlakova³

¹Department of Theoretical and Experimental Electrical Engineering
Brno University of Technology, Kolejní 4, Brno 612 00, Czech Republic

²Institute of Scientific Instruments of the ASCR, v.v.i
Královopolská 147, Brno 612 64, Czech Republic

³Radiological Clinic, The University Hospital Brno
Jihlavská 20, Brno 625 00, Czech Republic

Abstract— In this work the statistical evaluation of T_1 -weighted imaging and diffusion-weighted imaging of human tissues in then healthy people was made. In each patient the statistical data were evaluated from several tissues: bone, bone marrow, muscle, fat, white matter and gray matter. Based on this statistical data, we made a new statistics. By each tissue we evaluated following statistical quantities: standard deviation (S.D.), skewness and kurtosis. The box plots and small statistic database were created. This database is used to determine the tissues.

1. INTRODUCTION

The research of pathology of human tissues is currently very interesting [1]. Development of the magnetic resonance imaging represent very significant step because this technique provides images with excellent soft tissues contrast [2, 3]. We used two methods for measurement T_1 relaxation time weighted images (T1W) and diffusion weighted images (DWI). The first one variable is the spin-lattice relaxation T_1 . This variable describe the mechanism by which the z component of the magnetization vector comes into thermodynamic equilibrium with its surroundings. The second one variable is the diffusion coefficient D . This coefficient constitutes a random translational motion of molecules given by their thermal energy without requiring mass volumes motion. During diffusion time [4], the molecules may pass through regions having different diffusion coefficients D , by which means there occurs time dependence of the coefficient. Diffusion is often an anisotropic quantity (the D -value differs depending on the direction), and therefore coefficient D turns into tensor \mathbf{D} , which can be obtained only through measurement in six independent directions. The most commonly used method for measurement of diffusion coefficient is The Pulsed Field Gradient Spin Echo (PFGSE). It is Spin echo methods, with two diffusion gradients [5].

In our experiment we used a MR tomograph at the University Hospital Bohunice. The MR tomograph dispose of static field flux density $B_0 = 1.5$ T. Method of measurement and processing was tested on the healthy volunteers.

We defined the area of individual tissues in the measured images. We are interested in these tissues: gray matter, white matter, muscle, bone marrow and bone. The statistic analysis was made in these selected areas of the tissues. The value of maximum, minimum, means, standard deviation and also higher statistic orders such as skewness and kurtosis was obtained. With the knowledge of the individual tissues statistical quantities, the particular tissues can be automatically searched by using a special proposed algorithm.

2. STATISTICAL ANALYSIS

For our experiment we have to introduce the notion of a box plot. The box plot (a.k.a. box and whisker diagram) [6] is a standardized way of displaying the distribution of data based on the five number summaries: minimum, first quartile, median, third quartile, and maximum. In the simplest box plot the central rectangle spans the first quartile to the third quartile (the *interquartile range* or *IQR*). A segment inside the rectangle shows the median and “whiskers” above and below the box show the locations of the minimum and maximum, see Figure 1.

3. EXPERIMENT

To our experiment we used then healthy people. Each person was measured in MR tomograph and we obtained then sets of images (T1W and DWI), see Figure 2. We defined the area of individual tissues in the measured images [7, 8].

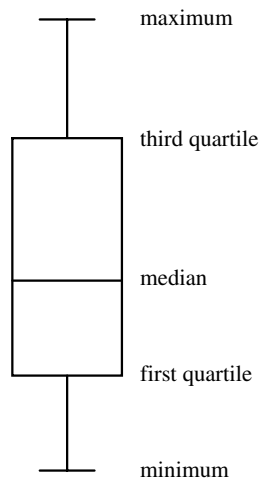


Figure 1: The box plot.

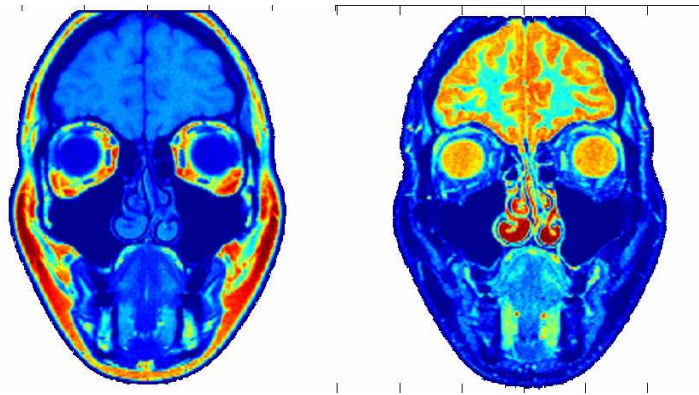


Figure 2: T1 weighted image (T1W) and the diffusion weighted image (DWI).

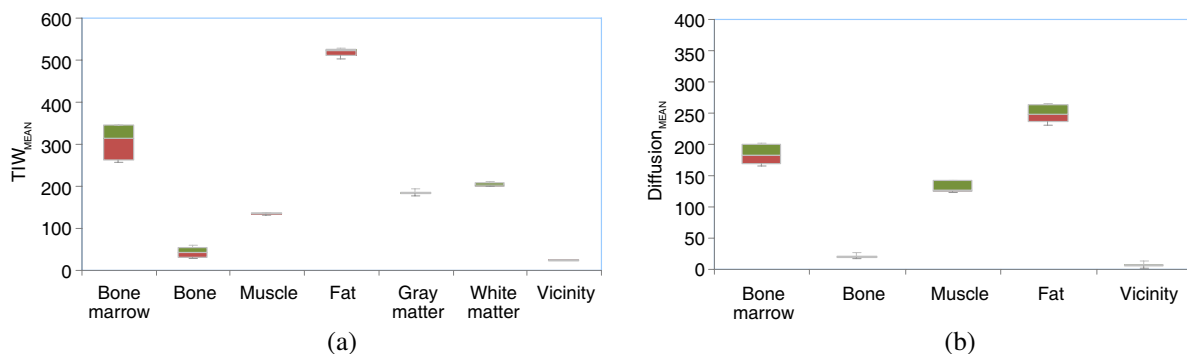


Figure 3: The box plot of the mean values: (a) T1W, (b) DWI.

In our experiment we used a MR tomograph at the University Hospital Bohunice. The MR tomograph dispose of static field flux density $B_0 = 1.5$ T. The statistical evaluation of obtained data from several individual tissues: bone, bone marrow, muscle, fat, white matter and gray matter, was performed [8, 9]. On the basis on this statistical data from individual human tissues, we made a new statistics (statistic from statistic). By each statistical evaluation of tissue we calculated following statistical quantities: standard deviation (S.D.), skewness and kurtosis. The box plots and small statistic database were created. This database is used to determine the tissues.

4. EVALUATION RESULT

In Figure 3 to Figure 6 you can see the box plots obtained by statistical analysis of individual tissues from a sample of then healthy people. The left column shows the box plots of statistical

evaluation of T1W images and the right column shows the box plots of statistical evaluation of diffusion weighted images (DWI). The Figure 3 shows the mean values box plot of individual tissues. The Figure 4 represent standard deviation (S.D.) box plot of the individual tissues. The Figure 5 displays the kurtosis box plot of individual tissues and on the Figure 6 you can see skewness box plot of individual tissues. Thus obtained box plots are very useful for determining the unknown tissues, see Section 5.

5. PRACTICAL APPLICATION

With the knowledge of the individual tissues statistical quantities (Figure 3–Figure 6), the unknown particular tissues can be automatically searched by using a special proposed algorithm. Based on the created statistical analysis the small database for individual tissues classification was created. The database contains the statistical data for human healthy tissues: bone, bone marrow, muscle, fat, gray and white matter.

Figure 7 shows diagram of the sample tissues identification. The input of this diagram is some unknown tissue sample. In the first step, a statistical analysis of unknown tissue sample is

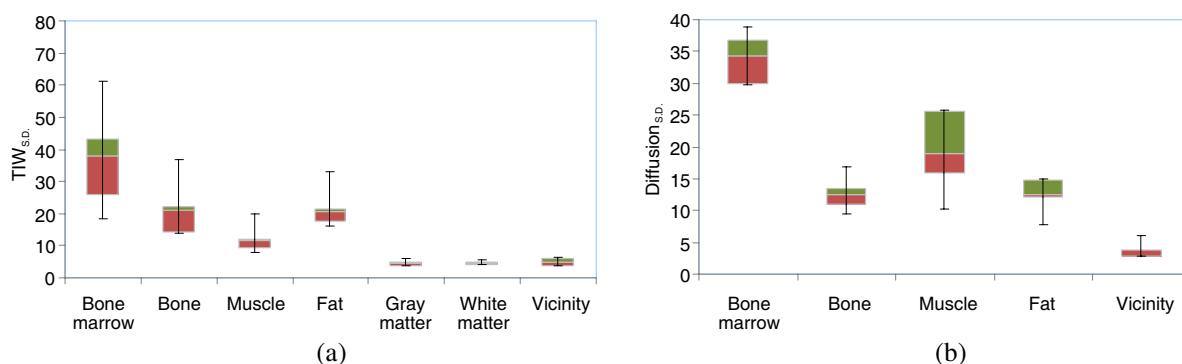


Figure 4: The box plot of the standard deviation (s.d.) values: (a) T1W, (b) DWI.

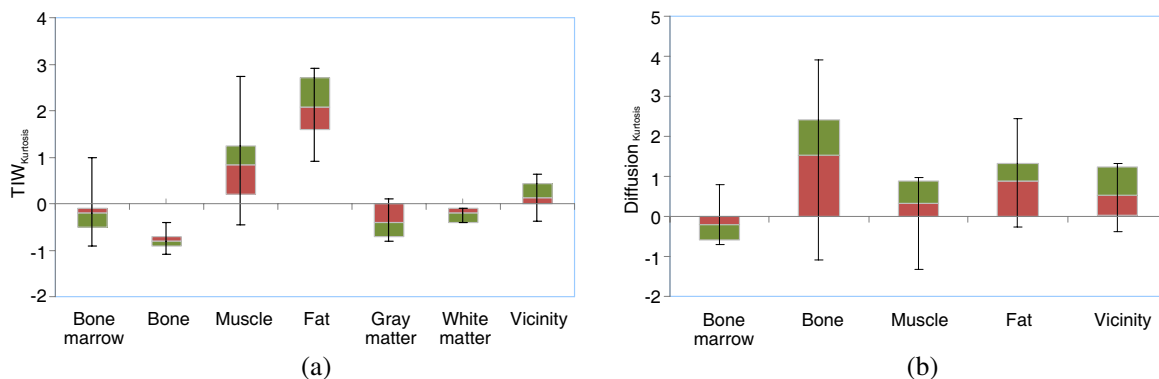


Figure 5: The box plot of the kurtosis values: (a) T1W, (b) DWI.

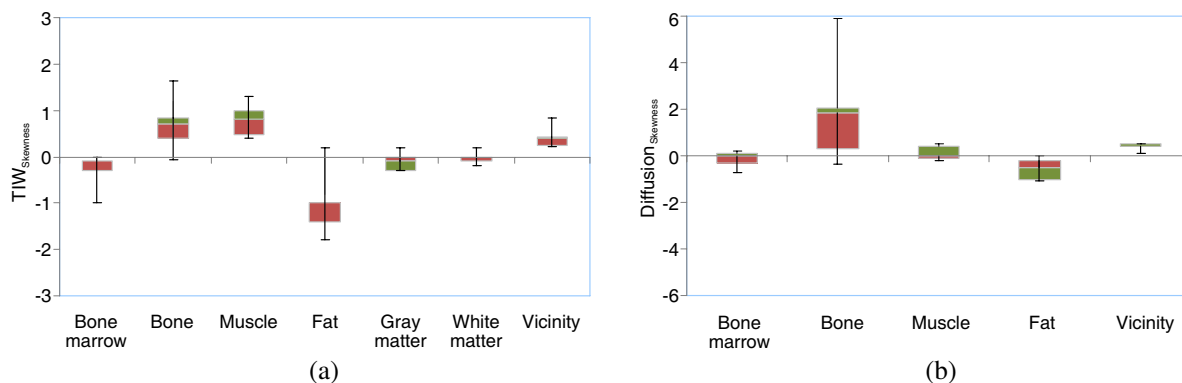


Figure 6: The box plot of the skewness values: (a) T1W, (b) DWI.

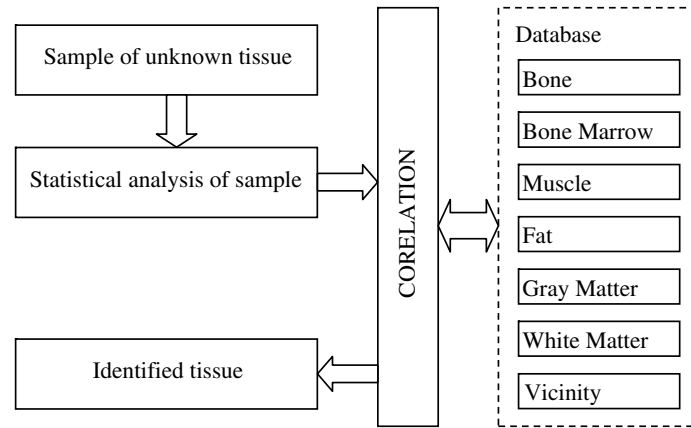


Figure 7: Diagram of the sample tissues identification.

performed. The evaluated statistical data of the tissue sample are correlated with our database statistical data. The result is the identification of unknown tissues. The diagram shown in the Figure 7 we can use for:

- Identification of healthy tissues.
- Finding the pathological tissues (the input of the diagram will be sample of known tissue and if we obtain on the output of diagram different identification of the sample tissue, we can say with certain probably, that the sample of tissues is pathological).

6. CONCLUSION

The statistical evaluation of T_1 -weighted imaging and diffusion-weighted imaging of human tissues in then healthy people we made. From the statistical evaluation we created the small database of healthy human tissues: bone, bone marrow, muscle, fat, white matter and gray matter. By each tissue we evaluated following statistical quantities: mean value, standard deviation (S.D.), skewness and kurtosis. The box plots and small statistic database were created. The results of the statistics data are presented in the Figure 3–Figure 6. This database is used to identification the unknown tissues or for diagnosis of the pathological known tissues (see Figure 7).

Currently the database of the statistical data is small, the task for further work will be expanded it. The results in the paper (database and diagram of the sample tissues identification) will be very important for next study for the comparison between healthy and pathology tissues.

ACKNOWLEDGMENT

This work was supported within GACR 102/11/0318 and GA102/12/1104 and GA FEKT-S-11-5/1012.

REFERENCES

1. Rupp, R. E., N. A. Ebraheim, and R. J. Coombs, “Magnetic resonance imaging differentiation of compression spine fractures or vertebral lesions caused by osteoporosis or tumore,” *Spine*, Vol. 20, 2499–2503, 1995.
2. Vladingerbroek, M. T. and J. A. Den Boer, *Magnetic Resonance Imaging*, Springer-Verlag, Heidelberg, Germany, 1999, ISBN 3-540-64877-1.
3. Frollo, I., P. Andris, J. Pribil, L. Vojtisek, T. Dermek, and L. Valkovic, “Measurement and imaging of planar electromagnetic phantoms based on NMR imaging methods,” *Measurement Science Review*, Vol. 10, No. 3, 97–101, 2010.
4. Marcon, P. and K. Bartušek, “Errors in diffusion coefficients measurement,” *PIERS Proceedings*, 1035–1039, Cambridge, USA, July 5–8, 2010.
5. Marcon, P., K. Bartusek, E. Gescheidtova, and Z. Dokoupil, “Diffusion MRI: Magnetic field inhomogeneities mitigation,” *Measurement Science Review*, Vol. 12, No. 5, 205–212, 2012.
6. McGill, R., J. W. Tukey, and W. A. Larsen, “Variations of boxplots,” *The American Statistician*, Vol. 32, No. 1, 12–16, 1978.

7. Marcon, P., K. Bartusek, M. Burdkova, and Z. Dokoupil, “Magnetic susceptibility measurement using 2D magnetic resonance imaging,” *Measurement Science and Technology*, Vol. 22, 2001.
8. Mikulka, J., E. Gescheidtova, and K. Bartusek, “Soft-tissues image processing: Comparison of traditional segmentation methods with 2D active contour methods,” *Measurement Science Review*, Vol. 12, No. 4, 153–161, 2012.
9. Mikulka, J., E. Gescheidtová, and K. Bartušek, “Processing of MR slices of human liver for volumetry,” *PIERS Proceedings*, 202–204, Xi’an, China, March 22–26, 2010.

Software for Partial Discharge and Localization

M. Cap, P. Drexler, P. Fiala, and R. Myska

Department of Theoretical and Experimental Electrical Engineering
Brno University of Technology, Kolejní 2906/4, Brno 612 00, Czech Republic

Abstract— This article deals with possibilities of localization of the partial discharges (PD) in oil power transformers. Localization can be performed on the basis of measured UHF waveforms analysis during activity of the partial discharges. The time-shifts of the waveforms related to transient process occurrence in the signals are the main input parameters for localization methods. In order to estimate the position of the signal source in the 3D space a minimum of four antennas has to be used, since the time of the PD is unknown. Designed application uses a numerical method for detection of the discharge spatial location. Diagnosis of the partial discharge is split into four Gross. At first, time graphs of detected signal are displayed for its visual verification. Each group of displayed signals include time stamp of the actual trigger. This time stamp is used as information for visualization of the position of the signal group in time range of the power voltage period. Third part is focused on the spatial detection of measured discharges in volume of the transformer. At least, statistical results are shown.

1. INTRODUCTION

Partial discharges (PD) in the high voltage transformer could cause risk of the transformer damage. Detection of the discharge presence is possible by several methods based on sound or electromagnetic signal measurement. This work is focused on measurement and evaluation of the UHF (Ultra High Frequencies) electromagnetic signal. Partial discharge is detected as a signal in range from hundreds of megahertz to units of gigahertz. Propagation delay of the signal from the place of the PD to the each detector can be used for spatial localization of the PD. Goal of this work to design software for detection, analysis and localization of the partial discharges.

2. MEASUREMENT SYSTEM AND LOCALIZATION METHOD

2.1. Diagnostic System

PD signal is detected by the special measuring system. Whole system contains 4 specially designed sensing heads (Fig. 1), central unit and software for PD analysis and localization. Sensing heads are mounted in to the front wall of the transformer. Heads are connected by triaxial cables. This type was chosen for higher EMC robustness. These cables are simultaneously used for RF signal transmission and DC powering of the sensing heads. Signal preprocessing part of each head includes conical antenna, controllable attenuators, amplifiers and high pass filter. Data are acquired by Agilent data acquisition system which uses a four-channel, 10 bit high speed cPCI digitizer. Acquired signal is preprocessed by sensing head and digitalized by each channel with preset parameters, see Table 1. Because of strong electromagnetic interference, diagnostic system is mounted in a shielded box. This two stage box contains all required powering [6], data acquisition and communication parts, Fig. 3.



Figure 1: Sensing head.



Figure 2: Head mounted on the transformer.

Table 1: Data acquisition parameters.

Number samples	2000
Time to be sampled	1000 ns
Sample interval	0.5 ns
Delay time	−50 ns
Channel full scale	0.5 V
Offset	0 V
Trigger level	10% of full scale
Trigger source	All input channels

2.2. Localization Method

Method of the partial discharge location is based on the signal time differences of arrival TDOA. Signal arrival time is determined from energy accumulation curve EAC given by equation [1, 2]:

$$w_i = \frac{t_s}{Z_0} \sum_{k=0}^i u_k^2, \quad k = 1 \dots N \quad (1)$$

Waveform point of the signal arriving time was set to 10% from maximal value of the EAC.

Due to given antenna arrangement shown in Fig. 2 the localization results lies on circle which plane is perpendicular to the straight line join of antennas. Therefore, solution can be found only in 2D space as a intersection of the circle with relevant part of tested transformer. The initial equation system defines source position towards three antennas

$$x^2 + y^2 = v^2 t_0^2, \quad (2)$$

$$x^2 + (y - y_2)^2 = v^2 (t_0 + t_{12})^2, \quad (3)$$

$$x^2 + (y - y_3)^2 = v^2 (t_0 + t_{13})^2, \quad (4)$$

Solution of Equations (2) and (3) leads to definition solution for t_0 , x , y as

$$t_0 = \frac{v^2 (y_2 t_{13}^2 - y_3 t_{12}^2) + y_3 y_2^2 - y_2 y_3^2}{2v^2 (y_3 t_{12} - y_2 t_{13})}, \quad (5)$$

$$y = \frac{y_2}{2} - \frac{v^2 (y_2 t_{13}^2 - y_3 t_{12}^2) + (y_3 y_2^2 - y_2 y_3^2)}{2y_2 (y_3 t_{12} - y_2 t_{13})} t_{12} - \frac{v^2 t_{12}^2}{2y_2}, \quad (6)$$

$$x = \sqrt{v^2 \left(\frac{v^2 (y_2 t_{13}^2 - y_3 t_{12}^2) + y_3 y_2^2 - y_2 y_3^2}{2v^2 (y_3 t_{12} - y_2 t_{13})} \right)^2 - \left(\frac{y_2}{2} - \frac{v^2 (y_2 t_{13}^2 - y_3 t_{12}^2) + (y_3 y_2^2 - y_2 y_3^2)}{2y_2 (y_3 t_{12} - y_2 t_{13})} t_{12} - \frac{v^2 t_{12}^2}{2y_2} \right)^2}. \quad (7)$$

Results of PD localization are calculated as a mean value from three partial solution obtained from different combination of channels.

3. PARTIAL DISCHARGE DIAGNOSTIC AND LOCALIZATION SOFTWARE APPLICATION

PD localization software application is designed as a multithread application. Basic function concept of this application is to split measurement and visualization into separate threads in order to achieve maximal possible computer performance for both application parts. Because of very short times which are acquired and theoretically large amount of discharges per one 50 Hz period is necessary to set up the acquisition hardware to the maximal performance.

3.1. Data Structures

Type of the data variable has to be chosen with respect to data transfer times and requirement of maximal number of acquisition in one 50 Hz period. Data which need to be transferred after one trigger depend on the type of variable used to store the data. Comparison for int, int16 and double are shown in Table 2. With respect to the maximal performance was the data variable type set to basic integer.

Table 2: Comparison of bit rate for different data types.

	bits of variable	Number of data packets per second		
		1	50 (One per period)	2500 (50 per period)
bits per second	8	64 000	3 200 000	160 000 000
	16	128 000	6 400 000	320 000 000
	64	512 000	25 600 000	1 280 000 000



Figure 3: Assembly of the diagnostic system in shielded box.

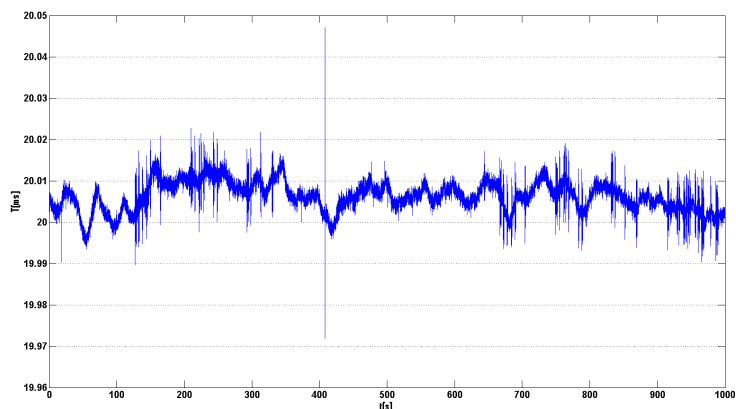


Figure 4: Analysis of the 50 Hz period time.

3.2. Trigger

Detection of the partial discharge is provided on all digitizer channels. Detected signal energy depends on the place of origin of the PD. If the PD will occur on the left or right side of the transformer winding the energy of detected signal will be biggest on the first or fourth channel. Therefore, trigger input is configured as a multichannel trigger so the trigger input is used all four input channels.

3.3. 50 Hz Detection

Diagnosis of the partial discharge requires information about time position of the actually acquired data in 20 ms time period. This value is necessary for the PD visualization in phase graph. Cross zero detection algorithm uses special hardware and external trigger input to detect position of the supply voltage. Stability of the 50 Hz frequency is in Czech Republic defined as $50 \text{ Hz} \pm 1\%$ in 99,5% the year and $50 \text{ Hz} \pm 6\%$ in 100% in the year. With requirements of the precise visualization of the PD in phase chart is necessary to detect actual frequency [5]. In case of one percent difference detected and real frequency can this cause an error 3.6° in one period or 180° in one second. This was solved by calculation of actual period time. Unfortunately, actual period is not stable and visualization error suppression require to refresh the period time after a several seconds. Fig. 4 shows fluctuation of the time period in time range of 1000 seconds (50 000 periods).

Detected time position of the zero value of the supply voltage and period time are calculated as a mean value from ten measured values with regard to eliminate influence of electromagnetic interference.

3.4. Acquisition Settings and Attenuators Control

Basic acquisition setting is shown in Table 1. These parameter are setted up with regard to signal parameters. Possibility of changing of acquisition parameters is crucial especially in case of first examination of signals in continual acquisition mode.

Controllable attenuators regulate transmission path output power. Attenuator attenuation depend on controll voltage which is set by usb controlled hardware in range 3–40 dB, see Fig. 5.

3.5. Application Modes

Diagnostic of partial discharge could be split into the two modes. First mode works in loop in order to acquire and visualize data continuously. This mode is to a certain extent similar to the

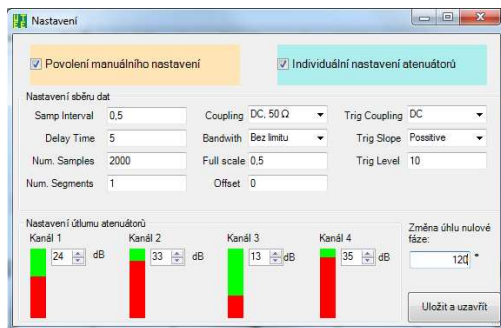


Figure 5: Setting.

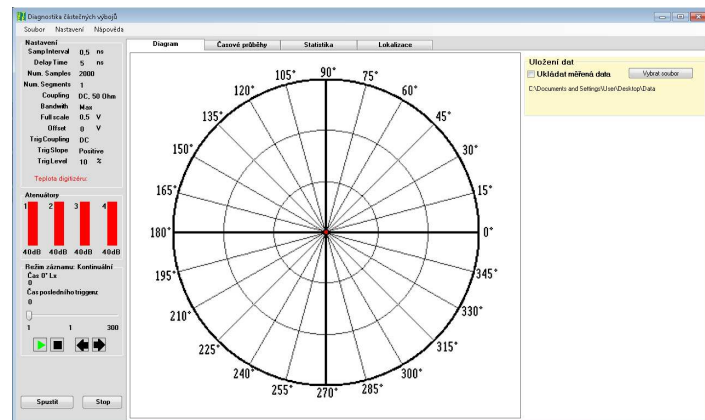


Figure 6: Main window with phase chart.

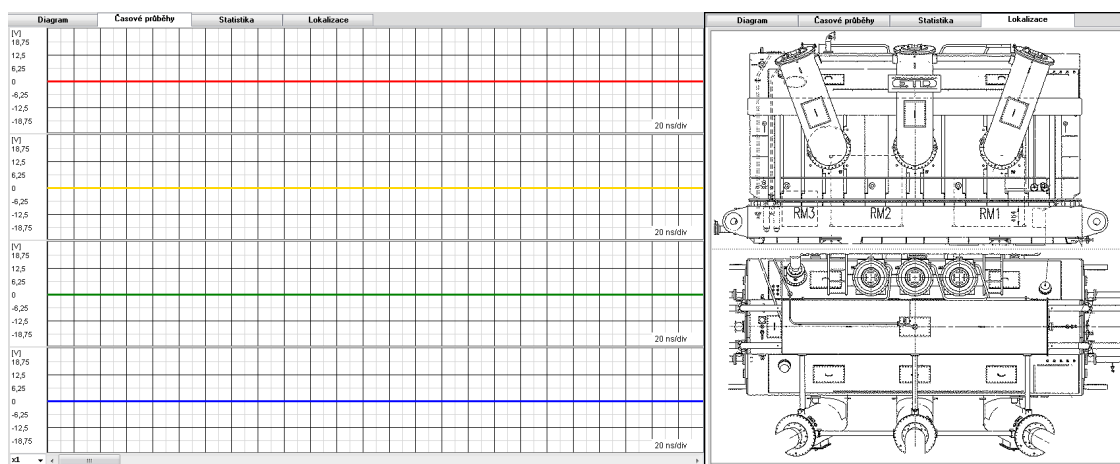


Figure 7: Time graphs and scheme of transformed for visualization of PD localization algorithm results.

basic function of the traditional oscilloscope. Second mode could be described as “acquire and wait”. In this case program will acquire 300 of data packets and stops acquisition. Both modes use two types of acquired signal visualization, phase chart and time graphs of all four channels which shows position of the acquired data to the zero supply voltage point. Chart uses two values, first is angle 0° – 360° calculated as the position of data to the time of the supply voltage zero time, Fig. 6. Actual angle need to be additionally corrected with power and transformer angle difference. Second parameter is mean value calculated from maximal voltage values in all channels [3].

Measurement of the partial discharges starts with examination of the signals in continual mode. Continual mode works similarly to the traditional oscilloscope, Fig. 7. User defines acquisition parameters to achieve the best visualization of various signals in transformer. Optimal attenuators and trigger settings have a crucial influence on selection of required signal. Second mode saves 300 data sets to memory and stops acquisition. This mode is designed for offline review of acquired data. Data could be played continually in loop or selected manually and examined one by one.

3.6. Partial Discharge Location

Partial discharge location uses TDOA method. Localization is because of large amount of processed data in online mode available only in memory mode. Use of four antennas allows locating position of partial discharge in three dimensions. Unfortunately, transformers in nuclear power plant Dukovany has all antenna plug-in points placed on the front side in line (see Fig. 2). Hence, localization is possible only in two dimensions.

4. CONCLUSION

Designed application uses TDOA method for partial discharge localization. Special requirements lead to online and offline function modes. Basics of the partial discharge analysis are shape of the wave and its time position examination. For this purpose, first two tabs were designed to show

this information clearly. PD location itself lies on the top of the application usage. Localization method allows locating of the PD origin in 3D space. Unfortunately, 3D location requires nonlinear placing of the sensing heads on the transformer wall. Therefore, application is not at this time able to locate PD origin in 3D space.

REFERENCES

1. Fiala, P., T. Jirku, P. Drexler, and P. Dohnal, “Detection of partial discharge inside of HV transformer, modeling, sensors and measurement,” *PIERS Proceedings*, 1013–1016, Cambridge, USA, July 5–8, 2010.
2. Myška, R. and P. Drexler, “Simulation and verification of methods for partial discharge source localization,” *PIERS Proceedings*, 704–708, Kuala Lumpur, Malaysia, March 27–30, 2012.
3. Polivka, J., P. Fiala, and J. Machac, “Microwave noise field behaves like white light,” *Progress In Electromagnetics Research*, Vol. 111, 311–330, 2011.
4. Fiala, P., “Pulse-powered virtual cathode oscillator,” *IEEE Trans. Dielectr. Electr. Insul.*, Vol. 18, No. 4, 1046–1053, 2011.
5. Szabó, Z., J. Sedláček, and M. Hadinec, “Optimization method of EMI power filters and its measurement,” *PIERS Proceedings*, 1085–1088, Hangzhou, China, March 24–28, 2008.
6. Fiala, P. and P. Drexler, “Power supply sources based on resonant energy harvesting,” *Microsystem Technologies-Micro-and Nanosystems-Information Storage and Processing Systems*, Vol. 18, Nos. 7–8, 1181–1192, 2012.
7. Szabó, Z. and P. Fiala, “Characterisation and testing shielding fabrics,” *PIERS Proceedings*, 1273–1276, Moscow, Russia, August 18–21, 2009.
8. Marcon, P., P. Fiala, M. Steinbauer, and M. Cap, “Special high voltage function generator,” *PIERS Proceedings*, 1000–1003, Suzhou, China, September 12–16, 2011.

Automatic Detection and Segmentation of the Tumor Tissue

M. Cap¹, E. Gescheidtova¹, P. Marcon¹, and K. Bartusek²

¹Department of Theoretical and Experimental Electrical Engineering
Brno University of Technology, Kolejní 2906/4, Brno 612 00, Czech Republic
²Institute of Scientific Instruments, Academy of Sciences of the Czech Republic
Kralovopolska 147, Brno 612 64, Czech Republic

Abstract— MRI is a constantly developing region of medicine, which is suitable for the study of soft tissues. The current methodologies for obtaining images weighted by relaxation times give only an idea of the distribution of soft tissues. Differential diagnosis of a high-grade glioms and solitary metastases is in some cases inconclusive. Investigators in several studies have demonstrated that in perfusion MRI (magnetic resonance imaging) of high-grade glioms and solitary metastases are differences. Analysis of the peritumoral region could be more useful than the analysis of the tumor itself. Precise evaluation of mentioned differences in peritumoral region gives a hopeful chance for tumor diagnosis.

This article describes automated detection and segmentation of the tumor and tumor edema. Automated detection of the tumor tissue area is based on the human brain symmetry. Healthy brain has a strong sagittal symmetry. Assuming the tumor is not placed symmetrically in both hemispheres, is possible use this method for its detection. Tumor area is evaluated from image which is obtained by summing partial results from all T2 weighted images. Segmentation and precise detection of the tumor in the by previous step marked area is based on Chan Vese algorithm. Segmentation is provided in T1 and T2 weighted images in order to achieve highest precision on the tumor border. Resulting masks are applied to the various perfusion maps.

1. INTRODUCTION

The aim of this work is to create system for tumor and peritumoral region automated detection and segmentation. Importance of the perfusion imaging method lies in its ability to describe anatomy and physiology of the tumor and peritumoral region microvasculature [1]. Several studies have demonstrated that in perfusion MRI of high-grade glioms and solitary metastases are differences [1–4]. Development of the magnetic resonance techniques reaches the point where the automated segmentation and other image processing methods becomes necessary for everyday practice. Consequent parts of this article describe methods for detection of brain cancer tissue and its segmentation.

2. METHODS

2.1. Data

MRI data contain three sets of images. Morphological images are T1 (FLAIR VISTA) and T2 (3D FFE KL) weighted. Third but in this article not shown data are perfusion weighted PWI images.

2.2. Image Registration

Image registration is necessary in case of use various number of different images. MR perfusion imaging require to measure time dependencies of blood pass throw the examined tissue. These dependencies are acquired in range of tens of seconds. Time necessary to acquire all required morphological and perfusion images could be in range of tens of minutes. During the time of examination are all images affected by small patient movements caused by breathing or heart beating. Moreover, large patient movements cause errors in tumor spatial localization and perfusion evaluation. Images could be registered in two ways. First way is to detect interhemispheric fissure

Table 1: Data sets and its parameters.

MRI data set	Data dimensions	Voxel dimension
FLAIR VISTA	432px × 432px × 300 slices	0.578 × 0.578 × 1.2 mm
T1W 3D FFE KL SENSE	320px × 320px × 209 slices	0.84 × 0.84 × 1.6 mm

which can be localized as a local minimum close to the center of gravity []. Second way is Matlab build-in intensity based segmentation method.

2.3. Localization of the Interhemispheric Fissure

Interhemispheric fissure is the space between right and left hemisphere. Because of strong sagittal symmetry, interhemispheric fissure can be used for detection of the unsymmetrical abnormalities [5]. Localization starts with localization of the center of gravity of the input image. Consequently, interhemispheric fissure is created from detected local minima in center of gravity neighborhood.

2.4. Abnormalities Detection

Detection could be split into the pixel and region based approaches. Purpose of this detection is to find position of the tumor or tumor edema but not to detect precise border of this areas. Resulted image pixels could be defined as:

$$O_{m,n} = \left(\left(\sum_{m=-2}^{m=+2} \sum_{n=-2}^{n=+2} I(m,n) \right) / 25 \right) - \left(\left(\sum_{k=-2}^{k=+2} \sum_{l=-2}^{l=+2} I(k,l) \right) / 25 \right) \quad (1)$$

where m row index, n column index, k row index placed symmetrically to m with regard to interhemispheric fissure, l column index placed symmetrically to n with regard to interhemispheric fissure.

Negative values of resulting image indicates higher intensity values on the left of the interhemispheric fissure and are placed to its right position from (m,n) to (k,l) . Consequently, value of $O(m,n)$ is set to zero [11]. Summing of all detection results enhance contrast in tumor area, see Fig. 1(a). High contrast represents target area for image segmentation. Consequent step, image segmentation, will use this detected area as input mask.

3. SEGMENTATION

Segmentation is based on the Chan-Vese algorithm [6–8]. Method minimizes energy F with respect to mean intensity value in areas c_1 and c_2 and curve C [6]:

$$F(c_1, c_2, \phi) = \int_{\Omega} (u_0(x, y) - c_1)^2 H(\phi) dx dy + \int_{\Omega} (u_0(x, y) - c_2)^2 (1 - H(\phi)) dx dy + v \int_{\Omega} |H(\phi)|, \quad (2)$$

where:

$$c_1(\phi) = \frac{\int_{\Omega} u_0(x, y) H(\phi(t, x, y)) dx dy}{\int_{\Omega} H(\phi(t, x, y)) dx dy} \quad (3)$$

$$\text{and } c_2(\phi) = \frac{\int_{\Omega} u_0(x, y) (1 - H(\phi(t, x, y))) dx dy}{\int_{\Omega} (1 - H(\phi(t, x, y))) dx dy}. \quad (4)$$

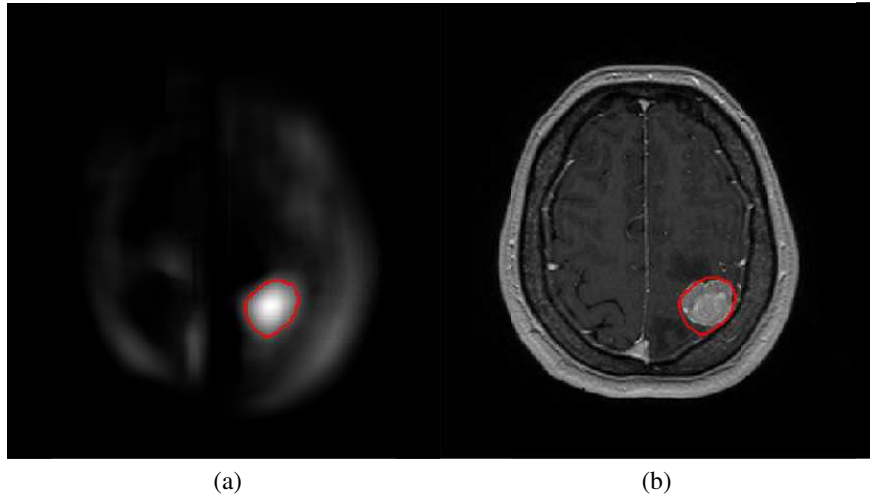


Figure 1: (a) Detected abnormalities in T1 weighted image. (b) Detected area in original image.

Following equation represent evolution of the level set function ϕ .

$$\frac{\partial \phi}{\partial t} = \delta_\varepsilon(\phi) \left[\mu \operatorname{div} \left(\frac{\nabla \phi}{|\nabla \phi|} \right) - v - \lambda_1 (u_0 - c_1)^2 + \lambda_2 (u_0 - c_2)^2 \right] \quad (5)$$

Solution of minimization energy problem can be found as [1]:

$$u(x, y) = c_1 H(\phi(x, y)) + c_2 (1 - H(\phi(x, y))) \quad (6)$$

Segmentation process continues till the change of the energy between two iterations reach limit value.

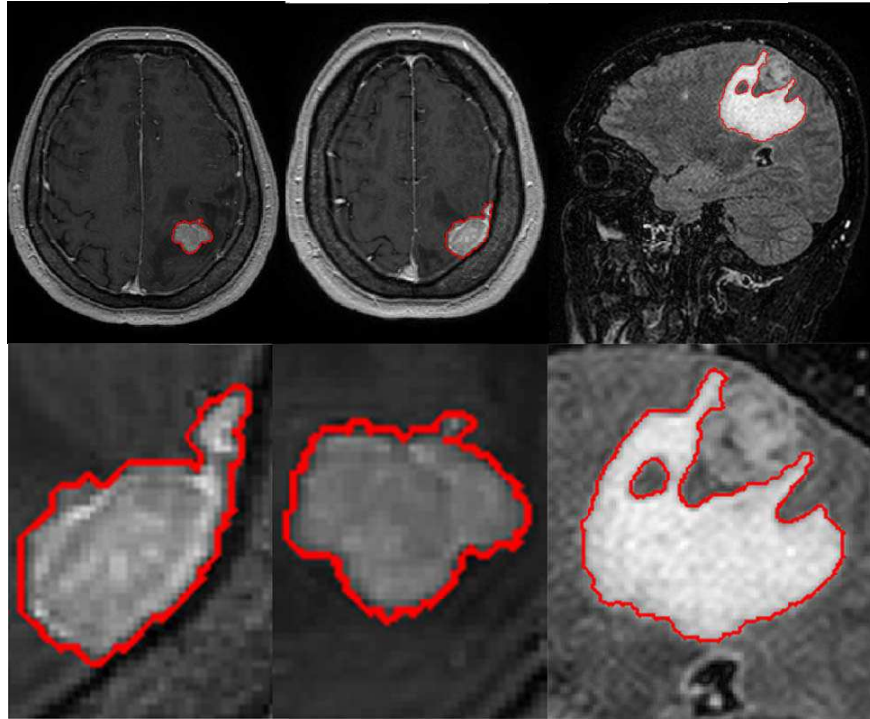


Figure 2: Results of the segmentation based on Chan Vese method.

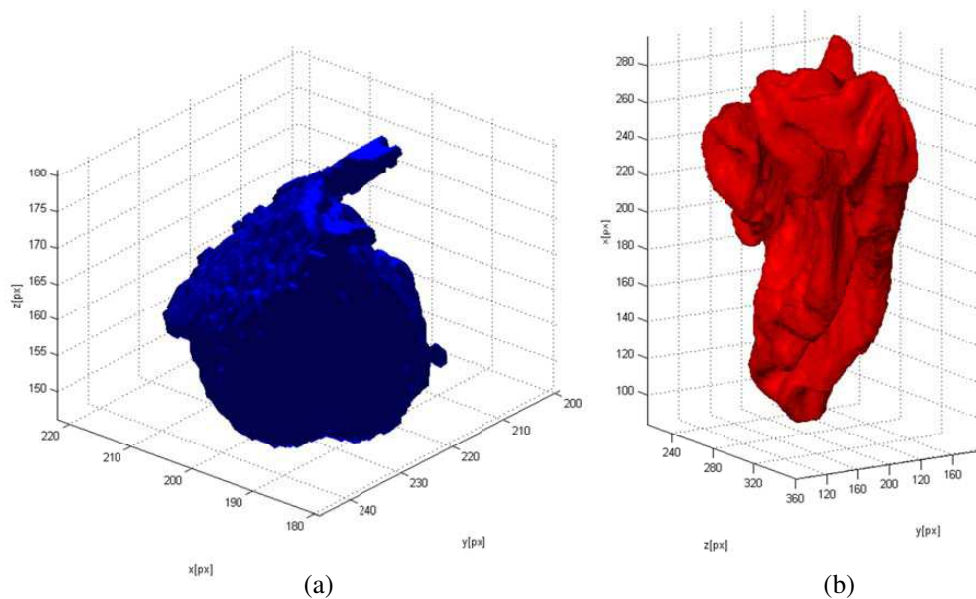


Figure 3: 3D models of the (a) tumor and (b) tumor edema.

Goal of this work is to create 3D binary matrix of tumor and tumor edema. Segmented images has high contrast for tumor (T1W 3D FFE KL SENSE) and tumor edema (FLAIR VISTA). Results of the tumor and tumor edema segmentation are shown in Fig. 2.

Created 3D matrix for tumor and tumor edema are used for processing of the perfusion weighted data and sisualization of perfusion parametric maps in mentioned areas. Three dimmensional model of both object are shown in Fig. 3.

4. CONCLUSION

Goal of this work was to detect and segment cancer tissue in human brain. In order to obtain the best possible spatial information about cancer tissue were data acquired with high spatial resolution and high with high number of slices. Automated method detects the tumor tissue in 38 slices of T1W 3D FFE KL SENSE data and tumor edema in 106 slices of FLAIR VISTA data. Automated abnormalities detection using brain symmetry with the use of Chan Vese segmentation method proof possibility to segment required areas with good precision.

ACKNOWLEDGMENT

This work was supported within GACR 102/11/0318 and GA102/12/1104 and GA FEKT-S-11-5/1012.

REFERENCES

1. Jackson, A., D. L. Buckley, and G. J. M. Parker, *Dynamic Contrast-enhanced Magnetic Resonance Imaging in Oncology*, 311, Elsevier, 2005.
2. Law, M., S. Cha, E. A. Knopp, G. Johnson, J. Arnett, and A. W. Litt, "High-grade gliomas and solitary metastases: Differentiation by using perfusion and proton spectroscopic MR imaging," *Radiology*, 715–721, 2002.
3. Hakyemez, B., C. Erdogan, N. Bolca, N. Yildirim, G. Gokalp, and M. Parlak, "Evaluation of different cerebral mass lesions by perfusion-weighted MR imaging," *J. Magn. Reson. Imaging*, Vol. 24, 817, 2006.
4. Rollin, N., J. Guyotat, N. Streichenberger, J. Honnorat, V. A. Tran Minh, and F. Cotton, "Clinical relevance of diffusion and perfusion magnetic resonance imaging in assessing intra-axial brain tumors," *Neuroradiology*, Vol. 9, 150, 2006.
5. Ray, N., B. N. Saha, and M. R. Graham Brown, "Locating brain tumors from MR imagery using symmetry," *Conference Record of the Forty-First Asilomar Conference on Signals, Systems and Computers*, 224–228, Nov. 4–7, 2007.
6. Vese, L. and F. Chan, "A multiphase level set framework for image segmentation using the Mumford and Shah model," *International Journal of Computer Vision*, Vol. 50, No. 3, 271–293, 2002.
7. Mikulka, J., E. Gescheidtová, and K. Bartusek, "Soft-tissues image processing: Comparison of traditional segmentation methods with 2D active contour methods," *Measurement Science Review*, Vol. 12, 153–161, 2012.
8. Mikulka, J., E. Gescheidtová, and K. Bartusek, "Processing of MR slices of human liver for volumetry," *PIERS Proceedings*, 202–204, Xi'an, China, March 22–26, 2010.
9. Cap, M., E. Gescheidtová, P. Marcon, K. Bartusek, and A. Sprlakova, "Fusion of the T1, T2 weighted and perfusion weighted images for peritumoral region evaluation," *PIERS Proceedings*, 103–105, Suzhou, China, September 12–16, 2011.
10. Marcon, P., K. Bartusek, M. Burdkova, et al., "Magnetic susceptibility measurement using 2D magnetic resonance imaging," *Measurement Science & Technology*, Vol. 22, No. 10, 2011.
11. Kubasek, R. and E. Gescheidtová, "Denoising of MR tomography signal with automatic adjustment of time-variant thresholds," *Proceedings of 27th Annual International Conference of the Engineering in Medicine and Biology Society*, 1–4, Shanghai, 2005, ISBN 0-7803-8741-4.

Study of the Influence of Magnetic Fields on Plants Tissues

E. Hutova¹, K. Bartusek², and J. Mikulka¹

¹Department of Theoretical and Experimental Electrical Engineering
Brno University of Technology, Kolejní 2906/4, Brno 612 00, Czech Republic
²Institute of Scientific Instruments, Academy of Sciences of the Czech Republic
Kralovopolska 147, Brno 612 64, Czech Republic

Abstract— If a magnetic field may influence behavior and movement of an electrically charged particle, can this field also affect cells in living organisms? The aim of the study is to determine the dependence of the growth of plant cultures on a stationary homogeneous and a gradient magnetic field. We created nine magnetic fields of various magnetic flux density values and defined the configurations. The magnetic fields were created by ferrite and neodymium magnets. The map of magnetic fields was simulated using the finite element method in the ANSYS program and experimentally measured with a Hall probe. The plant cultures applied in this experiment were early somatic embryos (ESEs) of *Picea abies* (/L./Karsten, clone 2.2/2) and *Pinus Engelmannii*. These cultures were derived at the Institute of Plant Biology, Mendel University in Brno. The clusters of early somatic embryos were placed in Petri dishes; each dish contained one cluster of the ESEs. The Petri dishes were placed in the magnetic fields. We used five dishes simultaneously as the reference group and located them in the Earth's magnetic field. Within the experiment, the ambient conditions were a very important aspect; it was demonstrated that the conditions, especially the outdoor temperature and humidity, have great influence on the growth of the ESEs.

The progress of growth was evaluated from 2D images of clusters in the Petri dishes, and the area of the ESEs was calculated. For better characterization of the quality of the ESEs, we used several magnetic resonance imaging (MRI) techniques with different types of contrast to measure a large number of slices of the ESEs. The contrast was obtained by means of the spin density (SD) method, relaxation times T_1 , T_2 , and magnetic field B_0 . This field characterizes the magnetic susceptibility of the plant cultures. The multi-contrast analysis of 2D images enables us to achieve better resolution of the clusters and obtain improved characterization of the plant culture growth.

1. INTRODUCTION

This article describes research into the influence of stationary and gradient magnetic fields on early somatic embryos (ESEs) in Norway spruce (*Picea abies*) and Apache Pine (*Pinus engelmannii*). The ESE clusters were placed in an induction medium located in Petri dishes; each dish contained exactly one cluster. We exposed all these ESE clusters to stationary and gradient magnetic fields of different intensities. The magnetic fields were created by ferrite and neodymium magnets [1]. The configurations of magnetic fields were determined using ANSYS. We exposed the ESE clusters to the influence of the magnetic fields and measured their size to calculate the growth rate; then, the influence of the magnetic fields on the plant culture was evaluated.

2. DESCRIPTION OF THE APPLIED MAGNETS

Magnetic flux density (\mathbf{B}) is a vector value that describes the magnetic field at any point around the magnet. Magnetic flux density is defined by the magnetic force \mathbf{F}_B acting on a moving electrically charged particle. Further, magnetic flux density is defined as a vector which has the direction $\mathbf{v}_F = 0$. For the velocity \mathbf{v} perpendicular to $\mathbf{v}_F = 0$, the angle φ is defined. This angle acts between \mathbf{v} and \mathbf{v}_F , always is 90° and equals to the force acting on the particle size of the maximum $\mathbf{F}_{B, \max}$. The magnitude of the magnetic flux density is defined by the size of the force relationship.

$$\mathbf{B} = \frac{\mathbf{F}_{B, \max}}{|Q|v}, \quad (1)$$

where Q is the charged particles.

The homogeneous gradient field is defined as a field whose magnetic lines are parallel; this magnetic field exhibits the same magnetic flux density value at all points. The gradient of the magnetic field is determined using the temporal characteristics of the magnetic flux density decrease in two parallel planes located at a defined distance $\pm r_0$ from the center of the gradients; another aspect participating in the process of gradient determination is the calculation of the size of the

field gradient. The spatial distribution of the magnetic field in excited layers of the sample in positions $\pm r_0$ can be described by the following relationships:

$$\mathbf{B}(r_0, t) = \mathbf{B}_{r_0}(t) + \mathbf{G}_r(t) \times r_0, \quad (2)$$

$$\mathbf{B}(-r_0, t) = \mathbf{B}_{r_0}(t) - \mathbf{G}_r(t) \times r_0. \quad (3)$$

The zeroth-order $\mathbf{B}_{r_0}(t)$ gradient is given by the sum of two flux density values of the magnetic fields $\mathbf{B}_{r_0}(r_0, t)$ and $\mathbf{B}_{r_0}(-r_0, t)$, which were measured in the positions $+r_0$ and $-r_0$.

$$\mathbf{B}_{r_0}(t) = \frac{1}{2} [\mathbf{B}(r_0, t) + \mathbf{B}(-r_0, t)]. \quad (4)$$

The difference of the measured magnetic flux density values defines the size of the magnetic flux density gradient $\mathbf{G}_r(t)$.

$$\mathbf{G}_r(t) = \frac{1}{2r_0} [\mathbf{B}(r_0, t) - \mathbf{B}(-r_0, t)]. \quad (5)$$

The size of the magnetic flux density gradient between two magnets was calculated based on the Hall effect:

$$U_H = \tilde{R}_H \frac{I B_y}{d}. \quad (6)$$

After expressing this relation, we obtain the formula for the calculation of the magnetic flux density

$$\mathbf{B}_y = \frac{U_H d}{\tilde{R}_H I}. \quad (7)$$

The characteristics of the applied magnetic fields were determined using the finite element method in the ANSYS system. The representation of the resulting magnetic flux density vectors is shown in Fig. 1.

In the experimental measurement of the magnetic flux density gradient, we assumed that the highest value of the gradient will be achieved between the magnets. However, this assumption was later refuted by the modeling in ANSYS; it is obvious from the results shown in Fig. 2 that the highest magnetic flux density value can be found at the edges of the magnets.

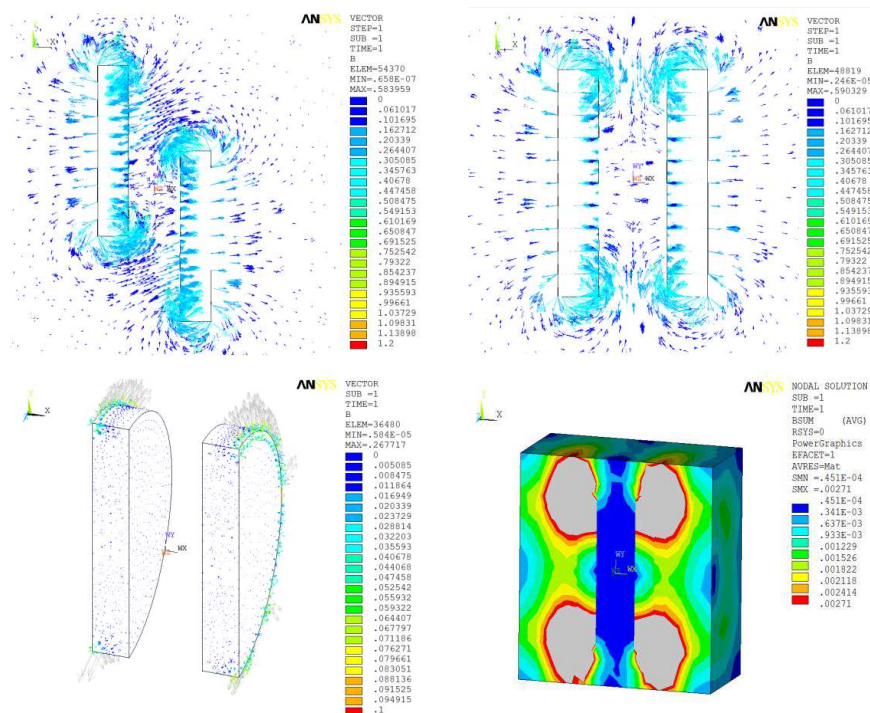


Figure 1: Results of the ANSYS-based modeling.

3. CHARACTERIZATION OF THE EXPERIMENT

The experiment was conducted in steps as shown in Fig. 3.

The acquired images of the ESEs were processed to provide the required data. For that reason, we created an application in C#. NET, which allows for the recognition and subsequent calculation of the area occupied by the ESEs [1]. The evaluated data were processed in Microsoft Excel; thus, we performed the calculation of the average increment in the ESE area. For this calculation, we utilized the equation

$$P_p = \left[\left(\frac{I_n}{I_0} \right) - 1 \right] \times 100, \tag{8}$$

where P_p is the area increment expressed in percent [%], I_n is the area after n days of cultivation [mm^2], and I_0 is the area at the beginning of the cultivation [mm^2].

4. RESULTS

It is obvious from the obtained values shown in Fig. 4 that the most stable and suitable conditions for the growth of the ESEs were provided by the ferrite magnet exhibiting the magnetic field gradient value of 5.68 T/m. Ferrite magnets are generally considered (mainly because of their properties and easier handling) a convenient solution for experiments with ESEs.

5. MULTI CONTRAST VIEW OF THE ESES OBTAINED USING THE MRI

We realized a measurement of the ESEs by means of MRI techniques. The aim was to measure slices of the grown cultures and to acquire images with the contrasts of SD, T_1 , T_2 , and B_0 [2]. The experiment was carried out on a Magnex 4.7 T 200 mm i.d. horizontal bore super conducting magnet at 200 MHz at the Institute of Scientific Instruments. A water-cooled Magnex 150 mm i.d. gradient set was employed; the apparatus is driven by IECO GPA 200–350 amplifiers, which

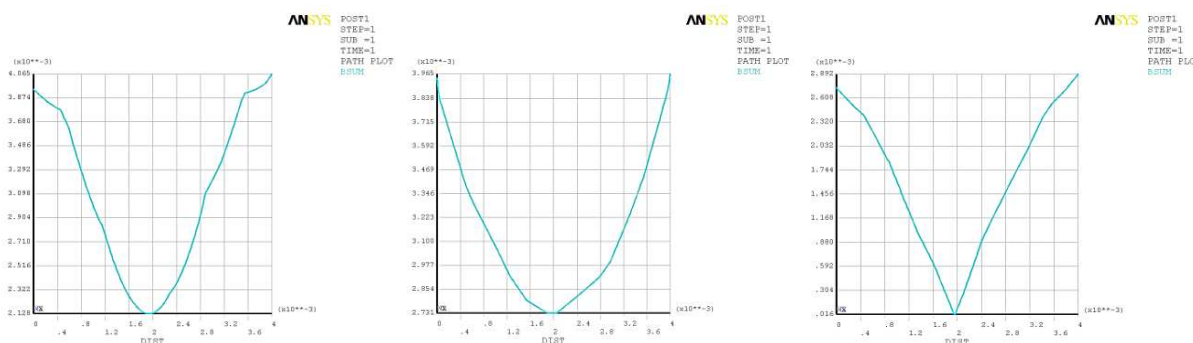


Figure 2: Behavior of the magnetic flux density gradient at the edges of the magnet.

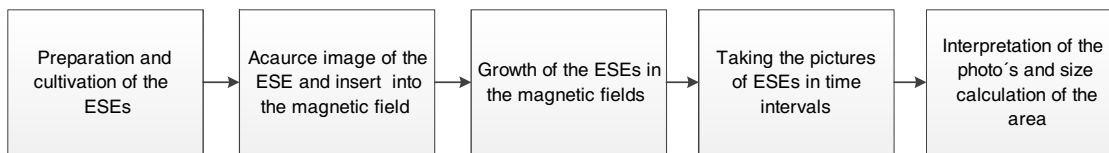


Figure 3: Description of the experiment by means of a processing diagram.

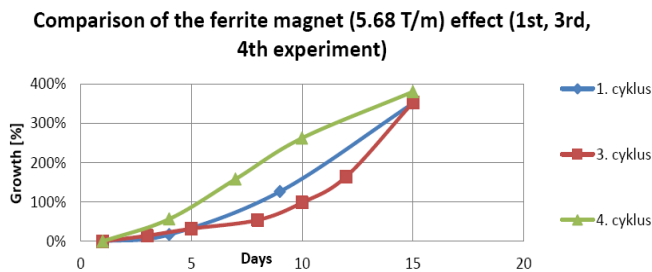


Figure 4: Diagram of the ESEs growth in the magnetic fields.

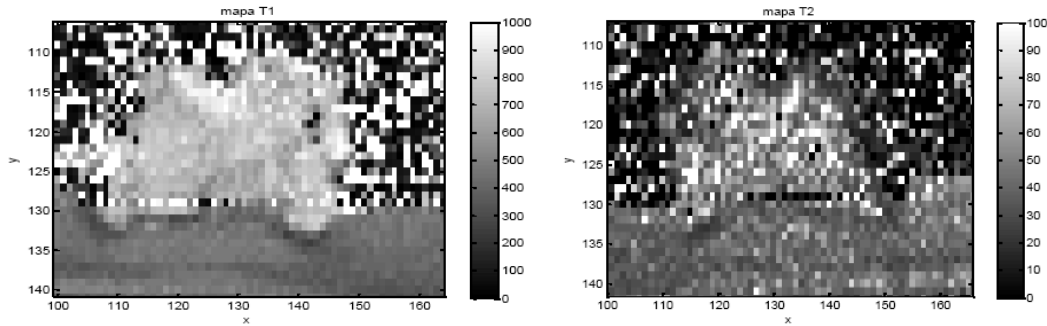


Figure 5: Map of the relaxation times T_1 and T_2 for the measured cluster.

can provide maximum gradients of 180 mT/m. All the experiments were performed with an MR solution console. The data measured were processed using the MAREVISI (8.2) and MATLAB (7.11.0) programs [3]. In the first measurement, we used clusters of the ESEs labeled 1 to 15 with the contrast of T_2 for $T_E = 16$ and 30 ms; at this instant, we also measured ESE clusters labeled 7, 14, and 15 having the B_0 contrast via the spin echo method ($SE = \pm 1$ ms). In the second measurement, one Petri dish (15) was measured, and the following contrast types were evaluated: spin density (SD), T_1 — the IR method at times $T_I = 10, 200, 500, 1000, 2800$ ms and T_2 — the SE method for $T_E = 16$ and 30 ms.

The size of the magnetic susceptibility in cluster 15 can be calculated from the change of the field in both the substrate and the cluster.

$$\chi = \frac{B_{SUB} - B_{CLU}}{B_0} \quad (9)$$

6. CONCLUSIONS

The experimental results show that the effect of gradient magnetic fields on ESEs varies considerably. Thus, it is not easy to answer the question of whether magnetic fields accelerate or suppress the growth of cultures; this problem will be the subject of further research. This paper provides overall clarification of the measurement methodology; this clarifying aspect is further accentuated by the basic program created to support the evaluation of the results.

ACKNOWLEDGMENT

This work was supported within the grant projects of the Grant Agency of the Czech Republic GA 102/12/1104 and GA 102/11/0318 and project of the BUT Grant Agency FEKT-S-11-5/1012.

REFERENCES

1. Pokludova, M. and E. Hutova, "The influence of magnetic field on the dew point of tissue culture," *Progress In Electromagnetics Research Symposium Abstracts*, 193–196, Moscow, Russia, August 19–23, 2012.
2. Marcon, P., K. Bartusek, E. Gescheidtova, and Z. Dokoupil, "Diffusion MRI: Magnetic field inhomogeneities mitigation," *Measurement Science Review*, Vol. 12, No. 5, 205–212, 2012.
3. Bartusek, K., E. Gescheidtova, and J. Mikulka, "Data processing in studying biological tissues, using MR imaging techniques," *33th International Conference on Telecommunications and Signal Processing*, 171–175, Assisztenda Szervezo, Budapest, 2010.

Combined X-ray Diagnostics of Heterogeneous Biological Material

P. Fiala¹, P. Koňas¹, M. Friedl¹, P. Šmíra², P. Dohnal¹, M. Hanzelka¹, and A. Nasswetrová²

¹Department of Theoretical and Experimental Electrical Engineering
Brno University of Technology, Kolejní 2906/4, Brno 612 00, Czech Republic

²Thermo Sanace s.r.o., Chamrádova 475/23, Ostrava-Kunčičky 718 00, Czech Republic

Abstract— The problem of finding a suitable diagnostic procedure for the examination of structural components of buildings has been closely analyzed in recent years. In this connection, the major interest is currently directed towards wood as a type of heterogeneous material; the utilized diagnostic procedures are under constant development to enable broad industrial application in the future. Within the research presented in this study, a new diagnostic method based on X-ray imaging has been proposed and tested. The technique utilizes the reduction of imaging information into 2D/3D planar projection, and it allows us to image clearly the rate of material damage by displaying the weighted damage rate. Another method is based on acoustic identification of structural elements infested with wood-destroying insects.

1. INTRODUCTION

Currently, the protection of wooden structural components against decay fungi and wood-destroying insects is widely realized through the use of the thermal treatment technique, which has been known and applied in Germany since the 1930s. The principle of this method consists in heating the related wooden structures by means of hot air whose temperature does not exceed 120°C; the duration of the process corresponds to 4–10 hours. The generated heat is accumulated inside wooden components of the structure under treatment, and the temperature of these components may reach as high as 60°C within the cross-section. The laboratory experiments involving the discussed diagnostic methods and damage recognition were described within reference [1]. In the following sections of our analysis, outdoor applications of these procedures will be described.

2. EVALUATION OF MECHANICAL PROPERTIES OF WOODEN STRUCTURAL ELEMENTS

The design of a mobile workstation which satisfies the requirements concerning the resolution accuracy of the evaluated image, (RTG image point $-87/125 \mu\text{m}$) [9], is shown in Fig. 1. The realized workstation is indicated in Fig. 2.

The following-described system can be used to monitor and evaluate the condition of wooden elements. As shown in Fig. 7 [1], the damage rate can be effectively determined and the presence of pests such as old-house borer (*Hylotrupes bajulus*) evaluated [2–11], Fig. 2.

The localization of wood-destroying insects was tested on laboratory samples which, in a defined manner, had been purposely infested with larvae of *Hylotrupes bajulus*, Figs. 3–4.

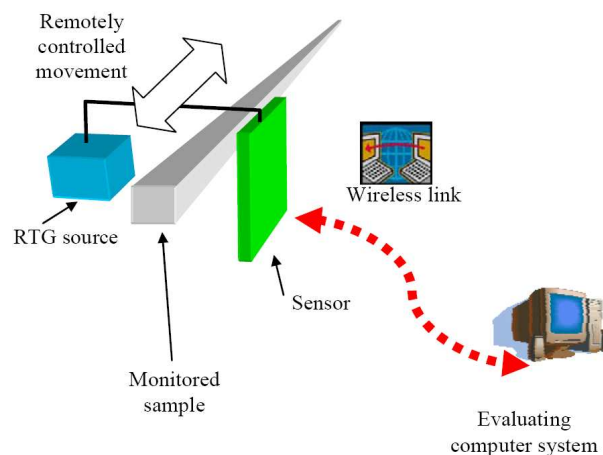


Figure 1: Diagram of the system for the monitoring of structural elements.

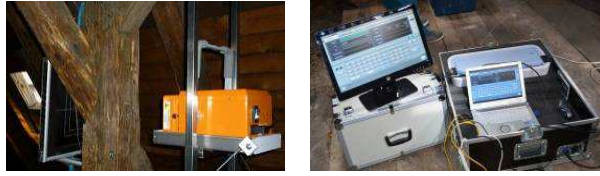


Figure 2: Experimental setup for the monitoring of structural elements.

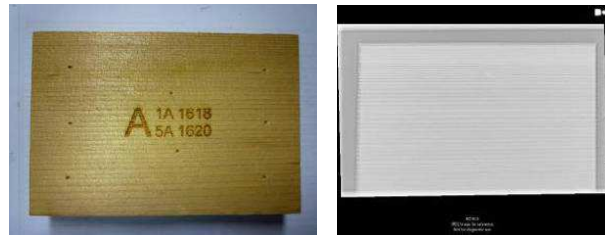


Figure 3: An uninfested sample wooden element.

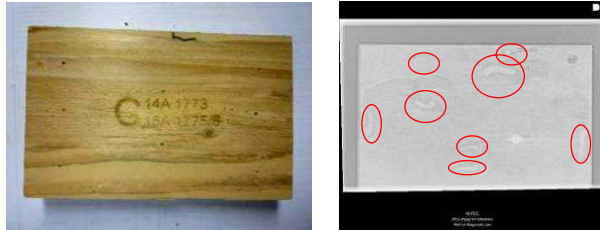


Figure 4: A sample wooden element attacked by the insect: Infested regions are marked in red.

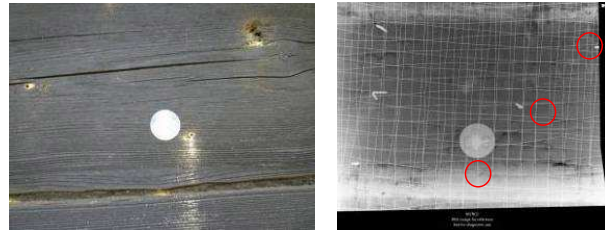


Figure 5: A sample wooden element attacked by the insect. The sample is combined with a plaster coating and netting wire; the larvae were found at spots marked by the red circles. Measured on 1 June 2012 at the gristmill in Kozlovice, the Czech Republic.

In real conditions, we conducted various experiments to obtain multiple types of information; thus, we also examined and obtained data on wooden elements combined with other materials (Fig. 5). In the data evaluation process, optical instruments are applied to create the 3D sharpening effect (image filtering), which enables us to determine the presence and position of *Hylotrupes bajulus* larvae with a probability of 60–90%. The evaluation may be impaired by image artefacts such as the netting wire in Fig. 5.

3. ACOUSTIC IDENTIFICATION OF AN ACTIVE WOODWORM LARVA

Sound recordings prove the presence of an active woodworm. However, as pest identification within such recordings would be time-intensive in outdoor measurements, which may last for several hours, special detection software was created. The software utilizes a suitable algorithm to ensure automatic and, in comparison with the manual mode, up to thirtyfold faster seeking of the moments of woodworm activity. Graphical output from the program is shown in Fig. 8; in the timeline, the pest active moments are indicated in red, while the noise is marked in green. The recordings presented in the figure are 4400s and 100s long, respectively. By means of this software, we can easily perform time analysis of a multi-hour record and locate spots of the woodworm activity. Then, the record (Fig. 7) can be started at red-marked times within the obtained diagram.

In the course of the trial outdoor RTG measurement, we also measured the sound track of the pest in a biological material, and the related processing results exhibited open activity of the pest. More concretely, the insect is active on a track recorded in one room of a house (Hukvaldy, Moravia, the Czech Republic) on 1 June 2012, Figs. 7 and 8. Using the software developed at the Department of Theoretical and Experimental Electrical Engineering, Brno University of Technology, the sound track can be accurately analyzed to enable the location of the pest activity spots.

Trial measurements of the insect activity in damaged 3D samples were realized by means of a sensor, and the related results are shown in Fig. 4.

The obtained results indicate that the applied measurement method can be successfully used to prove the activity of wood-destroying insects in a biological material, Fig. 7. The following diagrams introduce graphical output of the detecting program (Fig. 8) as well as the recording of the pest activity (Fig. 7).

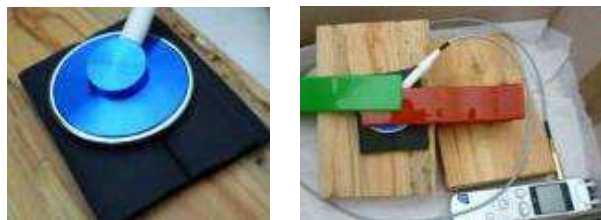


Figure 6: Measuring configuration of a fonendoscopic device for long-time recording.

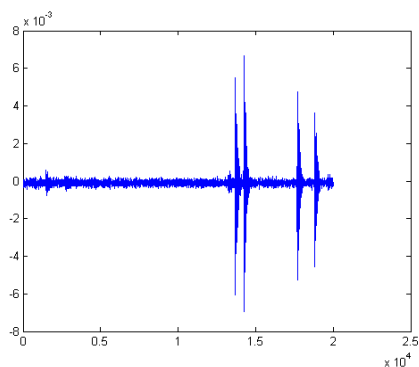


Figure 7: Recording of acoustic detection of an active pest.

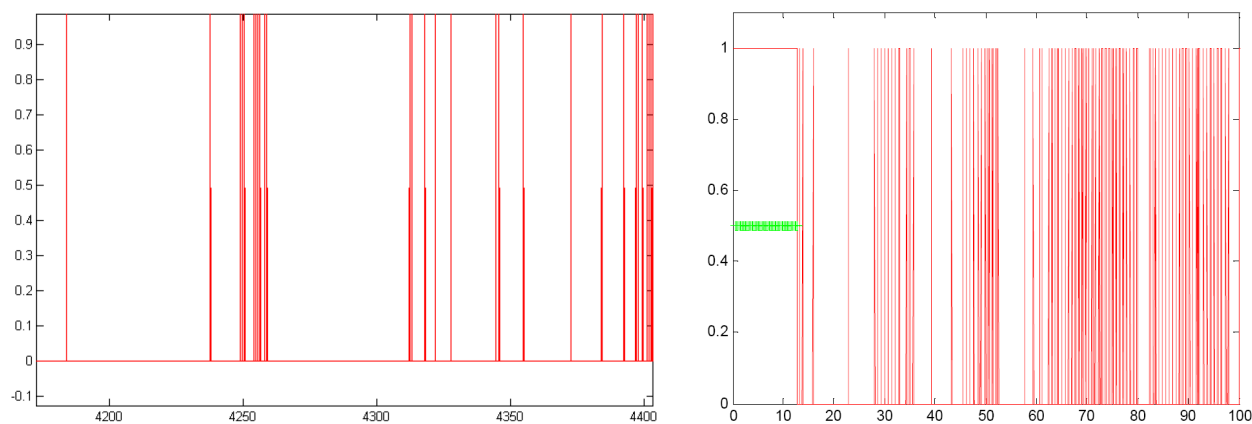


Figure 8: Graphical output of the program for acoustic detection of an active pest within the recording.

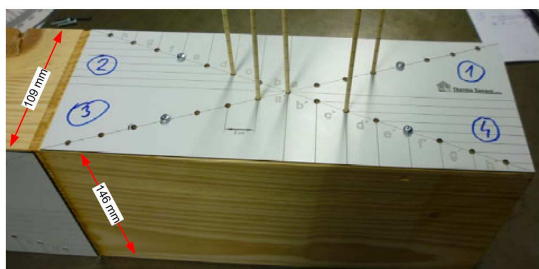


Figure 9: Instrumental box enabling the localization of an object inside a biological structure.



Figure 10: Tools for the localization of an object inside a biological structure.

4. LOCALIZATION OF AN OBJECT INSIDE A BIOLOGICAL STRUCTURE

To facilitate the localization of a woodworm inside a biological structure, the scanning of the object must be performed from no less than two angles (ideally 90°). In this measurement, the pest is represented by a pin, mainly because metal is perfectly identifiable in an RTG image. While laboratory conditions enable us to measure the object in all three axes of the three-dimensional system, real measurements performed on a saved (treated) roof may not allow such configuration owing to the structure of examined buildings. For that reason, the measurement was realized for two angles, namely 0° and 90°. Through further processing, the obtained images helped us to gain insight into the location of the object (a pest larva) in a biological structure. A convenient setup (phantom) was manufactured to support the measurement, Fig. 9.

We manufactured gauges with calibrated length guidelines to facilitate localization of the object inside the fabricated openings. The guidelines are applied (with 10 mm spacings) along the entire length of the gauges; this procedure allows pre-defined orientation and reading of the guidelines

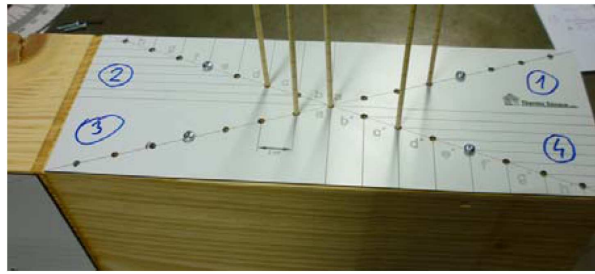


Figure 11: The measured study “A” for the localization of an object inside a biological structure (deployment of the objects is as follows: $d_1 = 7$ cm, $a = 6$ cm, $c_2 = 2$ cm, $b_3 = 12$ cm, $c_4 = 4$ cm).



Figure 12: Views of the study “A” configured for the measurement of object localization inside a biological structure.

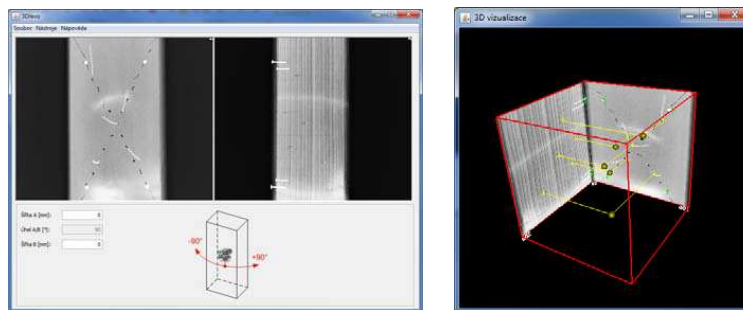


Figure 13: Final RTG images of situation “A”, 3D evaluation of the phantom object localization.

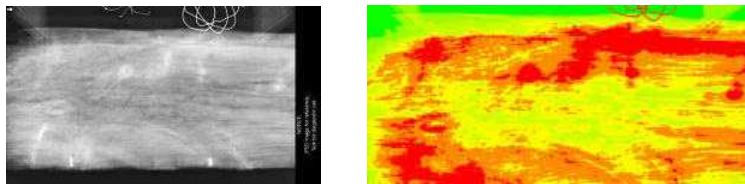


Figure 14: Sample PT23-SE2- evaluation of the object volume damage.

during their insertion into the measuring setup. Before the real measurement, an 8 mm long metal phantom was pressed into one end of each gauge (Fig. 10) to improve the contrast of the resulting RTG image and simplify the detection of the pest.

The actual measurement was performed from all three sides of the instrument (studies “A”, “B” and “C”), always from two views reversed by 90° . Within each study, metal rollers were inserted into engraved marks to facilitate the calibration of distance during the evaluation of the image. Below we present only the results for study A, Figs. 11, 12, and 13. The quality and/or damage rate evaluation of a structural element is shown in Fig. 14.

5. CONCLUSIONS

We designed and tested an X-ray transparent diagnostic method for 2-D imaging and 3-D quality evaluation with respect to the assigned image parameters. The parameters were set in such a manner as to enable the imaging of shot sections showing the rate of damage to the heterogeneous structure building.

In this context, we also tested acoustic monitoring methods for determining the presence and position of wood-destroying insects in wooden elements. The quality and/or damage rate diagnostics were realized using real structural timber, including wooden supporting members.

ACKNOWLEDGMENT

The research described in the paper was financially supported by a project from Education for Competitiveness Operative Programme CZ.1.07.2.3.00.20.0175 (Electro-researcher) and a project of the BUT Foundation Agency FEKT-S-11-5, and the Thermosanace Company Czech Republic. This paper also benefited from the use of the Insight Segmentation and Registration Toolkit (ITK), an open source software developed as an initiative of the U.S. National Library of Medicine.

REFERENCES

1. Fiala, P., P. Konas, M. Friedl, Z. Szabo, M. Hanzelka, and P. Smira, “Combined acoustic and X-ray diagnostics of heterogeneous,” *PIERS Proceedings*, Kuala Lumpur, Malaysia, Mar. 27–30, 2012.
2. Koňas, P., M. Rybníček, and T. Kolář, “Statistical processing and usage of incomplete tree-ring series,” *Proceedings of Abstracts of TRACE*, 44, 2011.
3. Vavrčík, H., V. Gryc, and P. Koňas, “Comparison of wood density in relation to growth rings of English oak and Sessile oak,” *TRACE — Tree Rings in Archaeology, Climatology and Ecology, Proceedings of the DENDROSYMPOSIUM 2009*, Vol. 8, 157–163, 2010, ISSN 1610-0956.
4. Gryc, V., H. Vavrčík, J. Šlezingerová, and P. Koňas, “Basic density of spruce wood, wood with bark, and bark of branches in locations in the czech republic,” *TRACE — Tree Rings in Archaeology, Climatology and Ecology, Proceedings of the DENDROSYMPOSIUM 2009*, Vol. 8, 151–156, 2010, ISSN 1610-0956.
5. Trecala, M. and P. Konas, “Modelling of coupled moisture and heat transfer during wood drying,” *Wood Research*, sv. 57, č 1, 2012, ISSN 1336-4561.
6. Mikulka, J., E. Gescheidtová, and K. Bartušek, “Evaluation of errors in manual image processing,” *PIERS Proceedings*, 84–86, Suzhou, China, Sep. 12–16, 2011.
7. Mikulka, J. and K. Bartušek, “3D reconstruction in magnetic resonance imaging,” *PIERS Online*, Vol. 6 No. 7, 617–620, 2010.
8. Thermosanace: Likvidace Dřevokazného Hmyzu Horkým Vzduchem, Mar. 8, 2012, [online] On: <http://www.thermosanace.eu/>.
9. FOMEI: divize RTG. Mar. 8, 2012, [online] On: <http://radiodiagnostika.fomei.com/>.
10. Drexler, P. and P. Fiala, “Methods for high-power EM pulse measurement,” *IEEE Sensors Journal*, Vol. 7, Nos. 7–8, 1006–1011, 2007.
11. Drexler, P., P. Fiala, and R. Kadlec, “Utilization of faraday mirror in fiber optic current sensors and experiments,” *PIERS Proceedings*, 137–141, Beijing, China, Mar. 23–27, 2009.
12. Drexler, P. and R. Kubasek, “Pulsed magnetic field fiber optic sensor,” *3rd IEEE International Conference on Signals, Circuits and Systems*, 784–789, 2009.

Miniature Planar Triple Passband Filter Using Embedded Resonators

S. P. Lim and K. M. Lum

School of Science and Technology, SIM University, Singapore

Abstract— A triple passband filter has been proposed using embedded resonators. The proposed filter consists of a main dual feeding structure that embeds four resonators. The topology of the four embedded stepped impedance resonators are designed to control and adjust the return loss and insertion loss of the three passband response characteristics. Two transmission zeros are realized for each passband and the selectivity of the filter is significantly improved. The proposed filter is prototyped using material FR4 substrate with dielectric constant of 4.06, thickness of 1.6 mm and loss tangent of 0.014, conductor thickness of 35 μm . The fabricated structure has a miniature dimensional about the size of 15 mm by 22 mm. The three passbands are observed at center frequency 1.8 GHz, 3.3 GHz and 5.2 GHz respectively with S_{11} value less than -10 dB. The corresponding passband insertion loss S_{21} is approximately -1 dB to -5 dB. Attenuation is greater than 20 dB for lower and upper stopband. Measurement and simulation results are discussed and presented.

1. INTRODUCTION

In this century, microwave and radio frequency have become a very important role in the communication world. Dual-band filters had been well known for low insertion loss, high selectivity, and size. In general, dual-band are designed by cascading a broadband bandpass filter (BPF) with narrowband bandstop filter [1]. Many had studied to improve and enhance on the performance using different kind of filter [2–8]. The proposed configuration seems particularly suitable for integration with multilayer transceiver antenna modules [9–13] and localization applications [14–18].

2. TRIPLE PASSBAND FILTER DESIGN AND CONCEPT

Figure 1 shows the design of the main dual feeding structure that embeds four resonators. The resonators can be configured using various types of design topology to tune the intercoupling effect.

Figure 2 presents the layout of the proposed triple passband filter. The main structure compose folded open loop half-wavelength resonator which embeds the four stepped impedance structures (SIR) to reduce the length of the transmission-line resonators. Two transmission zeros are realized for each passband and the selectivity of the filter is significantly improved. Table 1 details the specification of the proposed triple passband filter.

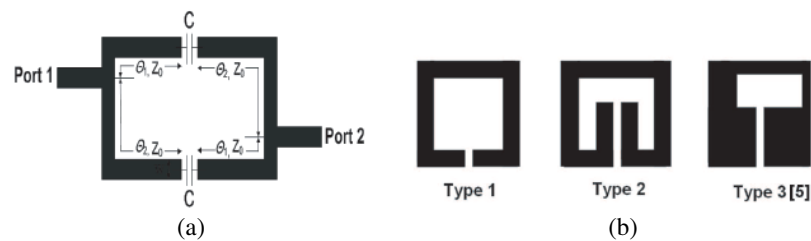


Figure 1: (a) Main dual feeding structure and (b) different topology for resonators.

Table 1: Design specifications of proposed triple passband filter design.

Parameter	Value
Passband 1 Center Frequency (GHz)	1.8
Passband 2 Center Frequency (GHz)	3.6
Passband 3 Center Frequency (GHz)	5.6
Return Loss, S_{11} (dB)	< -15
Passband Insertion Loss, S_{21} (dB)	> -3
Stopband Attenuation (dB)	> 20

–13 dB. The corresponding passband insertion loss S_{21} is approximately –2.5 dB. Attenuation is greater than 20 dB for lower and upper stopband.

Figure 4 shows the fabricated proposed filter using embedded resonators using FR4 substrate with dielectric constant 4.05 and thickness 1.6 mm. Measurement is done using network analyzer and the measured results are shown in Fig. 5.

The best matching S_{11} response for first passband is observed at 1.8 GHz with value less than –10 dB. The corresponding passband insertion loss S_{21} is approximately –1.7 dB. Attenuation is greater than 20 dB for lower and upper stopband. Next, the best matching S_{11} response for second passband is observed at 3.3 GHz with value less than –15 dB. The corresponding passband insertion loss S_{21} is approximately –3.8 dB. Attenuation is greater than 20 dB for lower and upper stopband. Lastly, the best matching S_{11} response for third passband is observed at 5.2 GHz with value less than –15 dB. The corresponding passband insertion loss S_{21} is approximately –5 dB. Attenuation is greater than 20 dB for lower and upper stopband.

4. CONCLUSION

A miniature planar triple passband filter using embedded open-loop resonators has been presented in this paper. With the presence of two transmission zeros, the frequency selectivity and insertion loss is improved. Good agreement is obtained between the simulated and measurement results.

REFERENCES

1. Vegesna, S. and M. Saed, “Microstrip dual-band bandpass and bandstop filters,” *Microw. and Optical Technology Lett.*, Vol. 54, No. 1, 168, Jan. 2012.
2. Lim, Y. T. and K. M. Lum, “A stepped impedance comb-line filter design using defective ground structure for wireless applications,” *PIERS Proceedings*, 598–601, Kuala Lumpur, Malaysia, Mar. 27–30, 2012.
3. Lau, J. W. and K. M. Lum, “Novel M-shaped defected ground structure for spurious suppressed dual mode bandpass filter design,” *PIERS Proceedings*, 583–587, Kuala Lumpur, Malaysia, Mar. 27–30, 2012.
4. Wong, C. Y. and K. M. Lum, “Miniaturized multilayered bandpass filter using microstrip hairpin resonator for C-band application,” *PIERS Proceedings*, 602–605, Kuala Lumpur, Malaysia, Mar. 27–30, 2012.
5. Lek, K. C. and K. M. Lum, “Stepped impedance key-shaped resonator for bandpass and bandstop filters design,” *PIERS Proceedings*, 588–592, Kuala Lumpur, Malaysia, Mar. 27–30, 2012.
6. Lim, P. L. and K. M. Lum, “A novel bandpass filter design using E-shaped resonator and dual square-loop defected ground structure,” *PIERS Proceedings*, 610–614, Kuala Lumpur, Malaysia, Mar. 27–30, 2012.
7. Lee, M. L. and K. M. Lum, “Multilayered miniaturized hairpin resonator for bandpass filter design,” *PIERS Proceedings*, 593–597, Kuala Lumpur, Malaysia, Mar. 27–30, 2012.
8. Ng, K. X. and K. M. Lum, “Compact lowpass filter design using cavity resonator and ladder-shaped defected ground structure,” *PIERS Proceedings*, 606–609, Kuala Lumpur, Malaysia, Mar. 27–30, 2012.
9. Lum, K. M. and C. Free, “A novel traveling-wave feed technique for circularly polarized planar microstrip antennas,” *IEEE International Symposium on Antennas and Propagation*, Vol. 2A, 250–253, Oct. 2005.
10. Lum, K. M., T. Tick, C. Free, and H. Jantunen, “Design and measurement data for a microwave CP antenna using a new travelling-wave feed concept,” *European Microwave Conf.*, Paris, France, Oct. 2005.
11. Lum, K. M., “A novel radiation enhancement technique for multilayer microwave circuits,” *PIERS Proceedings*, 578–582, Kuala Lumpur, Malaysia, Mar. 27–30, 2012.
12. Lum, K. M., C. Laohapensaeng, and C. E. Free, “A novel traveling-wave feed technique for circularly polarized planar antennas,” *IEEE Micro. and Wireless Components Letters*, Vol. 15, No. 3, 180–182, Mar. 2005.
13. Lum, K. M. and C. E. Free, “A novel dual circularly polarized planar and multi-layer LTCC antenna arrays using traveling-wave feed system,” *IEEE Trans. Micro. Theory Tech.*, Vol. 54, No 6, 2880–2886, Jun. 2006.
14. Seow, C. K. and S. Y. Tan, “Localization of omni-directional mobile device in multipath environments,” *Progress In Electromagnetics Research*, Vol. 85, 323–348, 2008.

15. Tai, C. S., S. Y. Tan, and C. K. Seow, “Robust non-line-of-sight localisation system in indoor environment,” *Electronics Letters*, Vol. 46, No. 8, 593–595, Apr. 2010.
16. Seow, C. K. and S. Y. Tan, “Non-line-of-sight unidirectional mobile localisation in multipath environment,” *Electronics Letters*, Vol. 44, No. 2, 141–142, Jan. 2008.
17. Seow, C. K. and S. Y. Tan, “Non-line-of-sight localization in multipath environments,” *IEEE Transactions on Mobile Computing*, Vol. 7, No. 5, 647–660, May 2008.
18. Seow, C. K. and S. Y. Tan, “Localisation of mobile device in multipath environment using bi-directional estimation,” *Electronics Letters*, Vol. 44, No. 7, 485–487, Mar. 2008.

Design of Planar Single-section and Cascaded Directional Filters

Y. H. Choo and K. M. Lum

School of Science and Technology, SIM University, Singapore

Abstract— In the proposed paper, a single-section and cascaded microstrip directional filters is designed for modern communication systems, such as mobile telephony, radiolocation and satellite links. The proposed filter takes on the structure of a Quadrature Hybrid coupler, where a parallel branch is capacitively coupled by two coupling resonators. It also has four ports which are completely match and exhibits a directional and filter-like frequency characteristics. This four-port device has a bandpass response between ports 1 and 4 (S_{41}), and its complementary reject-band response between ports 1 and 2 (S_{21}). No power is transmitted to port 3 (isolation), and none is reflected to port 1. By compensating the line length between the coupling resonators of the single-section directional filter, better performance can be achieved, notably in matching. Furthermore, cascading multiple single-section directional filters will lead to the generation of transmission zeros in the stopband and therefore will sharper the cut-off response characteristics. To validate the proposed directional filter configuration, related analysis, and design theory, a single-section and cascaded microstrip directional filters are designed and fabricated using FR-4 substrate with dielectric constant of 4.05, loss tangent of 0.014 and thickness of 1.6 mm. The overall dimension of the single-section and cascaded directional filter are 74.4 mm by 45 mm, and 122.2 mm by 50 mm respectively. For the single-section directional filter, the best matched measured return loss S_{11} is less than -20 dB around center frequency of 2.35 GHz. Good isolation S_{31} is obtained at values less than -25 dB. The filter response shows a bandstop characteristic with band elimination, S_{21} of -14.03 dB and a bandpass characteristic with coupling S_{41} of -3.64 dB. For the cascaded directional filter, the best matched measured return loss S_{11} is less than -25 dB. The measured S_{21} and S_{41} , are -20.43 dB and -2.74 dB respectively. Power at port 3 is well isolated with S_{31} values of less than -25 dB. The measured filter response showed good agreement with the simulation results. Both simulation and measurement data are presented and discussed.

1. INTRODUCTION

Many had studied to improve and enhance on the performance using different kind of bandpass filter [1–7]. A directional filter is designed to multiplex band of frequencies such that one portion of the band is used for east-to-west transmission and the other portion for west-to-east transmission. It may have several different configurations and geometry and has the following properties [8]: It has no reflection, i.e., when they are terminated in their own characteristic impedances, all the four ports will be matched. It is directional, i.e., signal entering into port 1 emerges at ports 2 and 4, and none at port 3. The transfer function between ports 1 and 2, and that between 1 and 4 are compliments of each other, i.e., if one has a bandpass characteristic, the other has a bandstop characteristic.

It has been known for many years about the principles of combining or separating different microwave channels for interfacing with a single port antenna system [9]. With the growth of satellite communication systems, the greatest technical advances were made in multiplexing structures [10]. There are a number of configurations employed for multiplexing network structures, such as hybrid-coupled, circulator-coupled, manifold filters and directional filters multiplexers [9–14]. The proposed configuration seems particularly suitable for integration with multilayer transceiver antenna modules [15–19] and localization applications [20–24].

2. DIRECTIONAL FILTER DESIGN AND CONCEPT

A single-section and cascaded directional filters can be implemented base on the theoretical concept of a branch-line coupler. Fig. 1 below shows the main configuration of a microstrip directional filter designed with two half-wavelength ($\lambda_g/2$) resonators. To ensure directional filtering effect, this configuration is base on the following assumptions made at the point where a parallel branch is capacitively coupled (at CP_1 , CP_2 , CP_3 and CP_4) is connected [11].

The principle of superposition is used to explain the mechanism of directivity in this filter based on the length of the lines between the coupling points CP_1 and CP_2 (90°), and points CP_3 and CP_4 (270°) [13]. At operating frequency, excitation of ports 1 and 4 at points CP_1 and CP_4 with $V/2$ (even mode) amplitude waves, and excitation of ports 1 and 4 at the same points with waves

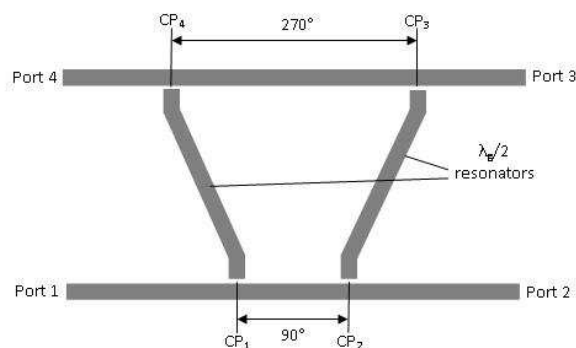


Figure 1: Configuration of microstrip directional filter with coupling resonators.

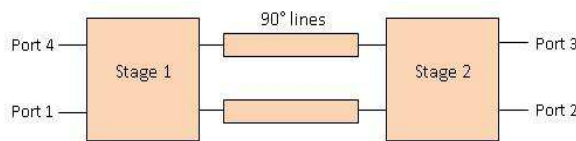


Figure 2: A cascaded two-stage directional filter.

of amplitude $V/2$ and $-V/2$ respectively (odd mode), are equivalent to the excitation of port 1 with a V amplitude wave. The resonator on the right side is excited by the even mode excitation of ports 1 and 4, and reflects $V/2$ amplitude waves at ports 1 and 4. The left resonator is excited by the odd mode excitation, reflecting waves of amplitude $-V/2$ and $V/2$ at ports 1 and 4 respectively. Hence, the amplitude of the wave at port 4 is V , while at ports 1, 2 and 3 is zero. At frequencies outside resonance, the signal entering into port 1 pass to port 2 with zero loss.

Resonator scalability can be realized by cascading the directional filters, operating at the same frequency, with quarter wavelength lines between each stage. Fig. 2 shows a block diagram of a two-stage directional filters with each stage correspond to a single-section directional filter.

The multi-stage design procedure is based on narrow stopband filter theory [14]. Due to the directional characteristic of these filters, a stopband response is obtained between ports 1 and 2 (S_{21}), and its complementary bandpass response is achieved between ports 1 and 4 (S_{41}), so each stage of the multi-pole directional filter from ports 1 to 2, acts as a notch resonator. By cascading several stages connected by 90° lines, it is possible to achieve a multi-pole stopband response between ports 1 and 2 (S_{21}) of the overall structure, and a multi-pole bandpass response generated between ports 1 and 4 (S_{41}) of the complete configuration.

In addition, better performance of single-section directional filters, especially in matching, can be gained by compensating the line length between coupling resonators. Transmission zeros in the stopband can be introduced by cascading identical directional filters, allowing sharper cut-off characteristic and improves the band elimination considerably with little degradation in coupling. The introduced transmission zeros can also be controlled by adjusting the connecting-line lengths between directional filters or the parameters related to the coupling resonators.

3. SIMULATION AND MEASUREMENT RESULTS

Figure 3 shows the design configuration of a single-section microstrip directional filter using FR4 specifications.

By performing compensation and tuning, the optimized electrical characteristics of the two parallel branch and two coupling lines are: $\theta_1 = 305^\circ$, $\theta_2 = 82.7^\circ$, $z_2 = 85.7\Omega$; $\phi_0 = 92.7^\circ$, $z_1 = 109\Omega$ respectively. The filter response of this single-section filter configuration is simulated from 1.5 GHz to 3.5 GHz. The numerical simulation of the filtering characteristics are displayed in Fig. 4.

The return loss (S_{11}) and band elimination (S_{21}) were tuned to center frequency 2.35 GHz. The results show good matching with S_{11} less than -30 dB, band elimination of S_{21} is -14.97 dB and coupling of S_{41} is -2.5 dB. There is also good isolation at S_{31} with values less than -25 dB around the center frequency. The computed 3-dB fractional bandwidth of the S_{21} bandstop response is 8.9%, and the 10-dB fractional bandwidth of the S_{41} bandpass response is 13.6%.

Subsequently, two identical single-section directional filters were cascaded with optimized transmission lines ($\theta_c = 43.2^\circ$) to form a cascaded directional filter design. Its configuration and simulated filtering responses are as shown in Fig. 5 and Fig. 6 respectively.

After cascading two identical directional filters, an improved filter response is achieved, with S_{11} return loss less than -30 dB around center frequency 2.35 GHz. Band elimination of S_{21} is -23.46 dB and isolation S_{31} at port 3 is less than -30 dB and the coupling of S_{41} is approximately

-2 dB. From the S_{41} plot, two transmission zeros, at 1.81 GHz and 3.14 GHz, are introduced nearer to the center frequency as compared to the single-section directional filter. The overall computed 3-dB fractional bandwidth of the S_{21} bandstop response is 16.6%, and the 10-dB fractional bandwidth of the S_{41} bandpass response is 21.7%.

The fabricated filters are depicted in Fig. 7 and the overall dimension of the single-section and cascaded directional filter are 74.4 mm by 45 mm, and 122.2 mm by 50 mm respectively. The

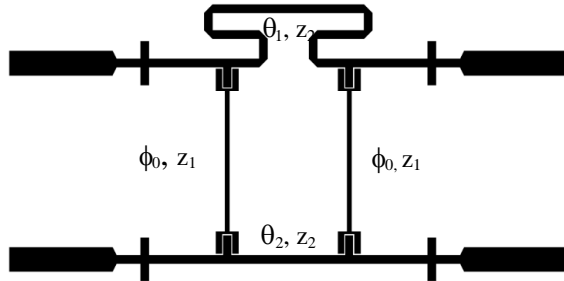


Figure 3: Single-section microstrip directional filter configuration.

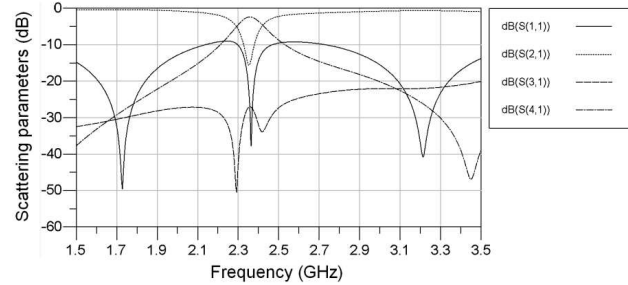


Figure 4: Simulation result of single-section microstrip directional filter.

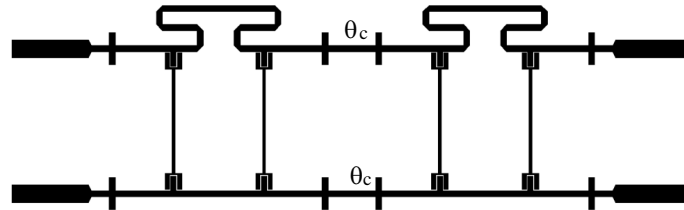


Figure 5: Cascaded microstrip directional filter configuration.

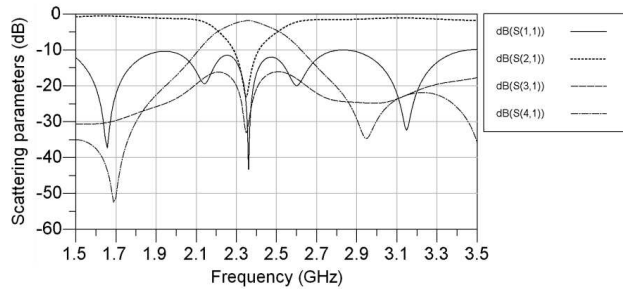


Figure 6: Simulation result of cascaded microstrip directional filter.

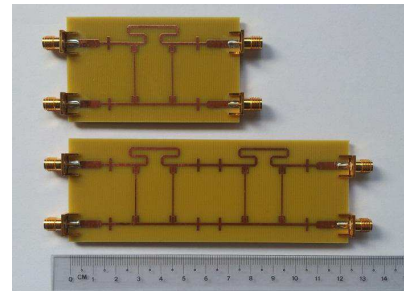
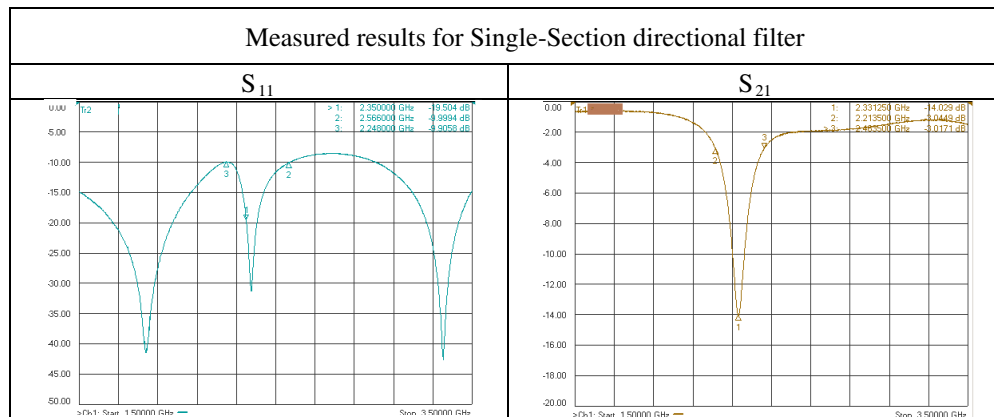


Figure 7: Fabricated directional filters.

Table 1: Measured results of fabricated single-section & cascaded directional filters.



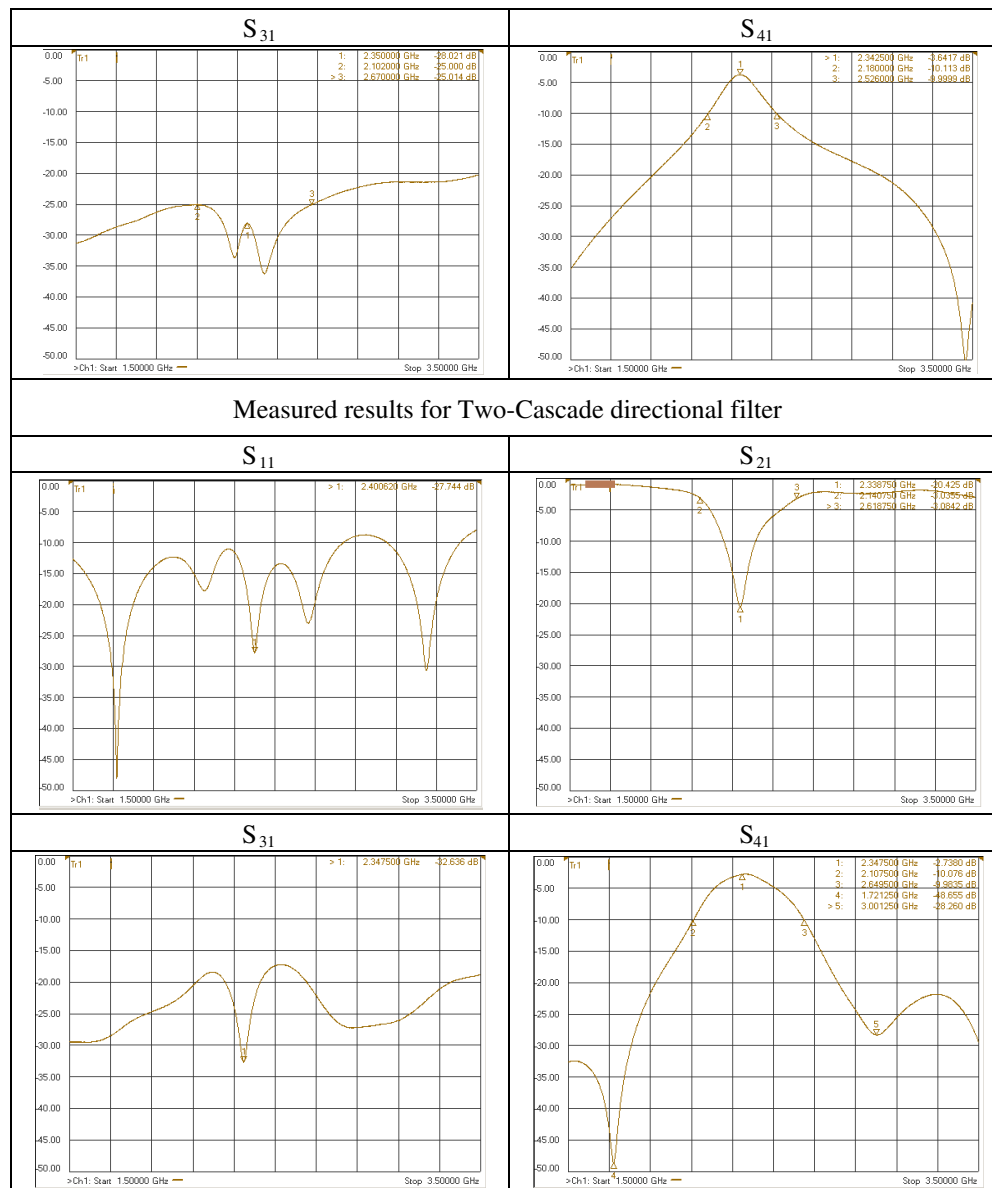


Table 2: Comparison of simulated and measured result of proposed filters.

Test Parameters	Single-Section		Two-Cascade	
	Simulated	Measured	Simulated	Measured
S_{11}	< -30 dB	< -30 dB	< -30 dB	< -25 dB
S_{21}	-14.97 dB	-14.03 dB	-23.46 dB	-20.43 dB
S_{31}	< -25 dB	< -25 dB	> -30 dB	> -30 dB
S_{41}	-2.5 dB	-3.64 dB	-1.71 dB	-2.74 dB

comparison of the simulated and measured results are tabulated in Table 1 and Table 2.

The measured 3-dB fractional bandwidth of the corresponding single-section S_{21} bandstop response is 10.7%, and the 10-dB fractional bandwidth of S_{41} bandpass response is 15%. The measured 3-dB fractional bandwidth of the two-cascade S_{21} bandstop response is 20.5%, and the 10-dB fractional bandwidth of the S_{41} bandpass response is 23%.

4. CONCLUSIONS

An analysis and design of a single-section and cascaded directional filters has been developed, based on approximate and exact microwave circuit analyses. In the single-section directional filter, its

performance is optimised, especially in matching, by compensating the line length between coupling resonators. In addition, by cascading two identical directional filters, higher attenuation in the stopband can be achieved due to the introduction of transmission zeros. By adjusting the connecting-line lengths between directional filters or the parameters related to the coupling resonator, these transmission zeros can be controlled. As a validation check, a single-section and cascaded directional filters was designed and implemented. Good agreement between the measurement and simulation is observed, validating the proposed configuration, related analysis, and design theory.

REFERENCES

1. Wong, C. Y. and K. M. Lum, "Miniaturized multilayered bandpass filter using microstrip hairpin resonator for C-band application," *PIERS Proceedings*, 602–605, Kuala Lumpur, Malaysia, Mar. 27–30, 2012.
2. Lim, P. L. and K. M. Lum, "A novel bandpass filter design using E-shaped resonator and dual square-loop defected ground structure," *PIERS Proceedings*, 610–614, Kuala Lumpur, Malaysia, Mar. 27–30, 2012.
3. Lim, Y. T. and K. M. Lum, "A stepped impedance comb-line filter design using defective ground structure for wireless applications," *PIERS Proceedings*, 598–601, Kuala Lumpur, Malaysia, Mar. 27–30, 2012.
4. Lee, M. L. and K. M. Lum, "Multilayered miniaturized Hairpin resonator for bandpass filter design," *PIERS Proceedings*, 593–597, Kuala Lumpur, Malaysia, Mar. 27–30, 2012.
5. Lek, K. C. and K. M. Lum, "Stepped impedance key-shaped resonator for bandpass and bandstop filters design," *PIERS Proceedings*, 588–592, Kuala Lumpur, Malaysia, Mar. 27–30, 2012.
6. Lau, J. W. and K. M. Lum, "Novel M-shaped defected ground structure for spurious suppressed dual mode bandpass filter design," *PIERS Proceedings*, 583–587, Kuala Lumpur, Malaysia, Mar. 27–30, 2012.
7. Ng, K. X. and K.M. Lum, "Compact lowpass filter design using cavity resonator and ladder-shaped defected ground structure," *PIERS Proceedings*, 606–609, Kuala Lumpur, Malaysia, Mar. 27–30, 2012.
8. Wing, O., "Cascade directional filter," *IRE Trans. Microw. Theory Tech.*, Vol. 7, No. 2, 197–201, Apr. 1959.
9. Wanselow, R. D. and L. P. Tuttle, Jr., "Practical design of strip transmission line half-wavelength resonator directional filters," *IRE Trans. Microw. Theory Tech.*, Vol. 7, No. 1, 168–173, Jan. 1959.
10. Cameron, R. J. and M. Yu, "Design of manifold coupled multiplexers," *IEEE Microwave Magazine*, Oct. 2007.
11. Matthaei, G. L., L. Young, and E. M. T. Jones, *Microwave Filters, Impedance-matching Networks, and Coupling Structures*, Artech House, 1985.
12. Cohn, S. B. and F. S. Coale, "Directional channel-separation filters," *Proceeding of the IRE*, Aug. 1956.
13. Pozar, D. M., *Microwave Engineering*, 2nd Edition, Wiley, New York, 1998.
14. Hong, J.-S. G. and M. J. Lancaster, *Microstrip Filters for RF/Microwave Applications*, John Wiley and Sons, 2001.
15. Lum, K. M., "A novel radiation enhancement technique for multilayer microwave circuits," *PIERS Proceedings*, 578–582, Kuala Lumpur, Malaysia, Mar. 27–30, 2012.
16. Lum, K. M., C. Laohapensaeng, and C. E. Free, "A novel traveling-wave feed technique for circularly polarized planar antennas," *IEEE Micro. and Wireless Components Letters*, Vol. 15, No. 3, 180–182, Mar. 2005.
17. Lum, K. M., T. Tick, C. Free, and H. Jantunen, "Design and measurement data for a microwave CP antenna using a new travelling-wave feed concept," *European Microwave Conf.*, Paris, France, Oct. 2005.
18. Lum, K. M. and C. Free, "A novel traveling-wave feed technique for circularly polarized planar microstrip antennas," *IEEE Antennas and Propag. International Symposium*, Vol. 2A, 250–253, Oct. 2005.
19. Lum, K. M. and C. E. Free, "A novel dual circularly polarized planar and multi-layer LTCC antenna arrays using traveling-wave feed system," *IEEE Trans. Micro. Theory Tech.*, Vol. 54, No. 6, 2880–2886, Jun. 2006.

20. Seow, C. K. and S. Y. Tan, “Localisation of mobile device in multipath environment using Bi-directional estimation,” *Electronics Letters*, Vol. 44, No. 7, 485–487, Mar. 2008.
21. Seow, C. K. and S. Y. Tan, “Non-line-of-sight unidirectional mobile localisation in multipath environment,” *Electronics Letters*, Vol. 44, No. 2, 141–142, Jan. 2008.
22. Tai, C. S., S. Y. Tan, and C. K. Seow, “Robust non-line-of-sight localisation system in indoor environment,” *Electronics Letters*, Vol. 46, No. 8, 593–595, Apr. 2010.
23. Seow, C. K. and S. Y. Tan, “Localization of omni-directional mobile device in multipath environments,” *Progress In Electromagnetics Research*, Vol. 85, 323–348, 2008.
24. Seow, C. K. and S. Y. Tan, “Non-line-of-sight localization in multipath environments,” *IEEE Transactions on Mobile Computing*, Vol. 7, No. 5, 647–660, May 2008.

Wideband Planar Filter Using Signal-interference Techniques

W. W. Hong and K. M. Lum

School of Science and Technology, SIM University, Singapore

Abstract— This paper presents a new wideband planar filter using signal-interference technique. The passband has a center frequency 1.5 GHz. The proposed filter topology has a $50\ \Omega$ input and output port respectively. The core design topology consists of a transversal signal-interference filtering section that embeds a miniature transversal filter. Thus, under signal-interaction principles, the filtering action comes about through the generation of multiple out-of-band power transmission zeros and constructive passband signal combinations. The proposed filter is prototyped using FR4 substrate with a dielectric constant of 4.4, thickness of 1.6 mm, loss tangent of 0.022 and conductor thickness of $35\ \mu\text{m}$. The fabricated structure has a dimensional size of 90 mm by 100 mm. The best matched measured return loss S_{11} is observed at 1.27 GHz with a value less than $-42\ \text{dB}$. The corresponding passband insertion loss S_{21} is approximately $-0.5\ \text{dB}$ with a $-10\ \text{dB}$ bandwidth of 1.2 GHz. The lower and upper stopband attenuation is greater than 40 dB respectively. Both simulation and measurement result are presented and discussed.

1. INTRODUCTION

Filters play important roles in many RF/microwave applications. They are used to separate or combine different frequencies. The electromagnetic spectrum is limited and has to be shared; filters are used to select or confine the radio frequency and microwave signals within assigned spectral limits. Emerging applications such as wireless communications continue to challenge RF/microwave filters with ever more stringent requirements such as higher performance, smaller size, lighter weight, and lower cost. Depending on the requirements and specifications, filters may be designed as lumped element or distributed element circuits; they may be realized in various transmission line structures, such as waveguide, coaxial line, and microstrip.

The design of wideband microwave filters has been a huge challenge over the last few years. Thus, several compact filter realizations exhibiting an extremely large passband bandwidth have been proposed using different technologies such as signal-interference [1]. Generally, planar transmission structures such as microstrip line are widely used because of low cost, compact size, and ease of implementation. Therefore, microstrip is commonly used to design filters.

Many had studied to improve and enhance on the performance using different kind of filters [2–8]. The proposed wideband planar filter configuration seems particularly suitable for integration with multilayer transceiver antenna modules [9–13] and localization applications [14–18].

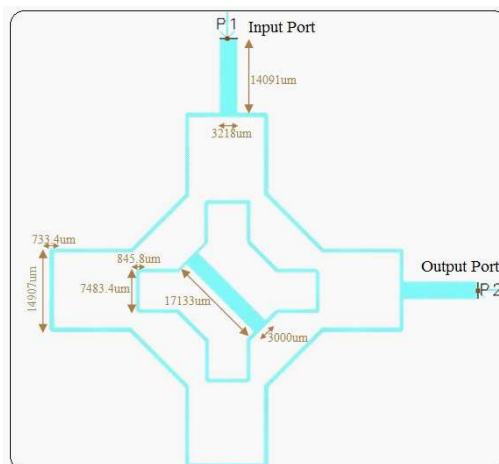


Figure 1: Proposed wideband filter design topology with key dimensional data.

Table 1: Design specifications of proposed wideband filter.

Parameters	Values
Center Frequency (GHz)	1.5
Return Loss, S_{11} (dB)	< -20
Insertion Loss, S_{21} (dB)	> -1
Bandwidth (GHz) at -10 dB	> 1
Stopband Attenuation (dB)	> 30

Table 2: Comparison of simulated and measured results.

Parameters	Simulation	Measurement
Center Frequency (GHz)	1.41	1.27
Return Loss, S_{11} (dB)	-40	-42
Insertion Loss, S_{21} (dB)	-0.35	-0.55
Bandwidth (GHz) at -10 dB	1.3	1.2
Stopband Attenuation (dB)	> 30	> 30

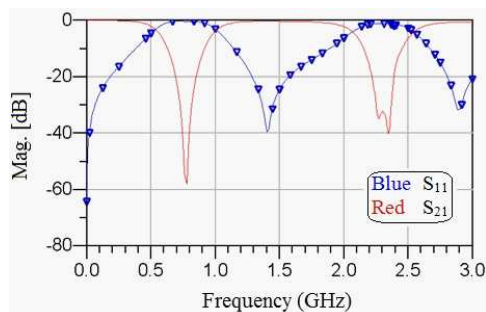
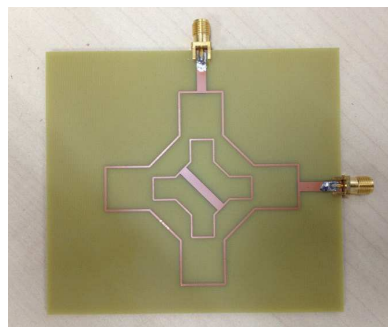
Figure 2: Simulated result for S_{11} and S_{21} .

Figure 3: Photograph of fabricated proposed wideband filter.

2. BANDPASS FILTER DESIGN AND CONCEPT

The proposed wideband planar filter design topology with its key dimensional data is shown in Figure 1. The design is arranged on the top layer laid on a FR4 dielectric substrate. Design specifications of the filter are shown in Table 1. The proposed filter topology has a 50Ω input and output port respectively. The core design topology consists of a transversal signal-interference filtering section that embeds a miniature transversal filter. Thus, under signal-interaction principles, the filtering action comes about through the generation of multiple out-of-band power transmission zeros and constructive passband signal combinations.

3. SIMULATION AND MEASUREMENT RESULT

The simulated result for S_{11} and S_{21} of the proposed wideband filter are shown in Figure 2. The best matched simulated return loss S_{11} is less than -35 dB at 1.41 GHz. The simulated corresponding passband insertion loss S_{21} is approximately -0.35 dB and the bandwidth at -10 dB is 1.3 GHz. The lower and upper stopband attenuation is greater than 30 dB respectively.

The wideband filter is prototyped using FR4 material. The board overall dimensional size is 90 mm by 100 mm. Figure 3 shows the fabricated wideband filter.

Measurement is done using Network Analyzer. As shown in Figure 4, the best matched measured return loss S_{11} is approximately -42 dB at 1.27 GHz and the corresponding S_{21} response is about -0.55 dB. The passband bandwidth at -10 dB is approximately 1.2 GHz. The lower and upper stopband attenuation is greater than -40 dB.

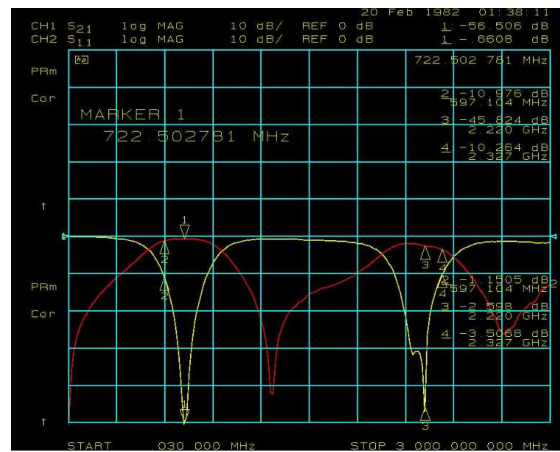


Figure 4: Measured S_{11} and S_{21} response of proposed wideband filter.

4. CONCLUSION

In this paper, a new wideband filter using signal interference techniques is proposed. Simulated and measurement results have shown reasonably good matching S_{11} and S_{21} response. Broad passband bandwidth at -10 dB is also obtained. High attenuation above 30 dB is also obtained at the lower and upper stopband.

REFERENCES

1. Gomez-Garcia, R. and J. I. Alonso, "Design of sharp-rejection and low-loss wide-band planar filters using signal-interference techniques," *IEEE Micro. and Wireless Components Letters*, Vol. 15, No. 8, Aug. 2005.
2. Lim, Y. T. and K. M. Lum, "A stepped impedance COMB-line filter design using defective ground structure for wireless applications," *PIERS Proceedings*, 598–601, Kuala Lumpur, Malaysia, Mar. 27–30, 2012.
3. Lek, K. C. and K. M. Lum, "Stepped impedance key-shaped resonator for bandpass and bandstop filters design," *PIERS Proceedings*, 588–592, Kuala Lumpur, Malaysia, Mar. 27–30, 2012.
4. Lim, P. L. and K. M. Lum, "A novel bandpass filter design using E-shaped resonator and dual square-loop defected ground structure," *PIERS Proceedings*, 610–614, Kuala Lumpur, Malaysia, Mar. 27–30, 2012.
5. Lau, J. W. and K. M. Lum, "Novel M-shaped defected ground structure for spurious suppressed dual mode bandpass filter design," *PIERS Proceedings*, 583–587, Kuala Lumpur, Malaysia, Mar. 27–30, 2012.
6. Lee, M. L. and K. M. Lum, "Multilayered miniaturized hairpin resonator for bandpass filter design," *PIERS Proceedings*, 593–597, Kuala Lumpur, Malaysia, Mar. 27–30, 2012.
7. Ng, K. X. and K. M. Lum, "Compact lowpass filter design using cavity resonator and ladder-shaped defected ground structure," *PIERS Proceedings*, 606–609, Kuala Lumpur, Malaysia, Mar. 27–30, 2012.
8. Wong, C. Y. and K. M. Lum, "Miniaturized multilayered bandpass filter using microstrip hairpin resonator for C-band application," *PIERS Proceedings*, 602–605, Kuala Lumpur, Malaysia, Mar. 27–30, 2012.
9. Lum, K. M. and C. Free, "A novel traveling-wave feed technique for circularly polarized planar microstrip antennas," *IEEE Antennas and Propag. International Symposium*, Vol. 2A, 250–253, Oct. 2005.
10. Lum, K. M., "A novel radiation enhancement technique for multilayer microwave circuits," *PIERS Proceedings*, 578–582, Kuala Lumpur, Malaysia, Mar. 27–30, 2012.
11. Lum, K. M., T. Tick, C. Free, and H. Jantunen, "Design and measurement data for a microwave CP antenna using a new travelling-wave feed concept," *European Microwave Conf.*, Paris, France, Oct. 2005.

12. Lum, K. M., C. Laohapensaeng, and C. E. Free, “A novel traveling-wave feed technique for circularly polarized planar antennas,” *IEEE Micro. and Wireless Components Letters*, Vol. 15, No. 3, 180–182, Mar. 2005.
13. Lum, K. M. and C. E. Free, “A novel dual circularly polarized planar and multi-layer LTCC antenna arrays using traveling-wave feed system,” *IEEE Trans. Micro. Theory Tech.*, Vol. 54, No. 6, 2880–2886, Jun. 2006.
14. Seow, C. K. and S. Y. Tan, “Localization of omni-directional mobile device in multipath environments,” *Progress In Electromagnetics Research*, Vol. 85, 323–348, 2008.
15. Seow, C. K. and S. Y. Tan, “Localisation of mobile device in multipath environment using bi-directional estimation,” *Electronics Letters*, Vol. 44, No. 7, 485–487, Mar. 2008.
16. Tai, C. S., S. Y. Tan, and C. K. Seow, “Robust non-line-of-sight localisation system in indoor environment,” *Electronics Letters*, Vol. 46, No. 8, 593–595, Apr. 2010.
17. Seow, C. K. and S. Y. Tan, “Non-line-of-sight localization in multipath environments,” *IEEE Transactions on Mobile Computing*, Vol. 7, No. 5, 647–660, May 2008.
18. Seow, C. K. and S. Y. Tan, “Non-line-of-sight unidirectional mobile localisation in multipath environment,” *Electronics Letters*, Vol. 44, No. 2, 141–142, Jan. 2008.

Planar Bandpass Filter Design Using Transversal Filtering

K. K. Oh and K. M. Lum

School of Science and Technology, SIM University, Singapore

Abstract— A new microwave single-passband planar filter using transversal filtering is presented. The proposed filter consists of transversal filtering sections. Three identical transversal sections are cascaded between the $50\ \Omega$ input and output terminations and two addition stubs are implemented at the input and output transmission line. These stubs vividly reduce the insertion losses. The center frequency of the proposed bandpass filter is 2.6 GHz. It is prototyped on FR4 substrate with dielectric constant 4.05, loss tangent 0.014 and thickness $1600\ \mu\text{m}$. The overall dimensional size is 72 mm by 46 mm. Best measured matching return loss S_{11} is observed at 2.6 GHz with a value less than $-15\ \text{dB}$. The passband insertion loss S_{21} is approximately $-2.5\ \text{dB}$. Attenuation for the lower stopband and upper stopband is greater than 40 dB respectively. Both simulation and measurement results are presented and discussed.

1. INTRODUCTION

With the increasing demand of wireless communication devices, the main key component is to improve the performance and reduce the circuit size of the filter. This had become the key challenge in order to emerge into the market today.

Many of the studied [1–7] had show the improvement and enhancement on the performance using different kind of filter such as conventional microstrip bandpass filter, parallel coupled half-wavelength resonator filters, hairpin-line filters, open-stub filter and many more. Filter using stub-loaded structure have a good selectivity for transmission zero that are close to the passband. Hence radial stub is being implemented as it is dimension is shorter compare to the equivalent transmission line. The proposed configuration seems particularly suitable for integration with multilayer transceiver antenna modules [8–12] and localization applications [13–17].

2. BANDPASS FILTER DESIGN AND CONCEPT

Design specifications of the proposed single passband filter are highlighted in Table 1 and the layout is presented in Figure 1. The single-passband filter consists of three identical transversal sections serially-cascaded between the $50\ \Omega$ input and output terminations. A microstrip stub is integrated

Table 1: Design specifications of bandpass filter.

Parameters	Value
Center Frequency	2.6 GHz
Return Loss, S_{11}	$< -100\ \text{dB}$
Passband Insertion Loss, S_{21}	$> -2\ \text{dB}$
Passband Bandwidth	$> 500\ \text{MHz}$
Stopband attenuation	$> 30\ \text{dB}$

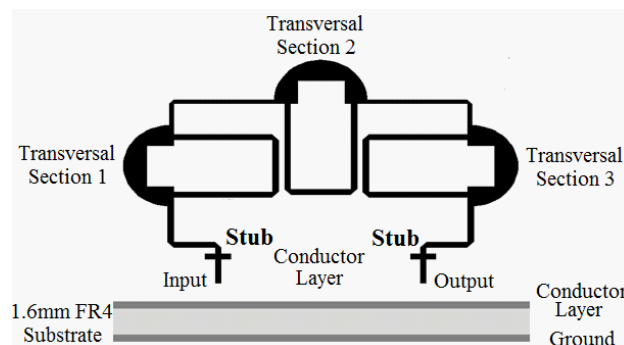


Figure 1: Design topology of proposed bandpass filter.

into the two microstrip transmission lines feeding the input and output terminations to achieve a better insertion loss.

3. SIMULATION AND MEASUREMENT RESULT

The simulated results for the propose passband filter are shown in Figure 3. The center frequency of the passband is observed at 2.7 GHz with S_{11} value less than -15 dB. The corresponding passband insertion loss S_{21} is approximately -1.7 dB. Passband bandwidth at -10 dB is 800 MHz. Attenuation is greater than 40 dB for lower and upper stopband respectively.

The proposed bandpass filter was fabricated on FR4 with dielectric constant 4.05, loss tangent 0.014 and thickness 1.6 mm as shown in Figure 4. The overall dimensional size is 72 mm by 46 mm.

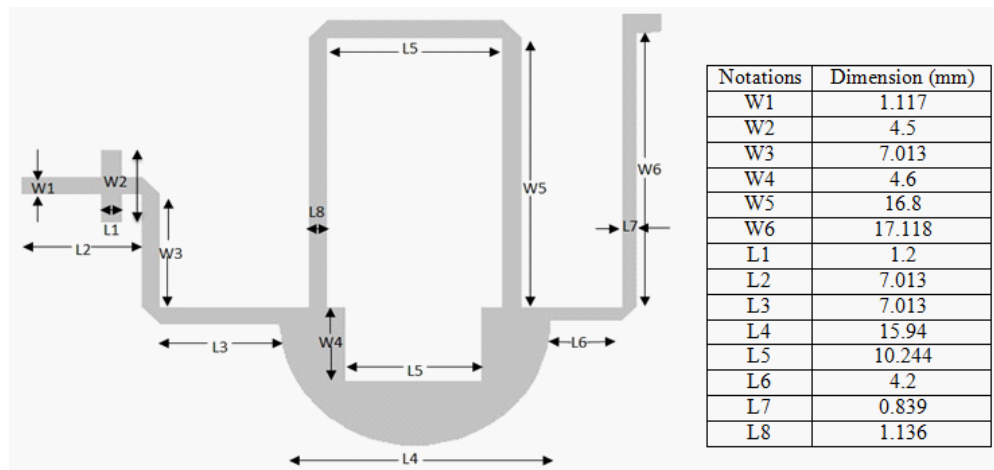


Figure 2: Key dimensional data of proposed bandpass filter.

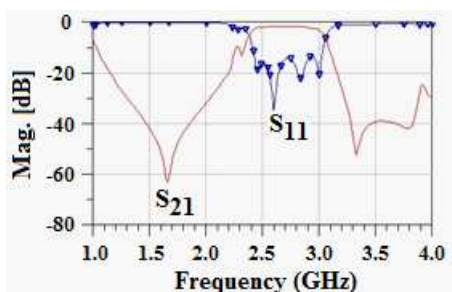


Figure 3: Simulated S_{11} and S_{21} response of proposed bandpass filter.

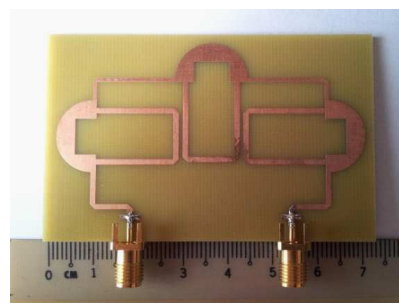


Figure 4: Fabricated bandpass filter.

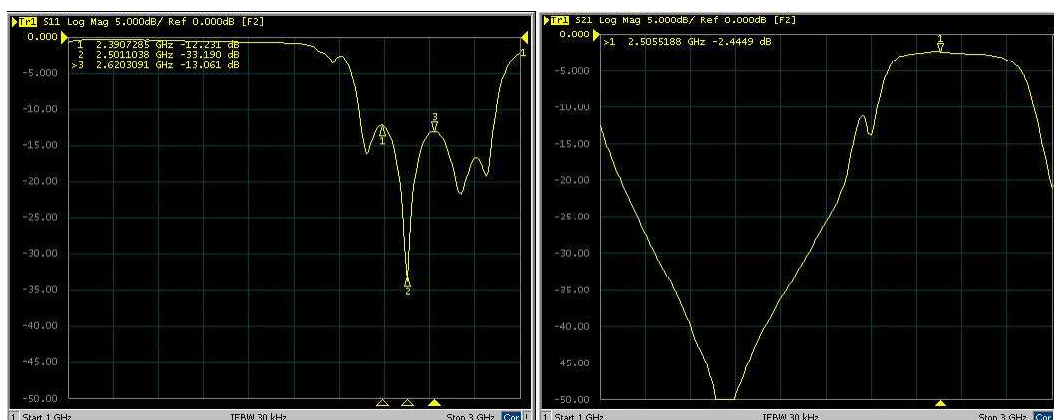


Figure 5: Measured S_{11} and S_{21} response of proposed bandpass filter.

Table 2: Comparison of simulated and measured result of proposed bandpass filter.

Key Parameters	Simulation	Measurement
Center Frequency (GHz)	2.7	2.6
Return Loss, S_{11} (dB)	< -15	< -15
Insertion Loss, S_{21} (dB)	-1.7	-2.5
Passband Bandwidth (MHz) at -10 dB	800	700
Stopband attenuation (dB)	> 40	> 40

Measurement is carried out using network analyzer. As presented in Figure 5, center frequency of the passband is observed at 2.6 GHz with S_{11} value less than -15 dB. The corresponding passband insertion loss S_{21} is approximately -2.5 dB. Passband bandwidth at -10 dB is 700 MHz. Attenuation is greater than 40 dB for lower and upper stopband respectively.

The presence of the degeneration in S_{21} response could be due to the accuracy of the fabrication. However, it is still clearly evident that good agreement exists between the overall simulated and measured results. The comparison is presented in Table 2.

4. CONCLUSION

In this paper, a new bandpass filter using identical transversal sections is proposed. Good agreement is presented between the simulated and measurement results and broad passband bandwidth of 700 MHz is obtained at -10 dB. High attenuation above 30 dB is also obtained at the lower and upper stopband.

REFERENCES

1. Lau, J. W. and K. M. Lum, "Novel M-shaped defected ground structure for spurious suppressed dual mode bandpass filter design," *PIERS Proceedings*, 583–587, Kuala Lumpur, Malaysia, Mar. 27–30, 2012.
2. Lee, M. L. and K. M. Lum, "Multilayered miniaturized hairpin resonator for bandpass filter design," *PIERS Proceedings*, 593–597, Kuala Lumpur, Malaysia, Mar. 27–30, 2012.
3. Wong, C. Y. and K. M. Lum, "Miniaturized multilayered bandpass filter using microstrip hairpin resonator for C-band application," *PIERS Proceedings*, 602–605, Kuala Lumpur, Malaysia, Mar. 27–30, 2012.
4. Lim, Y. T. and K. M. Lum, "A stepped impedance comb-line filter design using defective ground structure for wireless applications," *PIERS Proceedings*, 598–601, Kuala Lumpur, Malaysia, Mar. 27–30, 2012.
5. Lek, K. C. and K. M. Lum, "Stepped impedance key-shaped resonator for bandpass and bandstop filters design," *PIERS Proceedings*, 588–592, Kuala Lumpur, Malaysia, Mar. 27–30, 2012.
6. Lim, P. L. and K. M. Lum, "A novel bandpass filter design using E-shaped resonator and dual square-loop defected ground structure," *PIERS Proceedings*, 610–614, Kuala Lumpur, Malaysia, Mar. 27–30, 2012.
7. Ng, K. X. and K. M. Lum, "Compact lowpass filter design using cavity resonator and ladder-shaped defected ground structure," *PIERS Proceedings*, 606–609, Kuala Lumpur, Malaysia, Mar. 27–30, 2012.
8. Lum, K. M., T. Tick, C. Free, and H. Jantunen, "Design and measurement data for a microwave CP antenna using a new travelling-wave feed concept," *European Microwave Conf.*, Paris, France, Oct. 2005.
9. Lum, K. M., "A novel radiation enhancement technique for multilayer microwave circuits," *PIERS Proceedings*, 578–582, Kuala Lumpur, Malaysia, Mar. 27–30, 2012.
10. Lum, K. M. and C. Free, "A novel traveling-wave feed technique for circularly polarized planar microstrip antennas," *IEEE Antennas and Propag. International Symposium*, Vol. 2A, 250–253, Oct. 2005.
11. Lum, K. M., C. Laohapensaeng, and C. E. Free, "A novel traveling-wave feed technique for circularly polarized planar antennas," *IEEE Micro. and Wireless Components Letters*, Vol. 15, No. 3, 180–182, Mar. 2005.

12. Lum, K. M. and C. E. Free, “A novel dual circularly polarized planar and multi-layer LTCC antenna arrays using traveling-wave feed system,” *IEEE Trans. Micro. Theory Tech.*, Vol. 54, No. 6, 2880–2886, Jun. 2006.
13. Tai, C. S., S. Y. Tan, and C. K. Seow, “Robust non-line-of-sight localisation system in indoor environment,” *Electronics Letters*, Vol. 46, No. 8, 593–595, Apr. 2010.
14. Seow, C. K. and S. Y. Tan, “Localisation of mobile device in multipath environment using bi-directional estimation,” *Electronics Letters*, Vol. 44, No. 7, 485–487, Mar. 2008.
15. Seow, C. K. and S. Y. Tan, “Non-line-of-sight localization in multipath environments,” *IEEE Transactions on Mobile Computing*, Vol. 7, No. 5, 647–660, May 2008.
16. Seow, C. K. and S. Y. Tan, “Non-line-of-sight unidirectional mobile localisation in multipath environment,” *Electronics Letters*, Vol. 44, No. 2, 141–142, Jan. 2008.
17. Seow, C. K. and S. Y. Tan, “Localization of omni-directional mobile device in multipath environments,” *Progress In Electromagnetics Research*, Vol. 85, 323–348, 2008.

Performance of MIMO RADAR Using Two-way MUSIC

Pasan De Silva^{1,2} and Chee Kiat Seow^{1,2}

¹School of Science and Technology, SIM University, Singapore

²Nanyang Technological University, Singapore

Abstract— Multiple Input Multiple Output (MIMO) concept have been a prevalent technology in the wireless communication system (IEEE 802.11n and 4G), as it helps to increase transmit power and data throughput by array gain and diversity gain, while reducing multipath fading. In recent years, the concept of MIMO technology has been exploited for outdoor RADAR system for direction finding of targets besides using the conventional mono-static and bi-static radar system. Direction finding subspace algorithms such as MUSIC, ESPRIT have been often used to estimate the angle of arrival (AOA) of signal path that has been transmitted from the single element transmitters.

In this paper, we explore using the MUSIC algorithm for direction finding of the target in the space for RADAR system equipped with antenna array at both transmitter and receiver. This algorithm is known as Two-way MUSIC for MIMO RADAR system. We will assess the performance of the Two-way MUSIC algorithm for MIMO RADAR such as the advantages and limitations in terms of maximum number of target elements that can be detected for given number of transmitters and receivers. We will also explore the optimum performance of the system for different practical scenarios.

1. INTRODUCTION

Due to the inefficiency of the current RADAR systems to detect multiple targets, MIMO RADAR concept has been explored by scientists and engineers using numerous methods and algorithms. Two-way MUSIC comes handy out of other algorithms because of its ability to perform well in the presence of noise and target Radar Cross Section (RCS), which is a nuisance in other methods. Brief description and a derivation for MIMO concept and Two-way MUSIC algorithm are presented in the section below.

2. MIMO RADAR CONCEPT AND TWO-WAY MUSIC

MIMO RADAR concept was introduced to the world through Multistatic RADAR systems. The integration of MIMO concept used in communications systems with Multistatic RADAR system gave rise to the MIMO RADAR system. One reason behind the success achieved by MIMO RADAR Systems is the usage of multiple antennas for both transmitting and receiving purpose [1, 2].

When MIMO concept is being approached through Two-way MUSIC system, a key factor to be taken care of is the ability to detect different received signals with respect to different transmitters. In order to achieve that, orthogonality of the transmitted signals is adapted. In other words, antennae will transmit signals with orthogonality among them [1], so that through match filters at the receiver end, it is capable of identifying which transmitter transmit particular signal. Different transmitted signals \mathbf{S} , from different transmitters are shown in Figure 1. This is a key requirement when Two-way MUSIC algorithm is implemented to the MIMO RADAR system.

In order to derive the Two-way MUSIC algorithm, it's required to model the MIMO RADAR concept along with transmitters, receiver and targets, as given in Figure 2. For the purpose of identifying the transmitted signals emitted by different transmitters, orthogonal signals will be tagged with the transmitted steering vectors, given in Equation (1), with θ_t as Angle Of Departures (AOD), and θ_r the Angle Of Arrivals (AOA). Mt is the number of transmitters and Mr is the number of receivers. And λ is the wavelength of the transmitted signals [1, 5].

$$\begin{aligned} \mathbf{T}(\theta_t) &= \left[1e^{j2\pi \sin(\theta_t)*dt/\lambda} \ e^{j2\pi \sin(\theta_t)*2dt/\lambda} \ \dots \ e^{j2\pi \sin(\theta_t)*(Mt-1)dt/\lambda} \right]^T \\ \mathbf{T} &= [\mathbf{T}(\theta_{t1}), \ \mathbf{T}(\theta_{t2}), \ \dots, \ \mathbf{T}(\theta_{tQ})] \end{aligned} \quad (1)$$

Same way the receiving steering vector can be defined as explained in the Equation (2).

$$\begin{aligned} \mathbf{R}(\theta_r) &= \left[1e^{j2\pi \sin(\theta_r)*dr/\lambda} \ e^{j2\pi \sin(\theta_r)*2dr/\lambda} \ \dots \ e^{j2\pi \sin(\theta_r)*(Mr-1)dr/\lambda} \right]^T \\ \mathbf{R} &= [\mathbf{R}(\theta_{r1}), \ \mathbf{R}(\theta_{r2}), \ \dots, \ \mathbf{R}(\theta_{rQ})] \end{aligned} \quad (2)$$

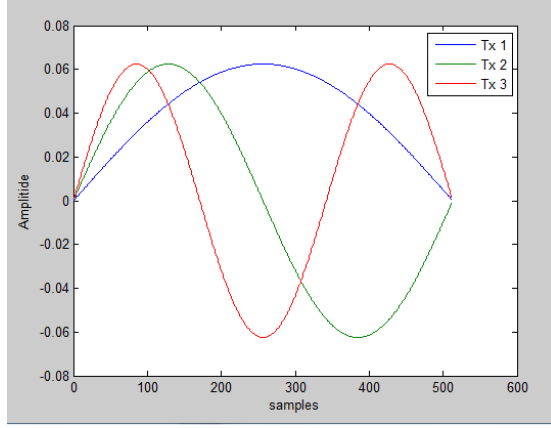


Figure 1: Transmitted signals from respective transmitters.

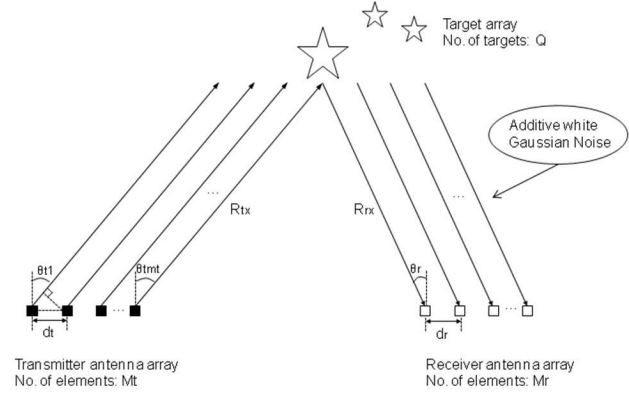


Figure 2: MIMO RADAR concept in Mathematical descriptive way.

And the target can be modeled by its reflection coefficient or RCS ζ , which is a complex random variable as shown in Equation (3). And Q is the number of targets [1, 2, 5].

$$\mathbf{\Sigma} = \left(1/\sqrt{2}Q\right) \text{diag}(\zeta_1, \dots, \zeta_Q) \quad (3)$$

By combining transmitting, receiving steering vectors and target model, the received signal can be modeled with the addition of Additive White Gaussian Noise, \mathbf{W} , which is also known as AWGN.

$$\mathbf{H} = \mathbf{R}\mathbf{\Sigma}(\mathbf{T})^T \mathbf{S} + \mathbf{W} \quad (4)$$

After passing through the matching filters of the receivers, the transmitted signal \mathbf{S} , where $\mathbf{S} = [s_0, s_1, \dots, s_{Mt-1}]$, and $s_i(t) = e^{jw_i t}$, will be cancelled off from the received signals. And the received signals can be rearranged in matrix format as in Equation (5), where N is the number of samples and \mathbf{C}^T is vectorised target RCS, and \mathbf{Z} is vectorised AWGN.

$$\mathbf{X}\mathbf{v} = 1/N^*(\mathbf{T} \odot \mathbf{R})\mathbf{C}^T + \mathbf{Z} \quad (5)$$

where \odot means Khatri-Rao product and $\mathbf{C}^T = [\mathbf{\Sigma}\mathbf{v}_1^T, \mathbf{\Sigma}\mathbf{v}_2^T, \dots, \mathbf{\Sigma}\mathbf{v}_{Mp}^T]$, where Mp is the number of samples, the covariance matrix will be created as given in the Equation (6) [5].

$$\mathbf{R}_{\mathbf{X}\mathbf{X}} = (\mathbf{X}\mathbf{v}\mathbf{X}\mathbf{v}^H) \quad (6)$$

Then the Eigen decomposition will be performed on the covariance matrix as given by the Equation (7), in order to separate signal Eigenvalues (v) and noise Eigenvalues (σ^2) and \mathbf{D} will be respective Eigenvectors [5].

$$\mathbf{R}_{\mathbf{X}\mathbf{X}} = \mathbf{D}\mathbf{V}\mathbf{D}^H = \mathbf{D}(\mathbf{v} + \sigma^2\mathbf{I})\mathbf{D}^H = \mathbf{D} \begin{bmatrix} v_1 + \sigma^2 & 0 & \dots & 0 & 0 & \dots & 0 \\ 0 & v_2 + \sigma^2 & \dots & 0 & 0 & \dots & 0 \\ \vdots & \vdots & \ddots & \vdots & \vdots & \vdots & \vdots \\ 0 & 0 & \dots & v_Q + \sigma^2 & 0 & \dots & 0 \\ 0 & 0 & \dots & 0 & \sigma^2 & \dots & 0 \\ \vdots & \vdots & \vdots & \vdots & \vdots & \ddots & \vdots \\ 0 & 0 & \dots & 0 & 0 & \dots & \sigma^2 \end{bmatrix} \mathbf{D}^H \quad (7)$$

So at the end, the spectrum for Two-way MUSIC can be defined as the reciprocal of the product of steering vectors and noise Eigenvectors \mathbf{D}_N , as given in the Equation (8) where $\mathbf{T}\mathbf{R} = \mathbf{T} \odot \mathbf{R}$ [1, 5]. As the Eigenvalues of \mathbf{D}_N are equal or close to zero, a spike can be observed in the pseudo spectrum where $\theta_t = \text{AOA}$, and $\theta_r = \text{AOD}$. In other words, the spike points to the location of targets.

$$P_{2way-MUSIC}(\theta_t, \theta_r) = \frac{1}{\mathbf{T}\mathbf{R}(\theta_t, \theta_r)^H \mathbf{D}_N \mathbf{D}_N^H \mathbf{T}\mathbf{R}(\theta_t, \theta_r)} \quad (8)$$

3. RESULTS AND DISCUSSIONS

The simulation was carried out under different environments in order to find out the performance as well as limitation of Two-way MUSIC when implemented in MIMO RADAR. All the results were simulated with 3 transmitters and 3 receivers. And the system can perform at a reasonable transmit power of 50–100 kW [8], and can detect targets located at a distance of 6–8 km. The operating frequency, or in other words carrier frequency is 2 GHz. The 3 different environments that the simulation results presented are scattered targets, linear targets (when the magnitude of AOA and AOD are the same), and either the AOA or AOD repeats more than 2 times.

3.1. Maximum Number of Targets

The maximum number of targets can be detected depends on the Eigen structure created. In the absence of noise, for 3×3 system, it can be detected up to 8 targets or $(M_t * M_r - 1)$ as only one noise Eigenvector is sufficient to generate the pseudo spectrum, as shown in the Figure 3. But in the presence of noise and path loss factor, as shown in the Figure 4, it is required at least 2 noise Eigenvectors to generate the pseudo spectrum, so that only 7 targets or $(M_t * M_r - 2)$ can be detected.

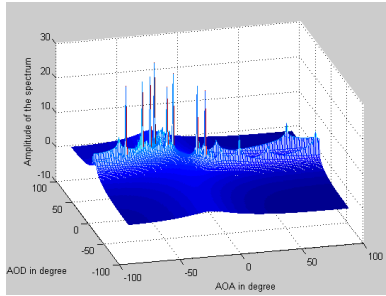


Figure 3: Maximum number of targets = 8 in the absence of noise and path loss.

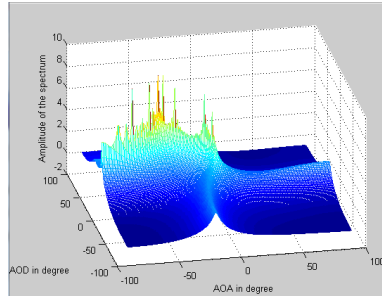


Figure 4: Maximum number of targets = 7 in the presence of noise and path loss.

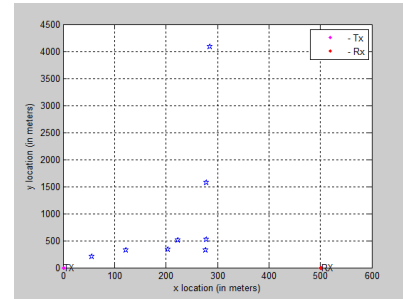


Figure 5: Physical location of the targets.

3.2. Linear Target (Magnitude of AOA and AOD are the Same)

When the magnitude of the AOA and AOD are the same, it can be detected only 4 targets, which is $(M_r + M_r - 2)$, as shown in the Figure 6. This is due to the unique behavior when combined steering vector is generated using Kronecker product. And it ultimately results in decreasing the rank of the matrix and therefore required more the 2 noise Eigenvectors for the detection of the targets and to generate the pseudo spectrum [5, 7].

3.3. When AOA or AOD Repeats

When AOA or AOD repeats more than two times, the rank for the transmitting and or receiving steering matrix will decrease and fail to detect the all the 7 targets. Instead, only 4 peaks can be observed, as shown in the Figure 8 [5, 7]. This is due to the drop in the rank of steering vectors. In other words, it follows the Kruskal's uniqueness [5, 7].

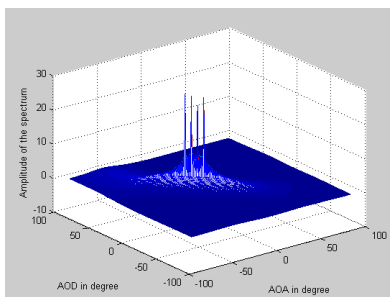


Figure 6: Maximum number of targets when the magnitude of AOA and AOD the same.

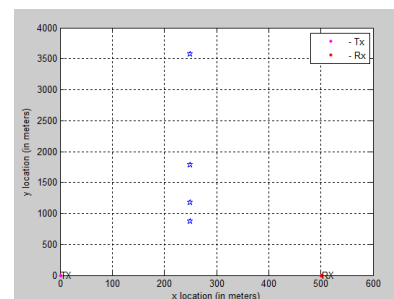


Figure 7: Physical location of the targets.

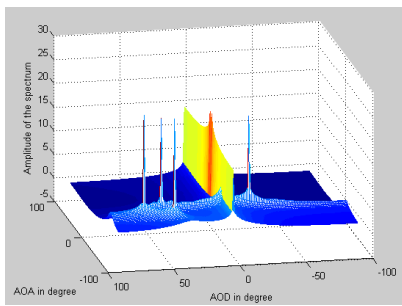


Figure 8: When AOA or AOD repeats more than two times.

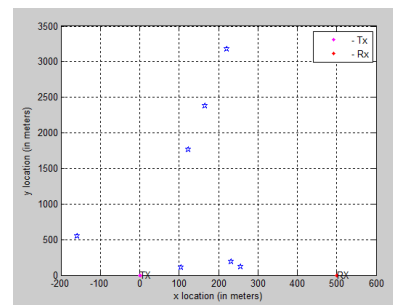


Figure 9: Physical location of the targets.

4. CONCLUSION

So it can be concluded that Two-way MUSIC algorithm is a viable solution to be implemented in MIMO RADAR system, which can be used in the systems such as Military RADAR and airport surveillance RADAR systems, with some limitations to be explored further.

REFERENCES

1. Fishler, E. and A. Haimovich, "MIMO radar: An idea whose time has come," *Proceedings of the IEEE Radar Conference*, Vol. 2, 71–78, Honolulu, Hawaii, USA, Apr. 2004.
2. Gogineni, S. and A. Nehorai, "Target estimation using sparse modeling for distributed MIMO radar," *IEEE Trans. Signal Processing*, Vol. 59, 5315–5325, Nov. 2011.
3. Hassanien, A. and S. A. Vorobyo, "Transmit/receive beamforming for MIMO radar with collocated antennas," *IEEE Transaction on Acoustic, Speech and Signal Processing*, 2089–2092, 2009.
4. Nageswara Rao, T. and V. Srinivasa Rao, "Implementation of MUSIC algorithm for a smart antenna system for mobile communications," *International Journal of Scientific and Engineering Research*, Vol. 2, No. 12, Dec. 2011.
5. Sidiropoulos, N. D. and R. Bro, "On the uniqueness of multilinear decomposition of n-way arrays," *Journal of Chemometrics*, Vol. 14, 229–239, 2000.
6. Adve, R., "Direction of arrival estimation," utoronto.ca, <http://www.comm.utoronto.ca/~rsa-dve/Notes/DOA.pdf>.
7. De Lathauwer, L., "A link between the canonical decomposition in multilinear algebra and simultaneous matrix diagonalization," *SIAM J. Matrix Anal. Appl.*, Vol. 28, No. 3, 642–666, 2006.
8. Szolnok, M. I., *Introduction to RADAR Systems*, 3rd Edition, McGraw-Hill Education, Asia, 2001.

On Multi-antenna Systems for Wireless Transmission Mediums

Mário Marques da Silva^{1,2}, Rui Dinis^{1,3}, and Américo Correia^{1,4}

¹Instituto de Telecomunicações, Portugal

²Universidade Autónoma de Lisboa, Portugal

³DEE-FCT-UNL, Portugal

⁴ISCTE-IUL, Portugal

Abstract— Current and emergent services are demanding higher data rates, improved spectral efficiency and increased network capacity. To face this new requirements, it is important to find schemes able to reduce the effects of fading and explore new types of diversity.

The current work performs a comparison between different multi-antenna techniques that can be employed to achieve the requirements of the Fourth Generation Cellular Systems (4G). The described schemes are studied at the link and system level using Bit Error Rate as the performance index.

1. INTRODUCTION

The use of multiple antennas at both the transmitter and receiver aims to improve performance or to increase symbol rate of systems, but it usually requires a higher implementation complexity. The antenna spacing must be larger than the coherence distance to ensure independent fading across different antennas elements [1, 2]. Alternatively, different antennas should use orthogonal polarizations to ensure independent fading across different antennas.

Multi-antenna systems are used in order to push the performance or capacity/throughput limits as high as possible without an increase of the spectrum bandwidth, although at the cost of an obvious increase of complexity. In the case of frequency selective fading channel, different symbols suffer from interference from each other, whose effect is usually known as Intersymbol Interference (ISI). This effect tends to increase with the used bandwidth. By exploiting diversity, multi-antenna systems can be employed to mitigate the effects of ISI.

The various multi-antenna configurations are referred to as Single Input Single Output (SISO), Multiple Input Single Output (MISO), Single Input Multiple Output (SIMO) or Multiple Input Multiple Output (MIMO). The SIMO and MISO architectures are forms of receive and transmit diversity schemes, respectively. MIMO architectures can be used for combined transmit and receive diversity, for the parallel transmission of data or for spatial multiplexing. When used for spatial multiplexing, MIMO technology promises high bit rates in a narrow bandwidth. Therefore, it is of high significance to spectrum users. In this case, MIMO system considers the transmission of different signals from each transmit antenna element so that the receiving antenna array receives a superposition of all transmitted signals.

The multiple-antenna techniques may present the following configurations:

- Space-time block coding (STBC).
- Multi-layer Transmission.
- Space Division Multiple Access (SDMA).
- Beamforming.

Although STBC is essentially a MISO system, the use of receive diversity makes it a MIMO, which corresponds to the most common configuration for this type of diversity. STBC based schemes focus on achieving a performance improvement through the exploitation of additional diversity, while keeping the symbol rate unchanged [2, 3]. On the other hand, multi-layer Transmission and SDMA belong to another group, entitled spatial multiplexing (SM), whose principles are similar but whose purposes are quite different. The goal of the MIMO based on multi-layer transmission scheme is to achieve higher data rates in a given bandwidth, whose increase rate corresponds to the number of transmit antennas [1]. In this case, the number of receive antennas must be equal or higher than the number of transmit antennas. The increase of symbol rate is achieved by “steering” the receive antennas to each one (separately) of the transmit antennas, in order to receive the corresponding data stream [5, 6]. This is achieved through the use of the nulling algorithm. Finally, the beamforming is implemented by antenna array with certain array elements

at the transmitter or receiver being closely located to form a beam array (typically half wavelength). This scheme is an effective solution to maximize the Signal-to-Noise Ratio (SNR), as it steers the transmit (or receive) beam towards the receiver (or transmitter) [4]. As a result, an improved performance or coverage can be achieved with beamforming.

1.1. Single-User MIMO and Multi-User MIMO

The MIMO techniques previously exposed are typically employed in the concept of Single-User MIMO (SU-MIMO). SU-MIMO considers data being transmitted from a single user into another individual user. An alternative concept is the Multi-User MIMO (MU-MIMO) where multiple streams of data are simultaneously allocated to different users, using the same frequency bands.

The approach behind MU-MIMO is similar to SDMA. Nevertheless, while SDMA is typically employed in the uplink (because the nulling algorithm requires higher number of antennas), the MU-MIMO can also be implemented in the downlink. This allows sending different data streams into different User Equipments (UE). In this case, instead of performing the nulling algorithm at the receiver side, the nulling algorithm is performed using a pre-coding approach at the transmitter side (BS). This is possible because the BS can accommodate a high number of transmit antennas and the UE can only accommodate a single or reduced number (lower) of receive antennas. In the downlink of a MU-MIMO configuration, the number of transmit antennas must be higher than the number of multiple data streams that is sent to multiple users, at the same time and occupying the same frequency bands (the opposite of the SDMA approach). In this configuration, the nulling algorithm is implemented at the transmitter side using a pre-processing algorithm such as Zero Forcing (ZF), Minimum Mean Square Error (MMSE), dirty paper coding, etc.. Alternatively, instead of implementing the above described spatial multiplexing principle, the MU-MIMO can be performed using the beamforming algorithm. In any case, MU-MIMO requires accurate downlink Channel State Information (CSI) at the transmitter side. Obtaining CSI is trivial using Time Division Duplexing (TDD) mode, being more difficult to be achieved when Frequency Division Duplexing (FDD) is employed. In FDD mode, CSI is normally obtained using a feedback link in the opposite direction.

Note that when the aim relies on achieving a performance improvement, a SU-MIMO is normally employed using an algorithm such as STBC. On the other hand, when the aim is to achieve higher throughputs using a constrained spectrum, we have two options: in the downlink, the MU-MIMO is typically the solution; in the uplink, SDMA is normally employed.

It is worth noting that users located at the cell edge, served by MU-MIMO, may experience a SNR degradation due to inter-cell interference, inter-user interference¹, additional path loss or due to limited BS transmit power (which results from the use of a pre-coding). A mechanism that can be implemented to mitigate such limitation is to employ a dynamic MIMO system, where MU-MIMO is employed everywhere, except at the cell edge. In this location, the BS switches into SU-MIMO, which translates in an improvement of performance [7]. Alternatively, base station cooperation is known as an effective mechanism which improves the performance at the cell edge, resulting in a more homogenous service quality, regardless the users' positions.

This paper is organized as follows: different MIMO systems are described in Section 2; in Section 3 a set of performance results is presented; finally, Section 4 summarizes this paper.

2. SYSTEM CHARACTERIZATION

This section describes different multi-antenna techniques which can be used to improve the performance, spectral efficiency or to achieve an increased network capacity.

2.1. Space-time Block Coding

Although Space-Time Block Coding (STBC) is essentially a MISO system, the use of receiver diversity makes it a MIMO, which corresponds to the most common configuration for this type of diversity. Transmit diversity (TD) techniques are particularly interesting for fading channels where it is difficult to have multiple receive antennas (as in conventional receiver diversity schemes). A possible scenario is the downlink transmission where the base station uses several transmit antennas and the mobile terminal only has a single one [2].

STBC based schemes focus on achieving a performance improvement through the exploitation of additional diversity, while keeping the symbol rate unchanged [2, 3]. Symbols are transmitted using an orthogonal block structure, which enables simple decoding algorithm at the receiver [2, 4].

¹ Users that share the spectrum and that are separated by the MU-MIMO spatial multiplexing.

2.1.1. Open Loop Techniques

Open Loop Transmit Diversity schemes are performed without previous knowledge of the channel state by the transmitter. Space Time Block Coding, also known as the Alamouti scheme, is the most known open loop technique [2].

If we employ Alamouti's transmit diversity we need some processing at the transmitter. The Alamouti's coding can be implemented either in the time domain or in the frequency domain. In this paper we consider time-domain coding (the extension to frequency domain coding is straightforward). By considering the Space Time Block Coding with two transmit antennas, the l th time-domain block to be transmitted by the m th antenna ($m = 1$ or 2) is $s_l^{(m)}$, with [2, 10]

$$s_{2l-1}^{(1)} = a_{2l-1} \quad s_{2l-1}^{(2)} = -a_{2l}^* \quad s_{2l}^{(1)} = a_{2l} \quad s_{2l}^{(2)} = a_{2l-1}^* \quad (1)$$

where a_l refers to the symbol selected from a given constellation, to be transmitted in the l th time domain block. Considering the matrix-vector representation, we define $\mathbf{s}_l^{[1,2]}$

$$\mathbf{s}_l^{[1,2]} = \begin{bmatrix} a_{2l-1} & a_{2l} \\ -a_{2l}^* & a_{2l-1}^* \end{bmatrix} \quad (2)$$

where different rows of the matrix refer to transmit antenna order and different columns refer to symbol period orders. The Alamouti's post-processing for two antennas comes [10],

$$\begin{aligned} \tilde{A}_{2l-1} &= \left[Y_{2l-1} H_l^{(1)*} + Y_{2l}^* H_l^{(2)} \right] \beta \\ \tilde{A}_{2l} &= \left[Y_{2l} H_l^{(1)*} - Y_{2l-1}^* H_l^{(2)} \right] \beta \end{aligned} \quad (3)$$

where $\beta = \left[\sum_{m=1}^M |H_l^{(m)}|^2 \right]^{-1}$. Defining $\mathbf{Y}_l^{[1,2]} = \begin{bmatrix} Y_{2l-1} & Y_{2l}^* \\ Y_{2l} & -Y_{2l-1}^* \end{bmatrix}$ and $\mathbf{H}_l^{[1,2]} = \left[H_l^{(1)*} \ H_l^{(2)} \right]^T$, (3) can be expressed in the matrix-vector representation as $\tilde{\mathbf{A}}_l^{[1,2]} = \left[\mathbf{Y}_l^{[1,2]} \times \mathbf{H}_l^{[1,2]} \right] \times \beta$, where $\tilde{\mathbf{A}}_l^{[1,2]} = \left[\tilde{A}_{2l-1} \ \tilde{A}_{2l} \right]^T$.

Finally, the decoded symbols come

$$\tilde{A}_{2l-j} = \overbrace{A_{2l-j} \sum_{m=1}^M |H_l^{(m)}|^2}^{\text{Desired Symbol}} \beta + \overbrace{N_{2l-j}^{eq}}^{\text{Noise Component}} \quad j = 0, 1 \quad (4)$$

where $N_{k,l}^{eq}$ denotes the equivalent noise for detection purposes.

Orthogonal code of rate 1 using more than two antennas does not exist. Schemes with 4 and 8 antennas with code rate one only exist in the case of binary transmission. If orthogonality is essential (fully loaded systems with significant interference levels), a code with $R < 1$ should be employed for such cases.

The signal processing for non-orthogonal 4 and 8 transmit antennas is defined in [10] and in the references therein. In both cases, the decoding does not achieve the maximum possible path diversity since in the decoding of all symbols there is always inter-symbolic interference from one symbol in the case of 4 antennas (c_0), and from 3 symbols in the case of 8 antennas (c_0, c_1, c_2).

It is worth noting that although the described STBC scheme is a MISO, by adopting receive diversity, this can be viewed as a MIMO system.

2.1.2. Closed Loop Techniques

In the case of the downlink, the space diversity provided by the STD scheme presents a low rate feedback link from the receiver (MS) informing the transmitter (BS) which antenna should be employed for transmission. There is a common or dedicated pilot sequence, which is transmitted. Different antennas with specific pilot patterns/codes enable antenna selection. Once the MS sends back to the transmitter the information about the M link qualities (number of transmit antennas), the BS transmits a single symbol stream over the best antenna. The receiver is supposed to re-acquire the carrier phase $\theta_k(t)$ after every switch between antennas. Moreover, the Antenna Switch (AS) has the capability to switch every slot duration.

2.2. Spatial Multiplexing

Multi-layer Transmission and SDMA belong to group entitled Spatial Multiplexing (SM), whose principles are similar but whose purposes are quite different. As long as the antennas are located sufficiently far apart, the transmitted and received signals from each antenna undergo independent fading.

The primary goal of the MIMO based on multi-layer transmission scheme is to achieve higher data rates in a given bandwidth, whose increase rate corresponds to the number of transmit antennas [1, 9]. An example of the multi-layer transmission scheme is the Vertical-Bell Laboratories Layered Space-Time (V-BLAST). In the Multi-Layer MIMO, the number of receive antennas N must be equal or higher than the number of transmit antennas M . The increase of symbol rate is achieved by “steering” the receive antennas to each one (separately) of the transmit antennas, in order to receive the corresponding data stream. This is achieved through the use of the nulling algorithm.

As depicted in Figure 2, two different Multi-Layer MIMO schemes are considered: scheme 1 and scheme 2 [4]. Scheme 1 directly allows an increase of the data rate whose increase rate corresponds to the number of transmit antennas. Scheme 2 allows the exploitation of diversity, without achieving an increase of data rate. The transmit diversity combining is achieved using any combining algorithm, namely the Mean-Square Error (MSE) based or the Maximum Ratio Combining (MRC). In case of the scheme 2 (depicted in Figure 2(b)), the antenna switching is performed at a symbol rate, where the red dashed lines represent the signal path at even symbol periods, in case of two transmit antennas. The diversity is achieved because each symbol is transmitted by different antennas, at different symbol periods. Output signals are then properly delayed and combined to provide diversity.

In Multi-Layer MIMO, the symbol with the highest SNR is first detected using a linear nulling algorithm such as zero forcing (ZF) or minimum mean square error (MMSE) [1]. The detected symbol is regenerated, and the corresponding signal portion is subtracted from the received signal vector using typically a Successive Interference Cancellation (SIC) algorithm. This cancellation process results in a modified received signal vector with fewer interfering signal components left. This process is repeated, until all symbols from different transmit antennas are detected. [1] provides the signal description for the V-BLAST MIMO scheme, while in [5] it is proposed an advanced receiver for the Multi-Layer MIMO scheme applied to Wideband Code Division Multiple Access (WCDMA) signals.

The goal of the SDMA scheme is to improve the cell capacity (more users per cell), while keeping the spectrum allocation unchanged. It is usually considered in the uplink, where the transmitter (UE) has a single antenna while the receiver (BS) has several antennas. Figure 3 depicts a SDMA configuration applied to the uplink. It requires that the number of antennas at the receiver is higher than the number of MSs that share the same spectrum. With such approach, the receiver is able to decode the signal from each transmitter, while avoiding the signal from the other transmitters. Similar to the decoding performed in multi-layer transmission, this can be

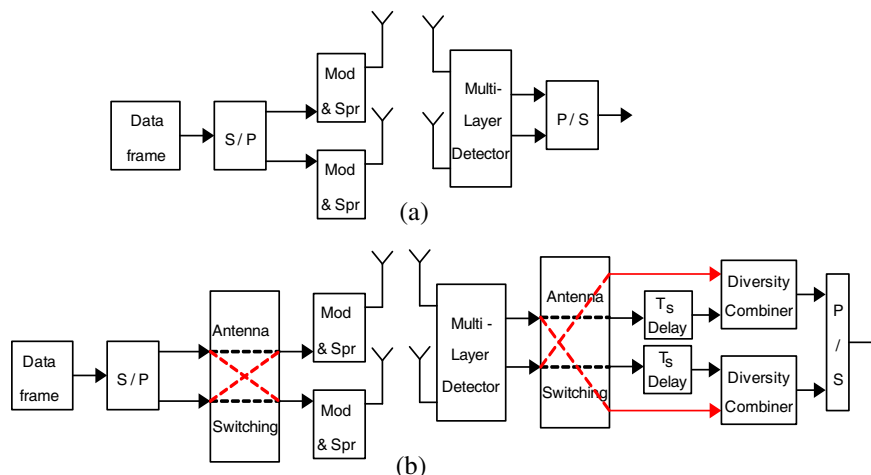
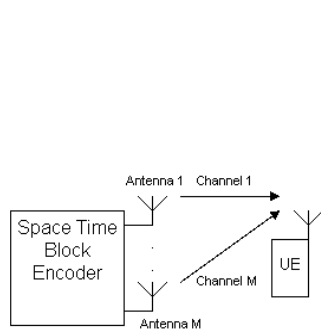


Figure 1: Generic block diagram of an open loop transmitter scheme.

Figure 2: Generic diagram of the 2×2 Multi-Layer MIMO. (a) Scheme 1 and (b) scheme 2.

achieved through the use of the nulling algorithm.

2.3. Beamforming

Contrary to STBC and SM MIMO schemes (sufficiently spaced to assure uncorrelated signals), the beamforming is implemented by antenna array with certain array elements at the transmitter or receiver being closely located to form a beam array. The antenna elements spacing is typically half wavelength. This scheme is an effective solution to maximize the SNR, as it steers the transmit (or receive) beam towards the receiver (or transmitter) [4]. As a result, an improved performance or coverage can be achieved with beamforming.

Figure 4 Simplified diagram of a beamforming transmitter depicts a BS transmitting a signal using the beamforming, generated with the Uniform Linear Antenna Array (ULA). As can be seen, the beamforming allows transmitting a higher power directed towards the desired station, while minimizing the transmitted power towards the other stations. It consists of M identical antenna elements with 120° Half Power Beam Width (HPBW) [4]. Each antenna element is connected to a complex weight w_m , $1 \leq m \leq M$. An analogy can be done with a receiving array antenna. The weighted elementary signals are summed together making an output signal as [4]:

$$y(t, \theta) = \sum_{m=1}^M w_m x \left[t - (m-1) \frac{d}{c} \sin \theta \right] \quad (5)$$

where $x(t)$ is the transmitted signal at the first element, d is the distance between elements (here considered $\lambda/2$), c is the propagation speed and θ is the DOA for the main sector, $-60^\circ < \theta < 60^\circ$. The other two array sectors are essentially the same as in the first one. In the frequency domain, the previous equation can be written as $Y(f, \theta) = \sum_{m=1}^M w_m X(f) e^{-j2\pi f(m-1) \frac{d}{c} \sin \theta}$, making

$$H(f, \theta) = \frac{Y(f, \theta)}{X(f)} = \sum_{m=1}^M w_m e^{-j2\pi f(m-1) \frac{d}{c} \sin \theta}.$$

For narrowband beamforming f is constant and θ is variable. For the beam to be directed towards the desired direction θ_1 , we have $w_m = e^{j2\pi f(m-1) \frac{d}{c} \sin \theta_1}$, in which, for the case of antenna elements spacing $d = \lambda/2$, this expression becomes [4] $w_m = e^{j\pi(m-1) \sin \theta_1}$. In other words, for $\theta = \theta_1$, $H(f, \theta_1)$ reduces to $H(f, \theta_1) = M$, which is the maximum attainable amplitude by beamforming.

2.4. Final MIMO Remarks

MIMO schemes require normally some additional processing and complexity from the receiver. Different receivers were analyzed in [4], in order to establish a trade-off between performance and complexity. An alternative approach that minimizes the level of computation from the receiver, transferring it to the transmitter, while keeping the ability to exploit diversity, has been proposed and studied in [8]. Such approach consists of a pre-coding scheme for MIMO systems.

3. PERFORMANCE RESULTS

In this section, we present a set of performance results concerning the proposed MIMO configurations, namely with one and two receive antennas, for a regular single carrier transmission (that is,

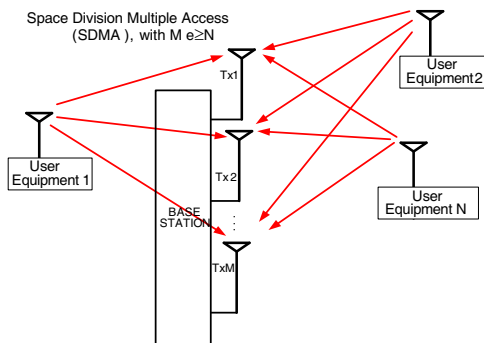


Figure 3: Example of SDMA scheme applied to the uplink.

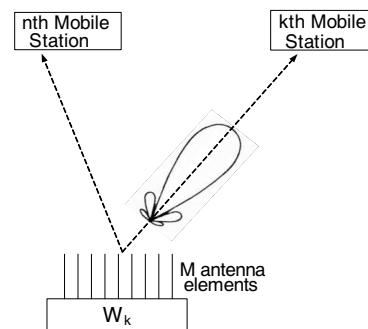


Figure 4: Simplified diagram of a beamforming transmitter.

without any advanced transmission technique such as multi-carrier or CDMA), and for the Pedestrian A and Vehicular A propagation environments (corresponds to a rich multipath propagation). Uncoded Bit Error Rate (BER) performance is considered, which is expressed as a function of E_b/N_0 , employing the QPSK constellation under a Gray mapping rule. Concerning the system level simulation, a total of four mobile terminals were considered in each cell. Different multi-antenna systems were considered in the simulations: the “equalizer” corresponds to the SISO, simply with an equalizer in the receiver; the STBC 2×1 and STBC 2×2 correspond to the Alamouti-like scheme with two transmit antennas and a single or two receive antennas, respectively; the STD 2×1 corresponds to the closed loop technique, with two transmit and a single receive antenna; the SPATIAL MUX 2×2 corresponds to the spatial multiplexing with two transmit and two receive antennas (see Figure 2 for layer 1 and 2); finally, BF8 corresponds to the beamforming with 8 antenna elements spaced half wavelength.

Figure 5 shows the performance results concerning the Pedestrian A propagation environment, and assuming a single receive antenna. As can be seen, the exploitation of diversity by the STBC and STD allows a performance improvement relating to the “equalizer”. Note that the STD performs better than the STTD for E_b/N_0 below 12 dB. Since the Pedestrian A presents a propagation environment close to the single path (flat fading), the selective diversity allows selecting the antenna which presents less fading, leading to good results even under noisy conditions. On the other hand, since the STBC always transmits the signals by the two antennas (antenna diversity), and since the corresponding channel presents low level of multipath diversity, it is only able to perform better than the STD for low levels of noise. Finally, the BF8 achieves a performance improvement relating to the “equalizer”, due to its inherent ability to focus energy in the desired mobile terminal (which tends to improve the SNR). Nevertheless, since the multipath diversity is low, its performance is below those of STD and STBC.

Figure 6 presents the performance for the Pedestrian A, but with double receive antennas. As expected, the performance obtained with the layer 2 is better than that of layer 1 due to its ability to explore diversity. Moreover, the Alamouti-like MIMO scheme (STBC) achieves a performance improvement relating to the layer 2.

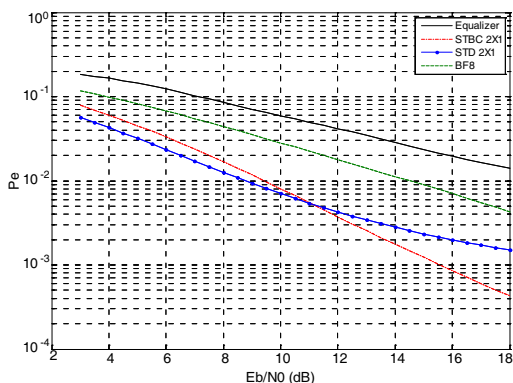


Figure 5: Pedestrian A propagation model (single receive antenna).

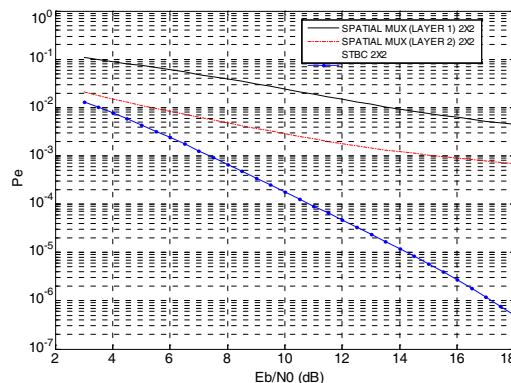


Figure 6: Pedestrian A propagation model (double receive antennas).

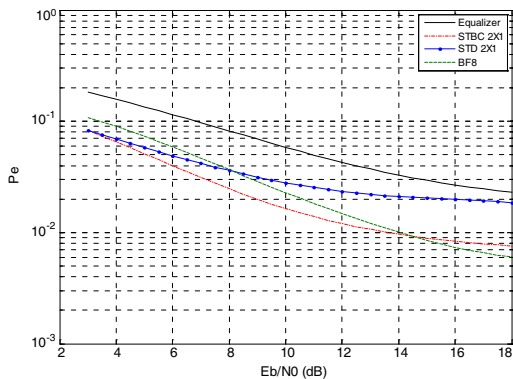


Figure 7: Vehicular A propagation model (single receive antenna).

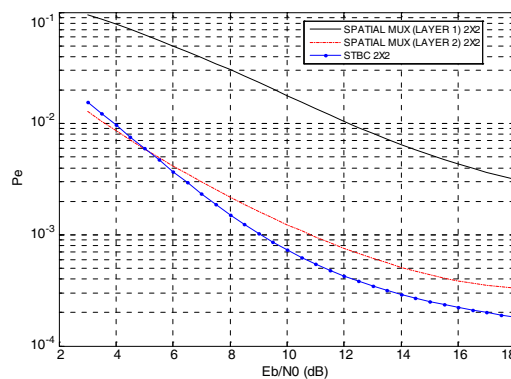


Figure 8: Vehicular A propagation model (double receive antennas).

Figure 7 corresponds to the results plotted in Figure 5 but concerning the Vehicular A, which is a rich multipath propagation and presents, *per se*, a high level of multipath diversity. Due to this fact, the best overall performance is achieved by the STBC for E_b/N_0 below 14 dB, and by the BF above this threshold. In the simulations, it was detected that, for higher number of interfering mobile terminals, the best overall performance is achieved by the beamforming scheme. Nevertheless, due to the lack of space, these results are not plotted in this paper.

Figure 8 corresponds to Figure 6 but for the Vehicular A propagation environment. As before, the best overall performance is achieved by the STBC. Nevertheless, due to the additional multipath diversity provided by the Vehicular A, relating to the Pedestrian A, the difference of performance between the layer 2 and the STBC is reduced.

4. CONCLUSIONS

This paper performed a comparison between different multi-antenna techniques that can be employed to achieve the requirements of 4G systems. It was shown that the best overall performance tends to be achieved by the Alamouti-like scheme. However, due to its inherent ability to increase the SNR, when the number of interfering mobile users increases, the best overall performance tends to be achieved by the beamforming. Naturally, when the aim is the increase of transmission rate, instead of performance improvement, the spatial multiplexing (layer 1) should be viewed as an option.

ACKNOWLEDGMENT

This work was supported by the FCT project PTDC/EEA-TEL/120666/2010, “LTE-Advanced Enhancements using Femtocells”. The authors would like also to thank to Instituto de Telecomunicações for their support.

REFERENCES

1. Foschini, G. J., “Layered space-time architecture for wireless communication in a fading environment when using multiple antennas,” *Bell Laboratories Technical Journal*, Vol. 1, No. 2, 41–59, Autumn, 1996.
2. Alamouti, S. M., “A simple transmitter diversity scheme for wireless communications,” *IEEE JSAC*, 1451–1458, Oct. 1998.
3. Tarokh, V., et al., “Space-time block codes from orthogonal designs,” *IEEE Trans. Inform. Theory*, 1456–1467, Jul. 1999.
4. Marques da Silva, M., et al., *Transmission Techniques for Emergent Multicast and Broadcast Systems*, 1st Edition, CRC Press, Boca Raton, USA, May 2010, ISBN: 9781439815939.
5. Marques da Silva, M., R. Dinis, and A. Correia, “A new V-BLAST detector approach for W-CDMA signals with frequency selective fading,” *PIMRC 2005*, Berlin, Germany, Sep. 2005.
6. Marques da Silva, M., *Multimedia Communications and Networking*, 1st Edition, CRC Press, Boca Raton, USA, Mar. 2012, ISBN: 9781439874844.
7. Liu, L., R. Chen, S. Geirhofer, K. Sayana, Z. Shi, and Y. Zhou, “Downlink MIMO in LTE-advanced: SU-MIMO vs. MU-MIMO,” *IEEE Communications Magazine*, Vol. 50, No. 2, 140–147, Feb. 2012.
8. Marques da Silva, M., A. Correia, and R. Dinis, “On pre-processing for MIMO W-CDMA,” *11th International Symposium on Wireless Personal Multimedia Communications (WPMC 2008)*, Lapland, Finland, Sep. 2008.
9. Foschini, G. J. and M. J. Gans, “On limits of wireless communications in fading environments when using multiple antennas,” *Wireless Personal Communications*, Vol. 6, 315–335, Mar. 1998.
10. Marques da Silva, M. and R. Dinis, “Iterative frequency-domain detection and channel estimation for space-time block codes,” *European Transactions on Telecommunications*, Vol. 22, No. 7, 339–351, John Wiley & Sons, Ltd., Nov. 2011.
11. Marques da Silva, M., et al., *Transmission Techniques for 4G Systems*, CRC Press Auerbach Publications, ISBN: 9781439815939, Boca Raton, USA, Nov. 2012, <http://www.crcpress.com/product/isbn/9781466512337>.

On the Multihop Relays with Multiple Antennas for LTE-A

Carlos Reis^{1,2}, Américo Correia^{1,2}, Nuno Souto^{1,2}, and Mário Marques da Silva^{1,3}

¹Instituto de Telecomunicações, Portugal

²ISCTE-IUL, Portugal

³Universidade Autónoma de Lisboa, Portugal

Abstract— In this paper, we analyze cooperative communications for broadcast/multicast wireless communication systems based on the LTE-A standard. Multihop relays utilizing the same frequency bands as the base station are considered. These relays are equipped with multiples antennas (MIMO), at least the double of those employed at the base station side. The simulation results show that multihop relays achieve an improvement of power efficiency, while keeping the average coverage and the overall network throughput unchanged. This can be viewed as an energy-efficient wireless transmission technique, which contributes to the implementation of the green cell networks concept, as it allows a reduction in the carbon emission footprint.

1. INTRODUCTION

Operators are required to continuously improve system capacity and coverage while cost saving and with a reduced carbon emission footprint. Many solutions are envisaged to meet these desiderates, but small cells deployments look promising as a way to improve coverage and capacity demand. LTE-Advanced (LTE-A) will be extensively deployed on 2.6 GHz band. As the majority of mobile traffic is generated indoors, coverage improvement is essential. Heterogeneous networks with many types of small cells will increasingly be deployed to address the need of coverage and capacity improvements.

Many solutions could be employed to improve the backhaul coverage. Fiber is an attractive solution, however very expensive and requiring a long time to deploy. The challenges with backhaul can be addressed by self-backhauling relay nodes.

Relay Nodes (RN) were introduced in 3GPP Release 9 as a special type of eNodeB that is not directly connected to the core network. A RN receives data which was forwarded by an eNodeB that is connected to the Evolved Packet Core (EPC) (see Figure 1). Upon receiving such data, the RN sends it to the User Equipments (UE) that are under its area of coverage. This is a very interesting option for operators, as usually RN present structures less expensive to deploy and to maintain, as compared to eNB. They can provide temporary network deployment and an outage of the services in an area (e.g., when a sporadic event that concentrates a lot of people in the same geographical area takes place, such as a summer festival). The use of a RN allows a fast deploying and inexpensive way to solve the problem, and can also provide coverage in small areas not covered by eNodeB (eNB).

In [1, 2], four relay architectures are proposed and studied. Those architectures differ from each other in terms of expected behaviour of the RN/DeNB¹ and how the data is sent within the EPC until it reaches the UE. That study concludes that an architecture where RN acts as a proxy for S_1/X_2 has the most overall benefits, having been incorporated in 3GPP Release 10 (LTE-Advanced). Type 1 half-duplex in-band relay does not transmit any signal to UE when it is supposed to receive data from the DeNB. The relay then configures these sub-frames as Multicast/Broadcast Single Frequency Network (MBSFN) sub-frames when UEs are not supposed to expect any downlink transmission.

In this paper, we consider Type 1 RN with advanced Multiple Input Multiple Output (MIMO) schemes with support of 4 antennas for enhancement to relay backhaul. The objective is to achieve the DeNB throughput in spite of its in-band half duplex mode.

We first analyse Base Station cooperation with MIMO and next we replace some BSs by Fixed Relays assuring that the overall throughput of the network is kept the same, but with an improved power efficiency. The 3GPP Release 10 (LTE-Advanced) parameters will be taken as reference in our system level simulations.

Section 2 presents the system model; the system level simulations are presented in Section 3; numerical results are then plotted in Section 4; finally, our conclusions are drawn in Section 5.

¹ DeNB stands for Donor eNB.

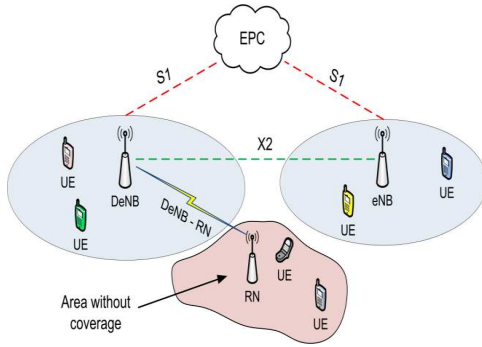


Figure 1: Example of relay node in E-UTRAN.

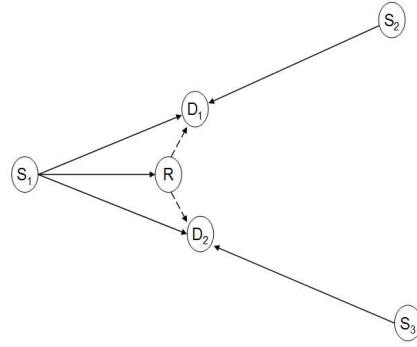


Figure 2: Cooperative multicast/broadcast network.

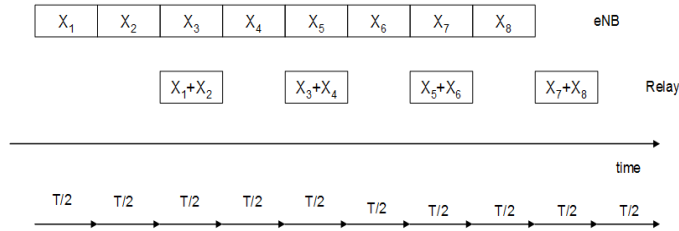


Figure 3: Time division channel allocation.

2. SYSTEM MODEL

The typical Multicast/Broadcast Multimedia Service (MBMS), such as video and audio, tends to be delay-sensitive and distortion-tolerant. Scalable video coding has been used for robust and flexible video transmissions, in which the source video is encoded into multiple streams with different priorities and transmitted using unequal error protection schemes. The basic streams, which contain the data with higher priority and describe the source at a basic quality are transmitted under higher protection. The enhancement streams with lower priority data, which are encoded progressively to further refine the quality of the basic stream. Under such a joint source and coding scheme, the multicast throughput can be improved, since users with different channel realizations can decode different number of streams, obtaining heterogeneous quality of service. We implement the unequal error protection function with hierarchical modulation and/or multi-layer transmission/spatial multiplexing (MIMO), as described in the following sub-section. We apply it to the relay-based cooperative multicast/broadcast cellular network.

Consider the system model as shown in Figure 2. It consists of 6 nodes with three source S_1 , S_2 and S_3 , one relay R and two destinations D_1 and D_2 . This 2-destination case can easily be extended to the multiple-destination case. In practice, the source may usually select a relay which is located between the source and destinations, where the R - D channels have relatively higher channel gains than the corresponding S - D channels. Two scenarios are considered: In the first scenario designated as Single Cell (SC) the sources transmit different signals, so S_2 and S_3 interfere with S_1 . The source node S_1 transmits the same signals to both D_1 and D_2 . In the second scenario, designated as Single Frequency Network (SFN), the nodes S_1 , S_2 and S_3 transmit the same signals to destination nodes. In any scenario only S_1 exploits R as a relay.

In this paper, a time division mechanism is assumed. Moreover, we shall assume that the relay node works in a half-duplex mode, while source nodes work in full-duplex mode (see Figure 3). Meanwhile, all channels are assumed to present mutually independent Rayleigh fading. In conventional cooperation schemes [3] such as Decode-and-Forward (DF), the source transmits a signal X_n in the first half time-slot, then the relay forwards the same symbol in the second half time-slot. In here, source transmits in every time slot continuously, while Relay stores the signals received and decode-and-forward in the first half time-slot of the next time-slot. Assuming that signal X_n is QPSK (Quadrature Phase Shift Keying) modulated, then the signal forwarded by relay has Hierarchical 16QAM (16 Quadrature Amplitude Modulation) modulation and/or MXN MIMO QPSK modulated. As a result, the spectral efficiency can be improved. It can exploit an increased diversity, while reducing the outage probability and increasing the coverage.

2.1. Multi-layer Transmission

Multi-layer Transmission and Space Division Multiple Access (SDMA) belong to the same group, entitled Spatial Multiplexing (SM), whose principles are similar but whose purposes are quite different. As long as the antennas are located sufficiently far apart, the transmitted and received signals from each antenna undergo independent fading.

The primary goal of the MIMO based on multi-layer transmission scheme is to achieve higher data rates in a given bandwidth, whose increase rate corresponds to the number of transmit antennas [7, 8]. An example of the multi-layer transmission scheme is the Vertical — Bell Laboratories Layered Space-Time (V-BLAST). In the Multi-Layer MIMO, the number of receive antennas N must be equal or higher than the number of transmit antennas M . The increase of symbol rate is achieved by “steering” the receive antennas to each one (separately) of the transmit antennas, in order to receive the corresponding data stream. This is achieved through the use of the nulling algorithm. With the sufficient number of receive antennas it is possible to resolve all data streams, as long as the antennas are sufficiently spaced so as to minimize the correlation [4].

As depicted in Figure 4, two different Multi-Layer MIMO schemes are considered: scheme 1 and scheme 2 [4]. Scheme 1 directly allows an increase of the data rate whose increase rate corresponds to the number of transmit antennas. Scheme 2 allows the exploitation of diversity, without achieving an increase of data rate. The transmit diversity combining is achieved using any combining algorithm, namely the Mean-Square Error (MSE) based or the Maximum Ratio Combining (MRC). In case of the scheme 2 (depicted in Figure 4(b)), the antenna switching is performed at a symbol rate, where the red dashed lines represent the signal path at even symbol periods, in case of two transmit antennas. The diversity is achieved because each symbol is transmitted by different antennas, at different symbol periods. Output signals are then properly delayed and combined to provide diversity.

In Multi-Layer MIMO, the symbol with the highest Signal to Noise Ratio (SNR) is first detected using a linear nulling algorithm such as zero forcing (ZF) or minimum mean square error (MMSE) [7]. The detected symbol is regenerated, and the corresponding signal portion is subtracted from the received signal vector using typically a Successive Interference Cancellation (SIC) algorithm. This cancellation process results in a modified received signal vector with fewer interfering signal components left. This process is repeated, until all symbols from different transmit antennas are detected.

3. SYSTEM-LEVEL SIMULATIONS

The considered system level simulator was originally developed as part of the work produced in [4]. The simulator was built in JAVA programming language, due to its characteristics such as portability, multi-platform compatibility, and ease of usage and configuration by users with low experience and familiarization with programming languages.

The core of the System Level Simulator (SLS) is composed by a discrete event generator with some grade of abstraction. The events generated consist of individual tasks such as Channel Quality

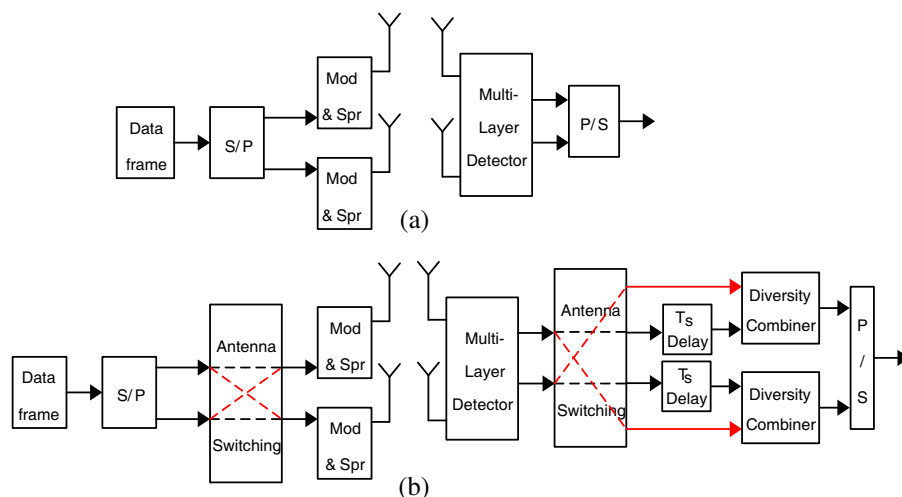


Figure 4: Generic diagram of the 2×2 multi-layer MIMO. (a) Scheme 1 and (b) scheme 2.

Indicator (CQI) reporting, packet processing, radio resources management, etc.. Propagation, traffic and mobility models are also part of the SLS, and have great impact in the results that will be obtained, especially in terms of coverage and radio link SNR estimation. Moreover, fast-fading and shadowing conditions are emulated, since channel conditions for every eNB/UE combination are time-varying and location dependent.

A scenario with nineteen sites was configured as the simulation environment. Moreover, two different configurations were assumed:

- a) Nineteen sites corresponding to nineteen eNBs without RNs;
- b) Nineteen sites corresponding to seven eNBs plus twelve RN.

The differences between these two configurations can be seen from Figure 5(a), where the black triangular shapes and the hexagons represent the location and coverage of eNBs respectively. From (b), the red triangular shapes and the yellow hexagons represent the location and coverage of RNs. The general parameterization used for all system-level simulations follows the 3GPP recommendations [5, 6]. The more specific parameters used for simulations can be obtained from Table 1.

4. SIMULATION RESULTS

In the system level simulations, mobile users receive blocks of bits transmitted from base stations. Each block undergoes small and large scale fading, as well as multi-cell interference. In terms of coverage or throughput, the SNR of each block is computed taking into account all the above impairments. Based on the comparison between the reference SNR at a Block Error Rate (BLER) of 1%, and the evaluated SNR, it is decided whether the block is or not correctly received. This is achieved for all the transmitted blocks, for all users, in all 57 sectors of the 19 cells, during 500 seconds.

Figure 6 presents the coverage as a function of the percentage of transmitted power from the base station (E_C/I_{0r}), for MIMO 2×2 and 4×4 , coding rate 1/2 and SC scenario. This corresponds to a scenario where there is interference with different patterns due to different frequency reuse

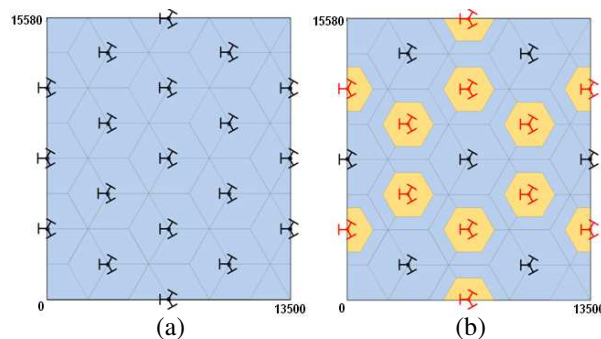


Figure 5: (a) Only eNBs scenario; (b) eNBs mixed with RNs.

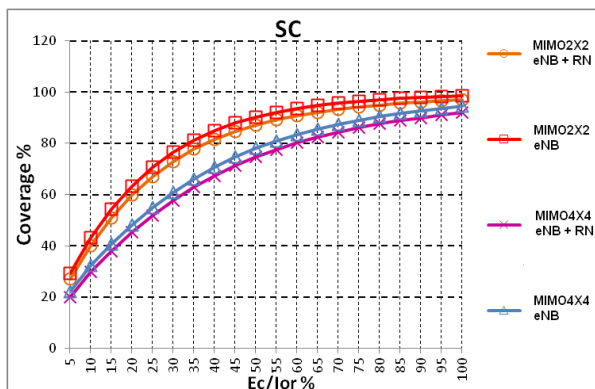


Figure 6: Coverage of SC scenario with and without relays.

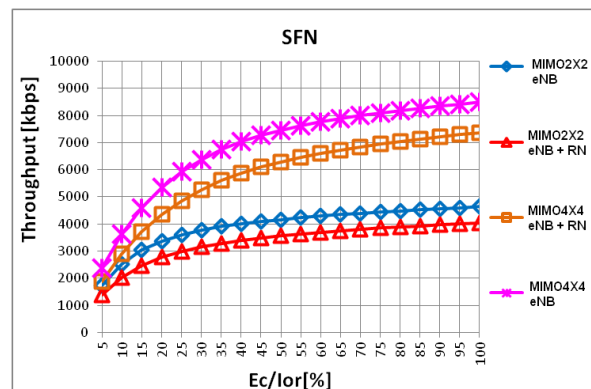


Figure 7: Throughput of SC scenario with and without relays.

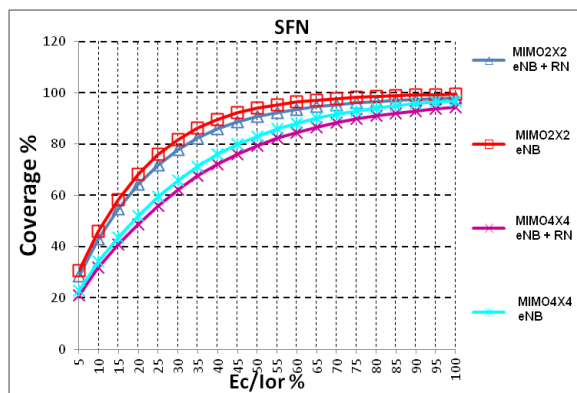


Figure 8: Coverage of SFN scenario with and without relays.

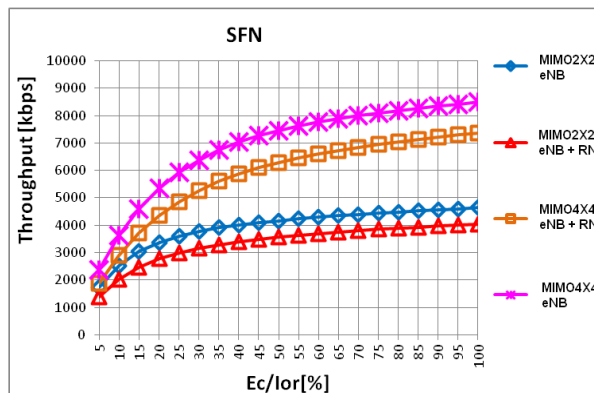


Figure 9: Throughput of SFN scenario with and without relays.

Table 1: Parameterization for SC and SFN simulation scenarios.

Parameter	Values
Cell Radius	2250 [m]
Modulations	H-16QAM
Coding rate	1/2
Number sectors per base station site	3 sectors/site
Sites layout	<ul style="list-style-type: none"> • 19 eNB • 7 eNB + 12 RN
eNB base station power/sector	<ul style="list-style-type: none"> • 46 [dBm] or 40 [W]
RN base station power/sector	<ul style="list-style-type: none"> • 34 [dBm] or 2.5 [W]
Number UEs per sector	20

factors. We have chosen the frequency reuse of $1/3$ in all simulations. All interfering sites transmit with the maximum power of 90%, according to the parameters indicated in Table 1. The cell radius R is 2250 meters (inter-site-distance 3900 m), and for the reuse factor chosen the reference coverage of 95% is achieved by all the schemes. However, it should be noticed that coverage values of MIMO 4×4 are lower than those of MIMO 2×2 due to higher levels of spatial interference. One of the curves almost superposed corresponds to configuration plotted in Figure 5(a) (eNB, without relays) and the other to Figure 5(b) (eNB+RN, with relays).

Figure 7 presents the average throughput distribution as function of E_C/I_{0r} for coding rate $1/2$ and the SC scenario, with the cell radius of $R = 2250$ meters, 2×2 and 4×4 MIMO, and with frequency reuse of $1/3$. We observe that the maximum throughput is achieved with MIMO 4×4 , in spite of its lower coverage due to higher spectral efficiency. Due to higher interference levels and lower transmitted power of relay nodes, the throughput achieved by the configuration of Figure 5(b) (with relays) indicates a loss of about 1 Mbps compared to the simulation of Figure 5(a) (only base stations). Figure 8 corresponds to Figure 6, but for the single frequency network (SFN). For comparison purposes, the reuse factor of $1/3$ is kept. The coverage values are only slightly higher than for SC. This means that the users that are being served by the relay nodes are much closer to them, as compared to the base stations of the adjacent cells. All the schemes achieve the reference coverage with lower E_C/I_{0r} .

Figure 9 corresponds to Figure 7 but for the SFN. For comparison purposes, the reuse factor of $1/3$ was also kept. The comparison between the two figures indicates slightly higher throughput values of Figure 9, as compared to those of Figure 7. Again, using 4×4 antennas, instead of 2×2 , allows increasing the maximum throughput from around 5000 kbps to 8500 kbps. Coding rate $1/2$ continues to be used to enable higher coverage values (and throughput).

5. CONCLUSIONS

We have analyzed cooperative communications with fixed multihop relays, working in half-duplex mode and equipped with multiple antennas MIMO. A cellular network was considered, where some of the BSs have been replaced by fixed relay stations with much less transmitted power, while keeping the same global area. We have confirmed that, by using multihop relays, it is possible to keep the average coverage and the overall network throughput, while achieving an improvement of power efficiency. This can be viewed as an energy-efficient wireless transmission technique, which contributes to the implementation of the green cell networks concept, as it allow a reduction in the carbon emission footprint.

ACKNOWLEDGMENT

This work was partially supported by FCT project PTDC/EEA-TEL/120666/2010, “LTE-Advanced Enhancements using Femtocells”.

The authors would like also to thank to Instituto de Telecomunicações for their support.

REFERENCES

1. 3GPP, “General aspects and principles for interfaces supporting Multimedia Broadcast Multicast Service (MBMS) within E-UTRAN,” TS 36.440 v9.1.0, Mar. 2010.
2. 3GPP, “Evolved Universal Terrestrial Radio Access (E-UTRA) and Evolved Universal Terrestrial Radio Access Network (E-UTRAN); overall description,” TS 36.300, 2010.
3. Tao, X., X. Xu, and Q. Cui, “An overview of cooperative communications,” *IEEE Communications*, Vol. 50, No. 6, 65–71, Jun. 2012.
4. Marques da Silva, M., A. Correia, R. Dinis, N. Souto, and J. Silva, “Transmission techniques for emergent multicast and broadcast systems,” 1st Edition, CRC Press Auerbach Publications, Boca Raton, USA, Jun. 2010, ISBN: 9781439815939.
5. 3GPP, “Evolved Universal Terrestrial Radio Access (E-UTRA); Radio Frequency (RF) system scenarios,” Technical Report TR 36.942 v9.0.1, Apr. 2010.
6. 3GPP, “Evolved Universal Terrestrial Radio Access (E-UTRA); User Equipment (UE) radio transmission and reception,” TS 36.101 v9.3.0, 2010.
7. Foschini, G. J., “Layered space-time architecture for wireless communication in a fading environment when using multiple antennas,” *Bell Laboratories Technical Journal*, Vol. 1, No. 2, 41–59, Autumn, 1996.
8. Marques da Silva, M. and R. Dinis, “Iterative frequency-domain detection and channel estimation for space-time block codes,” *European Transactions on Telecommunications*, Vol. 22, No. 7, 339–351, John Wiley & Sons, Ltd., Nov. 2011, DOI: 10.1002/ett.1484, <http://dx.doi.org/10.1002/ett.1484>.

Channel Capacity Improvement Dependency of the Number of Receiving Antennas for Aeronautical MIMO Systems

N. Kanada, Y. Sumiya, N. Yonemoto, S. Futatsumori, A. Kohmura, and E. Isozaki
Electronic Navigation Research Institute (ENRI), Tokyo 182-0012, Japan

Abstract— In this abstract, we discussed channel capacity improvement of Multiple-Input Multiple-Output (MIMO) antenna systems for new high-speed aeronautical digital communication technologies. It will be required to cope with increasing volumes of air traffic and airport surface congestion. Performance analysis under worse condition is important for safety communication such as air traffic control. Especially, the relationship between communication performance and the position of antennas around aircraft must be clarified due to the unknown effects of masking or reflection by aircraft components such as the fuselage, wings and empennage, and airport structures such as terminal buildings. We experimentally evaluated channel capacities for communication performance analysis. As the results, we show that increasing receiving antennas makes new aeronautical digital communication faster in an actual airport environment.

1. INTRODUCTION

Current Air Traffic Control (ATC) depends on analog voice communication or slow digital communications [1]. These systems remain because ATC communications must guarantee system interoperability and operational performance worldwide. However, new high-speed aeronautical digital communication technologies will be required to cope with recent air traffic growth [2]. Aeronautical Mobile Airport Communication System (AeroMACS), based on Mobile WiMAX (IEEE 802.16e) in 5 GHz band, from 5091 MHz to 5150 MHz [2], is a candidate system for high-speed digital communications on the airport surface. AeroMACS uses MIMO systems to increase channel capacity. MIMO systems have advantages of improvements of speed and reliability. Speed improvements mainly come from spatial division multiplexing. Reliability improvements mainly come from space diversity.

In this paper, we evaluate two MIMO effects, spatial division multiplexing and space diversity by calculating channel capacities in an airport surface condition.

2. MEASUREMENT CONFIGURATIONS

Transmission coefficient measurement experiments were conducted at Sendai Airport. The experimental layout is illustrated in Figure 1(a). An aircraft (a Beechcraft Model 99 Airliner) with two antennas was parked on an apron. A ground station was simulated by a ground-plane with six monopole antennas mounted on a vehicle. The alignments of the antennas are shown in Figures 1(b) and (c). Antennas on the aircraft are compatible Sensor Systems S65-5366-4M vertically polarized $1/4\lambda$ omnidirectional antennas. Radiation patterns of ground antennas are shown in Figure 1(d). A pattern of No. 4 antenna is not taken because of its breakout. Measurements were taken at vehicle positions at side and back, 90 and 180 degrees clockwise from the front of the aircraft. Distances between aircraft and ground antennas are 40 m.

Figure 2 shows the whole measurement system. Twelve transmission coefficients between the aircraft antennas and ground antennas were obtained by an Agilent E8364B Vector Network Analyzer (VNA). Port 1 of the VNA was connected to the ground-plane antennas via a Radio Frequency (RF) switch, while port 2 was connected to the antennas on the aircraft. A band pass filter (BPF) and amplifier (Amp) were inserted in line with each aircraft antenna to improve the measurement system's Signal to Noise Ratio (SNR). Cables from the two aircraft antennas were connected to an RF switch, with an additional amplifier inserted after the switch to compensate for cable losses. Channel capacities do not depend on direction of propagation because of reciprocity.

In order to cover the whole AeroMACS band, we measured the transmission coefficients from 5090 MHz to 5150 MHz. AeroMACS subcarriers are assigned at 5000/512 kHz steps within 5 MHz-wide band. However, a VNA Intermediate Frequency (IF) bandwidth of 1 kHz was used to improve the SNR of the measurements. The number of the measurement frequency points in each band was 6001. The effects of the wiring and amplifiers were corrected by post-processing. Each subcarrier was treated separately because the channel allocation plan is still under discussion. The system capacity will be calculated by summation of the subcarrier capacities of subcarriers after standardization.

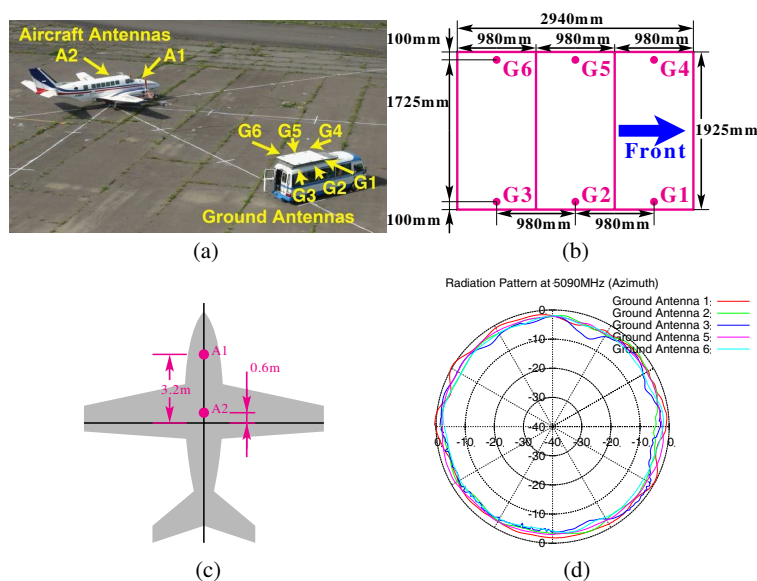


Figure 1: (a) Measurement overview. (b) Antenna configuration on the ground. (c) Antenna configuration on the aircraft. (d) Radiation pattern of ground antennas at 5090 MHz.

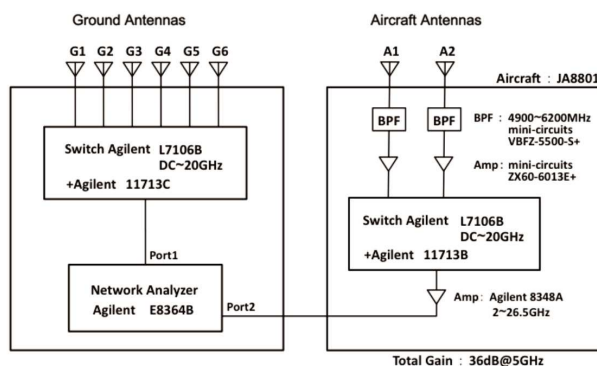


Figure 2: Measurement system.

3. RESULTS

Channel capacities between transmit antennas and receive antennas are calculated by measured transmission coefficients. Figure 3(a) shows the results of transmission coefficients. Horizontal axis of the graph is frequency, and vertical axis of it is transmission coefficients. Red line shows transmission coefficients between antenna A2 on the aircraft and G2 on the ground facility at side of the aircraft. Green line shows transmission coefficients between antenna A2 and G2 on the ground facility at backward of the aircraft. In the Figure 3(a), transmission coefficients of the backward is smaller than the side. We infer that aircraft's empennage masks aircraft antennas from ground antennas when the ground facility places behind the aircraft. Figure 3(b) shows channel capacities calculated from transmission coefficients. These capacities are calculated in equations given in [3], the same way as [4]. In the Figure 3(b), channel capacities of the backward is also smaller than the side.

4. DISCUSSION

In the previous analysis, visibility between antennas are important for channel capacity [4]. Therefore, in order to evaluate under good and bad condition, we choose side and backward of the aircraft cases. We analyze propagation characteristics by statistical analysis because they are varied by combination of the antenna, positional relationship, and frequencies. Table 1 is the minimum, average and standard deviation, and maximum of the channel capacities. The result is also illustrated in Figure 4.

Figure 4 illustrates relationship between number of the receiving antennas and channel capacity

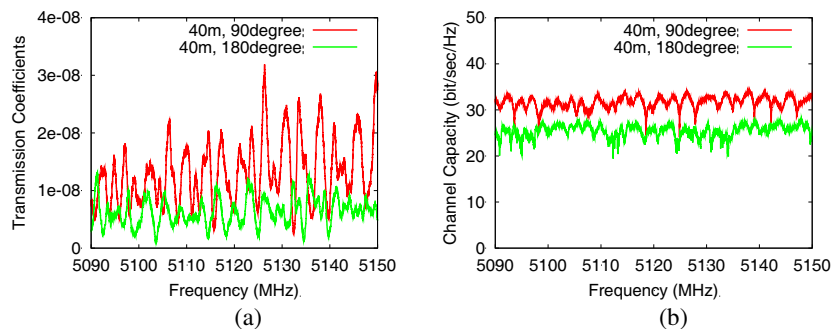


Figure 3: (a) Absolute of transmission coefficients between A2 and G2. (b) Channel capacities of 2×2 MIMO systems at 40 m.

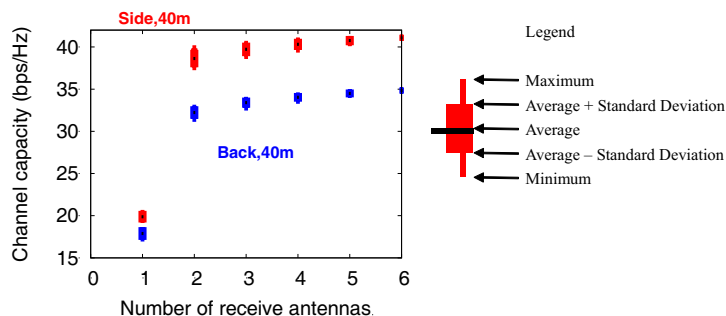


Figure 4: MIMO channel capacity improvement dependency of the number of receiving antennas.

Table 1: MIMO channel capacity improvements of the number of receiving antennas. Each unit is bit/sec/Hz.

# ANT	#ANT pairs	Side			Backward		
		Min	Ave.±Std. Dev.	Max	Min	Ave±Std. Dev.	Max
1	6	19.543	19.880±0.321	20.325	17.305	17.889±0.390	18.228
2	15	37.611	38.623±0.668	39.827	31.487	32.230±0.383	32.784
3	20	38.946	39.715±0.437	40.360	32.837	33.396±0.234	33.728
4	15	39.7	40.309±0.295	40.756	33.635	34.029±0.149	34.245
5	6	40.46	40.757±0.182	40.937	34.360	34.494±0.095	34.614
6	1	41.084	41.084	41.084	34.839	34.839	34.839

of MIMO antenna systems. Horizontal axis of the graph is the number of receiving antennas, and vertical axis of the graph is channel capacity of the systems. Red line shows the maximum, minimum, and average of channel capacities at the side of the aircraft. Blue line shows the maximum, minimum, and average channel capacity at the back of the aircraft. We compare channel capacities in the different angle at the same distance, 40 m. Figure 4 shows that the average of channel capacities increase, and the maximum, and the minimum channel capacities increase with respect to the number of receiving antennas. The same tendency is shown in the maximum, the minimum, and standard deviations of channel capacity.

In the both cases, The channel capacities twice increase with respect to the number of receiving antennas from 1 to 2. This effect causes from spatial division multiplexing. The channel capacities increase slowly when the number of receive antennas are greater than 2. This effect causes from spatial diversity. Therefore, the effect of space diversity and space division multiplexing do not depend on the location of ground facilities. For safety communications, such as aeronautical communications, it is important to improve performances in the bad conditions.

5. CONCLUSIONS

We experimentally evaluated the number of receive antennas dependency of MIMO antenna systems in real conditions. Effects of spacial division multiplexing and spacial diversity are shown in MIMO systems. They increase channel capacity and stability of communications. Therefore, MIMO is

effective for improvement of aeronautical communications. We will measure propagation in the whole airport in the future.

ACKNOWLEDGMENT

We would like to thank the Sendai Airport Office, Tokyo Regional Civil Aviation Bureau for their cooperation.

REFERENCES

1. Stacey, D., *Aeronautical Radio Communication Systems and Networks*, John Wiley&Sons, Ltd., Apr. 2008.
2. Philips, B. and J. Pouzet, “Communications operating concept and requirements,” ICAO ACP/1, Information Paper 5, <http://legacy.icao.int/anb/panels/acp/wgdoclist.cfm?MeetingID=188>.
3. Karasawa, Y., “MIMO propagation channel modeling,” *IEICE Trans. Commun., Special Section on Recent Progress in Antennas and Propagation Researches*, Vol. E88-B, No. 5, 1829–1842, 2005.
4. Kanada, N. et al., “Evaluation of antenna configuration for aeronautical WiMAX at 5.1 GHz,” *13th IEEE Wireless and Microwave Technology Conference (WAMICON)*, Apr. 2012.
5. Kanada, N., et al., “MIMO effect evaluation for aeronautical WiMAX in airport at 5.1 GHz,” *Integrated Communications, Navigation and Surveillance (ICNS) Conference*, Apr. 2012.

MIMO SC-FDE Transmission Techniques with Channel Estimation and High-order Modulations

João Carlos Silva¹, Rui Dinis², Nuno Souto¹, and Mário Marques da Silva³

¹ISCTE/Instituto de Telecomunicações, Lisboa, Portugal

²ISR/IST, Lisboa, Portugal

³UAL/Instituto de Telecomunicações, Lisboa, Portugal

Abstract— OFDM schemes have important limitations such as the high envelope fluctuations of the transmitted signals and its sensibility to carrier frequency errors. When these limitations bear critical we should consider SCFDE schemes (Single-Carrier Frequency Domain Equalization), which allow much higher power efficiency due to the lower envelope fluctuations. This can be further improved if the conventional linear FDE is replaced by an iterative FDE such as an IB-DFE (Iterative Block Decision Feedback Equalizer).

In order to obtain good performance results, accurate channel estimates must be available at the receiver, especially if MIMO (Multiple Input, Multiple Output) and high-order modulations are to be used. For this purpose, pilot symbols and/or training sequences are usually multiplexed with data symbols, which lead to spectral degradation. As an alternative, we can use implicit pilots.

In this paper, we consider SC-IB-FDE systems in MIMO 2×2 broadband with high order modulations and channel estimation.

1. INTRODUCTION

Block transmission techniques, with appropriate cyclic prefixes and employing FDE techniques (Frequency-Domain Equalization), have been shown to be suitable for high data rate transmission over severely time-dispersive channels [1, 2]. Two possible alternatives based on this principle are OFDM (Orthogonal Frequency Division Multiplexing) and Single Carrier (SC) modulation using FDE (or SC-FDE). Due to the lower envelope fluctuations of the transmitted signals (and, implicitly a lower PMEPR (Peak-to-Mean Envelope Power Ratio)), SC-FDE schemes are especially interesting for the uplink transmission (i.e., the transmission from the mobile terminal to the base station) [1, 2], being considered for use in the upcoming LTE (Long Term Evolution) cellular system.

A promising IFDE (Iterative FDE) technique for SC-FDE, denoted IB-DFE (Iterative Block Decision Feedback Equalizer), was proposed in [3]. This technique was later extended to diversity scenarios [4] and layered space-time schemes [5]. These IFDE receivers can be regarded as iterative DFE receivers with the feed-forward and the feedback operations implemented in the frequency domain. Since the feedback loop takes into account not just the hard decisions for each block but also the overall block reliability, error propagation is reduced. Consequently, IFDE techniques offer much better performance than non-iterative methods [3–5]. Within these IFDE receivers the equalization and channel decoding procedures are performed separately (i.e., the feedback loop uses the equalizer outputs instead of the channel decoder outputs). However, it is known that higher performance gains can be achieved if these procedures are performed jointly. This can be done by employing turbo equalization schemes, where the equalization and decoding procedures are repeated in an iterative way [6], being essential in MIMO schemes with high order modulations. Although initially proposed for time-domain receivers, turbo equalizers also allow frequency-domain implementations [7, 8].

In order for the above schemes to operate correctly, good channel estimates are required at the receiver. Typically, these channel estimates are obtained with the help of pilot/training symbols that are multiplexed with the data symbols, either in the time domain or in the frequency domain [9–11].

Overhead due to training symbols for channel estimation can be high, leading to decrease of system capacity, especially in fast-varying scenarios and/or high MIMO orders. A promising technique to overcome this problem is to use implicit training or implicit pilots, also called superimposed pilots, where the training block is added to the data block instead of being multiplexed with it [12–16]. This means that we can increase significantly the density of pilots (to the maximum extent of one pilot per data symbol), with zero pilot overhead. Normally, periodic pilot sequences are added

to data symbols in the time domain for single carrier systems [12, 16], or in the frequency domain for OFDM systems [13, 14].

In this paper, we consider the use of both multiplexed and implicit pilots for the SISO and MIMO settings with QPSK, 16QAM and 64QAM. For the implicit case, non-data-dependent pilots were used; i.e., the first approach mentioned above was used. We propose iterative receiver structures with joint channel estimation and detection. Unlike the iterative schemes of [16], our schemes do not employ the relatively complex Viterbi algorithm to jointly estimate channel and data. Instead, they incorporate iterative frequency domain equalization (either IB-DFE or turbo equalization) within the iterative channel estimation and detection/decoding framework.

The rest of this paper is organized as follows — the adopted system is introduced in Section 2 whilst Section 3 describes the proposed receiver structure. Furthermore, a set of performance results is presented in Section 4 and Section 5 contains the conclusions of this paper.

2. SYSTEM DESCRIPTION

We consider SC-FDE modulation. The l th transmitted block has the form

$$s_1^{ntx} = \sum_{n=-N_G}^{N-1} s_{n,l}^{ntx} h_T(t - nT_S), \quad (1)$$

with T_S denoting the symbol duration, N_G denoting the number of samples at the cyclic prefix, $h_T(t)$ representing the adopted pulse shaping filter, and $s_{n,l}^{ntx}$ denotes the length- N data block to be transmitted from the ntx transmit antenna. After passing the signal to the frequency domain, the implicit pilots can be added. It is better to add them in the frequency domain, since most of the processing is done there.

The transmitted sequences are thus given by (capital S being the signal in the frequency domain) [24]

$$X_{k,l}^{ntx} = S_{k,l}^{ntx} + S_{k,l}^{\text{Pilot}} \quad (2)$$

where, $S_{k,l}^{ntx}$ is the data symbol transmitted by the k th subcarrier (out of a total of N) of the l th FFT block and $S_{k,l}^{\text{Pilot}}$ is the corresponding implicit pilot. In Figure 1, we show a transmitter chain that incorporates for the SC-FDE scheme. The pilot symbols are added in the frequency domain, and the data is then passed through the IFFT for transmission (in practice, the resulting pilots could be added directly in the time domain, but Figure 2 makes things clearer).

Assuming only one user, the data bits are passed through a turbo coder, after which they are submitted to rate matching (taking into account the use of FFTs for faster processing, the antenna

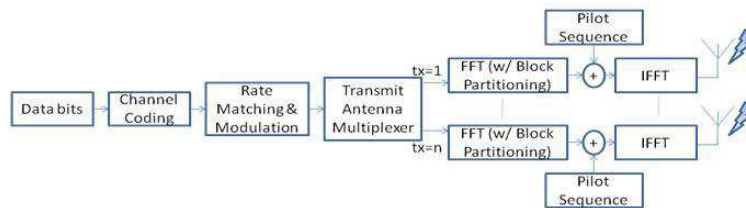


Figure 1: Transmitter scheme for the SC-FDE scheme.

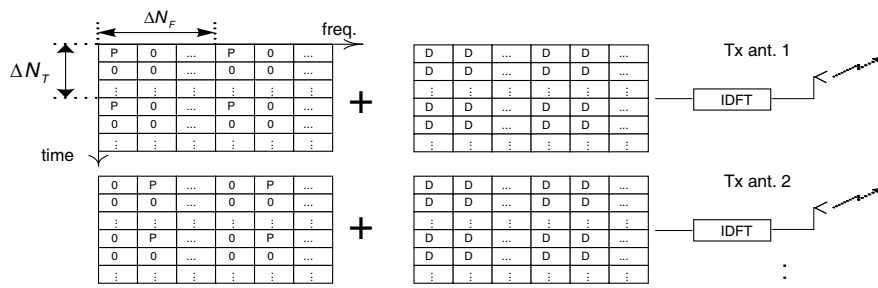


Figure 2: Proposed frame structure for a MIMO-SC-FDE transmission with implicit pilots (P — pilot symbol, D — data symbol).

multiplexer and block partitioning). All of the antennas will transmit a part of the message (if multiple users were to be employed, we could assign an antenna per user). The data bits are partitioned into blocks and the cyclic prefix is added to each block, so that the total size is a power of 2, for efficient use of the FFT.

We will consider the frame structure of Figure 2 for a SC-FDE system with N carriers. According to this structure the pilot grid is generated using a spacing of ΔN_T symbols in the time domain (number of blocks) and ΔN_F symbols in the frequency domain. The minimum ΔN_F should be equal to the number of transmit antennas, so that there is no interference between pilot symbols on different antennas.

3. ITERATIVE RECEIVER

3.1. Receiver Structure

The transmission of pilot symbols superimposed on data will clearly result in interference between them. To reduce the mutual interference and achieve reliable channel estimation and data detection we propose a receiver capable of jointly performing these tasks through iterative processing. The structure of the proposed iterative receiver is shown in Figure 3. According to the figure, the signal, which is considered to be sampled and with the cyclic prefix removed, is converted to the frequency domain after an appropriate size- N FFT operation. If the cyclic prefix is longer than the overall channel impulse response, the nrx receive antenna is given as [17]:

$$R_{k,l,nrx} = \sum_{ntx=1}^{Ntx} \left((S_{k,l,ntx} + S_{k,l,ntx}^{\text{Pilot}}) H_{k,l,ntx,nrx} + N_{k,l,nrx} \right) \quad (3)$$

with $H_{k,l,ntx,nrx}$ denoting the overall channel frequency response for the k th frequency of the l th time block between the ntx transmit and nrx receive antenna, and $N_{k,l,nrx}$ denoting the corresponding channel noise.

Before entering the equalization block, the pilot symbols are removed from the sequence resulting

$$(Y_{k,l,nrx})^{(q)} = R_{k,l,nrx} - \sum_{ntx=1}^{Ntx} \left(S_{k,l,ntx}^{\text{Pilot}} \left(\hat{H}_{k,l,ntx,nrx} \right)^{(q)} \right) \quad (4)$$

where $(\hat{H}_{k,l,ntx,nrx})^{(q)}$ are the channel frequency response estimates and q is the current iteration. Note that, in the case of a known channel without any pilots for estimation, $Y_{k,l,nrx} = R_{k,l,nrx}$.

The equalized samples are then simply computed as

$$\left(\hat{S}_{k,l,ntx} \right)^{(q)} = \frac{\left(\hat{H}_{k,l,ntx,nrx} \right)^{(q)*} Y_{k,l,ntx}^{(q)}}{\left| \hat{H}_{k,l,ntx,nrx}^{(q)} \right|^2} \quad (5)$$

where

$$Y_{k,l,ntx}^{(q)} = \sum_{nrx} \left((Y_{k,l,nrx})^{(q)} - \sum_{ntx1 \neq ntx} \left(S_{k,l,ntx1}^{\text{Pilot}} \left(\hat{H}_{k,l,ntx1,nrx} \right)^{(q)} \right) \right) \quad (6)$$

The sequences of the equalized samples are then passed through the IFFT, block grouping, demodulated and passed through the channel decoder. Each channel decoder has two outputs. One is the

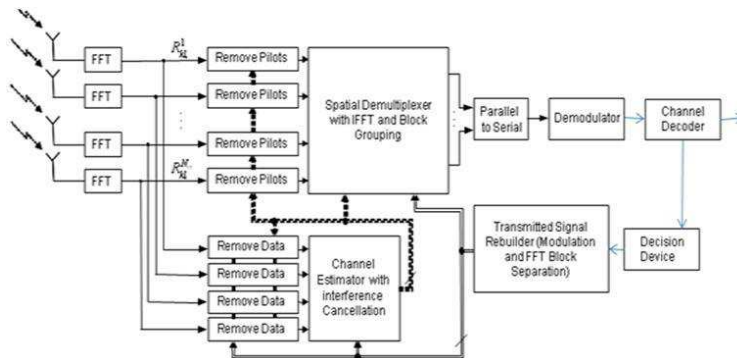


Figure 3: Iterative receiver structure.

estimated information sequence and the other is the sequence of log-likelihood ratio (LLR) estimates of the code symbols. These LLRs are passed through the Decision Device which outputs either soft-decision or hard decision estimates of the code symbols. These estimates enter the Transmitted Signal Rebuilder which performs the same operations of the transmitter (coding, modulation). The reconstructed symbol sequence can then be used for improving the channel estimates, as will be explained next, for the subsequent iteration.

3.2. Channel Estimation Using Pilots

Let us first assume that $S_{k,l} = 0$, i.e., there is no data overlapping the training block, as in conventional schemes. In that case, the channel frequency response is, for a SISO (Single Input, Single Output — used solely for simplification purposes) scheme:

$$\hat{H}_{k,l} = \frac{Y_{k,l}}{S_{k,l}^{TS}} = H_{k,l} + \frac{N_{k,l}}{S_{k,l}^{TS}} = H_{k,l} + \epsilon_{k,l}^H \quad (7)$$

The channel estimation error $\epsilon_{k,l}^H$ is Gaussian-distributed, with zero-mean and

$$E \left[|\epsilon_{k,l}^H|^2 S_{k,l} \right] = E \left[|N_{k,l}|^2 \right] E \left[\frac{1}{|S_{k,l}^{TS}|^2} \right] \quad (8)$$

3.2.1. Use of Implicit Pilots — General Case

Let us consider now the use of implicit pilots, i.e., $S_k \neq 0$ for the training blocks. In the following we will assume that

$$E \left[|S_{k,l}|^2 \right] = N E \left[|s_n|^2 \right] = 2\sigma_D^2 \quad (9)$$

and, for the frequencies that have pilots,

$$E \left[|S_{k,l}^{TS}|^2 \right] = N E \left[|s_n^{TS}|^2 \right] = 2\sigma_T^2 \quad (10)$$

Clearly, we will have interference between data symbols and pilots. This leads to performance degradation for two reasons:

- The data symbols produce interference on pilots, which might lead to inaccurate channel estimates. To reduce this effect, we should have

$$\sigma_D^2 \ll \sigma_T^2 \quad (11)$$

- The pilots produce interference on data symbols, which might lead to performance degradation (even if the channel estimation was perfect). To reduce this effect, we should have

$$\sigma_T^2 \ll \sigma_D^2 \quad (12)$$

Clearly, (11) and (12) are mutually exclusive. Moreover, the use of implicit pilots leads to increased envelope fluctuations on the transmitted signals [14]. To overcome these problems, we can employ pilots with relatively low power (i.e., $\sigma_T^2 \ll \sigma_D^2$) and average the pilots over a large number of blocks so as to obtain accurate channel estimates. This is very effective since the data symbols have usually zero mean and different data blocks are uncorrelated. Naturally, there are limitations on the length of this averaging window, since the channel should be constant within it (not to mention the associated delays). Once we have an accurate channel estimate, we can detect the data symbols, eventually removing first the signal associated to the pilots.

Let us assume a frame with N_T time-domain blocks, each with N subcarriers. If the cyclic prefix of each FFT block has $N_G = NT_g/T$ samples we will need N_G equally spaced frequency-domain pilots for the channel estimation. For pilot spacing in time and frequency ΔN_T and ΔN_F , respectively, the total number of pilots in the frame is given by:

$$N_P^{\text{Frame}} = \frac{N}{\Delta N_F} \cdot \frac{N_T}{\Delta N_T} \quad (13)$$

This means that we have a pilot multiplicity or redundancy of

$$N_R = \frac{N_P^{\text{Frame}}}{N_G} = \frac{N}{N_G \Delta N_F} \cdot \frac{N_T}{\Delta N_T} \quad (14)$$

Therefore, the SNR associated to the channel estimation procedure is

$$\text{SNR}_{\text{est}} = \frac{N_R \sigma_T^2}{\sigma_N^2 + \sigma_D^2} = N_R \frac{\sigma_T^2}{\sigma_D^2} \cdot \frac{\text{SNR}_{\text{data}}}{1 + \text{SNR}_{\text{data}}} \quad (15)$$

where $\sigma_N^2 = \frac{1}{2} E[|N_{k,l}|^2]$ and the SNR associated to data symbols is given by $\text{SNR}_{\text{data}} = \sigma_D^2 / \sigma_N^2$. For moderate and high SNR values,

$$\text{SNR}_{\text{est}} \approx N_R \frac{\sigma_T^2}{\sigma_D^2} \quad (16)$$

i.e., we have an irreducible noise floor of $N_R \frac{\sigma_T^2}{\sigma_D^2}$. To avoid significant performance degradation due to channel estimation errors, SNR_{est} should be much higher than SNR_{data} . This could be achieved with $\sigma_T^2 \ll \sigma_D^2$, provided that $N_R \gg 1$.

3.2.2. MIMO Estimation Algorithm with Implicit Pilots

To obtain the frequency channel response estimates the receiver applies the following steps in each iteration:

- a. Data symbols estimates are removed from the pilots. The resulting sequence becomes

$$\left(\tilde{R}_{k,l,nrx} \right)^{(q)} = R_{k,l,nrx} - \sum_{ntx=1}^{Ntx} \left(\left(\hat{S}_{k,l,ntx} \right)^{(q-1)} \left(\hat{H}_{k,l,ntx,nrx} \right)^{(q-1)} \right) \quad (17)$$

where $\left(\hat{S}_{k,l,ntx} \right)^{(q-1)}$ and $\left(\hat{H}_{k,l,ntx,nrx} \right)^{(q-1)}$ are the data and channel response estimates of the previous iteration. This step can only be applied after the first iteration. In the first iteration we set $\left(\tilde{R}_{k,l,nrx} \right)^{(1)} = R_{k,l,nrx}$.

- b. The channel frequency response estimates is computed using a moving average with size W , whilst at the same time removing the pilots, as follows (data is considered to be zero mean):

$$\left(\hat{H}_{k,l,ntx,nrx} \right)^{(q)} = \frac{1}{W} \sum_{l' = l - [W/2]}^{l + [W/2]} \frac{\left(\tilde{R}_{k,l',nrx} \right)^{(q-1)}}{S_{k,l',ntx}^{\text{Pilot}}} \quad (18)$$

- c. After the first iteration the data estimates can also be used as pilots for channel estimation refinement. This is especially useful if the spacing of pilot symbols in the time domain is $\Delta N_T > 1$. The respective channel estimates are computed as

$$\left(\tilde{H}_{k,l,ntx,nrx} \right)^{(q)} = \frac{(Y_{k,l,nrx})^{(q-1)} \left(\hat{S}_{k,l,ntx} \right)^{(q-1)*}}{\left| \left(\hat{S}_{k,l,ntx} \right)^{(q-1)} \right|^2} \quad (19)$$

- d. These channel estimates are enhanced by ensuring that the corresponding impulse response has a duration N_G . This is accomplished by computing the time domain impulse response of (18) and (19) through $\{(\tilde{h}_{i,l})^{(q)}; i = 0, 1, \dots, N - 1\} = \text{IDFT}\{(\tilde{H}_{k,l})^{(q)}; k = 0, 1, \dots, N - 1\}$ (zeros can be used for the missing carriers if $\Delta N_F > 1$, in order to perform a ‘‘FFT-interpolation’’), followed by the truncation of this sequence according to $\{(\hat{h}_{i,l})^{(q)} = w_i(\tilde{h}_{i,l})^{(q)}; i = 0, 1, \dots, N - 1\}$ with $w_i = 1$ if the i th time domain sample is inside the cyclic prefix duration and $w_i = 0$ otherwise. The final frequency response estimates are then simply computed using $\{(\hat{H}_{k,l})^{(q)}; k = 0, 1, \dots, N - 1\} = \text{DFT}\{(\hat{h}_{i,l})^{(q)}; i = 0, 1, \dots, N - 1\} * \Delta N_F$.

4. NUMERICAL RESULTS

The number of carriers employed was $N = 256$, each carrying a QPSK/16QAM/64QAM data symbol. Each information stream was encoded with a variable block size per antenna, yielding a deterministic number of 256-bit blocks after the FFT conversion. For the implicit case, the overall block size was of 2880 bits, whereas for the multiplexed pilots case, it was 720 bits per antenna — this way we had a fixed number of blocks per antenna for the multiplexed pilots case, and the same overall amount of bits for the implicit case, in order to avoid coding gains. The multiplexed pilots case used an extra block dedicated for channel estimation. The channel impulse response employed is characterized an exponential PDP (Power Delay Profile) with 32 symbol-spaced taps and normalized delay spread $\sum_{t_s=0}^{31} 10 \log_{10}(\frac{e^{-(t-t_s)}}{8})$. A symbol duration of $T_s = 260$ ns was used. The channel encoders were rate-1/2 turbo codes based on two identical recursive convolutional codes with two constituent codes characterized by $G(D) = [1(1 + D^2 + D^3)/(1 + D + D^3)]$. A random interleaver was used within the turbo encoders.

Most of the BER (Bit Error Rate) results presented next will be shown as a function of E_s/N_0 , where E_s is the average signal energy and N_0 is the single sided noise power spectral density. For channel estimation purposes, the moving average window size used was $W = 9$, considering different values of power ratio βP . The figures combine the use of perfect channel estimation, with estimation using multiplexed pilots (using $\Delta N_F = ntx$ and $\Delta N_T = N_T$) and estimation using implicit pilots (using $\Delta N_F = ntx$ and $\Delta N_T = 1$).

The power of the pilots is taken to be the same as the mean symbols' power throughout the block for the explicit case, and have a value of -6 dB for the implicit case. A fixed sliding window size of 45 was chosen.

In Figures 4–6, all the main performance results can be observed. Note that for the 16QAM and 64QAM, there are different orders of bit performance, and thus results were split into MSB — Most Significant Bit (highest protection); ISB — Intermediate Significance Bit (intermediate protection, only for 64QAM that modulates 3 bits) and LSB — Least Significant Bit (lowest protection).

In Figure 4, explicit channel estimation yields results similar to perfect estimation, and implicit estimation has a drawback of 2–3 dB. Note that the performance requires higher power for higher modulations, and that the offsets of using estimations also increase.

Comparing Figure 4 with Figures 6, we note that the MIMO 2×2 yields better results then SISO, due to high diversity and good equalization receiver. Between Figures 5–6 with a higher speed, the results require marginally more power, easily explained by the extrapolation error caused between pilot-exclusive blocks.

As regards for the implicit pilot estimation case, it can be seen throughout that it performs reasonably for modulations up to 16QAM (or 64QAM for SISO with “low” speed $v = 100$ km/h), with all its natural advantages of using the full bandwidth for data transmission — and a small amount of power for implicit pilot estimation.

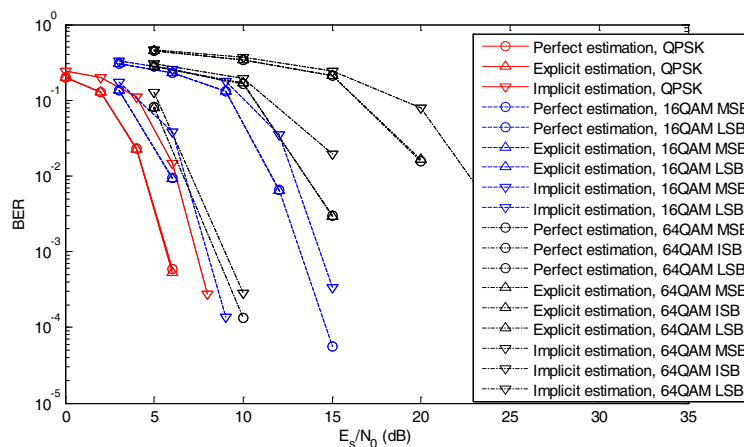


Figure 4: BER values for SC-FDE using IBDFE, SISO, QPSK/16QAM/64QAM, $v = 100$ km/h.

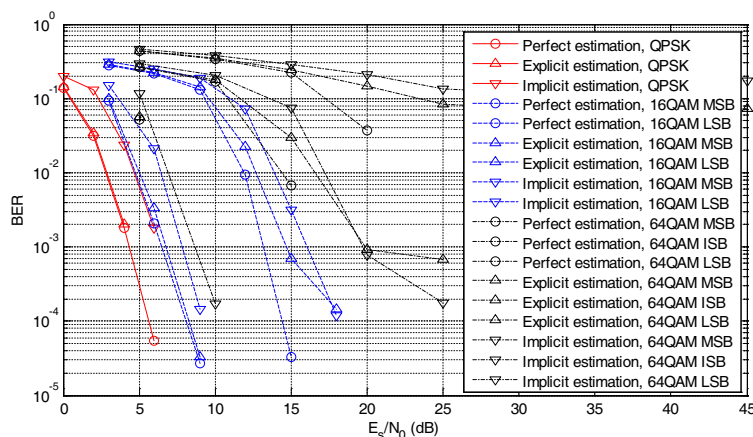


Figure 5: BER values for SC-FDE using IBDFFE, MIMO 2×2 , QPSK/16QAM/64QAM, $v = 100$ km/h.

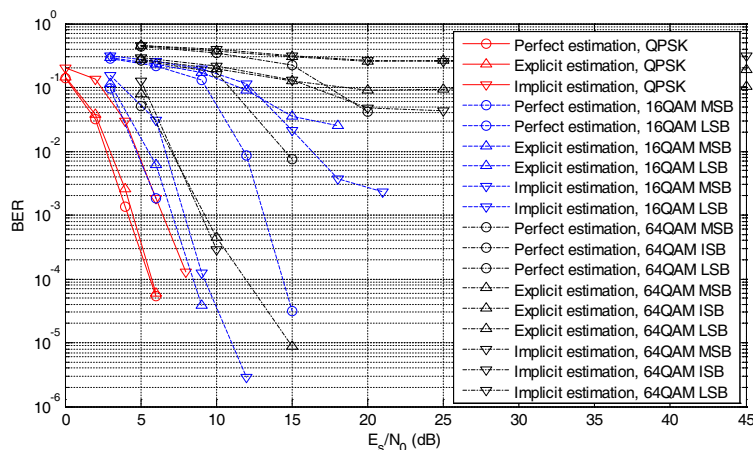


Figure 6: BER values for SC-FDE using IBDFFE, MIMO 2×2 , QPSK/16QAM/64QAM, $v = 200$ km/h.

5. CONCLUSIONS

In this paper, we have studied the use of SISO and MIMO 2×2 QPSK/16QAM/64QAM turbo-coding in a SC-FDE system employing both multiplexed and implicit pilots with the aim of supporting multicast and broadcast transmissions. To deal with the problem of the mutual interference between pilots and data symbols, which can severely affect the performance of QAM modulations, we proposed the use of an iterative receiver capable of accomplishing joint channel estimation and data detection. It was verified through simulations that, using channel estimation both with multiplexed pilots (at the cost of pilot bandwidth) and with implicit pilots (at the cost of around -6 dB more power), good performance results can be obtained.

ACKNOWLEDGMENT

This work was supported by the FCT project PTDC/EEA-TEL/120666/2010, “LTE-Advanced Enhancements using Femtocells”. The authors would like also to thank to Instituto de Telecomunicações for their support.

REFERENCES

1. Gusmão, A., R. Dinis, J. Conceição, and N. Esteves, “Comparison of two modulation choices for broadband wireless communications,” *Proc. IEEE VTC Spring*, 300–3305, May 2000.
2. Falconer, D., S. Ariyavisitakul, A. Benyamin-Seeyar, and B. Eidson, “Frequency domain equalization for single-carrier broadband wireless systems,” *IEEE Comm. Mag.*, Vol. 4, No. 4, 58–66, Apr. 2002.
3. Benvenuto, N. and S. Tomasin, “Block iterative DFE for single carrier modulation,” *IEE Electronic Letters*, Vol. 39, No. 19, Sep. 2002.

4. Dinis, R., A. Gusmão, and N. Esteves, “On broadband block transmission over strongly frequency-selective fading channels,” *Wireless 2003*, Calgary, Canada, Jul. 2003.
5. Dinis, R., R. Kalbasi, D. Falconer, and A. Banihashemi, “Iterative layered space-time receivers for single-carrier transmission over severe time-dispersive channels,” *IEEE Comm. Letters*, Vol. 8, No. 9, 579–581, Sep. 2004.
6. Tüchler, M., R. Koetter, and A. Singer, “Turbo equalization: principles and new results,” *IEEE Trans. on Comm.*, Vol. 50, May 2002.
7. Tüchler, M. and J. Hagenauer, “Turbo equalization using frequency domain equalizers,” *Allerton Conf.*, Oct. 2000.
8. Tüchler, M. and J. Hagenauer, “Linear time and frequency domain turbo equalization,” *IEEE VTC’01 (Fall)*, Oct. 2001.
9. Hoher, P., S. Kaiser, and P. Robertson, “Pilot-symbol-aided channel estimation in time and frequency,” *IEEE Communication Theory Mini-conference (CTMC), IEEE GLOBECOM97*, 90–96, 1997.
10. Sanzi, F. and J. Speidel, “An adaptive two-dimensional channel estimator for wireless OFDM with application to mobile DVB-T,” *IEEE Trans. on Broadcasting*, Vol. 46, 128–133, Jun. 2000.
11. Deneire, L., B. Gyselinckx, and M. Engels, “Training sequence versus cyclic prefix — A new look on single carrier communications,” *IEEE Comm. Letters*, Vol. 5, 292–294, Sep. 2001.
12. Orozco-Lugo, A., M. Lara, and D. McLernon, “Channel estimation using implicit training,” *IEEE Trans. on Sig. Proc.*, Vol. 52, No. 1, Jan. 2004.
13. Ho, C., B. Farhang-Boroujeny, and F. Chin, “Added pilot semi-blind channel estimation scheme for OFDM in fading channels,” *IEEE GLOBECOM’01*, Nov. 2001.
14. Zhu, H., B. Farhang-Boroujeny, and C. Schlegel, “Pilot embedding for joint channel estimation and data detection in MIMO communication systems,” *IEEE Comm. Letters*, Jan. 2003.
15. Lam, C., D. Falconer, F. Danilo-Lemoine, and R. Dinis, “Channel estimation for SC-FDE systems using frequency domain multiplexed pilots,” *IEEE VTC’06 (Fall)*, Sep. 2006.
16. Meng, X., J. Tugnait, and S. He, “Iterative joint channel estimation and data detection using superimposed training: Algorithms and performance analysis,” *IEEE Transactions on Vehicular Technology*, Vol. 56, No. 4, 1873–1880, Jul. 2007.
17. Marques da Silva, M., A. Correia, R. Dinis, N. Souto, and J. C. Silva, *Transmission Techniques for Emergent Multicast and Broadcast Systems*, CRC Press Auerbach Publications, Boca Raton, USA, May 2010, ISBN: 9781439815939.
18. Marques da Silva, M., et al., *Transmission Techniques for 4G Systems*, CRC Press Auerbach Publications, ISBN: 9781439815939, Boca Raton, USA, Nov. 2012, <http://www.crcpress.com/product/isbn/9781466512337>.

Single-stream Communication Using Orthogonal Signal Division Multiplexing with Multiple Antennas

T. Ebihara

Faculty of Engineering, Information and Systems, University of Tsukuba, Tsukuba, Japan

Abstract— Orthogonal signal division multiplexing (OSDM) is a new information transmission method using the Kronecker product between the rows of an IDFT matrix and the data sequences. This technique is designed to keep orthogonality among the data sequences over the frequency-selective fading channel. By sharing one data sequence as a pilot between the transmitter and the receiver, the receiver can obtain the channel matrix from the pilot and obtain the message by solving simultaneous equations. This technique has been extended to multistream communication with multiple antennas by the author. However, it was found that the simultaneous equation sometimes become ill-conditioned, which results in a loss of performance. This problem could be avoided with an increase in the number of antennas in the receiver. However, the increase in complexity remains an issue. In this paper, single-stream communication using OSDM with multiple antennas is proposed. By designing the data sequences in the transmitter, the ill-condition problem can be avoided with less complexity. The simulation results suggest that single-stream communication with multiple antennas can achieve better bit-error rate performance compared to the multistream case, with less complexity in exchange for an efficient data rate.

1. INTRODUCTION

The use of an array of antennas for both transmitting and receiving wireless communication is attractive to increase the throughput or spatial diversity. Greater throughput or spatial diversity in practical communication systems using multiple antennas can only be achieved if the channels are independent and identically distributed (e.g., an independent and identically distributed Rayleigh fading channel). Several communication systems using orthogonal frequency division multiplexing (OFDM) are in practical use. OFDM is attractive in terms of calculation complexity, because it makes frequency domain equalization possible at the receiver with the aid of fast Fourier transform (FFT), which is far simpler than time-domain equalization. I have been studying an alternative signal multiplexing scheme, orthogonal signal division multiplexing (OSDM), for wireless communication. The OSDM scheme is expected to be more robust against deep-fading channels because it combines some subcarriers for equalization, whereas the OFDM scheme equalizes the signal in each subcarrier [1–5]. Moreover, the OSDM technique has been extended to multi-stream communication with multiple antennas by the author [5–7]. However, it was found that the simultaneous equation in the equalization process sometimes becomes ill-conditioned, which results in the loss of communication quality. Although this problem could be avoided by increasing the number of antennas in the receiver, the increase in complexity remains problematic.

In this paper, single-stream communication using OSDM with multiple antennas is proposed to avoid such an ill-condition problem with less complexity. Section 2 provides an overview of single-stream communication using OSDM with multiple antennas. The performance evaluation of the proposed scheme in simulation is described in Section 3. The conclusions are summarized in Section 4.

2. SINGLE-STREAM COMMUNICATION USING ORTHOGONAL SIGNAL DIVISION MULTIPLEXING WITH MULTIPLE ANTENNAS

Although several communication schemes that use multiple antennas have been proposed, the focus of this paper is single-user communication in which the transmitter does not know the channel state information, and the signal power allocated for each transmitting antenna is equal. We assume that the transmitter and the receiver employ K_T and K_R antennas, respectively. Fig. 1 is a block diagram of OSDM for single-stream communication in the transmitter and the receiver when $K_T = K_R = 2$. The transmitter calculates the sum of the Kronecker products between the transmission message and the rows of an inverse discrete Fourier transform (IDFT) matrix, and it prepends a cyclic prefix (CP) as shown in the figure. As the transmission message, we consider data vectors of length M , $\mathbf{x}_{tn}^{k_T}$ ($n = 0, 1, \dots, N - 1$, $k_T = 0, 1, \dots, K_T - 1$), whose elements are modulated symbols expressed as complex numbers. In multi-stream communication, each element of $\mathbf{x}_{tn}^{k_T}$ is independent for all

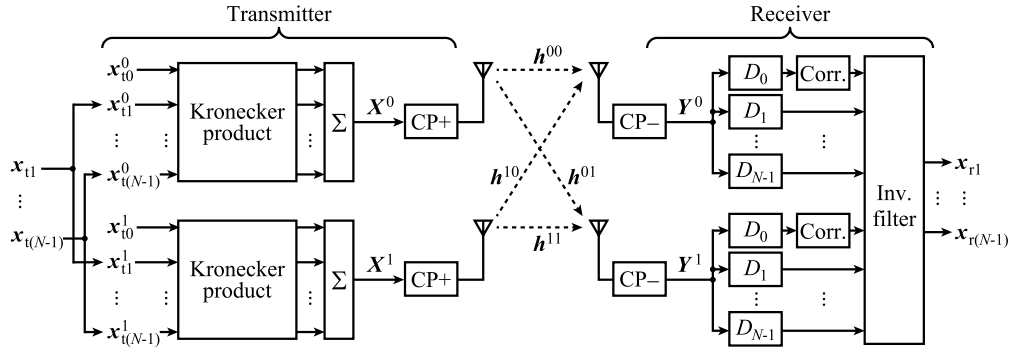


Figure 1: Block diagram of single-stream communication using OSDM with multiple (2×2) antennas.

n and k_T values. However, in this paper, we assume that $\mathbf{x}_{tn}^{k_T}$ is independent for only n , where $\mathbf{x}_{tn}^0 = \mathbf{x}_{tn}^1 = \dots = \mathbf{x}_{tn}^{K_T-1} \equiv \mathbf{x}_{tn}$ ($n = 1, 2, \dots, N-1$). This data vector, $\mathbf{x}_{tn}^{k_T}$, is multiplexed into the data stream of length MN , \mathbf{X}^{k_T} , as:

$$\mathbf{X}^{k_T} = \sum_{n=0}^{N-1} \mathbf{f}_{Nn} \otimes \mathbf{x}_{tn}^{k_T}, \quad (1)$$

where \mathbf{f}_{Nn} and ‘ \otimes ’ are the n -th row of the IDFT matrix of $N \times N$ and the Kronecker product, respectively. The transmitter prepends a CP of length L to \mathbf{X}^{k_T} , and transmits the signal through the channel from the antenna $\#k_T$.

We assume that the channel has a maximal delay of length L and is stable throughout the communication. The receiver removes the CP, applies the matched filter D_n , and applies the inverse filter to obtain the message, as shown in (Fig. 1). The CP-removed sequence obtained from the antenna $\#k_R$ ($k_R = 0, 1, \dots, K_R - 1$) can be expressed as:

$$\mathbf{Y}^{k_R} = \sum_{k_T=0}^{K_T-1} \mathbf{X}^{k_T} \begin{pmatrix} h^{k_T k_R}[0] & h^{k_T k_R}[1] & \dots & h^{k_T k_R}[MN-1] \\ h^{k_T k_R}[MN-1] & h^{k_T k_R}[0] & \dots & h^{k_T k_R}[MN-2] \\ \vdots & \vdots & \ddots & \vdots \\ h^{k_T k_R}[1] & h^{k_T k_R}[2] & \dots & h^{k_T k_R}[0] \end{pmatrix}, \quad (2)$$

where $h^{k_T k_R}[l]$ ($l = 0, 1, \dots, MN-1$) is a channel impulse response from the antenna $\#k_T$ to $\#k_R$ and $h^{k_T k_R}[l] = 0$ if $l \geq L$. The relationship between \mathbf{Y}^{k_R} and \mathbf{x}_{tn} is expressed by the following equation:

$$\begin{aligned} & (\mathbf{Y}^0 D_n \quad \mathbf{Y}^1 D_n \quad \dots \quad \mathbf{Y}^{K_R-1} D_n) \\ &= (\mathbf{x}_{tn}^0 \quad \mathbf{x}_{tn}^1 \quad \dots \quad \mathbf{x}_{tn}^{K_T-1}) \begin{pmatrix} C_n^{00} & C_n^{01} & \dots & C_n^{0(K_R-1)} \\ C_n^{10} & C_n^{11} & \dots & C_n^{1(K_R-1)} \\ \vdots & \vdots & \ddots & \vdots \\ C_n^{(K_T-1)0} & C_n^{(K_T-1)1} & \dots & C_n^{(K_T-1)(K_R-1)} \end{pmatrix}, \quad (3) \end{aligned}$$

$$= \mathbf{x}_{tn} \begin{pmatrix} \sum_{k_T=0}^{K_T-1} C_n^{k_T 0} & \sum_{k_T=0}^{K_T-1} C_n^{k_T 1} & \dots & \sum_{k_T=0}^{K_T-1} C_n^{k_T (K_R-1)} \end{pmatrix}, \quad (4)$$

where $D_n = \mathbf{f}_{Nn}^* \otimes I_M$, \mathbf{f}_{Nn}^* is a complex conjugate of the transposition of \mathbf{f}_{Nn} , I_M is an identity matrix of $M \times M$,

$$C_n^{k_T k_R} = \begin{pmatrix} \overline{W_N^n} h^{k_T k_R}[0] & h^{k_T k_R}[1] & \dots & h^{k_T k_R}[M-1] \\ \overline{W_N^n} h^{k_T k_R}[M-1] & h^{k_T k_R}[0] & \dots & h^{k_T k_R}[M-2] \\ \vdots & \vdots & \ddots & \vdots \\ \overline{W_N^n} h^{k_T k_R}[1] & \overline{W_N^n} h^{k_T k_R}[2] & \dots & h^{k_T k_R}[0] \end{pmatrix}, \quad (5)$$

and \overline{W}_N^n is a complex conjugate of $W_N^n = \exp(2\pi\sqrt{-1}n/N)$. It is clear that if the receiver knows the channel response, $h^{k_T k_R}[l]$, the received message, \mathbf{x}_{rn} , can successfully be obtained as;

$$\mathbf{x}_{rn} = \left(\mathbf{Y}^0 D_n \quad \mathbf{Y}^1 D_n \quad \dots \quad \mathbf{Y}^{K_R-1} D_n \right) C_n^{s*} (C_n^s C_n^{s*})^{-1}, \quad (6)$$

where C_n^s is the matrix on the right-hand side in Eq. (4). In OSDM, the channel response, $h^{k_T k_R}[l]$, can be obtained by sharing $\mathbf{x}_{t0}^0, \mathbf{x}_{t0}^1, \dots, \mathbf{x}_{t0}^{K_T-1}$ in both the transmitter and the receiver, as a pilot. Further details regarding the channel measurement are as described [6, 7].

From Eqs. (4) and (6), it is clear that the receiver must solve the ill-condition problem if the condition number of C_n^s is large. In the single-stream scheme, the receiver combines $K_T K_R$ channel matrices for equalization, as shown in Eq. (4), whereas the multi-stream scheme combines K_R channel matrices. Because the condition number of C_n^s becomes small as the number of channel matrices for combining increases, the single-stream scheme is attractive to avoid the ill-condition problem with a limited number of reception antennas.

Moreover, the complexity of single-stream scheme in the receiver is far less than that of the multi-stream scheme. The required number of complex multiplications for the receiver in the single-stream scheme is on the order of $K_R M^3 N$, whereas that in the multi-stream scheme is $(K_T^3 + K_T^2 K_R) M^3 N$. Although the efficient data rate of the single-stream scheme remains $1/K_T$ of that of the multistream scheme, the single-stream communication is attractive because it may achieve better communication quality compared to the multi-stream case with far less complexity.

3. PERFORMANCE EVALUATION IN SIMULATION

The performance of single-stream communication using OSDM was evaluated in simulation. In the simulation, baseband transmission (which did not include carrier modulation or demodulation processes) was performed under the condition that $M = 31$, $N = 2$, and $K_T = K_R = 2$. The channel response in simulation was assumed to be a Rayleigh fading channel of $L = 15$ with an exponentially decaying amplitude profile. In this paper, the communication quality is discussed in light of the relationship between the signal-to-noise ratio (SNR) and the bit-error rate (BER). The SNR is defined as the ratio between the total power of the received sequence and that of additive noise.

Figure 2 shows the relationship between the SNR and BER of single-stream communication using OSDM with multiple antennas (2×2). For comparison, the relationships between the SNR and BER of multistream communication using OSDM with multiple antennas (2×2 , 2×3 , and 2×4) are also shown in the figure. The single-stream scheme (2×2) achieves better performance compared to the multistream scheme with the same number of reception antennas (2×2), and its performance is almost the same as that of the multistream scheme with more reception antennas (2×4) (Fig. 2). This is because the receiver in the single-stream scheme can combine more channel matrices for equalization compared to the multistream scheme, as was noted in Section 2.

Although the efficient data rate of the single-stream scheme is still one-half of that of the multi-stream scheme in this simulation, the single-stream communication is attractive because the complexity of the single-stream scheme in the receiver is about $1/8$ and $1/12$ of that of the multistream scheme in (2×2) and (2×4), respectively.

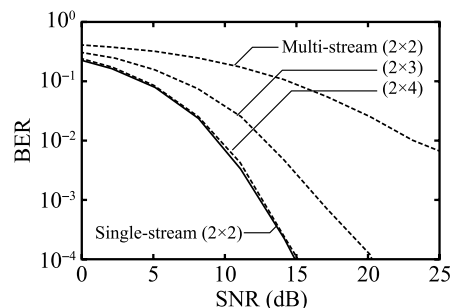


Figure 2: Performance comparison of single-stream communication and multi-stream communication using OSDM with multiple antennas.

4. CONCLUSION

Single-stream communication using OSDM with multiple antennas is proposed to increase the communication quality with less complexity, compared to multistream communication using OSDM with multiple antennas. In the multistream scheme, the simultaneous equation sometimes become ill-conditioned, which results in loss of performance. This problem could be avoided with an increase in the number of antennas in the receiver. However, the increase in complexity remains an issue. In this paper, single-stream communication using OSDM with multiple antennas was proposed to avoid the ill-condition problem with less complexity. By designing the data sequences in the transmitter, the ill-condition problem could be avoided with less complexity. We evaluated the performance of the proposed scheme in a baseband simulation. The simulation results suggest that the single-stream communication achieved better bit-error rate performance compared to the multistream case with less complexity in exchange for an efficient data rate, and it may be suitable for wireless communication systems with a limited number of reception antennas.

ACKNOWLEDGMENT

This work was partially supported by a Grant-in-Aid for Young Scientists (B) by the Japan Society for Promotion of Science (24760672).

REFERENCES

1. Suehiro, N., C. Han, and T. Imoto, "Very efficient wireless frequency usage based on pseudo-coherent addition of multipath signals using Kronecker product with rows of DFT matrix," *Proc. IEEE Int. Symp. Information Theory*, 385, Yokohama, Japan, Jul. 2003.
2. Suehiro, N., R. Jin, C. Han, and T. Hashimoto, "Performance of very efficient wireless frequency usage system using Kronecker product with rows of DFT matrix," *Proc. IEEE Information Theory Workshop*, 526, Chengdu, China, Oct. 2006.
3. Han, C., N. Suehiro, and T. Hashimoto, "Study of OSDM over Quasi-Static channel," *IEICE Technical Report*, RS207-35, 37–42, 2007.
4. Ebihara, T. and K. Mizutani, "Underwater acoustic communication with an orthogonal signal division multiplexing scheme in doubly spread channels," *IEEE Journal of Oceanic Engineering*, (in press).
5. Ebihara, T. and N. Suehiro, "The orthogonal signal division multiplexing and its performance evaluation," *Denshi Joho Tsushin Gakkai Ronbunshi B*, Vol. 91-B, No. 9, 1086–1094, 2008.
6. Ebihara, T., "High-speed underwater acoustic communication using orthogonal signal division multiplexing: A MIMO approach," *Proc. Symp. Ultrasonic Electronics*, Vol. 33, 509–510, 2012.
7. Ebihara, T., "Improvement of power efficiency for underwater acoustic communication using orthogonal signal division multiplexing over multiple transducers," *Japanese Journal of Applied Physics*, (in press).

General Ray Method for Solution of Dirichlet Boundary Value Problem for Helmholtz Equations

Alexandre Grebennikov and A. Lizbeth Cortés Cortés

Facultad de Ciencias Físico Matemáticas, Benemérita Universidad Autónoma de Puebla
Av. San Claudio y Río verde, Ciudad Universitaria, Puebla, Pue., CP 72570, Mexico

Abstract— An approach for solution of the Dirichlet boundary value problems for Helmholtz equations on the base of the General Rays Principle is considered. The proposed approach to the problem under investigation consists in constructing for considering PDE an analogue as family of ODE, describing the distribution of the electrical potential function $u(x, y)$ along of “General Rays”, which are presented by straight lines. The scheme of reduction PDE to the family of ODE uses the application of the direct Radon transform to PDE. This reduction leads to ODE with respect to variable p . Development of proposed scheme leads to the General Ray method, which presents the solution of the considering problem by explicit analytical formulas that include the direct and inverse Radon transforms. Developed versions of the General Ray method for considering class of problems is realized as algorithms and program package in MATLAB system, illustrated by numerical experiments.

1. INTRODUCTION

There are two main approaches for solving boundary value problems for partial differential equations in analytical form: the Fourier decomposition and the Green function method [1]. The Fourier decomposition is used, as the rule, only in theoretical investigations. The Green function method is the explicit one, but it is difficult to construct the Green function for the complex geometry of the considered domain Ω . The known numerical algorithms are based on the Finite Differences method, Finite Elements (Finite Volume) method and the Boundary Integral Equation method. Numerical approaches lead to solving systems of linear algebraic equations [2] that require a lot of computer time and memory.

A new approach for the solution of boundary value problems on the base of the General Ray Principle (*GRP*) was proposed by the author in [3, 4] for the stationary waves field. *GRP* leads to explicit analytical formulas (*GR*-method) and fast algorithms, developed and illustrated by numerical experiments in [4] for solution of the boundary value problems for the Laplace equation. Here we extend the proposed approach to construct p -version of *GR*-method, based on application of the direct Radon transform to Helmholtz equations. Developed p -version of *GR*-method is realized as algorithms and program package in MATLAB system, illustrated by numerical experiments.

2. GENERAL RAY PRINCIPLE AND P -VERSION OF *GR*-METHOD

The General Ray Principle gives no traditional mathematical model for considered physical field and corresponding boundary problems. *GRP* consists in the next main assumptions:

- 1) the physical field can be simulated mathematically by the superposition of plane vectors (general rays) that form field $\vec{V}(l)$ for some fixed straight line l ; each vector of field $\vec{V}(l)$ is parallel to the direction along this line l , and the superposition corresponds to all possible lines l that intersect domain Ω ;
- 2) the field $\vec{V}(l)$ is characterized by some potential function $u(x, y)$;
- 3) we know some characteristics such as values of function $u(x, y)$ and/or flow of the vector $\vec{V}(l)$ in any boundary point $P_0 = (x^0, y^0)$ of the domain.

Application of the *GRP* to the problem under investigation means to construct for considering PDE an analogue as a family of ODE, describing the distribution of the function $u(x, y)$ along of “General Rays”, which are presented by a straight line l with some parameterization. We use the traditional Radon parameterization with a parameter t : $x = p \cos \varphi - t \sin \varphi$, $y = p \sin \varphi + t \cos \varphi$. Here $|p|$ is a length of the perpendicular from the centre of coordinates to the line l , $\varphi \in [0, \pi]$ is the angle between the axis x and this perpendicular.

Let us consider the Dirichlet boundary problem for the Helmholtz equation:

$$\Delta u(x, y) + k^2 u(x, y) = \psi(x, y), \quad (x, y) \in \Omega; \quad (1)$$

$$u(x, y) = f(x, y), \quad (x, y) \in \Gamma, \quad (2)$$

with respect to the function $u(x, y)$ that has two continuous derivatives on bought variables inside the plane domain Ω , bounded with a continuous curve Γ . Here $\psi(x, y)$, $(x, y) \in \Omega$ and $f(x, y)$, $(x, y) \in \Gamma$ are given functions.

The p -version of the GR -method can be explained as the consequence of the next steps:

- 1) reduce the boundary value problem to homogeneous one;
- 2) extend the desired solution $u_0(x, y)$ of the reduced problem to all plane, such that $u_0(x, y) = 0$, $(x, y) \notin \Omega$, and describe its distribution along the general ray (a straight line l) by the direct Radon transform $\hat{u}_0(p, \varphi)$;
- 3) construct the family of ODE on the variable p with respect the function $\hat{u}_0(p, \varphi)$, applying the direct Radon transform to no homogeneous equation and supposing the fulfillment of formula (2) at the pp. 3 in [5];
- 4) solution of the constructed ODE with zero boundary conditions;
- 5) calculate the inverse Radon transform of the obtained solution;
- 6) regress to the initial boundary conditions.

We present bellow the realization of this scheme, supposing that the boundary Γ can be described in the polar coordinates (r, α) by some one-valued positive function that we denote $r_0(\alpha)$, $\alpha \in [0, 2\pi]$. It is always possible for the simple connected star region Ω with the centre at the coordinate origin. Let us write the boundary function $\bar{f}(\alpha) = f(r_0(\alpha) \cos \alpha, r_0(\alpha) \sin \alpha)$. Supposing that functions $r_0(\alpha)$ and $\bar{f}(\alpha)$ have the second derivative, we introduce functions $f_0(\alpha) = \bar{f}(\alpha)/r_0^2(\alpha)$, $(x, y) \in \Omega$, $\psi_0(x, y) = \psi(x, y) - 4f_0(\alpha) - f_0''(\alpha) - k^2 r^2 f_0(\alpha)$, $u_0(x, y) = u(x, y) - r^2 f_0(\alpha)$.

To realize the first step of the scheme we can write the boundary problem with respect the function $u_0(x, y)$ as the next two equations:

$$\Delta u_0(x, y) + k^2 u_0(x, y) = \psi_0(x, y), \quad (x, y) \in \Omega; \quad (3)$$

$$u_0(x, y) = 0, \quad (x, y) \in \Gamma. \quad (4)$$

To make the second and the third steps we need to extend $u_0(x, y)$ as zero out of the domain Ω and use the direct Radon transform:

$$R[u](p, \varphi) = \int_{-\infty}^{+\infty} u(p \cos \varphi - t \sin \varphi, p \sin \varphi + t \cos \varphi) dt$$

After application the Radon transform to the Equation (3) we obtain, using formula (2) at the pp. 3 of [9], the family of the ODE with respect the variable p :

$$\frac{d^2 \hat{u}_0(p, \varphi)}{dp^2} + k^2 \hat{u}_0(p, \varphi) = R[\psi_0](p, \varphi), \quad (p, \varphi) \in \hat{\Omega}; \quad (5)$$

where $\hat{\Omega}$ is the domain of the change of parameters p , φ . As the rule, $\varphi \in [0, \pi]$, module of the parameter p is equal to the radius in the polar coordinates and changes in the limits, determined by the boundary curve Γ . In the considered case for some fixed φ parameter p is in the limits: $-r_0(\varphi - \pi) < p < r_0(\varphi)$.

For the fourth step, we propose to use the next boundary conditions for every fixed $\varphi \in [0, \pi]$:

$$\hat{u}_0(-r_0(\varphi - \pi), \varphi) = 0; \quad \hat{u}_0(r_0(\varphi), \varphi) = 0. \quad (6)$$

Result of the fourth step for $(p, \varphi) \in \hat{\Omega}$ is presented by formula:

$$\begin{aligned} \hat{u}_0(p, \varphi) = & \frac{\left(\int_{-r_0(\varphi-\pi)}^{r_0(\varphi)} \hat{\psi}_0(\varphi, p) \text{sen}(kp) dp \right) \cos(kr_0(\varphi)) - \left(\int_{-r_0(\varphi-\pi)}^{r_0(\varphi)} \hat{\psi}_0(\varphi, p) \cos(kp) dp \right) \text{sen}(kr_0(\varphi))}{k(\text{sen}(kr_0(\varphi)) - \tan(-kr_0(\varphi - \pi)) \cos(kr_0(\varphi)))} \text{sen}(kp) \\ & + \frac{\tan(-kr_0(\varphi - \pi)) \left(\int_{-r_0(\varphi-\pi)}^{r_0(\varphi)} \hat{\psi}_0(\varphi, p) \cos(kp) dp \right) \text{sen}(kr_0(\varphi))}{k(\text{sen}(kr_0(\varphi)) - \tan(-kr_0(\varphi - \pi)) \cos(kr_0(\varphi)))} \cos(kp) \\ & - \frac{\tan(-kr_0(\varphi - \pi)) \left(\int_{-r_0(\varphi-\pi)}^{r_0(\varphi)} \hat{\psi}_0(\varphi, p) \text{sen}(kp) dp \right) \cos(kr_0(\varphi))}{k(\text{sen}(kr_0(\varphi)) - \tan(-kr_0(\varphi - \pi)) \cos(kr_0(\varphi)))} \cos(kp) \\ & + \frac{1}{k} \left(\int_{-r_0(\varphi-\pi)}^p \hat{\psi}_0(\varphi, p) \cos(kp) dp \right) \text{sen}(kp) \\ & - \frac{1}{k} \left(\int_{-r_0(\varphi-\pi)}^p \hat{\psi}_0(\varphi, p) \text{sen}(kp) dp \right) \cos(kp) \end{aligned}$$

and out of the $\hat{\Omega}$ we extend $\hat{u}_0(p, \varphi) \equiv 0$.

Let us denote the inverse Radon transform as operator R^{-1} , then the fifth and sixth steps of the scheme are concentrated in the next formula

$$\bar{u}(x, y) = R^{-1}[\hat{u}_0(p, \varphi)] + r^2 f_0(\alpha), \quad (x, y) \in \Omega \tag{7}$$

The inverse Radon transforms in explicit formula (7) can be realized numerically by fast Fourier discrete transformation (FFDT) that guarantees the rapidity of proposed method and developed algorithmic realization.

3. NUMERICAL EXPERIMENTS

We have constructed the fast algorithmic and program realization of *GR*-method for considered problem in MATLAB system. We used the uniform discretization of variables $p \in [-1, 1]$, $\varphi \in$

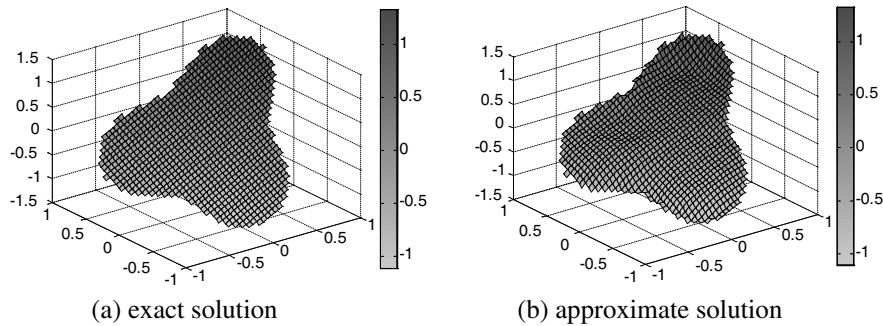


Figure 1.

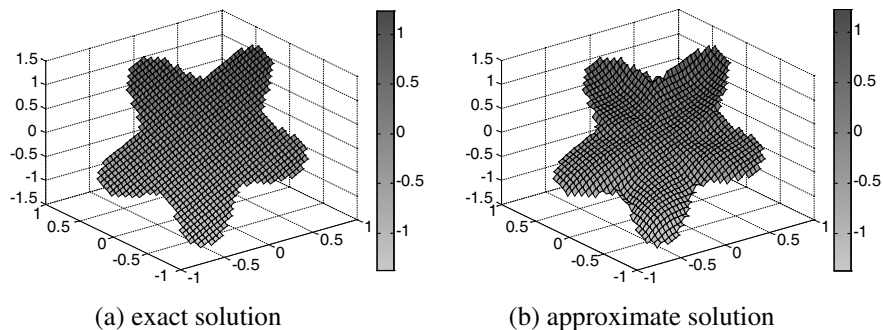


Figure 2.

$[0, \pi]$, so as for variables x, y , with \mathbf{N} nodes. We made testes on mathematically simulated model examples with known exact functions $u(x, y), f(x, y), \psi(x, y)$. Graphic illustrations of solution of numerical examples by GR -method for the Helmholtz equation are presented at Figures 1 and 2. Boundary curves Γ are determined for these figures by formula $r_0(\alpha) = 0.8 + 0.2 * \sin(k * \alpha)$ parameter $k = 3$ for Figure 1 and $k = 5$ for Figure 2. Exact solution is the bilinear function $u = x + y$.

4. CONCLUSION

The p -version of GR -method is constructed for solution of the Dirichlet boundary value problems for Helmholtz equation. It is based on application of the Radon transform directly to the partial differential equation. This version of GR -method for arbitrary simple connected star domains is realized as fast algorithms and program package in MATLAB system, illustrated by numerical experiments.

ACKNOWLEDGMENT

The author acknowledges to CONACYT Mexico, Merited Autonomous University of Puebla Mexico and Aerospace School of Moscow Aviation Institute for approval of this investigation in the frame of the Probation Period at 2012–2013 years.

REFERENCES

1. Sobolev, S. L., *Equations of Mathematical Physics*, Moscow, 1966.
2. Samarsky, A. A., *Theory of Difference Schemes*, Moscow, 1977.
3. Grebennikov, A. I., “Fast algorithm for solution of Dirichlet problem for Laplace equation,” *WSEAS Transaction on Computers Journal*, Vol. 2, No. 4, 1039–1043, 2003.
4. Grebennikov, A., “Fast algorithms and MATLAB software for solution of the dirichlet boundary value problems for elliptic partial differential equations in domains with complicated geometry,” *WSEAS Transactions on Mathematics J.*, Vol. 7, No. 4, 173–182, 2008.
5. Sigurdur, H., *The Radon Transform*, Birkhauser, Boston-Basel-Berlin, 1999.

High Resolvability of Electrical Tomography Based on General Ray Method

Alexandre Grebennikov

Facultad de Ciencias Físico Matemáticas, Benemérita Universidad Autónoma de Puebla
Av. San Claudio y Río verde, Ciudad Universitaria, Puebla, Pue., CP 72570, Mexico

Abstract— A computer simulation of a new special Electrical Tomography method of high resolvability is proposed. Its mathematical model and the measurement scheme of external data are constructed on the basis of General Ray Principle, proposed by the author for distribution of different, in particular electromagnetic, fields. Proposed model leads to the classic Radon transformation that appears as specific element in new General Ray Method, constructed by the author and realized as a simple linear fast numerical algorithm. Proposed measurement scheme and General Ray algorithms open possibility of high resolvability and fast computer recognition of compound structures with micro components. Developed scheme is realized as MATLAB software and justified by numerical experiments.

1. INTRODUCTION

In creation and construction of modern artificial materials it appears the necessity of recognition of compound structures with micro and nano-particles. Recognition of compound structures with elements that have different electro-conductivities or permittivity is possible using scanning by Electrical Tomography (ET). In a plane case it can be mathematically described [1] as a coefficient inverse problem for the Laplace equation, written in the divergent form

$$\frac{\partial}{\partial x} (\varepsilon(x, y)u'_x(x, y)) + \frac{\partial}{\partial y} (\varepsilon(x, y)u'_y(x, y)) = 0, \quad (1)$$

where $(x, y) \in \Omega$ some limited open region on a plane, $u(x, y)$ is potential, the function $\varepsilon = \varepsilon(x, y)$ characterize the conductivity or permittivity of a media.

In traditional statement [1] it is supposed also that functions $J_n(x, y)$, $u^0(x, y)$ are known on the boundary curve Γ and the next boundary conditions are satisfied:

$$\varepsilon(x, y) \frac{\partial u(x, y)}{\partial n} = J_n(x, y), \quad (x, y) \in \Gamma, \quad (2)$$

$$u(x, y) = u^0(x, y), \quad (x, y) \in \Gamma, \quad (3)$$

where $\frac{\partial}{\partial n}$ is the normal derivative in the points of the curve Γ .

Equations (1)–(3) serve as the model of ET, when there is a family of potential and boundary conditions that corresponds to different angles of scanning scheme. Traditional approach for solving ET leads to nonlinear ill-posed problem.

In traditional schemes [1] the electric field is produced by the same electrodes that serve as measuring elements, i.e., the electrodes are active. May be this activity of electrodes, which provokes its mutual influence, is the cause of impossibility to use a great number of electrodes and obtain the sufficiently large number of measurements. It is very important that in proposing scheme electrodes on the boundary Γ do not produce the external electric field (are not active) and serve only for measurement of data. Therefore, the proposed approach gives in principal the possibility to use a large number of electrodes and measurements of the input values of data and reconstruct the desired image more perfectly.

2. NEW MEASUREMENT SCHEME FOR ELECTRIC TOMOGRAPHY AND GENERAL RAY METHOD

In [2], a new variant of the ET is proposed, when the external electromagnetic field $\vec{V}(l)$, is produced by active electrodes, located outside of the Ω , initiates some distribution of the electric potential inside the domain Ω . At that, we propose that measurements of necessary values would be realized on the boundary curve Γ with another, no active electrodes. To construct a mathematical model of proposed ET we use the General Ray Principle [3], i.e., consider the electric field as the stream

flow of “general rays”. Each one of these rays corresponds to some straight line l . The main idea of the General Ray Principle consists in reduction a Partial Differential Equation to a family of Ordinary Differential Equations. Let the line l has the parametric presentation: $x = p \cos \varphi - t \sin \varphi$, $y = p \sin \varphi + t \cos \varphi$, where $|p|$ is a length of the perpendicular, passed from the centre of coordinates to the line l , φ is the angle between the axis X and this perpendicular [4]. Hence, using this parameterization for the line l , we shall consider the potential $u(x, y)$ and function $\varepsilon(x, y)$ for $(x, y) \in l$ as functions (traces) $\bar{u}(t)$ and $\bar{\varepsilon}(t)$ of variable t . Let suppose that domain Ω is the circle of radius r . Considering the Equation (1) on the line l we obtain for every fixed p and φ the ordinary differential equation for traces

$$(\bar{\varepsilon}(t)\bar{u}'_t(t))'_t = 0, \quad |t| < \bar{t}, \quad \bar{t} = \sqrt{r^2 - p^2}. \quad (4)$$

We suppose that functions $v(p, \varphi)$ and $J(p, \varphi)$ are given and we can write boundary conditions

$$\bar{\varepsilon}(-\bar{t})\bar{u}'_t(-\bar{t}) = J(p, \varphi), \quad (5)$$

$$\bar{u}(\bar{t}) - \bar{u}(-\bar{t}) = v(p, \varphi) \quad (6)$$

Equations (4)–(6) are considered as the basic mathematical model for new type of ET [2].

If different components in the considered structure have the smooth distribution, therefore functions $\bar{\varepsilon}(t)\bar{u}'_t(t)$ and $\bar{u}'_t(t)$ are continuous. Integrating twice the Equation (4) on t and using boundary conditions (5)–(6), we obtain for $\varepsilon(x, y)$ the next formula for scanning General Ray (*GR*) method

$$\varepsilon(x, y) = 1/R^{-1} \left[\frac{v(p, \varphi)}{J(p, \varphi)} \right], \quad (7)$$

where R^{-1} is the inverse Radon transform operator [4]. *GR*-method gives the explicit solution of the inverse coefficient problem for considering case. It is generalized and applied also for structures with piecewise constant characteristics. We have constructed the numerical realization of formula (7) that we call “*GR*-algorithm”. This algorithm is fast, because it does not require solving any equation and the Radon transform can be inverted by fast manner using discrete Fast Fourier Transform algorithm.

3. NUMERICAL EXPERIMENTS

We tested scanning *GR*-algorithm on mathematically simulated model examples for structure with piecewise-constant permittivity. The scheme of solution of the corresponding example consists of the steps presented in details at [5]. Here we considered a plane circle of radius 1 mm with basic permittivity $\varepsilon_0(x, y) = 1$ and two different internal elements as circles of radiuses r_i , $i = 1, 2$, with permittivity $\varepsilon_1(x, y) = 2$, $\varepsilon_2(x, y) = 3$.

At part (a) of Figures 1, 2, the exact structures are shown; at part (b) — reconstructed structures, for $r_1 = 0.05$ mm, $r_2 = 0.005$ mm, $r_1 = 0.0015$ mm, $r_2 = 0.001$ mm correspondently. We have used discretization on the bi-dimensional red with $N \times N$ nodes and made calculation at the PC with processor INTEL CORE 2 DUO T5250. For the first example $N = 1001$, time of reconstruction — 207.1 sec; in the second example $N = 3001$, time of reconstruction — 5950 sec.

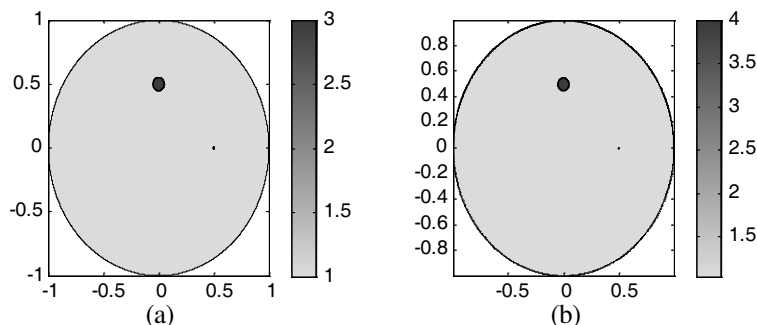


Figure 1: The first example, $r_1 = 0.05$, $r_2 = 0.005$; (a) — exact distribution; (b) — reconstructed distribution. $N = 1001$, time of reconstruction — 207.1 sec.

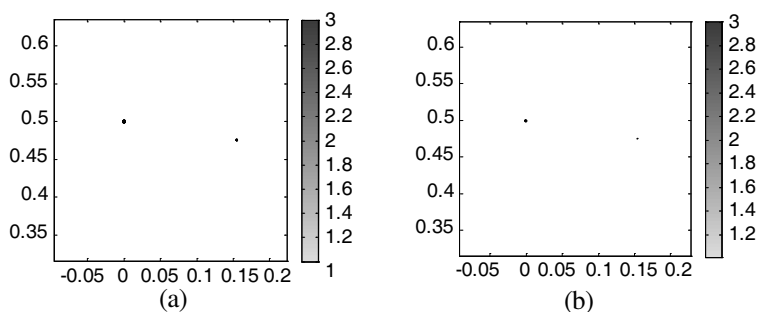


Figure 2: Scaled image of the second synthetic example; $r_1 = 0.0015$, $r_2 = 0.001$; (a) — exact distribution; (b) — reconstructed distribution. $N = 3001$, time of reconstruction — 5950 sec.

4. CONCLUSIONS

A new measurement scheme and a new mathematical model on the base of the *GRP* for ET are considered. To resolve this scheme fast algorithms and MATLAB software are constructed. The properties of the constructed algorithms and computer programs are illustrated by numerical experiments that demonstrate the possibility to reconstruct structures with micro-scale elements.

ACKNOWLEDGMENT

The author acknowledges to CONACYT Mexico, Merited Autonomous University of Puebla Mexico and Aerospace School of Moscow Aviation Institute for approval of this investigation in the frame of the Probation Period at 2012–2013 years.

REFERENCES

1. Williams, R. A. and M. S. Beck, *Process Tomography: Principles, Techniques and Applications*, Butterworth-Heinemann, Oxford, 1995.
2. Grebennikov, A., “New mathematical model and measurement scheme of electrical tomography and its fast resolution by general ray method,” *PIERS Proceedings*, 256–259, Moscow, Russia, Aug. 19–23, 2012.
3. Grebennikov, A. I., “A novel approach for solution of direct and inverse problems for some equations of mathematical physics,” *Proceedings of the 5th International Conference on Inverse Problems in Engineering: Theory and Practice*, D. Lesnic, Ed., Vol. II, Chapter G04, 1–10, Leeds University Press, Leeds, UK, 2005.
4. Radon, J., “Über die bestimmung von funktionen durch ihre integrawerte langs gewisser mannigfaltigkeiten,” *J. Math. Phys.*, Vol. K1, No. 69, 262–267, Berichte Sachsische Academic der Wissenschaften, Leipzig, 1917.
5. Reyes Mora, S. and A. I. Grebennikov, “Unicidad de solución del problema inverso de identificación de coeficiente en ecuación de tipo laplace con condiciones de contorno parcialmente reducidos,” *Boletín de la Sociedad Cubana de Matemática y Computación*, M-99, Numero especial Editorial de Universidad de Ciencias Pedagógicas “Enrique Jose Varona”, 2009.

Fast Numerical Solution of Dirichlet Boundary Problem for Laplace Equation in 3D Domains with Complicated Geometry

Alexandre Grebennikov

Facultad de Ciencias Físico Matemáticas, Benemérita Universidad Autónoma de Puebla
Av. San Claudio y Río verde, Ciudad Universitaria, Puebla, Pue., CP 72570, Mexico

Abstract— The Dirichlet boundary value problem for Laplace equation in 3D simply connected star domain Ω with continue boundary surface is considered. The proposed approach to the numerical solution of the problem consists in the next scheme: 1) apply the two-dimensional p -version of the General Ray Method for some sufficient number of slices in 3D domain; 2) construct 3D approximation of obtained 2D results by explicit spline-approximation formulas for 3 variables. We suppose that in every slice the corresponding sub domain is 2D simply connected star domain. Bought steps of the scheme can be realized by fast algorithms that guarantees rapidness of the calculation by scheme in general. Developed scheme is illustrated by numerical experiments realized on model examples, using constructed MATLAB software.

1. INTRODUCTION

Boundary problems for the Laplace equation appear as the main mathematical models in different areas of applied physics, particularly for the electrostatic stationary field [1].

One of the main approaches for solving these problems consists in constructing numerical algorithms based on the Finite Differences method, Finite Elements method and the Boundary Integral Equation method. All methods and algorithms constructed on the bases of this approach have some difficulties in realization for the complicated geometrical form of the domain Ω . Numerical approach leads to solving systems of linear algebraic equations that require a lot of computer time and memory. Another approach is analytical, based on the Fourier decomposition and the Green function method. The Fourier decomposition is used more for theoretical investigation, because the calculation of the coefficients of the Fourier series also requires essential numerical expenses.

The Green function method is the explicit one, which permits to construct solution of the boundary problem in explicit form by the Poisson integral. But concrete formulas of Green functions for the domains Ω with the complicated geometry were unknown. Some advantages in construction such formulas were achieved in [2] on the basis of Incompressible Influence Elements method that uses representation for Green's functions in the form of integrals and also require sufficiently large volume of calculations. Hence, construction of fast methods and algorithms of solution of mentioned problems for domains with complicated geometrical form is very actual.

In this paper, we consider the Dirichlet boundary value problem for Laplace equation in 3D simply connected star domain Ω with continue boundary surface Γ :

$$\Delta u(x, y, z) = 0, \quad (x, y) \in \Omega, \quad (1)$$

$$u|_{\Gamma} = f, \quad (2)$$

for a given function f .

The proposed approach to the numerical solution of the problem consists in the next scheme: 1) apply the two-dimensional p -version of the General Ray Method (*GR*-method) [3] for some sufficient number slices of the domain; 2) construct 3D approximation of obtained results by explicit spline-approximation formulas for 3 variables [4]. We suppose that in every slice the corresponding sub domain is also 2D simply connected star domain. Bought steps of the scheme can be realized by fast algorithms that guarantees rapidness of the calculation by scheme in general. Developed scheme is illustrated by numerical experiments realized on model examples, using constructed MATLAB software.

2. P-VERSION OF GR-METHOD FOR 2D DOMAIN

Let us consider plane slices S_k with coordinates z_k , $k = 1, \dots, N$ for points inside the domain Ω . We define Ω_k corresponding plane subdomains with contour Γ_k , presented in plane S_k by equation $r = r_k(\alpha)$ in polar coordinates, and consider for each one the particular problem

$$\Delta u_k(x, y) = 0, \quad (x, y) \in \Omega_k; \quad (3)$$

$$u_k(x, y) = f(x, y, z_k), \quad (x, y) \in \Gamma_k. \quad (4)$$

The p -version of the GR -method for 2D domain can be explained as the consequence of the next steps [3]:

- 1) reduce the problem to equivalent one with no homogeneous equation and homogeneous boundary condition:

$$\Delta u_{k,0}(x, y) = \psi_k(x, y), \quad (x, y) \in \Omega_k; \quad (5)$$

$$u_{k,0}(x, y) = 0, \quad (x, y) \in \Gamma_k; \quad (6)$$

- 2) extend the desired solution $u_{k,0}(x, y)$ of the reduced problem to all slice-plane S_k , such that $u_{k,0}(x, y) = 0$, $(x, y) \notin \Omega_k$, and describe it along the general ray (a straight line l) by its direct Radon transform $\hat{u}_k(p, \varphi) = R[u_{k,0}(x, y)]$;
- 3) construct the family of ODE on the variable p with respect the function $\hat{u}_k(p, \varphi)$, supposing the fulfillment of formula (2) at the pp. 3 in [5] and applying the direct Radon transform to no homogeneous equation;
- 4) resolve of the constructed ODE with zero boundary conditions;
- 5) calculate $u_{k,0}(x, y)$ as the inverse Radon transform of the obtained solution;
- 6) regress to the initial boundary condition calculating the function $u_k(x, y)$.

The concrete formulas corresponding to this scheme, presented in [3], are realized numerically by fast algorithms [6]. Constructed package of MATLAB programs present results in discreet form as a matrix of approximate values of functions $u_k(x, y)$ in the points of the uniform greed $\{x_{i,k}, y_{j,k}\}$, $i, j = 1, \dots, N$ that covers the domain Ω_k .

2.1. Observation

The supposition, mentioned in step 3), consists in fulfillment of the formula

$$R[\Delta u_{k,0}(x, y)] = \frac{d^2 \hat{u}_k(p, \varphi)}{dp^2}, \quad (7)$$

which is true, if the extended function $u_{k,0}(x, y)$ has continues derivatives of the second order in all the plane S_k . If corresponding derivatives are not continues (that frequently can occur) we consider our scheme for some approximation $u_{k,0}^\varepsilon(x, y)$ of the function $u_{k,0}(x, y)$. This approximation can be considered as solution of the problem

$$\Delta u_{k,0}^\varepsilon(x, y) = \psi_k^\varepsilon(x, y), \quad (x, y) \in \Omega_k; \quad (8)$$

$$u_{k,0}^\varepsilon(x, y) = 0, \quad (x, y) \in \Gamma_k; \quad (9)$$

where

$$\psi_k^\varepsilon(x, y) = \begin{cases} \psi_k(x, y), & (x, y) \in \Omega_k^\varepsilon; \\ 2\psi_k(r_k(\alpha) - \varepsilon, \alpha) \frac{r_k(\alpha) - \varepsilon/2 - r}{\varepsilon}, & (x, y) \in \Omega_k^{\varepsilon/2} / \Omega_k^\varepsilon; \\ 0, & (x, y) \notin \Omega_k^{\varepsilon/2}; \end{cases}$$

sub domain Ω_k^ε is defined as a part of Ω_k , such that for every α : $r < r_k(\alpha) - \varepsilon$. For continue function $\psi_k(x, y)$ solution $u_{k,0}^\varepsilon(x, y)$ of problem (8)–(9) exists, is unique and has continues derivatives of the second order in $\Omega_k \cup \Gamma_k$. Let us construct extension of $u_{k,0}^\varepsilon(x, y)$ as zero out of Ω_k , then this extension has continues second derivatives at all the plane S_k . So, for this extension and its Radon transform the relation (7) is fulfilled. Hence, the steps 3)–5) of the scheme can be realized for $u_{k,0}^\varepsilon(x, y)$. It is simple to justify, using presentation of solutions by the Green formula, that

$$u_{k,0}^\varepsilon(x, y) \rightarrow u_{k,0}(x, y), \quad \varepsilon \rightarrow 0, \quad (x, y) \in \Omega.$$

At the same time, the numerical realization of all steps 1)–6) of the scheme, which do not use values of the function $\psi_k(x, y)$ at the Γ_k , for sufficient little ε is the same for bought functions $u_{k,0}^\varepsilon(x, y)$ and $u_{k,0}(x, y)$. So, we justified possibility to construct the approximation for $u_{k,0}(x, y)$ by numerical realization of the proposed scheme without the additional supposition on fulfillment of relation (7).

3. EXPLICIT SPLINE APPROXIMATION OF 3D FUNCTIONS

The explicit method for approximation functions of one and many variables by splines was developed by the author, justified theoretically and by numerical experiments [7, 8]. We use the explicit formula for approximation of function $u(x, y, z)$ by three-dimensional spline on the grid $\{x_{i,k}, y_{j,k}, z_k\}$ $i, j, k = -1, \dots, N + 2$, which covers the domain Ω and some its neighborhood. Let $s_{i,k}(u)$ be a local basic cubic splines [7], constructed on the nodes $w_{i-2,k}, \dots, w_{i+2,k}$; $i = 1, \dots, N$; where w is x o y . For variable z , we also construct local basic cubic splines $s_k(z)$ on the red $\{z_k\}$. Mentioned formula is the next one:

$$S(x, y, z) = \sum_{k=1}^N \sum_{i=1}^N \sum_{j=1}^N u_k(x_{i,k}, y_{j,k}) s_{i,k}(x) s_{j,k}(y) s_k(z). \tag{10}$$

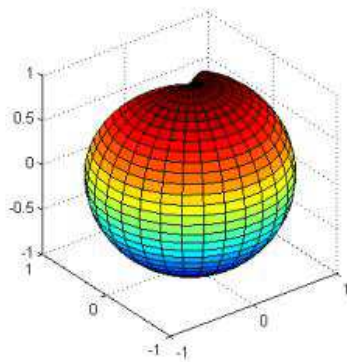


Figure 1.

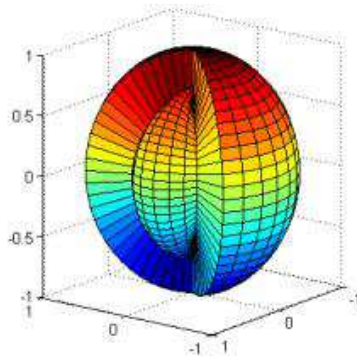


Figure 2.

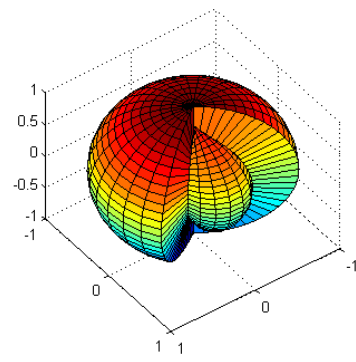


Figure 3.

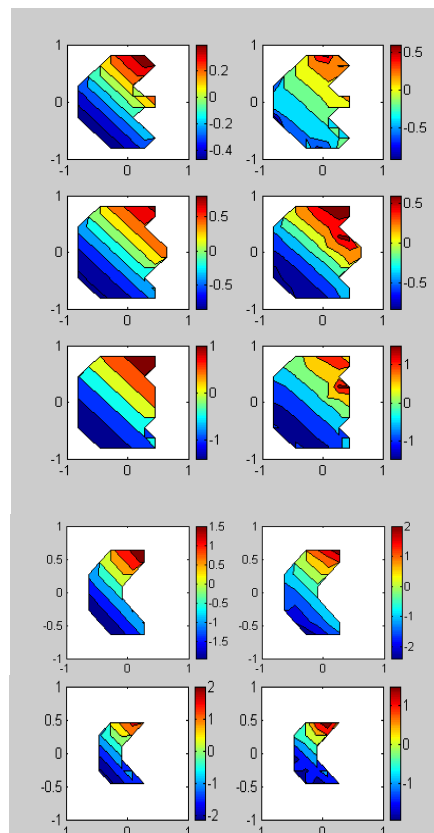


Figure 4.

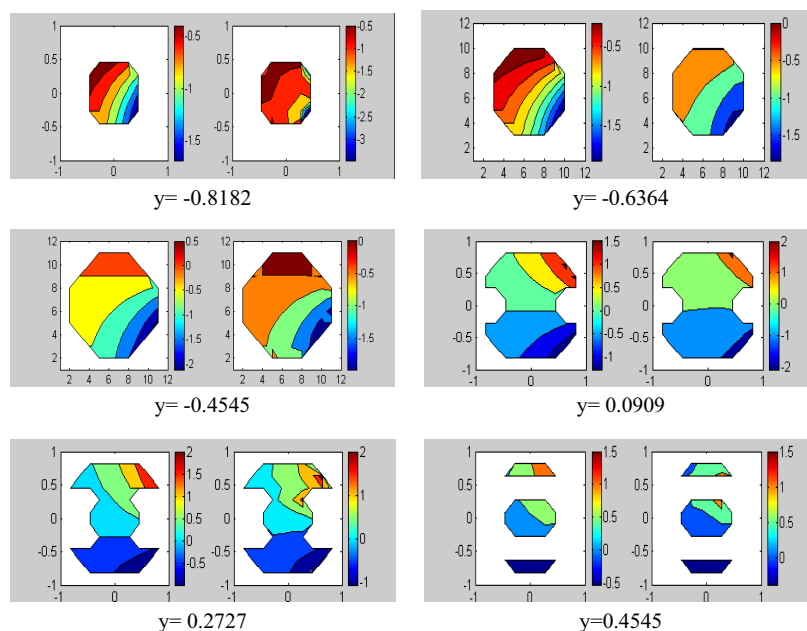


Figure 5.

4. NUMERICAL EXPERIMENTS

We have constructed the algorithmic and program realization of proposed schemes and formulas in MATLAB system, which we tested on mathematically simulated model examples with known exact function u .

Bellow we present example for the exact solution of the Laplace equation $u(x, y, z) = \sin(x + y) \exp(\sqrt{2}z)$ and domain Ω painted in Figures 1, 2, 3 for different points of view.

We calculated the approximate solution on the red with $N = 12$ points for every variable. In Figure 4, we see isoline maps of: 1) the exact solution (the left column of graphics); 2) the recuperated by GR -method and approximated by formula (10) solution (the right column of graphics), for intersections of the domain Ω by planes parallel to the coordinate plane xOy , which correspond to values $z = -0.4545, -0.0909, 0.2727; 0.4545, 0.6364$.

In Figure 5, we see similar isoline maps for intersections of the domain Ω by planes parallel to the coordinate plane xOz , which correspond to values of variable y , marked bellow the graphics.

5. CONCLUSIONS AND ACKNOWLEDGEMENTS

A new scheme for the approximate solution of the Dirichlet boundary value problem for Laplace equation in 3D simply connected star domain is developed, justified by theoretical reasons and realized numerically by fast algorithms. Constructed package of MATLAB programs is tested by simulated numerical examples, which confirm the validity and good approximation properties of constructed scheme.

The author acknowledges to CONACYT Mexico, Merited Autonomous University of Puebla Mexico and Aerospace School of Moscow Aviation Institute for approval of this investigation in the frame of the Probation Period at 2012–2013 years.

REFERENCES

1. Sobolev, S. L., *Equations of Mathematical Physics*, Moscow, 1966.
2. Seremet, V. D., *Handbook of Green's Functions and Matrices*, WIT Press, London, 2002.
3. Grebennikov, A. I., "General ray method for solution of dirichlet boundary value problems for poisson equation in arbitrary simple connected star domain," *Proceedings of 2nd International Symposium "Inverse Problems, Design and Optimization"*, 101–106, Miami, Florida, USA, Apr. 2007.
4. Grebennikov, A. I., *Spline Approximation Method and Its Applications*, MAX Press, Russia, 2004.
5. Helgason, S., *The Radon Transform*, Birkhauser, Boston-Basel-Berlin, 1999.

6. Grebennikov, A., “Fast algorithms and MATLAB software for solution of the dirichlet boundary value problems for elliptic partial differential equations in domains with complicated geometry,” *WSEAS Transactions on Mathematics J.*, Vol. 7, No. 4, 173–182, 2008.
7. Grebennikov, A. I., *Method of Splines and Solution of Ill-posed Problems of Approximations Theory*, Moscow University Publishers, Russia, 1983.
8. Grebennikov, A. I., *Algorithms and Programs of Approximation Functions of One and Some Variables by Splines and Applications*, Moscow University Publishers, Russia, 1987.

Electromagnetic Eigen-field Characteristics of Acousto-optic Waveguides with Transverse SAW

Yasumitsu Miyazaki

Faculty of Engineering, Aichi University of Technology
50-2 Manori, Nishihassama-cho, Gamagori 443-0047, Japan

Abstract— Among several optical devices, fundamental characteristics and processing systems of collinear optical switching device have been studied about optical dielectric waveguides on LiNbO₃ crystal substrates. Conventional waveguide-type A-O devices use collinear interaction with mode coupling based on Bragg condition between optical waves and SAW both propagating in same directions. Collinear A-O devices of waveguide-type show sufficient performance for wavelength selective switching with narrow bandwidths. However, in these collinear A-O devices, since SAW propagation speed is very slow, interaction time is several micro seconds for 10 mm waveguide device length.

In A-O devices of optical waveguides using transverse A-O interaction, where SAW propagates transversely and at right angles to optical wave propagation direction, SAW propagation lengths needed for complete A-O interaction may become 10 μm and interaction time may be several nano seconds, with ultra high speed switching. In this paper, fundamental characteristics of transverse A-O interaction are studied as electromagnetic boundary value problem.

Refractive indexes in optical waveguides induced by A-O effects with SAW are shown by sine functions. Wave field characteristics in inhomogeneous media of periodic structures for transverse directions given by A-O effects are analyzed by analytic method of Hill's equations for transverse spectral functions. Electromagnetic fields in core and clad regions with periodic structures are shown by Mathieu functions. By boundary conditions, eigen equations of transverse type A-O waveguides are derived. Dispersion characteristics of A-O eigen modes are studied for wavelengths of optical waves and SAW, with acousto-optic coefficients for stable pass and unstable forbidden bands. Based on these fundamental field characteristics of A-O waveguides, mode couplings and switchings in transverse A-O waveguide devices consisting of coupled several optical waveguides controlled by SAW may be shown.

1. INTRODUCTION

Integrated optics and optical devices consisting of active and passive waveguides have been rapidly developed recently. Among several optical devices, for optical switch using acoustoptic (A-O) effects, fundamental characteristics and application processing systems of collinear optical switching device using acoustoptic (A-O) effects, have been studied about optical dielectric waveguides on LiNbO₃ crystal substrates [1–3]. Conventional waveguide-type A-O devices use collinear interaction with mode coupling based on Bragg condition between optical waves and SAW both propagating in same directions. Collinear A-O devices of waveguide-type show sufficient performance for wavelength selective switching with narrow bandwidths in case of low switch speed [4, 5]. However, since SAW propagation speed is very slow, comparing with optical wave speeds, and in these collinear A-O devices, interaction time is several micro seconds for 10 mm waveguide device length.

In A-O devices of optical waveguides using transverse A-O interaction, where SAW propagates transversely and at right angles to optical wave propagation direction, SAW propagation lengths needed for complete A-O interaction may become 10 μm and interaction time may be several nano seconds [6, 7]. Ultra high speed switching can be accomplished, in A-O waveguide devices with transverse interaction of optical modes and SAW. In this paper, fundamental characteristics of transverse A-O interaction are studied as electromagnetic boundary value problem.

Refractive indexes in optical waveguides induced by A-O effects of SAW are shown by sine functions in the transverse direction and yield wave equations with functional coefficients. Wave field characteristics in inhomogeneous media of periodic structures for transverse directions given by A-O effects due to SAW, are analyzed by analytic method of Hill's equations for transverse spectral functions. Electromagnetic fields in core and clad regions with periodic structures expressed by sine functions corresponding to SAW fields are shown by Mathieu functions with parameters and concerned with eigen values. By boundary conditions for electric and magnetic fields at boundaries between core and clad regions, eigen equations for eigen modes in transverse type A-O waveguides are derived. Dispersion characteristics of A-O eigen modes are studied for wavelengths of optical

waves and SAW, with acousto-optic coefficients. Stable pass and unstable forbidden bands are discussed. Based on these fundamental field characteristics of A-O waveguides, mode couplings and switchings in transverse A-O waveguide devices consisting of coupled several optical waveguides controlled by SAW may be shown.

2. STRUCTURE OF TRANSVERSE A-O WAVEGUIDE DEVICE

Interactions between surface acoustic waves (SAW) and optical waves are expressed by refractive index tensors. For acousto-optic effects, physical relations among electric fields E_k , electric displacement D_i , particle displacement u_j , stress tensor T_{ij} and strain tensor S_{kj} are expressed using physical coefficients of elastic coefficients C_{ijkl}^E , piezoelectric co-efficients e_{kij} , dielectric constants ε_{ij} , acousto-optic co-efficients p_{ijkl} .

Refractive index changes Δn_{il} due to strains of SAW are

$$\Delta n_{il} = -\frac{1}{2} \sum_{k,j} \frac{n_{ik}^2}{n_{il}} \left(\sum_{\alpha,\beta} p_{kj\alpha\beta} S_{\alpha\beta} \right) n_{jl}^2 \quad (1)$$

For one dimensional case,

$$\Delta n = -\frac{n^3}{2} p S \quad (2)$$

Refractive index changes induced by acoustic longitudinal wave with angular frequency Ω , wave number K and amplitude S_0 propagating in the z direction in homogeneous media are given

$$\Delta n_1 = -\frac{1}{2} n^3 p_{12} S_3, \quad \Delta n_3 = -\frac{1}{2} n^3 p_{11} S_3 \quad (3)$$

where $S_3 = S_0 \sin(\Omega t - Kz)$, $S_1 = S_2 = 0$.

Figure 1 shows optical waveguide of two dimensional case with SAW propagating in the z direction. For optical A-O devices such as optical modulators, switches, couplers and separators using A-O effects, one or two A-O waveguides are combined. In transverse A-O waveguides shown in Fig. 2, optical waves propagate in the longitudinal z direction and SAW propagates in the transverse x direction, where in the y direction, waveguides have uniform characteristics. Region I is core part with refractive index n_1 and width d , and regions II and III are clad parts with refractive indexes n_2 and n_3 . Transverse plane of the waveguide is xy cross section. Strain $S(x, t)$ induced by SAW with velocity Ω/K is given by Eq. (3) and refractive index changes in homogeneous media of regions i with refractive indexes n_i , using elasto-optic coefficients p_i , are

$$\Delta n_i = -\frac{1}{2} n_i^3 p_i S(x, t) \quad (4)$$

When dielectric constants of core and clad regions in transverse A-O waveguides are $\tilde{\varepsilon}_1$, $\tilde{\varepsilon}_2$ and $\tilde{\varepsilon}_3$, wave numbers of optical waves in the transverse x direction change to $\beta_x \pm K$ by SAW with wave numbers, and propagation constants β_z in the longitudinal z direction are controlled to be $\sqrt{\beta^2 - (\beta_x \pm K)^2}$ where β is wave number of media $\omega\sqrt{\mu\tilde{\varepsilon}}$ without SAW. These characteristics of wave spectrum and dispersions are shown in Fig. 3.

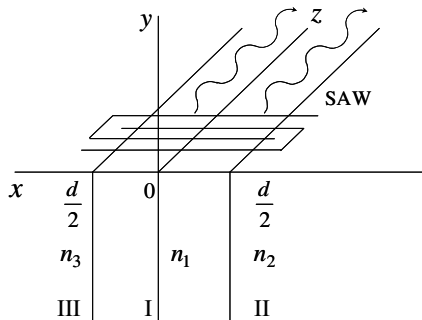


Figure 1: Collinear A-O waveguide device.

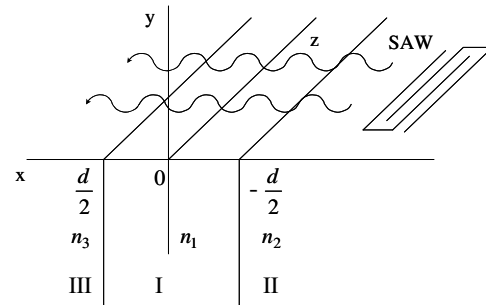


Figure 2: Transverse A-O waveguide device.

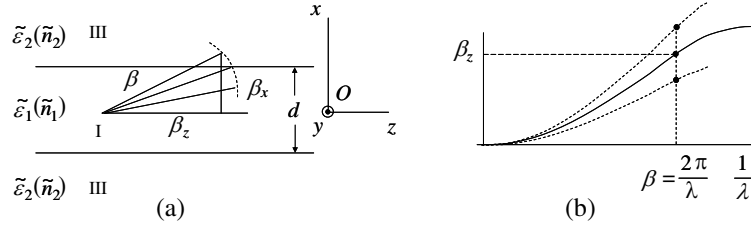


Figure 3: Two-dimensional A-O waveguide.

3. ELECTROMAGNETIC FIELD IN TRANSVERSE A-O WAVEGUIDE

Field and wave equations in the core and clad regions of transverse A-O waveguides controlled by SAW are shown by changes of refractive indexes and dielectric constants in each region as

$$\begin{aligned} \tilde{\varepsilon}_i &= \varepsilon_i + \Delta\varepsilon_i, & \tilde{\varepsilon}_i &= \tilde{n}_i^2 \varepsilon_0, & \Delta\varepsilon_i &= \Delta n_i^2 \varepsilon_0, & \tilde{n}_1 &= n_1 + \Delta n_1, \\ \tilde{n}_2 (= \tilde{n}_3) &= n_2 + \Delta n_2, & \Delta\varepsilon_i &= -\Delta\varepsilon_{is} \sin(\Omega t - Kx - \phi) \end{aligned} \quad (5)$$

where the phase factor of SAW is ϕ .

From the Maxwell equation

$$\nabla \times \mathbf{E} = -\mu \frac{\partial \mathbf{H}}{\partial t}, \quad \nabla \times \mathbf{H} = \tilde{\varepsilon} \frac{\partial \mathbf{E}}{\partial t} \quad (6)$$

we have vector wave equation as

$$\nabla \times \nabla \times \mathbf{E} - \mu \frac{\partial^2}{\partial t^2} \tilde{\varepsilon} \mathbf{E} = 0 \quad (7)$$

Hence

$$\left(\nabla^2 - \mu \tilde{\varepsilon} \frac{\partial^2}{\partial t^2} \right) \mathbf{E} = \mu \Delta \varepsilon \frac{\partial^2 \mathbf{E}}{\partial t^2} - \nabla (\nabla \ln \tilde{\varepsilon} \mathbf{E}) \quad (8)$$

From Eq. (5), in the region of A-O effects, the electric field is given as

$$\left(\nabla^2 - \mu \tilde{\varepsilon} \frac{\partial^2}{\partial t^2} \right) \mathbf{E} = -\mu \Delta \varepsilon_{is} \sin(\Omega t - Kx - \phi) \frac{\partial^2 \mathbf{E}}{\partial t^2} - \nabla (\nabla \ln \tilde{\varepsilon} \mathbf{E}) \quad (9)$$

The magnetic field is shown by, when angular frequency of SAW Ω is smaller than optical frequency ω , $\omega \gg \Omega$

$$\mathbf{H} = \frac{j}{\mu\omega} \nabla \times \mathbf{E} \quad (10)$$

Here, electromagnetic fields $\mathbf{E}^{(i)}(x, z, t)$ in the core and clad regions for uniform field in the y direction are shown as, if propagation factor of the z direction is $e^{-j\beta_z z}$ and time factor is $e^{j\omega t}$

$$\mathbf{E}^{(i)}(x, z, t) = \mathbf{E}_t^{(i)}(x) e^{-j\beta_z z + j\omega t} \quad (11)$$

Transverse electric fields satisfy, using frequency relation of $\omega \gg \Omega$

$$\left[\frac{\partial^2}{\partial x^2} + \mu\omega^2 (\varepsilon_i + \Delta\varepsilon_{is} \sin(Kx + \phi)) - \beta_z^2 \right] \mathbf{E}_t^{(i)}(x) = 0 \quad (12)$$

In Eq. (12), when $\phi = \frac{\pi}{2}$, and we define parameters W , η , a_i , q_i following as, for y polarization and $\mathbf{E}_t^{(i)} = E_y^{(i)} \mathbf{i}_y$,

$$Kx = 2\eta, \quad a_i = W^2 (\mu\omega^2 \varepsilon_i - \beta_z^2) = \frac{4(\mu\omega^2 \varepsilon_i - \beta_z^2)}{K^2}, \quad -2q_i = W^2 \mu\omega^2 \Delta\varepsilon_{is} = \frac{4\mu\omega^2 \Delta\varepsilon_{is}}{K^2} \quad (13)$$

Here, for wavelength Λ of SAW

$$W = \frac{2}{K} = \frac{\Lambda}{\pi}, \quad K = \frac{2}{W} = \frac{2\pi}{\Lambda}$$

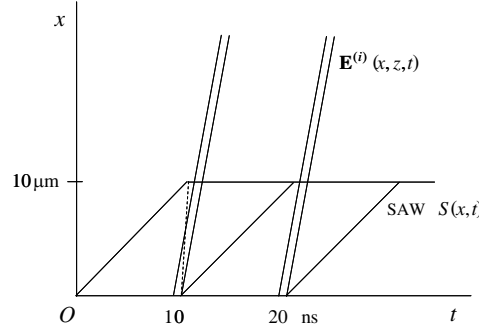


Figure 4: Interaction of optical modes and SAW.

Equation (12) of transverse electric fields $\mathbf{E}_t^{(i)}(x)$ is reduced to Mathieu equation with parameter q and eigen values a for η coordinate variable.

$$\left[\frac{d^2}{d\eta^2} + (a_i - 2q_i \cos 2\eta) \right] E_t^{(i)}(\eta) = 0 \quad (14)$$

In transverse A-O waveguide, propagation characteristics of optical waves and SAW are shown for distance x and time t in Fig. 4. Propagation velocity of SAW $V = \frac{\Omega}{K}$ is smaller than those of optical modes $v = \frac{1}{\sqrt{\varepsilon_{eq}\mu}}$, and optical waves pass through transverse cross section of SAW xy plane with short time interactions, giving high speed responses. Where ε_{eq} is equivalent dielectric constant of optical modes, $\frac{\beta_z}{\beta} = \sqrt{\varepsilon_{eq}}$.

Electric fields in core (I) and clad (II), (III) regions, for y polarization, $\mathbf{E}_t^{(i)}(x) = \mathbf{i}_y E_y^{(i)}(x)$, using Mathieu functions and coefficients $C_\nu^{(i)}$, $S_\nu^{(i)}$, and z component $H_z^{(i)}$ of magnetic fields are

$$E_y^{(i)}(\eta) = \sum_{\nu=0}^{\infty} \left(C_\nu^{(i)} c e_\nu(\eta, q_i) + S_\nu^{(i)} s e_\nu(\eta, q_i) \right), \quad H_z^{(i)}(\eta) = \frac{1}{j\omega\mu} \sum_{\nu=0}^{\infty} \left[C_\nu^{(i)} c e'_\nu(\eta, q_i) + S_\nu^{(i)} s e'_\nu(\eta, q_i) \right] \quad (15)$$

Here, $a_i = \nu^2 + \sum_{r=0}^{\infty} \alpha_r q_i^r$, $\alpha_2 = \frac{1}{2(\nu^2-1)}$, $c e_\nu(\eta, q) = \cos \nu z - \frac{1}{4}q \left[\frac{\cos(\nu+2)\eta}{(\nu+1)} - \frac{\cos(\nu-2)\eta}{(\nu-1)} \right] + O(q^2)$, $s e_\nu(\eta, q) = \sin \nu z - \frac{1}{4}q \left[\frac{\sin(\nu+2)\eta}{(\nu+1)} - \frac{\sin(\nu-2)\eta}{(\nu-1)} \right] + O(q^2)$.

From continuity conditions of electric and magnetic fields at boundary interface between core and clad, $x = \pm \frac{d}{2}$, when refractive indexes of clad regions II and III, $\tilde{n}_2 = \tilde{n}_3$ using coefficients $C_\nu^{(1)}$, $S_\nu^{(1)}$, $C_\nu^{(2)}$, $S_\nu^{(2)}$ and defining $\eta_\pm = \frac{K}{2} (\pm \frac{d}{2})$, we have

$$\begin{pmatrix} c e_\nu(\eta_+, q_1) & s e_\nu(\eta_+, q_1) & c e_\nu(\eta_+, q_2) & s e_\nu(\eta_+, q_2) \\ c e_\nu(\eta_-, q_1) & s e_\nu(\eta_-, q_1) & c e_\nu(\eta_-, q_2) & s e_\nu(\eta_-, q_2) \\ c e'_\nu(\eta_+, q_1) & s e'_\nu(\eta_+, q_1) & c e'_\nu(\eta_+, q_2) & s e'_\nu(\eta_+, q_2) \\ c e'_\nu(\eta_-, q_1) & s e'_\nu(\eta_-, q_1) & c e'_\nu(\eta_-, q_2) & s e'_\nu(\eta_-, q_2) \end{pmatrix} \begin{bmatrix} C_\nu^{(1)} \\ S_\nu^{(1)} \\ C_\nu^{(2)} \\ S_\nu^{(2)} \end{bmatrix} = 0 \quad (16)$$

For expansion coefficients of Eq. (15), determinant of matrix Eq. (16) gives eigen equation and derives dispersion characteristics of eigen modes giving propagation constants $\beta_z^{(\nu)}$ of ν modes as eigen values.

$$\begin{aligned} \Delta \varepsilon_2 = \Delta \varepsilon_3 = 0, \quad \beta_i^2 = \mu \omega^2 \tilde{\varepsilon}_i = \tilde{n}_i^2 \varepsilon_0, \quad \tilde{\varepsilon}_1 = \varepsilon_1 + \Delta \varepsilon_1, \\ \Delta \varepsilon_1 = \Delta n_1^2 \varepsilon_0, \quad \Delta n_1 = -\frac{1}{2} n_1^3 p_1 S(t), \quad \Delta \varepsilon_1 = -\Delta \varepsilon_{1s} \sin(\Omega t - Kx - \phi) \end{aligned} \quad (17)$$

where strain is given by SAW as $S(x, t) = S_0 \sin(\Omega t - Kx - \phi)$.

TE symmetric (even) mode for y polarization electric and magnetic fields $E_y^{(1)}$, $E_y^{(2)}$, $H_z^{(1)}$, $H_z^{(2)}$

are, using Mathieu functions and $C_\nu^{(1)}$, $C_\nu^{(2)}$, in core and clad regions

$$\begin{aligned} E_y^{(1)} &= C_\nu^{(1)} c e_\nu(\eta, q_1) e^{-j\beta_z z}, & H_z^{(1)} &= -\frac{j}{\omega\mu} \frac{1}{W} C_\nu^{(1)} c e'_\nu(\eta, q_1) e^{-j\beta_z z} \quad |x| \leq \frac{d}{2}, \\ E_y^{(2)} &= C_\nu^{(2)} e^{-j\beta_z z} e^{\pm\alpha_x^{(2)} x}, & H_z^{(2)} &= \frac{\pm\alpha_x^{(2)}}{\omega\mu} j C_\nu^{(2)} e^{-j\beta_z z} e^{\pm\alpha_x^{(2)} x}, \quad x \leq -\frac{d}{2}, \quad x \geq \frac{d}{2} \end{aligned} \quad (18)$$

As simple case, we next consider transverse A-O effects in core region without A-O effects in clad regions, as follows.

Here,

$$a_1 = \nu^2 + \sum_{r=0}^{\infty} \alpha_{r1} q_1^r, \quad \frac{d}{dx} = \frac{K}{2} \frac{d}{d\eta} = \frac{1}{W} \frac{d}{d\eta} \quad (19)$$

for spectrum parameters,

$$-\alpha_x^{(i)2} = \beta_i^2 - \beta_z^2 = \beta_x^{(i)2}, \quad \alpha_x^{(2)} = \alpha_x^{(3)} \quad (20)$$

and coefficients

$$C^{(2)} = C^{(3)}$$

Boundary condition of electric and magnetic fields E_y and H_z at the boundary interface at $x = \pm\frac{d}{2}$, and $\eta = \frac{K}{2} (\pm\frac{d}{2})$, are

$$\begin{aligned} C_\nu^{(1)} c e_\nu(\eta^{(d)}, q_1) &= C_\nu^{(2)} e^{-\alpha_x \frac{d}{2}}, & \frac{1}{W} C_\nu^{(1)} c e'_\nu(\eta^{(d)}, q_1) &= \alpha_x C_\nu^{(2)} e^{-\alpha_x \frac{d}{2}} \\ -c_\nu e'_\nu(\eta, q_1) \Big|_{\eta=+\frac{K}{4}d} &= +c_\nu e'_\nu(\eta, q_1) \Big|_{\eta=-\frac{K}{4}d} \end{aligned} \quad (21)$$

where, $\eta^{(d)} = \frac{K}{4}d$, $\alpha_x = \alpha_x^{(2)}$.

From field continuity condition of Eq. (21), we have mode dispersion relations of TE symmetric modes as

$$\frac{C_\nu^{(1)}}{C_\nu^{(2)}} = \frac{e^{-\alpha_x \frac{d}{2}}}{c e_\nu(\eta^{(d)}, q_1)} = \frac{\alpha_x e^{-\alpha_x \frac{d}{2}}}{\frac{1}{W} c e'_\nu(\eta^{(d)}, q_1)}, \quad \frac{c_\nu e'_\nu(\eta^{(d)}, q_1)}{c_\nu e_\nu(\eta^{(d)}, q_1)} = -\alpha_x W \quad (22)$$

where, $\beta_z^2 - \alpha_x^2 = \beta_2^2$, $\alpha_x W = \sqrt{(\beta_1^2 - \beta_2^2) W^2 - 1}$, $\beta_z^2 + (\frac{1}{W})^2 = \beta_1^2$.

From eigen equation of Eq. (22), propagation constants $\beta_z^{(\nu)}$ of optical guided ν modes and dispersion characteristics are derived. Eigen characteristics of Mathieu function yield stable (pass) and unstable (decay) regions for parameters of q and a concerned with TE symmetric modes as shown in Fig. 5.

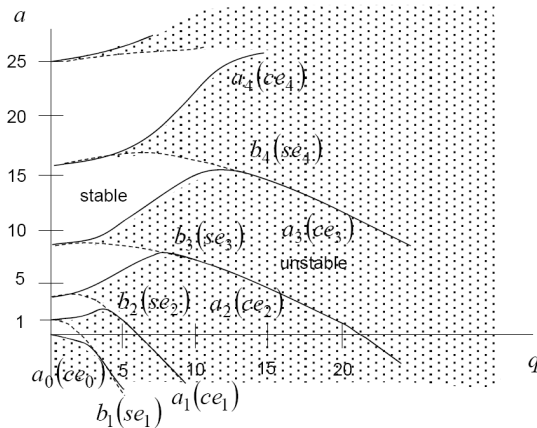


Figure 5: Eigen characteristics of TE symmetric modes.

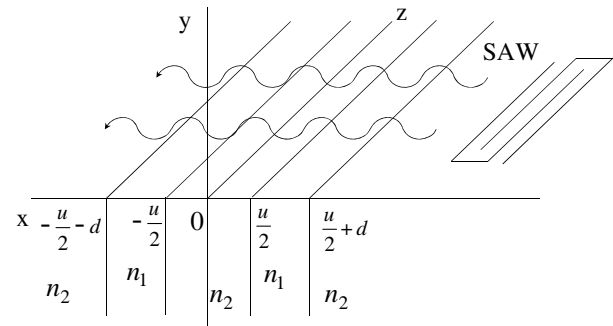


Figure 6: Transverse A-O couplers and wave separator.

Parameters a_ν and b_ν are represented for Mathieu functions ce_ν and se_ν , as eigen values a in Eq. (14).

Optical transverse A-O coupler and wave separators consisting of parallel waveguides with transversely propagating SAW shown in Fig. 6, can be discussed based on eigen mode characteristics of transverse A-O waveguide.

4. CONCLUSION

Transverse A-O waveguides with SAW have high efficient and high speed switching characteristics. Electromagnetic field characteristics in transverse A-O waveguides with transversely controlled refractive indexes by SAW are studied by eigen function expansion methods for Hill's equations. Field characteristics are discussed by Mathieu function expansion method for core and clad regions with acousto-optic effects due to SAW. Eigen equations and eigen modes are shown using field expression of Mathieu functions by field boundary condition. Stable and unstable dispersion characteristics for wave numbers and wavelengths of optical waves and SAW are shown.

REFERENCES

1. Kondo, T., Y. Miyazaki, and Y. Akao, "Optical tunable switched directional couplers consisting of two thin-film waveguides using surface acoustic waves," *Jpn. J. Appl. Phys.*, Vol. 17, No. 7, 1231–1243, 1978.
2. Goto, N. and Y. Miyazaki, "Integrated optical multi-/demultiplexer using acoustooptic effect for multiwavelength optical communications," *IEEE J. on Selected Areas in Commun.*, Vol. 8, No. 6, 1160–1168, 1190.
3. Goto, N. and Y. Miyazaki, "Multi-wavelength separation characteristics in integrated acoustooptic devices for photonic switching system," *Jpn. J. Appl. Phys.*, Vol. 40, No. 5B, 3762–3767, 2001.
4. Goto, N. and Y. Miyazaki, "FDTD analysis of wavelength-selective characteristics in weighted acoustooptic switches for wavelength-division-multiplexed photonic routing," *Jpn. J. Appl. Phys.*, Vol. 43, No. 5B, 2958–2964, 2004.
5. Von Helmlolt, C. H., "Integrated optic strip waveguides driven by surface acoustic waves," *Jour. of Opt. Commun.*, Vol. 2, No. 4, 142–154, 1981.
6. Miyazaki, Y., "Optical modes in dielectric thin film fiber with convex surface by conformal mapping technique," *Trans. IECE Japan*, Vol. E59, No. 10, 1–6, 1976.
7. McLachlan, N. W., *Theory and Application of Mathieu Functions*, Dover Pub., New York, 1964.

Permittivity Determination of Multi-sectional Diaphragm with Metamaterial Layers in Rectangular Waveguide

Yu. G. Smirnov¹, Yu. V. Shestopalov², and E. D. Derevyanchuk¹

¹Penza State University, Russia

²Karlstad University, Sweden

Abstract— In this paper we consider the inverse problem of the permittivity determination of a multi-sectional diaphragm with metamaterial layers. Based on the developed recursive method of the solution to the inverse problem we perform a detailed analysis for a three-sectional diaphragm.

1. INTRODUCTION

Determination of electromagnetic parameters of dielectric bodies that have complicated geometry or structure is an urgent problem as far as investigation of the properties and creation of nanocomposite materials are concerned. As a rule, these parameters cannot be directly measured which leads to the necessity of applying methods of mathematical modeling and numerical solution of the corresponding forward and inverse electromagnetic problems [1–3]. In [4] we proposed a numerical–analytical approach and determined in the closed form the permittivity of layered materials loaded in a waveguide. The aim of this work is the development of the proposed technique to the analysis of electromagnetic properties and solution to the inverse problem in the case of a multi-sectional diaphragm with metamaterial layers placed in a rectangular waveguide. We consider different fillings of the diaphragm sections and present the results of numerical modeling.

2. INVERSE PROBLEM

Assume that a waveguide $P = \{x : 0 < x_1 < a, 0 < x_2 < b, -\infty < x_3 < \infty\}$ with the perfectly conducting boundary surface ∂P is given in the cartesian coordinate system. A three-dimensional body Q ($Q \subset P$)

$$Q = \{x : 0 < x_1 < a, 0 < x_2 < b, 0 < x_3 < l\}$$

is placed in the waveguide; the body has the form of a diaphragm (an insert); namely, a parallelepiped divided into n sections adjacent to the waveguide walls. Domain $P \setminus \bar{Q}$ is filled with an isotropic and homogeneous layered medium having constant permeability ($\mu_0 > 0$) in whole waveguide P , the sections of the diaphragm

$$\begin{aligned} Q_0 &= \{x : 0 < x_1 < a, 0 < x_2 < b, -\infty < x_3 < 0\} \\ Q_j &= \{x : 0 < x_1 < a, 0 < x_2 < b, l_{j-1} < x_3 < l_j\}, \quad j = 1, \dots, n \\ Q_{n+1} &= \{x : 0 < x_1 < a, 0 < x_2 < b, l < x_3 < +\infty\} \end{aligned}$$

are filled each with a medium having constant permittivity $\varepsilon_j > 0$; $l_0 := 0$, $l_n := l$.

The electromagnetic field inside and outside the object in the waveguide is governed by Maxwell's equations

$$\begin{aligned} \operatorname{rot} \mathbf{H} &= -i\omega \varepsilon \mathbf{E} + \mathbf{j}_E^0 \\ \operatorname{rot} \mathbf{E} &= i\omega \mu_0 \mathbf{H}, \end{aligned} \quad (1)$$

where \mathbf{E} and \mathbf{H} are the vectors of the electric and magnetic field intensity, \mathbf{j} is the electric polarization current, and ω is the circular frequency.

Assume that $\pi/a < k_0 < \pi/b$, where k_0 is the wavenumber, $k_0^2 = \omega^2 \varepsilon_0 \mu_0$ [5]. In this case, only one wave H_{10} propagates in the waveguide without attenuation (we have a single-mode waveguide [5]).

The incident electrical field is

$$\mathbf{E}^0 = \mathbf{e}_2 A \sin\left(\frac{\pi x_1}{a}\right) e^{-i\gamma_0 x_3} \quad (2)$$

with a known A and $\gamma_0 = \sqrt{k_0^2 - \pi^2/a^2}$.

Solving the forward problem for Maxwell's equations with the aid of (1) and the propagation scheme in Fig. 1, we obtain explicit expressions for the field inside every section of diaphragm Q and outside the diaphragm:

$$E_{(0)} = \sin\left(\frac{\pi x_1}{a}\right) (Ae^{-i\gamma_0 x_3} + Be^{i\gamma_0 x_3}), \quad x \in Q_0, \quad (3)$$

$$E_{(j)} = \sin\left(\frac{\pi x_1}{a}\right) (C_j e^{-i\gamma_j x_3} + D_j e^{i\gamma_j x_3}), \quad (4)$$

$$j = 1, \dots, n+1; \quad D_{n+1} = 0, \quad x \in Q_j,$$

where $\gamma_j = \sqrt{k_j^2 - \pi^2/a^2}$ and $k_j^2 = \omega^2 \varepsilon_j \mu_0$, $\gamma_{n+1} = \gamma_0$.

From the conditions on the boundary surfaces $L := \{x_3 = 0, x_3 = l_1, \dots, x_3 = l_n\}$ of the diaphragm sections

$$[E]|_L = 0, \quad [H]|_L = 0, \quad (5)$$

where square brackets $[\cdot]$ denote the function jump over the boundary surfaces, applied to (3) and (4) we obtain using conditions (5) a system of equations for the unknown coefficients

$$\begin{cases} A + B = C_1 + D_1 \\ \gamma_0 (B - A) = \gamma_1 (D_1 - C_1) \\ C_j e^{-i\gamma_j l_j} + D_j e^{i\gamma_j l_j} = C_{j+1} e^{-i\gamma_{j+1} l_j} + D_{j+1} e^{i\gamma_{j+1} l_j} \\ \gamma_j (D_j e^{i\gamma_j l_j} - C_j e^{-i\gamma_j l_j}) = \gamma_{j+1} (D_{j+1} e^{i\gamma_{j+1} l_j} - C_{j+1} e^{-i\gamma_{j+1} l_j}), \quad j = 1, \dots, n, \end{cases} \quad (6)$$

where $C_{n+1} = F$, $D_{n+1} = 0$. In system (6) coefficients A , B , C_j , D_j are supposed to be complex and ε_j ($j = 1, \dots, n$) are supposed to be real. Formulate the inverse problem for a multisectional diaphragm.

Inverse problem P: find (real) permittivity ε_j of each section from the known amplitude A of the incident wave and amplitude F of the transmitted wave at different frequencies.

Expressing C_j , D_j via C_{j+1} , D_{j+1} we obtain a recurrent formula that couples amplitudes A and F :

$$A = \frac{1}{2 \prod_{j=0}^n \gamma_j} (\gamma_n p_{n+1} + \gamma_0 q_{n+1}) F e^{-i\gamma_0 l_n}, \quad (7)$$

where

$$\begin{aligned} p_{j+1} &= \gamma_{j-1} p_j \cos \alpha_j + \gamma_j q_j i \sin \alpha_j, & p_1 &:= 1, \\ q_{j+1} &= \gamma_{j-1} p_j i \sin \alpha_j + \gamma_j q_j \cos \alpha_j, & q_1 &:= 1. \end{aligned} \quad (8)$$

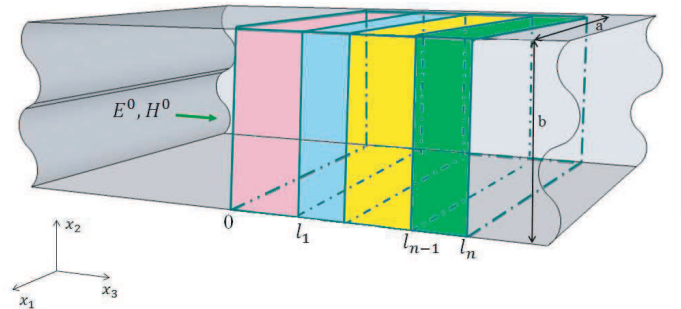


Figure 1. Multilayered diaphragms in a waveguide.

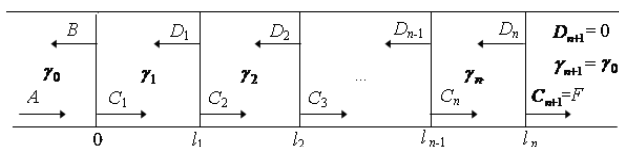


Figure 2. Scheme of the wave propagation through the diaphragms.

Here $\alpha_j = \gamma_j(l_j - l_{j-1})$, $j = 1, \dots, n$. Note that similar formulas are obtained in classical monographs dealing with wave propagation in layered media, e.g., in [6].

It should be noted that we solve the inverse problem under study assuming that permittivities ε_j ($j = 1, \dots, n$) are real. In the case of an n -sectional diaphragm, we obtain a system of n equations with n unknown permittivities by duplicating (8) at different frequencies:

$$\operatorname{Re}(A(\omega_j)) = \operatorname{Re} \left(\frac{1}{2 \prod_{j=0}^n \gamma_j} (\gamma_n p_{n+1} + \gamma_0 q_{n+1}) F(\omega_j) e^{-i\gamma_0 l_n} \right), \quad j = 1, \dots, n, \quad (9)$$

where all the necessary quantities are given by (8). Solving system (9) numerically we find permittivities ε_j ($j = 1, \dots, n$).

3. NUMERICAL

In this section we present examples of numerical solutions to inverse problem P. The tables show the test results of numerical solution to the inverse problem of reconstructing permittivities of one-, two-, or three-sectional diaphragm at one, two, three frequencies correspondingly. The test values of the transmission coefficient are taken from the solution to the forward problem.

Based on the developed recursive method we obtain the results for n -sectional diaphragms with $n = 1, 2, 3$.

For a one-sectional diaphragm from (9) we obtain the formula

$$\operatorname{Re}(A(\omega_1)) = \operatorname{Re} \left(\frac{1}{2\gamma_0\gamma_1} (\gamma_1 p_2 + \gamma_0 q_2) F(\omega_1) e^{-i\gamma_0 l_1} \right), \quad (10)$$

where

$$\begin{aligned} p_2 &= \gamma_0 p_1 \cos \alpha_1 + \gamma_1 q_1 i \sin \alpha_1, & p_1 &:= 1, \\ q_2 &= \gamma_0 p_1 i \sin \alpha_1 + \gamma_1 q_1 \cos \alpha_1, & q_1 &:= 1. \end{aligned}$$

Here $\alpha_1 = \gamma_1 l_1$.

In Table 1 numerical results for a one-sectional diaphragm are presented.

Parameters of the one-sectional diaphragm are $a = 2$ cm, $b = 1$ cm, $c = 2$ cm, and $l_1 = 0.9$ cm; the excitation frequencies $f = 11.94$ GHz. The first, second, and third columns of the table show, respectively, the values of transmission coefficient $\frac{F}{A}$ and the calculated and true values of the (real) permittivity of a section.

For a two-sectional diaphragm from (9) we obtain the system of 2 equations with 2 unknown permittivities

$$\begin{aligned} \operatorname{Re}(A(\omega_1)) &= \operatorname{Re} \left(\frac{1}{2\gamma_0\gamma_1\gamma_2} (\gamma_2 p_3 + \gamma_0 q_3) F(\omega_1) e^{-i\gamma_0 l_2} \right), \\ \operatorname{Re}(A(\omega_2)) &= \operatorname{Re} \left(\frac{1}{2\gamma_0\gamma_1\gamma_2} (\gamma_2 p_3 + \gamma_0 q_3) F(\omega_2) e^{-i\gamma_0 l_2} \right), \end{aligned} \quad (11)$$

Table 1.

$\frac{F}{A}(\omega_i)$	Calculated ε_i	True ε_i
$-0.044 + i \cdot 0.046$	-1.7095	-1.7
$0.691 - i \cdot 0.693$	1.69997	1.7
$-0.381 - i \cdot 0.855$	3.0004	3
$-0.018 + i \cdot 0.013$	-3.029	-3

where

$$\begin{aligned} p_3 &= \gamma_1 p_2 \cos \alpha_2 + \gamma_2 q_2 i \sin \alpha_2, \\ p_2 &= \gamma_0 p_1 \cos \alpha_1 + \gamma_1 q_1 i \sin \alpha_1, \quad p_1 := 1, \\ q_3 &= \gamma_1 p_2 i \sin \alpha_2 + \gamma_2 q_2 \cos \alpha_2, \\ q_2 &= \gamma_0 p_1 i \sin \alpha_1 + \gamma_1 q_1 \cos \alpha_1, \quad q_1 := 1. \end{aligned}$$

Here $\alpha_j = \gamma_j(l_j - l_{j-1})$, $j = 1, 2$.

In Table 2 numerical results for a two-sectional diaphragm with one or more metamaterial layers are presented.

Parameters of the two-sectional diaphragm are $a = 2$ cm, $b = 1$ cm, $c = 2$ cm, $l_1 = 1$ cm, and $l_2 = 1.5$ cm; the excitation frequencies $f = 11.94$ GHz and $f = 8.12$ GHz. The first, second, and third columns of the table show, respectively, the values of transmission coefficient $\frac{F}{A}$ and the calculated and true values of the (real) permittivity of a section.

For a three-sectional diaphragm from (9) we obtain the system of 3 equations with 3 unknown permittivities

$$\begin{aligned} \operatorname{Re}(A(\omega_1)) &= \operatorname{Re} \left(\frac{1}{2\gamma_0\gamma_1\gamma_2\gamma_3} (\gamma_3 p_4 + \gamma_0 q_4) F(\omega_1) e^{-i\gamma_0 l_3} \right), \\ \operatorname{Re}(A(\omega_2)) &= \operatorname{Re} \left(\frac{1}{2\gamma_0\gamma_1\gamma_2\gamma_3} (\gamma_3 p_4 + \gamma_0 q_4) F(\omega_2) e^{-i\gamma_0 l_3} \right), \\ \operatorname{Re}(A(\omega_3)) &= \operatorname{Re} \left(\frac{1}{2\gamma_0\gamma_1\gamma_2\gamma_3} (\gamma_3 p_4 + \gamma_0 q_4) F(\omega_3) e^{-i\gamma_0 l_3} \right), \end{aligned} \quad (12)$$

where

$$\begin{aligned} p_4 &= \gamma_2 p_3 \cos \alpha_3 + \gamma_3 q_3 i \sin \alpha_3, & p_3 &= \gamma_1 p_2 \cos \alpha_2 + \gamma_2 q_2 i \sin \alpha_2, \\ p_2 &= \gamma_0 p_1 \cos \alpha_1 + \gamma_1 q_1 i \sin \alpha_1, & p_1 &:= 1, \\ q_4 &= \gamma_2 p_3 i \sin \alpha_3 + \gamma_3 q_3 \cos \alpha_3, & q_3 &= \gamma_1 p_2 i \sin \alpha_2 + \gamma_2 q_2 \cos \alpha_2, \\ q_2 &= \gamma_0 p_1 i \sin \alpha_1 + \gamma_1 q_1 \cos \alpha_1, & q_1 &:= 1. \end{aligned}$$

Table 2.

$\frac{F}{A}(\omega_i)$	Calculated ε_i	True ε_i
$-0.017 - i \cdot 0.00393$	-1.09995	-1.1
$-0.012 + i \cdot 0.025$	-1.2013281	-1.2
$0.132 + i \cdot 0.33$	1.10077	1.1
$0.164 + i \cdot 0.33$	-1.20084	-1.2
$-0.05 + i \cdot 0.079$	-1.09815	-1.1
$-0.0015 + i \cdot 0.113$	1.20156	1.2

Table 3.

$\frac{F}{A}(\omega_i)$	Calculated ε_i	True ε_i
$-0.002476 - i \cdot 0.004015$	-1.10193	-1.1
$-0.006608 + i \cdot 0.007652$	-1.19769	-1.2
$-0.009451 + i \cdot 0.0007723$	-1.2981	-1.3
$-0.019 - i \cdot 0.026$	-1.01787	-1.1
$-0.017 + i \cdot 0.021$	1.18248	1.2
$-0.034 + i \cdot 0.0049$	-1.41637	-1.3
$0.195 + i \cdot 0.064$	1.70101	1.7
$0.138 - i \cdot 0.045$	1.49818	1.5
$0.166 + i \cdot 0.049$	-4.00463	-4

Here $\alpha_j = \gamma_j(l_j - l_{j-1})$, $j = 1, 2, 3$.

In Table 3 numerical results for a three-sectional diaphragm with one or more metamaterial layers are presented.

Parameters of the three-sectional diaphragm are $a = 2$ cm, $b = 1$ cm, $c = 2$ cm, $l_1 = 1$ cm, $l_2 = 1.5$ cm, and $l_3 = 1.9$ cm; the excitation frequencies $f = 11.94$ GHz, $f = 8.12$ GHz, and $f = 9.55$ GHz.

The first, second, and third columns of the table contain, respectively, the values of transmission coefficient $\frac{F}{A}$ and the calculated and true values of the (real) permittivity of a section.

4. CONCLUSION

In this work, we have constructed a mathematical model of the wave propagation through a multi-layered dielectric in a waveguide and analyzed electromagnetic properties of multi-sectional diaphragms with metamaterial layers placed in a rectangular waveguide. Note an important feature of the method of solution to the inverse problem under study: for the case of an n -sectional diaphragm, the system for finding the layer permittivities is obtained by duplicating the general formula that couples the transmission coefficient and the incident field amplitude at different frequencies. Using the developed recursive method we have obtained analytical results and performed numerical simulation and solution to the inverse problem of the permittivity determination for multi-sectional diaphragms with one, two, and three layers. Numerical results confirm the efficiency of the method.

ACKNOWLEDGMENT

This work is partially supported by the Russian Foundation for Basic Research, projects 11-07-00330-a and 12-07-97010-p-a, by a grant of the Ministry of Education and Science of the Russian Federation 14.B37.21.1950, and the Visby Program of the Swedish Institute.

REFERENCES

1. Akleman, F., "Reconstruction of complex permittivity of a longitudinally inhomogeneous material loaded in a rectangular waveguide," *IEEE Microwave and Wireless Components Letters*, Vol. 18, No. 3, 158–160, 2008.
2. Baginski, M. E., D. L. Faircloth, and M. D. Deshpande, "Comparison of two optimization techniques for the estimation of complex permittivities of multilayered structures using waveguide measurements," *IEEE Trans. Microw. Theory Tech.*, Vol. 53, No. 10, 3251–3259, 2005.
3. Baker-Jarvis, J. and E. J. Vanzura, "Improved technique for determining complex permittivity with the transmission-reflection method," *IEEE Trans. Microw. Theory Tech.*, Vol. 38, No. 8, 1096–1103, 1990.
4. Shestopalov, Y. and Y. Smirnov, "Inverse scattering in guides," *J. Phys.: Conf. Ser.*, Vol. 346, 012019, 2012.
5. Jackson, J. D., *Classical Electromagnetics*, John Wiley & Sons, New York, 1967.
6. Brekhovskikh, L., *Waves in Layered Media*, Academic Press, New York, 1980.

Multi Bands Reconfigurable Antenna for Mobile Phone Application

Dau-Chyrh Chang and Hsin-Chi Li

Institute of Information and Communication Engineering
Oriental Institute of Technology, New Taipei City, Taiwan

Abstract— The design of multi-band reconfigurable antenna with compact size and high efficiency is presented. The antenna is composed of one main loop radiator, one monopole radiator, and coupling loop radiator. The size of the antenna is $50 \times 75 \times 0.8$ mm which is printed on FR4-exopy substrate with permittivity 4.4. There are four PIN diodes switch to control the antenna with multiple frequency capability. By adjusting the PIN diode switches, the antenna frequency can be switched for GSM850, GSM900, GSM1800, GSM1900, UMTS2100, and IEEE 802.11a/b/g.

1. INTRODUCTION

In recent years, for wireless communication products are integrating with different antennas for multi-communication systems. In generally the operating frequency of antenna can be reconfigurable by controlling the reactance for multi-band operation. By using this reconfigurable technique, the size of wireless mobile communication system can be reduced. The technology can improve signal transmission quality that not only can be applied to systems integration, can also increase bandwidth and improve transmission speed.

The structure of the proposed reconfigurable antenna is shown in Figure 1. The structure of the proposed frequency reconfigurable antenna is based on the multi-band antenna structure with the combination of the pin diodes switch. The size of the antenna is $50 \times 75 \times 0.8$ mm which is printed on FR4-exopy substrate with permittivity 4.4. The antenna is composed of one main loop radiator, one monopole radiator, and coupling loop radiator, and supports different frequency respectively. Main antenna and ground plane are printed on the same plane, and use coaxial cable to excite the antenna. The PIN diodes are placed inside loop radiator and monopole radiator. The switch states at each model are given in Table 1. The model 1 is all the PIN diodes are OFF state, and the return loss of simulated is shown in Figure 2.

2. ANTENNA DESIGN

From the result that can found the antenna has four resonant points from 0.5 GHz to 6.5 GHz. In order to confirm the current distribution of the resonant frequency, the current distribution of the four resonant frequencies of simulated is shown in Figure 3. From the Figure 3(a) can be found that the current through the monopole radiator and therefore the monopole radiator is resonated for 900 MHz The current distribution of 1800 MHz is shown in Figure 3(b), the current through the

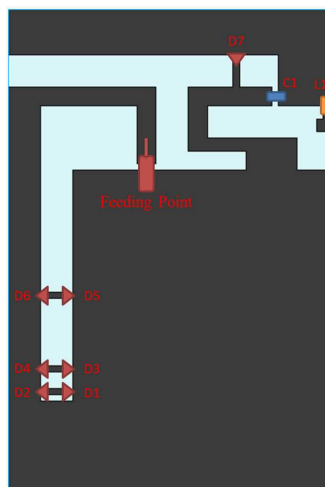


Figure 1: The proposed structure of multi-band antenna.

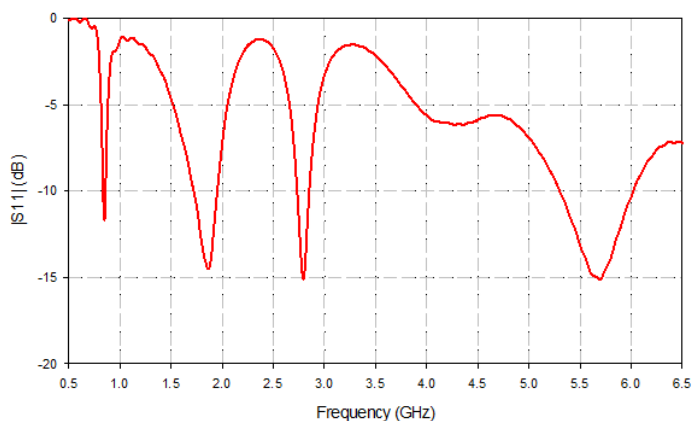


Figure 2: The simulation result of return loss.

Table 1: Reconfigurable antenna models of operation.

Diodes combination	Pin diodes state				
	Model 1	Model 2	Model 3	Model 4	Model 5
D1, D2	OFF	ON	OFF	OFF	OFF
D3, D4	OFF	OFF	ON	OFF	OFF
D5, D6	OFF	OFF	OFF	ON	OFF
D7	OFF	OFF	OFF	OFF	ON

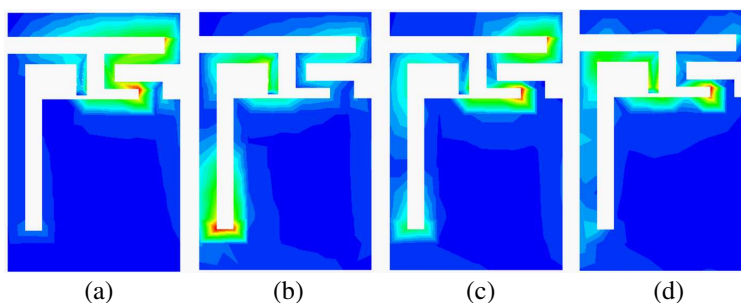


Figure 3: The current distribution of antenna at the frequency of (a) 900 MHz, (b) 1800 MHz, (c) 2700 MHz, (d) 5500 MHz.

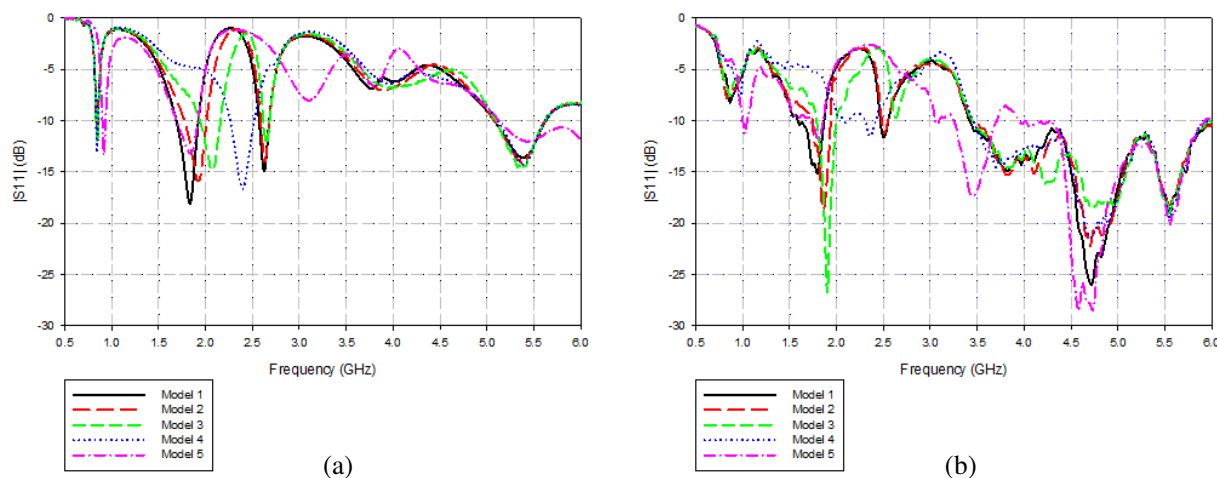


Figure 4: (a) Simulated, (b) measured return loss of the reconfigurable antenna

loop radiator and there are two nodes in the middle of the loop radiator, so the loop radiator is resonated for 1800 MHz. Figure 3(c) shows the current distribution of 2700 MHz and the current is flowing the monopole radiator, but there is one node in the middle of the monopole. According to the analysis of the resonant frequency, that is generated by the third harmonic of the resonant frequency of the monopole radiator. The current distribution of 5500 MHz is shown in Figure 3(d), current is mainly concentrated in the monopole radiator and the loop radiator. From the current distribution can be found that have two nodes in the middle, according to the analysis of the resonance frequency that generated by the coupling loop antenna resonance.

Use analyzed the simulation results of the current distribution that can understand the resonant structure of the antenna at different frequencies. Using the combination of the PIN diodes and antenna to switch the current path, and then completed the switching of resonant frequency. On the other hand, we have to add the DC bias to control the PIN diodes state. And need to use the inductor and capacitor to isolate the AC and DC signals, that to avoid the impact and interference between signals. In this article, the inductor (L_1) is 150 nH and the capacitor (C_1) is 100 pF.

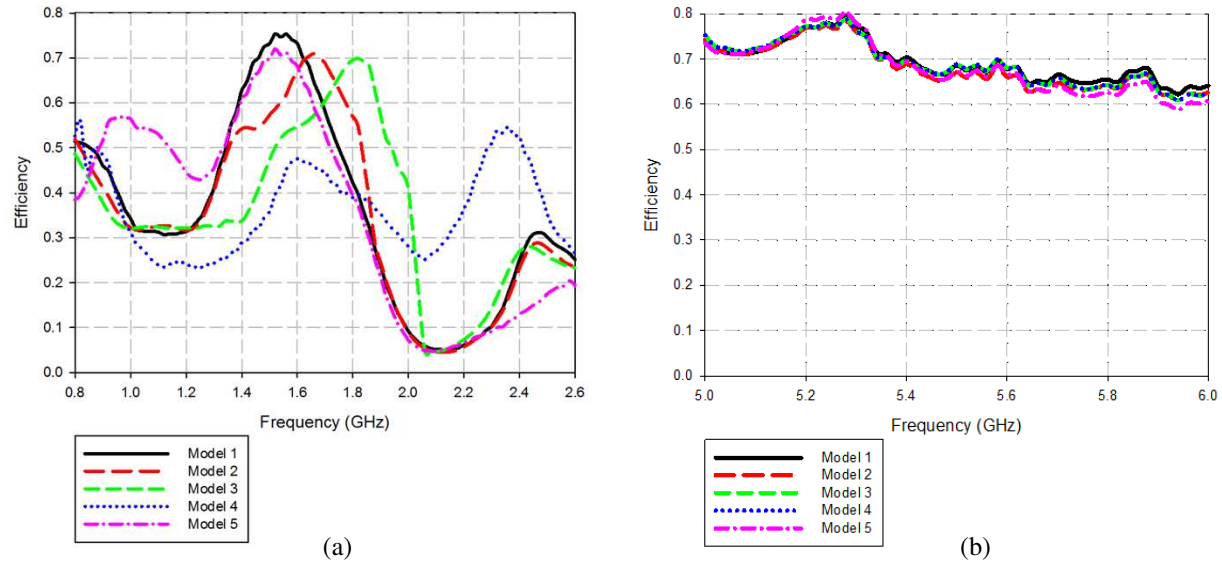


Figure 5: Measured overall efficiency of the reconfigurable antenna at (a) lower band, (b) higher band.

3. ANTENNA PARAMETER OF THE STUDY

Figure 4 shows the result of return loss, use of the switch of PIN diodes can be completed tune the resonant frequency of antenna. Figure 4(a) shows the simulation result of return loss, according to the switching of PIN diodes state that can achieve five kinds of reconfigured frequency model and support different bands respectively. In the bands for return loss is higher than 6 dB that include GSM850, GSM900, GSM1800, GSM1900, UMTS2100 and IEEE 802.11 b/g/n. Figure 4(b) is the return loss of measured, from the result were be found have significant frequency shift. Figure 5 shows the efficiency of measured, the efficiency of lower band (generated by the monopole radiator) is approximately about 50%, the efficiency of middle band (generated by the loop radiator) is about 60–70%, the efficiency of higher band (generated by the coupling loop radiator) is approximately about 70%. The difference of simulation and measurement result is because the loss of component, DC bias and the implement error.

4. CONCLUSIONS

In this article, a novel multi bands reconfigurable antenna employing a tunable loop/monopole antenna has been presented. By using the characteristics of equivalent circuit of the PIN diode, the resonance of loop/monopole antenna can be reconfigurable by switching the diode either in “ON” or “OFF” state. The trend of both simulation and measurement results are agreed. This type of reconfigurable technique can be used for compact size mobile communication system for different communication purposes.

REFERENCES

1. Weedon, W. H., W. J. Payne, and G. M. Rebeiz, “MEMS-switched reconfigurable antennas,” *Proc. IEEE AP-S Int. Symp. Antennas and Propagation*, 654–657, 2001.
2. Yang, F. and Y. Rahmat-Samii, “Patch antennas with switchable slots (PASS) in wireless communications: Concepts, designs, and applications,” *IEEE Antennas Propagat. Mag.*, Vol. 47, 13–29, Feb. 2005.
3. Yang, S., H. K. Pan, A. E. Fathy, S. M. El-Ghazaly, and V. K. Nair, “A novel reconfigurable maze antenna for multi-service wireless universal receivers,” *Proc. IEEE Radio and Wireless Symp.*, 195–198, 2006.
4. Boyle, K. R. and P. G. Steeneken, “A five-band reconfigurable PIFA for mobile phones,” *IEEE Trans. Antennas Propagat.*, Vol. 55, No. 11, 3300–3309, 2007.
5. Yu, W., GEMS at <http://www.2comu.com/>.

Reconfigurable Antenna with Tri-polarization Capability

Dau-Chyrh Chang and Hsin-Chi Li

Institute of Information and Communication Engineering
Oriental Institute of Technology, New Taipei City, Taiwan

Abstract— The design of the polarization reconfigurable antenna for tri-polarization diversity is presented. In order to satisfy the requirement of polarization diversity in the integrated communication systems, we propose the concept of switching the polarization state of antennas by controlling high speed PIN diodes. In order to reduce the impact of antenna performance, the lumped elements, capacitor and inductor, are used to isolate the direct current source and RF signal respectively. Used of the pin diodes switch that can complete the characteristic of polarization diversity for LP (linear polarization), LHCP (left hand circular polarization) and RHCP (right hand circular polarization).

1. INTRODUCTION

The use of polarization diversity is increasingly important in the modern wireless communication system. In the WLAN (Wireless Local Area Networks) system, can be used polarization diversity to avoid the fading of multi-path. The reflected process in the transmission environment, the reflective will be change the characteristic of polarization. It makes the changes of the signal amplitude and phase has the difference. After multiple reflect, the signal on the different polarization into mutually independent or nearly independent of each other. In the process of the wireless communication, fading generated the impact on the quality of transmission signals and also deterioration in the BER (Bit Error Rate). With the development of electronic communication technology, diversity reception technology has become an effective anti-fading measures.

This article mainly applied the pin diodes and meander monopole radiator, by controlling the bias voltage of the pin diodes to change the antenna resonant structure and resonant modes. Depending on the bias of the given way, the antenna will be formed LP, RHCP and LHCP. The reconfigurable antenna with has the radiation characteristics of tri-polarization in the limited volume.

2. ANTENNA DESIGN

When the two orthogonal vectors have the same amplitude and has the 90 degree phase difference and that will became circular polarization. Electric field vector changes over time that can divide into LHCP and RHCP. Observe the changes in the electric field vector trajectory and the electric field assuming of the following formula:

$$\vec{E} = E_{0x}e^{-jkz}\hat{a}_x + E_{0y}e^{-jkz} * e^{j\phi}\hat{a}_y = E_{0x} \cos(\omega t - kz)\hat{a}_x + E_{0y} \cos(\omega t - kz + \phi)\hat{a}_y \quad (1)$$

In the space, when the two orthogonal vectors have the same amplitude and had the 90 degree phase difference, i.e., $E_{0x} = E_{0y}$ and assuming the $\phi = 90^\circ$, the changes of electric field vector is LHCP, and conversely if $\phi = -90^\circ$, that the changes of electric field vector is RHCP.

The antenna is illustrated in Figure 1. It is printed on $50 \times 50 \times 0.8 \text{ mm}^3$ a FR4-epoxy substrate with relative permittivity 44. The CPW feeding line is used for the tri-polarization antenna. The tri-polarization antenna is composed of three meander radiators 1, 2, and 3. The distance between meander radiator 1 and meander radiators 2, 3 is quarter wavelength (about 90 degree phase difference). The meander radiators 2 and 3 are controlled by the PIN diode switches. The switch states at each model are given in Table 1. The main contribution of meander radiator 1 is for LP (model 1). The contributions of meander radiators 1 and 2 (3) are for LHCP (RHCP). When the two diodes near meander radiators 2 and 3 are off then most of the current will flow at radiator 1 which will cause LP radiation. When one of the two diodes (D1D2) is on then the current will flow the radiator 1 and radiator 2 (3), and because there have 90 degree phase difference between two radiators so that will cause CP radiation.

3. ANTENNA PARAMETER OF THE STUDY

Figure 2 is the return loss of simulated and measured, from the result can be found that have error between simulation and Implementation, but the measured return loss still lower than -10 dB in

Table 1: Reconfigurable antenna models of operation.

Diode Combination	Diode State		
	Model 1 (LP)	Model 2 (LHCP)	Model 3 (RHCP)
D1	OFF	ON	OFF
D2	OFF	OFF	ON

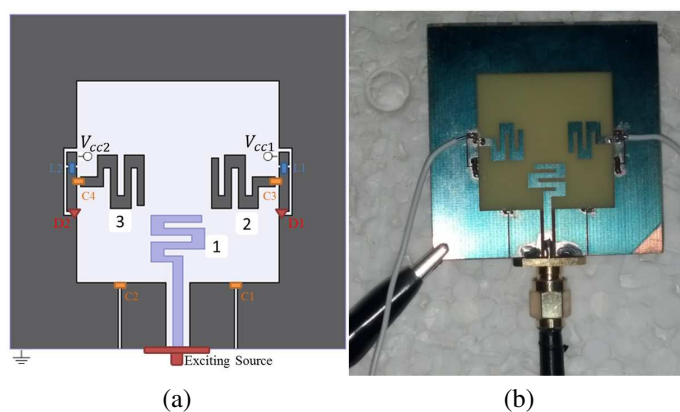


Figure 1: The proposed structure of reconfigurable antenna. (a) Simulation mode. (b) Prototype.

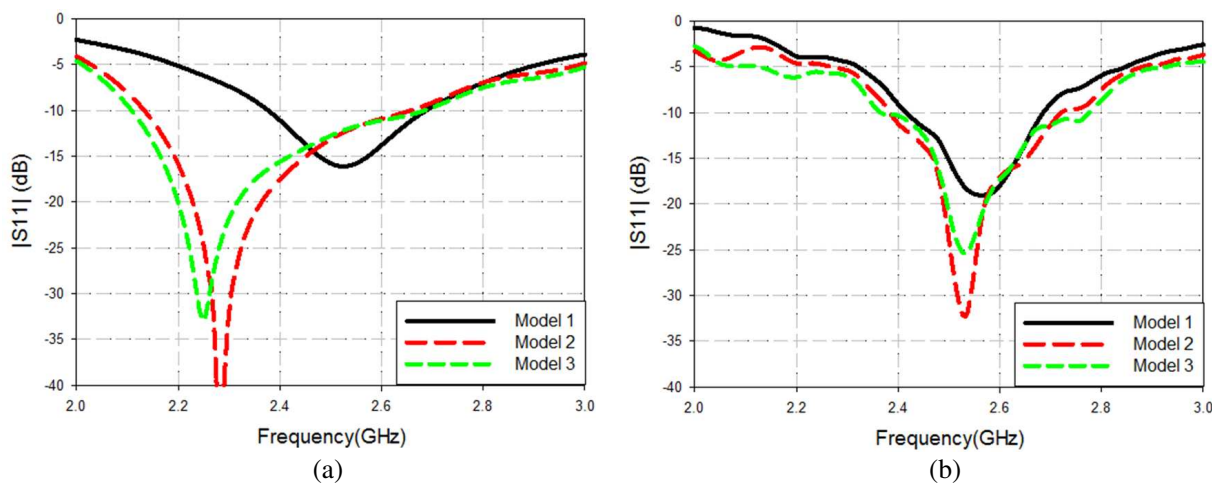


Figure 2: Result of return loss. (a) Simulation. (b) Measurement.

the requirement band (2412–2472 MHz). The difference of simulation and measurement result is because the loss of component and the implement error. Figure 3 is the axial ratio of simulated, the model 1 is LP so that axial ratio is higher, and the model 2 and 3 are CP so that axial ratio is lower than 3 dB in the requirement bands.

Figure 4 is the E -plane pattern of model 1 that because there is one monopole radiated, so that is LP and the E -phi is more lower than E -theta. Figure 5 is the E -plane pattern of model 2, the results of measurement and simulation is very close that the value of E -theta is close to E -phi in the direction of $\phi = 0^\circ$, and 180° , so in the direction is CP radiation. Figure 6 is the E -plane pattern of model 3, the results of measurement and simulation is very close that the value of E -theta is close to E -phi in the direction of $\phi = 0^\circ$ and 180° , so in the direction is CP radiation. According to the switch of pin diodes that can complete switch the characteristic of antenna polarization.

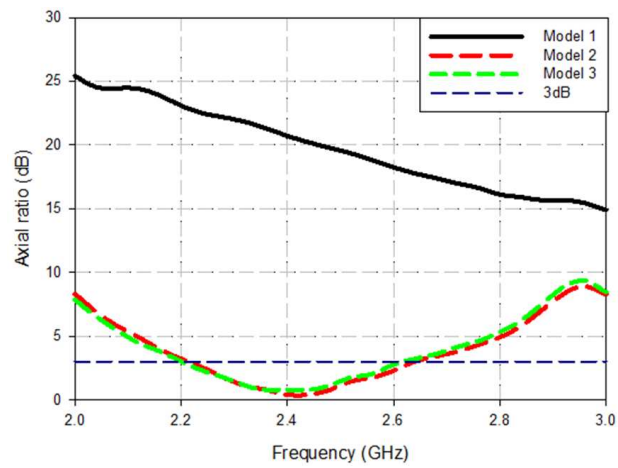


Figure 3: Simulation result of axial ratio.

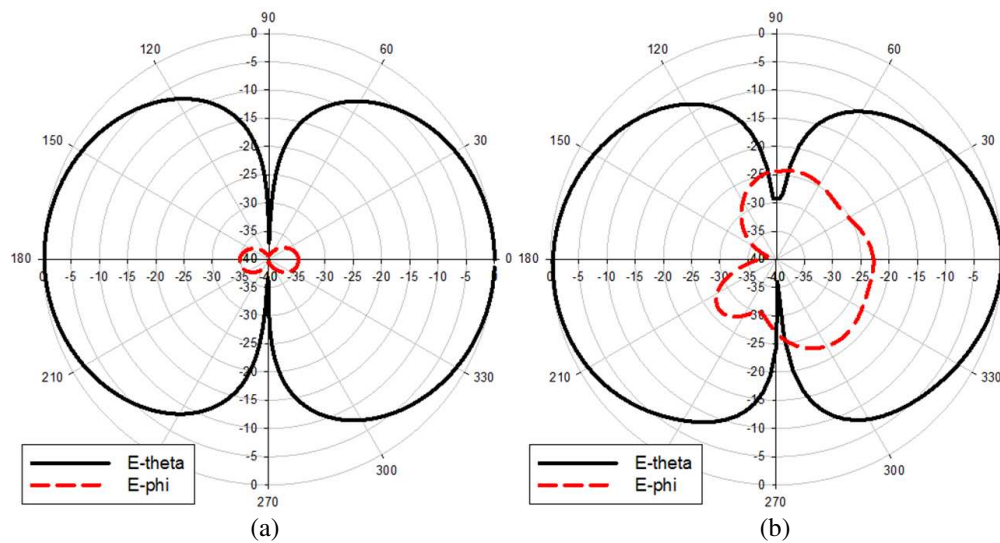


Figure 4: *E*-plane pattern for model 1. (a) Simulation. (b) Measurement.

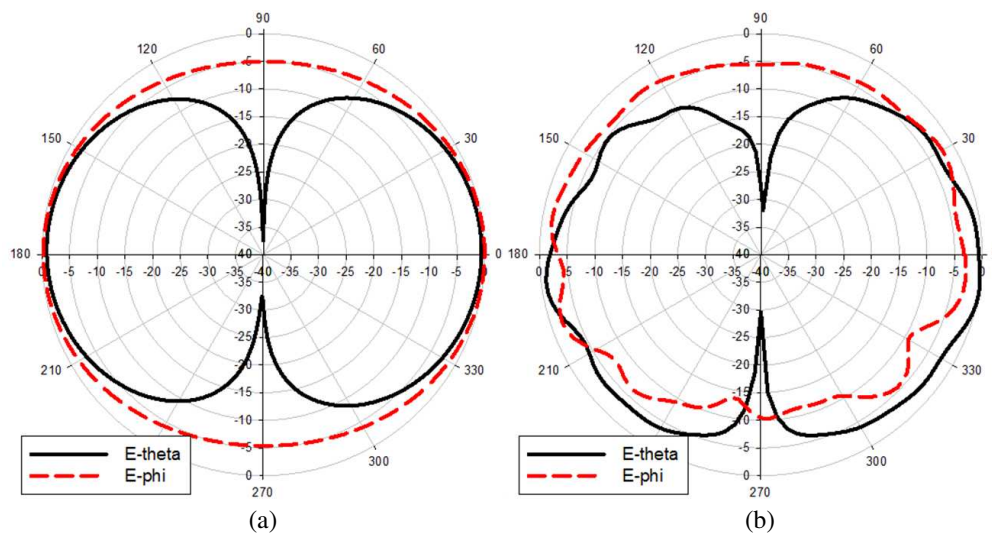


Figure 5: *E*-plane pattern for model 2. (a) Simulation. (b) Measurement.

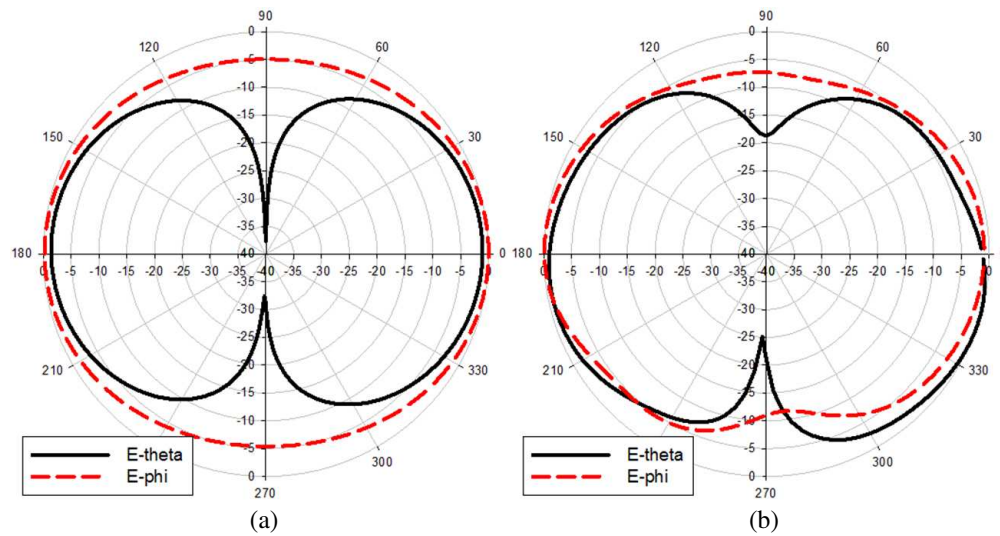


Figure 6: E -plane pattern for model 3. (a) Simulation. (b) Measurement.

4. CONCLUSIONS

This article is using pin diodes to design the tri-polarization reconfigurable antenna, and from the measurement result that can be found the trends is close to the simulation analysis. By using the bias voltage of pin diodes that can change the resonant structure of antenna, thereby change the exciting mode of antenna and achieve the tri-polarization radiation patterns.

REFERENCES

1. Gupta, R. K., U. C. Sharma, P. Sayanu, and G. Kumar, "MEMS based reconfigurable dual band antenna," *Microwave Opt. Technol. Lett.*, Vol. 50, 1570–1575, Mar. 2008.
2. Yang, S., A. E. Fathy, S. M. El-Ghazaly, and V. K. Nair, "Novel reconfigurable multi-band antennas for multi-radio platforms," *Proc. IEEE Radio and Wireless Symp.*, 723–726, 2008.
3. Sung, Y. J. and T. U. Jang, "A reconfigurable microstrip antenna for switchable polarization," *IEEE Microwave and Wireless Components Letters*, Vol. 14, 534–536, Nov. 2004.
4. Fries, M. K., M. Grani, and R. Vahldieck, "A reconfigurable slot antenna with switchable polarization," *IEEE Microwave and Wireless Components Letters*, Vol. 13, 490–492, Nov. 2003.
5. Yu, W., GEMS at <http://www.2comu.com/>.

Analysis of Phase Range Distribution of Different Reflectarray Elements on Polycrystalline Silicon Cell

A. Selamat¹, N. Misran^{1,2}, M. T. Islam^{1,2}, and M. F. Mansor¹

¹Department of Electrical, Electronic and System Engineering
Universiti Kebangsaan Malaysia, Bangi, Selangor 43600, Malaysia

²Institute of Space Science (ANGKASA), Universiti Kebangsaan Malaysia
Bangi, Selangor 43600, Malaysia

Abstract— The bandwidth behavior of reflectarray elements are discussed in this paper to overcome the intrinsic limitation of narrow bandwidth it offers. This is done by analyzing the relationship between bandwidth and phasing distribution characteristics of the elements. Five shapes of elements, i.e., ring, rectangular loop, triangular loop, square loop and ellipse loop have been investigated. Each element is designed on Kapton sheet positioned on top of a coverglass layer that protects the silicon layer. Rogers RT/Duroid 5880 dielectric substrate ($\epsilon_r = 2.2$ and $\tan \delta = 0.0009$) is used to support the layers above. These elements are designed to operate at Ku-band frequency range using CST microwave studio. The elements dimension are varied thus modifies the surface current distribution that leads to variation of phase reflection from the elements. The relationship of bandwidth performance with the obtained reflection loss of each element is then investigated. It has been demonstrated from this work that triangular element can offer the highest static linear phase range about 263° , whereas the square element gives the lowest static linear phase range of 153° . The surface area of resonating element has significantly control the current distribution hence leads the triangular element with the lowest surface area to has steep phase variation. While square element with greater surface area is shown to exhibit smoother phase variation with broader bandwidth performance. Moreover, the CST simulation results also shown that triangular element can operate at two resonant frequencies within Ku-band at 12.22 GHz and 14.09 GHz which can be further exploited for satellite and communication applications.

1. INTRODUCTION

Nowadays, study on reflectarray antenna to replace the conventional parabolic reflector antenna is becoming a trend. Various advantages including flat surface, light weight and low cost to manufacture have made this antenna the choice of study. However, one major obstacle need to be faced is the bandwidth limitation. Various studies have been carried out to overcome this problem. Bandwidth can be increased using two layer grounded array of rings [1], whereas the linearity of reflection phase response are controlled by the diameter ratio of the ring [2, 5]. Introduction of split concept into the element has also improved bandwidth significantly [3]. Thus, this paper discusses the basic design procedure using five different shapes of element that is printed on silicon solar cell and to study the phase performance of each resonant element.

2. DESIGN METHODOLOGY

The reflectarray elements are designed to be operated at Ku-band with five different shapes comprising rectangular loop, square loop, ellipse loop, triangular loop and ring. Figure 1 shows the details design for each element used in this experiment. Each design has passed through an optimization process to get the exact nominal value so that all designs are resonated around 14 GHz frequencies. Table 1 depicted the detail dimensions of each design respectively.

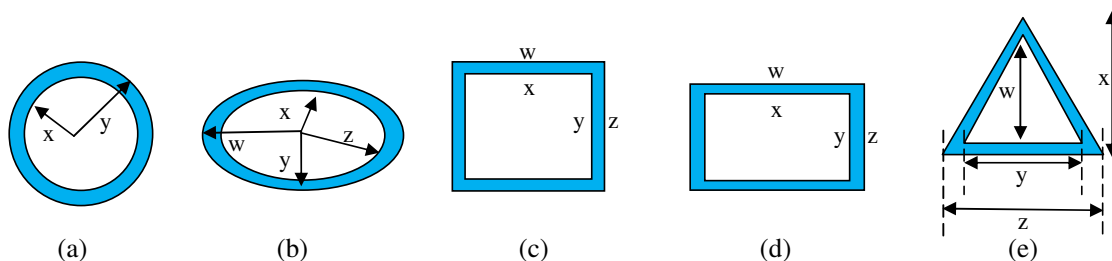


Figure 1: Geometries of (a) ring, (b) ellipse loop, (c) square loop, (d) rectangular loop, (e) triangular loop.

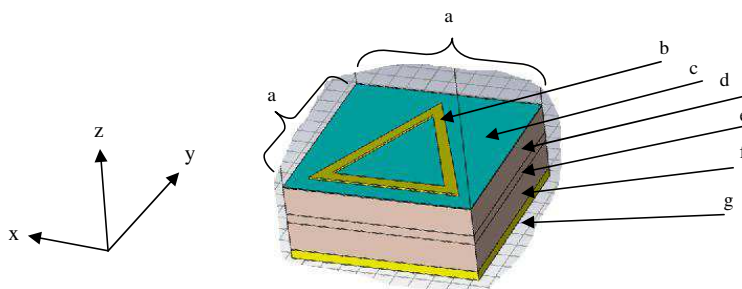


Figure 2: A 3-D geometrical view.

Table 1: Dimension of each element.

Element/Dimension	w (mm)	x (mm)	y (mm)	z (mm)
Ring	-	3.4	4.5	-
Ellipse loop	4	2	3	3
Rectangular loop	8	5.5	5	7
Square loop	9	5.8	5.8	9
Triangular loop	6.2	8	6	8

Table 2: Geometry of each layer.

	Layer/Dimension	x (mm)	y (mm)	z (mm)
a	Periodicity	10	10	4.246
b	Copper (Top)	-	-	0.1
c	Kapton sheet	10	10	0.051
d	Silica glass	10	10	1.52
e	Silicon Solar Cell	10	10	0.5
f	RT/Duroid 5880	10	10	1.575
g	Copper (Bottom)	10	10	0.5

All the above mentioned copper elements are constructed on top of a Kapton sheet of 0.051 mm thickness and secured on top of a cover-glass [4] as shown in Figure 2. The 1.52 mm cover-glass is used to protect a solar cell layer of 0.5 mm thickness situated in-between the silica glass and RT/Duroid substrate. The Rogers RT/Duroid 5880 substrate layer of 1.575 mm thickness is used to support all the above mentioned layers. Meanwhile, copper layer at the bottom of the RT 5880 substrate acts as a ground plane. Example of the complete 3-D geometrical dimension of a triangular element is shown in Table 2.

3. RESULTS AND DISCUSSIONS

The study focuses on two main criteria, namely the static linear phase range and the bandwidth obtained from the S-shaped curve of each element. Investigation on these parameters will determine the best element which has the low loss performance and greater phase range to be selected as the reflectarray element candidate. Figure 4(a) shows the reflection phase curve of the five different elements that have been analyzed using the commercial full-wave electromagnetic software CST Microwave Studio. The results show three resonant elements including ring, rectangular loop and square loop have very close value of linear phase range. Referring to Figure 3, the linear phase range can be calculated using Equation (1) below.

$$\Delta\varphi = \varphi_1 - \varphi_2 \quad (1)$$

Table 3 summarizes the detail results of the static linear phase range as well as the reflection loss values for each element. It can be observed that triangular loop element with reflection loss of -1.2 dB offers a maximum static phase range of around 263° . Conversely, the elements of square

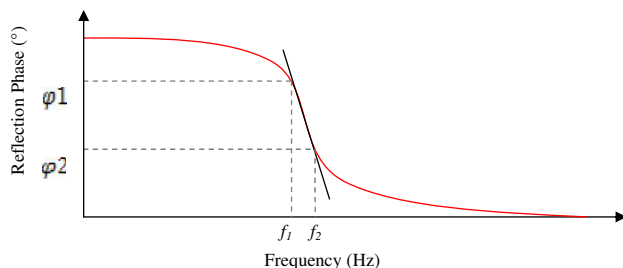


Figure 3: Reflection phase versus frequency.

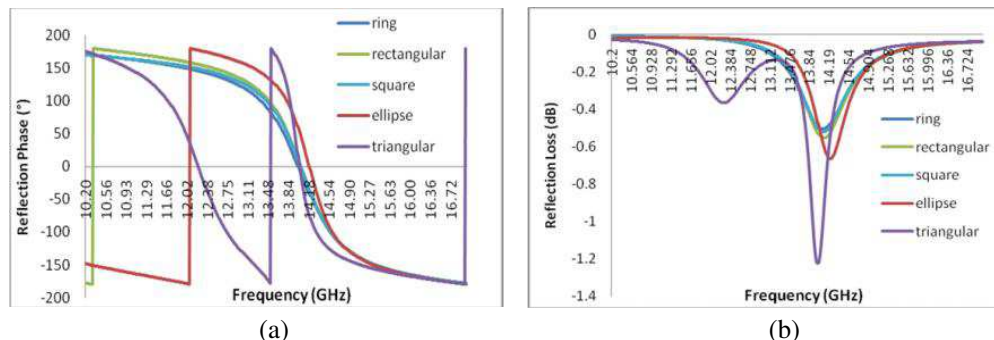


Figure 4: Comparison of simulated results among different reflectarray elements (a) reflection phase (°) vs frequency (GHz), (b) reflection loss (dB) vs frequency (GHz).

Table 3: Simulated linear phase range, reflection loss and bandwidth of different resonant elements.

Case	Element	Linear Phase Range (°)	Reflection Loss (dB)	Bandwidth (%)
1	Triangular	262.815	-1.20	5.13
2	Ellipse	197.114	-0.65	5.27
3	Ring	165.044	-0.51	6.36
4	Rectangular	162.329	-0.53	5.34
5	Square	153.449	-0.52	5.56

loop, ellipse loop, ring, and rectangular loop have linear phase range values less than 200° . The square loop element with -0.5 dB reflection loss gives the minimum static linear phase range value of about 153° . Meanwhile, it is observed that highest bandwidth value of 6.36% offered by ring element at the lowest reflection loss. Conversely, the lowest bandwidth happened at triangular loop element as it contributes the largest loss.

The simulated result in Figure 4(b) shows the triangular loop element has both the highest and the lowest loss compared to the other shapes of element. It is happened because the triangular element resonates at dual frequencies. At the resonant frequency of 14.09 GHz it has reflection loss of -1.2 dB, while at the resonant frequency of 12.22 GHz the reflection loss is about -0.4 dB. This is significantly due to the surface shape of the triangular loop element itself as shown in Figure 5(e). One of the triangular loop element vertices has allowed higher current distribution in that particular region which refers to the second resonant frequency. However, the other vertices have low current distribution which results for the first resonant frequency. The red color in the surface current density result generated by the CST computer model represents the region with the higher current distribution.

Figure 5 shows the current distribution from the five different resonating elements. It can be seen that triangular loop element has the maximum current density of 2128 A/m while the square loop element has the lowest maximum current density of 444 A/m. These results occur due to the fact that concentration of the current distribution depends on reflective area of each design element. It is also noticed that, resonant frequency of each element straightly depends on the length, width and diameter of the reflective area. As depicted in Table 4, triangular loop element has reflecting

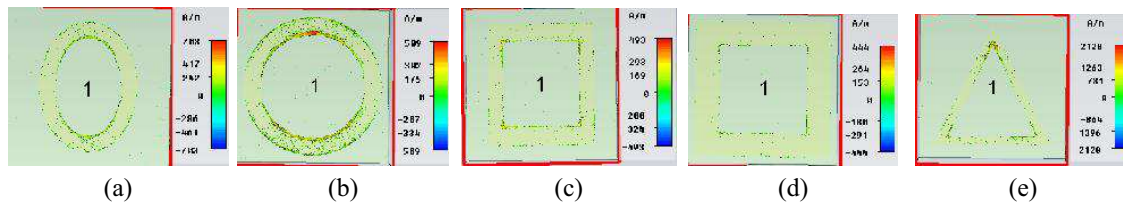


Figure 5: Surface current density on reflectarray elements, (a) ellipse loop, (b) ring, (c) rectangular loop, (d) square loop, (e) triangular loop.

Table 4: Surface current density and area of different element.

Case	Element	Surface Current (A/m)	Area of Resonating Element (mm ²)
1	Triangular	2128	13.4
2	Ellipse	703	18.8
3	Ring	509	27.3
4	Rectangular	493	28.5
5	Square	444	47.4

area of 13.4 mm² thus it has the maximum surface current. Meanwhile, the square loop element has reflecting area of 47.4 mm² and this contributes to the lowest surface current value compared to other elements. In conclusion, any modification made to the reflecting area of resonant element will affect the surface current density.

4. CONCLUSIONS

Five different shapes of elements have been designed as a radiating element on a polycrystalline silicon cell. The simulation results presented have shown that the elements phase performance depends on size of the design area thus influence bandwidth. It also noted that shape of element also contributes indirectly to the performance of resonant frequency. The results have shown that triangular shape is the best candidate as the reflectarray antenna element as it offers the largest linear phase range and the lowest reflection loss. Besides it also can operate at dual frequencies within Ku-band.

ACKNOWLEDGMENT

The authors would like to thank the staff of Institute of Space Science (ANGKASA) of Universiti Kebangsaan Malaysia for the technical support.

REFERENCES

1. Misran, N., R. Cahill, and V. F. Fusco, "Reflection phase response of microstip stacked ring elements," *Electronics Letters*, Vol. 38, No. 8, 2002.
2. Misran, N., R. Cahill, and V. F. Fusco, "Performance of a broadband ring element reflectarray," *IEEE*, No. 3, 111–114, 2003.
3. Yusop, S. H., N. Misran, M. T. Islam, and M. Y. Ismail, "Analysis on split concept of reflectarray antenna element for bandwidth enhancement," *Proceeding of IEEE International Conference on Space Science and Communication (IconSpace)*, Penang, Malaysia, Jul. 2011.
4. Zawadzki, M. and J. Huang, "Integrated RF antenna and solar array for spacecraft application," *Proceeding of IEEE International Conference on Phased Array Systems and Technology*, 239–242, 2000.
5. Bialkowski, M. E. and K. H. Sayidmarie, "Investigation into phase characteristics of a single-layer reflectarray employing patch or ring elements of variable size," *IEEE Tran. Antenna & Prop.*, Vol. 56, No. 11, 2008.

Photon Generation from Quantum Vacuum Using a Josephson Metamaterial

P. Lähteenmäki¹, G. S. Paraoanu¹, J. Hassel², and P. J. Hakonen¹

¹Low Temperature Laboratory, Aalto University, P. O. Box 15100, FI-00076 AALTO, Finland

²VTT Technical Research Centre of Finland, P. O. BOX 1000, FI-02044 VTT, Finland

Abstract— When one of the parameters in the Euler-Lagrange equations of motion of a system is modulated, particles can be generated out of the quantum vacuum. This phenomenon is known as the dynamical Casimir effect, and it was recently realized experimentally in systems of superconducting circuits, for example by using modulated resonators made of coplanar waveguides, or arrays of superconducting quantum interference devices (SQUIDs) forming a Josephson metamaterial. In this paper, we consider a simple electrical circuit model for dynamical Casimir effects, consisting of an LC resonator, with the inductor modulated externally at 10.8 GHz and with the resonant frequency tunable over a range of ± 400 MHz around 5.4 GHz. The circuit is analyzed classically using a circuit simulator (APLAC). We demonstrate that if an additional source of classical noise couples to the resonator (on top of the quantum vacuum), for example *via* dissipative “internal modes”, then the resulting spectrum of the photons in the cavity will present two strongly asymmetric branches. However, according to the theory of the dynamical Casimir effect, these branches should be symmetric, a prediction which is confirmed by our experimental data. The simulation presented here therefore shows that the origin of the photons generated in our experiment with Josephson metamaterials is the quantum vacuum, and not a spurious classical noise source.

1. INTRODUCTION

The picture about vacuum that emerges from modern quantum field theory is very different from that offered by classical physics. In classical field theory, the vacuum is the zero-energy state of the field, defined by the absence of any excitation. In quantum field theory, the vacuum state has a finite zero-point energy associated with it, and the uncertainty principle indicates that fluctuations exist even in this state. Due to the existence of fluctuations, the quantum vacuum can become unstable under certain perturbations, and the energy of the perturbation is converted into creation of real particles [1]. In the Schwinger effect for example, a static intense electric field can create pairs of electrons and positrons. In very strong gravitational fields, at the event horizon of black holes, the vacuum becomes unstable and energy is radiated away (Hawking effect). By the equivalence principle, an accelerated observer in the Minkowski vacuum will detect a finite-temperature field (Unruh effect).

In a previous paper, we reported the observation of the dynamical Casimir effect using a flux-biased Josephson metamaterial embedded in a microwave cavity at 5.4 GHz [2]. A non-adiabatic change in the index of refraction of the cavity (or in the electrical length) was realized by modulating the flux at values close to double the resonant frequency of the cavity. We measured also the frequency-correlated photons emitted from the cavity (which is kept at a temperature $T = 50$ mK), and we obtained a power spectrum displaying a bimodal, “sparrow-tail” distribution, with two symmetric branches. Furthermore, we demonstrated that the generated photons are squeezed below the vacuum level and that the state of the two-photon field is nonseparable. The experimental results are in excellent agreement with the theoretical predictions. An alternative realization of the dynamical Casimir effect consists in modulating an effective boundary condition, realized experimentally as a SQUID structure placed at the end of a coplanar waveguide resonator [3]. Remarkably, the experiments presented in Refs. [2, 3] are the only existing measurements of the dynamical Casimir effect, which was predicted theoretically in 1970 [4].

2. MODEL FOR NOISE ANALYSIS

A SQUID array was used in Ref. [2] to test the dynamical Casimir effect. This array was coupled to the external circuit by a capacitor. The entire system behaved as an electromagnetic cavity with tunable index of refraction. A simple analog model for this system, realized with electronic components, can be constructed as an LC circuit with the resonant frequency $1/2\pi\sqrt{LC}$ tunable in a range of ± 400 MHz around 5.4 GHz. The inductance L is modulated at a frequency of at

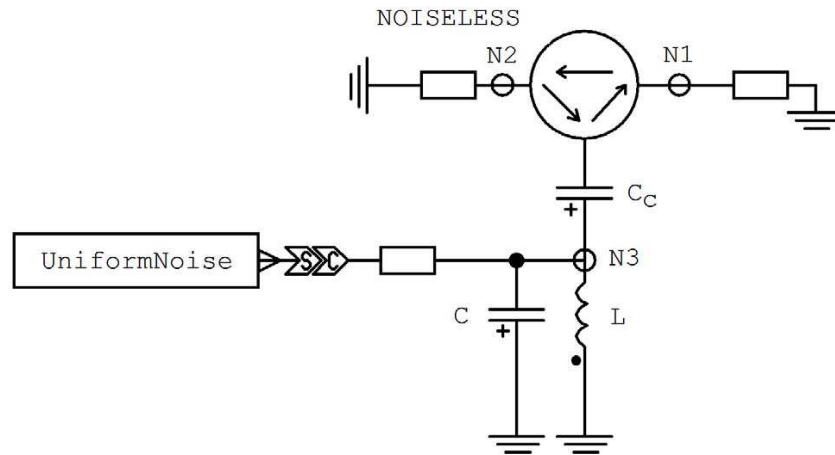


Figure 1: Schematic of the circuit used in the APLAC simulation. An LC circuit is formed between node N_3 and the ground. This circuit is coupled through a capacitor C_c to an external circuit consisting of a circulator and two resistors. White (uniform) noise is injected in the circuit through a resistor, and the spectrum at node N_1 is recorded.

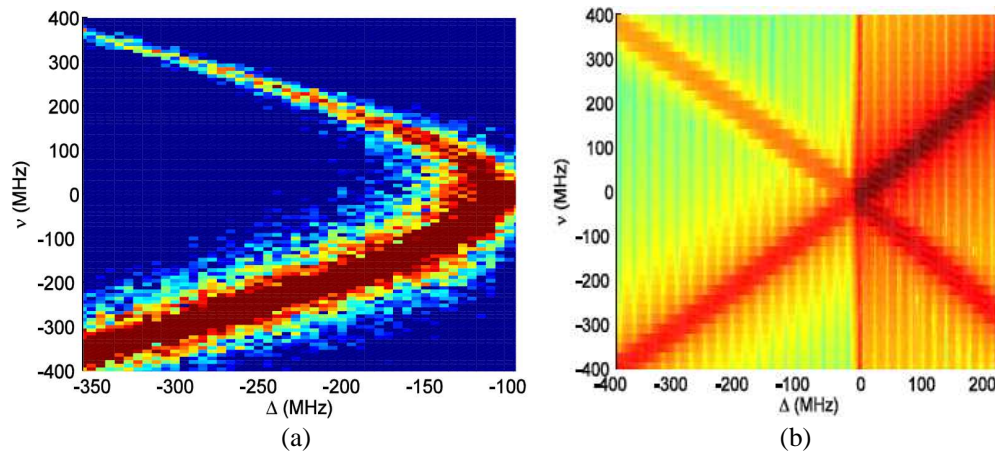


Figure 2: (a) Energy spectrum measured at the node N_1 of the modulated LC circuit with a classical noise input. The vertical axis ν (MHz) is the frequency measured from half the pumping frequency ($10.8 \text{ GHz}/2 = 5.4 \text{ GHz}$), while the horizontal axis Δ (MHz) is the detuning of the resonator frequency with respect to half the pumping frequency ($10.8 \text{ GHz}/2 = 5.4 \text{ GHz}$). The figure is obtained by averaging over 100 realizations of the simulation. (b) Alternate realization of the simulation: the energy in an initially-excited and pumped LC resonator is partly kept at the resonant frequency and partly upconverted, resulting again in the appearance of two asymmetric branches in the spectrum.

10.8 GHz, and classical white noise is fed in the circuit (see Fig. 1). The purpose of this simulation is to see the effect produced by spurious sources of noise on top of the quantum vacuum. In the experiment presented in Ref. [2] (see also its Supplementary Material) this could be for example additional thermal noise coming through the electromagnetic modes that couple to the cavity. Some of these modes are not directly accessible to the experimentalist (they are the so-called “internal modes”) and they might not thermalize well with the rest of the sample, at the base temperature of the refrigerator ($T = 50 \text{ mK}$, corresponding to a negligible thermal occupation of 0.0056 at the frequency of 5.4 GHz).

The circuit is simulated using APLAC, and the spectrum at node N_1 can be obtained (Fig. 2). The vertical axis ν (MHz) is the frequency at a given measurement point, while the horizontal axis Δ (MHz) is the frequency of the resonator; both frequencies are measured with respect to half the pumping frequency ($10.8 \text{ GHz}/2 = 5.4 \text{ GHz}$). The value of the capacitance used in this simulation is $C = 40 \text{ fF}$, and the coupling capacitor is $C_c = 5 \text{ fF}$. The spectrum in Fig. 2(a) is obtained by modulating the inductor at a constant amplitude of 2 nH and at a constant frequency

of 10.8 GHz around its average value. This average value is then slowly decreased from $L = 25.3$ nH to $L = 21.71$ nH, resulting in an increase in the LC resonant frequency from 5 to 5.4 GHz.

An alternate realization of this simulation consists of using the same LC circuit as in Fig. 1, again with the inductance being modulated at a frequency nearly twice the resonant frequency of the LC resonator, but with the capacitor C_c decoupled. We start the simulation by depositing an initial amount of energy in the LC resonator and we monitor the spectrum at the node N_3 as the frequency of the resonator is slowly swept, reaching and passing the parametric instability threshold ($\Delta = 0$). The resulting spectrum shown in Fig. 2(b) looks similar to the previous simulation.

3. CONCLUSIONS

The energy and the fluctuations of the electromagnetic vacuum confined in a cavity have real, measurable effects: they produce an attractive force between the walls of the cavity (static Casimir effect), and, if the boundary conditions or the index of refraction are changed, photons are created (dynamical Casimir effect). The experimental demonstration of the dynamical Casimir effect by the modulation of the effective electrical length (or the index of refraction) of a cavity constitutes an important milestone in quantum field theory. To establish this effect, we should check that the input state of any mode that couples to the cavity is the quantum vacuum state. In this paper, we show by a simple circuit simulation that any spurious (uncontrolled) classical source of noise that enter the cavity (the rest of the circuit being kept at the base temperature of the dilution refrigerator) should produce a spectral pattern with strongly asymmetric branches. Since the spectrum predicted by the theory of the dynamical Casimir effect is symmetric, the result presented here shows that the observed effect cannot be explained simply by the parametric amplification of a classical signal present at the input of the device, thus supporting the quantum origin of the phenomenon. Our experiment demonstrates the potential of superconducting quantum circuits to serve as a platform for simulating effects from cosmology and quantum field theory [5].

ACKNOWLEDGMENT

We wish to acknowledge the Academy of Finland for financial support through projects Nos. 135135 and 263457, and through the Center of Excellence in Low Temperature Quantum Phenomena and Devices (project 250280).

REFERENCES

1. Nation, P. D., J. R. Johansson, M. P. Blencowe, and F. Nori, "Stimulating uncertainty: Amplifying the quantum vacuum with superconducting circuits," *Rev. Mod. Phys.*, Vol. 84, 1–24, 2012.
2. Lähteenmäki, P., G. S. Paraoanu, J. Hassel, and P. J. Hakonen, "Dynamical casimir effect in a josephson metamaterial," *Proc. Natl. Acad. Sci.*, Vol. 110, 4234, USA, 2013.
3. Wilson, C. M., G. Johansson, A. Pourkabirian, M. Simoen, J. R. Johansson, T. Duty, F. Nori, and P. Delsing, "Observation of the dynamical Casimir effect in a superconducting circuit," *Nature*, Vol. 479, 376–379, 2011.
4. Moore, G. T., "Quantum theory of the electromagnetic field in a variable-length one-dimensional cavity," *J. Math. Phys.*, Vol. 11, 2679–2691, 1970.
5. Fulling, S. A., *Aspects of Quantum Field Theory in Curved Space-time*, Cambridge Univ. Press, Cambridge, 1989.

Filtration Properties of a System for the Measurement of Air Ions

Z. Szabó, Z. Roubal, and K. Bartušek

Department of Theoretical and Experimental Electrical Engineering
Brno University of Technology, Kolejní 2906/4, Brno 612 00, Czech Republic

Abstract— The measurement of air ion properties and concentration is a topical problem examined by a large number of research institutes. Detailed medical analyses have proved that negative light ions exhibit a positive effect on human health; conversely, a deficiency of these ions is known to cause fatigue, health problems, and poor work performance.

A significant precondition for the evaluation of these effects consists in determining the concentration, polarity, and mobility spectrum of air ions in the given area.

The measurement of air ion concentration can be realized via a wide variety of methods, including the technique based on the application of an aspiration condenser (AC). This research study presents a methodology for the measurement of air ion concentration using an AC and comprises the formulation of systematic and random errors.

1. INTRODUCTION

Air ions are extremely important for human health: they affect the metabolic function of cells in the lungs, the blood supply in the organism, and also the human mental capabilities. Through their electric charge, air ions also influence the Earth's atmosphere and the environment. The metrology of air ions has been known for a long time. One of the methods applied within this field is based on measurement using an AC; this technique is utilized in the measurement described within this paper.

2. MEASURING METHOD

An aspiration condenser having a variable electric field and an electrometer for measuring small currents were used to measure ions of different types (light-weight, light heavy-weight, heavy-weight) and polarities. The principle of the measuring method is obvious from Figure 1; it has been taken over from [1] and [2]. A known amount of air under examination $M = 1.021 \cdot 10^{-3}$ m/s (volume rate of flow) flows through a cylindrical capacitor, which exhibits polarization voltage U ($U = 0-100$ V).

Electrostatic forces attract the air ions to the electrodes. The number of ions captured by the electrode create a small electric current I . The concentration of ions of one polarity is proportional to the magnitude of this current according to the relation

$$n = \frac{I}{M \cdot e} \quad (1)$$

where $e = 1.6 \cdot 10^{-19}$ C is the electron charge.

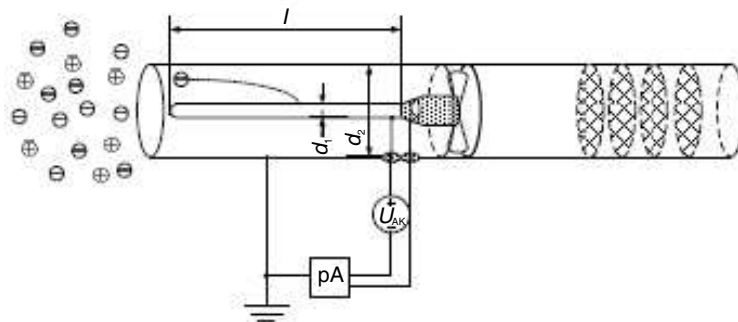


Figure 1: Principle of measuring air ions by using an AC.



Figure 2: AC design.

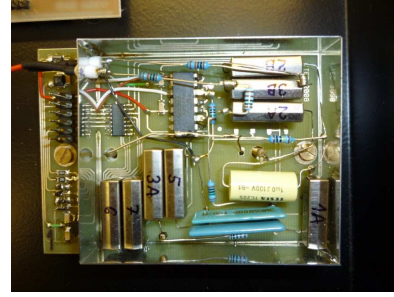


Figure 3: Design of the low-level amplifier.

The capacitor collector captures all ions whose mobility is lower than the minimum mobility given by the relation

$$k_m = \frac{M}{4 \cdot \pi \cdot C \cdot U} = \frac{M \cdot \ln \frac{d_2}{d_1}}{2 \cdot \pi \cdot l \cdot U}, \quad (2)$$

where M is the volume rate air flow through the condenser, C is the condenser capacitance, U is the voltage across the electrodes, and d_1 , d_2 , and l are the dimensions of the AC. The methodology of measuring and the calculations are described in more detail in [1], [2], and [3].

The shape of the condenser ensures that the air flow is laminar. Air flow turbulence can distort the measurement accuracy. The surface of the electrodes is required to be as smooth as possible. The realized design of the AC is shown in Figure 2.

The current flowing through the AC is based on the ion concentration. The current intensity depends on the polarization voltage, on the dimension and parameters of the AC, and on the ion concentration. The specific current range for the designed AC is 10^{-10} A– 10^{-13} A. The low-level amplifier is realized with INA 116 — Figure 3. The design of the amplifier is shown in Figure 3.

3. MEASUREMENT ERRORS

The measurement of air ion concentration based on an AC includes systematic and random errors caused by leakage resistance, parasitic capacitance in the circuit, ion field fluctuation, and the measuring amplifier noise. The noise voltage magnitude is greatly influenced by the source of the applied polarization voltage, because the impedance against the reference ground potential has to be very high ($> 10^{13} \Omega$).

There are two different approaches to realizing the source of auxiliary voltage. The first method utilizes a voltage source and offers the advantage of very low internal resistance; the disadvantage related to this technique consists in that real leakage resistance of the source has to be taken into account. The second solution exploits a charged condenser, and the leakage resistance can be neglected; the main disadvantages of this approach can be identified in the necessity to charge the condenser and in the small transmission for direct current.

To facilitate the analysis of systematic errors, we need to examine the influence exerted by parasitic elements on the accuracy of the measurement. Thus, it is necessary to consider leakage resistance of the AC (insulation resistance of the condenser and leakage resistance to ground), leakage resistance of the electrometer input terminals to ground, and insulation resistance of the source of auxiliary voltage for the intermediate electrode of the condenser to ground. Simultaneously, the measured value is influenced by internal resistance of both the electrometer and the auxiliary voltage source. To facilitate configuration of the measuring connection according to Figure 1, an equivalent diagram can be set up (Figure 4); this circuit includes all types of parasitic resistance and capacitance in the measuring system, including internal resistance of the electrometer and capacitance of the AC.

Notation of the individual elements (the values measured for the realization of the AC at the DTEEE are indicated in brackets)

R_{AK} , C_{AK} are the leakage resistance and capacitance of the AC ($R_{AK} = 470 \text{ T}\Omega$, $C_{AK} = 8 \text{ pF}$),
 R_P denotes the teflon leadthrough resistance and insulation resistance of the auxiliary voltage source ($R_P = 10^{18} \Omega$),
 R_V , C_U are the internal resistance and capacitance of the auxiliary voltage source ($R_V = 100 \text{ T}\Omega$, $C_U = 1 \mu\text{F}$),

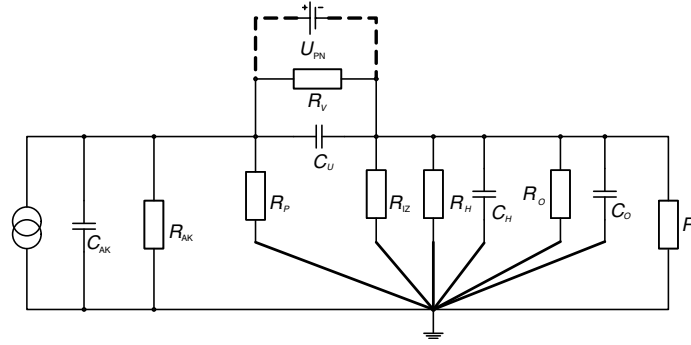


Figure 4: Equivalent diagram of the ion concentration measurement.

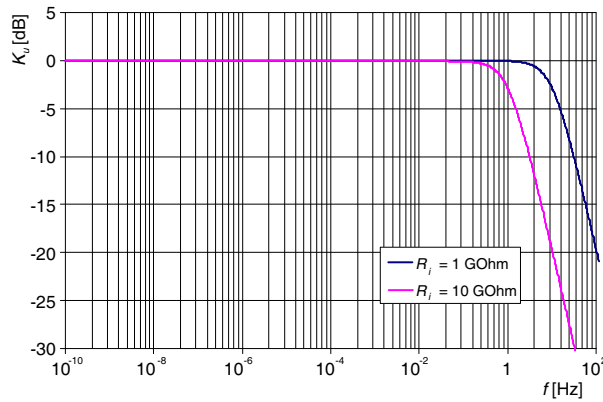


Figure 5: Transmission through the AC in relation to the frequency.

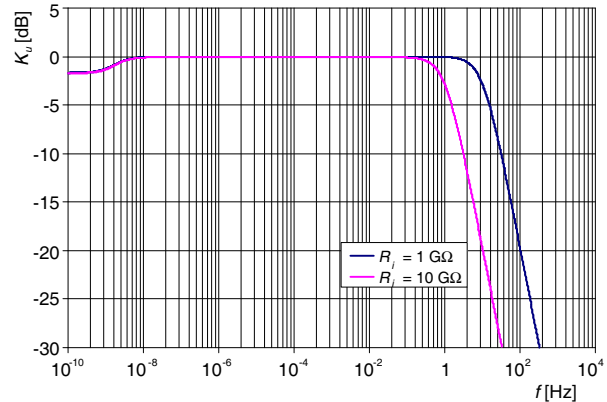


Figure 6: Transmission through the AC in relation to the frequency; the voltage source consists of a condenser.

U_{PN} is the auxiliary voltage source,

R_i denotes the sensing resistor or internal resistance of the electrometer,

R_{IZ} denotes the insulation resistance of the auxiliary voltage source ($R_{IZ} = 5 \cdot 10^{17} \Omega$),

R_H is the leakage resistance of the sensing resistor between the intake and ground ($R_H = 10^{15} \Omega$),

C_H is the capacitance of the sensing resistor intake ($C_H = 200 \text{ fF}$),

R_O denotes the leakage resistance of the electrometer input terminal,

C_O capacitance of the electrometer input terminal ($C_O = 7 \text{ pF}$).

The measuring system including an AC can be described as a circuit with the conversion of input current formed by incident ions to an output voltage that corresponds to the concentration of the ions. Frequency characteristics of the measuring system transmission related to various values of the sensing resistor R_i and to both circuit solutions of the auxiliary voltage source are indicated in Figures 5 and 6. Analysis of the frequency transmission and measurement errors was carried out using the Micro-Cap program.

An increase of the sensing resistor R_i value (the auxiliary voltage source is composed of a condenser) decreases frequency transmission in the low frequency range. The measured current will be filtered through the bandwidth of up to 1 Hz and will correspond to the mean value of the ion field fluctuations. It is obvious from the frequency characteristics (Figure 5.) that, in the source generating auxiliary voltage, the frequency transmission is constant also for direct current; the maximum frequency transmission is 10 Hz for $R_i = 1 \text{ G}\Omega$ and 1 Hz for $R_i = 10 \text{ G}\Omega$.

If a condenser is used to create auxiliary voltage, the frequency transmission of current through the device decreases only for lower frequencies (Figure 6). The limitation at higher frequencies is the same as with a voltage source. However, at the lower frequencies of the spectrum are the periods of harmonic changes longer than 3 years; thus, it is proved that, for real times, we can ensure satisfactory accuracy of the measurement.

Table 1: Magnitude of the measurement error and bandwidth in relation to the electrometer internal resistance.

Internal resistance [Ω]	Bandwidth [Hz]	Measurement error [%]
100 G	10 nHz–100 Hz	24
10 G	10 nHz–40 mHz	1.35
1 G	10 nHz–100 mHz	0.12
1 M	10 nHz–1 Hz	0.002

The configuration including a condenser auxiliary source filters the measured ion current with maximum frequency of 1 Hz pro $R_i = 10 \text{ G}\Omega$. The limitation does not influence the use of the above-mentioned configuration in the measurement of the air ion field concentration.

The dependence of transmission of the magnitude of internal resistance R_i is exactly expressed in Table 1. With the resistance value of $1 \cdot 10^6 \Omega$, the magnitude of relative error is as low as 0.002%. If the electrometer internal resistance rises to the value of approximately $1 \cdot 10^{10} \Omega$, the relative error increases to 0.12%. With the resistance value of $1 \cdot 10^{11} \Omega$, however, the relative error is larger, attaining the value of 1.35%. In the case of further increase of the electrometer internal resistance, the error rises exponentially; with the resistance value of $1 \cdot 10^{12} \Omega$, the error amounts to 24%, resulting in substantial measurement distortion.

The data in Table 1 indicate that a decrease in the value of the electrometer internal resistance is accompanied by an increase in the accuracy of the air ion field concentration; thus, the relative error of the measurement decreases significantly. Simultaneously, it is obvious that the bandwidth of accurate measurement extends with a decrease in the electrometer internal resistance. Thus, the data can be applied to improve the accuracy of the entire process of measuring air ion concentration.

4. CONCLUSIONS

As is evident from the above-presented results, the error changes substantially with an upward alteration of resistance. Furthermore, the bandwidth for “accurate” measurement varies significantly with the magnitude of the electrometer internal resistance. Given the resistance of $1 \cdot 10^6 \Omega$, the bandwidth is from 10 nHz to 1 Hz; however, if the electrometer internal resistance R_i changes to the value of $1 \cdot 10^{12}$, the bandwidth is defined by the limits of 10 nHz and 100 Hz. The dependence of the error of measurement holds for both connections of the source of auxiliary voltage.

It is also important to note that, in general, the use of a voltage source producing auxiliary voltage enables us to obtain higher measurement accuracy in the entire frequency spectrum. If a condenser is used to create auxiliary voltage, the frequency bandwidth without damping is markedly narrower; however, the connection behaves identically in real periods of harmonic changes and can be fully utilized for these purposes.

ACKNOWLEDGMENT

The research described in the paper was financially supported by a grant of Czech Ministry of Industry and Trade No. FR-TI1/368, project of the BUT Grant Agency FEKT-S-11-5/1012, and project CZ.1.07.2.3.00.20.0175, Elektro-výzkumník.

REFERENCES

1. Roubal, Z., M. Steinbauer, Z. Szabó, and R. Kubasek, “Real-time measurement of air ion spectrum using gerdien tube with segmented inner electrode,” *PIERS Proceedings*, 1744–1748, Moscow, Russia, Aug. 18–21, 2009.
2. Fiala, P. and Z. Szabó, VUT v Brně, “Ion filtr for gerdien tube type sensor,” PV-2010-780, Praha, 2010.
3. Bartušek, K., “Měření spektrálních charakteristik iontových polí,” <http://www.elektrorevue.cz/clanky/01038/index.html>, 2001.
4. Bartušek, K., “Měření s aspiračním kondenzátorem,” <http://www.elektrorevue.cz/>.
5. Vojtek, T., M. Steinbauer, P. Drexler, and E. Kroutilová, “Methods of air ion concentration measurement,” *Applied Electronics*, 181–184, Department of Applied Electronics and Telecommunications, University of West Bohemia, Pilsen, Czech Republic, 2006, ISBN 80-7043-442-2.
6. Hörrak, U., “Air ion mobility spektrum at a rural area,” *Dissertationes Geophysicales Universitatis Tartuensis*, Tartu, 2001.

7. Kondrashova, M. N., E. V. Grigigorreko, A. N. Tikhonov, T. V. Sirota, A. V. Temnov, I. G. Stavrovskaya, N. I. Kosyakova, N. V. Lange, and V. P. Tikonov, “The primary physicochemical mechanism for the beneficia biological/medical effects of negative air ions,” *IEEE Trans. Plasma Sci.*, 230–237, 2000.
8. Moody, N. F., “Measurement of ion-induced noise in atmospheric counting chambers, and a novel chamber for its elimination,” *Int. J. Biometeor.*, Vol. 25, No. 4, 331–339, 1981.
9. Grambarczyk, Z., “Frequency characteristic of an aspiration integrating small ion counter with a shielded collector,” *Journal of Electrostatics*, Vol. 51, 284–289, 2001.
10. Tammet, H. F., *The Aspiration Method for Determination of Atmospheric-ion Spectra*, IPST, Jerusalem, 1970.

A Comparison of the Dynamic Range of FDNR Building Blocks

Z. Szabó, J. Sedláček, and M. Friedl

Department of Theoretical and Experimental Electrical Engineering
Brno University of Technology, Kolejní 2906/4, Brno 612 00, Czech Republic

Abstract— A multitude of various active selective blocks are utilized for the design of active filters based on RLC prototypes. The design of low-pass filters is often realized by means of the Bruton transformation, in which the RLC prototype structure is transformed into an RCD structure. The basic building blocks applied within the latter structure are denoted as dual capacitors (FDNR). These active blocks, realized in various circuit configurations with different numbers of active circuit elements (operational amplifiers, OA), have recently been described by several authors [1, 2].

At present, it is possible to fabricate ARC filters for the frequency range within units of MHz, using simple and economical selective FDNR building blocks that work successfully with one active element (OA). The fabrication is enabled by modern active elements (such as voltage operational amplifiers working in the GBW of approximately 1 GHz or CFA amplifiers applicable up to higher frequencies) and by the synthesis method based on purposefully lossy RLC prototypes [3, 4].

This research report presents a comparison of the dynamic ranges of the most widely utilized lossy FDNR building blocks (types I and V), and the authors intend to employ the proposed comparative outline to help improve the practical exploitation of these capacitors in the process of optimizing active frequency filters.

1. DESIGN AND REALIZATION OF FILTERS HAVING LOSSY PARAMETERS

The process of designing active filters based on RLC prototypes involves the application of several different types of active selective blocks. The design of low-pass filters very often employs the Bruton transformation, in which the structure of an RLC prototype is transformed to the RCD structure. Here, the elementary structural blocks applied are active elements known as dual capacitors (and frequently referred to in literature as FDNRs — frequency dependent negative resistors). In high-pass ARC filters, synthetic inductors (SI) are often utilized as active blocks simulating the properties of a coil. These active blocks, realized in different circuit configurations and having different numbers of active circuit elements (operational amplifiers or OAs), have been described in sources such as [1, 2, 4].

In order to provide experimental verification of partial conclusions made within previous investigation into the properties of the designed active lossy block filters, several above-specified networks were realized as test samples on printed circuits. The related transmission properties (mainly the modular frequency characteristics and the circuit dynamics) obtained by means of computer modeling were compared with the experimentally measured values.

2. UNIVERSAL MEASURING STATION

A universal measuring station was set up together with the concept of a suitable measurement methodology in order to facilitate the measurement of transmission properties of various two-port networks within a wider frequency range. A block diagram of the measuring station is presented in Figure 1. Figure 2 then shows the first-designed model connection of the realized 5th order low-pass sample filter with lossy dual capacitors; the buffer amplifiers are indicated as well.

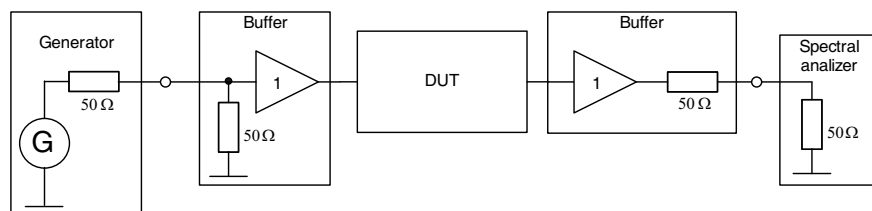


Figure 1: Block diagram of the measurement apparatus testing the designed filtering circuits.

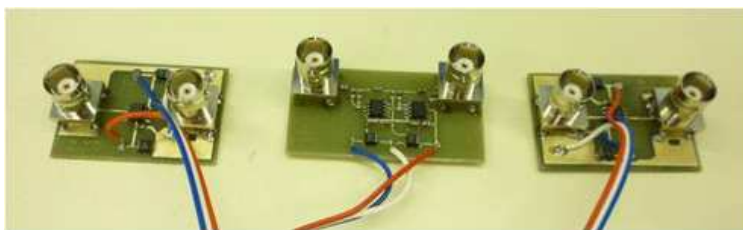


Figure 2: Block amplifiers and the filtering circuit.

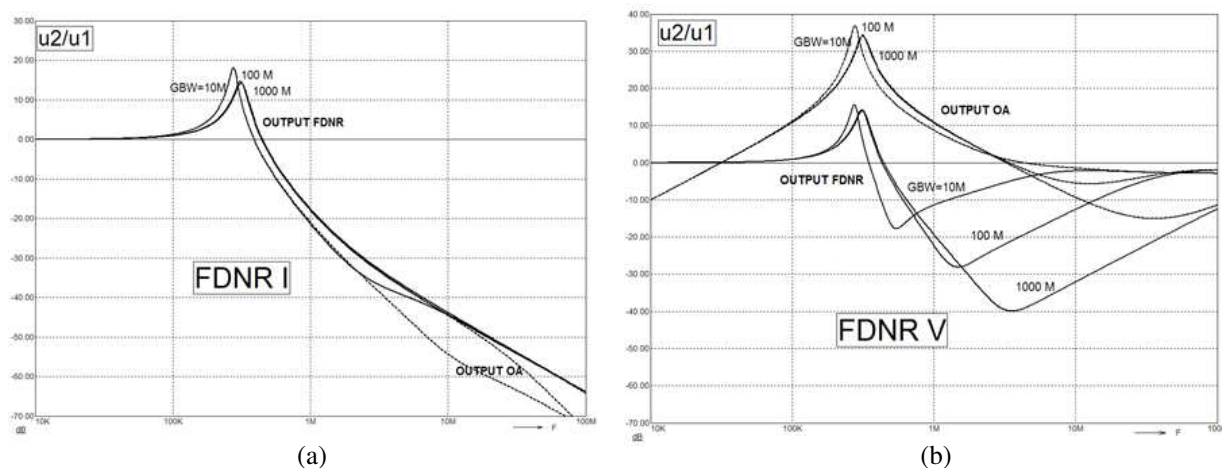


Figure 3: Comparison of voltage transmission functions in various FDNR building blocks. (a) FDNR I (series loss), (b) FDNR V (parallel loss).

3. COMPARISON OF THE DYNAMIC RANGE OF LOSSY DUAL CAPACITOR CIRCUITS

In addition to comparing the transmission characteristics of individual types of lossy dual capacitors in relation to real parameters of active elements, we employed computer modelling techniques to examine possible dynamic range of the above-described connections. A comparison of the circuit types most frequently applied in practice (types I and V) is presented in Figure 3, which shows the graphs of the resulting transmission functions in individual circuit types on the outputs of the dual capacitors and the actual active elements (OA).

The diagrams (Figure 3) clearly indicate that in type I circuits connected in series, the dynamic range over which the active block can operate is larger by about 20 dB compared to type V dual capacitors connected in parallel. The status is caused by the fact that, at the resonance point, the output of the active element (OA) included in a type V circuit exhibits a voltage gain larger by approximately 20 dB compared to the functional block output. This significantly increases the risk of the active element saturation and reduces the potential dynamic range for this circuit (type V) with parallel connection of the lossy element. Therefore, it is possible to conclude that, compared to the series connection (type I circuit), the hitherto frequently applied connection of low-pass filters with a parallel lossy element (type V circuit) exhibits a potential dynamic range smaller by approximately 20 dB. This precondition substantially reduces application possibilities of the type V circuit, especially in cases where the highest attainable dynamic range of the processes signals is required.

3.1. Measurement Results for the Low-pass filter with a Type V FDNR (Parallel Loss)

Figure 4 shows a connection diagram for the designed filter. The filter dynamics measurement (Figure 5) confirmed the result following from the modelling of the circuits, namely that this type of circuit exhibits a comparatively low dynamic range (approximately 300 mV with the supply voltage of 5 V, and approximately 200 mV with the supply voltage of 3.5 V).

3.2. Measurement Results for the Low-pass Filter with a Type I FDNR (Series Loss)

The connection diagram related to the designed filter is shown in Figure 6; the measured characteristics are indicated in the graphs provided in Figure 7.

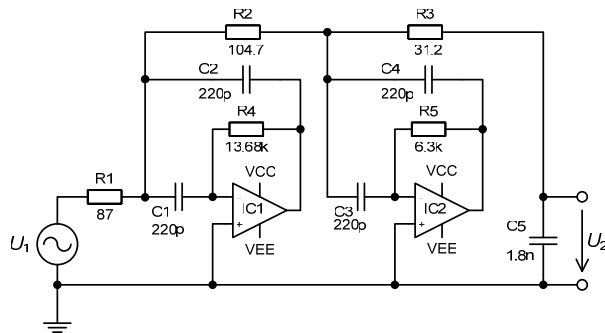


Figure 4: Connection of the 5th order low-pass with the threshold frequency of 1 MHz — type V FDNR — parallel loss.

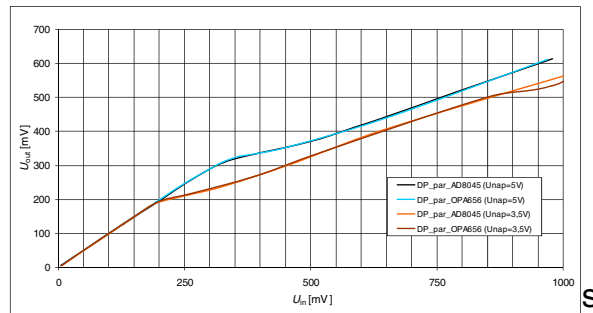


Figure 5: Dependence of the LP output voltage on the input voltage at the frequency of 500 kHz.

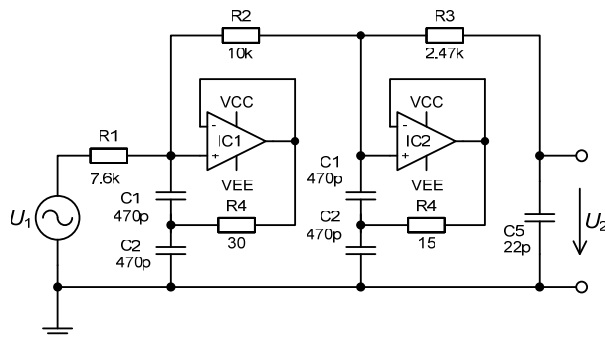


Figure 6: Connection of the 5th order low-pass with the threshold frequency of 1 MHz — type 1 FDNR — series loss.

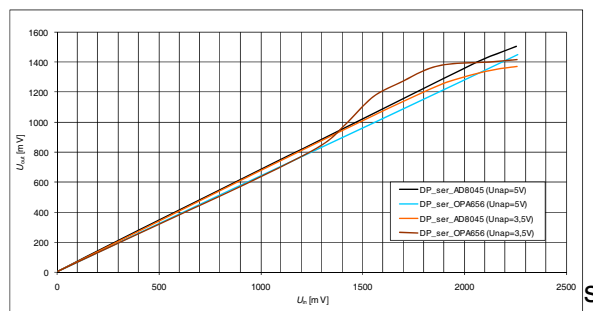


Figure 7: Dependence of the LP output voltage on the input voltage at the frequency of 500 kHz.

The measurement of attainable dynamics (Figure 7) enabled us to verify the correctness of the conclusions made in the previous subchapters. The measurement results exhibit a markedly higher level of attainable dynamics in this type of circuit (transmission linearity may rise up to 2000 mV even with the reduced supply voltage of 3.5 V), which fully corresponds to the theoretical conclusions presented within chapter 3 of this article. The measured values indicate that, at lower supply voltage levels, the AD 8045 operational amplifier provides better results.

4. CONCLUSION

The authors performed a comprehensive analysis of the dynamic properties of lossy active functional blocks (lossy dual capacitors FDNR and synthetic inductors SI).

The realized research showed that the connection of active blocks with a series equivalent model offers a large number of advantages compared to the most frequently applied connection including a parallel equivalent diagram. Substantial benefits of the examined type of connection consist in the fact that, at higher frequencies, it does not exhibit the parasitic transmission zero that causes problems in a parallel connection. Another advantage is the significantly larger (even by 20 dB) attainable circuit dynamics.

The conclusions made on the basis of computer modelling of the above-described circuits were fully verified via measurements performed on the related filter samples. We realized practical connections of various types of second or higher-order low-pass and high-pass filters to verify possible application of these blocks with modern operational amplifiers up to the frequency range of units of MHz.

ACKNOWLEDGMENT

The research described in the paper was financially supported by the grant of the Czech Ministry of Industry and Trade No. FR-TI1/368, project of the BUT Grant Agency FEKT-S-11-5/1012 and project CZ.1.07.2.3.00.20.0175, Elektro-výzkumník.

REFERENCES

1. Szabó, Z. and J. Sedláček, “A simple economical building FDNR blocks with modern operational amplifiers,” *PIERS Proceedings*, 1113–1117, Moscow, Russia, Aug. 18–21, 2009.
2. Hájek, K., V. Michal, J. Sedláček, and M. Steinbauer, “A simple method of goal — Directed lossy synthesis and network optimization,” *Advances in Electrical and Electronic Engineering*, 249–253, Žilina, 2006, ISSN 1336-1376.
3. Szabó, Z., “A contribution to optimal synthesis of filters,” Dissertation Thesis, 118 s, Faculty of Electrical Engineering and Communication, Brno University of Technology, 2012.
4. Sedláček, J., Z. Szabó, and V. Michal, “A non cascade synthesis of optimized ARC filters,” *TIEF 2007*, 1–7, UTEE, FEKT VUT v Brne, Paris, 2007, ISBN 978-80-214-3476-9.
5. Hájek, K. and J. Sedláček, “Lossy LC ladder prototypes and their use for ARC filter optimization,” *WSEAS Transactions on Electronics*, Vol. 2, No. 3, 94–99, Jul. 2005, ISSN 1109-9445.
6. Martinek, P. and T. Daša, “Evolutionary algoritmes by ARC filter synthesis,” *ECCTD 05*, 155–159, Cork, 2005.

Analysis of Leap-frog Filter in the Programme NAF

L. Fröhlich, J. Sedláček, M. Friedl, and M. Čáp
FECC BUT, UTEE, Kolejní 2906/4, Brno 612 00, Czech Republic

Abstract— The method of design of ARC filters with the help of non-cascade realization Leap-Frog, which combines qualities of block realizations and realizations concerning ladder RLC filters, is considerably difficult. The programme for the complete synthesis of these ARC filters was created.

This article describes the complete description of the programme NAF. It includes the correct depiction of the set values of RLC filters concerned with required user's parameters. The user's parameters can be for instance filters LP, HP, BP, and BR, the type of approximation with or without zero transfers and the kind of filter configuration T or PI. From the following depiction of RLC filters the programme already realizes ARC depiction of Leap-Frog filter, even with certain values of individual elements.

However, the most important part for the design of this programme is the depiction of modular characteristics for already defined outputs of certain filters, with the regard to the following setting of dynamic ratios inside the filter including particular real OAs. With the help of depiction of module characteristics in individual filter outputs, it is not problematic to change norms of particular elements' values so that the individual transfers from the input to the output of the filter would be the same for their maximums.

The programme should serve mainly to bigger use of these circuits in practice, when a user can compare several ARC filter designs designed in different ways and he can judge which of the stated applications would be the most suitable.

1. INTRODUCTION

As it has already been mentioned in the introduction part, for the development of this method in practice it is necessary to create a suitable programme for a complete synthesis of these circuit structures. The complete idea for creating and implementation of this programme to the current programme NAF is obvious in the Fig. 1.

Developing diagram depicts the implementation of the Leap-Frog method to the programme NAF, see Fig. 1. For the depiction of the particular circuit, firstly the choice of filter type is done, for instance LP, HP, BP or BR. For individual filter types the choice of input parameters is then defined (e.g., for the choice LP: F_M , F_P , A_{ZVL} and A_{POT}). Finally, the choice of approximation is done, which is possible also with the zero transfer but also without it (e.g., Butterworth), where the filter order is later depicted. On the first page, there are several more functions such as depiction of coefficients of certain approximation or depiction of frequency and time characteristics. After inputting and depicting of certain data, it is also necessary to set the value of ending resistors (identical ending) and their values and also the type of the ending of the complete RLC filter (e.g., PI or T configuration).

2. DEPICTION OF GIVEN CIRCUIT

For the depiction of final RLC filter it is necessary to use a certain variable, which defined parameters of complete RLC circuits. For our defined input data we then gain following data from the programme: (example of the depiction of variables)

- HP [0 1000 0, 0113 5, 3296e-08 5, 3296e-08 1000],
- KP [R L C C R],
- $PR1$ [0 -1 1 1 0],
- $PR2$ [1 2 2 3 3],
- $PR3$ [2 3 0 0 0],

where

HP : element value,

KP : element name,

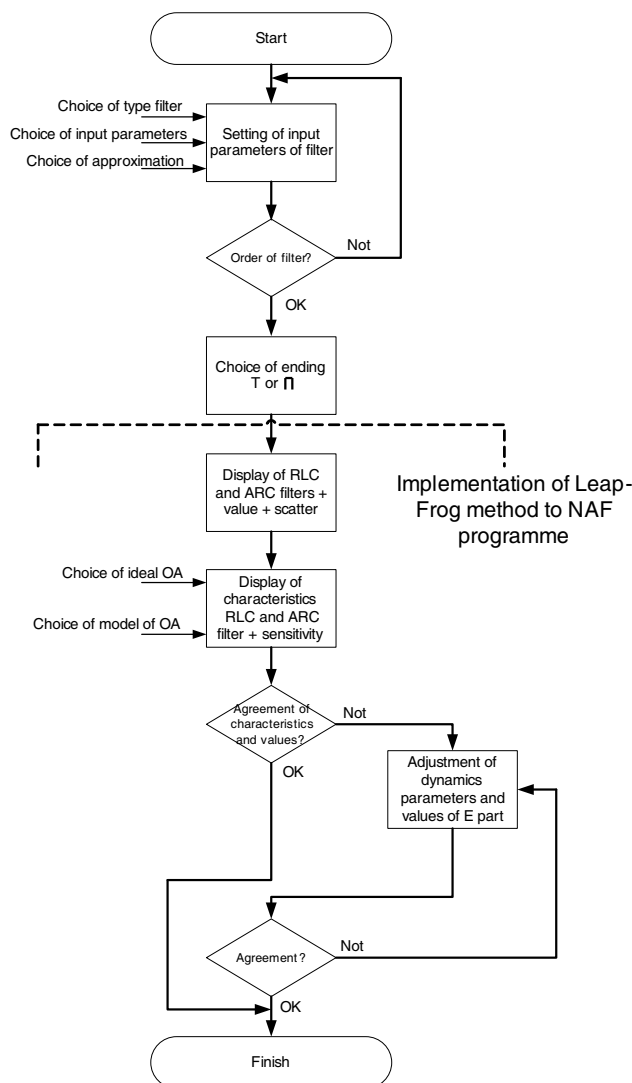


Figure 1: Developing diagram for implementation of the part of ARC_LF to programme NAF.

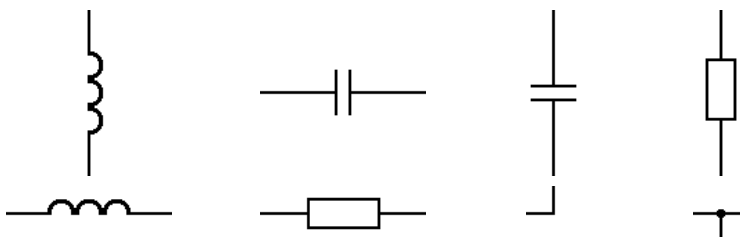


Figure 2: Particular examples of elements, which are contained in RLC filter.

PR1: element code (0 — resistor, -1 — coil, 1 — capacitor),

PR2: the beginning of the element in given knot,

PR3: the end of the element in given knot.

With the help of these data it is very simple to depict a demanded circuit, which will contain individual parts. The example of certain element types serving for the depiction of final RLC circuit is obvious in the Fig. 2.

The particular depiction of the final RLC circuit in the programme NAF can be seen in the Fig. 3. Apart from RLC circuit, the value of the given element and the value normed according to a user's chosen capacitor's value is depicted, in our case according to the value $C_1 = 10 \text{ nF}$. In

the Fig. 4, there is a depiction of the principle of division of RLC circuit to individual parts, which are later defined by equations, which set the qualities of the graph of signal flows out of which is finally depicted ARC circuit.

For the above stated DP 3rd order there are defined relations (1) up to (5) for ending type PI.

$$I_{R1} = \frac{U_{R1}}{R_1} = \frac{U_1 - U_{C1}}{R_1}, \tag{1}$$

$$U_{C1} = \frac{I_{C1}}{pC_1} = \frac{I_{R1} - I_{L2}}{pC_1}, \tag{2}$$

$$I_{L2} = \frac{U_{L2}}{pL_2} = \frac{U_{C1} - U_{C3}}{pL_2}, \tag{3}$$

$$U_{C3} = \frac{I_{C3}}{pC_3} = \frac{I_{L2} - I_{R2}}{pC_3}, \tag{4}$$

$$I_{R2} = \frac{U_{R2}}{R_2} = \frac{U_2}{R_2}. \tag{5}$$

From above stated equations it is not problematic to create final GST, see Fig. 5, which serves for creation of ARC circuit with the help of individual integrators, see Fig. 6.

In the same way as the forming of RLC circuit was created, the similar is forming of ARC circuit with the help of individual integrators. The final scheme of ARC circuits also with the depiction of values of individual parts, the number of knots and also the number of individual R and C and OA serve for depiction of transfer characteristics. Individual parameters for the depiction of transfer

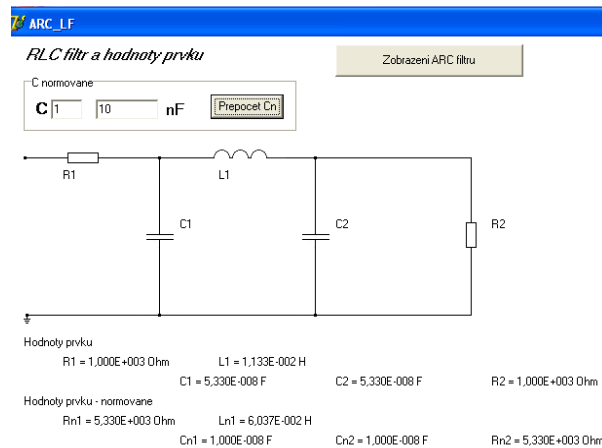


Figure 3: Depiction of RLC filter in the programme NAF.

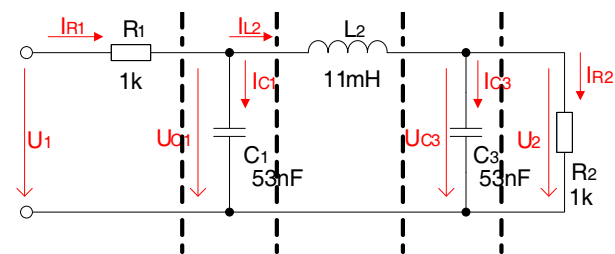


Figure 4: Depiction of division of RLC filter.

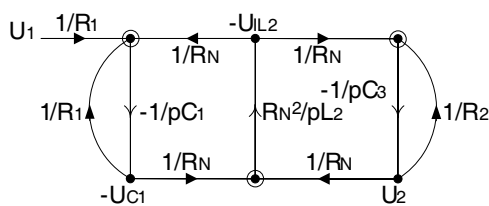


Figure 5: Final depiction of GST for circuit in the Fig. 4 — LP 3rd order — ending PI.

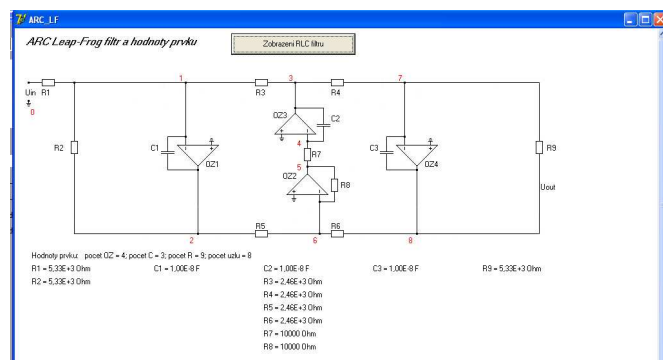


Figure 6: Final depiction of ARC circuit with the help of Leap-Frog method in programme NAF.

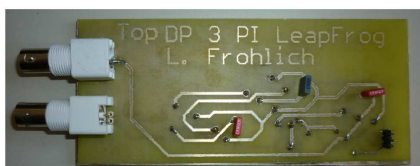


Figure 7: Real filter LP 3rd order PI.



Figure 8: Real filter LP 3rd order PI.

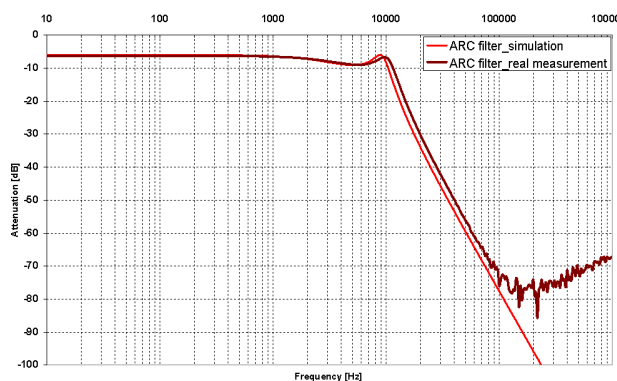


Figure 9: Simulation and real measuring.

characteristics must be input into the programme manually. Individual parameters are gradually recorded into the matrix, out of which the transfer characteristic will be later created, after defining of the knot number and output.

3. REAL CIRCUIT CREATED BY LEAP-FROG METHOD

For the verification of real and correct calculations, the real sample of the filter — type DP of 3rd order with the ending PI was created. It can be seen in the Figs. 7, 8 and 9.

4. CONCLUSIONS

The article described and depicted the illustration from the programme for the complete analysis of the ARC filter synthesis concerning Leap-Frog method. The main reason for the creation of this programme was the spread of this method due to the quite difficult of manual design and the following synthesis. As this method has certain advantages — for instance excellent dynamical ratios, practically the lowest sensitiveness, small scatter of the building elements and the possibility to design mainly capacitors in E order, it is possible to use certain filters in practice, mainly LP and BP. These filters are suitable for using in NMR application.

ACKNOWLEDGMENT

The research described in the paper was financially supported by grant of Czech ministry of industry and trade No. FR-TI1/001, GACR 102/09/0314 and project of the BUT Grant Agency FEKT-S-11-15.

REFERENCES

1. Sedláček, J. and K. Hájek, “Kmitočtové filtry, 1. vydání,” 535, BEN — Technická Literatura, Praha, 2002, ISBN 80-7300-023-7.
2. Sedra, A. and K. Martin, “Design of signal-flow graph (SFG) active filters,” *IEEE Trans. CAS*, Vol. 25, No. 4, 185–195, 1978.
3. Biolek, D., “Řešíme elektronické obvody, 1. vydání,” 520, BEN — Technická Literature, Praha, 2004, ISBN 80-7300-125-X.
4. Hájek, K., “Optimalizovaný návrh filtrů ARC s využitím počítače,” *Habilitační Práce*, VA, Brno, 1994.
5. Sedláček, J., “Optimalizace v syntéze filtrů RLC,” *Habilitační Práce*, VA, Brno, 1994.

Application of the Level Set Method in MR-EIT Inverse Problems

T. Kříž and J. Dědková

Department of Theoretical and Experimental Electrical Engineering
Brno University of Technology, Kolejní 4, Brno 612 00, Czech Republic

Abstract— The authors describe the possibilities of utilizing the Level set method for conductivity reconstruction based on techniques used in electrical impedance tomography. Standard electrical tomography exploits voltages measured on the surface of the used samples, to which a current source is connected. Even though an EIT-based method is applied within this study, the authors utilize the values of components of the magnetic flux density measured in the vicinity of samples, to which a direct current source is connected. Conductivity reconstructions realized by means of EIT-based deterministic methods.

1. INTRODUCTION

The electrical impedance tomography (EIT) is a widely investigated problem with many applications in the industry and biological sciences. The aim is to reconstruct the internal conductivity distributions in two or three dimensional models. Standard electrical tomography exploits voltages measured on the surface of the used samples, to which a current source is connected. Even though an EIT-based method is applied within this study, the algorithm utilizes the values of components of the magnetic flux density measured in the vicinity of samples, to which a direct current source is connected. Magnetic flux density components can be calculated by Biot-Savart Law by Equation (1). If we apply two dimensional models we suppose the electric field in very thin layer of electrical conductive medium which can be described by the surface current density \mathbf{K} . The surface current density K inside a specimen produces also a magnetic field. The magnetic flux density \mathbf{B} corresponding to \mathbf{K} , can be obtained according to the Biot-Savart Law.

$$\vec{B} = \frac{\mu_0}{4\pi} \int_S \frac{\vec{K} \times \vec{R}}{R^3} dS \quad (1)$$

For further numerical simulations we divided the sample into NE triangle elements with centers $[x_t, y_t, z_t]$. We suppose that the current density \mathbf{K} is constant on each element. The magnetic field in general point given by coordinates $[x_i, y_i, z_i]$ we can calculate components of magnetic flux density with using superposition principle

$$\vec{B}_i \approx \frac{\mu_0}{4\pi} \sum_{j=1}^{NE} \frac{\vec{K}_j \times \vec{R}_{ij}}{R_{ij}^3} \Delta S_j \quad (2)$$

The vector \mathbf{R} represents the distance between centre of actual element $[x_t, y_t, z_t]$ and point $[x_i, y_i, z_i]$. If we know certain components of magnetic field we can obtain the current density distribution. If we would like to obtain the NE values of K_x and K_y components of surface current density \mathbf{K} , we have to know for example the same number of B_x and B_y components of magnetic field

$$B_{ix} = \frac{\mu_0}{4\pi} \sum_{j=1}^{NE} R_{ijz} \frac{\Delta S_j}{R_{ij}^3} K_{jy}, \quad B_{iy} = -\frac{\mu_0}{4\pi} \sum_{j=1}^{NE} R_{ijz} \frac{\Delta S_j}{R_{ij}^3} K_{jx}, \quad i = 1, \dots, NE \quad (3)$$

The matrix notation for these $2 \cdot NE$ algebraic equations is

$$\begin{bmatrix} B_{koefx} & 0 \\ 0 & B_{koefy} \end{bmatrix} \begin{bmatrix} K_x \\ K_y \end{bmatrix} = \begin{bmatrix} B_x \\ B_y \end{bmatrix} \Leftrightarrow \mathbf{B}_{koef} \mathbf{K} = \mathbf{B} \quad (4)$$

From system (6) we can obtain very easy wanted current density distribution

$$\mathbf{K} = \mathbf{B}_{koef}^{-1} \mathbf{B} \quad (5)$$

Conductivity reconstruction is an inverse, non-linear, and very ill-posed problem. Conductivity reconstructions realized by means of EIT-based deterministic methods are defined as the minimization of the suitably chosen objective function $\Psi(\sigma)$ related to σ . The objective function is most often minimized using the method of the least squares, which converges very quickly. Stability of the minimization process is ensured by means of regularization techniques such as the Tikhonov regularization method or a total variation method. The application of regularization methods consists in the introduction of a regularization term, which is added to the objective function. The objective function for the Tikhonov regularization method is expressed in the following formula:

$$\Psi(\sigma) = \frac{1}{2} \sum \|\mathbf{J}_M - \mathbf{J}_{\text{FEM}}(\sigma)\|^2 + \alpha \|\mathbf{R}\sigma\|^2, \quad (6)$$

where \mathbf{J}_M is the vector of current density obtained from the magnetic flux density components, \mathbf{J}_{FEM} is the vector of current density obtained via forward solution using the Finite element method, σ is the vector of conductivity on individual elements, and \mathbf{R} is the regularization matrix connecting adjacent elements of different conductivities.

The applications of the Tikhonov regularization method was used to find regions with different conductivities and their close surroundings.

The level set method was applied in identifying the location of the regions with different conductivities. The method is used to identify regions with different image or material properties. The level set method (LS) [3–5] is based on the deformation of function ϕ . Then, the border of the object is given by the zero level of function ϕ . The evolution equation of level set function ϕ in the general form is

$$\frac{\partial \phi}{\partial t} + F |\text{grad} \phi| = 0, \quad (7)$$

where ϕ is the level set function, F the speed function, t the time step.

The distribution of the searched unknown conductivity can be described in terms of level set function F depending on the position of point \mathbf{r} with respect to boundary D between regions with different values of conductivity. During the iteration process based on minimizing objective function $\Psi(\sigma)$, boundary D is searched in accordance with the request that $\sigma(r)$ minimize $\Psi(\sigma)$.

$$\sigma(r) = \begin{cases} \sigma_{int} & \{r : F(r) < 0\} \\ \sigma_{ext} & \{r : F(r) > 0\} \end{cases} \quad D = \{r : F(r) = 0\} \quad (8)$$

After select location with non-homogenous regions there is applied Tikhonov regularization method again to calculate final value of conductivity of selected region by Level set method only.

2. NUMERICAL SIMULATION AND TESTS

Numerical models were built for testing of algorithm that calculating conductivity distribution in the investigating samples in Matlab. A numerical model consists of 210 elements and 122 nodes. The linear triangles elements were used for numerical analysis. The FEM grid is shown in Fig. 1. The current electrodes were placed on boundary of investigated samples. Current electrodes are shown in Fig. 1. (green triangles). The current value was adjust to $I = 1$ A. There were defined two values of conductivity for the model. The first material has conductivity 60 MS/m (copper) and the second one has 10 pS/m (cracks).

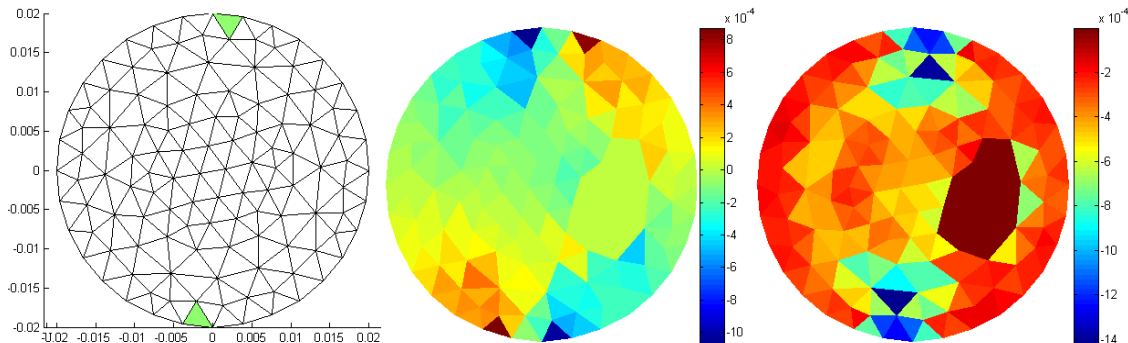


Figure 1: FEM grid with 210 elements and 122 nodes, x - and y -components of magnetic flux density.

Three numerical models were built. There were defined regions with different conductivity inside (non-homogenous regions). There is one large non-homogenous region in the first model, two small non-homogenous regions in the second model and one small non-homogenous region in the third one. We can see the original conductivity distribution for all models in Fig. 2.

The components B_x and B_y were used to current density. The count of measured calculated

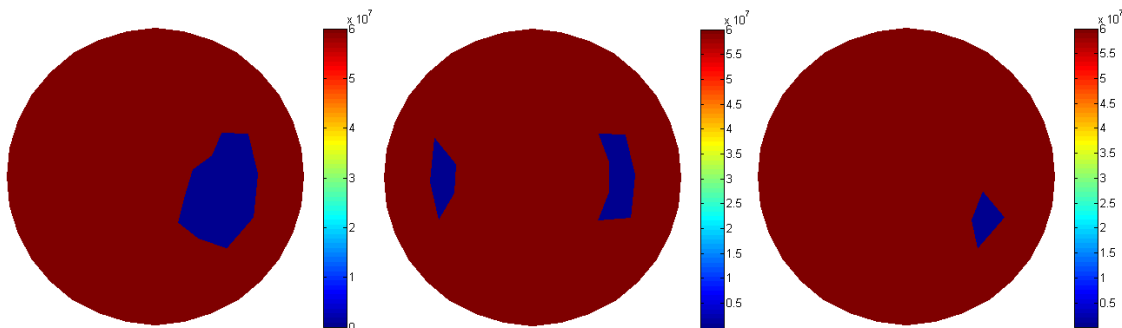


Figure 2: Original conductivity distribution for all samples.

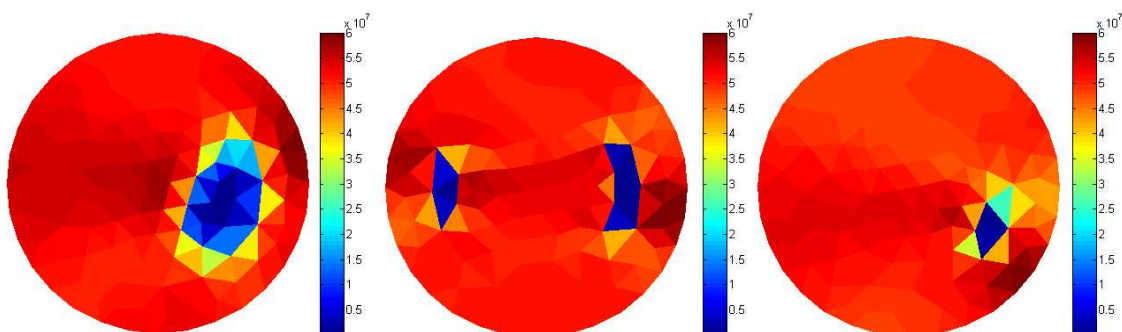


Figure 3: Conductivity distribution after first use of Tikhonov regularization method.

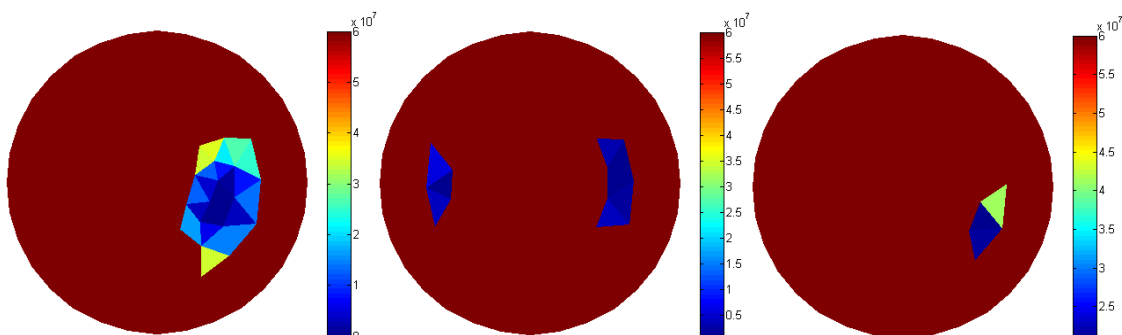


Figure 4: Specified zero level set boundary for all samples.

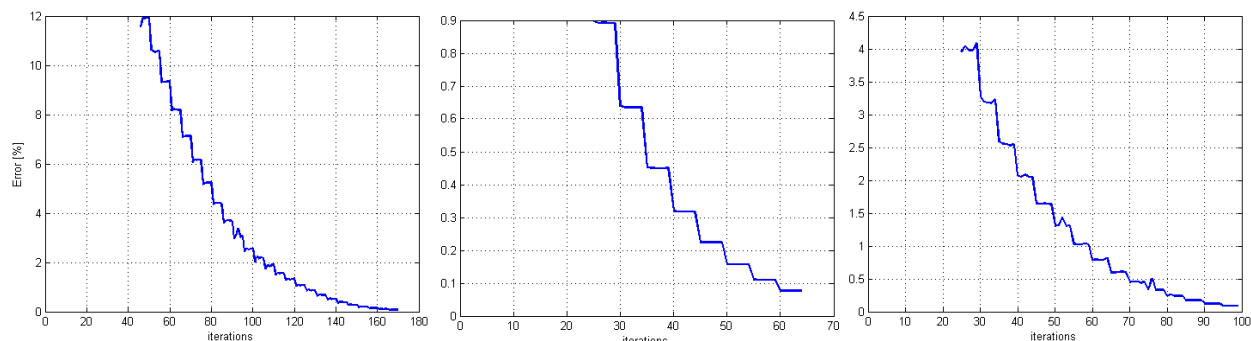


Figure 5: Evolution of objective function for second use of Tikhonov regularization method.

Table 1: Results of tests.

sample	$\Psi_1 (\sigma)$	Err_1 [%]	t_1 [s]	$\Psi_2 (\sigma)$	Err_2 [%]	t_2 [s]
1	6.39e3	12.23	17.51	0.0357	0.0736	30.77
2	157.62	5.66	13.13	0.3014	0.0775	10.12
3	1.03e3	6.19	13.09	0.1653	0.0875	18.64

values of B_x and B_y has to be same as count of elements. The magnetic flux density components used to calculation of surface current density is in the Fig. 1.

Conductivity distribution after first use of Tikhonov regularization method is in the Fig. 3. This first part of reconstruction process approximately determined cracks in the models. You can see that values of calculated conductivity aren't accurate.

Selected cracks by level set method after first use of Tikhonov regularization method is shown in the Fig. 4. Tikhonov regularization method was used second time to calculate final conductivity in these selected regions.

Evolution of the objective functions of all samples is in the Fig. 5. You can see different count of iterations in dependence on cracks location.

Steps in the graph are due to change value of regularization parameter during minimizing process.

All tested results are in the Table 1. Conductivity values calculated in the regions with cracks by Tikhonov regularization method are same as original conductivity distribution in the Fig. 2.

Index one illustrates results after first application of Tikhonov regularization method and index two is for results after second application of Tikhonov regularization method.

3. CONCLUSIONS

If the results obtained by Tikhonov regularization method and combination of Tikhonov regularization method with level set method are compared combinations of both methods gives better results. Disadvantage of this approach is more time consuming that using Tikhonov regularization only.

ACKNOWLEDGMENT

The research described in the paper was financially supported by project of the BUT Grant Agency FEKT-S-11-5/1012 and projekt CZ.1.07.2.3.00.20.0175, Elektro-vyzkumnik.

REFERENCES

1. Vladingerbroek, M. T. and J. A. Den Boer, *Magnetic Resonance Imaging*, Springer-Verlag, Heidelberg, Germany, 1999, ISBN 3-540-64877-1.
2. Borsic, A., "Regularization methods for imaging from electrical measurement," Ph.D. Thesis, Oxford Brookes University, 2002.
3. Zhang, X., D. Yan, S. Zhu, and B. He, "Noninvasive imaging of head-brain conductivity profiles," *IEEE Engineering in Medicine and Biology Magazine*, Vol. 27, No. 5, 78–83, 2008.
4. Seo, J. K., O. Kwon, and E. J. Woo, "Magnetic resonance electrical impedance tomography (MREIT): Conductivity and current density imaging," *Journal of Physics: Conference Series*, Vol. 12, 140–155, 2005.

Influence of Initial Conditions on Conductivity Calculation via the MR-EIT Inverse Problem

T. Kříž and J. Dědková

Department of Theoretical and Experimental Electrical Engineering
Brno University of Technology, Kolejní 4, Brno 612 00, Czech Republic

Abstract— The article describes the testing of an algorithm for conductivity reconstruction based on regularization techniques. For the calculation of conductivity in tested samples, the algorithm exploits the measured values of magnetic flux density \mathbf{B} in the vicinity of these samples. Generally, problems based on electrical impedance tomography are non-linear and ill-posed. The reconstruction process is described as the minimization of the suitably chosen objective function $\Psi(\sigma)$ with respect to σ . In the algorithm for the conductivity image reconstruction, we tested the values of initial conditions that exert significant influence on both the stability of the solution and the accuracy of the resulting conductivity image. The influence of the initial value of regularization parameter σ was subject to testing; the initial value was changed within several orders. Moreover, we tested the magnitude of the change of regularization parameter $\Delta\alpha$ during the iteration process. The testing of the conductivity initial value was realized in such a manner that the initial value was selected within several intervals and as a random value on each element. In all the parameters tested, we evaluated the relative error, solution time, and stability of the reconstruction process. The conductivity reconstruction result, the accuracy, the time consumption, and the reconstruction time are presented in the article.

1. INTRODUCTION

The electrical impedance tomography (EIT) is a widely investigated problem with many applications in physical and biological sciences. The aim is to reconstruct the internal conductivity distributions in two dimensional models. The EIT algorithm for a conductivity reconstruction is an inverse and an ill-posed problem. The solution of this problem is described as a minimization of a suitable objective function $\Psi(\sigma)$ which is dependent on a conductivity σ . The least squares method is very often used for a minimization of the objective function. The regularization methods are used for better stability of the solution. The Tikhonov regularization method can be used. The regularization term is added to the objective function if the Tikhonov regularization method is used. This term makes the solution stable. The square of the norm of measured voltages and calculated voltages by finite element method is involved in the standard EIT objective function. Objective function in general form can be written

$$\Psi(\sigma) = \frac{1}{2} \sum \|\bar{U}_M - \bar{U}_{\text{FEM}}(\sigma)\|^2 + \alpha \|\mathbf{R}\bar{\sigma}\|^2 \quad (1)$$

where σ is the unknown conductivity distribution vector in the object, U_M is the vector of measured voltages on the object boundary, $U_{\text{FEM}}(\sigma)$ is the vector of peripheral voltages in respect to σ which can be obtained using finite element method, α is a regularization parameter and \mathbf{R} is a regularization matrix connecting adjacent elements of the different conductivities.

2. BASIC THEORY

Further we suppose the electric field in very thin layer of electrical conductive medium which can be described by the surface current density \mathbf{K} . The surface current density \mathbf{K} inside a specimen produces also a magnetic field. The magnetic flux density \mathbf{B} corresponding to \mathbf{K} , can be obtained according to the Biot-Savart Law

$$\bar{\mathbf{B}} = \frac{\mu_0}{4\pi} \int_S \frac{\bar{\mathbf{K}} \times \bar{\mathbf{R}}}{R^3} dS \quad (2)$$

For further numerical simulations we divided the sample into NE triangle elements with centers $[x_t, y_t, z_t]$. We suppose that the current density \mathbf{K} is constant on each element. The magnetic field in general point given by coordinates $[x_i, y_i, z_i]$ we can calculate components of magnetic flux

density with using superposition principle

$$\vec{B}_i \approx \frac{\mu_0}{4\pi} \sum_{j=1}^{NE} \frac{\bar{K}_j \times \bar{R}_{ij}}{R_{ij}^3} \Delta S_j \quad (3)$$

The vector \mathbf{R} represents the distance between centre of actual element $[x_t, y_t, z_t]$ and point $[x_i, y_i, z_i]$. If we know certain components of magnetic field we can obtain the current density distribution. If we would like to obtain the NE values of K_x and K_y components of surface current density \mathbf{K} , we have to know for example the same number of B_x and B_y components of magnetic field

$$B_{ix} = \frac{\mu_0}{4\pi} \sum_{j=1}^{NE} R_{ijz} \frac{\Delta S_j}{R_{ij}^3} K_{jy}, \quad B_{iy} = -\frac{\mu_0}{4\pi} \sum_{j=1}^{NE} R_{ijz} \frac{\Delta S_j}{R_{ij}^3} K_{jx}, \quad i = 1, \dots, NE \quad (4)$$

The matrix notation for these $2 \cdot NE$ algebraic equations is

$$\begin{bmatrix} B_{koefx} & 0 \\ 0 & B_{koefy} \end{bmatrix} \begin{bmatrix} K_x \\ K_y \end{bmatrix} = \begin{bmatrix} B_x \\ B_y \end{bmatrix} \Leftrightarrow \mathbf{B}_{koef} \mathbf{K} = \mathbf{B} \quad (5)$$

From system (6) we can obtain very easy wanted current density distribution

$$\mathbf{K} = \mathbf{B}_{koef}^{-1} \mathbf{B} \quad (6)$$

In the following part is shown an example of the magnetic field distribution and the corresponding surface current density distribution and the influence of the non-homogeneity inside tested samples.

The current density is calculated on each element by means of superposition of the outside magnetic field values. We suppose that the current density is constant on elements. The created objective function for the minimization by the least squares method for a conductivity image reconstruction is

$$\Psi(\sigma) = \frac{1}{2} \sum \|\bar{J}_M - \bar{J}_{FEM}(\sigma)\|^2 + \alpha \|\mathbf{R}\bar{\sigma}\|^2, \quad (7)$$

where σ is the unknown conductivity distribution vector in the object, J_M is the vector of calculated surfaces current density from measured magnetic flux components outside sample, $J_{FEM}(\sigma)$ is the vector of computed current density in respect to σ which can be obtained using finite element method, α is a regularization parameter and \mathbf{R} is a regularization matrix connecting adjacent elements of the different conductivities.

3. NUMERICAL SIMULATIONS AND TESTS

Numerical models were built for testing of algorithm that calculating conductivity distribution in the investigating samples in Matlab. Start conductivity and regularization parameter value were tested. A numerical model consists of 210 elements and 122 nodes. The linear triangles elements were used for numerical analysis. The FEM grid is shown in Fig. 1. The current electrodes were placed on boundary of investigated samples. Current electrodes are shown in Fig. 1. (green

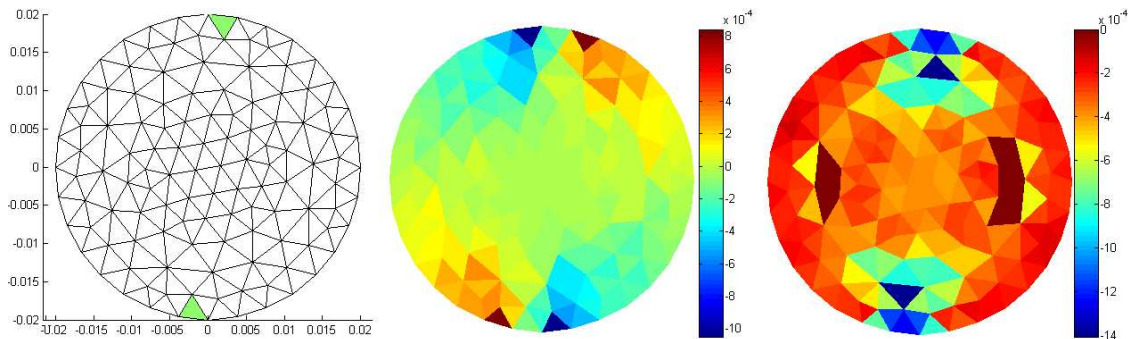


Figure 1: FEM grid with 210 elements and 122 nodes, original conductivity distribution sample one and two.

triangles). The current value was adjusted to $I = 1$ A. There were defined two values of conductivity for the model. The first material has conductivity 60 MS/m (copper) and the second one has 10 pS/m (cracks).

Two numerical models were built. There were defined regions with different conductivity inside (non-homogenous regions). There is one small non-homogenous regions in the first model and two small non-homogenous regions in the second model.

Magnetic flux density components were calculated by Biot-Savart law 1 mm above the sample. Calculated components B_x , B_y are shown in Fig. 1 for sample 2. These values of magnetic field substitute measured values for reconstruction algorithm testing. The current density components were computed from magnetic flux components with usage equation. The components B_x and B_y were used to current density. The count of measured (calculated) values of B_y and B_x has to be same as count of elements. The start value of regularization parameter was tested. Different values of regularization parameter were tested. Optimal value was set to $\alpha = 1e-14$ and change of regularization parameter during conductivity calculation process $\Delta\alpha$ was tested. Parameter $\Delta\alpha$ was changed from 0.5 to 0.8. Results are in the Table 1. How we can see from Table 1, choose of the parameter $\Delta\alpha$ change during reconstruction process is parameter $\Delta\alpha = 0.7$ considering to accuracy and solution time.

Evolution of the objective function for $\Delta\alpha = 0.7$ is in the Fig. 2. Steps in the graph are due to change value of regularization parameter $\Delta\alpha$ during minimizing process.

Start conductivity was in sequence set up to values $\sigma = 6, 6e5, 6e6, 6e7, 6e8$ and $6e9$ S/m for the testing of start conductivity value. Time of solution, accuracy and final value of conductivity

Table 1: Parameter $\Delta\alpha$ dependence.

$\Delta\alpha$	Sample 1			Sample 2		
	$\Psi(\sigma)$	Err [%]	t [s]	$\Psi(\sigma)$	Err [%]	t [s]
0.5	6.7e-3	0.6367	35.96	5.37e-3	1.69	38.24
0.6	4.99e-4	0.43	29.09	3.24e-3	2.19	35.61
0.7	1.4e-2	0.46	27.16	1.14e-2	1.56	34.61
0.8	1.399	1.63	16.23	8.51e1	14.92	28.53

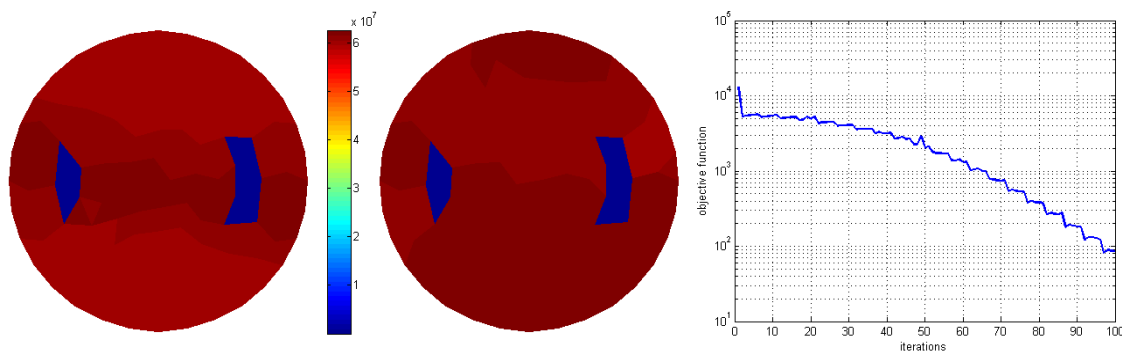


Figure 2: Final conductivity distribution for $\Delta\alpha = 0.5$ and 0.7 , objective function evolution for $\Delta\alpha = 0.7$.

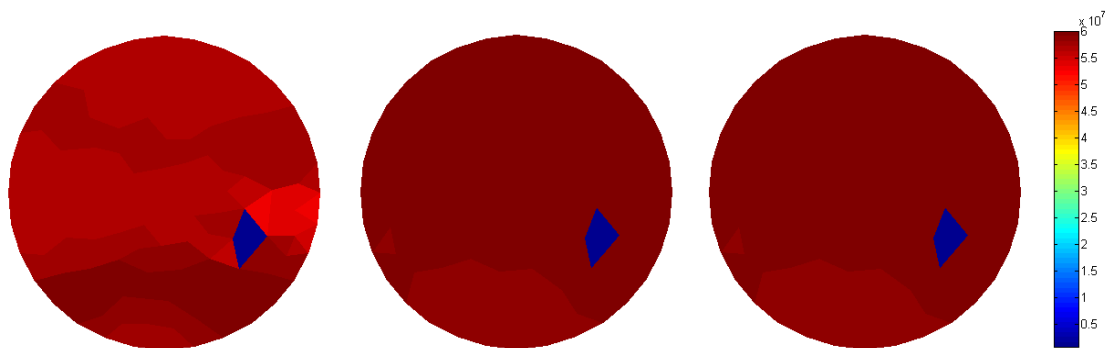


Figure 3: Final conductivity distribution for start conductivity $6e6$, $6e7$ and $6e8$ — sample 1.

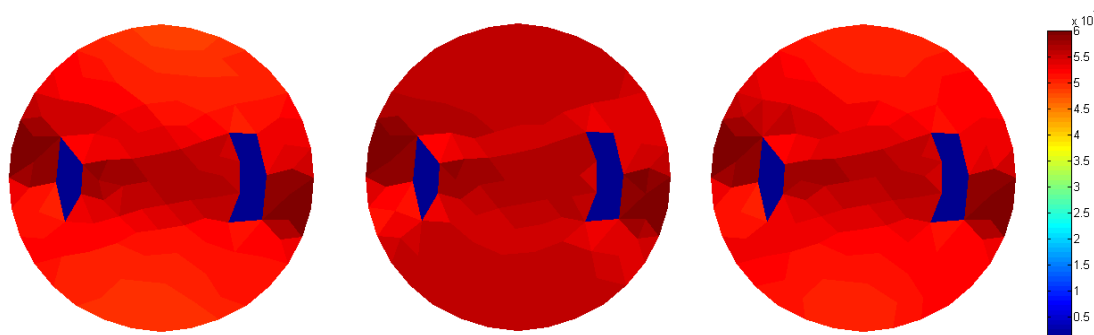


Figure 4: Final conductivity distribution for start conductivity 6e6, 6e7 and 6e8 — sample 2.

Table 2: Starting conductivity value dependence.

σ [S/m]	Sample 1				Sample 2			
	$\Psi(\sigma)$	Err [%]	t [s]	α	$\Psi(\sigma)$	Err [%]	t [s]	α
6e0	2.23e-4	0.99	3605	1e-06	5056	1238	4838	1e-09
6e5	0.18	0.98	3613	1e-11	322	989	3113	1e-09
6e6	3.34e-4	0.90	3596	1e-12	554	901	1936	1e-12
6e7	145e-2	0.46	2716	1e-14	0.01	156	3461	1e-14
6e8	2.45e-2	0.82	3725	1e-15	331	9,71	3724	5e-15
6e9	0.718	102e-4	3606	1e-16	284	1.05	5127	1e-17

were observed during reconstruction process. The results of testing are presented in the Table 2.

Examples of final conductivity distribution for different start conductivity are shown in the Fig. 3 and for sample 1 and in the Fig. 4 for sample 2.

4. CONCLUSIONS

How, we can see from results of testing in the Tables 1 and 2 that algorithm for reconstruction is very sensitive to choice value of regularization parameter α and algorithm is less sensitive to change parameter α during reconstruction algorithm. Start conductivity can be set up in the interval 6e5 to 6e9 S/m.

ACKNOWLEDGMENT

The research described in the paper was financially supported by project of the BUT Grant Agency FEKT-S-11-5/1012 and projektCZ.1.07.2.3.00.20.0175, Elektro-vyzkumnik.

REFERENCES

1. Vladingerbroek, M. T. and J. A. Den Boer, *Magnetic Resonance Imaging*, Springer-Verlag, Heidelberg, Germany, 1999, ISBN 3-540-64877-1.
2. Borsic, A., "Regularization methods for imaging from electrical measurement," Ph.D. Thesis, Oxford Brookes University, 2002.
3. Zhang, X., D. Yan, S. Zhu, and B. He, "Noninvasive imaging of head-brain conductivity profiles," *IEEE Engineering in Medicine and Biology Magazine*, Vol. 27, No. 5, 78–83, 2008.
4. Seo, J. K., O. Kwon, and E. J. Woo, "Magnetic resonance electrical impedance tomography (MREIT): Conductivity and current density imaging," *Journal of Physics: Conference Series*, Vol. 12, 140–155, 2005.

EM Field and Biological Systems Interactions

J. Vrba

Department of EM Field, Czech Technical University in Prague, Prague, Czech Republic

Abstract— Research of interactions between em field and biological systems is of growing interests elsewhere. Also here in czech republic there are several groups working in this field, often in international co-operations. We will describe here mainly basic technical equipment developed for 5 different research projects in the discussed area of interactions of em field and biological systems.

1. INTRODUCTION

In present time four research institutions here in the Czech Republic run research projects focused on studies of interactions between EM field and biological systems. These institutions are technically supported by Dept. of EM Field of the Czech Technical University in Prague. In this contribution we would like to give more details about that projects and obtained technical results (i.e., description of developed exposition systems).

Three of discussed projects (1 in Germany and 2 here in Czech Republic) are basic research for simulation of the microwave hyperthermia treatment. Other two projects (both in Czech Republic) are focused on simulation of the case of exposition by mobile phone.

In the modern view, cancer is intended as a complex illness, involving the cells that undergo to transformation, their environment, and the general responses at biochemical and biological levels induced in the host. Consequently, the anti-cancer btreatment protocols need to be multi-modal to reach curative effects. Especially after the technical improvements achieved in the last 15 years by bio-medical engineering, microscopy devices, and molecular biology methods, the combinations of therapeutic procedures are growing in interest in basic and clinical research.

The combination of applied biological research together to the physical sciences can offer important perspectives in anticancer therapy (e.g., different methodologies and technical devices for application of energies to pathological tissues).

The modern bioengineering knowledge applied to traditional tools, as the microscopy, has largely renewed and expanded the fields of their applications (e.g.,: *in vivo* imaging), pushing the interest for direct morpho-functional investigations of the biomedical problems.

2. WAVEGUIDE APPLICATOR

Very good results of EM field expositions in biological experiments can be obtained by simple but efficient waveguide applicators, see example in Fig. 1.



Figure 1: Waveguide applicator for biological experiments.

Waveguide offer a very big advantage — in approximately of fifty percents of its aperture the irradiated electromagnetic field is very near to a plane wave, which is basic assumption for good homogeneity of the heating and optimal treatment penetration.

Here described system is being used (shared) for research projects by two two institutions (Institute of Radiation Oncology in Prague and Institute of Microbiology of the Czech Academy of Sciences). Aperture of this waveguide is 4.8×2.4 cm and it is excited at frequency 2.45 GHz. Effective heating is in the middle of the real aperture — its size is approximately 2.4×2.4 cm. Waveguide is filled by teflon to reduce its cut-off frequency. Power from generator is possible to control from 10 to 180 W, in these experiments we work between 10 and 20 W mostly.

3. EVALUATION OF WAVEGUIDE APPLICATOR

To evaluate this applicator from technical point of view we made a series of experiments, see, e.g., Fig. 2, where you can see example of measurement of temperature distribution by IR camera.

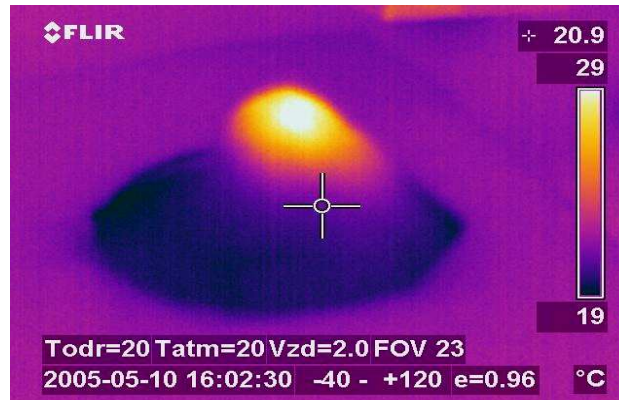


Figure 2: Temperature distribution obtained on surface of a model of mouse.

Here you can see temperature distribution obtained on surface of a model of mouse made from agar — with a simulated tumour on mouse back. Experiment has been done by heating phantom during 2 minutes delivering a power of 10 W. Maximum of temperature increase has been found approximately 10°C . Similar results with different increase in temperature we have got also in other technical experiments on phantom or live mouse when power or heating time was changed.

4. ARRAY APPLICATOR

The main goal of the planned biological experiment is a hyperthermia treatment of the experimentally induced pedicle tumours of the rat to verify the feasibility of ultrasound diagnostics and magnetic resonance imaging respectively to map the temperature distribution in the target area of the treatment. That means to heat effective volume of approximately cylindrical shape (diameter approx. 2 cm, height approx. 3 cm). Temperature to be reached is 41°C or more (i.e., temperature increase of at least 4°C from starting point 37°C), time period of heating is 45 minutes.

Therefore the applicator itself (see Fig. 3) is created by two inductive loops tuned to resonance by capacitive elements. Dimensions of these resonant loops were designed by our software, developed for this purpose. Coupling between coaxial feeder and resonant loops (not shown in Fig. 1) as well as a mutual coupling between resonating loops could be adjusted to optimum by microwave network analyzer. The position of the loops is fixed by Perspex holder. There is a special cylindrical space for experimental animal in lower part of this holder. As the heated tissue has high dielectric losses, both loops are very well separated and so no significant resonance in heated area can occur. From this follows, that either the position of the loops with respect to heated area or the distance between the loops is not very critical. Evaluation of the discussed applicator: First measurements to evaluate the basic properties of the discussed applicator were done on agar phantom of muscle tissue:

- evaluation of basic microwave properties (transfer of EM energy to the tissue, reflections),
- evaluation of compatibility with US and MR,
- calculation and measurement of SAR and temperature distribution and its homogeneity.

Exact tuning of the resonant loops to frequency 915 MHz has been easy and we could optimize the coupling between the coaxial feeder and resonant loops as well, reflection coefficient less than 0.1.

We have tested the power to be delivered to the applicator to obtain sufficient temperature increase (approximately 4°C in less than 5 minutes is required). With power 10 W delivered to each loop for period of 2 minutes we succeeded to obtain the temperature increase of approximately 7°C .

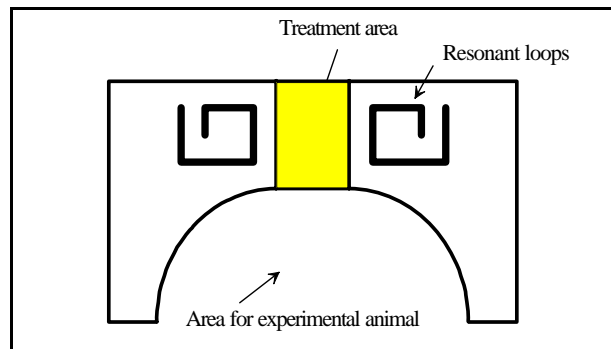


Figure 3: Arrangement of discussed microwave hyperthermia applicator.

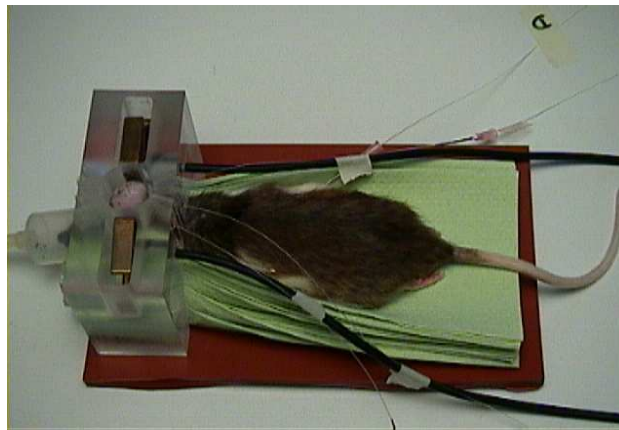


Figure 4: Photograph of the discussed applicator.

To keep the increased temperature for a long time, 2 W in each loops were sufficient. Similar values were obtained during first experiments on rats also. Even with higher level of delivered microwave power we did not observe the change of resonant frequency (caused by increased temperature of the loops).

5. CONCLUSIONS

Considering the necessary effective heating depth for the planned experiments, we have found 915 MHz to be suitable frequency. This applicator has been developed for German Cancer Research Institute in Heidelberg. And it is being used there for a series of animal experiments to study effect of hyperthermia on tumours and possibility to combine hyperthermia with chemotherapy etc.. Compatibility of this applicator with a Magnetic resonance unit (MR) has been studied and it has been demonstrated.

ACKNOWLEDGMENT

This research is supported by the Czech Science Foundation by project P102/11/0649: “Research and measurements of signals generated by nanostructures”.

REFERENCES

1. Vrba, J., *Medical Applications of Microwaves*, CTU Press, Prague, 2003 (In Czech).
2. Hand, J. and J. R. James, editors, *Physical Techniques in Clinical Hyperthermia*, Wiley, New York, 1986.

3. Franconi, C., J. Vrba, et al., “27 MHz hybrid evanescent-mode applicators,” *Int. Journal of Hyperthermia*, Vol. 9, No. 5, 655–674, 1993.
4. Vrba, J., C. Franconi, et al., “Evanescent-mode applicators for hyperthermia,” *IEEE Trans. on Biomedical Engineering*, Vol. 40, No. 5, 397–407, May 1993.

Electromagnetic Modeling and Simulation for Interconnect Structures Based on Volume-surface Integral Equations

Y. Q. Zhang, M. H. Wei, Y. R. Cao, Y. Q. Wang, and M. S. Tong

Department of Electronic Science and Technology, Tongji University
4800 Cao'an Road, Shanghai 201804, China

Abstract— Electromagnetic (EM) analysis for interconnect and packaging structures usually relies on the solutions of surface integral equations (SIEs) in integral equation solvers. Though the SIEs are necessary for the conductors in the structures, one has to assume a homogeneity of material for each layer of substrate if SIEs are used for the substrate. When the inhomogeneity of materials in the substrate has to be taken into account, then volume integral equations (VIEs) are indispensable. In this work, we consider the inhomogeneous materials of substrate and replace the SIEs with the VIEs to form volume-surface integral equations (VSIEs) for the entire structures. The VSIEs are solved with the method of moments (MoM) by using the Rao-Wilton-Glisson (RWG) basis function to represent the surface current on the conductors and Schaubert-Wilton-Glisson (SWG) basis function to expand the volume current inside the substrate. A numerical example is presented to demonstrate the effectiveness of the approach.

1. INTRODUCTION

Electromagnetic (EM) modeling and simulation are crucial for understanding the electrical performance of interconnect structures in microelectronic or nanoelectronic devices. The structures are usually small compared with the wavelength within a certain range of frequency, so extra care is required for achieving a good numerical accuracy [1]. Also, the structures include multiscale features, namely, some dimensions are much smaller than others in geometries, leading to deteriorating the conditioning of system matrix. Moreover, the EM analysis usually requires covering a wide range of frequency with significant low-frequency components, resulting in a perplexity of low-frequency effects [2]. These factors have caused much challenge in numerical implementation and thus choosing appropriate governing equations, robust numerical method, and wise implementation scheme has become essential. Traditionally, the EM modeling for interconnect structures is formulated with surface integral equations (SIEs) in integral equation approach [3] and one has to assume the homogeneity of materials in the dielectric substrate. However, the inhomogeneity of materials could exist due to their impurity in some interconnect structures and the SIEs may not be appropriate for such a case.

In this work, we use the VIEs to replace the SIEs for the substrate and they are coupled with the SIEs for the conductors to form the volume-surface integral equations (VSIEs) for describing the EM features of the interconnect structures. The use of VIEs in the substrate allows the inhomogeneity of materials and may provide more flexibility in the analysis [4–7]. The VSIEs are usually solved with the MoM in which the Rao-Wilton-Glisson (RWG) basis function is used to expand the surface current on the conductors with a triangular tessellation [8] while the Schaubert-Wilton-Glisson (SWG) basis function is applied to represent the flux density in the substrate with a tetrahedral discretization [9]. To facilitate the implementation, we suggest that the dyadic Green's function be kept in its original form without moving the gradient operator onto the basis and testing functions. We can avoid the inconvenience of conventional implementation in this way though requiring a good treatment for the hypersingularity in the dyadic Green's function [10]. Numerical example for analyzing a typical inhomogeneous interconnect structure is presented to illustrate the approach and good result can be observed.

2. VOLUME-SURFACE INTEGRAL EQUATIONS

The interconnect and packaging structures include both conducting signal lines (transmission lines) and ground and dielectric substrates as sketched in Fig. 1. We assume that the signal lines and ground are perfectly electric conductors (PECs) and the involved EM features can be described by the following electric field integral equation (EFIE) [3]

$$-\hat{n} \times \mathbf{E}^{ex}(\mathbf{r}) = \hat{n} \times i\omega\mu_0 \int_S \bar{\mathbf{G}}(\mathbf{r}, \mathbf{r}') \cdot \mathbf{J}_S(\mathbf{r}') dS', \quad \mathbf{r} \in S \quad (1)$$

where $\mathbf{J}_S(\mathbf{r}')$ is the electric current induced on the conductor surface S whose unit normal vector is \hat{n} and $\mathbf{E}^{ex}(\mathbf{r})$ represents a delta-gap excitation at an appropriate position on the conductors. Also, $\bar{\mathbf{G}}(\mathbf{r}, \mathbf{r}')$ is the dyadic Green's function defined by

$$\bar{\mathbf{G}}(\mathbf{r}, \mathbf{r}') = \left(\bar{\mathbf{I}} + \frac{\nabla\nabla}{k_0^2} \right) g(\mathbf{r}, \mathbf{r}') \quad (2)$$

where $\bar{\mathbf{I}}$ is the identity dyad, $g(\mathbf{r}, \mathbf{r}') = e^{ik_0R}/(4\pi R)$ is the three-dimensional (3D) scalar Green's function in which $R = |\mathbf{r} - \mathbf{r}'|$ is the distance between an observation point \mathbf{r} and a source point \mathbf{r}' , and k_0 is the wavenumber of the free space with a permittivity ϵ_0 and a permeability μ_0 . For the substrate which could consist of inhomogeneous materials with a permittivity $\epsilon(\mathbf{r}')$ and a permeability $\mu(\mathbf{r}')$, we can use the VIEs to catch up its EM characteristics, i.e., [3]

$$\mathbf{E}(\mathbf{r}) = \mathbf{E}^{ex}(\mathbf{r}) + i\omega\mu_0 \int_V \bar{\mathbf{G}}(\mathbf{r}, \mathbf{r}') \cdot \mathbf{J}_V(\mathbf{r}') d\mathbf{r}' - \nabla \times \int_V \bar{\mathbf{G}}(\mathbf{r}, \mathbf{r}') \cdot \mathbf{M}_V(\mathbf{r}') d\mathbf{r}', \quad \mathbf{r} \in V \quad (3)$$

$$\mathbf{H}(\mathbf{r}) = \mathbf{H}^{ex}(\mathbf{r}) + i\omega\epsilon_0 \int_V \bar{\mathbf{G}}(\mathbf{r}, \mathbf{r}') \cdot \mathbf{M}_V(\mathbf{r}') d\mathbf{r}' + \nabla \times \int_V \bar{\mathbf{G}}(\mathbf{r}, \mathbf{r}') \cdot \mathbf{J}_V(\mathbf{r}') d\mathbf{r}', \quad \mathbf{r} \in V \quad (4)$$

where $\mathbf{E}^{ex}(\mathbf{r}) = \mathbf{H}^{ex}(\mathbf{r}) = 0$ in the substrate in general, and

$$\begin{aligned} \mathbf{J}_V(\mathbf{r}') &= i\omega[\epsilon_0 - \epsilon(\mathbf{r}')] \mathbf{E}(\mathbf{r}') \\ \mathbf{M}_V(\mathbf{r}') &= i\omega[\mu_0 - \mu(\mathbf{r}')] \mathbf{H}(\mathbf{r}') \end{aligned} \quad (5)$$

are the induced volumetric electric and magnetic currents inside the substrate, respectively. If the substrate is nonmagnetic or has the same permeability as the background, which is usually true, then $\mathbf{M}_V(\mathbf{r}') = 0$ and only Eq. (3) is needed, which can be reduced to

$$\mathbf{E}(\mathbf{r}) = i\omega\mu_0 \int_V \bar{\mathbf{G}}(\mathbf{r}, \mathbf{r}') \cdot \mathbf{J}_V(\mathbf{r}') d\mathbf{r}', \quad \mathbf{r} \in V. \quad (6)$$

When considering the coupling of fields produced by the surface current on the conductors and the volume current inside the substrate, we can form the following VSIEs

$$0 = \hat{n} \times \left[\mathbf{E}^{ex}(\mathbf{r}) + i\omega\mu_0 \int_S \bar{\mathbf{G}}(\mathbf{r}, \mathbf{r}') \cdot \mathbf{J}_S(\mathbf{r}') dS' + i\omega\mu_0 \int_V \bar{\mathbf{G}}(\mathbf{r}, \mathbf{r}') \cdot \mathbf{J}_V(\mathbf{r}') d\mathbf{r}' \right], \quad \mathbf{r} \in S \quad (7)$$

$$\mathbf{E}(\mathbf{r}) = i\omega\mu_0 \int_S \bar{\mathbf{G}}(\mathbf{r}, \mathbf{r}') \cdot \mathbf{J}_S(\mathbf{r}') dS' + i\omega\mu_0 \int_V \bar{\mathbf{G}}(\mathbf{r}, \mathbf{r}') \cdot \mathbf{J}_V(\mathbf{r}') d\mathbf{r}', \quad \mathbf{r} \in V \quad (8)$$

from which the unknown currents can be solved and equivalent circuit parameters of the structure can subsequently be extracted.

3. THE METHOD OF MOMENTS SOLUTION

The above VSIEs can be solved by the traditional MoM in which the surface current on the conductors is expanded by the RWG basis function while the electric flux density inside the substrate is represented with the SWG basis function, i.e.,

$$\mathbf{J}_S(\mathbf{r}') = \sum_{n=1}^{N_c} J_n \mathbf{e}_n(\mathbf{r}') \quad (9)$$

$$\mathbf{D}(\mathbf{r}') = \sum_{n=1}^{N_d} D_n \mathbf{f}_n(\mathbf{r}') \quad (10)$$

where $\mathbf{e}_n(\mathbf{r}')$ is the RWG basis function and N_c is the number of RWG triangle pairs while $\mathbf{f}_n(\mathbf{r}')$ is the SWG basis function and N_d is the number of SWG tetrahedron pairs. Also, J_n and D_n are the expansion coefficients for the two basis functions, respectively. The flux density instead of current density is chosen as an unknown function in the substrate because it is normally continuous across material interfaces. The current density is related to the flux density through

$$\mathbf{J}(\mathbf{r}') = -i\omega\kappa(\mathbf{r}') \mathbf{D}(\mathbf{r}') \quad (11)$$

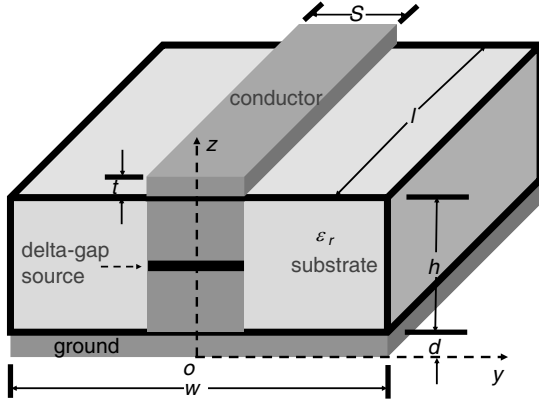


Figure 1: Geometry of a typical interconnect and packaging structure. A conducting signal line is at the top of a one-layer dielectric substrate with a ground.

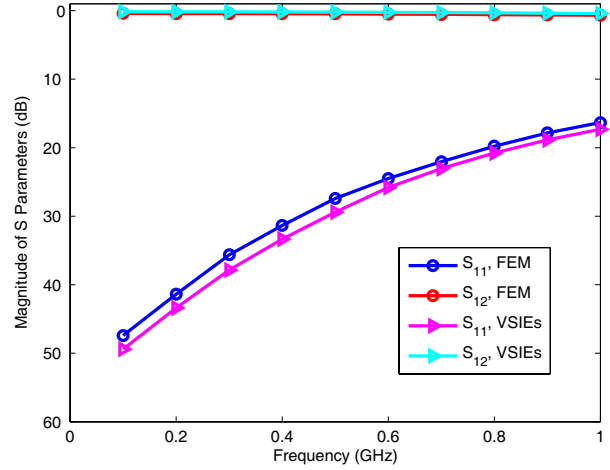


Figure 2: S parameter for the interconnect and packaging structure including a signal line and a one-layer dielectric substrate. The geometry is defined with $l = 10.0$, $w = 5.0$, $d = 0.1$, $s = 0.2$, $t = 0.05$, and $h = 0.3$, all in millimeters, and the substrate has an inhomogeneous relative permittivity $\epsilon_r(y) = \cos(2.0\pi|y|/w) + 4.0$ in the y direction.

where

$$\kappa(\mathbf{r}') = [\epsilon(\mathbf{r}') - \epsilon_0]/\epsilon(\mathbf{r}') \quad (12)$$

is the contrast ratio of permittivity. Using the RWG and SWG basis function as a testing function to test Eq. (7) and Eq. (8), respectively, we can obtain the following matrix equation

$$-\left\langle \mathbf{e}_m(\mathbf{r}), \frac{\mathbf{E}^{ex}(\mathbf{r})}{i\omega\mu_0} \right\rangle = \sum_{n=1}^{N_c} J_n \langle \mathbf{e}_m(\mathbf{r}), \bar{\mathbf{G}}(\mathbf{r}, \mathbf{r}'), \mathbf{e}_n(\mathbf{r}') \rangle + \sum_{n=1}^{N_d} D_n \langle \mathbf{e}_m(\mathbf{r}), \bar{\mathbf{G}}_0(\mathbf{r}, \mathbf{r}'), \mathbf{f}_n(\mathbf{r}') \rangle, \quad m = 1, 2, \dots, N_c \quad (13)$$

$$D_m \left\langle \mathbf{f}_m(\mathbf{r}), \frac{\mathbf{f}_m(\mathbf{r})}{i\omega\mu_0\epsilon(\mathbf{r})} \right\rangle = \sum_{n=1}^{N_c} J_n \langle \mathbf{f}_m(\mathbf{r}), \bar{\mathbf{G}}(\mathbf{r}, \mathbf{r}'), \mathbf{e}_n(\mathbf{r}') \rangle + \sum_{n=1}^{N_d} D_n \langle \mathbf{f}_m(\mathbf{r}), \bar{\mathbf{G}}_0(\mathbf{r}, \mathbf{r}'), \mathbf{f}_n(\mathbf{r}') \rangle, \quad m = 1, 2, \dots, N_d \quad (14)$$

where $\bar{\mathbf{G}}_0(\mathbf{r}, \mathbf{r}') = -i\omega\kappa(\mathbf{r}')\bar{\mathbf{G}}(\mathbf{r}, \mathbf{r}')$. The above matrix equation can be solved with any matrix solver so that the unknown current density and flux density can be found.

4. NUMERICAL EXAMPLE

To illustrate the proposed approach, we present a numerical example for the EM analysis of typical interconnect and packaging structure which include inhomogeneous materials. The geometry of the structure is shown in Fig. 1, i.e., a conducting signal line is at the top of a one-layer dielectric substrate with a ground. It is assumed that the signal line and ground are made of PECs and the dielectric substrate is also lossless but inhomogeneous. The structure is strictly in 3D and both the interconnect and ground have a nonnegligible thickness. The dimensions of the geometry are characterized as follows (all in millimeters): the length, width, and height of the substrate are $l = 10.0$, $w = 5.0$, and $h = 0.3$, respectively, and the thickness of the ground is $d = 0.1$. The signal line has a width $s = 0.2$, a thickness $t = 0.05$. We assume that the relative permittivity of the inhomogeneous dielectric substrate has a distribution defined by

$$\epsilon_r(y) = \cos(2.0\pi|y|/w) + 4.0 \quad (15)$$

in the y direction. Fig. 2 shows the solution of S parameters for the structure and it is close to the result from a finite element method (FEM) solver.

5. CONCLUSION

EM modeling and simulation are essential for analyzing and designing interconnect and packaging structures. The SIEs of integral equation approach are widely employed in formulating the solvers due to their less number of unknowns in the discretization of formulations. Nevertheless, the SIEs require a homogeneity of materials in the substrate and may not be convenient for discretizing structures with many material interfaces. In this work, we develop a VSIE approach by replacing the SIEs with the VIEs in the substrate for the EM analysis of interconnect and packaging structures. This replacement allows the inhomogeneity of materials in the substrate and removes the drawbacks of the SIEs. The resultant VSIEs are solved with the MoM in which the surface current on the conductors is expanded with the RWG basis function while the flux density inside the substrate is represented by the SWG basis function. A numerical example for the EM analysis of inhomogeneous interconnect and packaging structure has demonstrated the effectiveness of the proposed approach.

ACKNOWLEDGMENT

This work was supported by the National Natural Science Foundation of China with the Project No. 61271097.

REFERENCES

1. Li, M. K. and W. C. Chew, "Multiscale simulation of complex structures using equivalence principle algorithm with high-order field point sampling scheme," *IEEE Trans. Antennas Propagat.*, Vol. 56, No. 8, 2389–2397, 2008.
2. Qian, Z.-G. and W. C. Chew, "Fast full-wave surface integral equation solver for multiscale structure modeling," *IEEE Trans. Antennas Propagat.*, Vol. 57, No. 11, 3594–3601, 2009.
3. Chew, W. C., M. S. Tong, and B. Hu, *Integral Equation Methods for Electromagnetic and Elastic Waves*, Morgan & Claypool, San Rafael, CA, 2008.
4. Lu, C. C. and W. C. Chew, "A coupled surface-volume integral equation approach for the calculation of electromagnetic scattering from composite metallic and material targets," *IEEE Trans. Antennas Propagat.*, Vol. 48, No. 12, 1866–1868, 2000.
5. Ewe, W.-B., L.-W. Li, and M.-S. Leong, "Fast solution of mixed dielectric/conducting scattering problem using volume-surface adaptive integral method," *IEEE Trans. Antennas Propagat.*, Vol. 52, No. 11, 3071–3077, 2004.
6. Nie, X.-C., N. Yuan, L.-W. Li, Y.-B. Gan, and T. S. Yeo, "A fast volume-surface integral equation solver for scattering from composite conducting-dielectric objects," *IEEE Trans. Antennas Propagat.*, Vol. 53, No. 2, 818–824, 2005.
7. Usner, B. C., K. Sertel, M. A. Carr, and J. L. Volakis, "Generalized volume-surface integral equation for modeling inhomogeneities within high contrast composite structures," *IEEE Trans. Antennas Propagat.*, Vol. 54, No. 1, 68–75, 2006.
8. Rao, S. M., D. R. Wilton, and A. W. Glisson, "Electromagnetic scattering by surfaces of arbitrary shape," *IEEE Trans. Antennas Propagat.*, Vol. 30, No. 3, 409–418, 1982.
9. Schaubert, D. H., D. R. Wilton, and A. W. Glisson, "A tetrahedral modeling method for electromagnetic scattering by arbitrary shaped inhomogeneous dielectric bodies," *IEEE Trans. Antennas Propagat.*, Vol. 32, No. 1, 77–85, 1984.
10. Tong, M. S. and W. C. Chew, "Super-hyper singularity treatment for solving 3D electric field integral equations," *Microw. Opt. Technol. Lett.*, Vol. 49, No. 6, 1383–1388, 2007.

Refractive Index Profiling of Metal-diffused Planar Waveguides Using a Differential Near-field Optical Microscopy

W.-S. Tsai¹ and P. K. Wei^{2,3}

¹Department of Applied Materials and Optoelectronics Engineering
National Chi-Nan University, Taiwan

²Research Center for Applied Sciences, Academia Sinica, Taiwan

³Department of Optoelectronics, National Taiwan Ocean University, Taiwan

Abstract— A differential near-field scanning optical microscopy (DNSOM) was used to reconstruct the refractive index profile of a Ti:LiNbO₃ planar waveguide. The waveguide was measured at 633 nm for single-mode operation. The reconstructed index profile matches well with known index model of Ti:LiNbO₃ waveguides. Guiding mode profile calculated from fitted index model also shows good agreement with measured mode profile.

1. INTRODUCTION

Refractive index profiles of optical waveguides are crucial in determining optical characteristics of integrated optical waveguides, such as guiding mode behaviors, coupling condition, and so on. However, for the metal-diffused optical waveguides, the index profiles were mainly determined by the fabrication process. Therefore, several methods were proposed to determine accurate refractive index profiles of optical waveguides. Secondary ion mass spectrometry (SIMS) measures the concentration distribution of diffused metal ions and reconstructs index profiles indirectly and destructively [1–3]. Prism coupling method measures the effective indexes of optical waveguides, and obtains index profiles using WKB approximation with measured effective indexes of multimode waveguides [4, 5]. For the nondestructive measurement of single-mode waveguide, guiding mode intensities were measured to relate index profiles with scalar wave equation, which were called near-field methods [6–8].

Previously, differential near-field optical microscopy (DNSOM) was proposed in measuring the symmetric index profile of an optical fiber [9]. Modified end-fire coupling method was also proposed to reconstruct two-dimensional index profiles of optical waveguides [10, 11]. In this work, the DNSOM system was applied to reconstruct asymmetric index profile of a metal-diffused planar waveguide. The index model of Ti:LiNbO₃ waveguides has been determined [12], however, exact index profile depends on the fabrication process. Therefore, we would like to apply DNSOM system on this waveguide, and compare the results with existing model.

2. DIFFERENTIAL INVERSE ALGORITHM

For a weakly guiding waveguide, since the index difference $\Delta n(x)$ is very small compared with substrate index n_s , the refractive index profile, $n(x)$, can be assumed as [7, 8]

$$n^2(x) = (n_s + \Delta n(x))^2 \approx n_s^2 + 2n_s\Delta n(x). \quad (1)$$

Based on scalar wave equation, $\nabla^2 E(x) + [k^2 n^2(x) - \beta^2]E(x) = 0$, the refractive index profile of an optical waveguide can be solved if its guiding mode profile was measured. k is the free space wave number and $\beta = k \times n_{eff}$ is the propagation constant of the modal field $E(x)$. Assume $n_{eff} \approx n_s$, the inverse algorithm can be written as [9]

$$\Delta n(x) \approx -\frac{1}{2} \frac{E''}{n_s k^2 E} + \Delta n_{eff}, \quad (2)$$

where $\Delta n_{eff} = n_{eff} - n_s$. The differential inverse algorithm is based on the concept that the derivatives of modal field can be measured directly, without the need of numerical differentiation that amplified measured noises. Eq. (2) can thus be rewritten as

$$\Delta n(x) \approx -\frac{1}{2} \frac{(\sqrt{I})''}{n_s k^2 \sqrt{I}} + \Delta n_{eff} = -\frac{1}{4n_s k^2} \left[\frac{I''}{I} - \frac{1}{2} \frac{(I')^2}{I^2} \right] + \Delta n_{eff}. \quad (3)$$

Simultaneous measurements of I , I' and I'' enable the reconstruction of corresponding index profile directly.

3. EXPERIMENTS

The DNSOM system was built on an atomic-force microscope with a tapered fiber probe [13] and a shear-force feedback [14], as shown in Fig. 1. A 632.8 nm-wavelength He-Ne laser, modulated by an optical chopper at frequency f_0 ($= 390$ Hz), was coupled into the optical waveguide by the fiber coupling method. At the output end, the fiber probe was allowed to scan over the waveguide area within the near-field region by using a tuning-fork feedback mechanism [15]. The probe is a tapered fiber coated with a gold layer of thickness 80 nm around the tip region to enhance the resolution. The diameter of fiber tip coated with gold is 100 nm, and therefore subwavelength resolution can be obtained in the near-field measurement. The probe was mounted on a tuning fork that oscillates the probe along the x -direction with an amplitude Δx at frequency f_1 ($= 33.48$ kHz). The probe was connected to a photomultiplier tube and the signal was read by three lock-in amplifiers (LIAs), referenced at frequencies f_0 , f_1 and $2f_1$, respectively. The amplitude and phase signals were sent to the computer to render the near-field images. Since the position of tip vibration was described by

$$x(t) = x(0) + \Delta x \sin \omega_1 t, \quad (4)$$

where $x(0)$ is the equilibrium position and ω_1 ($= 2\pi f_1$) is the angular frequency of the dither vibration. The optical intensity $I(x)$ on the detector can then be approximated by

$$I[x(t)] \approx I[x(0)] + \Delta x I'[x(0)] \sin \omega_1 t + \frac{1}{4} \Delta x^2 I''[x(0)] \cos 2\omega_1 t, \quad (5)$$

Hence, during the scan of the fiber tip, the image signal from LIA gives the optical intensity I as that of the conventional method, whereas the image signals from LIA1 and LIA2 generate optical intensity derivatives I' and I'' , respectively, as required by the proposed method.

A Ti-diffused planar waveguide on LiNbO₃ substrate was fabricated for measuring. In order to have a planar waveguide with single guiding mode at 632.8 nm, a 325 Å-thick Ti layer was deposited on a Z -cut LiNbO₃ by RF sputtering. The diffusion process was controlled at 1020°C for 2.5 hr. Both ends of the sample were then polished before measurement. The optical images measured by DNSOM are shown in Fig. 2. Fig. 2(a) is the measured optical intensity. The upper and lower parts of Fig. 2(b) are the images of the first and second derivative of intensity, respectively. Fig. 2(c) shows the phase images of Fig. 2(b). According to Eq. (5), the measured first-derivative of intensity in the upper part of Fig. 2(b) is equal to $I'\Delta x$. And the measured second-derivative of intensity in the lower part of Fig. 2(b) is equal to $I''\Delta x^2/4$. Using the small amplitude measurement method [16], Δx is found to be 0.12 μm in our measurement setup. The images calibrated with the vibration amplitude rendered the one-dimensional intensities I , I' , and I'' .

It is noticeable that optical intensity has a large change at the air and substrate interface. Such abrupt change causes large edge diffraction when light propagates in the air. That results in a non-smooth and asymmetric waveguide mode when measured in the far-field [6]. The optical intensity at the output surface of the waveguide was directly measured by DNSOM. It takes the advantage of free of edge diffraction and thus is suitable for the refractive-index profile reconstruction of a strong asymmetric integrated optical waveguide. For example, the asymmetrical patterns of optical intensities in a Ti:LiNbO₃ waveguide are clearly observed in Fig. 2(b), especially for I' and I'' .

The calculated index profile was reconstructed by substituting I , I' , and I'' in Eq. (3). Note that there is an offset Δn_{eff} between the calculated and actual refractive index profile [2]. As the refractive index difference in the deep substrate region is known to be equal to zero, Δn_{eff} is

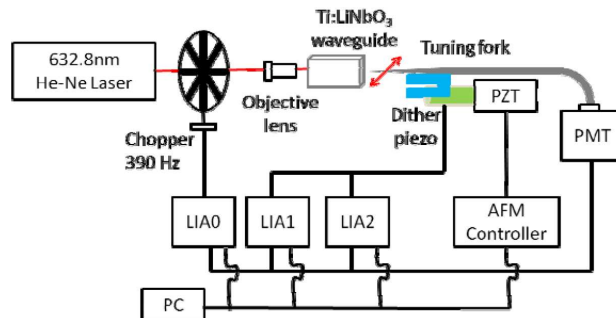


Figure 1: System setup of the differential near-field scanning optical microscopy.

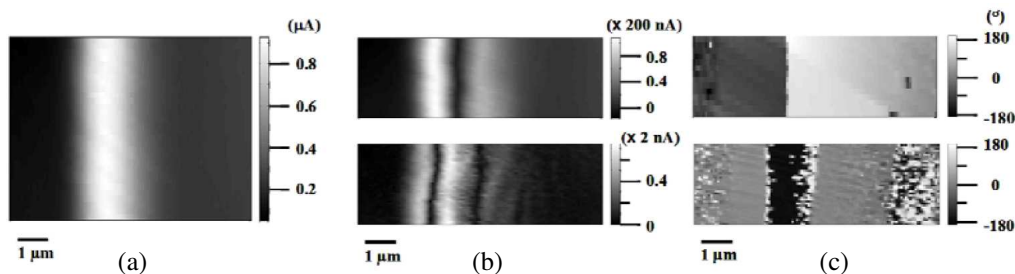


Figure 2: (a) Measured image of output field intensity, I . (b) Measured images of the first-, I' (upper part) and the second derivative, I'' (lower part) of output field intensity. (c) The phase signals of (b).

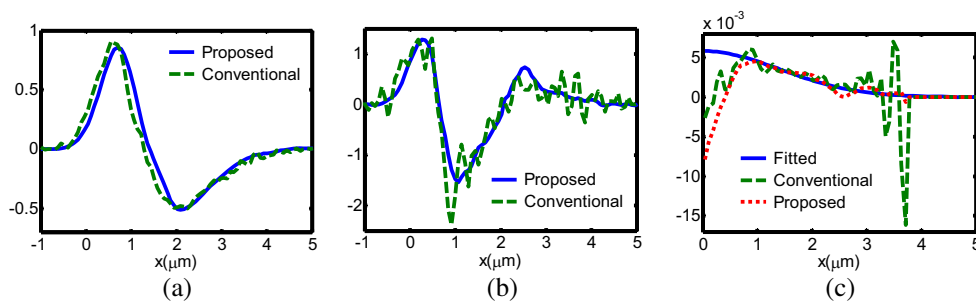


Figure 3: (a) The first derivative field intensity I' . (b) The second derivative field intensity I'' . (c) The reconstructed index profiles and the fitted index profile.

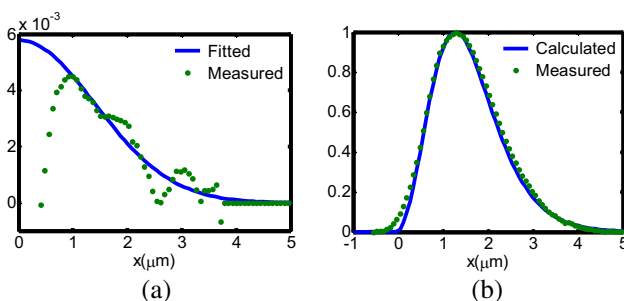


Figure 4: (a) The reconstructed index profile by the proposed method and the fitted index profile. (b) Comparison of the optical field intensity calculated by using the fitted index profile in (a) and the measured optical field intensity I .

estimated to be 0.0018 by Eq. (3). This offset value was confirmed by the effective refractive index measured by a prism coupler (Metricron[®] 2010), which showed a single-mode dip at the index of 2.2892 with $n_s = 2.2874$. The difference of these two values is also 0.0018, which is consistent with the previous estimation. Using the offset and the measured I , I' and I'' , the refractive index profile was obtained. Figs. 3(a) and (b) showed a comparison of the derivatives of field intensity, I' and I'' , by measurement and numerical differentiation. For comparison, the best fitting of the reconstructed index profile obtained by the proposed method was also shown in Fig. 3(c). As can be seen, the index profile obtained by the proposed method is less noisy than that by the conventional one. Fig. 4(a) shows the reconstructed index profile by the proposed method. It can be seen that the index profiles are well matched with a known diffusion profile for the Ti:LiNbO₃ waveguide. The diffusion depth is 2.0 μm and the maximum refractive index difference is 0.0058. For verification, the fitted refractive index profile is used to calculate the intensity distribution in the waveguide as shown in Fig. 4(b). As can be seen, the calculated intensity profile is in good agreement with that measured from our DNSOM system.

4. CONCLUSIONS

The refractive index profile of a Ti:LiNbO₃ planar waveguide was measured at 633 nm for single-mode operation, using a differential near-field optical microscopy. Experimental results show that the reconstructed index profiles are in good agreement with the known ones. Moreover, the measured optical field intensity distributions agree quite well with those calculated with the known index profile. Refractive index profiling of optical waveguides with unknown materials would be of great interests in the future.

ACKNOWLEDGMENT

This work was supported by National Science Council, Taipei, Taiwan, under contract No. NSC-101-2221-E-260-021.

REFERENCES

1. Betts, R. A., C. W. Pitt, K. R. Riddle, and L. M. Walpita, "A comparative study of the dopant profiles in diffused planar optical waveguides by SIMS and guided wave probe," *Appl. Phys. A*, Vol. 31, 29–35, 1983.
2. Caccavale, F., P. Chakraborty, A. Quaranta, I. Mansour, G. Gianello, S. Bosso, R. Corsini, and G. Mussi, "Secondary-ion-mass spectrometry and near-field studies of Ti:LiNbO₃ optical waveguides," *J. Appl. Phys.*, Vol. 78, 5345–5350, 1995.
3. Caccavale, F., A. Morbiato, M. Natali, C. Sada, and F. Segato, "Correlation between optical and compositional properties of Ti:LiNbO₃ channel optical waveguides," *J. Appl. Phys.*, Vol. 87, 1007–1011, 2000.
4. White, J. M. and P. F. Heidrich, "Optical waveguide refractive index profiles determined from measurement of mode indices: A simple analysis," *Appl. Optics*, Vol. 15, 151–155, 1976.
5. Chiang, K. S., "Construction of refractive-index profiles of planar dielectric waveguides from the distribution of effective indexes," *J. Lightwave Technol.*, Vol. 3, 385–391, 1985.
6. Caccavale, F., F. Segato, I. Mansour, and M. Gianesin, "A finite differences method for the reconstruction of refractive index profiles from near-field measurements," *J. Lightwave Technol.*, Vol. 16, 1348–1353, 1998.
7. Mansour, I. and F. Caccavale, "An improved procedure to calculate the refractive index profile from the measured near-field intensity," *J. Lightwave Technol.*, Vol. 14, 423–428, 1996.
8. Morishita, K., "Index profiling of three-dimensional optical waveguides by the propagation-mode near-field method," *J. Lightwave Technol.*, Vol. 4, 1120–1124, 1986.
9. Tsai, W.-S., W.-S. Wang, and P.-K. Wei, "Two-dimensional refractive index profiling by using differential near-field scanning optical microscopy," *Appl. Phys. Lett.*, Vol. 91, 061123, 2007.
10. Tsai, W.-S., S.-C. Piao, and P.-K. Wei, "Refractive index measurement of optical waveguides using modified end-fire coupling method," *Opt. Lett.*, Vol. 36, 2008–2011, 2011.
11. Tsai, W.-S., S.-Y. Ting, and P.-K. Wei, "Refractive index profiling of an optical waveguide from the determination of the effective index with measured differential fields," *Optics Express*, Vol. 20, 26766–26777, 2012.
12. Fouchet, S., A. Carencio, C. Daguet, R. Guglielmi, and L. Riviere, "Wavelength dispersion of Ti induced refractive index change in LiNbO₃ as a function of diffusion parameters," *J. Lightwave Technol.*, Vol. 5, 700–708, 1987.
13. Stöckle, R., C. Fokas, V. Deckert, R. Zenobi, B. Sick, B. Hecht, and U. P. Wild, "High-quality near-field optical probes by tube etching," *Appl. Phys. Lett.*, Vol. 75, 160–162, 1999.
14. Betzig, E., P. L. Finn, and J. S. Weiner, "Combined shear force and near-field scanning optical microscopy," *Appl. Phys. Lett.*, Vol. 60, 2484–2486, 1992.
15. Karrai, K. and R. D. Grober, "Piezoelectric tip-sample distance control for near field optical microscopes," *Appl. Phys. Lett.*, Vol. 66, 1842–1844, 1995.
16. Wei, C.-C., P.-K. Wei, and W. Fann, "Direct measurements of the true vibrational amplitudes in shear force microscopy," *Appl. Phys. Lett.*, Vol. 67, 3835–3837, 1995.

Interference Cancellation and DOA Estimation by Generalized Receiver Applying LMS and MUSIC Algorithms

Jingui Liu, Modar Safir Shbat, and Vyacheslav Tuzlukov

College of IT Engineering, Kyungpook National University, South Korea

Abstract— Under implementation of the generalized receiver (GR) constructed based on the generalized approach to signal processing (GASP) in noise there is a need to cancel an interference to improve the GR performance. In this paper, we discuss an interference cancellation technique based on the non-blind beamforming algorithm, namely, the least mean square (LMS) algorithm employed by GR. The direction of arrival (DOA) estimation is also used by LMS algorithm to provide a priori knowledge about the desired signal in GR. The simulation results demonstrate a superiority of GR performance in comparison with the Neyman-Pearson (NP) receiver.

1. INTRODUCTION

The generalized receiver (GR) is constructed based on the generalized approach to signal processing (GASP) in noise discussed in [1–5]. The GR is a combination of Neyman-Pearson (NP) detector that is optimal for detection of signals with known parameters and the energy detector that is optimal for detection of signals with unknown parameters. With the purpose to improve the GR performance under noise and interference conditions, the least mean square (LMS) algorithm is proposed for interference cancellation [6]. LMS beamforming algorithm is a non-blind beamforming algorithm that needs a reference signal to update the weight vectors of array antenna with the purpose to form a desired direction vector and generate nulls towards an interference direction [7].

Employment of GR with LMS algorithm requires a prior knowledge about the desired signal. The direction of arrival (DOA) estimation is used to provide the GR with the required information about arrival angles of the received signals. For the past few decades, a wide variety of techniques have been proposed for the DOA estimation. The subspace algorithms such as the multiple signal classification (MUSIC) and estimation of signal parameter via rotational invariance technique (ESPRIT) algorithms are widely used owing to their high resolution [8]. In this paper, the MUSIC algorithm for DOA is employed with LMS algorithm with the purpose to cancel interference. The simulation results demonstrate a good performance at the output of GR with LMS algorithm and MUSIC DOA estimation under the interference cancellation. The rest of this paper is organized as follows: Section 2 presents the simple GR flowchart and main functioning principles. Section 3 discusses the LMS beamformer employed by GR. Implementation of DOA estimation algorithm is introduced in Section 4. The simulation results are discussed in Section 5. The conclusion remarks are given in Section 6.

2. GR STRUCTURE

GR flowchart is presented in Fig. 1. Here, AF is the additional filter used to generate the reference noise and PF is the preliminary filter that can be considered as a band pass filter matched by bandwidth with the desired signal. The AF resonance frequency is detuned relative to the PF resonant frequency on such a value that both the signal and noise can be appeared at the PF output, whereas only the noise is appeared at the AF output. The detuning value must be more than $4 \sim 5$ signal bandwidth. In this case, the correlation coefficient between the processes forming at the PF and AF outputs is not more than 0.05. MSG is the model signal generator generating the reference signal or model signal a_i^M . The stochastic process at the GR output takes the following form:

$$Z_g = \sum_{i=1}^N (2X_i a_i^M - X_i^2 + \eta_i^2), \quad (1)$$

where

$$a_i^M = \gamma a_i, \quad (2)$$

$$X_i = a_i + \xi_i, \quad (3)$$

a_i is the sample of desired received signal at the PF output, γ is the coefficient of proportionality, X_i is the sample of observed stochastic process at the PF output. η_i and ξ_i are the samples of

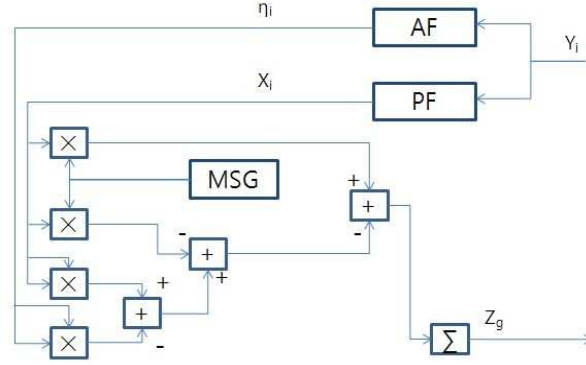


Figure 1: The main structure of GR.

the observed noise at the AF and PF outputs respectively, and $i = 1, 2, \dots, N$, where N is the sample size. If the reference signal or model signal is identical to the desired signal, i.e., $\gamma = 1$, Equation (1) can be written as

$$Z_g = \sum_{i=1}^N (a_i^2 + \eta_i^2 - \xi_i^2). \quad (4)$$

It is well known that $\sum_{i=1}^N a_i^2$ is the received signal energy, and $\sum_{i=1}^N (\eta_i^2 - \xi_i^2)$ is the background noise formed by AF and PF.

3. GR WITH LMS BEAMFORMER

LMS algorithm is a basic non-blind beamforming algorithm used to reject the interfering signals based on the minimum mean square error (MMSE) criterion and the steepest descent method. Updating the coefficients in weight vector W_i adjusts the phase and amplitude of the input signal, respectively, and the output signal (beamformer output) will be closed to the desired signal. LMS algorithm can be defined by the following equations:

$$M_i = W_{i-1}^T S_i, \quad (5)$$

$$e_i^* = M_i - d_i, \quad (6)$$

$$W_i = W_{i-1} + \mu e_i^* S_i, \quad (7)$$

where M_i is the beamformer output, S_i is the received signal or the beamformer input, d_i is the reference signal in the beamformer, e_i^* is the error between the beamformer output and reference signal, μ is the step size that is called the adaptation rate and must be chosen based on the correlation matrix of S_i , and $*$ denotes the complex conjugate.

In the case when there are interfering signals, the LMS algorithm can be applied at the output of GR to cancel them. The structure of GR with LMS beamformer is shown in Fig. 2. Statistics forming at the GR output when the interference signals are present takes the following form:

$$Z_g = \sum_{i=1}^N (a_i^2 - 2I_i \xi_i - I_i^2 + \eta_i^2 - \xi_i^2), \quad (8)$$

where I_i is the sample of the observed interference signal. In (8), the term $-2I_i \xi_i - I_i^2$ is caused by interaction between the interference and noise that deteriorates the GR performance.

In GR with LMS beamformer, the model signal of LMS beamforming algorithm should be the square of the signal a_i^M due to the fact that the output of the GR is presented as the energy of the signal. According to (5)–(7), we can obtain the following equations:

$$d_i = (a_i^M)^2, \quad (9)$$

$$M_i = W_{i-1}^T Z_{g_i}, \quad (10)$$

$$e_i^* = W_{i-1}^T Z_{g_i} - (a_i^M)^2, \quad (11)$$

$$W_i = W_{i-1} + \mu e_i^* Z_{g_i}. \quad (12)$$

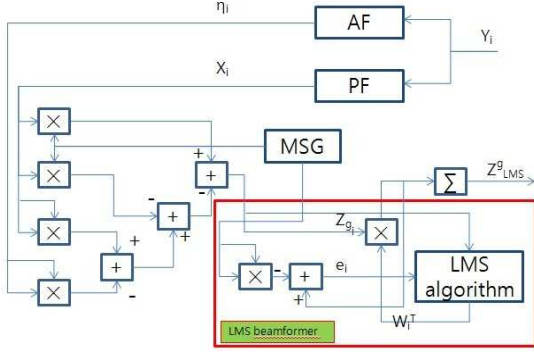


Figure 2: GR with LMS beamformer.

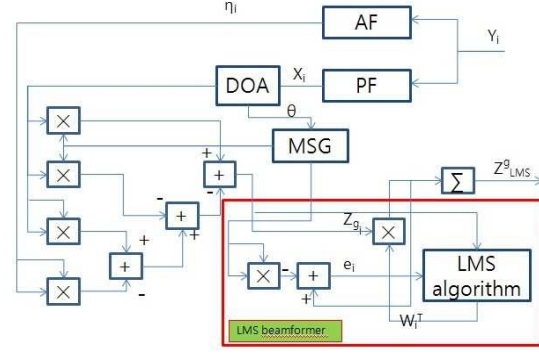


Figure 3: GR with LMS beamformer applying MUSIC algorithm.

Updating the weight vector W_i , the component $-2I_i\xi_i - I_i^2$ in (8) caused by interaction between the interference and noise can be cancelled, and the final output of GR with LMS beamformer can be approximated by (4).

4. UNKNOWN DOA

Both GR and LMS beamformer need a prior knowledge about the desired signal, namely, the DOA to process the received signal. However, the DOA of signals is usually unknown in practical situation, e.g., mobile communication systems. Therefore, it's necessary to apply the DOA estimation technique that estimates the DOA of signals based on array response in the received signal.

The MUSIC algorithm is one of subspace DOA estimation algorithms and has a high resolution technique based on exploiting the eigenstructure of input covariance matrix. MUSIC algorithm assumes that the noise in each channel is uncorrelated and the correlation matrix is diagonal. The incident signals are to be correlated and generate the nondiagonal correlation matrix. The number of incident signals should be less than the number of array elements. If D is the number of signals, M is the number of array elements, the number of signal eigenvalues and eigenvectors is D , and the number of noise eigenvalues and eigenvectors is $M - D$. The array correlation matrix with uncorrelated noise and equal variance is given by

$$\mathbf{R}_{xx} = \mathbf{A}\mathbf{R}_{ss}\mathbf{A}^H + \sigma_n^2\mathbf{I}, \quad (13)$$

where $\mathbf{A} = [a(\theta_1) \ a(\theta_2) \ \dots \ a(\theta_D)]$ is the $M \times D$ array steering matrix, $\mathbf{R}_{ss} = [s_1(t) \ s_2(t) \ \dots \ s_D(t)]^T$ is the $D \times D$ signal correlation matrix, σ_n^2 is the noise variance, and \mathbf{I} is means the identity matrix. \mathbf{R}_{xx} has D eigenvectors associated with signals and $M - D$ eigenvectors associated with the noise. Thus, it is possible to construct the $M \times (M - D)$ noise subspace spanned by the noise eigenvectors using eigenvalue decomposition such that $\mathbf{V}_N = [V_1 \ V_2 \ \dots \ V_{M-D}]$. The noise subspace eigenvectors are orthogonal to array steering vectors at the angles of arrivals θ_D , and the MUSIC pseudospectrum is given as

$$P_{MUSIC}(\theta) = 1/abs\{\mathbf{a}^H(\theta)\mathbf{V}_N\mathbf{V}_N^H\mathbf{a}(\theta)\}. \quad (14)$$

where $abs\{\cdot\}$ means to take the absolute value. By this way, the DOA can be estimated by searching the spectrum peak.

Figure 3 shows the GR with MUSIC algorithm and LMS beamformer. Here, the MUSIC algorithm is applied at the GR PF output. The estimated DOA is transmitted to MSG to generate the reference signal or model signal. The reference signal or model signal has some error compared with the true value. However, we can neglect this error owing to the high resolution of MUSIC algorithm.

5. SIMULATION RESULTS

The simulation results are presented to evaluate the performance of GR with LMS beamformer when DOA of signals is unknown. Four element uniform linear array (ULA) antenna with half wavelength distance is used to receive signals, and there are three incident signals. The first signal is the desired signal arriving at 10° , the second and third signals are interference arriving at -60° and 60° respectively. These angles are assumed to be unknown and should be estimated by MUSIC

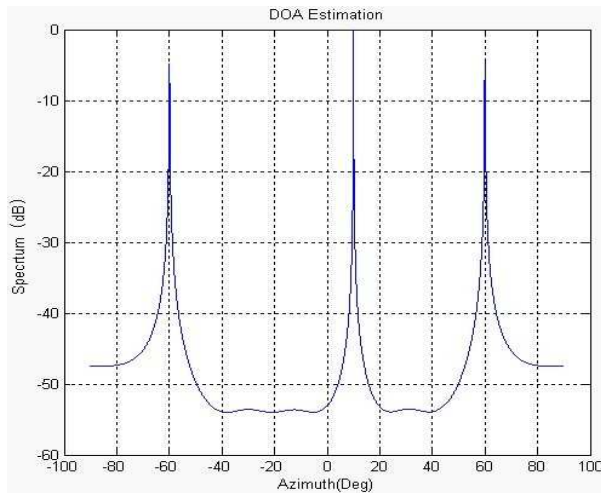


Figure 4: DOA estimation by MUSIC algorithm.

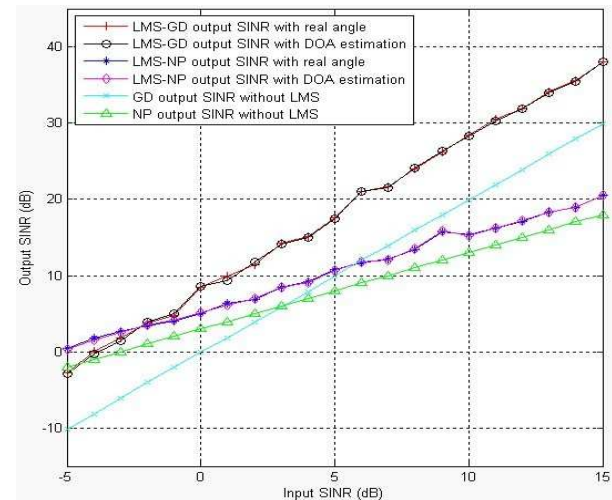


Figure 5: Performance comparison between GR and NP.

algorithm. All signals are set as Gaussian random sequences with the mean equal to 0. We compare the NP receiver and GR by performance under identical input conditions.

Figure 4 presents the DOA estimation results of MUSIC algorithm. After DOA estimation process, the MSG gets the DOA information about the desired signal and generates the reference signal. The simulation results comparing the NP receiver and GR performances are presented in Fig. 5 in the form of the relation between the input signal-to-interference-noise ratio (SINR) and the output SINR for both receivers. In general case, the output SINR increases when the input SINR increases and the DOA estimation error decrease. We can see from Fig. 5 that GR with LMS beamformer has a good performance for interference cancellation in both cases when LMS beamformer is used. In practice, the GR overcomes NP by detection performance applying the LMS algorithm with and without DOA estimation.

6. CONCLUSION

The GR with LMS beamformer has a good ability for interference cancellation, and MUSIC algorithm is a high resolution technique for DOA estimation. This paper deals with the employment of DOA estimation algorithm (MUSIC) and GR with LMS beamformer when the DOA is unknown. The simulation results show a promising performance that for a practical SINR values, GR overcomes the NP receiver under the same conditions using MUSIC algorithm and LMS beamformer.

REFERENCES

1. Tuzlukov, V., "A new approach to signal detection theory," *Digital Signal Processing*, Vol. 8, No. 3, 166–184, 1998.
2. Tuzlukov, V., *Signal Detection Theory*, Springer Verlag, New York, USA, 2001.
3. Tuzlukov, V., *Signal Processing Noise*, CRC Press, Boca Raton, FL, USA, 2002.
4. Tuzlukov, V., *Signal and Image Processing in Navigational Systems*, CRC Press, Boca Raton, FL, USA, 2005
5. Tuzlukov, V., *Signal Processing in Radar Systems*, CRC Press, Boca Raton, FL, USA 2012.
6. Jin Gui, L., S. S. Modar, and V. Tuzlukov, "Generalized receiver with non-blind beamforming based on LMS algorithm," *Proceedings of International Conference on ICT Convergence 2012*, 635–638, Jeju Island, Korea, Oct. 15–17, 2012.
7. Usha, M., K. Nalini, and P. Ganesh, "Non-blind adaptive beamforming algorithms for smart antennas," *IJRRAS*, Vol. 6, No. 4, 491–496, 2011.
8. Lavate, T. B., "Performance analysis of MUSIC and ESPRIT DOA estimation algorithms for adaptive array smart antenna in mobile communication," *Proceedings of International Conference on Computer and Network Technology 2010*, 153–158, Bangkok, Thailand, Apr. 2010.

Rain Attenuation Prediction Using Frequency Scaling Technique at Tropical Region for Terrestrial Link

Ulaganathen Kesavan^{1,2}, A. R. Tharek¹, and M. Rafiqul Islam³

¹Wireless Communication Centre, Fakulti Kejuruteraan Elektrik
Universiti Teknologi Malaysia, Skudai, Johor 81310, Malaysia

²Electrical Engineering Department

Sultan Haji Ahmad Shah Polytechnic of Malaysia, Malaysia

³Faculty of Engineering, International Islamic University, Malaysia

Abstract— The radio waves propagates through the earth atmosphere will be attenuated due to presence of the atmosphere particles such as water vapor, water drops and the ice particles. Meantime the atmospheric gases and rain will absorb the scatter the radio path consequently degrade the performance of the link. This paper presents studies on rain attenuation at 26 GHz, which is widely used for local multipoint distribution service deployment by using the measured and prediction methods for terrestrial microwave links point to point in tropical regions. Basically the models described in this paper include those of the ITU-R, revised Moupfouma and revised Silva Mello model. The main objective of these studies to identify most suitable rain attenuation prediction model for tropical region like Malaysia. In another hand comparison in term of attenuation on Ku band and Ka band. at various reduction factor models are also been discuss. It was found at lower operating frequency and lower rain rates the ITU-R models fits well whereby at the higher operating frequency with higher rain rates the Moupfouma model is more adequate compare with other models. This paper will help provide useful information for researchers to make good considerations in rain attenuation predictions for a terrestrial link operating frequency at 26 GHz in a tropical region.

1. INTRODUCTION

Generally at frequencies below 7 GHz, excess attenuation due to rainfall and atmospheric gaseous, frozen particles such as snow, ice crystals is very small and can be neglected in radio system design. However at frequencies above 7 GHz liquid rain drops in the form of absorption and scattering do become serious contributes to transmission losses [1–3]. The attenuation on any given path depends on the value of specific attenuation, frequency, polarization, temperature, path length and latitude [4]. The rainfall causes absorption and scattering of radio waves which result in the reduction of the receive signal level. Most of the researchers and studies related to rain attenuation are based on data obtained from the temperate region. The models do not give an accurate prediction of rain attenuation in tropical and equatorial regions. Therefore, more studies are needed in order to obtain a better rain attenuation prediction models that suits the tropical and equatorial climates and establishing a reliable prediction method for rain attenuation. The 26-GHz frequency band is allocated to broadband wireless access (BWA) in many parts of the world. However, little is known about the effects of persistent heavy rainfall in tropical regions. The 26-GHz band offers advantages such as relatively high bandwidth resulting in a much higher bit rates available to individual users when compared to a carrier of around 10 GHz used typically in tropical regions. It also allows the reuse of spectrum with a higher density of smaller cells resulting in a higher network capacity in urban and rural areas [5]. These networks are particularly suited for network connection to small offices or suburban homes to high-capacity public switching and backbone networks for wireless multimedia services. Wireless information required by customers on the move includes internet, multimedia, and voice. The study of radio wave propagation in such an environment is necessary for optimization of system deployment.

2. EXPERIMENTAL SET-UP

A link of path length 5.83 km was set up in Johor Bahru, Malaysia. Both the transmitter and receiver operate at a frequency of 15 GHz. The received signal levels were sampled every minute. Three years precipitation data were collected from the Casella rain gauge installed at the measurement site (Jan. 2006–Dec. 2008). These data have been used to investigate the link. The precipitation data and rain attenuation data was recorded at the same period of time. The rain gauge used is a tipping bucket type and it has sensitivity of 0.5 mm. It records the total rainfall

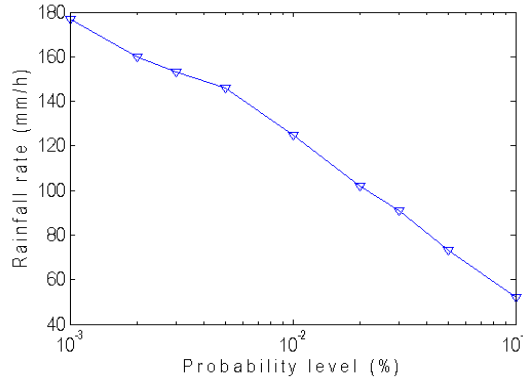


Figure 1: Rainfall rate CCDF for Johor Bahru (3 years).

Table 1: Specifications of the 15 GHz link.

Link location	Hop length (km)	Frequency band (GHz)	Maximum transmit power (dBm)	10^{-6} BER (2×2 Mbs) received threshold	Antenna for both transmit and receive side	
					Size (m)	Gain (dBi)
Johor Bahru	5.83	15	+18.0	-84.0	0.6	37.0

occurring in each minute without recording non rainy events; therefore the rain rate is recorded as an integral multiple of 30 mm/h or 0.5 mm/min. Table 1 shows the link specifications, while Figure 1 presents the complementary cumulative distribution function (CCDF) of the rainfall rate for an average of three years in Johor Bahru. This graph been plotted to show the relationship of the rain rate at various percentage of time throughout the period of the data collected during this experimental. It was observed at 0.01% of time, the rain rate was 125 mm/hr recorded.

Further analysis have been conducted to study the effects of rain attenuation on this link at higher frequencies, 26 GHz. The rain attenuation values at these frequencies have been obtained by inverting the available 15 GHz rain attenuation data, using the frequency scaling technique as follows [6]:

$$A_1(f_1)/A_2(f_2) = (\Phi_2/\Phi_1)^{1-H(\Phi_1,\Phi_2,A_1)} \quad (1)$$

$$\text{where, } \Phi(f) = f^2/1 + 10^{-4}f^2 \quad (2)$$

$$H(\Phi_1, \Phi_2, A_1) = 1.12 \cdot 10^{-3}(\Phi_2/\Phi_1)^{0.6}(\Phi_1 A_1)^{0.55} \quad (3)$$

A_1 and A_2 are the equivalent probable values of the excess rain attenuation at frequencies f_1 and f_2 respectively and frequency f is in GHz. Figure 2 shows the comparison of measured attenuation at 26 GHz with those predicted by Mello, Moupfouma and ITU-R at different probability levels of the rainfall rate.

3. RESULTS AND DISCUSSIONS

The CCDF of measured rain attenuation at 15 GHz is compared with the predictions of ITU-R, revised Moupfouma and revised Silva Mello.el. As per shown in Figure 2, the measured rain attenuation is 18.08 dB and 35.5 dB, at 0.1% and 0.01%, respectively. In comparison, the predicted attenuations at 0.1% are 12.40 dB, 22.33 dB and 12.60 dB by Mello, Moupfouma and ITU-R models, respectively. Similarly, the corresponding predicted values at 0.01% are 24.50 dB, 57.16 dB and 32.40 dB, respectively. These indicate that Moupfouma predictions are very close at 0.1% (almost 22.32 dB), which overestimate the measured value by 23.5%; whereas at 0.01%, the predictions are 57.16 dB, respectively, which overestimates the measured values by 61%.

Silva Mello.el predictions largely underestimate the measured attenuation at 0.1% and 0.01% of the time. For instance, the prediction errors (overestimates) at these time percentages are almost the same, 31% and 30%. It has been observed that the ITU-R model at 0.1% of time, with prediction errors around 30% but closely agrees with the measured value at 0.01% of the time,

with little error 8.7%. However, it underestimates the measurements at other percentages, more especially at higher rain rates.

As seen in Figure 3, the measured rain attenuation at 26 GHz is 43.18 dB and 87.23 dB, at 0.1% and 0.01%, respectively. In comparison, the predicted attenuations at 0.1% are 29.56 dB, 50.43 dB and 28.58 dB by Mello, Moupfouma and ITU-R models, respectively. Similarly, the corresponding predictions at 0.01% are 53.67 dB, 115.24 dB and 65.33 dB, respectively. Also, it can be seen Moupfouma predictions are very close at 0.1% (almost 50.4 dB), which overestimate the measured value by 14.3%; whereas at 0.01%, the predictions are 115.24 dB, respectively. Therefore these model largely overestimate the measured attenuation at all percentages of time, worse still at higher rain rates. On the other hand, Mello predictions largely underestimate the measured attenuation at 0.1% and 0.01% of the time. For instance, the prediction errors at these time percentages are 31.5% and 38.5%.

From the figure it can be seen Moupfouma predictions largely overestimate the measured attenuation at all percentages, compared to the other two models. At 0.1% of the time, Moupfouma models predicted same value for rain attenuation, but the values are different at other percentages. In the case of ITU-R, the predictions are 28.58 dB and 65.33 dB, respectively. From these results, one can say that the ITU-R model most closely agrees with the measurements compared to other models. For instance, it has been observed that the percentage error, at 0.1% and 0.01% of the time, in ITU-R model is approximately 33.6% and 25%. The prediction errors are worse at higher rain rates, implying that the model is not suitable at higher frequencies.

Further analysis been conducted by comparing the rain attenuation on 15 GHz and 26 GHz which is at Ku Band and Ka band. Based on data presented in Table 2, it is clearly indicates the rain attenuation at 0.01% of time exceeded for operating frequency at 26 GHz is higher by 52.72 dB.

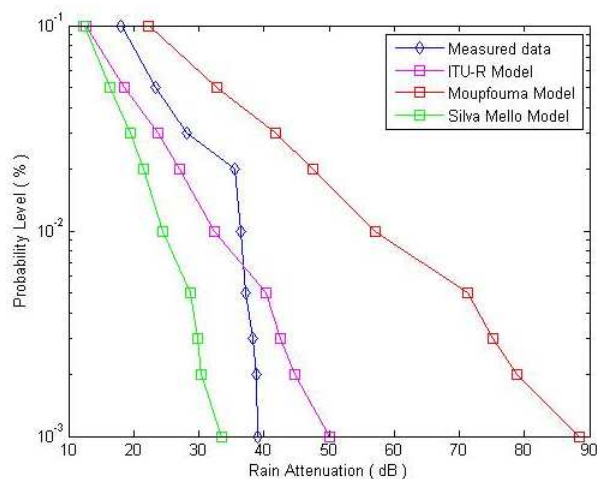


Figure 2: Comparison of rain attenuation CCDF at 15 GHz.

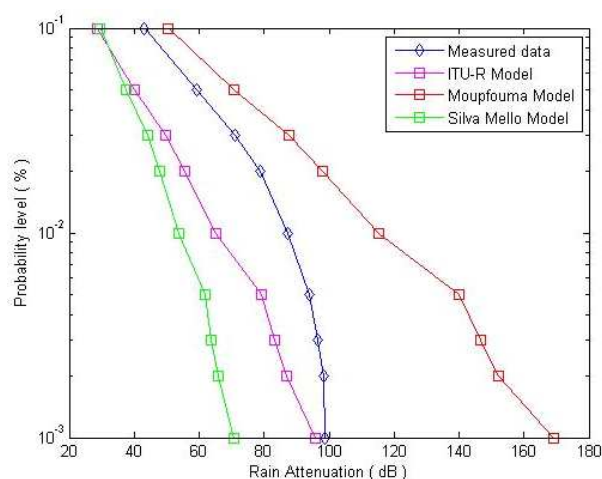


Figure 3: Comparison of rain attenuation CCDF at 26 GHz.

Table 2: Comparison of measured rain attenuation at 15 GHz and 26 GHz.

Percentage of Time (%)	Rain Attenuation (dB)	
	$f = 15$ GHz	$f = 26$ GHz
0.1	17.08	43.18
0.05	23.44	59.26
0.03	28.14	71.14
0.02	31.18	78.83
0.01	34.50	87.22
0.005	37.12	93.84
0.003	38.23	96.65
0.002	38.92	98.40
0.001	39.00	98.60

It is almost same recommended in a reviewed literature review [9] to use fade margin more than 40 dB when a link is operating at higher frequency such as Ka Band. The outcome of this finding conclude the literature findings. Even one of the author in his published paper title “Case Study of Rain Attenuation At Ka Band” [10] has mentioned the attenuation at Ka Band is 30 dB compare to the Ku Band is only 12 dB using different model for validation purpose.

4. CONCLUSIONS

From the results presented, ITU-R predictions are the closest to the measured attenuation, compared to the other three models studied in this work. For the 15 GHz link, it has been observed that the ITU-R model closely agrees with the measured value at 0.01% of the time, with little error (8.7%). However, it underestimates the measurements at other percentages, more especially at higher rain rates. The ITU-R model seems to be most suitable for predicting terrestrial rain attenuation in tropical like Malaysia at lower operating frequency, compared to other models. The rain attenuation at higher operating frequency is more than double in term of percentages, most likely the Moupfouma model is suitable with little error (14.3%). However this result is still preliminary and more data need to be collected for accurate results. For future work it is necessary to collect longer rainfall rate data in order to carry out further analyse with more effectively and collect actual measured rain attenuation data for 26 GHz link. This information will be very useful to implement frequency diversity technique for mitigating rain effects in future especially for the tropical region.

ACKNOWLEDGMENT

The authors would like to acknowledge and express sincere appreciation to Technology University of Malaysia (UTM) and Ministry of Higher Education (MOHE) for financing the research project under the Research University Grant (RUG), title: Rain propagation studies and mitigation technique at 26 GHz using 5.8 GHz for point to point application, vote No. Q. J130000.7123.01H05.

REFERENCES

1. Crane, R. K., *Electromagnetic Wave Propagation Through Rain*, John Wiley & Son Series, 1996.
2. Crane, R. K., “Prediction of attenuation by rain,” *IEEE Transaction on Communication*, Vol. 28, No. 9, September 1980.
3. Panagopoulos, A. D., P.-D. M. Arapoglou, and P. G. Cottis, “Satellite communications at Ku, Ka and V bands: Propagation impairments and mitigation techniques,” *IEEE Communications Surveys and Tutorials*, 2004.
4. Kanellopoulos, J. D., et al., “Rain attenuation problems affecting the performance of microwave communication systems,” *Ann. Telecommun.*, Vol. 45, Nos. 7–8, 1990.
5. La Maire, R. O., A. Krishna, P. Bhagwat, and J. Panian, “Wireless LAN’s and mobile networking: Standards and future directions,” *IEEE Commun. Mag.*, Vol. 34, No. 8, 86–94, August 1996.
6. Recommendation ITU-R P.530-13 (10/2009), “Propagation data and prediction methods required for the design of terrestrial line of sight systems,” October 2009.
7. Moupfouma, F., “Electromagnetic waves attenuation due to rain: A prediction model for terrestrial or L.O.S SHF and EHF radio communication,” *J. Infrared Milli. Terahz. Waves*, Vol. 30, 622–632, 2009.
8. Silva Mello, L. A. R., M. S. Pontes, R. S. L. Souza, and N. A. Garcia, “Prediction of rain attenuation in terrestrial link using full rain rate distribution,” *Electron Lett.*, Vol. 43, No. 25, 1442–1443, 2007.
9. Freeman, R. L., *Radio System Design for Telecommunication*, 3rd Edition, Wiley-IEEE Press, April 2007, ISBN: 978-0-471-75713-9.
10. Mandeep, J. S., N. Y. Yann, and S. I. S. Hassan, “Case study of the rain attenuation at Ka band,” *Journal of Electromagnetic Waves and Applications*, Vol. 22, Nos. 11–12, 1517–1525, 2008.

New Indoor Propagation Channel Model for Location Purposes

Alain Moretto and Elizabeth Colin

Allianstic, ESIGETEL, Villejuif, France

Abstract— In this paper, we propose a deterministic, close to indoor physical phenomena and hall orientated indoor propagation model for localization purposes. This multi-frequency, multi-path indoor channel model is based on geometrical optics (GO). The received electromagnetic power is given as a function of the carrier frequency, the distance between emitting and receiving antennas, the ceiling height and takes into account both building materials dielectric properties and radiation Rx/Tx antenna’s pattern. Received power simulations are compared to measurements with an UHF RFID system using active tags at 868 MHz and 433 MHz in a 20 m long ground floor environment. A good match is noticed.

1. INTRODUCTION

Accuracy and reliability are critical features for indoor location systems; however, nowadays techniques don’t provide enough accuracy for distance evaluation. Metrics as receiver signal power, Angle of Arrival (AoA), Time of Flight (ToF) are not directly related to distance or relative position between emitter and receiver. This is due to multi-path and fading phenomena that can be dominating in indoor environments. Improving indoor channel model is a way to allow a more accurate positioning, but indoor channel has very particular and complex properties. Indoor channel is site specific, multi-path and, most of the time, Non Light-of-Sight (NLOS).

The paper is organized as follows. In Section 2, we present the most commonly used indoor propagation models for distance estimation purposes and we focus on the strengths and limits of these models so as to propose our propagation model. Section 3 compares simulated received power with measurements to validate our model. The dependence of the received power according to two environment parameter that are of great interest in a location context within a hall, ceiling height and building material properties, is studied in Section 4.

2. INDOOR PROPAGATION CHANNEL MODELING

2.1. Indoor Channel Models

We can find two main kinds of models, statistical (also called empirical) ones, based on large measurement campaigns and deterministic ones, based on physical laws such as Maxwell laws [1, 2].

Empirical models as One-slope, Motley-Keenan [3] and COST231 are widely used in location applications because of their simplicity [4, 5]. However, those path-loss models do not take into account multi-paths phenomena; as a consequence, a sub-meter distance estimation precision cannot be reached even with a robust signal post-processing.

Ray-tracing techniques can be found among deterministic models [6]. These latter models are based on geometrical optics (GO) and diffraction theory [7, 8]. Their computation may be time consuming but predictions are closer to measurements than those given by empirical models.

The model we suggest afterwards, is based on GO and estimates the received electromagnetic power as a function of the distance to the emitting antenna and its radiation pattern, the ceiling height, the number of vertical bounces (reflections on ground/ceiling) and building materials dielectric properties.

2.2. Suggested Model

In an open space indoor environment (flat amphitheater, airport/hospital hall ...), that’s to say every time ceiling height is “small” compared to ground dimensions, we can simply model the propagation channel with two perfectly smooth parallel diopters. Thus we can neglect diffraction phenomena which will speed up calculations.

Our 2D model (see Figure 1) takes into account the radiation pattern of the emitting (A on Figure 1) and receiving (B on Figure 1) antennas and assumes that the incident power is reflected by the floor and the ceiling with respective reflection indexes ρ_{floor} and ρ_{ceiling} .

Once we know the height of the emitting and the receiving antennas (h_E and h_R), the distance d between them as well as the height of the ceiling (H), we calculate the angle that allows the power to be received. This angle “ i ” is different if the power initially spreads out of antenna A towards the roof (i_{up}) or towards the floor (i_{low}) and depends on the number N of successive bounces.

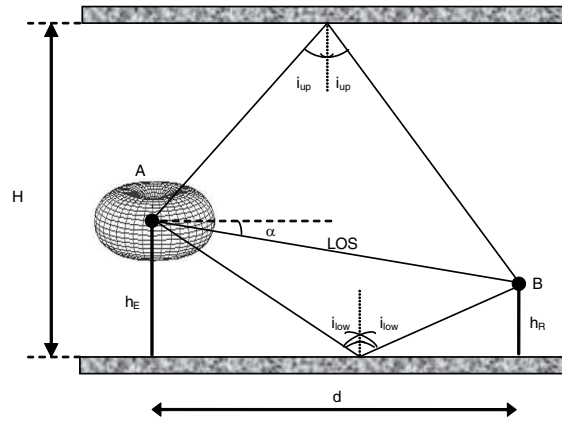


Figure 1: Reflexion of electromagnetic energy emitted by a dipole antenna on the floor (low index) and the ceiling (up index). Only one reflection is drawn for readability considerations.

The orientated angle α refers to the angle between the horizon and the line of sight path (LOS).

The incident electrical Field \vec{E} at the Rx Antenna B is the vector sum of the LOS (\vec{E}_{LOS}) and the so-called “low” (\vec{E}_{low}) and “up” (\vec{E}_{up}) contributions.

$$\vec{E} = \vec{E}_{LOS} + \vec{E}_{up} + \vec{E}_{low} \quad (1)$$

If we assume both antennas to be isotropic, the electric Field mathematical classical expression is, at a distance r from the antenna:

$$E = A \exp(j\omega t - kr) \quad (2)$$

A is the amplitude and depends on the emission power ISO/IEC and ETSI standards and $k = \frac{2\pi}{\lambda} = \frac{\omega}{c}$ in the air.

Each contribution, as well as the global received electrical Field is given below:

$$\vec{E}_{LOS} = \frac{A \exp(j\omega t) \exp(-jkd_{LOS})}{d_{LOS}} \begin{vmatrix} \cos(\alpha) \\ -\sin(\alpha) \end{vmatrix} \quad (3)$$

$$\vec{E}_{up} = A \exp(j\omega t) \times \begin{vmatrix} \sum_{i \text{ odd}}^n \frac{\exp(-jkd(\text{up},i))}{d_{\text{odd},i}} \rho_{\text{ceiling}}^i \rho_{\text{floor}}^{i-1} \sin(i_{sup}) + \sum_{i \text{ even}}^n \frac{\exp(-jkd(\text{up},i))}{d_{\text{up},i}} \rho_{\text{ceiling}}^{\frac{i}{2}} \rho_{\text{floor}}^{\frac{i}{2}} \sin(i_{sup}) \\ - \sum_{i \text{ odd}}^n \frac{\exp(-jkd(\text{up},i))}{d_{\text{up},i}} \rho_{\text{ceiling}}^i \rho_{\text{floor}}^{i-1} \cos(i_{sup}) + \sum_{i \text{ even}}^n \frac{\exp(-jkd(\text{up},i))}{d_{\text{up},i}} \rho_{\text{ceiling}}^{\frac{i}{2}} \rho_{\text{floor}}^{\frac{i}{2}} \cos(i_{sup}) \end{vmatrix} \quad (4)$$

$$\vec{E}_{low} = A \exp(j\omega t) \times \begin{vmatrix} \sum_{i \text{ odd}}^n \frac{\exp(-jkd(\text{low},i))}{d_{\text{odd},i}} \rho_{\text{floor}}^i \rho_{\text{ceiling}}^{i-1} \sin(i_{low}) + \sum_{i \text{ even}}^n \frac{\exp(-jkd(\text{low},i))}{d_{\text{up},i}} \rho_{\text{floor}}^{\frac{i}{2}} \rho_{\text{ceiling}}^{\frac{i}{2}} \sin(i_{sup}) \\ \sum_{i \text{ odd}}^n \frac{\exp(-jkd(\text{low},i))}{d_{\text{low},i}} \rho_{\text{floor}}^i \rho_{\text{ceiling}}^{i-1} \cos(i_{low}) - \sum_{i \text{ even}}^n \frac{\exp(-jkd(\text{low},i))}{d_{\text{low},i}} \rho_{\text{floor}}^{\frac{i}{2}} \rho_{\text{ceiling}}^{\frac{i}{2}} \cos(i_{sup}) \end{vmatrix} \quad (5)$$

In the far Field approximation, in so far as both antennas are adapted the received electromagnetic power P_R is given by the Poynting relation:

$$P_R = \frac{1}{2} Z_0 \left\| \vec{E} \right\|^2 \quad (6)$$

where Z_0 is the air impedance.

It is quite easy to adapt these previous formulas to a Hertz or a dipole antenna for instance by simply taking into account the weighting factor of the radiation pattern.

3. COMPARISON WITH MEASUREMENT AND VALIDATION

Measurements are taken every meter in the ground floor of a 2.50 m ceiling height building. Our tracking device uses 433 MHz (ISO 18000-7) or 868 MHz (ISO 18000-6) RFID technology. We used the material “UTP Diff2” reader from ELA-Innovation with vertical dipole Rx/Tx antennas as well as their active “Thin line” RFID tags. Each measurement point is averaged over 20 successive acquisitions.

There are an infinite number of possible paths between antennas A and B, however it can be shown that the contribution of additional paths beyond $N = 100$ can be neglected. This will speed

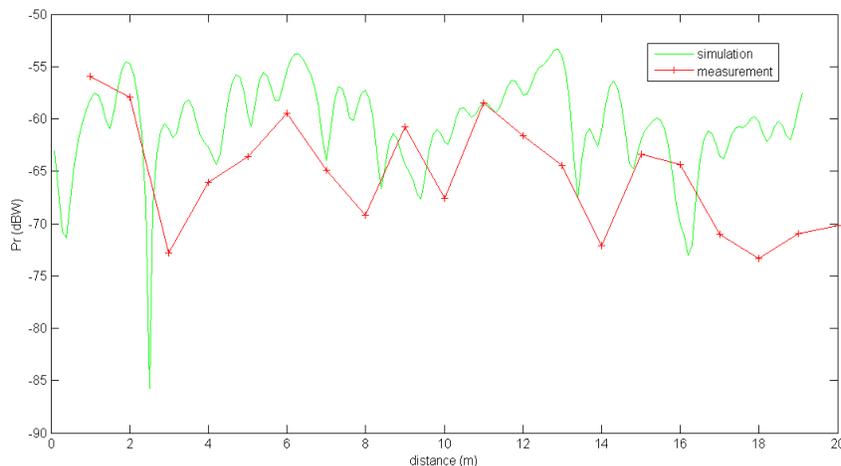


Figure 2: Comparison between measurements and simulation at 868 MHz in 20 m \times 20 m, 2.5 m high reinforced concrete.

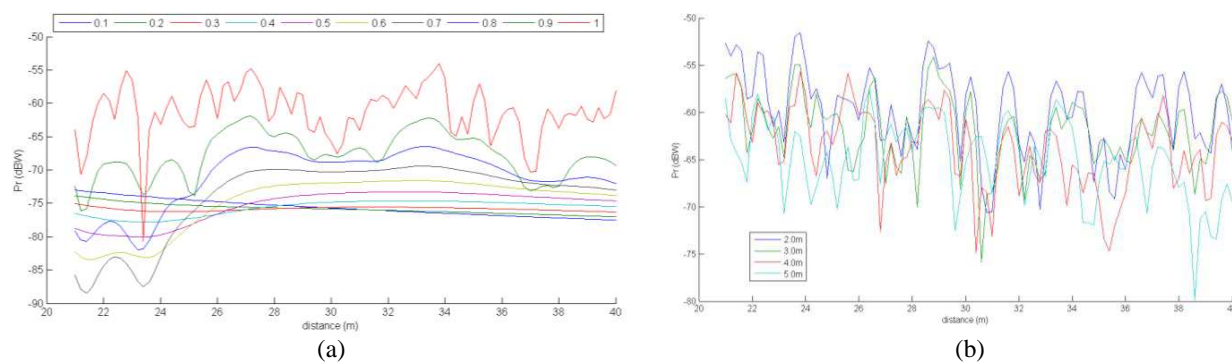


Figure 3: Received 868 MHz electromagnetic power in a 20 m \times 20 m, (a) 2.5 m high hall for different reflection indexes corresponding to different materials, (b) for different ceiling heights. Reflection index is 100%.

up the calculation time even more. Received power is simulated every 10 cm at 868 MHz with $\rho_{\text{floor}} = \rho_{\text{ceiling}} = 99\%$.

Despite its simplicity, our model shows a good agreement with measurements, both on a received signal level standpoint but also on a behavioral point of view. Not only the average simulated received power is compliant to a traditional One slope model but also the evolution of the simulated curve as a function of distance reflects the multipath phenomena. A field measurement campaign at 433 MHz, not presented in this paper, also validates our model.

4. PARAMETERS OF INTEREST FOR LOCALISATION IN A HALL

4.1. Dependence on Construction Materials

Many construction materials can be found in a building such as concrete, reinforced concrete, steel, wood, glass, doped glasses, plaster, brick mortar and composite material. Each one of these materials can be very complex and the key parameter, from an electromagnetic point of view, is their complex relative dielectric permittivity ϵ_r (as well as their conductivity σ that we won't use in this simplified model) [9–11].

As expected, absorbing materials reduce multi-paths and hence fast fading effects (see Figure 3(a)). In this case, path-loss models such as One-Slope model perfectly apply. On the contrary, high reflection indexes lead to numerous and deep fading effects. Since halls are made of composite materials, reflection indexes are difficult to evaluate; they should be considered as fitting parameters between simulation and measurements.

4.2. Dependence on the Ceiling Height

This simplified model can apply to many indoor empty (no people, no furniture) places such as gateways and airport or hospital halls. These different places can be characterized by the parameter H (height of the ceiling).

Figure 3(b) clearly points out the consequences of multipath propagation on the received signal strength for four different hall heights in the worst case (metallic environment). The same global behavior is observed for the four hall heights. As expected, the higher the ceiling is the greater the attenuation is and the lower the ceiling is the deeper fadings are. This theoretical study seems to prove the scalability of our model from office to vast airport or hospital halls.

5. CONCLUSIONS

Location systems mainly use simple models like One-Slope complemented by spatial filtering techniques like sequential Monte-Carlo methods. However, the performance of these methods is based on a priori knowledge of the channel. To improve the estimation of the position in a hall, we propose a propagation model based on geometrical optics that is simple enough not to influence the computation time, but that takes into account the multipath, the ceiling height and the type of materials.

ACKNOWLEDGMENT

Special thanks to Chouarhi Yacine for endless hours of Received Signal Strength Information measurements and for data acquisition interface programming. Thanks to ELA-Innovation support.

REFERENCES

1. Feuerstein, M. and T. S. Rappaport, *Wireless Personal Communications*, Kluwer Academic Publishers, 1993.
2. Sizun, H., *La Propagation des ondes Radioé Lectriques*, Springer, 2003.
3. Keenan, J. and A. Motley, "Radio coverage in buildings," *British Telecom Technology Journal*, Vol. 8, No. 11, Jan. 1990.
4. Joho, D., et al., "Modeling RFID signal strength and tag detection for localization and mapping," *IEEE Conference on Robotics and Automation*, 2009.
5. Nikitin, P. et al., "Phase based spatial identification of UHF RFID tags," *IEEE Conference RFID*, 2010.
6. Valenzuela, R., "Ray tracing prediction of indoor radio propagation," *PIMRC'94*, Sep. 1994.
7. Smulders, P. F. M., "Geometrical optics model for millimeter-wave indoor radio propagation," *Electronic Letters*, Vol. 29, No. 13, Jun. 1993.
8. Mudhafar, H.-A. and P. Kaveh, "A new statistical model for site-specific indoor radio propagation prediction based on geometric optics and geometric probability," *IEEE Transactions on Wireless Communications*, Vol. 1, 1, Jan. 2002.
9. Büyükköztürk, O., T.-Y. Yu, and J. A. Ortega, "A methodology for determining complex permittivity of construction materials based on transmission-only coherent, wide-bandwidth free-space measurements," *Cement & Concrete Composites*, Vol. 28, 349–359, 2006.
10. Sagnard, F., et al., "Microwave measurements of the complex permittivity of construction materials using Fresnel reflection coefficients and reflection ellipsometry," *IEEE AP-S International Symposium and USNC/URSI National Radio Science meeting*, 626–629, Boston, Jul. 8–13, 2001.
11. Thajudeen, C., A. Hoorfar, F. Ahmad, and T. Dogaru, "Measured complex permittivity of walls with different hydration levels and the effect on power estimation of TWRI target returns," *Progress In Electromagnetics Research B*, Vol. 30, 177–199, 2011.

Access Point Selection for WLAN Indoor Localization Systems Using RF Walk Test Data

C. Sapumohotti, M. Y. Alias, and S. W. Tan
Multimedia University, Malaysia

Abstract— Location fingerprinting utilizes periodic beacons transmitted by Wireless Local Area Network (WLAN) Access Points (APs) to provide localization in indoor environments. Currently there is lack of methods to quantify the amount of localization information provided by individual APs. Such a metric would enable the optimal placement of new APs as well as filtering out excess APs so as to reduce the resources consumed by indoor localization software in client devices. This paper proposes LocationInfo, a metric that utilizes walk test data for quantifying the localization efficacy of APs. Simulation based studies shows that LocationInfo is able to accurately select APs with high localization information.

1. INTRODUCTION

Availability of accurate location information in indoor environments adds significant value to mobile device users. Location information enables navigation in large indoor environments as well as context aware information delivery [1]. For outdoor localization, the Global Positioning System (GPS) [2] technology is the de-facto standard. However, as GPS requires line-of-sight (LOS) between GPS satellites and the client device for accurate localization [1, 3, 4], it has limited application in indoor environments. Recent proliferation of WLAN devices presents an opportunity to provide indoor localization by utilizing the unique WLAN beacon received signal strengths (RSS) corresponding to different locations in the map. This method is referred to as location fingerprinting.

Location fingerprinting utilizes periodic beacons broadcasted by WLAN AP to client devices. A typical location fingerprinting implementation consists of two phases which are referred to as online phase and offline phase [5]. In the offline phase which is also known as calibration phase, RSS data collected at predefined locations (referred to as calibration points) and the corresponding location information is stored in a database (referred to as radio map). In the online phase, the beacon RSS measured in real-time by a client device is compared with the radio map to infer its location. The most costly operation associated with location fingerprinting systems is the offline calibration phase. This is non-trivial and requires significant amount of manual labor.

There are several challenges when deploying location fingerprinting systems. For example, there is no reliable method to identify the optimal locations to place APs prior to the calibration phase. Placing APs in non-optimal positions could result in poor localization accuracy in the online phase and cause the offline phase to be repeated. Another challenge is associated with the limited processing and communication resources in client devices. This is most significant when there are a large number of APs in the radio map as the computation power required by the localization algorithm increases with the number of APs. In addition, not all APs provide the same localization accuracy. Hence, filtering out APs which have a low impact on localization accuracy can reduce the computation and bandwidth requirement imposed by the localization software. For example, *MaxMean* [6] metric and *InfoGain* [7] metric have been proposed for this purpose. However, a filtering process prior to the calibration phase for assessing which APs provide the best accuracy would be helpful in order to verify the long-term availability of these APs.

In the *MaxMean* method, the mean AP RSS was used as a metric and the set of APs with the highest mean was chosen to be included in the radio map. While the *MaxMean* method is simple, it does not work well in scenarios such as the case when APs are located in the corridors. This is because of the multipath propagation effect which is highly pronounced in such environments. Consequently, APs that have high RSS may result in low localization accuracy. The *InfoGain* metric adopts information theory to model the localization capabilities of APs. InfoGain of an AP is defined as

$$InfoGain(AP_i) = H(G) - H(G|AP_i) \quad (1)$$

Assuming the user locations are uniform distributed, the initial entropy of the system is given by

$$H(G) = -\log\left(\frac{1}{N}\right) \quad (2)$$

where N is the number of calibration points (grids) in the system. The conditional entropy of an AP is given by

$$H(G|AP_i) = - \sum_v \sum_{j=1}^n P(G_j, AP_i = v) \log(P(G_j|AP_i = v)) \quad (3)$$

where summation is carried out at each grid point for all possible set of RSS for the AP.

This paper proposes a novel metric referred to as LocationInfo for the purpose of quantifying the localization efficacy of APs. First, LocationInfo computes an information theory based metric using walk test data. A walk test as the name suggested uses the device to automatically collect RSS samples at a periodic scan interval while walking through the corridors covered by the radio map. A scan interval of 1 second is used in this work. Typically a walk test can be completed in a few minutes while an offline calibration phase which could take a few hours. In other words, walk test is much more trivial and could be repeated multiple times with low overhead. Next, the APs with the highest LocationInfo will be selected for to generate radio map. Compared to InfoGain which is also based on information theory, LocationInfo exploits the spatial relationship between adjacent walk test points and is able to include the discriminative ability of ambient APs. Furthermore, LocationInfo uses probability distributions to represent the RSS likelihood at each walk test point.

2. LOCATIONINFO METRIC

In order to calculate LocationInfo, the walk test is sampled at 1 m resolution and the resulting walk test points are interpreted as a set of grids with 1 m separation. The problem of localization is then viewed as determining the grid when a RSS vector is given. The Information value of each AP is given by the amount of uncertainty of localization removed due to the RSS information of that AP.

The marginal RSS likelihood distribution for the i th AP in a th grid is defined as

$$P(AP_i = b|G = a) = \int_{b-0.5}^{b+0.5} N(x) dx \quad (4)$$

In Eq. (4), the function $N(X)$, given in Eq. (5), is the normal distribution with mean \bar{x} given by the RSS of the walk test sample collected in the grid, while the variance s is equal to 2 dB.

$$N(x) = \frac{1}{\sigma\sqrt{2\pi}} e^{-0.5\left(\frac{x-\bar{x}}{s}\right)^2} \quad (5)$$

In order to represent the effect of other APs in the radio map, a random variable known as *ambient discriminator* is introduced. The expected value of ambient discriminator at a th grid is given as

$$E[(D|G = a)] = AS \times a \quad (6)$$

The probability distribution of the *ambient discriminator* is given by a uniform distribution given by

$$P[(D|G = a)] = \frac{1}{W + 1} \quad (7)$$

where the window size is W and the range of value for D is such that

$$|D - E[(D|G = a)]| \leq \frac{W}{2} \quad (8)$$

For this research, a window size of 8 was chosen. This allows for comparison of grids up to 4 m away from the current grid in both directions. Given the marginal likelihood distributions for AP RSS in a grid and ambient discriminator, the *LocationInfo* metric is defined as

$$LocationInfo(AP_i) = I(G; AP_i, D) = H(G) - H(G|AP_i, D) \quad (9)$$

Assuming uniform probability distribution for user locations, the initial entropy of the system is defined similar to *InfoGain*. The conditional entropy in the equation is defined as

$$H(G|AP_i, D) = - \sum_{a=1}^N \sum_{b=RL}^{RU} \sum_{c=AL}^{AU} P(AP_i = b, D = c, G = a) \log(P(G = a|AP_i = b, D = c)) \quad (10)$$

The summation limits for the AP beacon RSS is from $RL = -96$ dBm to $RU = -20$ dBm. A lower limit of -96 dBm was chosen because the minimum value reported by the WLAN device is -95 dBm and a RSS value of -96 dBm is assigned for missing beacons. The -20 dBm is the upper limit and is valid unless the AP and client are very close, e.g., in the range of a few centimetres. The summation limits for the ambient discriminator is given by AL and AU .

3. SIMULATION RESULTS AND DISCUSSION

The simulation was conducted using WiLocSim [8] simulation testbed for a large rectangular space (see Figure 1) with dimension of $30\text{ m} \times 50\text{ m}$ where the coordinate origin is located at the upper left corner. 22 APs are located as shown in Figure 2. The objective of the simulation is to determine the localization error of the radio map as the APs with low localization information are removed from the radio map based on localization efficacy metrics (*MaxMean*, *InfoGain* and *LocationInfo*). The walk test path is given by the dotted line at $x = 15\text{ m}$ line and the radio map is built on the same line with 1 m separation between calibration points. 60 samples are collected at each of these calibration points. The test points which are used to evaluate the localization error are located within the dashed lines which are located at $x = 14.5\text{ m}$ and $x = 15.5\text{ m}$. 5000 test points are simulated and the localization error is calculated by considering the average difference between location estimates and actual locations of these test points. The nearest neighbour classification [5, 9] was used as the localization algorithm.

The simulation results are given in Figure 2. The results clearly show the localization error of the set of APs selected by *LocationInfo* is less than those of *MaxMean* and *InfoGain*, especially when the number of APs is low (i.e., ≤ 4). In other words, *LocationInfo* can be used to select APs to yield good localization accuracy while maintaining low overhead at client devices. As the

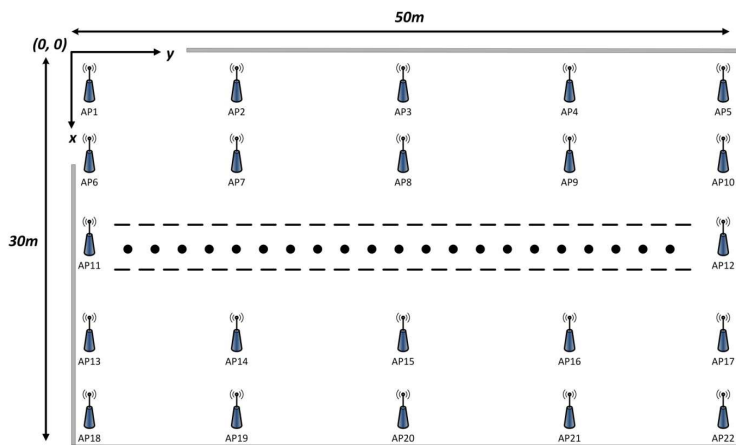


Figure 1: Simulation setup.

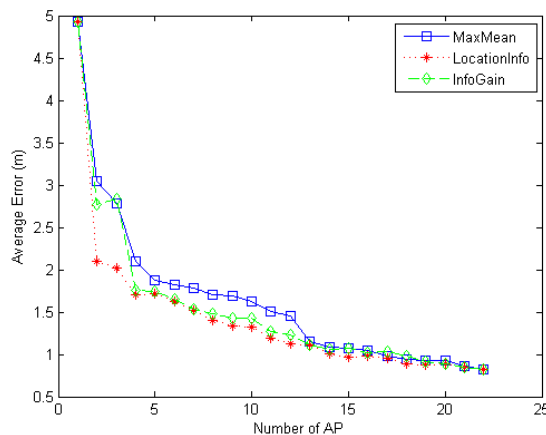


Figure 2: Simulation results.

number of APs included in the Radio Map is increased, the curves converge and the reduction of localization error shows diminishing returns.

4. CONCLUSIONS

In this paper, a metric for quantifying the localization ability of WLAN AP was proposed. The proposed metric is developed based on information theory and it is referred to as *LocationInfo*. This metric can be used to solve optimal AP placement as well as optimization of the radio map. Our simulation results show that *LocationInfo* outperformed the methods available in literature.

ACKNOWLEDGMENT

The authors would like to thank Ministry of Higher Education (MOHE), Malaysia for supporting this work.

REFERENCES

1. Zeimpekis, V., G. M. Giaglis, and G. Lekakos, "A taxonomy of indoor and outdoor positioning techniques for mobile location services," *Journal of ACM Special Interest Group on Electronic Commerce*, Vol. 3, 19–27, 2002.
2. Engee, P. K., "The global positioning system: Signals, measurements and performance," *Int. J. Wireless Inf. Netw.*, Vol. 1, No. 2, 83–105, 1994.
3. Hightower, J. and G. Borriello, "Location systems for ubiquitous computing," *IEEE Computer Mag.*, Vol. 34, No. 8, 57–66, 2001.
4. Alsindi, N., X. Li, and K. Pahlavan, "Performance of TOA estimation algorithms in different indoor multipath conditions," *2004 IEEE Wireless Communications and Networking Conference*, Vol. 1, 495–500, Mar. 21–25, 2004.
5. Honkavirta, V., T. Perala, S. Ali-Loytty, and R. Piche, "A comparative survey of WLAN location fingerprinting methods," *6th Workshop on Positioning, Navigation and Communication*, 243–251, Mar. 19, 2009.
6. Youssef, M. A., A. Agrawala, and A. Udaya Shankar, "WLAN location determination via clustering and probability distributions," *Proceedings of the First IEEE International Conference on Pervasive Computing and Communications*, 143–150, Mar. 23–26, 2003.
7. Chen, Y., Y. Qiang, Y. Jie, and X. Chai, "Power-efficient access-point selection for indoor location estimation," *IEEE Transactions on Knowledge and Data Engineering*, Vol. 18, No. 7, 877–888, Jul. 2006.
8. Sapumohotti, C., M. Y. Alias, and S. W. Tan, "Wilocsim: Simulation testbed for WLAN location fingerprinting systems," *Progress In Electromagnetics Research B*, Vol. 46, 1–22, 2013.
9. Bahl, P. and V. N. Padmanabhan, "RADAR: An in-building RF-based user location and tracking system," *Proc. IEEE Conf. Comput. Commun.*, 775–784, 2000.

Evaluation of Singular Potential Integrals with Linear Source Distribution

W. T. Sheng, Z. Y. Zhu, G. C. Wan, and M. S. Tong

Department of Electronic Science and Technology, Tongji University
4800 Cao'an Road, Shanghai 201804, China

Abstract— In the method of moments (MoM) with the Rao-Wilton-Glisson (RWG) basis function for solving electromagnetic (EM) surface integral equations (SIEs), one needs to evaluate singular potential integrals with linear source distribution. The weakly singular integrals could be evaluated with the well-known Duffy's method, but it requires a two-fold numerical integration. In this work, we develop a novel approach to handle the singular potential integrals by using a local polar coordinate system. The approach can automatically cancel the singularity and reduce the integrals to a one-fold numerical integration by deriving a closed-form expression for the integral over the polar coordinate. Numerical example is presented to demonstrate the effectiveness of the approach.

1. INTRODUCTION

Integral equation method is widely used for solving electromagnetic (EM) problems due to its unique features compared to other approaches [1]. The surface integral equations (SIEs) are preferred whenever available because they require less number of unknowns in the domain discretization. One fundamental problem in the integral equation method is the treatment of singularity or evaluation of singular potential integrals related to the Green's function. In the method of moments (MoM) with Rao-Wilton-Glisson (RWG) basis function [2] for solving the electric field integral equation (EFIE), one needs to handle the $1/R$ weak singularity, where R is the distance between an observation point and a source point. This is because one can move the gradient operator of the integral kernel, which is the dyadic Green's function, onto the basis function and testing function and lower the degree of singularity to facilitate the evaluation.

The $1/R$ weak singularity has been widely studied and many efficient evaluation techniques have been developed [3–5]. The well-known Duffy's method [6] is the earliest work on this subject and it mainly uses a variable change to produce an extra zero in the Jacobian which can be used to cancel the singularity and regularize the integrand. The resultant integrals are regular and can be accurately evaluated with numerical quadrature rules.

However, the Duffy's method requires a two-fold numerical integration after regularizing the integral kernel and may be inconvenient in implementation. In this work, we develop a novel approach to evaluate the singular potential integrals with a linear source distribution by using a special polar coordinate system. The approach can automatically cancel the singularity without using a variable change or coordinate transform and reduce the integral to a one-fold numerical integration by deriving a closed-form expression for the integral over the polar coordinate. The one-fold numerical integration is for the angular coordinate and has a very simple integrand which can be easily evaluated. The numerical example for EM scattering by a conducting object is presented to demonstrate the approach and good result can be observed.

2. SURFACE INTEGRAL EQUATIONS

To illustrate the novel approach for evaluating the weakly singular integral, we consider the EM scattering problem for a three-dimensional (3D) conducting object embedded in the free space with a permittivity ϵ_0 and a permeability μ_0 . The governing equation for the problem is the electric field integral equation (EFIE) which can be written as [1]

$$-\hat{n} \times \mathbf{E}^{inc}(\mathbf{r}) = \hat{n} \times i\omega\mu_0 \int_S \bar{\mathbf{G}}(\mathbf{r}, \mathbf{r}') \cdot \mathbf{J}_S(\mathbf{r}') dS', \quad \mathbf{r} \in S \quad (1)$$

where $\mathbf{E}^{inc}(\mathbf{r})$ is the incident electric field, $\mathbf{J}_S(\mathbf{r}')$ is the electric current induced on the conducting surface S , and \hat{n} is the unit normal vector of the surface. Also, $\bar{\mathbf{G}}(\mathbf{r}, \mathbf{r}')$ is the dyadic Green's function defined by

$$\bar{\mathbf{G}}(\mathbf{r}, \mathbf{r}') = \left(\bar{\mathbf{I}} + \frac{\nabla\nabla}{k_0^2} \right) g(\mathbf{r}, \mathbf{r}') \quad (2)$$

where $\bar{\mathbf{I}}$ is the identity dyad, k_0 is the wavenumber in the free space, and $g(\mathbf{r}, \mathbf{r}') = e^{ik_0 R}/(4\pi R)$ is the 3D scalar Green's function in which $R = |\mathbf{r} - \mathbf{r}'|$ is the distance between an observation point \mathbf{r} and a source point \mathbf{r}' . If the unknown current $\mathbf{J}_S(\mathbf{r}')$ is expanded by the RWG basis function, i.e.,

$$\mathbf{J}_S(\mathbf{r}') = \sum_{n=1}^N I_n \mathbf{\Lambda}_n(\mathbf{r}') \quad (3)$$

where $\mathbf{\Lambda}_n(\mathbf{r}')$ is the RWG basic function defined over the n th pair of triangular patches, I_n is the corresponding expansion coefficient, and N is the number of all pairs of triangular patches, then we can obtain the following matrix equation after using the RWG basic function as a testing function to test the EFIE

$$\begin{aligned} -\langle \mathbf{\Lambda}_m(\mathbf{r}), \mathbf{E}^{inc}(\mathbf{r}) \rangle &= i\omega\mu_0 \sum_{n=1}^N I_n \langle \mathbf{\Lambda}_m(\mathbf{r}), \bar{\mathbf{G}}(\mathbf{r}, \mathbf{r}'), \mathbf{\Lambda}_n(\mathbf{r}') \rangle \\ &= i\omega\mu_0 \sum_{n=1}^N I_n [\langle \mathbf{\Lambda}_m(\mathbf{r}), g(\mathbf{r}, \mathbf{r}') \mathbf{\Lambda}_n(\mathbf{r}') \rangle + \langle \nabla \cdot \mathbf{\Lambda}_m(\mathbf{r}), g(\mathbf{r}, \mathbf{r}') \nabla' \cdot \mathbf{\Lambda}_n(\mathbf{r}') \rangle] \end{aligned} \quad (4)$$

where we have moved the gradient operator in the dyadic Green's function onto the basis function and testing function, respectively. The integral kernel in the matrix equation is only in a $1/R$ weak singularity now and can be handled with the following novel approach. Note that the same singularity appears in the integral equations for dielectric or composite objects, so the developed treatment technique can be applied to those scenarios as well.

3. NOVEL APPROACH FOR EVALUATING THE SINGULAR POTENTIAL INTEGRALS

From Eq. (4), we can see that the singular integral takes two kinds of form resulting from the scalar potential and vector potential, respectively, i.e.,

$$I_1 = \int_{\Delta S} \frac{e^{ik_0 R}}{R} dS, \quad I_2 = \int_{\Delta S} \mathbf{\Lambda}_n(\mathbf{r}) \frac{e^{ik_0 R}}{R} dS \quad (5)$$

where ΔS is a triangular patch $\Delta p_1 p_2 p_3$ or integral domain as shown in Fig. 1. We establish a local Cartesian coordinate system (u, v, w) and polar coordinate system (ρ, θ) over the triangle plane, in which the projection of the observation point on the plane is chosen as the origin. Fig. 1(a) and Fig. 1(b) illustrate the situations when the origin is outside and inside the triangle, respectively. In such a coordinate system, the observation point is located at $(0, 0, w_0)$ while the source point lies on $(u, v, 0)$ or (ρ, θ) within the triangle, leading to $R = \sqrt{\rho^2 + w_0^2}$. Note that we have used the unprimed (u, v, w) or \mathbf{r} to indicate a source point and (u_0, v_0, w_0) to denote an observation point in the above. For the first integral I_1 , there is no singularity in fact in the situation of Fig. 1(a) since the origin is outside the triangle, but we can still derive a more friendly formulation to calculate

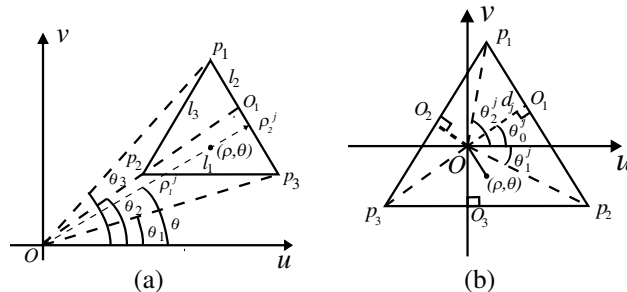


Figure 1: A local Cartesian coordinate system (u, v, w) and polar coordinate system (ρ, θ) are established over the plane of a triangular patch $\Delta p_1 p_2 p_3$. The projection of the observation point on the plane is chosen as the origin. (a) The origin is outside the triangle. (b) The origin is inside the triangle.

it, i.e.,

$$\begin{aligned}
I_1 &= \sum_{j=1}^2 \int_{\theta_j}^{\theta_{j+1}} d\theta \int_{\rho_1^j(\theta)}^{\rho_2^j(\theta)} \frac{e^{ik_0\sqrt{\rho^2+w_0^2}}}{\sqrt{\rho^2+w_0^2}} \rho d\rho \\
&= \sum_{j=1}^2 \int_{\theta_j}^{\theta_{j+1}} d\theta \int_{R_1^j(\theta)}^{R_2^j(\theta)} \frac{e^{ik_0R}}{R} \sqrt{R^2-w_0^2} d\left(\sqrt{R^2-w_0^2}\right) \\
&= \sum_{j=1}^2 \int_{\theta_j}^{\theta_{j+1}} d\theta \int_{R_1^j(\theta)}^{R_2^j(\theta)} e^{ik_0R} dR \\
&= \sum_{j=1}^2 \frac{1}{ik_0} \int_{\theta_j}^{\theta_{j+1}} \left[e^{ik_0R_2^j(\theta)} - e^{ik_0R_1^j(\theta)} \right] d\theta
\end{aligned} \tag{6}$$

where

$$R_1^j(\theta) = \sqrt{\rho_1^j(\theta) + w_0^2}, \quad R_2^j(\theta) = \sqrt{\rho_2^j(\theta) + w_0^2} \tag{7}$$

and $\rho_1^j(\theta)$ and $\rho_2^j(\theta)$ are the radial coordinates of the intersection points formed by the polar axis at the angle θ and two sides of the triangle and they can be easily determined by the slopes and intercepts of the sides. If b_1 and b_2 denote the intercepts and k_1 and k_2 denote the slopes of the two sides, respectively, then they can be found as

$$\rho_\ell^j(\theta) = \frac{b_\ell}{\sin(\theta) - k_\ell \cos(\theta)}, \quad \ell = 1, 2. \tag{8}$$

From the formulas, we can see that the singularity, if existing, moves to $R_1^j(\theta)$ or $R_2^j(\theta)$ when $\tan(\theta)$ is equal to one of slopes of the sides. This situation occurs only when one of the sides coincides with the line connecting the point o and the point o_1 . Fortunately, this singularity vanishes because the upper bound and lower bound of the integral with respect to θ are the same in this case and this result matches the reality, i.e., no singularity. On the other hand, there exists a singularity in the situation of Fig. 1(b) because the origin is inside the triangle. We divide the triangle patch into three subtriangles by connecting the origin with three vertices of the triangle and each subtriangle is specified by the parameters d_j , θ_0^j , θ_1^j , and θ_2^j as shown in the figure. In this case, the integral I_1 can be derived as

$$\begin{aligned}
I_1 &= \sum_{j=1}^3 \int_{\theta_1^j}^{\theta_2^j} d\theta \int_0^{d_j^\theta(\theta)} \frac{e^{ik_0\sqrt{\rho^2+w_0^2}}}{\sqrt{\rho^2+w_0^2}} \rho d\rho \\
&= \sum_{j=1}^3 \int_{\theta_1^j}^{\theta_2^j} d\theta \int_{R_0}^{R_j(\theta)} \frac{e^{ik_0R}}{R} \sqrt{R^2-w_0^2} d\left(\sqrt{R^2-w_0^2}\right) \\
&= \sum_{j=1}^3 \int_{\theta_1^j}^{\theta_2^j} d\theta \int_{R_0}^{R_j(\theta)} e^{ik_0R} dR \\
&= \frac{1}{ik_0} \sum_{j=1}^3 \int_{\theta_1^j}^{\theta_2^j} \left[e^{ik_0R_j(\theta)} - e^{ik_0R_0} \right] d\theta
\end{aligned} \tag{9}$$

where

$$R_0 = w_0, \quad R_j(\theta) = \sqrt{[d_j^\theta(\theta)]^2 + w_0^2} \tag{10}$$

and $d_j^\theta(\theta) = d_j / \cos(\theta - \theta_0^j)$. Obviously, there is no singularity in the above final formulation because $\theta - \theta_0^j$ cannot be 90° or $\cos(\theta - \theta_0^j)$ cannot be zero for a triangle and we can use a numerical quadrature rule to conveniently evaluate the one-fold integral with a very simple integrand. The above formulas are valid for all w_0 , including $w_0 = 0$ which is the singular case.

For the second integral I_2 , the involved RWG basis function is actually a first-order (linear) polynomial vector and its component could be written as $a_0 + a_1u + a_2v = a_0 + a_1\rho \cos \theta + a_2\rho \sin \theta$ in the local coordinate system, where a_0, a_1, a_2 are the known constants. When the basis function combines with the scalar Green's function, the combination of the first term a_0 will result in the integral I_1 which we have addressed above. The combination of the second and third term will yield the following integrals

$$\begin{aligned} \begin{pmatrix} I_{2a} \\ I_{2b} \end{pmatrix} &= \sum_{j=1}^2 \int_{\theta_j}^{\theta_{j+1}} \begin{pmatrix} \cos \theta \\ \sin \theta \end{pmatrix} d\theta \int_{\rho_1^j(\theta)}^{\rho_2^j(\theta)} \rho \frac{e^{ik_0\sqrt{\rho^2+w_0^2}}}{\sqrt{\rho^2+w_0^2}} \rho d\rho \\ &= \sum_{j=1}^2 \int_{\theta_j}^{\theta_{j+1}} \begin{pmatrix} \cos \theta \\ \sin \theta \end{pmatrix} d\theta \int_{R_1^j(\theta)}^{R_2^j(\theta)} \sqrt{R^2-w_0^2} e^{ik_0R} dR \end{aligned} \quad (11)$$

respectively, for the case of Fig. 1(a), and

$$\begin{aligned} \begin{pmatrix} I_{2a} \\ I_{2b} \end{pmatrix} &= \sum_{j=1}^3 \int_{\theta_1^j}^{\theta_2^j} \begin{pmatrix} \cos \theta \\ \sin \theta \end{pmatrix} d\theta \int_0^{d_j^{\theta}(\theta)} \rho \frac{e^{ik_0\sqrt{\rho^2+w_0^2}}}{\sqrt{\rho^2+w_0^2}} \rho d\rho \\ &= \sum_{j=1}^3 \int_{\theta_1^j}^{\theta_2^j} \begin{pmatrix} \cos \theta \\ \sin \theta \end{pmatrix} d\theta \int_0^{d_j^{\theta}(\theta)} \sqrt{R^2-w_0^2} e^{ik_0R} dR \end{aligned} \quad (12)$$

respectively, for the case of Fig. 1(b). For the nonsingular case or $w_0 \neq 0$, we cannot derive a closed-form formula for the inner integrals in the above and they are evaluated with the numerical quadrature rule. For the singular case, namely, $w_0 \rightarrow 0$ in the situation of Fig. 1(b), we can derive a closed-form formula for the inner integrals in the above, i.e.,

$$\begin{aligned} \begin{pmatrix} I_{2a}^s \\ I_{2b}^s \end{pmatrix} &= \sum_{j=1}^3 \lim_{w_0 \rightarrow 0} \int_{\theta_1^j}^{\theta_2^j} \begin{pmatrix} \cos \theta \\ \sin \theta \end{pmatrix} d\theta \int_0^{d_j^{\theta}(\theta)} \sqrt{R^2-w_0^2} e^{ik_0R} dR \\ &= \sum_{j=1}^3 \int_{\theta_1^j}^{\theta_2^j} \begin{pmatrix} \cos \theta \\ \sin \theta \end{pmatrix} \left[\frac{e^{ik_0d_j}}{ik_0} \left(d_j^{\theta}(\theta) - \frac{1}{ik_0} \right) - \frac{1}{k_0^2} \right] d\theta. \end{aligned} \quad (13)$$

4. NUMERICAL EXAMPLE

To demonstrate the effectiveness of the novel approach for evaluating the singular potential integrals, we present a typical numerical example for EM scattering by a perfectly electric conducting (PEC) object, but the technique can also be used in the problems with non-PEC objects. It is assumed that the incident wave is a plane wave with a frequency $f = 300$ MHz and is propagating along the $-z$ direction in free space. We calculate the bistatic radar cross section (RCS) of the object observed along the principal cut ($\phi = 0^\circ$ and $\theta = 0^\circ-180^\circ$) for the scatterer with both vertical

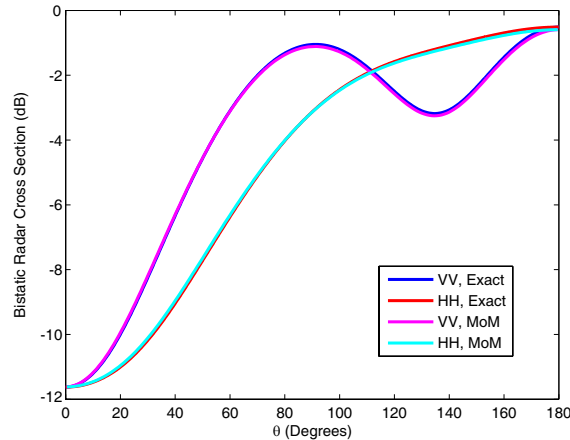


Figure 2: Bistatic RCS solutions for a PEC sphere with a radius $a = 0.2758\lambda$.

polarization (VV) and horizontal polarization (HH). The scatterer is a PEC sphere with a radius $a = 0.2758\lambda$ (the origin of the coordinate system is the center of the sphere) and we discretize the spherical surface into 4216 triangular patches. Fig. 2 plots the RCS solutions and they are very close to the corresponding Mie-series solutions.

5. CONCLUSION

Although many techniques have been developed for evaluating the singular potential integrals arising from the SIEs in the MoM with the RWG basis function, we provide an alternative approach to handle the singular integrals in this work. The approach can automatically cancel the singularity without using a variable change or coordinate transform and reduce the integrals to a one-fold numerical integration with a very simple integrand. Compared with the Duffy's method which requires a two-fold numerical integration, the approach could be more convenient in implementation and more efficient in calculation as illustrated by the numerical example.

ACKNOWLEDGMENT

This work was supported by the Program of Shanghai Pujiang Talents, Shanghai, China, with the Project No. 12PJ1408600.

REFERENCES

1. Chew, W. C., M. S. Tong, and B. Hu, *Integral Equation Methods for Electromagnetic and Elastic Waves*, Morgan & Claypool, San Rafael, CA, 2008.
2. Rao, S. M., D. R. Wilton, and A. W. Glisson, "Electromagnetic scattering by surfaces of arbitrary shape," *IEEE Trans. Antennas Propagat.*, Vol. 30, No. 3, 409–418, 1982.
3. Wilton, D. R., S. M. Rao, A. W. Glisson, D. H. Schaubert, O. M. Al-Bundak, and C. M. Butler, "Potential integrals for uniform and linear source distributions on polygonal and polyhedral domains," *IEEE Trans. Antennas Propagat.*, Vol. 32, No. 3, 276–281, 1987.
4. Graglia, R. D., "Static and Dynamic potential integrals for linearly varying source distributions in two- and three-dimensional problems," *IEEE Trans. Antennas Propagat.*, Vol. 35, No. 6, 662–669, 1987.
5. Khayat, M. A. and D. R. Wilton, "Numerical evaluation of singular and near-singular potential integrals," *IEEE Trans. Antennas Propagat.*, Vol. 53, No. 10, 3180–3190, 2005.
6. Duffy, M. G., "Quadrature over a pyramid or cube of integrands with a singularity at a vertex," *SIAM J. Numer. Anal.*, Vol. 19, No. 6, 1260–1262, 1982.

A Multi-arm Coupled-fed Monopole Antenna for WWAN Mobile Systems

Wen-Shan Chen¹, Bau-Yi Lee², Hung-Ying Lin¹, Chien-Min Cheng¹,
Shih-Chiang Chiu¹, and Jing-Yen Chen¹

¹Department of Electronic Engineering
Southern Taiwan University of Science and Technology, Tainan City 710, Taiwan

²Department of Electrical Engineering
Tung Fang Design University, Kaohsiung City 82941, Taiwan

Abstract— This paper proposes a printed monopole antenna, which is fabricated on a 0.8 mm thick FR-4 substrate for WWAN 5-band application. On one side of the substrate, a monopole patch and a $50\ \Omega$ micro-strip feed-line with length of 25 mm are etched. The monopole patch is directed fed by the feed-line and operates a resonant mode at 2.66 GHz. On the other side of the substrate, a coupled-fed monopole with four arms (an L-shaped arm, a left arm, a right arm, and an F-shaped arm) and a ground plane are printed. The coupled-fed monopole is connected to the ground plane through one of the arms (the F-shaped arm). Beside, each arm of the monopole excites its own resonant mode, except one of the arms (the left arm) is used for improving the impedance matching. By adjusting the length of the four arms, the antenna's operating bandwidth based on the 6-dB return loss is from 0.72–1.15 GHz and 1.45–2.2 GHz for GSM 850/900, GSM 1800/1900, and UMTS applications. The overall dimension of the proposed antenna is $60 \times 110 \times 0.8\ \text{mm}^3$ that contains an antenna portion of $60 \times 15\ \text{mm}^2$ and a ground plane of $60 \times 95\ \text{mm}^2$. The proposed antenna having dual wide operating bandwidth and a small size with planar structure are suitable for smart phone handset. This article also provides the studies of measured radiation patterns, antenna gain, and radiation efficiency. Furthermore, the simulated results of antenna SAR obtained by SEMCAD-X are presented and discussed. Both the measured results and antenna SAR demonstrate the reliability of the proposed antenna.

1. INTRODUCTION

Owing to the portable requirement of modern wireless communication systems, the components for the wireless devices such as mobile phones, laptop computers, and tablet PCs are needed to be small, low profile, light, low cost, and easy integration with circuit boards. Beside the constraint of portable, these products must also carry multi functions to attract the consumer's interests. Therefore, the antennas used in these products are required to have multi operating bands for multi functions and small size for placing inside of them. Printed antennas that have the advantages of compact, low cost, and wide operating bandwidth become the optimal selection for manufacturers. In 1–4), the proposed designs used 3D structure to operate penta-bands for WWAN applications, whose operating bandwidths are within 824–960 and 1710–2170 MHz. The reference antennas 5–8) with planar geometric were also designed for WWAN applications. Indeed, the planar antenna has benefit of compact and easy fabrication to the 3D structure. To excite border impedance bandwidths of an antenna, coupled-fed mechanism becomes a popular feeding method because it produces more uniform surface current distributions and less input impedance variations. In 2, 7, 9–10), monopole, PIFA, and loop antennas were employed coupled-fed method to obtain multi-band and broad-band applications. In this paper, a WWAN five-band antenna for mobile phone application is proposed. The proposed antenna consists of a monopole patch connected with a $50\ \Omega$ micro-strip feed-line on front side of an FR4 substrate and a multi-arm monopole coupled fed by the monopole patch. The multi-arm monopole is printed on back side of the substrate and connected with the system ground plane. The 6-dB operating bandwidths (0.72–1.15 and 1.45–2.2 GHz) are all excited by the multi-arm monopole and can be used in the WWAN five-band applications. Note that the monopole patch excites a resonant mode at 2.66 GHz, which is not used in this design.

2. ANTENNA DESIGN AND ITS RESONANT MODES

The geometric of the proposed monopole antenna shown in Figure 1 is fabricated on a 0.8 mm FR4 substrate with relative permittivity constant of 4.4 and loss tangent of 0.0245. On front side of the substrate, a monopole patch connected with a $50\ \Omega$ micro-strip feed-line is printed. An SMA connector at end of the micro-strip feed-line is used for RF signal inputs. The monopole patch is

excited to obtain a resonant mode at 2.66 GHz. On back side of the substrate a multi-arm monopole connected with the system ground plane is designed. The system ground plane occupies an area of $60 \times 95 \text{ mm}^2$, while the antenna portion is $60 \times 15 \text{ mm}^2$. The multi-arm monopole is coupled fed by the monopole patch and consists of four arms, which are an L-shaped arm, a left arm, a right arm, and an F-shaped arm. On the left hand side of the coupled-fed monopole, the monopole with the L-shaped arm ($W_2 + L_3$) excites a resonant mode at 0.85 GHz and its higher modes at 1.73 and 2.14 GHz and the monopole with the left arm (W_4) is used for increasing impedance matching of higher operating band. On the right hand side, the monopole with the right arm (W_3) excites a resonant mode at 1.85 GHz and the monopole with the F-shaped arm operates a resonant mode at 1.93 GHz. Note that the F-shaped arm connects to the system ground plane and the detailed dimensions are listed in Table 1. Figure 2 shows the measured and simulated return losses of the proposed antenna. The simulated results are obtained through the HFSS simulation software by Ansoft. From the results, the correspondences between the measured and simulated results are observed, except an excited mode at 1.6 GHz occurred in the measured result is owing to the measured cable line. Based on the 6-dB return loss, the measured result from 0.72–1.15 GHz and 1.45–2.2 GHz can be applied in GSM 850/900, GSM 1800/1900, and UMTS systems.

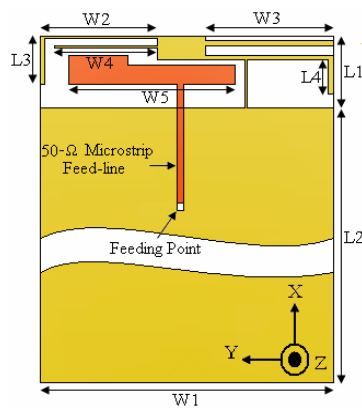


Figure 1: Geometric of the proposed monopole antenna.

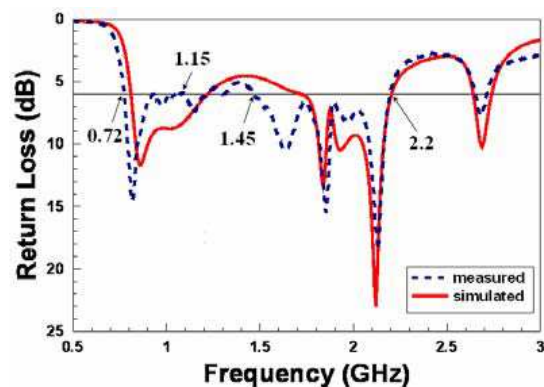


Figure 2: Measured and simulated return losses of the proposed antenna.

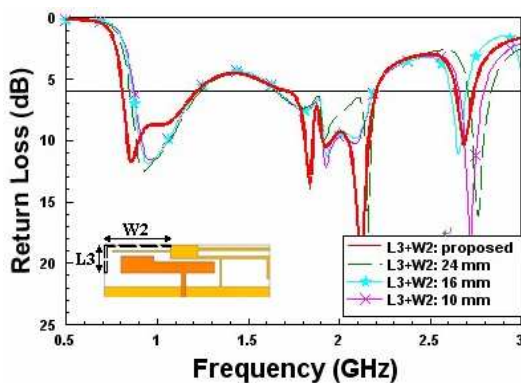


Figure 3: Simulated return losses with different lengths of L-shaped arm ($W_2 + L_3$).

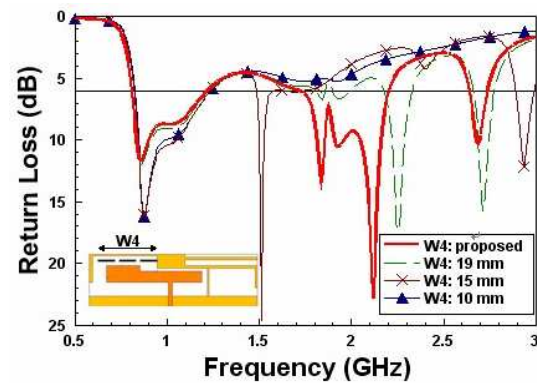


Figure 4: Simulated return losses with different lengths of left arm (W_4).

Table 1: Parameters of proposed design (Unit: mm).

L1	L2	L3	L4	W1	W2	W3	W4	W5
15	95	10	7	60	23	26	21	34

Table 2: Simulated results of SAR at different operating bands.

Frequency (MHz)	859	925	1795	1920	2045
1g SAR (W/Kg)	1.52	1.71	0.62	0.47	0.43

3. PARAMETRIC STUDY AND EXPERIMENTAL RESULTS

This paragraph presents the parameters that control the resonant modes. Figures 3, 4, 5, and 6 demonstrate the different lengths of the four arms of the coupled-fed monopole while Figure 7 shows the different lengths of the direct-fed monopole. In Figure 3, the L-shaped arm ($W_2 + L_3$) is decreased from 33 to 10 mm. The resonant mode of 0.85 GHz and its higher modes at 1.73 and 2.14 GHz are shifted to higher band and the other modes only affect their impedance matching. The results verify that the L-shaped arm controls these resonant modes. Figure 4 shows the simulated return losses of different lengths of the left arm (W_4). The left arm is surrounded by the L-shaped arm therefore the left arm influences the antenna's impedance matching. On the right hand side, the simulated return losses of different length of the right arm (W_3) are shown in Figure 5. The results indicate that the resonant mode at 1.85 GHz moves to higher band as W_3 decreases and verifies that the 1.85 GHz mode is obtained by it. Figure 6 shows the simulated return losses of different lengths of the F-shaped arm. When the length of L_4 equals 7 mm, the 1.93 GHz mode separates with the higher mode of the L-shaped arm at 2.14 GHz to create wider operating bandwidth. The other bands have minor influences by this change. Figure 7 shows the simulated return losses of different lengths of the direct-fed monopole (W_5). Although the resonant mode at 2.66 GHz is not used in this design, it moves to higher band as the length W_5 decreases. The resonant modes excited by the coupled-fed monopole have only slight effects.

Figure 8 shows the measured 2-D radiation patterns at 859, 924, 1795, 1920, and 2045 MHz. The patterns in X - Y plane at 859 and 924 MHz have an omni-directional characteristic. The patterns at higher bands, which are twisted and have more nulls, are due to the nulls of current path in both resonant path and ground plane. Figures 9(a) and 9(b) show the measured antenna gain and radiation efficiency at 824–960 MHz and 1710–2170 MHz, respectively. From the results, the antenna gain at 824–960 MHz is from 0.6 to 1.9 dBi and radiation efficiency is above 64.5% with smooth variation. At 1710–2170 MHz, the antenna gain is from 2.4 to 3.4 dBi and radiation

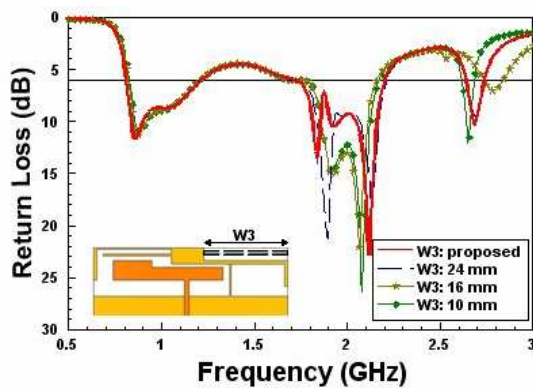


Figure 5: Simulated return losses with different lengths of W_3 .

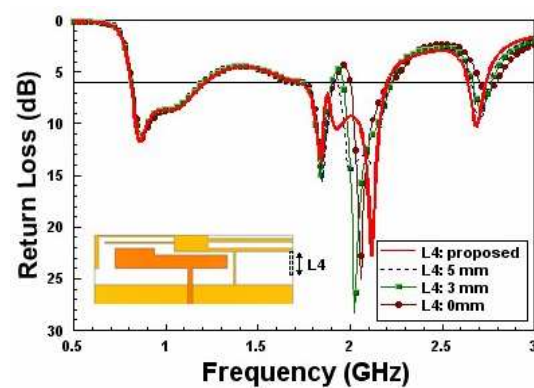


Figure 6: Simulated return losses with different lengths of L_4 .

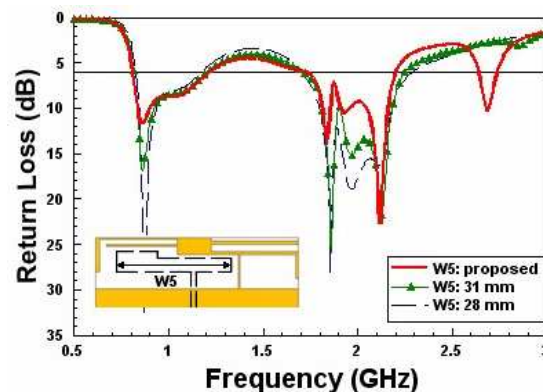


Figure 7: Simulated return losses of the proposed antenna with different lengths of W_5 .

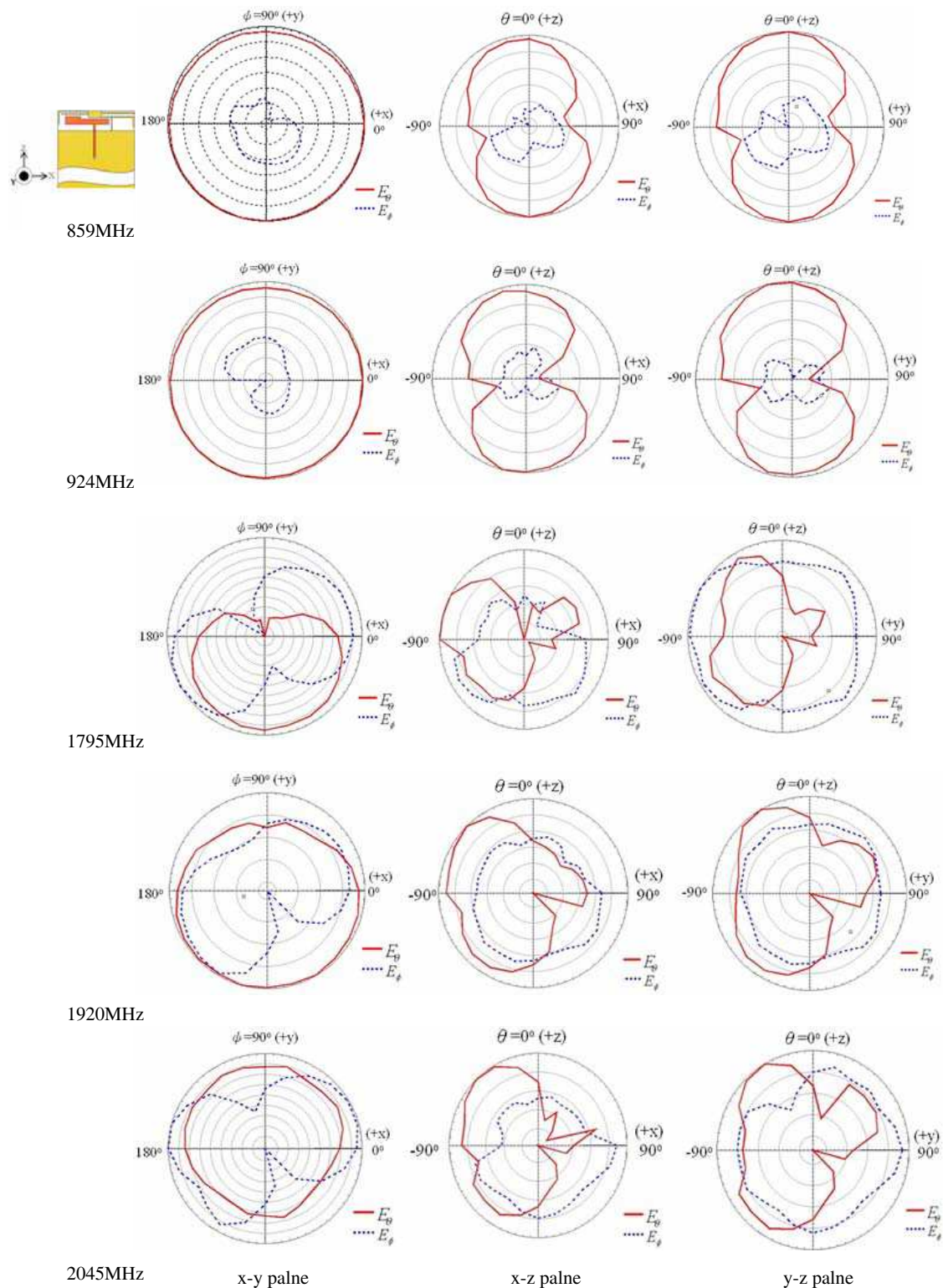


Figure 8: Measured 2-D radiation patterns at 859, 924, 1795, 1920, and 2045 MHz.

efficiency is higher than 65.7%. The simulated antenna SAR listed in Table 2 pass the FCC regulation except at 925 MHz, which has SAR value of 1.71 W/kg. The value is a little over the FCC standard of 1-g SAR less than 1.6 W/kg. Note that the proposed antenna is placed inside of a 1-mm thick plastic casing for the simulation and the results are obtained through SEMCAD-X software.

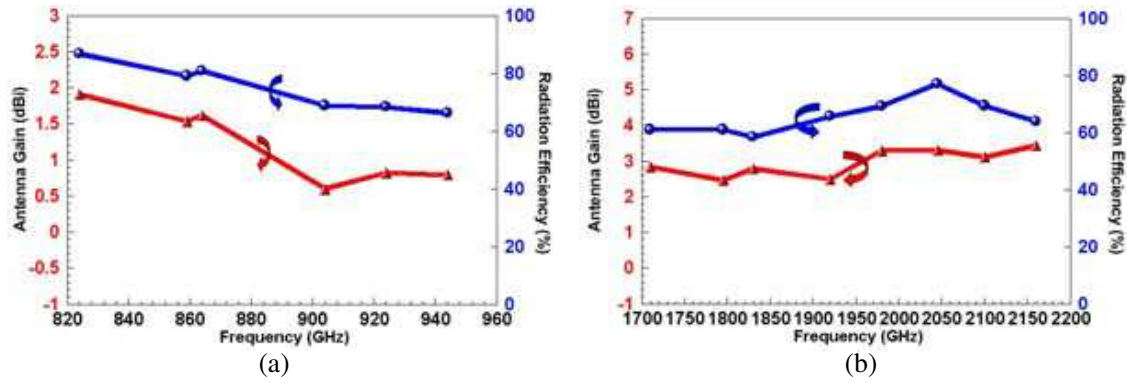


Figure 9: Measured antenna gain and radiation efficiency at (a) 824–960 MHz and (b) 1710–2170 MHz.

4. CONCLUSIONS

A direct-fed monopole and a coupled-fed monopole with four arms designed on an FR 4 substrate have been proposed for WWAN mobile applications. The resonant bands excited by the coupled-fed monopole are verified and the dual operating bandwidths based on the 6-dB return loss are 0.72–1.15 GHz and 1.45–2.2 GHz that cover GSM 850/900, GSM 1800/1900, and UMTS applications. To the antenna's performances, good antenna gains and efficiency are obtained and measured 3-D radiation patterns in X - Y plane show an omni-directional characteristic. In addition, the simulated SARs almost meet the FCC regulations at the operating frequency bands. The overall dimensions of $60 \times 110 \times 0.8 \text{ mm}^3$ with planar two-dimensional structure make the proposed antenna attractive great interests in the modern slim mobile phones.

ACKNOWLEDGMENT

This work was supported by the National Science Council of Taiwan under grant numbers of NSC 101-2221-E-218-032 and NSC 101-2632-E-218-001-MY3 and measured at Advanced Connectek Inc. (ACON).

REFERENCES

1. Wong, K. L., W. J. Chen, and T. W. Kang, "Small-size loop antenna with a parasitic shorted strip monopole for internal WWAN notebook computer antenna," *IEEE Trans. Antennas Propagat.*, Vol. 59, 1733–1738, 2011.
2. Wong, K. L. and C. H. Chang, "Internal coupled-fed shorted monopole antenna for GSM 850/900/1800/1900/UMTS operation in the laptop computer," *IEEE Trans. Antennas Propagat.*, Vol. 56, 3600–3604, 2008.
3. Wang, X., W. Chen, and Z. Feng, "Multiband antenna with parasitic branches for laptop applications," *Electron. Lett.*, Vol. 43, 1012–1013, 2007.
4. Chen, H. M., C. L. Liu, Y. F. Lin, C. M. Liang, and S. C. Pan, "Miniature internal penta-band monopole antenna for mobile phones," *IEEE Trans. Antennas Propagat.*, Vol. 58, 1008–1011, 2010.
5. Wong, K. L. and S. C. Chen, "Study of a hearing aid-compatible internal LTE/WWAN bar-type mobile phone antenna," *Proc. 2010 Asia Pacific Microwave Conf.*, 1793–1796, Yokohama, Japan, Dec. 2010.
6. Chen, W. S., L. M. Liou, and B. Y. Lee, "A compact meandered antenna with multifrequency bands for mobile phone applications," *Microwave Opt. Technol. Lett.*, Vol. 53, 2216–2221, 2011.
7. Wong, K. L. and C. H. Chang, "Printed $\lambda/8$ -PIFA for penta-band WWAN operation in the mobile phone," *IEEE Trans. Antennas Propagat.*, Vol. 57, 1373–1381, 2009.
8. Wong, K. L. and S. J. Liao, "Uniplanar coupled-fed printed PIFA for WWAN operation in the laptop computer," *Microwave Opt. Technol. Lett.*, Vol. 51, 549–554, 2009.
9. Lee, S. H., K. J. Kim, B. Kim, J. K. Oh, and Y. J. Yoon, "Multi-band coupled feed loop antenna for mobile handset," *Proc. 2009 Asia Pacific Microwave Conf.*, 2703–2706, Suntec, Singapore, Dec. 2009.
10. Chen, W. S., Y. T. Liu, and W. H. Hsu, "Multi-frequency printed loop antenna for mobile phone application," *2011 IEEE Antenna Propagat. Soc. Int. Symp. Dig.*, 1926–1928, Spokane, Washington, USA, Jul. 2011.

Design of Two-layer Hemispherical Dielectric Resonator Antenna

Xiaosheng Fang and Kwok Wa Leung

The State Key Laboratory of Millimeter Waves, Department of Electronic Engineering
City University of Hong Kong, Kowloon, Hong Kong, China

Abstract— The two-layer hemispherical dielectric resonator antenna (DRA) excited in the TE₁₁₁ mode is studied. Its resonance frequency is found rigorously by solving the TE-mode characteristic equation. By using the covariance matrix adaptation evolutionary strategy (CMA-ES), results that determine the outer and inner radii of the two-layer hemispherical DRA are found for the first time. The results are compared with the exact solutions and good agreement is obtained.

1. INTRODUCTION

The dielectric resonator antenna (DRA) [1, 2] has received tremendous attention due to a number of attractive advantages such as its small size, light weight, low loss, and ease of excitation. The shape of the DRA can be rectangular, cylindrical, or hemispherical, but only the last one admits an analytical solution.

A number of studies on the two-layer hemispherical DRA [3–6] have been carried out owing to its wideband characteristic. In designing a two-layer hemispherical DRA, the characteristic equation [3] can be solved to determine the resonance frequency. However, the equation has spherical Bessel and Hankel functions that engineers may not be familiar with. Also, it difficult to solve the solution using a pocket calculator and a computer is normally needed. To address these problems, an engineering formula that gives the TE₁₁₁-mode resonance frequency of the two-layer hemispherical DRA has been obtained [4], but the solution is limited to the hollow case only.

In this paper, a more general formula for designing the two-layer hemispherical DRA is obtained by using the covariance matrix adaptation evolutionary strategy (CMA-ES). The superiority of the CMA-ES over the least square method as used in [4] has been discussed in [7] and is therefore not repeated here. The formula can be used to determine the outer radius of the two-layer hemispherical DRA when given the design frequency and dimension ratio. From outer radius, the inner radius can be obtained easily from the given dimension ratio. It was found that the maximum error of the formula is less than 3.1% over the ranges of $6 \leq \varepsilon_{r1} \leq 21$, $2 \leq \varepsilon_{r1}/\varepsilon_{r2} \leq 6$, and $0.07 \leq b/a \leq 0.67$.

2. THEORY

Figure 1 shows the geometry of a two-layer hemispherical DRA resting on the ground plane. The outer layer of the DR has radius a and dielectric constant ε_{r1} , whereas the inner layer has radius b and dielectric constant ε_{r2} . In this paper, the free-space wavenumber is denoted by k_0 , whereas the wavenumbers of the outer and inner dielectric layers are denoted by $k_1 = \sqrt{\varepsilon_{r1}}k_0$ and $k_2 = \sqrt{\varepsilon_{r2}}k_0$, respectively. The TE₁₁₁-mode resonance frequency f_r of the DRA can be obtained by finding the first root (k) of k_0 using the following TE-mode characteristic equation [3] (the indices n , m , and r of a TE _{n m r} mode refer to field variations along the θ , ϕ , and r directions, respectively):

$$\Gamma_1\Gamma_2 - \Gamma_3\Gamma_4 = 0 \quad (1)$$

where

$$\begin{aligned} \Gamma_1 &= \hat{J}'_1(k_2b)\hat{H}_1^{(2)}(k_1b) - \sqrt{\frac{\varepsilon_{r1}}{\varepsilon_{r2}}}\hat{J}_1(k_2b)\hat{H}'_1^{(2)}(k_1b) \\ \Gamma_2 &= \hat{J}_1(k_1a)\hat{H}'_1^{(2)}(k_0a) - \sqrt{\varepsilon_{r1}}\hat{J}'_1(k_1a)\hat{H}_1^{(2)}(k_0a) \\ \Gamma_3 &= \hat{J}'_1(k_2b)\hat{J}_1(k_1b) - \sqrt{\frac{\varepsilon_{r1}}{\varepsilon_{r2}}}\hat{J}_1(k_2b)\hat{J}'_1(k_1b) \\ \Gamma_4 &= \hat{H}_1^{(2)}(k_1a)\hat{H}'_1^{(2)}(k_0a) - \sqrt{\varepsilon_{r1}}\hat{H}'_1^{(2)}(k_1a)\hat{H}_1^{(2)}(k_0a) \end{aligned}$$

in which $\hat{J}_n(x)$ and $\hat{H}_n^{(2)}(x)$ are the first-order Schelkunoff-type spherical Bessel (first kind) and Hankel (second kind) functions, respectively. A prime of a function denotes a derivative with

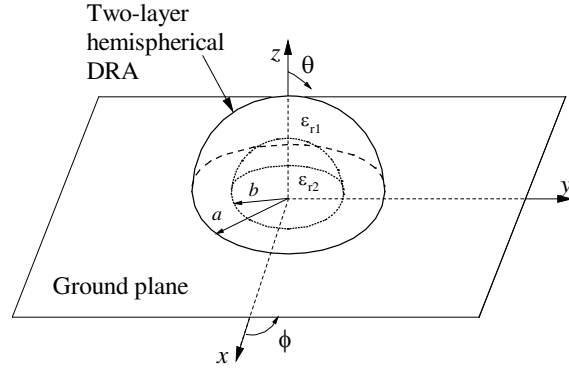


Figure 1: Geometry of the two-layer hemispherical DRA resting on a ground plane.

respect to the whole argument. After the first root k is obtained, the frequency f_r can be obtained as follows:

$$f_r = \frac{c \cdot \text{Re}(k)}{2\pi} \quad (2)$$

where c is the speed of light in vacuum.

3. RESULTS

The following part is to obtain engineering formulas that determine the dimensions a , b of the DRA when $\varepsilon_{r1,2}$, f_r , and b/a are given. Since f_r is inversely proportional to a [4], it can be expressed as follows:

$$f_r = \frac{1}{a} F \left(\varepsilon_{r1}, \frac{\varepsilon_{r1}}{\varepsilon_{r2}}, \frac{b}{a} \right) \quad (3)$$

where the function F is to be determined from (1), (2). For convenience, (3) can be written as:

$$f_r a = F \left(\varepsilon_{r1}, \frac{\varepsilon_{r1}}{\varepsilon_{r2}}, \frac{b}{a} \right) \quad (4)$$

Let $x_1 = \varepsilon_{r1}$, $x_2 = \varepsilon_{r1}/\varepsilon_{r2}$, $x_3 = b/a$, and $y = f_r a$, (4) then becomes $y = F(x_1, x_2, x_3)$. To determine F , a number of data sets were generated by solving (1) numerically. The data was curve-fitted using the following mathematical form:

$$y = \frac{A(x_3)}{\sqrt{d_0 x_1 + d_1}} [B(x_3) + x_2]^{C(x_3)} \quad (5)$$

where

$$\begin{aligned} A(x_3) &= a_3 x_3^3 + a_2 x_3^2 + a_1 x_3 + a_0 \\ B(x_3) &= b_3 x_3^3 + b_2 x_3^2 + b_1 x_3 + b_0 \\ C(x_3) &= c_3 x_3^3 + c_2 x_3^2 + c_1 x_3 + c_0 \end{aligned}$$

A 4×4 matrix \mathbf{M} containing the unknown parameters is defined as follows:

$$\mathbf{M} = \begin{bmatrix} a_0 & b_0 & c_0 & d_0 \\ a_1 & b_1 & c_1 & d_1 \\ a_2 & b_2 & c_2 & 0 \\ a_3 & b_3 & c_3 & 0 \end{bmatrix} \quad (6)$$

The CMA-ES method is used here to determine the parameters. An optimal parameter matrix \mathbf{M}_O can be obtained by minimizing the maximum percentage error as done in [7]. In our study, the optimization process was independently repeated for 100 times and the following optimal parameter matrix \mathbf{M}_O was obtained:

$$\mathbf{M}_O = \begin{bmatrix} 49.59 & 18.78 & -0.024 & 0.183 \\ -32.08 & -5.02 & 0.07 & -0.1 \\ 5.05 & -17.77 & -0.012 & 0 \\ 57.01 & 6.89 & -0.004 & 0 \end{bmatrix} \quad (7)$$

After the various parameters have been found, the outer radius a can be calculated straightforwardly from (5) and (7), while the inner radius b can be obtained easily from the given ratio of b/a . The result was tested and it was found that it is valid over the ranges of $6 \leq \varepsilon_{r1} \leq 21$, $2 \leq \varepsilon_{r1}/\varepsilon_{r2} \leq 6$, and $0.07 \leq b/a \leq 0.67$, with errors less than 3.1%.

4. CONCLUSIONS

New results that facilitate designs of the TE₁₁₁-mode two-layer hemispherical DRA have been presented. In the first part of this paper, the TE₁₁₁-mode resonance frequency f_r has been found for given a , b , ε_{r1} , and ε_{r2} . It has been obtained rigorously by solving the TE-mode characteristic equation. For the second part, an engineering formula which determines the outer radius a of the DRA for given $\varepsilon_{r1,2}$, f_r , and b/a has been found. After a has been found, the inner radius b can be obtained easily from the dimension ratio b/a . The result has been obtained by using the CMA-ES method. It was found that its error is less than 3.1% over the ranges of $6 \leq \varepsilon_{r1} \leq 21$, $2 \leq \varepsilon_{r1}/\varepsilon_{r2} \leq 6$, and $0.07 \leq b/a \leq 0.67$. The results should be useful for designs of two-layer hemispherical DRAs.

ACKNOWLEDGMENT

This work was supported by a GRF grant from the Research Grants Council of Hong Kong Special Administrative Region, China (Project No. CityU 115912).

REFERENCES

1. Long, S. A., M. W. McAllister, and L. C. Shen, "The resonant cylindrical dielectric cavity antenna," *IEEE Trans. Antennas Propagat.*, Vol. 31, No. 5, 406–412, May 1983.
2. Luk, K. M. and K. W. Leung, *Dielectric Resonator Antennas*, Research Studies Press, Baldock, U.K., 2003.
3. So, K. K., "Slot-excited dielectric resonator antenna," PhD Dissertation, City University of Hong Kong, Hong Kong, Aug. 2005.
4. Leung, K. W. and K. K. So, "Dimensional analysis of two-layer spherical dielectric resonator," *IEEE Microwave and Guided Wave Lett.*, Vol. 10, 139–141, Apr. 2000.
5. Chen, N. C., H. C. Su, K. L. Wong, and K. W. Leung, "Analysis of a broadband slot-coupled dielectric-coated hemispherical dielectric resonator antenna," *Microw. Opt. Techn. Lett.*, Vol. 8, No. 1, 13–16, Jan. 1995.
6. Leung, K. W., X. S. Fang, Y. M. Pan, E. H. Lim, K. M. Luk, and H. P. Chan, "Dualfunction radiating glass for antennas and light covers — Part II: Dualband glass dielectric resonator antennas," *IEEE Trans. Antennas Propagat.*, to be published.
7. Fang, X. S., C. K. Chow, K. W. Leung, and E. H. Lim, "New single-/dual-mode design formulas of the rectangular dielectric resonator antenna using covariance matrix adaptation evolutionary strategy," *IEEE Antennas Wireless Propag. Lett.*, Vol. 10, 734–737, 2011.

Use of Transparent Dielectric Resonator Antenna as a Light Cover

Xiaosheng Fang and Kwok Wa Leung

The State Key Laboratory of Millimeter Waves, Department of Electronic Engineering
City University of Hong Kong, Kowloon, Hong Kong, China

Abstract— This paper presents a dualband transparent hollow hemispherical dielectric resonator antenna (DRA) functioning as a light cover. The dualband DRA is excited by a coaxial-cable-fed aperture. The lower and upper bands of the antenna can cover the IEEE 802.11b WLAN band (2.4–2.48 GHz) and IEEE 802.11a WLAN band (5.15–5.35 GHz), respectively. ANSYS HFSS was used to simulate the reflection coefficient, radiation pattern, and gain of the antenna. Measurements were carried out to verify the simulations and reasonable agreement between them is obtained. Results of using the transparent DRA as a light cover are reported.

1. INTRODUCTION

Due to attractive features such as its small size, light weight, low loss, and ease of excitation, tremendous research efforts have been paid on the dielectric resonator antenna (DRA) over the last two decades [1, 2]. Different dielectric materials including ceramics, composite material, and glass can be used for fabrications of DRA. Among them glass is the most interesting because of its transparent characteristic. The first transparent glass DRA [3] has been proposed by Lim and Leung in 2010.

Today, it is a trend to provide dual- or multi-function designs [4] to reduce the system size and cut the system cost. Recently, the idea of using the glass DRA as a light cover has been proposed [5–7]. In [7], the dualband hollow glass hemispherical DRA is excited by a microstripline-fed slot. It is part of a lighting system and is an excellent hidden antenna. In this paper, the coupling slot of the dualband transparent hollow glass hemispherical DRA is fed by a coaxial cable instead of the microstripline. As a result, no microwave substrate is required. Instead, an aluminum ground plane is used to support the glass DRA. The proposed dualband DRA is operated in 2.4- and 5.2-GHz WLAN bands. Its reflection coefficient, radiation pattern, and gain of the antenna were simulated by using ANSYS HFSS, and the results are in reasonable agreement with our measurements.

2. CONFIGURATION

Figure 1 shows the configuration of the dualband transparent hollow hemispherical DRA. The DRA has outer and inner radii of $a_1 = 20.8$ mm and $a_2 = 9$ mm, respectively. The dielectric constant ϵ_r of the glass was measured and found to be 6.85. An aluminum ground plane with a size of 10×10 cm² is used to support the DRA. The DRA is excited by a coupling slot with a length of $L = 39$ mm and a width of $W = 2$ mm, which is fed with a coaxial cable beneath the ground plane. An LED, driven by a 3-V DC power supply, is inserted into the hollow region of the DRA through the slot to serve as the light source. Fig. 2 shows a photo of the DRA prototype.

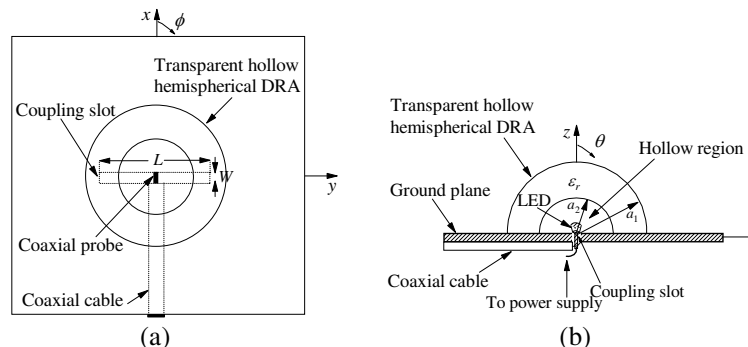


Figure 1: Configuration of the dualband hollow glass hemispherical DRA. (a) Top view. (b) Side view.



Figure 2: A photo of the DRA prototype. An LED is inserted into the hollow region of the DRA to serve as the light source.

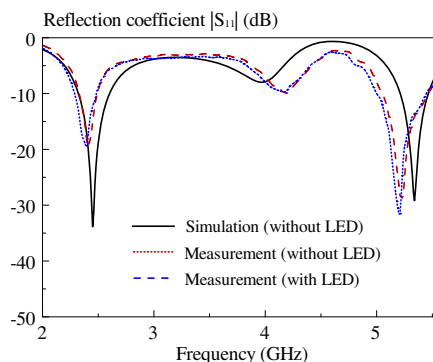


Figure 3: Measured and simulated reflection coefficients of the dualband hollow glass hemispherical DRA with and without the LED as a function of frequency: $a_1 = 20.8$ mm, $a_2 = 9$ mm, $\varepsilon_r = 6.85$, $L = 39$ mm and $W = 2$ mm.

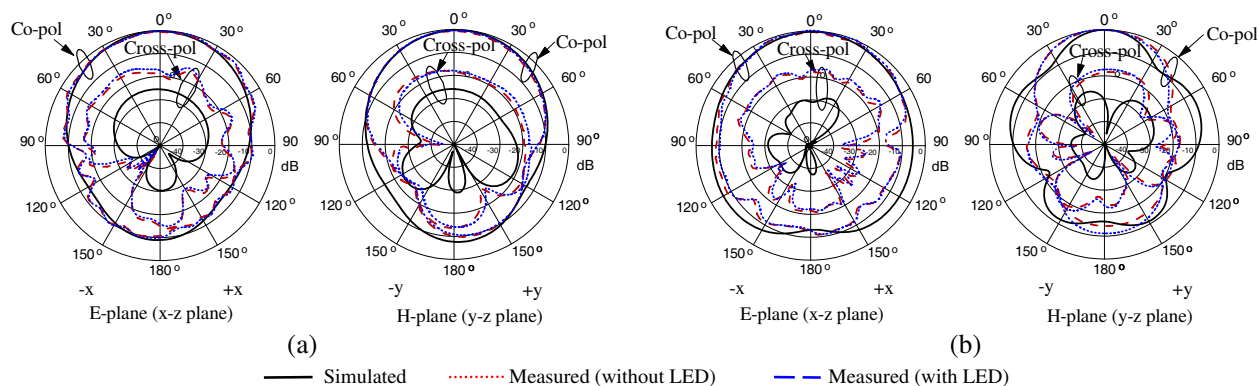


Figure 4: Measured and simulated radiation patterns of the dualband transparent glass hemispherical DRA with and without the LED. The parameters are the same as in Fig. 3. (a) 2.40 GHz. (b) 5.20 GHz.

3. RESULTS

Figure 3 shows the measured and simulated reflection coefficients of the prototype. Reasonable agreement between the measured and simulated results is observed. With reference to the figure, three resonant modes are found. The first and third resonant modes are caused by the TE_{111} and TE_{311} modes of the hollow hemispherical DRA, respectively, whereas the second resonant mode is due to the coupling slot. The measured resonance frequencies (min. $|S_{11}|$) of the TE_{111} and TE_{311} mode are given by 2.41 GHz and 5.23 GHz, respectively, which agree reasonably well with simulated frequencies of 2.45 GHz (1.65% error) and 5.34 GHz (2.08% error). It can be found from the figure that the measured impedance bandwidths ($|S_{11}| < -10$ dB) of the lower and upper bands are 6.6% (2.33–2.49 GHz) and 7.8% (5.05–5.46 GHz), respectively, entirely covering the 2.4- and 5.2-GHz WLAN bands.

The measured and simulated radiation patterns of the prototype at the WLAN frequencies are shown in Fig. 4 and reasonable agreement between them is seen. With reference to the figure, broadside field patterns are observed for the two resonant modes. For each resonant mode, the co-polarized fields are stronger than the cross-polarized fields by more than 18 dB in the boresight direction ($\theta = 0^\circ$).

Figure 5 shows the measured antenna gain of the DRA. With reference to the figure, the measured peak gains of the lower and upper bands are ~ 6.07 dBi and ~ 7.78 dBi, respectively, which are found at around the match points, as expected.

The dualband hollow glass hemispherical DRA with the LED inserted was also studied. The reflection coefficient, radiation pattern and antenna gain of this light-cover DRA were measured and the results are also shown in Figs. 3–5 for ease of comparison. With reference to the figures, the results with and without the LED are almost the same. Also, it was experimentally found that the results do not change when the LEDs are turned on or off, which is highly desirable.

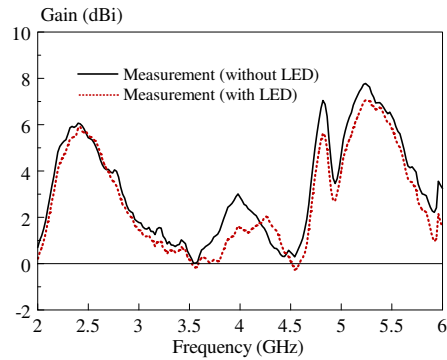


Figure 5: Measured antenna gains of the dualband hollow hemispherical DRA with and without the LED. The parameters are the same as in Fig. 3.

4. CONCLUSIONS

A slot-coupled dualband hollow glass hemispherical DRA has been investigated. The slot is fed by a coaxial cable. It has been shown that the proposed antenna can completely cover the 2.4- and 5.2-GHz WLAN bands. The glass DRA can simultaneously serve as a light cover. To demonstrate this, an LED has been inserted into the hollow region of the DRA through the coupling slot. It has been found that the LED has negligible effects on the antenna performance, therefore it is needless to take it into account when designing the light-cover DRA.

ACKNOWLEDGMENT

This work was supported by a GRF grant from the Research Grants Council of Hong Kong Special Administrative Region, China (Project No. CityU 116911).

REFERENCES

1. Long, S. A., M. W. McAllister, and L. C. Shen, "The resonant cylindrical dielectric cavity antenna," *IEEE Trans. Antennas Propagat.*, Vol. 31, No. 5, 406–412, May 1983.
2. Luk, K. M. and K. W. Leung, *Dielectric Resonator Antennas*, Research Studies Press, Baldock, UK, 2003.
3. Lim, E. H. and K. W. Leung, "Transparent dielectric resonator antennas for optical applications," *IEEE Trans. Antennas Propagat.*, Vol. 58, No. 4, 1054–1059, Apr. 2010.
4. Lim, E. H. and K. W. Leung, *Compact Multifunctional Antennas for Wireless Systems*, Wiley, 2012.
5. Leung, K. W., E. H. Lim, and X. S. Fang, "Dielectric resonator antennas: From the basic to the aesthetic," *Proceedings of the IEEE*, Vol. 100, No. 7, 2181–2193, Jul. 2012.
6. Leung, K. W., X. S. Fang, Y. M. Pan, E. H. Lim, K. M. Luk, and H. P. Chan, "Dualfunction radiating glass for antennas and light covers — Part I: Omnidirectional glass dielectric resonator antennas," *IEEE Trans. Antennas Propagat.*, Vol. 61, No. 2, Feb. 2013 (in Press).
7. Leung, K. W., X. S. Fang, Y. M. Pan, E. H. Lim, K. M. Luk, and H. P. Chan, "Dualfunction radiating glass for antennas and light covers — Part II: Dualband glass dielectric resonator antennas," *IEEE Trans. Antennas Propagat.*, Vol. 61, No. 2, Feb. 2013 (in Press).

A Compact Loop Antenna with Parasitic Split Ring for UHF RFID Application

Kittima Lertsakwimarn, Rattapong Suwalak, and Chuwong Phongcharoenpanich

Faculty of Engineering, King Mongkut's Institute of Technology Ladkrabang
Bangkok 10520, Thailand

Abstract— This paper presents a compact loop antenna with parasitic split ring for the reader of the UHF RFID application. The proposed antenna is made up of the rectangular loop structure (feeding element) and the parasitic split ring to reduce the overall antenna dimension. It is found that the size can be decreased by 50% of the typical single loop antenna. The simulation is carried out by using CST Microwave Studio program based on the Finite Integral Technique (FIT). Furthermore, the antenna parameters are optimized using the Quasi Newton method. The effect of the antenna parameters on the impedance bandwidth are investigated in this paper. The comparison between the simulation and experimental results are also discussed. From the results, the antenna has the $|S_{11}|$ less than -10 dB along the bandwidth of 12 MHz (1.6%). It can be operated in UHF RFID system in Thailand with the frequency band from 920 MHz to 925 MHz. The omnidirectional beam is obtained with the maximum gain of 1.5 dBi at the center frequency of 922.5 MHz. The antenna is designed on FR4-substrate. The overall size of the proposed antenna is $51 \text{ mm} \times 38 \text{ mm} \times 0.8 \text{ mm}$ ($0.15\lambda \times 0.11\lambda \times 0.02\lambda$). It is easily embedded inside handheld reader. Moreover, the proposed antenna is simple structure, low profile and easy fabrication. Therefore, the compact loop antenna with parasitic split ring can be employed with a handheld UHF RFID reader.

1. INTRODUCTION

Radio frequency identification (RFID) is a technology used for object identification. The RFID technology has been used for many applications such as retail, transportation, manufacturing and goods flow systems [1]. There are various frequency bands of RFID systems such as low frequency (LF), high frequency (HF), ultra high frequency (UHF), and microwave frequency. The UHF-RFID systems are very popular because the operating range is further than the LF- and HF-RFID systems. The LF- and HF-RFID systems use the near-field coupling techniques whereas the UHF-RFID utilizes the far-field radiation technique. The typical system operation consists of tag, reader and information management system. The reader uses an antenna to transmit radio energy to interrogate a transponder or tag that is attached to the item to be identified.

Generally, the RFID reader can be classified into two different categories: stationary and handheld readers. The advantage of handheld reader is used to read the data from the tags attached on goods or materials that are not convenient to move. For this reason, the handheld reader is suitable to use for crawl items in a retail store or warehouse management, including gathered information about pallets of goods. The special considerations in the design of handheld reader antenna are compact size, light weight, strong structure, durable use and convenient movement [2].

In recent years, there are many types of studied antennas for handheld RFID reader such as a printed dipole antenna [3], three-element printed Yagi antenna [4], helical antenna [2] and four non-meandered printed inverted-F antenna [5], that mainly focus on the design of the compact size antenna. By using the same fashion as the printed dipole antenna in [3], the proposed antenna design utilizes the printed loop antenna with parasitic split ring on FR4-substrate.

This paper proposes the compact loop antenna and parasitic split ring on FR4-substrate for the reader of RFID applications. The allocated UHF band in Thailand is 920–925 MHz. In Section 2, antenna design is shown. The simulation and experimental results of the proposed antennas are given in Section 3. Finally, conclusion is given in Section 4.

2. ANTENNA DESIGN

In this section, the antenna design and the simulation results will be addressed. The antenna is simulated using the CST Microwave Studio [6], and the antenna evolution is initialized with rectangular loop structure with total length of perimeter of one wavelength to study various characteristics. Next, two parasitic parallel lines of the same size will be added which are placed above and below of the rectangular loop. It is noted that the width of the loop and length of the parasitic

parallel lines have identical size. The last step is to add the parasitic split ring in place of parasitic parallel lines. The width and the length of the rectangular loop and parasitic split ring can be adjusted to meet the required characteristics.

2.1. Rectangular Loop Antenna with Parasitic Parallel Lines

The simulation of the antenna evolution is initialized with the rectangular loop antenna with perimeter of one wavelength on FR4-substrate as shown in Fig. 1(a). The antenna is designed to operate at 922.5 MHz where it is the center frequency of UHF RFID band in Thailand. It is found that the rectangular loop antenna can be operated at 922.5 MHz with omnidirectional pattern in vertical plane. According to the principle of loop antenna when the circumference is about the wavelength, the maximum radiation will be perpendicular to the plane of the loop. When the loop size is smaller than one wavelength, the radiation is gradually changed from an omnidirectional pattern in vertical plane to an omnidirectional pattern in horizontal plane [7]. Therefore, the requirement of the antenna design is to radiate in horizontal plane of the loop. Then, parasitic parallel lines will be added with the same size which are placed above and below the loop, in order to reduce the size of loop antenna. Fig. 1(b) illustrates the rectangular loop antenna with parasitic parallel lines configuration.

From the result of $|S_{11}|$ at the operating frequency of 922.5 MHz as shown in Fig. 2, it can be seen that when add parasitic parallel lines, the $|S_{11}|$ is decreased. However, with the added parasitic parallel lines of the loop antenna, the total size of the antenna cannot be sufficiently reduced. The next step is to add the parasitic split ring structure in place of the parasitic parallel lines which will be discussed in the next section.

2.2. Rectangular Loop Antenna with Parasitic Split Ring

In order to apply the antenna for handheld reader application in horizontal plane, the size of the antenna and radiation pattern must be suitable for implementation with handheld RFID reader. Fig. 3 shows the structure of the rectangular loop antenna and parasitic split ring. This structure can be further reduced the overall size of the antenna. The proposed antenna parameters must be optimized.

3. SIMULATION AND EXPERIMENTAL RESULTS

All simulations were performed by using CST Microwave Studio. The optimum antenna parameters are tabulated in Table 1. The $|S_{11}|$ versus frequency of the proposed antenna is shown in Fig. 4. This antenna can be operated along the UHF RFID band. It is found that the $|S_{11}|$ is lower than -10 dB from 915 MHz to 930 MHz or 1.6% bandwidth of UHF band. For the measurement, a photograph of the proposed prototype tag antenna is depicted in Fig. 5. The measurement of $|S_{11}|$

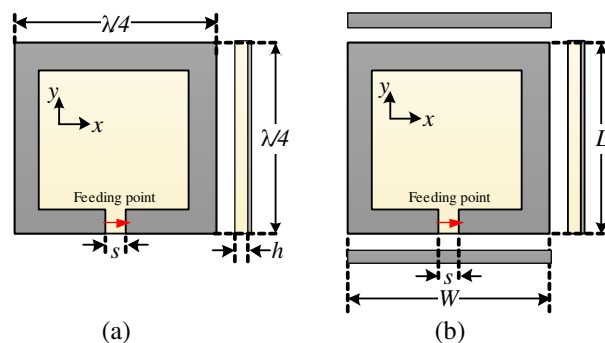


Figure 1: The antenna structure. (a) The single rectangular loop antenna structure. (b) The rectangular loop antenna with parasitic parallel lines structure.

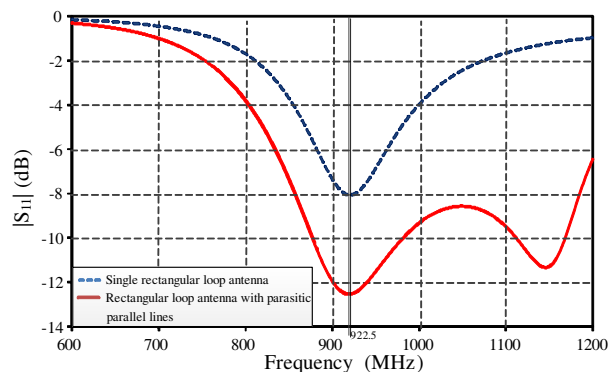


Figure 2: The simulation result of the $|S_{11}|$ of the single rectangular loop antenna and rectangular loop antenna with parasitic parallel lines structure.

Table 1: The optimum antenna parameters.

Parameters	W	L	w_1	l_1	t_1	t_2	t_3	s_1	s_2	h
Size in mm	51	38	26.5	23.5	4	7	3	2	7	0.8

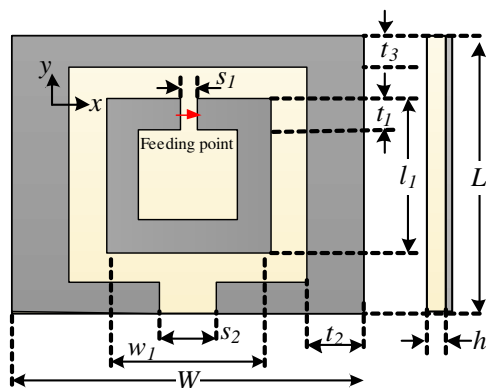


Figure 3: The proposed antenna configuration.

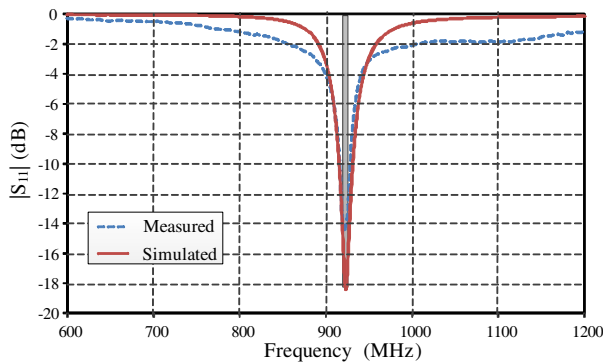


Figure 4: Simulated and measured $|S_{11}|$ versus frequency.

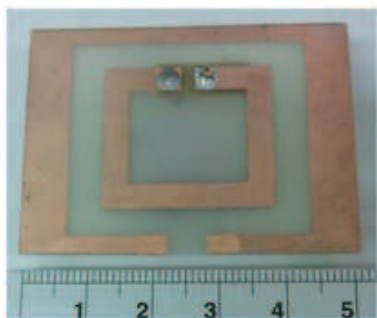


Figure 5: Photograph of the proposed prototype antenna.

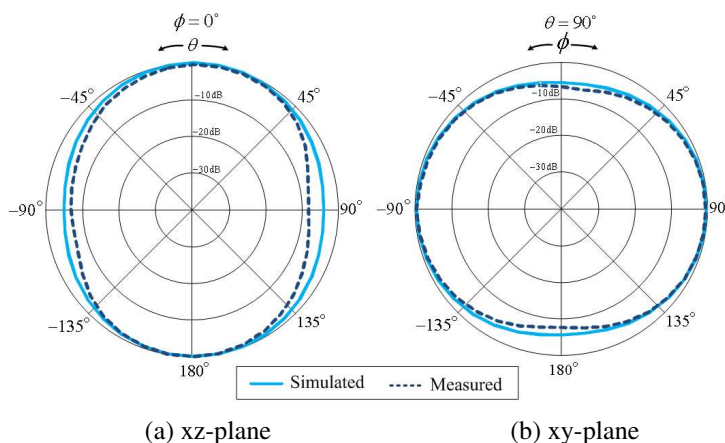


Figure 6: Simulated and measured radiation patterns at 922.5 MHz.

and radiation pattern was carried out using the Agilent E5230A vector network analyzer (VNA), which agree fairly well with the simulation result, as shown in Fig. 4 and Fig. 6. The measurement of $|S_{11}|$ is lower than -10 dB from 916 MHz to 928 MHz (1.2% bandwidth).

4. CONCLUSIONS

A compact loop antenna with parasitic split ring is proposed in this paper. The proposed antenna can be operated from 920 MHz to 925 MHz for the reader of the UHF RFID application. The proposed antenna is achieved by using the rectangular loop structure (feeding element) together with the parasitic split ring to reduce the overall antenna dimension. It is found that the size can be decreased by 50% of the typical single loop antenna. The overall size of the proposed antenna is $51 \text{ mm} \times 38 \text{ mm} \times 0.8 \text{ mm}$ ($0.15\lambda \times 0.11\lambda \times 0.02\lambda$). The antenna radiates the omnidirectional beam. The directivity is 1.7 dBi at 922.5 MHz. The prototype was fabricated and measured to verify the simulations. The measurement results show good agreement with the simulations ones. Therefore, the characteristics of the proposed compact loop antenna with parasitic split ring can achieve the requirement of the UHF RFID application.

ACKNOWLEDGMENT

This work is supported by the Thailand Research Fund (TRF) through the Royal Golden Jubilee Ph.D. Program under Grant No. PHD/0324/2552.

REFERENCES

1. Finkenzeller, K., *RFID Handbook*, 2nd Edition, Wiley, New York, 2003.
2. Nikitin, P. V. and K. V. Rao, "Helical antenna for handheld UHF RFID reader," *Proc. IEEE Int. Conf. RFID*, 166–173, Apr. 14–16, 2010.

3. Hua, R. C. and T. G. Ma, “A printed dipole antenna for ultra high frequency (UHF) radio frequency identification (RFID) handheld reader,” *IEEE Transactions on Antennas and Propagation*, Vol. 55, No. 12, 3742–3745, 2007.
4. Nikitin, P. V. and K. V. S. Rao, “Compact printed Yagi antenna for handheld UHF RFID reader,” *Proc. IEEE Antennas and Propagation Society International Symposium (APSURSI)*, 1–4, Jul. 11–17, 2010.
5. Xie, Z. M., X. Z. Lai, and R. J. Hu, “Compact UHF RFID reader antenna using bended fold dipole structure for mobile RFID system,” *Proceedings of the 2011 International Conference on Machine Learning and Cybernetics*, 414–417, Jul. 10–13, 2011.
6. CST-Microwave Studio, *User’s Manual*, 2006.
7. Huang, Y. and K. Boyle, *Antennas from Theory to Practice*, John Wiley & Sons, 2008.

Compact Size Antenna for Car FM Radio

Dau-Chyrh Chang¹, Fong-Yi Lin¹, Bing-Hao Zeng², and Jay Chen²

¹Oriental Institute of Technology, Taiwan

²Lorom Industrial Co. Ltd, Taiwan

Abstract— Car antenna can be divided into different types, various forms of car antenna is like below types: internal antenna, external antenna, hidden antenna and we have seen in the car is almost the mast antenna, but the mast antenna is easy to collide when we driving in the restricted space of occasions. Therefore the structure of shark fin antenna doesn't easily to influence at narrow space and that have appearance and function of advantages but the drawback is the poor reception. This paper describes combination of the antenna board and the car FM amplifier, and to set the shape of the car antenna board to the shark fin antenna that in order to achieve compact size, ease assembly and lower manufacturing costs, and kept to good reception on the FM radio.

1. INTRODUCTION

FM radio is almost required for any kinds of car. From the FCC regulation, the frequency band for FM radio is from 88 MHz to 108 MHz that means the wavelength the FM car radio is around 3 meters. Due to the car environment, the size of antenna should be as small as possible to reduce the wind resistance when the car is moving. For the size of quarter wavelength monopole antenna for this band is about 75 cm. It is large in length for the car. In order to reduce the size of the wire antenna, broadside mode helix antenna with height about 6 cm is used for the traditional FM car radio. This paper describes a wire antenna, which is printed on FR4 with thickness 0.8 mm, is used for car FM radio.

2. WIRE ANTENNA

The car FM radio, which is composed of a wire antenna and a printed circuit board FM amplifier, and they was etched on an FR4/Epoxy substrate with a thickness of 0.8 mm. This wire antenna is a metal strip, and the metal strip is bent around the printed circuit board FM amplifier. The ground plane area is 50×30 cm, and it is below the wire antenna and is simulated as roof of the car. The shape of the car antenna board is for a shark fin antenna, which size is 10×6 cm. The wire width is 1 mm, the wire between each other is 1 mm meter. The wavelength of FM is 3 meters, and this band of the quarter-wave length is 75 cm, but now this wire antenna isn't enough for the quarter-wave length. The wire antenna simulations the FM band impedance of the imaginary parts is capacitive. so we used the parallel LC, by using the equating of the imaginary parts to solve the jX_c . We were used lumped elements such as SMD capacitors/inductors, and let the wire antenna to achieve compact size. Figure 2 shown the Equivalent circuit model of the wire antenna, and jB is Equivalent circuit as parallel LC.

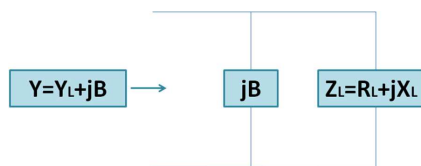


Figure 1: The Equivalent circuit model of the wire antenna.

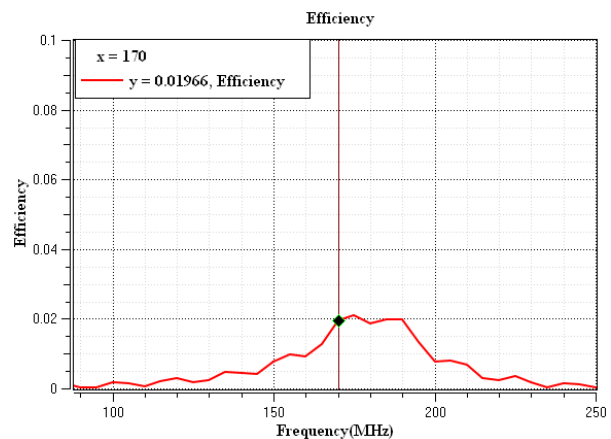


Figure 2: Efficiency of wire antenna.



Figure 3: The car FM wire antenna.

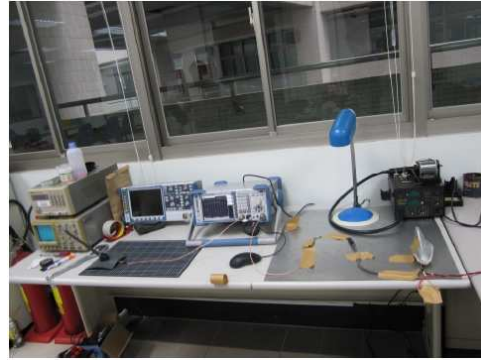


Figure 4: The environment of performance test for S_{21} .

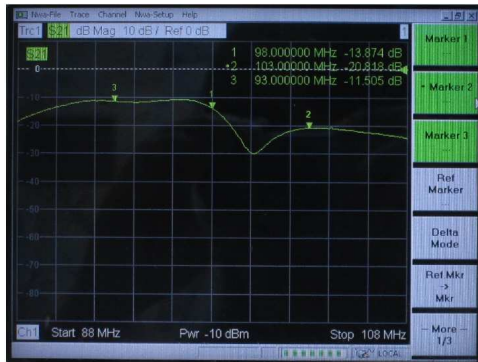


Figure 5: Test S_{21} of car FM wire antenna.

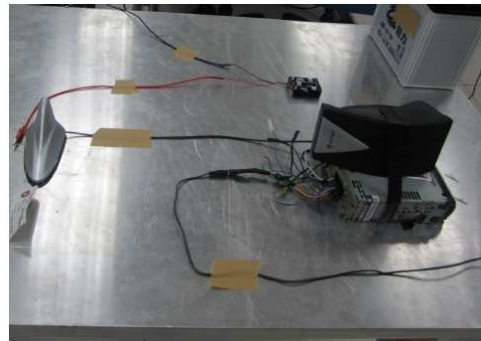


Figure 6: The environment of performance test for car FM radio.

3. MEASUREMENT RESULTS

When measured, we have to simulate the car of the roof, so the wire antenna was placed in the metal plane, and connected a 12V battery to make it work. We compared the wire antenna and other commercially available shark fin antenna, the wire antenna of the S_{21} is better than the other. Figure 3 the car FM wire antenna. Figure 4 is the environment of performance test for S_{21} . Figure 5 shows that test S_{21} of the car antenna.

4. CONCLUSIONS

The car FM wire antenna full use of shark fin antenna some of the space, and does not interfere with the reception of the signal, such a combination of methods, making the car antenna can be compact size, low-cost, and also to simplify the complicated assembly, and the test result shows that there are 38 radio base station are received with good audio quality. Figure 6 is the environment of performance test for the car FM wire antenna with amplifier and radio receiver mounted on the 1 meter by 1.5 meter ground. This paper had patent applications by Lorom Industrial Co. Ltd, Taiwan.

REFERENCES

1. Ali, M. and S. S. Stuchly, "A meander-line bow tie antenna," *IEEE Antenna and Propagation Society International Symposium*, Vol. 3, 1566–1569, 1996.
2. Best, S. R. and J. D. Morrow, "Limitations of inductive circuit model representations of meander line antenna," *IEEE Antenna and Propagation Society International Symposium*, Vol. 1, 852–855, 2003.

Gain Enhancement of Circularly Polarized Slender Antenna Using a Wider Helical Element

Ye Zhang and Takeshi Fukusako

Department of Computer Science & Electrical Engineering, Kumamoto University, Japan

Abstract— This paper presents a gain enhancement of a small circularly polarized (CP), slender helical antennas with a wider of helical line in a limit space. The gain of helical element is increased to 0 dBic, which is higher by 6 dB than previous study. The antenna can generate circular polarization in the normal direction to the helical axis. A number of conventional circularly polarized antennas have roughly a square or circular shape for generating two orthogonal, linearly polarized modes of equal amplitude with a phase difference of 90° . The slender sharp antenna is novel and convenient for installation in some devices. The measured and simulated characteristics of the antenna are in good agreement. Furthermore, in order to apply the antenna to small handset devices, the antenna is installed on a large ground plane ($60\text{ mm} \times 40\text{ mm}$) to discuss the effect of the ground, since the AR is affected by the radiation from both the antenna element and the large ground plane. Such planar and slender shaped antenna is useful to be installed in handsets or used as RFID tags.

1. INTRODUCTION

In recent years, small and circularly polarized antennas have become attractive for several types of applications, including wireless telecommunication, wireless sensors, GPS, and RFIDs [1–3]. A number of conventional circularly polarized antennas have roughly a square or circular shape in order to generate two orthogonal, linearly polarized modes of equal amplitude with a phase difference of 90° . On the other hand, a slender, rectangular antenna is convenient for installation in some devices. However, in previous study, the capacitive feed helical element CP antenna shown in [1], the gains are lower than that of a conventional small antenna. This paper presents the techniques to enhance the gain of previous antenna. A wider helical element is used to enhance the antenna gain. As a result, the gain of helical element is increased to 0 dBic, which is higher by 6 dB than previous study. Such planar and slender shaped antenna is useful to be installed in handsets or used as RFID tags.

2. ANTENNA STRUCTURE

The structure of the proposed antenna is shown in Figs. 1(a), (b). The antenna has a height (the distance between the antenna and the ground plane) of $1.6\text{ mm} + d$ (the height of helical element) and uses a 0.8 mm thick RT/Duroid 5880 substrate with a permittivity (ϵ_r) of 2.2 and a dielectric loss ($\tan \delta$) of 0.001. The helical element has a width w of 2 mm or 4 mm and spaced 0.25 mm between the adjacent lines. The substrate dimension is fixed as (g_x) 28 mm ($0.09\lambda_0$, λ_0 : wavelength at resonance frequency) \times (g_y) 8.75 mm ($0.03\lambda_0$, $w = 2\text{ mm}$) or 16.75 mm ($0.06\lambda_0$, $w = 4\text{ mm}$) and

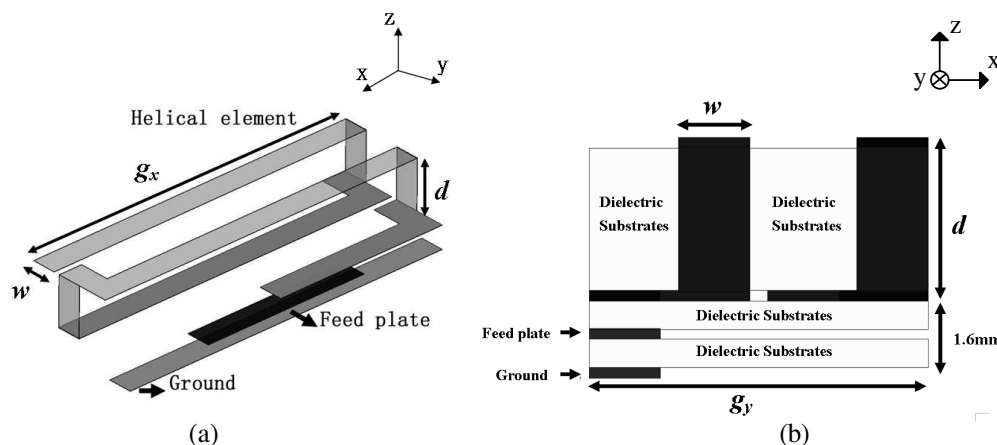


Figure 1: Geometry of the proposed antenna. (a) Structure of the helical element, feed plate and ground plane. The dielectric substrates have been removed from this figure. (b) Side view in the x - z plane.

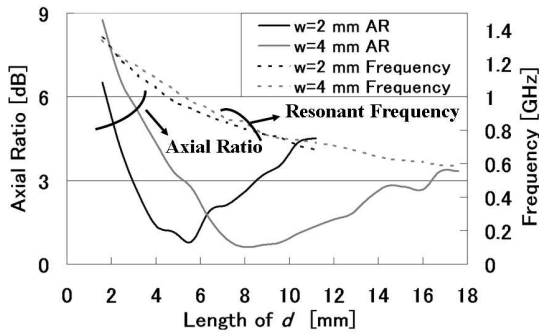


Figure 2: Axial ratio characteristics and frequency variations with varying lengths d .

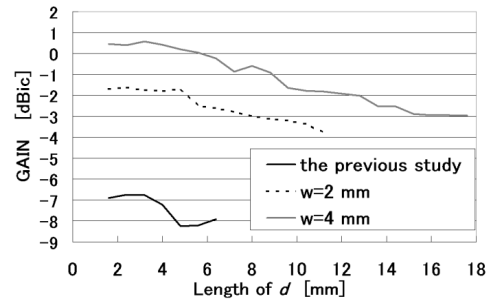


Figure 3: The gain characteristics.

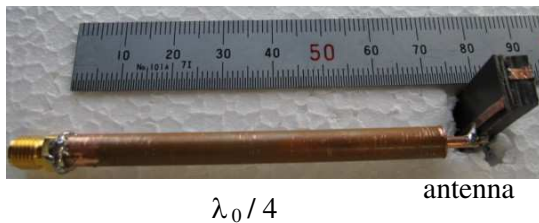


Figure 4: The proposed antenna with the feeding cable and the $\lambda_0/4$ spertop of balun.

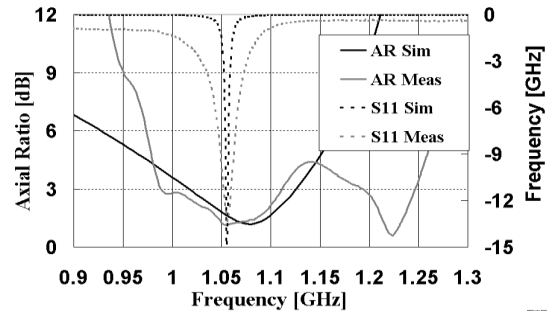


Figure 5: S_{11} characteristics and Axial ratio characteristics.

satisfies the condition of electrically small antennas ($ka < 0.5$). The length of the element is approximately half-wavelength to provide inductive impedance at the resonant frequency. At the feed point, a capacitive feed structure, as reported in [1–3] is used. The feed plate has a length of 3 mm and a width of 20 mm to give a capacitive impedance.

3. RESULTS ANTENNA CHARACTERISTICS

The structure is simulated using Ansoft HFSS ver. 10 simulations software, which utilizes 3D full-wave finite element methods (FEM). In order to keep the size of the small antenna as much as possible, the width of helical element adjusted to $w = 2$ mm which is wider than the previous study $w = 1$ mm at first. The simulated result of axial ratio characteristics and frequency variations with varying lengths d are shown in Fig. 2. The CP can be achieved in the frequency band of 0.8 GHz to 1.2 GHz, which depends on the total length of helical element. Moreover, for keeping the slender sharp of antenna, $w = 4$ mm has been also discussed. The CP can be achieved form 0.61 GHz to 1.02 GHz.

The gain is enhanced about 5 dB ($w = 2$ mm, $g_y = 8.75$ mm) and 6 dB ($w = 4$ mm, $g_y = 16.75$ mm) as shown in Fig. 3. The maximum of gain is increased to 0 dBic, the present results are practical values for applications such as short range wireless communication.

The fabricated antenna is ($w = 2$ mm, $d = 4$ mm, $g_y = 8.75$ mm easy fabrication) shown in Fig. 4. The fabricated antenna has a ka value of 0.33. A coaxial cable has been soldered to the feeding point, and a spertopf balun of quarter-wavelength has been mounted on to the feeding cable in order to eliminate the leakage current from the cable [4].

Figure 5 shows the simulated and measured results of the S_{11} and axial ratio characteristics (+z direction). The simulated and measured results are reasonably identical.

The simulated and measured gains are -2.07 dBic and -1.74 dBic at the resonant frequencies as shown in Fig. 6.

Figure 7 shows the measured and simulated radiation patterns for x - z and y - z planes. These results shows similar radiation pattern as dipole antenna and are in a reasonably good agreement in both planes.

In order to apply the antenna to devices having a large ground plane [1, 5], the antenna is placed at the top of a 60 mm \times 40 mm ($0.2\lambda_0 \times 0.13\lambda_0$) ground plane as shown in Fig. 8, which maybe used

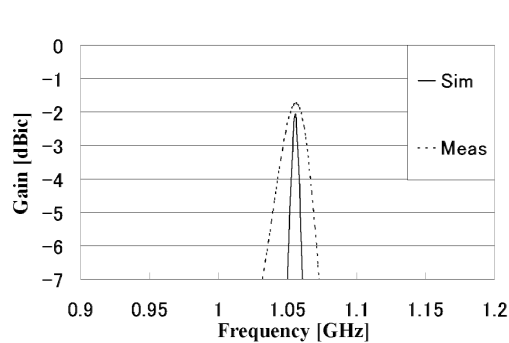


Figure 6: Gain characteristics.

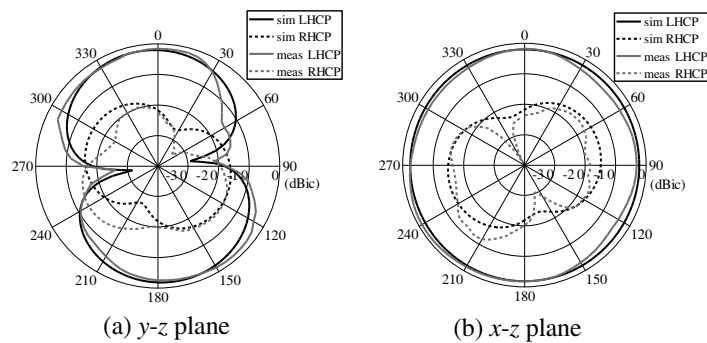


Figure 7: Radiation patterns.

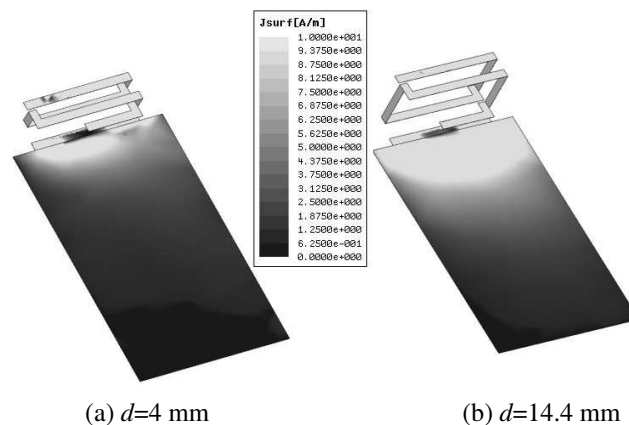
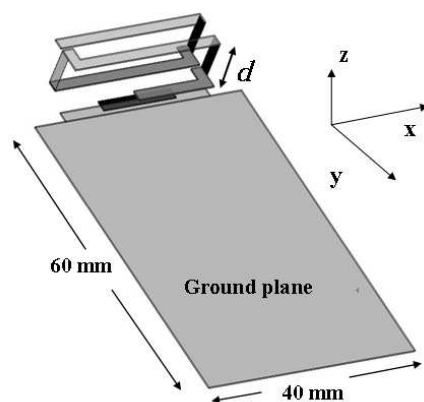


Figure 8: Geometry of the proposed antenna which is installed on 60 mm \times 40 mm. Figure 9: Current distribution of the proposed antenna.

for small handsets. However, because of the different current distribution on the ground plane, as shown in Fig. 9, the antenna needs to adjust $d = 14.4$ mm for CP when the AR is affected by the radiation from both the antenna element and the large ground plane.

4. CONCLUSION

Gain enhancement of a small circularly polarized, slender helical antenna with a wider of helical line had been presented. The maximum gain of helical element can be increased to 0 dBic, which is higher by 6 dB than previous study. This CP antenna can find its applications in RFID and small handsets.

REFERENCES

1. Zhang, Y. and T. Fukusako, "Design of circularly polarized low-profile and slender antenna with a helical element," *IEEE Antennas and Wireless Propagation Letters*, Vol. 11, 523–526, 2012.
2. Ide, K. and T. Fukusako, "Low-profile, electrically small meander antenna using a capacitive feed structure," *Microwave & Optical Tech. Lett.*, Vol. 52, No. 10, 2269–2274, Oct. 2010.
3. Ide, K., S. Ijiguchi, and T. Fukusako, "Gain enhancement of low-profile electrically small capacitive-feed antennas using stacked meander lines," *Int. J. on Antennas & Propag.*, Vol. 2010, Article ID 606717, 8 pages (Open access journal), 2010.
4. Icheln, C., J. Krogerus, and P. Vainikainen, "Use of balun chokes in small-antenna radiation measurements," *IEEE Trans. on Instrum. Meas.*, Vol. 53, No. 2, 498–506, Apr. 2004.
5. Hasebe, N., K. Sakaguchi, and S. Sumimoto, "Radiation of circularly polarized wave from a small helical antenna set on the corner of a rectangular ground plane," *IEICE Trans. Communications*, Vol. J92-B, No. 5, 874–882, May 2009.

Resonantly Confined Modes in Optical Fibers with Circularly Aligned High-index Rods

Yasuo Ohtera, Haruka Hirose, and Hirohito Yamada

Department of Communication Engineering, Graduate School of Engineering
Tohoku University, Japan

Abstract— An optical fiber with novel waveguiding mechanism is proposed. The proposed fiber consists of a circularly-arranged array of high index rods and low index cladding and core region. The wave is confined in the inner region surrounded by the rods by guided-mode resonance (GMR). Different from the conventional circular fibers in which wave is confined by total internal reflection, the proposed fiber exhibit relatively narrow guiding condition due to its GMR-confinement. Some of the optical characteristics such as dispersion relations, mode field profiles, and loss spectra are analyzed using Finite-Difference Time-Domain (FDTD) method.

1. INTRODUCTION

Optical fiber-based sensing has become a key technology in a number of industrial fields due to its robustness to electromagnetic noise, low power consumption and multi-point detection capability. Especially, a class of micro-structured fibers such as photonic crystal fibers (PCFs) has been regarded as a promising building block for the above application, for its characteristic propagation properties. To date, for example, high-sensitive refractive index sensors [1] and gas sensors [2] have been demonstrated utilizing PCFs. To further improve the system's sensitivity, it is straightforward to sharpen the wavelength dependence of the propagation characteristics (loss, etc.) of such fibers. To fulfill this requirement, in this paper, we demonstrate that a class of optical fibers having an array of high-index rods can support highly wavelength dependent propagation modes.

Figure 1 shows a schematic view of the proposed fiber structure. High index rods ($n = 1.8$) are circularly arranged with assist holes ($n = 1.0$) in a host medium ($n = 1.45$) with a constant azimuthal pitch. This rod array functions as a curved version of sub-wavelength grating. It exhibits guided-mode resonance (GMR [3]) for diverging and converging waves inside the fiber. Conventionally, GMR phenomena have been studied and demonstrated in a flat geometry [3]. On the other hand, recently, several groups reported that curved gratings shows resonant reflection for diverging waves, and can be useful for light focusing applications [4, 5]. In proposed fiber, at a resonance wavelength the array of rods function as a highly reflective mirror, resulting in a field confinement inside the circular region surrounded by the rods. The role of assist holes is to reduce refractive index near the outer edge of the fiber, and suppress the radiation loss of the leaky mode that contributes the formation of GMR. Transverse field confinement of circular optical cavity having such curved grating was already confirmed by FDTD simulation for a perfect 2-D system [6]. As the resonance condition is highly wavelength dependent, the propagation loss rapidly changes along with the detuning from the resonance wavelength. The largest difference between this fiber and PCFs photonic bandgap fibers (PBFs) are that the propagation condition is quite sensitive to both wavelength and structural variation.

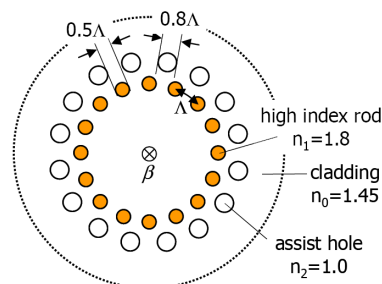


Figure 1: Index profile of the proposed fiber. β means the propagation constant.

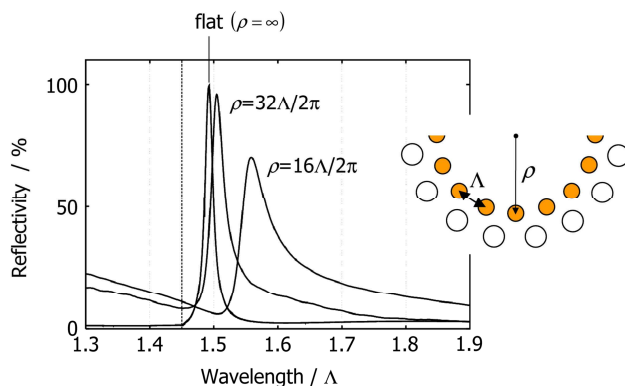


Figure 2: Calculated in-plane reflectivity of the rod arrays with various curvature radius (ρ). Polarization was assumed to be TM (E -field is normal to the plane). For the finite ρ structures the reflectivity is that for diverging circular waves incident from the center of the curvature. The vertical dotted line indicate the cut-off wavelength above which no higher order diffracted waves are radiated to the background medium for the flat structure.

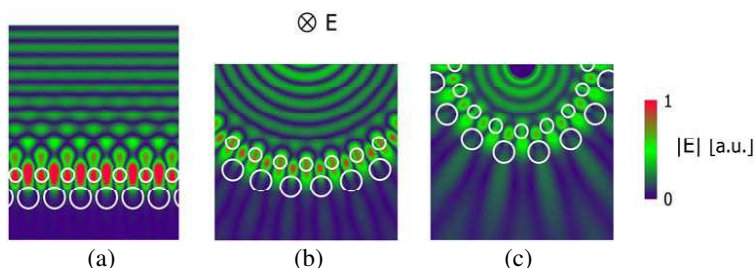


Figure 3: Calculated E -field patterns at GMR peaks. (a) Flat, (b), (c) finite curvature structures with $\rho = 32\Lambda/2\pi$ and $\rho = 16\Lambda/2\pi$, respectively. Incident wave was launched from the top of the figure.

2. BASIC MIRROR PERFORMANCE OF THE ROD ARRAY

First, the reflection characteristics of the rods/holes array are analyzed. Fig. 2 shows calculated reflection spectra for various curvature radii. In a flat structure we assumed that the neighboring rods and holes form an equilateral triangle. For curved structures we kept the diameters of rods and holes the same as the flat structure. Simulations were carried out using in-plane version of FDTD. The field is assumed to be TM (E -field is normal to the plane, H -field lies in the plane). In the flat structure ($\rho = \text{infinity}$), sharp GMR peak feature as high as $R = 100\%$ appeared at wavelength $\sim 1.5\Lambda$. Similar peaks appeared also for finite curvature structures. For the curved structures reflectivity is defined for a diverging cylindrical wave incident from the center of the curvature (reflected wave becomes a converging cylindrical wave propagating back to the center of the curvature). From this result, it was confirmed that this type of curved rods/holes array function as a mirror for cylindrical waves.

Figure 3 shows calculated electric field profiles at the GMR peaks for each structure. For the flat structure (a), we used Cartesian version of 2D-FDTD. The top and bottom of the analytical space were terminated by perfectly matched layers (PMLs). Horizontal extent was truncated by one period and the boundary walls were connected by periodic boundary condition. In (b) and (c), 2-D FDTD of cylindrical coordinate system version was used. The inner and outer edges of the space were terminated by radiation boundaries [7].

In Fig. 3(a), typical GMR properties can be observable: i.e., field is strongly localized in the grating (rod array) region. In addition, Field experiences 2π phase shift per period along the transverse (horizontal) direction. We can see horizontally-oscillating feature, which is created by the evanescent field, in the vicinity of the rod region. This feature rapidly vanishes as the position goes far from the array, resulting in the mirror operation for only the zeroth-order diffracted waves. Figs. 3(b) and 3(c) show that the above GMR mirror function is preserved for finite curvature structures; field confinement still occurs in the array region and cylindrical standing wave is formed inside the curvature. In addition, no higher order diffracted waves are generated inside the curvature

region. However, small portion of diffracted waves exists outside the array. This can be explained as follows: in the resonant grating, the incident wave first couples to the leaky guided mode which propagates horizontally within the array layer. This leaky mode re-radiates small portion of the modal power toward both sides of the array. When directly reflected wave and all the radiated waves interfere constructively, 100% reflectivity is achieved. In the curved structure, the above leaky mode is that for a “curved” periodic waveguide. Therefore it always suffers from a bending loss. The smaller the bending radius, the larger the loss becomes. This is the reason for the field leakage observed outside the array in Fig. 3(b) and Fig. 3(c). We can suppress it by, for example, locating more assist holes or increasing the curvature radius.

3. CHARACTERISTICS OF THE FIBER STRUCTURE

Next, we calculated characteristics of a fiber structure. The base structure is Fig. 2(c) and Fig. 3(c), in which 16 pairs of rods and holes surround the core region. Calculation was carried out using the Cartesian coordinate version of the compact 2-D FDTD method [8]. In this method, time evolution of the fields for a given excitation is calculated for a specified out-of-plane wavenumber (propagation constant of the fiber, β). A point E -source with a gaussian-enveloped sinusoidal waveform was located at the center of the curvature. The time-domain signal of E was monitored at the center. Finite temporal portions of the signal were extracted by applying a time-window and passed to Fast Fourier Transformation to obtain a short-time spectrum. Frequencies of confined modes were determined by picking up the peak frequencies of the spectrum. Also, by changing the center time of the window at a constant interval, and calculating the decay rate of each peak, we can estimate the propagation loss of each mode. Fig. 4 shows a calculated dispersion relation (β vs frequency) of the fiber. We found two types of modes: resonantly confined modes (RGM, indicated

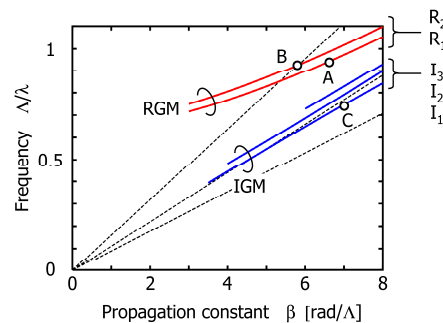


Figure 4: Dispersion relation of resonantly guided modes (RGMs) and index guided modes (IGMs), respectively. Three dashed lines correspond to the lightlines of the rod, cladding, and air holes (from bottom to top), respectively.

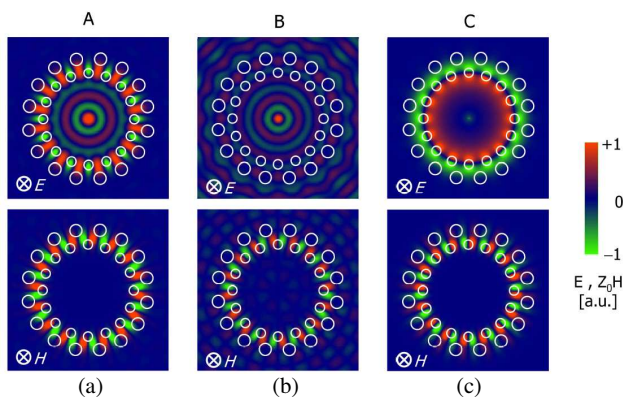


Figure 5: Mode field profiles of (a), (b) RGMs and (c) IGM. The upper and lower figures correspond to the axial component of E - and H -fields, respectively. The H amplitudes are multiplied by impedance in vacuum (Z_0).

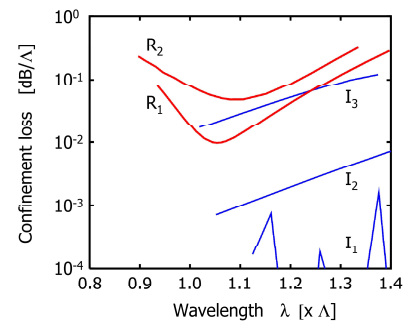


Figure 6: Confinement loss of the RGM and IGM. R_1 , R_2 , etc. correspond to each mode displayed in Fig. 2. Note that the rapid variation of I_1 mainly originates from calculation error.

by R_1 and R_2), and ordinary index-guided mode (IGM, marked by $I_1 \sim I_3$). Significant feature is that the dispersion relation of RGMs extends beyond the lightline of the cladding. This should be a clear evidence of that the RGMs are not reflected by total internal reflection, but resonant reflection (which can occur at large reflection angle at core/clad boundary).

Figure 5 shows the field profiles for RGMs (A and B in Fig. 4) and IGM (C in Fig. 4). Figs. 5(a) and 5(b) clearly show the feature of GMR: azimuthal standing wave pattern is formed along the high-index rod array. On the other hand, the E -field pattern of IGM (Fig. 5(c)) shows no nulls along the azimuthal direction near the rod region. According to the calculation of temporal decay rate of each mode, the RGMs were found to have loss minima at a specific wavelength whereas IGMs have no such characteristics.

Figure 6 shows the relation between the wavelength and propagation loss. The loss minima can only be seen for RGMs. Such characteristic implies the RGM's potential usefulness as a sensing probe, which detects environmental fluctuation via the change of propagation loss. Although the calculated order of propagation loss is quite large, structural design having moderate loss will be found by proper selection of constituent materials and appropriate rods/assist holes arrangement.

4. CONCLUSIONS

We proposed a novel class of optical fibers that confine and guide light utilizing guided-mode resonance phenomenon of circularly arranged rods embedded in a host material. Calculation result of dispersion relation indicated that the mode can exist in the (conventionally) continuum region. Calculated mode field profiles also exhibited a typical feature of GMR: field is strongly confined in the rod array region. The challenge is to optimize the loss spectra will be investigated as our next task.

ACKNOWLEDGMENT

This study has been supported by JSPS KAKENHI Grant Number 24656041.

REFERENCES

1. Wu, D. K. C., B. T. Kuhlmeiy, and B. J. Eggleton, "Ultrasensitive photonic crystal fiber refractive index sensor," *Opt. Lett.*, Vol. 34, No. 3, 322–324, 2009.
2. Li, S.-G., S.-Y. Liu, Z.-Y. Song, Y. Han, T.-L. Cheng, G.-Y. Zhou, and L.-T. Hou, "Study of the sensitivity of gas sensing by use of index-guiding photonic crystal fibers," *Appl. Opt.*, Vol. 46, No. 22, 5183–5188, 2007.
3. Wang, S. S. and R. Magnusson, "Theory and applications of guided-mode resonance filters," *Appl. Opt.*, Vol. 32, No. 14, 2606–2613, 1993.
4. Cannistra, A. T., M. K. Poutous, E. G. Johnson, and T. J. Suleski, "Performance of conformal guided resonance filters," *Opt. Lett.*, Vol. 36, No. 7, 1155–1157, 2011.
5. Ohtera, Y., S. Iijima, and H. Yamada, "Guided-mode resonance in curved grating structures," *Opt. Lett.*, Vol. 36, No. 9, 1689–1691, 2011.
6. Ohtera, Y., S. Iijima, and H. Yamada, "Cylindrical resonator utilizing curved resonant grating as a cavity wall," *Micromachines*, Vol. 3, No. 1, 101–113, 2012.
7. Xu, Y., J. S. Vuckovic, R. K. Lee, O. J. Painter, A. Scherer, and A. Yariv, "Finite-difference time-domain calculation of spontaneous emission lifetime in a microcavity," *J. Opt. Soc. Am. B*, Vol. 16, No. 3, 465–474, 1999.
8. Xiao, S. and R. Vahldieck, "An efficient 2-D FDTD algorithm using real variables," *IEEE Microwave Guided Wave Lett.*, Vol. 3, No. 5, 127–129, 1993.

Terahertz Metamaterial Absorbers for Sensing and Imaging

P. Kung and S. M. Kim

Department of Electrical and Computer Engineering, The University of Alabama, Tuscaloosa, USA

Abstract— The development of devices and structures with functionality in the terahertz (THz) portion of the electromagnetic spectrum is of great interest because of potential applications in sensing and imaging in the THz, including molecular spectroscopy and medical imaging. One of such devices is a THz absorber that has the ability to absorb THz radiation with specific characteristics, including polarization, bandwidth, or multiband capability.

In this work, we present the design and finite-element simulation of thin, tunable, polarization insensitive metamaterial THz absorbers. We further propose a novel metamaterial structure with a broadened bandwidth of absorption in the THz. This concept is based on multiple band absorption and is achieved by bringing absorption bands close enough to one another in a multi-layered pattern, which decreases the negative interaction between rings and corresponding resonances. Physically, the structure consists of multilayer concentric copper rings, interspaced with polyimide as the dielectric and a final copper plane to reflect selected frequencies back into the absorbing layered rings. These rings are tightly stacked in order to reduce their destructive interaction compared to when the rings are all placed on the same plane normal to the incident wave.

1. INTRODUCTION

The Terahertz (THz) range (0.1 ~ 10 THz) of the electromagnetic spectrum has attracted increasing attention because of a growing number of applications. Because it lies between the microwave and far infrared frequencies, it shares some properties from each of these regimes. Like microwave, THz wave can penetrate through wide variety of non-conducting materials like clothing, paper, plastic, wood, etc.. THz radiation is also non-ionizing and can be absorbed by molecules like water and DNA. These properties make THz waves very attractive for a large variety of application including medical imaging [1], environmental monitoring of Earth [2], remote sensing of explosives [3], and semiconductor electrical property determination [4]. However, conventional microwave technology cannot measure and detect THz radiation. As a result, there is intense research focused on developing appropriate devices to sense THz electromagnetic waves. Although terahertz time domain spectroscopy (THz-TDS) is a method which has been extensively used to measure terahertz transmission and reflection from materials, it suffers from indirect measurement in frequency domain and a large experimental setup size. Therefore, it is highly challenging to design compact THz devices capable of measuring terahertz radiation directly.

Metamaterials, which are artificially subwavelength structures capable of manipulating electromagnetic waves in a desired fashion [5, 6], represent a promising approach to meet this need. The first metamaterial THz absorber was introduced in 2008 and used the major drawback of metamaterials, loss in a metal, as a key factor to absorb terahertz waves [8]. It consisted of three subwavelength layers including a frequency selective surface (FSS), a dielectric spacer followed by a metallic back layer. Many articles have discussed the principle of these kind of absorbers. Basically, the FSS determines the absorption frequency, the metallic back layer reflects the transmitted resonance frequency, and the spacer layer acts as a subwavelength cavity which makes the waves reflected from the metallic layer out of phase with respect to the reflected waves from the FSS [7]. Soon after the first demonstration of THz absorber, different structures have been fabricated to enhance the functionality of the absorber including polarization independent [8, 9], dual band [8, 10], triple band [9], multiband [7] and broadband perfect absorbers [11–13].

2. ABSORBER STRUCTURE AND SIMULATION PROCEDURE

The absorber structure considered here consists of a periodic 2D array of two stacked-layered concentric rings acting as the FSS layers, as shown in Figure 1 (one unit cell shown). A thin dielectric (polyimide) layer separated the two ring layers, and another separated the back FSS layer from a back metallic full layer. The metal used in this study was copper. The spacer between the metallic back layer and the back FSS layer is also polyimide.

Finite element analysis (FEA) was carried out using commercial COMSOL Multiphysics package in order to determine the response of the structure to an incident THz electromagnetic wave. The

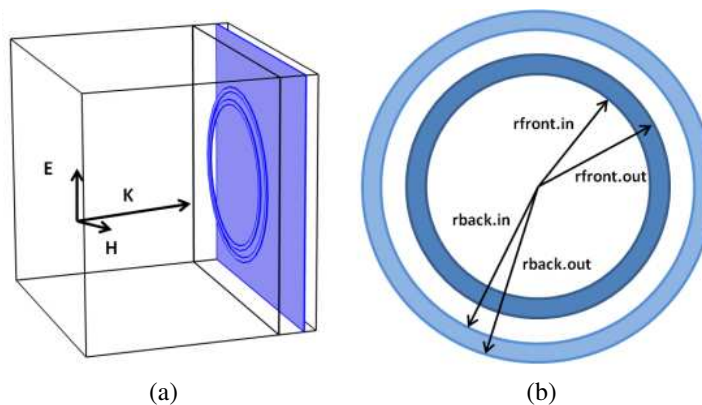


Figure 1: (a) 3D illustration of the hybrid multilayer absorber with polarization and wave vector directions. (b) Planar view of the front and back FSS layers showing their respective ring arrangement.

response from a unit cell containing the structure under study was considered in the simulation. The incident THz wave propagates perpendicularly to the plane of the structure and perfect boundary conditions in the directions perpendicular to electric and magnetic field vectors were used. For absorption calculations, both Poynting theorem method and scattering matrix calculations were used. In the former, the incident power (I) was calculated as $0.5 \times E_0^2 / Z_0$ which E_0 is the incident electric field (V/m) and Z_0 is the free space impedance (Ω), while the reflected power (R) was calculated through Comsol. Because our structure contains a metallic back plane parallel to the plane of the ring structure, there is no transmission through the absorber and its absorption can therefore be determined as $1 - R/I$. Lumped port boundary conditions were also employed to calculate scattering matrix parameters and the absorption was calculated by using $1 - |S_{11}|^2 - |S_{21}|^2$. Both calculations were in agreement with each other. For the simulation, the conductivity used for the copper was $\sigma = 6 \times 10^7$ S/m. For the polyimide material, a conductivity of $\sigma = 6.7 \times 10^{-16}$ S/m and a relative permittivity of $\varepsilon = 3.15$ were used. The thickness of the copper layers (ring and back plane) was 200 nm.

3. RESULTS AND DISCUSSION

Each ring of the two FSS layers was first simulated separately prior to combining them together to make a multilayer hybrid absorber. The aim of this part of the work consisted of determining the proper radii for the rings and optimal polyimide spatter thicknesses through sweeps. Simulation results the first (front) FSS ring yielded 29 and 31 μm for the inner and outer radii respectively (rfront.in and rfront.out), and a polyimide thickness of 10.5 μm , in order to achieve an absorption peak of 99.9% at 1.06 THz. The unit cell dimension was 104 μm . For the second (back) FSS ring, its inner and outer radii, as well as its distance from the first FSS ring were parameters that were swept. The optimal distance between the two FSS layers was found to be 1 μm and the ring radii 34 and 36 μm (rback.in and rback.out) to achieve a 99.9% absorption at 0.82 THz. After putting both FSS together, the absorption frequencies remained almost unchanged. However, due to the interaction between the rings in the two stacked layers, the peak of absorption decreased slightly to 98%. The bandwidth of the absorption peak at half maximum for each resonance frequency was almost 50 GHz.

In order to broaden the absorption band, the radius of the front ring was first changed as a means to bring the resonances closer in frequency. Table 1 lists the dimensions of three different absorber structures investigated, with the resulting absorption peak frequencies. By increasing the radius of the front ring while keeping other structure parameters unchanged, the resonance frequencies are brought closer, which can also be observed in the absorption spectra in Figure 2. But by doing so, the rings get closer to each other in the plane normal to the incidence direction and therefore the effect of the electric field of one ring onto another ring gets considerable, which reduces the peak absorption of the back FSS ring at the lower frequency. At the same time, the resonance frequency bears a slight red shift.

To achieve a broadband absorber, the front ring radius was further increased until it exceeded the size of the back ring. Figure 3 illustrates the resulting absorption spectra of structures with dimensions listed in Table 2. For comparison, we have also depicted the first resonance absorption of

absorber #1. In structure #4, the absorption peaks mostly overlapped, resulting in an absorption bandwidth increase up to 70 GHz which was 20 GHz more than the bandwidth of one ring absorber. In absorber #5, the front ring size was even larger until the resonance frequencies are distinguishable once more. Similar to the case of absorber #3, the amplitude of second (back ring) absorption also decreased but its resonance frequency experienced a small blue shift compared to the single ring absorber case. The bandwidth at half maximum of absorber #5 was 100 GHz, which was 2 times as high as that of single ring absorbers.

Table 1: Dimensions of three different absorbers.

Name	rfront. in (μm)	rfront. out (μm)	Front Res. (THz)	Abs. (%)	rback. in (μm)	rback. out (μm)	Back Res. (THz)	Abs. (%)
29–31, 34–36 (1)	29	31	1.06	98	34	36	0.82	98
31–33, 34–36 (2)	31	33	1	98	34	36	0.812	79
32–34, 34–36 (3)	32	34	0.94	98	34	36	0.80	56

Table 2: Dimensions of three different absorbers where the back ring radii are fixed but the front ring radii increase and exceed the size of those in back ring.

Structure	rfront. in (μm)	rfront. out (μm)	Front Res. (THz)	Abs. (%)	rback. in (μm)	rback. out (μm)	Back Res. (THz)	Abs. (%)
38–40, 34–36 (4)	38	40	0.80	98	34	36	—	—
39–41, 34–36 (5)	39	41	0.775	98	34	36	0.835	61

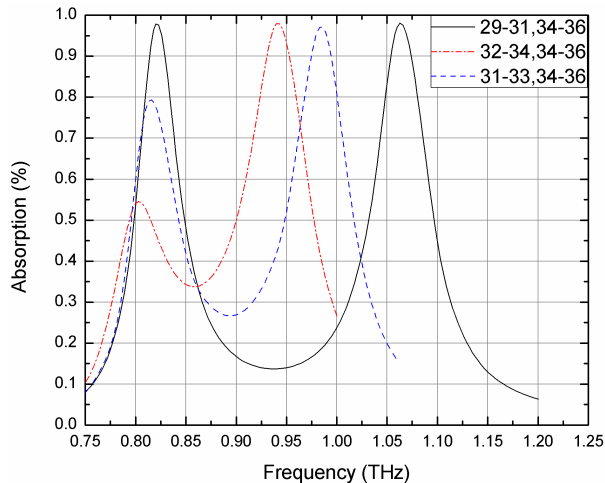


Figure 2: Absorption spectra for the three absorber structures of Table 1.

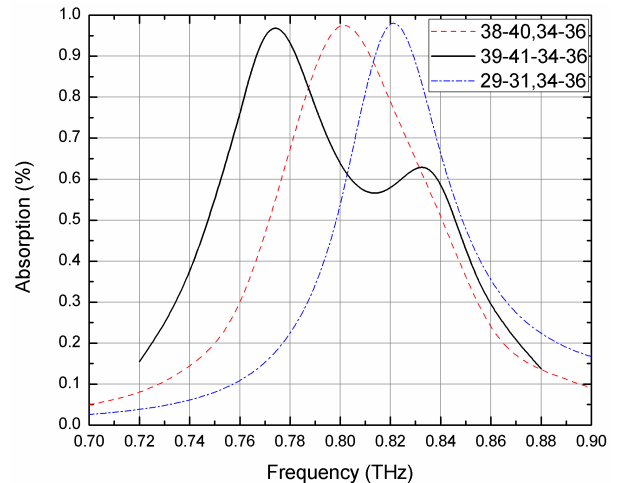


Figure 3: Absorption spectra for the three absorber structures of Table 2.

4. CONCLUSIONS

We have investigated a multilayer polarization independent THz absorber consisting of two copper rings in two tightly stacked layers separated by a polyimide layer, followed by another polyimide layer and a metallic back layer. Design and simulation were carried out using finite element analysis. First, the proper radii for the individual rings and polyimide thickness were optimized, resulting in an absorption resonance bandwidth at half maximum of almost 50 GHz. By changing the dimension of the ring in the front layer, we have brought the resonance closer in frequency, which led to a doubling of the bandwidth to 100 GHz. However, the peak absorption associated with the back ring dropped to 60%, which is attributed to the spatial overlap between the two rings.

ACKNOWLEDGMENT

We would like to acknowledge the National Science Foundation (EECS-0824452, CAREER, and IIT-1127831) for support of this work.

REFERENCES

1. Woodward, R. M., B. E. Cole, V. P. Wallace, R. J. Pye, D. D. Arnone, E. H. Linfield, and M. Pepper, "Terahertz pulse imaging in reflection geometry of human skin cancer and skin tissue," *Phys. Med. Biol.*, Vol. 47, 3853–3863, 2002.
2. Waters, J. W., L. Froidevaux, R. S. Harwood, R. F. Jarnot, H. M. Pickett, W. G. Read, P. H. Siegel, R. E. Cofield, M. J. Filipiak, D. A. Flower, J. R. Holden, G. K. Lau, N. J. Livesey, G. L. Manney, H. C. Pumphrey, M. L. Santee, D. L. Wu, D. T. Cuddy, R. R. Lay, M. S. Loo, V. S. Perun, M. J. Schwartz, P. C. Stek, R. P. Thurstans, M. A. Boyles, K. M. Chandra, M. C. Chavez, G. S. Chen, B. V. Chudasama, R. Dodge, R. A. Fuller, M. A. Girard, J. H. Jiang, Y. Jiang, B. W. Knosp, R. C. LaBelle, J. C. Lam, K. A. Lee, D. Miller, J. E. Oswald, N. C. Patel, D. M. Pukala, O. Quintero, D. M. Scaff, W. Van Snyder, M. C. Tope, P. A. Wagner, and M. J. Walch, "The earth observing system microwave limb sounder (EOS MLS) on the Aura satellite," *IEEE Trans. Geosci. Remote Sensing*, Vol. 44, No. 5, 1075–1092, 2006.
3. Appleby, R., "Standoff detection of weapons and contraband in the 100 GHz to 1 THz region," *IEEE Trans. Ant. Prop.*, Vol. 55, No. 11, 2944–2956, 2007.
4. Dawahre, N., J. Brewer, G. Shen, N. Harris, D. S. Wilbert, L. Butler, S. Balci, W. Baughman, S. M. Kim, and P. Kung, "Nanoscale characterization of single crystal zinc oxide nanowires," *11th IEEE International Conference on Nanotechnology*, 640–645, Portland, Oregon, 2011.
5. Zhang, J, K. F. MacDonald, and N. I. Zheludev, "Controlling light-with-light without nonlinearity," *Light: Science and Applications*, Vol. 1, 1–5, 2012.
6. Iwanaga, M., "Photonic metamaterials: A new class of material for manipulating light waves," *Sci. Technol. Adv. Mater.*, Vol. 13, 053002-17, 2012.
7. Peng, X. Y., B. Wang, S. Lai, D. H. Zhang, and J. H. Teng, "Ultrathin multi-band planar metamaterial absorber based on standing wave resonances," *Opt. Exp.*, Vol. 20, No. 25, 27756–27765, 2012.
8. Ma, Y., Q. Chen, J. Grant, S. C. Saha, A. Khalid, and D. R. S. Cumming, "A terahertz polarization insensitive dual band metamaterial absorber," *Opt. Lett.*, Vol. 36, No. 6, 945–947, 2011.
9. Shen, X., T. J. Cui, J. Zhao, H. F. Ma, W. X. Jiang, and H. Li, "Polarization independent wide-angle triple-band metamaterial absorber," *Opt. Exp.*, Vol. 19, No. 10, 9401–9407, 2011.
10. Tao, H., C. M. Bingham, D. Pilon, K. Fan, A. C. Strikwerda, D. shrekenhamer, W. J. Padilla, X. Zhang, and R. D. Averitt, "A dual band terahertz metamaterial absorber," *J. Phys. D: App. Phys.*, Vol. 43, 225102-5, 2010.
11. Huang, L., R. D. Chowdhury, S. Ramani, M. T. Reiten, S. N. Luo, A. J. Taylor, and H. T. Chen, "Experimental demonstration of terahertz metamaterial absorbers with a broad and flat absorption band," *Opt. Lett.*, Vol. 37, No. 2, 154–156, 2012.
12. Kim, D. H., D. S. Kim, S. Hwang, and J. H. Jang, "Surface relief structure for a flexible broadband terahertz absorber," *Opt. Exp.*, Vol. 20, No. 15, 16815–16822, 2012.
13. Kim, D. S., D. H. Kim, S. Hwang, and J. H. Jang, "Broadband terahertz absorber realized by self-assembled multilayer glass spheres," *Opt. Exp.*, Vol. 20, No. 12, 13566–13572, 2012.

Operational Slow Line Underpinned by a 1D Metamaterial

D. Dowlett, T. Ditchi, E. Géron, and J. Lucas

Laboratoire de Physique et d'Étude des Matériaux, ESPCI-ParisTech
UPMC Univ. Paris 06, CNRS UMR8213, 10, Rue Vauquelin, Paris 75005, France

Abstract— In this paper, we demonstrate how to take advantage of the forbidden bands that present 1D meta-material to design a line that exhibits a low group velocity. The theoretical aspect and an application along with its design rules are presented. Finally, the usability of the line to transmit some piece of information at low velocity is practically verified.

1. INTRODUCTION

Many hyperfrequencies applications require slow lines. They can be used as delay lines, for data buffering or to increase interactions between the electromagnetic wave and matter, by increasing the interaction time as in electro-optic applications [1]. There are two ways to obtain a significant delay using a line. Whether a long line is used or it is possible to use a shorter line if the electromagnetic velocity is significantly smaller. In some radar applications, the required delays are very large. They imply such length that they are realized using optical fibers.

Without dispersion, the only way to obtain a slow velocity in a line or a material consists in using high dielectric constant material. Unfortunately only small velocity reduction can be obtained this way. It is possible though to obtain large velocity reduction by taking advantage of dispersion. Many applications are not wide band and can therefore withstand smaller bandwidth. It is possible to obtain a significant velocity reduction when the line or material is resonant over the considered bandwidth. Many works based on this effect have been carried out recently [2]. In this paper, we propose to use the properties of some metamaterial lines to obtain the same result.

In this work, we demonstrate how to calculate the required gain to obtain a given group velocity reduction using the Kramers-Kronig relations [3] and how it applies to 1D metamaterials. Then we expose the key features that control the behavior of such lines: characteristic impedance, group velocity and bandwidth and how they interact with each others. The design of the line is then checked using a circuit simulation software that can take into account some internal propagation phenomena. At this point the losses in both substrate and lumped components as well as impedance matching with the standard $50\ \Omega$ lines are taken into account.

Finally the results obtained with a prototype are presented. The usability of such a system to obtain large delays is verified and discussed focusing on ability to transmit data.

2. SLOW LINES BASICS

A slow line exhibits a low group velocity V_g defined as follows:

$$V_g = \frac{d\omega}{dk} \quad (1)$$

where ω is the circular frequency and k the wave vector modulus in the direction of propagation, which is to say, in the case of a line, minus the phase shift per length unit.

2.1. Slowing Down

Considering the Kramers-Kronig relations [4, 5], group velocity variations can be obtained by modifying the amplitude of the frequency response (i.e., the gain). This is illustrated in Figure 1. In this figure, curve a) presents the relative targeted velocity variation of the group velocity, where V_0 is the “normal” group velocity. By using Equation (1), one can calculate the corresponding wave vector modulus which is presented in the Figure 1(b). It is then possible to compute [3] the required gain variation G for a given length of line L as presented in Figure 1(c).

The results of Figure 1 can be applied to any frequency domain ranging from zero to F_{\max} . The K-K relation yields the logarithm of the gain variation which has been converted to dB for convenience in Figure 1(c). One can see considering the legend of this figure that the greater the initial group velocity V_0 , the easier it is to reduce it. Accordingly, The greater the frequency range F_{\max} , the higher the required gain. By plotting those graphs for narrower velocity reduction bandwidth, it shows as well that the greater the bandwidth, the larger the required gain.

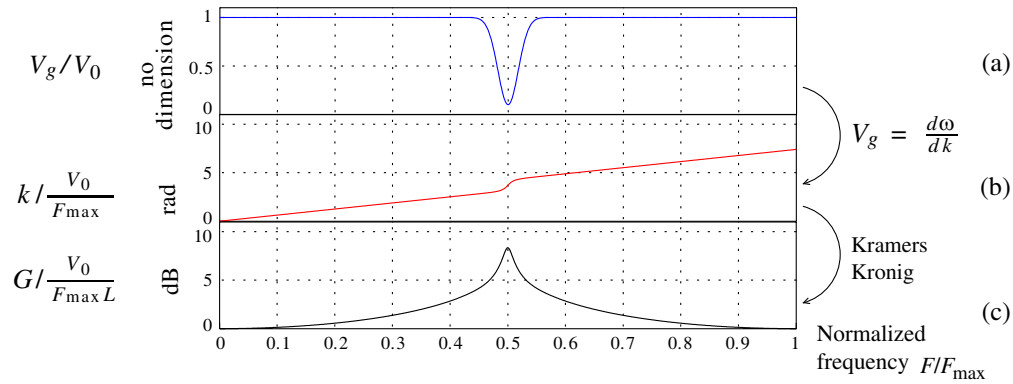


Figure 1: Targeted velocity reduction and corresponding gain variation.

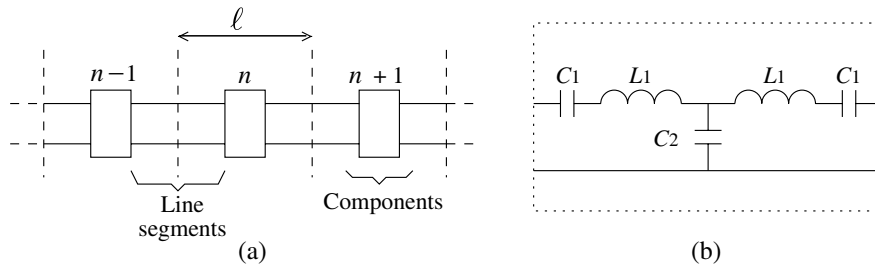


Figure 2: Theoretical structure of the slow 1D metamaterial line. (a) General structure. (b) Components details.

2.2. Dimensioning

In a microstrip line or $50\ \Omega$ coaxial wire where the group velocity is about $\frac{2}{3}$ of c the speed of light in vacuum, by taking $F_{\max} = 4$ GHz in order to have a central frequency of 2 GHz (Telecommunications applications), the required gain variation according to Figure 1 is of $G \approx 8 \times \frac{F_{\max}}{V_0} \approx 160$ dB per length unit. This value is indeed titanic. It cannot be reached via some amplification. The Hilbert transform that underlies the Kramers-Kronig produces a result up to an additive constant. Consequently, the gain variation presented in Figure 1 can be shifted down. Finally it is possible to consider a pass band line, where the gain is 0 dB at 2 GHz and that presents a strong attenuation outside the bandwidth.

This might be achieved using filters, but it is much more judicious to consider a passband line where the bandwidth is created by two adjacent forbidden bands.

3. 1D META-MATERIAL LINE

A 1D meta-material is a line build up of a succession of elementary cells whose length ℓ is such that the line appears homogeneous to the electromagnetic wave it carries. This condition can be stated as:

$$\ell < \frac{\lambda}{10} \quad (2)$$

where λ is the wave length of the carried wave.

Such a structure is presented in Figure 2(a). The cells of the metamaterial are constituted of lumped or printed components connected with classical line segments.

This kind of line is easier to study when the length of the line segment is small which is compatible with the condition of Equation (2). One can simply consider the components values and the classical telegraphist model of the line segments to calculate the behavior of the metamaterial [6]. In this work, the target frequency is about 2 GHz therefore the Equation (2) yields $\ell \ll 1$ cm when using microstrip lines over a PTFE woven glass substrate. This condition can be respected using classical hybrid technology [7]. Consequently, the 1D metamaterial line used will be studied in a first time without considering the line segment, the design is then post corrected to take into account their influence which is assumed to be small enough.

3.1. Band-gaps

1D metamaterials are known to exhibit bandgaps which is what we are looking for. In a first time an elementary cell such as the one presented in Figure 2(b) without the capacitor C_1 is considered. The propagation in such a structure has been studied by Brillouin [8]. As long as the condition of Equation (2) is respected, this 1D metamaterial behaves as a right handed line up to the circular frequency $\frac{1}{\sqrt{L_1 C_2}}$. After this frequency, the propagation is forbidden. In order to begin with a forbidden band, we have added the serial capacitor C_1 which prevents propagation at low frequencies. Finally, the behavior of the metamaterial can be calculated using the Floquet theorem and the Kirchhoff laws and one obtains [9] the behavior presented in Table 1.

This table shows that it is possible with such a structure to flank a RH propagation band with a forbidden band on each side.

4. TUNNING THE SLOW LINE

There are three parameters to take into account when designing a slow line: the velocity reduction, the bandwidth and the characteristic impedance of the line. Each of those parameters influences the other. For instance enlarging the bandwidth increases the velocity, and modifies the characteristic impedance. In the realization presented hereafter, we have chosen to favor velocity reduction over characteristic impedance.

One can find in Table 2 the values calculated to obtain a bandwidth of about 100 MHz around 2 GHz. In the same table one will find as well the values corrected by simulating [10] a line of 10 cells of the metamaterial, in order to take into account the 50Ω line segments used to practically build the line.

The obtained line presents a low characteristic impedance of about 3Ω which makes it necessary to use quarter wave line segment at its input and output in order to avoid reflections. As these quarter wave line segment are not slow line segments we assume that the multiple reflection they induce are short lived compared to the propagation time in the line itself and that they will not perturb the line unduly. This point will be verified later.

Figure 3(a) presents an overview of the behavior of the transmission. It exhibits a narrow

Table 1: Nature of the waves in the slow line metamaterial.

ω	0	$\omega_1 = \frac{1}{\sqrt{L_1 C_1}}$	$\sqrt{\omega_1^2 + 2\omega_2^2}$	$\omega_2 = \frac{1}{\sqrt{L_2 C_2}}$
Nature of the waves	Evanescent	Right handed		Evanescent

Table 2: Values calculated and corrected by simulation for the 1D slow metamaterial line.

	Ideal metamaterial	Corrected values
L_1	4.5 nH	3.4 nH
C_1	1.5 pF	1.4 pF
C_2	26 pF	21 pF

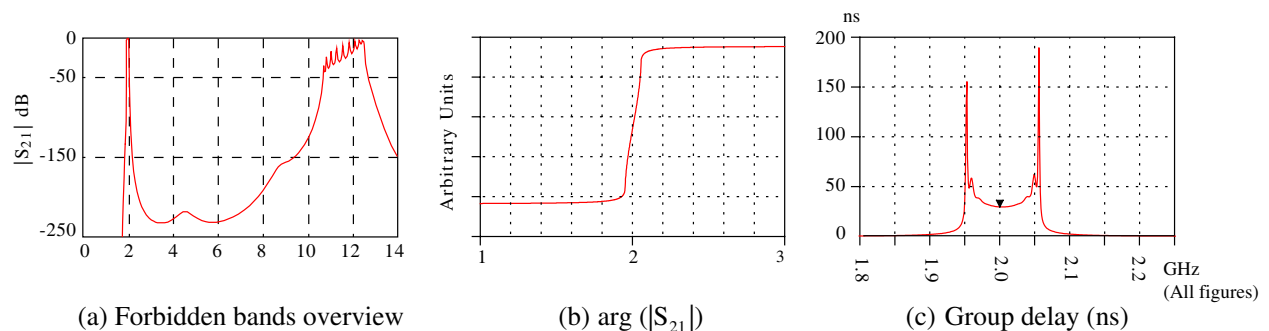


Figure 3: Simulated slow line forbidden bands and performances.

passband with very steep slopes around 2 GHz as required to significantly reduce the group velocity. Figure 3(b) presents the corresponding shape of the argument of the transmission coefficient which shows that there is indeed a strong variation of the group velocity in the considered passband. Finally, 3(c) presents the corresponding group delay which is to be compared to the ≈ 0.35 ns that would be obtained in a classical 7 cm long microstrip line.

5. BUILDING AND CHARACTERIZING THE SLOW LINE

5.1. Realization

The line calculated and simulated has been realized and is presented in Figure 4.

5.2. Performances

We have firstly verified the value of the group velocity for the prototype. This measurement was simply realized using a Vector Network Analyzer (VNA) to measure the argument of S_{21} . The measurement was performed inside and outside of the passband in order to measure the velocity reduction ratio. This corresponds to a steady state measurement. The ratio measured is 32 as presented in Table 3 along with an high attenuation which is mainly due to the losses in the components. At this level, these losses prevent of course to use such a line for industrial applications. Nevertheless it allows to validate the concept. Though being high, the losses do not prevent to measure the effective data transmission ability of the the slow line.

Schuster demonstrated in 1920 as reported by Brillouin in his book [11] that the group velocity is the velocity of any king of signal modulation given a constant transmission amplitude. It is not the case for the slow line. Nevertheless, the passband is sufficiently large to allow to transmit modulated signals. Consequently, we measured the effective signal velocity by comparing the transit time of a GFSK (Gaussian Frequency Shift Keying) modulated data frame time between the slow line and a reference microstrip line of the same length. By doing so, we are sure to effectively measure the information velocity which would have not been fully the case if we had used a Gaussian modulated signal for instance [12]. The experimental setup is presented in Figure 5.

A data set chosen to easily recognize its middle bit is used to modulate a carrier at the central frequency of the slow line. The GFSK modulator generates a synchronization signal. The modulated signal alternatively propagates in the slow line and in a reference microstrip line of the same overall length than the slow line. After its transit in the slow line, or in the reference line, the signal

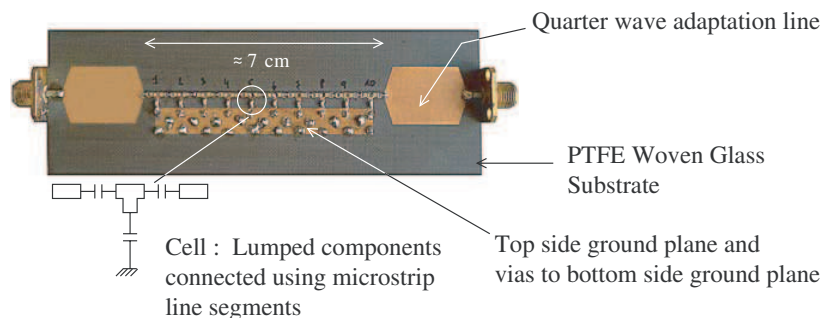


Figure 4: Slow line prototype.

Table 3: Summary of the performances of the slow line.

	$V_{g_{ref}}$	$V_{g_{Slow}}$	$\frac{V_{g_{ref}}}{V_{g_{Slow}}}$	Reflection ($ S_{11} $)	Losses
Simulated	$2.06 \cdot 10^8$ m/s	$4.2 \cdot 10^6$ m/s	48	**	**
Steady State measurement (via VNA S_{21})	$1.65 \cdot 10^8$ m/v	$5.12 \cdot 10^8$ m/s	32	-40 dB	40 dB
Transient measurement (Zero span SPA)	$2.14 \cdot 10^8$ m/s	$5.84 \cdot 10^8$ m/s	37	**	40 dB

** = Not measured or calculated

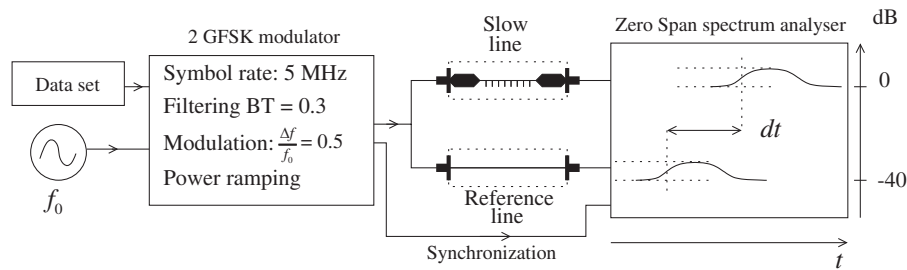


Figure 5: Experimental signal velocity measurement setup.

is demodulated using a spectrum analyzer in zero span mode with the same settings in both cases (reference level, resolution filter, sweep time). This way we verified that the information is correctly transmitted, and we measured the effective delay for the information introduced by the slow line. The middle bit is identified inside the data frame by demodulating the whole frame and its start date is measured as the middle of the rising time in both cases. This method for measuring the information velocity is insensitive to any bias that would result from some reshaping of the signal.

6. CONCLUSION

In this paper we used, the previously well-tryed from previous work, Kramers-Kronig technique to estimate the gain variation required to obtain a significant reduction of the group velocity. Considering the magnitude of the gain variation, we concluded that the best way to reach this goal is to take advantage of the strong attenuation that occurs in frequency bands where the waves are evanescent. Consequently we designed a slow line by flanking its working band by two forbidden bands. Simulations validated the concept and allowed to tune the design by taking into accounts the losses in the components and the dimension of the connecting microstrip lines we used for the hybrid technology prototype. By working as expected, this prototype validates the conception method. Further more it has allowed us to verify that though the transmission amplitude in the working band is not strictly constant, the group velocity reduction effectively corresponds to a reduction of the velocity of information in spite of strong amplitude variations.

REFERENCES

1. Brosi, J. M., C. Koos, L. C. Andreani, M. Waldow, J. Leuthold, and W. Freude, "High-speed low-voltage electro-optic modulator with a polymer infiltrated silicon photonic crystal waveguide," *Optics Express*, 2008.
2. Editorial, "Taking things slow," *Nature Photonics*, Vol. 2 No. 8, 447, 2008, <http://www.nature.com/nphoton/focus/slowlight/>.
3. Lucas, J., E. Géron, T. Ditchi, and S. Holé, "A fast fourier transform implementation of the Kramers-Kronig relations: Application to anomalous and left handed propagation," *AIP Advances*, Vol. 2, 032144-1, 2012, <http://dx.doi.org/10.1063/1.4747813>.
4. De Laer Kronig, R., "On the theory of dispersion of x-rays," *J. Opt. Soc. Am. Rev. Sci. Instrum.*, Vol. 12, 547–557, 1926.
5. Bohren, C. F., "What did Kramers and Kronig do and how did they do it?," *Eur. J. Phys.*, Vol. 31, 573–577, 2010, doi:10.1088/0143-0807/31/3/014.
6. Caloz, C. and T. Itoh, *Electromagnetic Metamaterials: Transmission Line Theory and Microwave Applications/The Engineering Approach*, Wiley Interscience, 2006.
7. Géron, E., T. Ditchi, J. Lucas, and S. Holé, "Electronically controlled asymmetric microstrip line coupler underpinned by an hybrid right-left-handed line," *IET Microwaves, Antenas & Propagation*, August 2012, doi: 10.1049/iet-map.2011.0426.
8. Brillouin, L. and M. Parodi, *Propagation des Ondes dans les Milieu Périodiques*, Masson TE cie Dunod, 1956.
9. Eleftheriades, G. V., and K. G. Balmain, *NEgative-Refractive Metamaterials*, 95–97, IEE Press Wiley-Interscience, 2005, ISBN 13: 978-0-471-60146-3.
10. ADS Simulation Software, Technical Report, Agilent Technologies.
11. Brillouin, L., *Wave Propagation and Group Velocity*, 7–9, Library of Congress Catalog Card Number: 59-13829, Academic Press INC, 1960.
12. Sauter, T., "Gaussian pulses and superluminality," *J. Phys. A: Math. Gen.*, Vol. 35, 6743–6754, 2002, PII: S0305-4470(02)34090-3.

An Optimized Design of Cylindrical Acoustic Cloak with Two-phase Isotropic Layered Composites

C. N. Weng, W. H. Chung, and T. Chen

Department of Civil Engineering, National Cheng Kung University, Tainan, Taiwan

Abstract— In this paper, we present a genetic algorithm as the optimization procedure in the design of a two-phase multilayered acoustic cloak. Examples on refining the material parameters of anisotropic layers as well as thickness distributions are demonstrate. Numerical results show that the proposed optimization can efficiently reduce the scattering fields with simpler structure configurations.

1. INTRODUCTION

Recently, the use of coordinate transformations to design materials specifications that control the propagation of electromagnetic waves as desire has been extensively discussed. This starts with the pioneering study of invisibility cloaks by Pendry [1] and Leonhardt [2]. They proposed that one can enclose a region by a properly engineered material, whose refractive index are tailored according to the result of geometric transformation, while light pass through, the fields would be bent around the region without penetrating and finally return to their original trajectories. The idea is soon confirmed by a few works of theoretical models [3, 4], numerical ray tracing [5], full wave simulation [6] and experiment in microwave regime [7]. Similar concept can be extended to the design of acoustic cloak [8–10]. Experiment for protecting underwater structure from sonar detection [11] is performed as well. Unfortunately, such media usually appears strong anisotropy and nonhomogeneity which is not easy to fabricate even using metamaterials. In practice, a possible way to yield this property is the use of anisotropic multilayered structures [7, 12] or bi-layer isotropic media [13–16]. However, the unavoidable scattering will occur due to impedance mismatch. For electromagnetics, some researches devoted to the reduction of scattering of multilayered cloak through optimizations [17–19]. Similar concept is also performed in acoustic cloaking by Cai [20]. In this paper, we extent the concept in the design of cylindrical acoustic cloaks with a genetic algorithm based optimization procedure. Through the proposed optimization procedure, a simpler cloak structure which consists of a multilayered composite made of only two isotropic materials is presented. In addition, with suitable constraints in calculations, the material parameters can be restricted within a certain range so that the constituent materials are close to nature materials.

2. LAYERED DESIGN AND OPTIMIZATION OF ACOUSTIC CLOAKS

According to the transformation techniques, the bulk modulus and mass density tensor of a cylindrical acoustic cloak can be written as

$$\frac{\kappa}{\kappa_0} = \left(\frac{b-a}{b}\right)^2 \frac{r}{r-a}, \quad \frac{\rho_r}{\rho_0} = \frac{r}{r-a}, \quad \frac{\rho_\theta}{\rho_0} = \frac{r-a}{r},$$

in which a and b are the inner and outer radius of the cloak, respectively, and the subscript zero denotes the properties of background material. Such graded anisotropic material can be approached by using discrete homogeneous cylindrical shells as shown in Fig. 1 when the incident wavelength is much larger than the thickness of each layer. A few proposed works have demonstrated that multilayered cloaks comprised of either anisotropic or bi-layer isotropic media can perform well with respect to a given frequency through optimization. In this letter, we propose an alternative layered structure which consists of only two kinds of isotropic media periodically arranged along radial direction and each thickness t_i ($i = 1 - M$) can be varying.

Our design is implemented by the following steps: First, we break the cloaking shell into a step-wise discrete N -layer structure and each was characterized by a homogeneous anisotropic media as shown in Fig. 1(b). Then, we individually approximate each anisotropic layer by alternating layers of isotropic materials as shown in Fig. 1(c) and thus total number of layers of the structure becomes $2N$. Finally, we replace the previous structure by a two phase concentric multilayered structures with identical number of layers as shown in Fig. 1(d). Actually, the first two steps are the same with other reported works of electromagnetic and acoustic cloaking. The key point of the proposed

design is the last step. We utilize GA optimization to search for optimal solutions for these two materials as well as the geometric configurations. Before we start, let us introduce the objective function of the problem, scattering width, a quantitative parameter in scattering studies, which is the measure of power scattered in a given direction when an object is illuminated by an incident wave. For the proposed model, the angle distribution of scattering cross section can be expressed as

$$\sigma = \lim_{r \rightarrow \infty} \left[2\pi r \frac{|p_{sc}|^2}{|p_{inc}|^2} \right]. \quad (1)$$

In far-fields, Eq. (1) can be expressed through asymptotic approximation and yields

$$\sigma = \frac{4}{k_0} \left| \sum_n i^n A_n e^{in\theta} \right|^2, \quad (2)$$

where A_n is the coefficients of scattering field induce by a unit-amplitude incident plane wave. If the incident frequency and observation angle are prescribed, Eq. (2) is only in terms of material parameters and thickness with $M + 4$ unknowns. For simplicity, we focus on the bistatic scattering width in the forward direction ($\theta = 0$) since the strongest scattering occurs in this direction generally. For better cloaking efficiency, the smaller value of σ is demanded, and hence our optimization aims to the reduction of scattering width by adjusting the material pair $\rho_{A(B)}$, $\kappa_{A(B)}$ and corresponding thickness t_i for each layer.

3. OPTIMIZATION SCHEME AND NUMERICAL RESULTS

We illustrate a simple design of a six layered cloak as an example with respect to sound frequency 9875 Hz. Background material is water with density $\rho_0 = 998 \text{ kg/m}^3$ and bulk modulus $\kappa_0 = 1.9 \text{ Gpa}$. The geometric parameters are selected as $a = 0.1 \text{ m}$ and $b = \lambda = 0.15 \text{ m}$ which forms the diameters of cloaking region about 1.2 times the incident wavelengths. Note that the outer

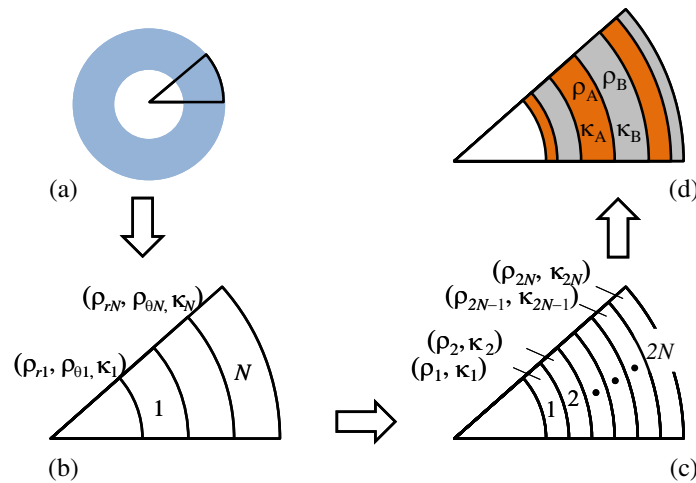


Figure 1: (a) Schematic representation for an ideal acoustic cloak and (b)–(d) the design procedure of the two-phase multilayered cloak.

Table 1: Material parameters for the six-layer cloak in step 2.

Layer	t_i/λ	ρ_i/ρ_0	κ_i/κ_0
1	0.056	0.0385	
2	0.056	25.962	1.4444
3	0.056	0.1010	
4	0.056	9.8990	0.5556
5	0.056	0.1504	
6	0.056	6.6496	0.3778

Table 2: Optimized parameters for the two phase multilayered cloak.

Layer	t_i/λ	ρ_i/ρ_0	κ_i/κ_0
1	0.0661	0.0627	0.9400
2	0.0538	8.6889	0.7151
3	0.0403	0.0627	0.9400
4	0.1157	8.6889	0.7151
5	0.0135	0.0627	0.9400
6	0.0134	8.6889	0.7151

radius b is changeable after optimization but here we just assign a moderate initial value. Sound hard condition is assumed at the innermost interface ($r = a$) to mimic a rigid acoustic object. When applying the GA, the inner radius of the cloak is fixed and the chromosome is arranged as a string representing variables $\{\rho_A, \rho_B, \kappa_A, \kappa_B, t_i\}$, $i = 1-6$. It is mentioned that the second step in the previous section is essential since the initial guesses and constrain condition in our GA process are determined from this step. According to the example, processing first two steps acquires the parameters for each layer in Table 1. It is observed that the constituents can be classified into two groups. Group A, correspond to layer 1, 3 and 5, is the low density materials (in contrast to water). Group B, correspond to layer 2, 4 and 6, is the high density materials. Both groups share the same value of bulk modulus. In this regard, we suppose our two-phase model is also constructed by the combination of a low density ρ_A and a high density shell ρ_B , and assume the value of these two materials locate on somewhere between the maximum and minimum values of group A and B respectively. Thus the constrain can be expressed calculationas

$$\begin{aligned} \min(\rho_1, \rho_3, \rho_5) \leq \rho_A \leq \max(\rho_1, \rho_3, \rho_5), \quad \min(\rho_2, \rho_4, \rho_6) \leq \rho_B \leq \max(\rho_2, \rho_4, \rho_6), \\ \min(\kappa_1, \kappa_3, \kappa_5) \leq \kappa_{A,B} \leq \max(\kappa_1, \kappa_3, \kappa_5), \quad \lambda/100 \leq t_i \leq \lambda/5. \end{aligned} \quad (3)$$

The average densities $\rho_A = (\rho_1 + \rho_3 + \rho_5)/3$, $\rho_B = (\rho_2 + \rho_4 + \rho_6)/3$ together with uniform thickness $t_i = (b - a)/6$, $i = 1-6$ are set as the initial guesses. The roulette wheel selection and heuristic

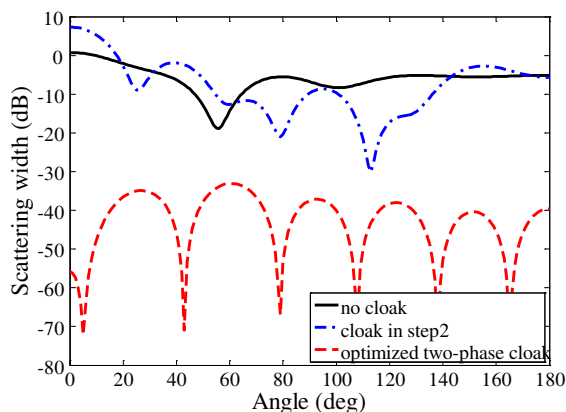


Figure 2: Normalized scattering efficiency for a sound rigid scatterer without cloak (black), the same scatterer covered by a layered cloak with parameters in Table 1 (blue) and Table 2 (red).

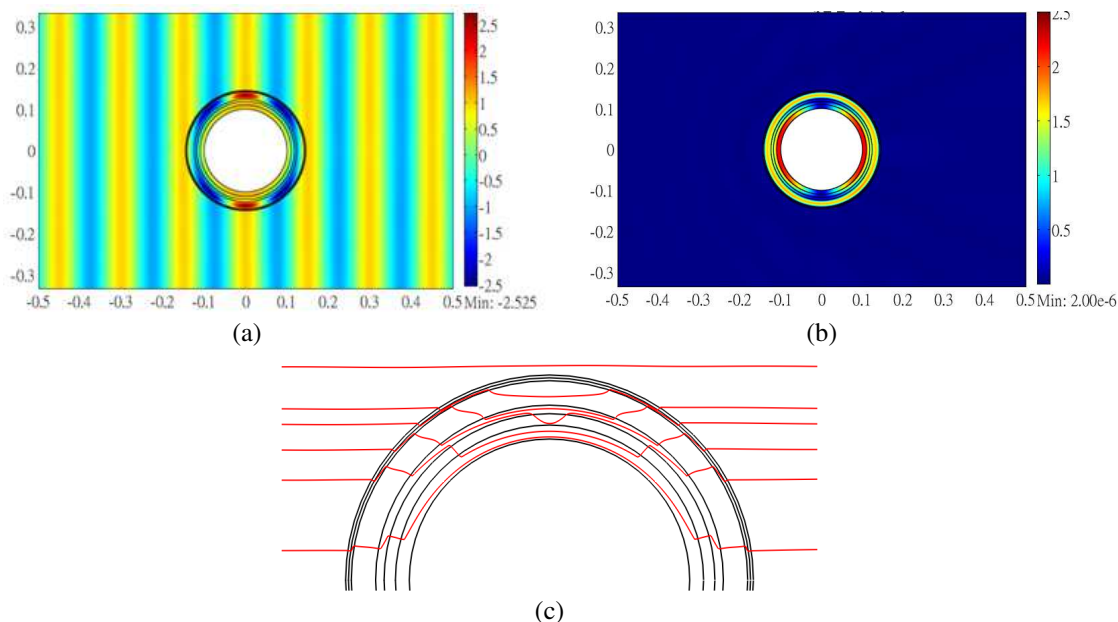


Figure 3: (a) Snapshot of the pressure field distribution (unit: Pa), (b) the norm of scattered field, and (c) the streamlines.

crossover function are used in our GA process, and numerical optimization proceeds until the stopping criteria $\sigma/2a < 0.002$ is satisfied. Table 2 shows the final optimized results. It is interesting to see that the optimized material for the low density shell (ρ_A, κ_A) is very close to the properties of some conventional materials such as polyetherimide (PEI), polyimide (PI), and specific types of aluminum honeycomb [21]. It appears a great advantage in fabrication. We plot the angle distributions of scattering width normalized to geometrical cross section in Fig. 2. The black curve represents the normalized scattering efficiency of a sound rigid cylinder without any cloak. The blue and red curves represent the cases of layered cloak with parameters of Tables 1 and 2, respectively. It can be observed that the scattering width is significantly reduced in every direction compared to non-cloak case. To further verify the optimization results, the full wave simulations based on finite element method are demonstrated. The snapshot of pressure field and norm of scattered field in the vicinity of the optimized two-phase cloak are shown in Figs. 3(a) and (b) respectively. It is found that strong scattering is induced within the shell region $a < r < b$, whereas the scattering field outside the cloak is diminished. This indicates that most scattering energies are cancelled by the multilayered structure so that a good cloaking performance is presented. Fig. 3 illustrates the streamlines of energy flux in the optimized two-phase multilayered cloak. The fluxes flow around the inner region but with different paths than that of an ideal cloak. After passing through the cloak, the fluxes return to their original trajectories without any distortion.

4. CONCLUSIONS

In conclusion, we introduced an optimization design of a two-phase isotropic multilayered cylindrical cloak. We demonstrate that an ideal acoustic with anisotropic and inhomogeneous materials can be approached by simple multilayered structure which only consist of two kinds of materials. By moderately adjusting their material and geometrical parameters, we found that at certain configurations the scattering width of this multilayered cloak can be efficiently minimized. In addition, one of these two materials of the structure is very close to conventional material which indicate that it is more feasible in practice to fabricate. For further study, the proposed procedure can be extended to three dimensional cases or applied to the design of other structures with complex materials.

ACKNOWLEDGMENT

This work was supported by the National Science Council, Taiwan, under Contract No. NSC97-2221-E-006-117-MY3.

REFERENCES

1. Pendry, J. B., D. Schurig, and D. R. Smith, "Controlling electromagnetic fields," *Science*, Vol. 312, 1780–1782, 2006.
2. Leonhardt, U., "Optical conformal mapping," *Science*, Vol. 312, 1777–1780, 2006.
3. Ruan, Z., M. Yan, C. W. Neff, and M. Qiu, "Ideal cylindrical cloak: Perfect but sensitive to tiny perturbations," *Phys. Revs. Lett.*, Vol. 99, 113903, 2007.
4. Chen, H., B. I. Wu, B. Zhang, and J. A. Kong, "Electromagnetic wave interactions with a metamaterial cloak," *Phys. Rev. Lett.*, Vol. 99, 063903, 2007.
5. Schurig, D., J. B. Pendry, and D. R. Smith, "Calculation of material properties and ray tracing in transformation media," *Opt. Express*, Vol. 14, No. 21, 9794–9804, 2006.
6. Cummer, S. A., B.-I. Popa, D. Schurig, and D. R. Smith, "Full-wave simulations of electromagnetic cloaking structures," *Phys. Rev. E*, Vol. 74, 036621, 2006.
7. Schurig, D., J. J. Mock, B. J. Justice, S. A. Cummer, J. B. Pendry, A. F. Starr, and D. R. Smith, "Metamaterial electromagnetic cloak at microwave frequencies," *Science*, Vol. 314, 977, 2006.
8. Milton, G. W., M. Briane, and J. R. Willis, "On cloaking for elasticity and physical equations with a transformation invariant form," *New J. Phys.*, Vol. 8, 248, 2006.
9. Cummer, S. A. and D. Schurig, "One path to acoustic cloaking," *New J. Phys.*, Vol. 9, 45, 2007.
10. Chen, H. and C. T. Chan, "Acoustic cloaking in three dimensions using acoustic metamaterials," *Appl. Phys. Lett.*, Vol. 91, 183518, 2007.
11. Zhang, S., C. Xia, and N. Fang, "Broadband acoustic cloak for ultrasound waves," *Phys. Rev. Lett.*, Vol. 106, 024301, 2011.
12. Cai, W., U. K. Chettiar, A. V. Kildishev, and V. M. Shalaev, "Optical cloaking with metamaterials," *Nat. Photon.*, Vol. 1, 224–227, 2007.

13. Huang, Y., Y. Feng, and T. Jiang, “Electromagnetic cloaking by layered structure of homogeneous isotropic materials,” *Opt. Express*, Vol. 15, 11133, 2007.
14. Torrent, D. and J. Sánchez-Dehesa, “Acoustic cloaking in two dimensions a feasible approach,” *New J. Phys.*, Vol. 10, 063015, 2008.
15. Qiu, C. W., L. Hu, X. Xu, and Y. Feng, “Spherical cloaking with homogeneous isotropic multilayered structures,” *Phys. Rev. E*, Vol. 79, 047602, 2009.
16. Cheng, Y., F. Yang, J. Y. Xu, and X. J. Liu, “A multilayer structured acoustic cloak with homogeneous isotropic materials,” *Appl. Phys. Lett.*, Vol. 92, 151913, 2008.
17. Popa, B.-I. and S. A. Cummer, “Cloaking with optimized anisotropic layers,” *Phys. Rev. A*, Vol. 79, 023806, 2009.
18. Xi, S., H. Chen, B. Zhang, B.-I. Wu, and J. A. Kong, “Route to low-scattering cylindrical cloaks with finite permittivity and permeability,” *Phys. Rev. B*, Vol. 79, 155122, 2009.
19. Yu, Z., Y. Feng, X. Xu, J. Zhao, and T. Jiang, “Optimized cylindrical invisibility cloak with minimum layers of non-magnetic isotropic materials” *J. Phys. D: Appl. Phys.*, Vol. 44, No. 18, 185102, 2011.
20. Cai, L. W., “Optimizing imperfect cloaks to perfection,” *J. Acoust. Soc. Am.*, Vol. 132, No. 4 2923–2931, 2012.
21. MatWeb online source: <http://www.matweb.com/>.

3D Active Imaging Models and Systems to See through Adverse Conditions: Application to the Surveillance of an Aircraft Environment

N. Riviere¹, R. Ceolato¹, E. Bernard¹, L. Hespel¹, and M. Renaudat²

¹The French Aerospace Lab, Onera, Toulouse 31055, France

²Sagem Security and Defense, Massy 91344, France

Abstract— Onera, the French Aerospace Lab, develops and models active imaging systems to understand the relevant physical phenomena impacting on their performances. As a consequence, efforts have been done both on the propagation of a pulse through the atmosphere and on target geometries and their surface properties. But these imaging systems must operate at night in all ambient illuminations and weather conditions in order to perform the strategic surveillance of the environment for various worldwide operations or to perform the enhanced navigation of an aircraft. Onera has implemented codes for 3D laser imaging systems. As we aim to image a scene even in the presence of rain, snow, fog or haze, Onera introduces such meteorological effects in its numerical model and compares simulated images with measurements provided by commercial laser scanner.

1. INTRODUCTION

Weather conditions influence the incidence of aircraft (A/C) accidents in a number of ways. As an example, one can remember the 11th April 2011 when an Air France A380, taxiing along the runway of JFK Airport in New York, clipped the wing of a smaller Comair CRJ jet, sending it into a spin. There were no reports of injuries but both aircrafts have been grounded pending an investigation. This accident is mainly due to bad weather (strong rain) and low visibility (night vision) conditions. Onera identified different sensor technologies in order to detect, to recognize and to localize objects of the scene in all weather conditions to provide enhanced visions to the crew. One distinguishes two kinds of sensors to fulfill the target: large Field of View (FOV) sensors (passive visible/IR Camera, Radar) and, high spatial resolution — small FOV optical laser sensors prototypes. On the one hand, large FOV sensors technologies are often chosen to offer the best solution to the pilot to maneuver on the taxi way. On the other hand, the small FOV sensors study is dedicated to recognize and to localize fixed and mobile objects on the taxiway. Onera will improve the obstacle detection, the localization of obstacles previously detected and the recognition of these objects. Bad weather conditions (rain, snow, fog, haze, dust wind. . .) impacts the visibility and also the contrast of the scene. Several technologies can be considered like 2D flash ladar or 3D ladar (laser scanner, new Focal Plane Area. . .) [1, 2]. Onera develops new laser imaging systems and simulates images obtained with such systems by modeling all physical phenomena including meteorological ones. For small FOV applications, we distinguish 2D and 3D active imaging devices as physical phenomena can be different in these two cases. Here, we focus on 3D active imaging systems from simulations to experiments.

2. ACTIVE IMAGING MODELS

3D imaging can be done with either scanning or non-scanning systems. In this paper, we present a scanning technique to image in three dimensions the environment of an A/C. The purpose of a 3D scanner is usually to create a point cloud of geometric samples on the surface of an object. Then, these points can be used to extrapolate the shape of the object (a process called reconstruction). 3D scanners collect distance information about surfaces within its FOV and the retro-diffused flux by the surface to the detector device. If a spherical coordinate system is defined in which the scanner is the origin and the vector out from the front of the scanner is $\varphi = 0$ and $\theta = 0$, then each point in the picture is associated with a φ and θ . Together with distance, which corresponds to the r component, these spherical coordinates fully describe the three dimensional position of each point in the picture, in a local coordinate system relative to the scanner. The intensity backscattered by the scene mainly depends on the type of material (backscattered reflectance for a fixed wavelength). Its value can be stored and associated to each point in the picture. The accuracy observed on a scene depends on applications and experimental conditions. To define the characteristics of a specific

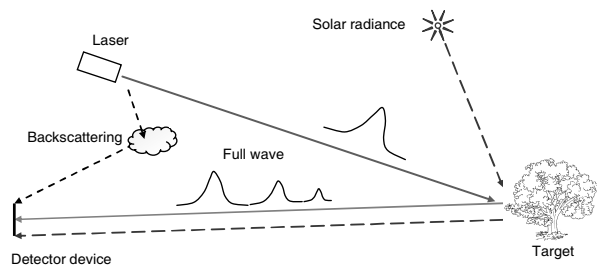


Figure 1: General approach adopted to study a 3D fullwave form laser scanner.

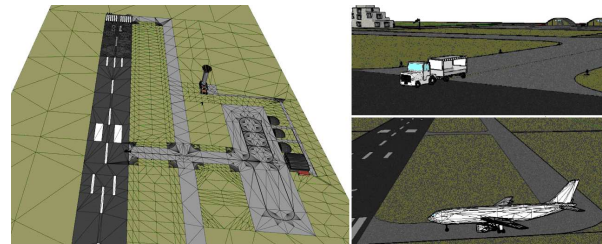


Figure 2: Description of an airport with optical properties of materials on facets.

imager and its associated performances, Onera developed a model (Matlis code) to simulate the entire process. Many papers deal with the acquisition of a distance using but few of them provide a result taking into account the entire imaging process (from the laser source to the detection). Matlis code allows simulating 3D point clouds obtained by a static (for terrestrial applications) or a moving laser scanner (for aerial applications) with a linear or a circular scan law. The general description is shown on Figure 1. Each physical phenomenon is simulated in a dedicated module where physical or simplified models are used [3–5].

First, we describe a 3D scene with a large number of facets including optical properties of materials, coordinates of facet summits, directions and positions of normal vectors. This description is commonly used for Onera's applications: Figure 2 represents the runway, taxiways, buildings and typical objects of an airport. To simulate the effect of the target shape, the laser pulse is separated into a temporal (in the direction of propagation) and a spatial (perpendicular to the direction of propagation) contribution. The beam's irradiance profile is assumed to be Gaussian. The temporal shape of the pulse is an adaptable parameter that can be changed by the user (e.g., Gaussian form and temporal width set to 5 ns).

The received component power from the target is calculated from the radar equation [6, 7]. It depends on the material and the bidirectional reflectance distribution function (BRDF) applied to each facet. The BRDF takes into account surface and subsurface local light scattering. Then, we add the background solar irradiance and the backscattering component to the signal received by the sensor. The received power is modulated by speckle phenomena which are estimated by the diameter of the speckle cells. Furthermore, atmospheric turbulences affect the received signal in several ways: laser beam expansion and deviation, scintillation (random intensity fluctuation). The received signal is degraded by such phenomenon and the estimated distance can be affected. By convoluting the shape of the laser output signal with the temporal response of the target we obtain the shape of the reflected signal. Different electrical and optical properties of the sensor are simulated. We limit this study to an avalanche photodiode sensor with different kinds of electronic noises [8]. The output of our code is a 3D point cloud (position and intensity value coded on N bits). Figure 3 shows a validation.

As a result, we model a 3D laser imaging system taking into account the propagation of a laser pulse through a clear atmosphere, its reflection on a target and its detection by a sensor. We also developed signal processing and current works are dedicated to introduce bad weather conditions in our code [9].

3. ACTIVE IMAGING EXPERIMENTS

Onera performs evaluations of laser scanner to address operational requirements and scenarios both previously selected and defined. These evaluations have been based on laser sensor modeling considering 3D objects database (airport, vehicles...) associated with realistic bad weather conditions and optical properties measured or issued from an Onera specific database [10]. For some critical items, we used small-scale test benches providing water spray, water wall environment (equivalent to monsoon phenomena), field trials using fog generators, natural bad weather conditions (characterized using adequate instruments). We characterize microphysical parameters such as particle size distribution, concentration of particles, extinction, and absorption of adverse media generated on these benches. As an example, next figure represents the particle size distribution of the fog obtained with a typical nozzle. Specific "performance evaluation" targets were also designed.

We planed to evaluate technologies regarding to taxi operation improved vision operational requirements and to evaluate the capability of detection and recognition of taxiway objects under

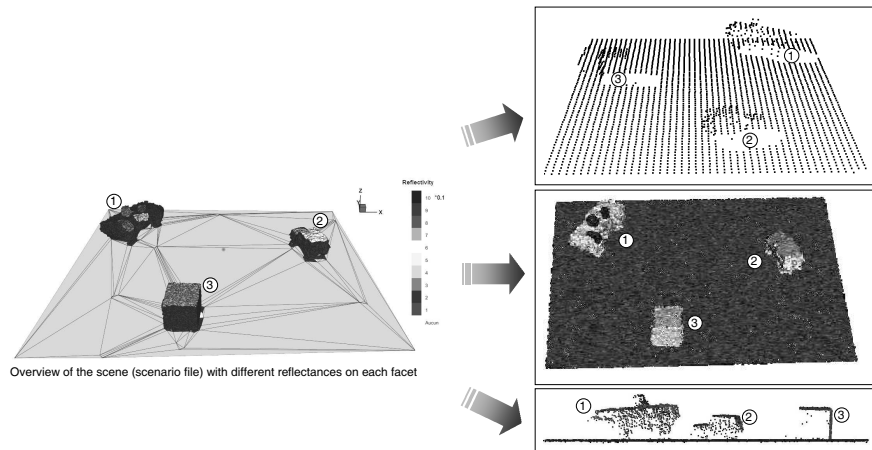


Figure 3: Overview of the scene and 3 representations of the results obtained with Matlis code (linear scanner, altitude 200 m, frequency range 50 kHz and speed $500 \text{ km} \cdot \text{h}^{-1}$).

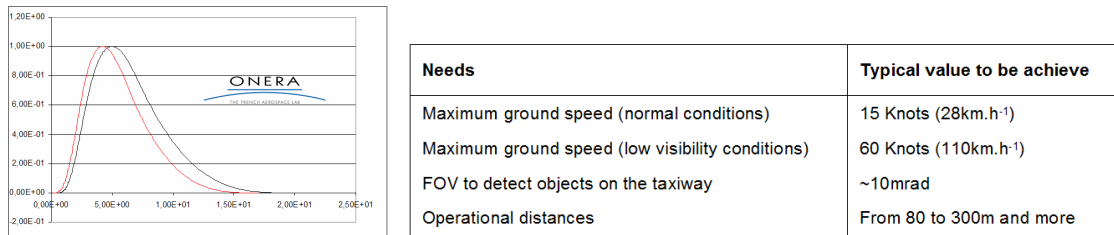


Figure 4: Normalized PSD for a typical nozzle used on a test bench to generate fog and Pilot's requirements.

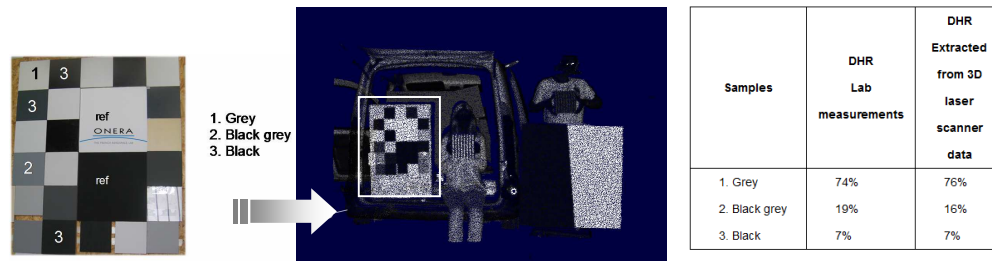


Figure 5: Typical paint coatings observed with a 3D laser scanner and the associated optical properties.

all meteorological conditions. The flight crew needs information about the environment of the A/C on a taxiway (orientation, obstacles...). The table included in Figure 4 gives examples of pilots' requirements. We evaluate the geometric aspect of different technical patterns in lab, the spectral reflectance of typical material (natural or man-made material, Visible and IR range) and the transmission through the adverse media [11, 12]. We verified retrieved values of reflectances on technical targets observed with a laser scanner. We distinguish the BRDF and the DHR (Directional Hemispherical Reflectance) components for different types of materials [13]. The spectral DHR is an integrated parameter calculated as a ratio of the total energy reflected by the sample to the total incident energy from a given direction. It could be measured by lab instruments on small scaled samples. Also, it can be computed by integrating the BRDF over the half-space. If we consider samples to be lambertian, the DHR is determined by the backscattered light (from/to a ladar system) [14]. Figure 5 shows the good agreement between lab measurements and results extracted from laser scanner experiments.

To evaluate the transmission through an adverse media (fog, haze, rain...), we realize an experiment with a lambertian panel in front of the laser scanner. Next figure represents the point cloud obtained with our laser scanner. The target and the fog can be easily separated (geometric and radiometric aspects). We also verify the temporal transmission (Figure 6). We demonstrate

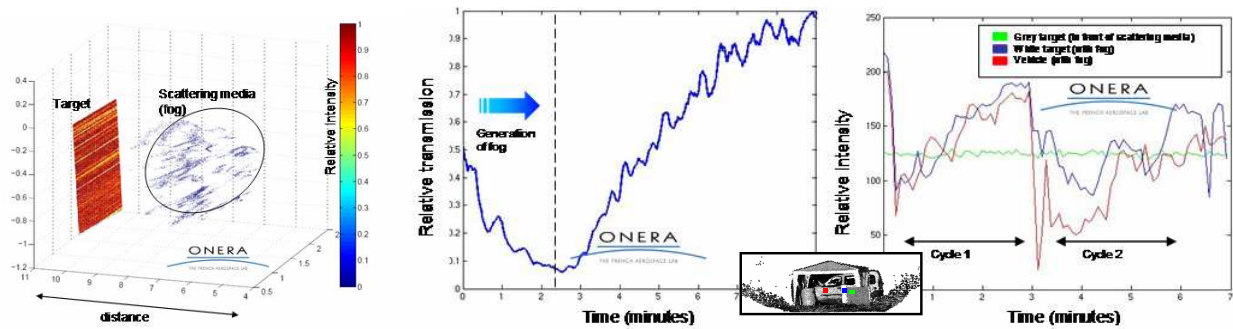


Figure 6: Detection of a target and relative transmission through fog by night.



Figure 7: Detection of a vehicle and identification of the fog contribution (red dots).

that it is possible to detect targets with different reflectance values, even if there is fog between the scanner and the scene. All of these experiments were done by night in low visibility conditions. 3D laser scanner systems create a point cloud of the object as show on Figure 7. After post-treatments, we separate the object from adverse media. We bring to light the embedded capability and the good resolution of such devices.

4. CONCLUSIONS

Active imaging systems are useful to see with bad visibility (night vision) and with bad weather conditions (fog, rain...). We identify sensor technologies in order to detect, to recognize and to localize objects of a scene under all weather conditions to provide enhanced visions of an A/C. New technologies can be considered to achieve this objective. The next step would consider mobile objects and it would integrate new physical models of bad weather conditions Matlis code. A full validation of the concept by comparison between experiments and models under adverse conditions will be done.

REFERENCES

1. Riviere, N., G. Anna, L. Hespel, B. Tanguy, M. T. Velluet, and Y. M. Frédéric, "Modeling of an active burst illumination imaging system: Comparison between experimental and modelled 3D scene," *Proc. SPIE*, Vol. 7835, 783509, 2010.
2. Riviere, N., L. Hespel, M. T. Velluet, and Y. M. Frederic, "Validation of an end to end model for 2D flash laser imaging," *Proc. OPTRO*, Paris, 2010.
3. Kogelnik, H. and T. Li, "Laser beams and resonators," *Appl. Opt.*, Vol. 5, No. 10, 1550–1567, 1966.
4. Kogelnik, H., "On the propagation of Gaussian beams of light through lens like media including those with a loss or gain variation," *Appl. Opt.*, Vol. 4, No. 12, 1562–1569, 1965.
5. Martin, J. M. and S. M. Flatte, "Intensity images and statistics from numerical simulation of wave propagation in 3D random media," *Appl. Opt.*, Vol. 27, 2111, 1988.
6. Der, S., B. Redman, and R. Chellapa, "Simulation of error in optical radar range measurement," *Applied Optics*, Vol. 36, No. 27, 1997.
7. Anna, G., L. Hespel, N. Riviere, D. Hamoir, and B. Tanguy, "Physical modeling of point cloud (3D) and full-wave form (4D) laser Imaging," *Proc. SPIE*, Vol. 7835, 78350A, 2010.
8. Overbeck, J. A., M. S. Salisbury, M. B. Mark, and E. A. Watson, "Required energy for a laser radar system incorporating a fiber amplifier or an avalanche photodiode," *Applied Optics*, Vol. 34, No. 36, 1995.

9. Rivière, N. and L. Hespel, “Identification of radiative parameters of dense scattering media with polarization analysis,” *Tenth Conference on Electromagnetic and Light Scattering*, Bodrum, Turkey, 2007.
10. www.onera.fr/dota/memoires.
11. Ceolato, R., N. Riviere, and L. Hespel, “Reflectances from a supercontinuum laser-based instrument: Hyperspectral, polarimetric and angular measurements,” *Opt. Express*, Vol. 20, 2012.
12. Riviere, N., R. Ceolato, and L. Hespel, “Multispectral polarized BRDF: Design of a highly resolved reflectometer and development of a data inversion method,” *Opt. App.*, Vol. 42, No. 1, 2012.
13. Ceolato, R., N. Riviere, L. Hespel, and B. Biscans, “Probing optical properties of nanomaterials,” *SPIE Newsroom*, 2012.
14. Ceolato, R., N. Riviere, L. Hespel, and B. Biscans, “Supercontinuum laser-based instrument to measure hyperspectral polarized BRDF,” *Proc. SPIE*, 8189B-44, 2011.

A Multi-scale SAR Segmentation Based on Hierarchical Merging

Xi Ye^{1,2}, Meng Liu^{1,2}, Hong Zhang¹, and Chao Wang¹

¹Center for Earth Observation and Digital Earth, CAS, Beijing 100094, China

²Graduate University of the Chinese Academy of Sciences, Beijing 100049, China

Abstract— SAR image segmentation is the base problem of SAR processing, and the premise of the scene interpretation. Be corrupted by speckle noise, SAR image segmentation is a recognized problem. The paper presents an approach using the method based on hierarchical region merging. According to the mechanism of speckle, the backscatter of SAR image obeys the negative exponent distribution in homogeneous region. We proposed the measure of the homogeneity based on negative exponent distribution and Mumford-Shah function. The Local mutual best fitting, which has lower algorithm complexity, will be used in our algorithm. Unlike the traditional hybrid segmentation, the method presented in our paper can afford the segmentation result in continuous scales from pixel level to the whole scene. The comparison of the method and Level Set validates that segmentation method can overcome the speckle noise and better in keep the structure of the parcel.

1. INTRODUCTION

With the launches of new SAR sensors, such as the German TerraSAR-X/TanDEM-X and the Italian COSMO-SkyMed satellites, SAR remote sensing from space has made a big leap forward with a very high spatial resolution of up to 1 m, and hence open up for the first time opportunities to use SAR for fine imaging of urban area. High resolution SAR imagery has become a promising tool to provide updated geo-information. However, the mass data and complex noise characteristics are really a challenge to SAR image processing and analysis.

Object-based image analysis (OBIA) technique provides a feasible idea to solve the problem. Image segmentation is the premise and basis of OBIA. Be different from classification, the main purpose of the image segmentation is the reconstruction and analysis of image details. Due to the side-glance imaging and random walk of multiplicative speckle noise, homogeneous area in SAR image may present different characteristics and the parcel has no continuous contour. At present there are a lot of research literatures about SAR image segmentation. The algorithm can be divided into three categories: 1) method based on contour detection, 2) method based on clustering, 3) method based on region split/merging. In the existing segmentation algorithm, method based on region split/merging is robust and effective in reconstructing the scene corrupted by speckle noise, and is widely used in remote sensing analysis [1].

Method based on region split/merging usually consists of the following three parts, 1) the merging rule, 2) the heterogeneity measure, 3) iterative termination conditions. Heterogeneity measure is the most critical part of regional segmentation. Region statistics is usually adopted to measure heterogeneity. In literature [2], the Gaussian distribution is used to describe the statistical characteristic and t test is utilized to measure the heterogeneity of merging regions. In literature [3], the Gamma distribution is used to describe the statistical characteristic and maximum likelihood estimation is utilized to determine region merge. In fact, gamma distribution is more proper in describing SAR texture [4]. In order to guarantee the edge of merge area is smooth, and eliminate internal hole, a shape parameter is used in literature [5, 6]. It can get a more reasonable result, combine statistical characteristic with shape parameter.

The merging rule is an important part of graph based segmentation algorithm. Different rules will greatly affect the results of image segmentation [7]. In literature [6], the simulated annealing algorithm is used to segmentation. Each “boundary point” is randomly changed to an adjacent region. If it causes a better result, the change will be accepted. Otherwise, the change will be accepted by a certain probability. The common procedure is based on greedy programming. Only global optimal result is accepted at every time. These methods can have a good result. But it is inefficient and time-consuming. In literature [5], the algorithm called local mutual best fitting is employed, which can get the approximate optimal result and reduces the complexity of time.

The paper adopts the region split/merging algorithm and proposes the heterogeneity measure of SAR image segmentation. To overcome the problem that the statistical characteristic is not

effective, we amend the heterogeneity measure. The local mutual best fitting will be used in our algorithm, which has lower algorithm complexity. The method presented can afford the segmentation result in continuous scales from pixel level to the whole scene.

2. COST FUNCTION OF REGION MERGE

The cost function has two competing terms. The first is the measure of heterogeneity, which is derived from the single-point statistical model of SAR intensity imagery and Mumford-shah function. The second one is the shape term, which is related to the boundaries of the regions. The shape term is helpful to maintain smooth edges or a more or less compact form. The function is shown as follow,

$$C = sC_{\text{hetero}} + (1 - s)C_{\text{shape}} \quad (1)$$

where C_{hetero} is the measure of heterogeneity, and C_{shape} is the shape term, s is the weight between terms. The introduction to the terms is provided in the following sections.

2.1. The Measure of Heterogeneity

The high resolution images provided by TerraSAR and Cosmo-SkyMed are mostly one look intensity images. According to priori knowledge, SAR intensity image obeys the negative exponential distribution in homogeneous area. The Probability Distribution Function (PDF) can be written as follows:

$$P(I) = \frac{1}{\sigma} \exp\left(-\frac{I}{\sigma}\right) \quad (2)$$

where I is the intensity and σ is the standard deviation.

Assuming that there is n_A pixels in region A, n_B pixels in region B, and the PDF of each pixel is independent. The joint probability distribution of region A and B can be written as follow:

$$P_{A,B}(\sigma_A, \sigma_B, I_i, I_j) = \prod_{i=1}^{n_A} \frac{1}{\sigma_A} \exp\left(-\frac{I_i}{\sigma_A}\right) \cdot \prod_{j=1}^{n_B} \frac{1}{\sigma_B} \exp\left(-\frac{I_j}{\sigma_B}\right) \quad (3)$$

The cost function of merging region A and B is described as the deviation between the PDF of merged region and the joint probability of region A and B.

$$\ln P_0 - \ln P_{A,B} = n_A \cdot \left(\ln \sigma_A + \frac{\mu_A}{\sigma_A}\right) + n_B \cdot \left(\ln \sigma_B + \frac{\mu_B}{\sigma_B}\right) - (n_A + n_B) \cdot \left(\ln \sigma_0 + \frac{\mu_0}{\sigma_0}\right) \quad (4)$$

where P_0 is the PDF of merged region, $P_{A,B}$ is the joint probability of region A and B, σ_A , μ_A , σ_B , μ_B is the mean value and standard deviation of region A and B respectively. σ_0 , μ_0 is the mean value and standard deviation of merged region. In SAR images, the mean value and standard deviation of negative exponential distribution are equal. So the merge cost C_{diff} can be rewritten as:

$$C_{\text{diff}} = n_A \ln \sigma_A + n_B \ln \sigma_B - (n_A + n_B) \ln \sigma_0 \quad (5)$$

Due to the property $\mu = \sigma$, use $(\mu + \sigma)/2$ to replace σ :

$$C_{\text{diff}} = n_A \ln(\sigma_A + \mu_A) + n_B \ln(\sigma_B + \mu_B) - (n_A + n_B) \ln(\sigma_0 + \mu_0) \quad (6)$$

When merging between single pixels, σ equals to 0, Equation (6) avoids two problems: 1) the cost function may get a singular value in merging single pixels. 2) standard deviation has poor ability to describe the heterogeneity between regions.

Furthermore, according to the Mumford-shah function, which is a frame of image segmentation, the boundary of region is important in describing the heterogeneity between regions. Several segmentation algorithms are compared in article [8] using SAR data. We can find that the algorithms based on Mumford-shah function are better than the algorithm only based on the region statistics. We rewrite the Equation (6) according to Mumford-shah function,

$$C_{\text{diff}} = [n_A \ln(\sigma_A + \mu_A) + n_B \ln(\sigma_B + \mu_B) - n_A + n_B \ln(\sigma_0 + \mu_0)] / l(\partial(A, B)) \quad (7)$$

where $l(\partial(A, B))$ is the length of the common boundary of region A, B.

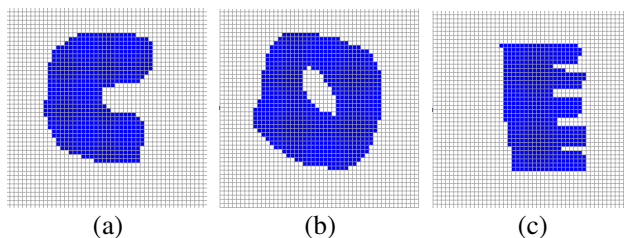


Figure 1: The unreasonable cases of region.

2.2. Shape Term

We hope the region in image segmentation reasonable as far as possible. The main unreasonable cases are shown in Fig. 1(a) the hollow region shape, (b) the region has a hole, (c) the region has sawtooth.

Two parameters called compactness and smoothness, are used to control the shape of the region. The compactness is defined as the ratio of the region length and the square root of the region size. It is used to reduce the cases (a) and (b). When cases (a) and (b) appear, the cost function will reach high value. The smoothness is defined as the ratio of the region length and the edge length of the bounding box. It is used to reduce the case (c). In case (c), the region length is longer than the edge length of the bounding box, and it will result in a higher value in smoothness parameter, as well as the cost function.

$$\begin{aligned} \text{compact} &= \frac{l}{\sqrt{n}} \\ \text{smooth} &= \frac{l}{b} \end{aligned} \quad (8)$$

where l is the region length, b is edge length of the bounding box, n is the region size (that is the number of pixels in the region).

2.3. Local mutual best fitting

Local mutual best fitting is a bottom-up strategy. The processing can be expressed as follows:

- (1) The segmentation starts from the single pixel, the single pixel is viewed as object.
- (2) For each object A in the current image, find the best fitting neighbor of A. Assuming that object B is the best fitting neighbor of A.
- (3) Investigated the best fitting neighbor C of object B, if C and A are not the same, then choose the object B as the current object, go back to step (2).
- (4) If C and A are the same, merge the object A and object B. If the object D and object E are the best fitting neighbor of each other, than merge the object D and object E.
- (5) Traverse the whole image each iteration.
- (6) Repeat these steps until there are no objects need to merge in the image. A limit can be used to control the merging between objects.

3. EXPERIMENT AND ANALYSIS

The experiment is carried out with the artificially and real SAR images. We want to validate that the method can segment meaningful parcel with reasonable boundary. Fig. 2 shows the artificially image contaminated by speckle noise of one look Gamma distribution and the edge map of the segmentation result. One can observe that the algorithm success to detect all the regions in the scene. And the edges of the regions are close to ideal edges.

In the real SAR image, a compare with Level Set, which is famous for keeping reasonable border in SAR image segmentation, is proposed in the first experiment. The test data is acquired by ERS-1, the size of the image is 250×250 pixels and the scene is farmland. The result is shown in Fig. 3. It's shown that, the proposed method can overcome the interference of speckle noise and get meaningful parcel with reasonable border.

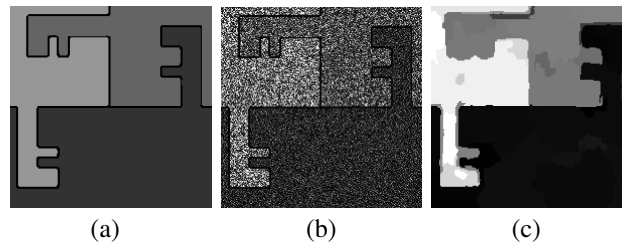


Figure 2: (a) Artificially image. (b) Artificially image corrupted by multiplicative noise. (c) The segmentation result.

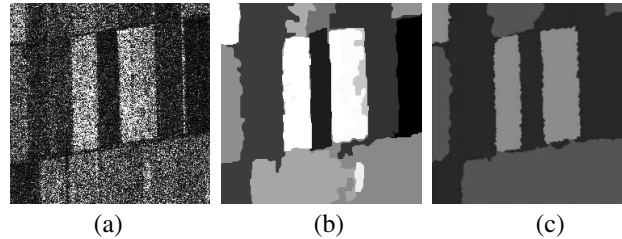


Figure 3: (a) Original image. (b) Proposed method. (c) Level set.

4. CONCLUSION

The paper adopts the graph based segmentation algorithm and proposes the heterogeneity measure of SAR image segmentation. The Mumford-shah theory is adopted to complete the description of homogeneity measurement. The local mutual best fitting is employed in the algorithm, which has lower algorithm complexity. The proposed method is robust in SAR image segmentation. The comparison of the method and Level Set validates that segmentation method can overcome the speckle noise and better in keep the structure of the parcel.

ACKNOWLEDGMENT

This work was supported in part by Director Innovation Fund of CEODE, and in part by the National Natural Science Foundation of China under Grants 40971198.

The authors would like to thank the Machine Learning Centre of the Hebei University, Hong Kong Polytechnic University, and the IEEE Systems, Man and Cybernetics Society.

REFERENCES

1. Development, L.I.o.E.U.a.R., <http://www.ioer.de/segmentation-evaluation/results.html>.
2. Cook, R., et al., "MUM (merge using moments) segmentation for SAR images." *Proceeding of the SPIE*, Vol. 2316, 92–103, 1994.
3. Cook, R., et al., "Segmentation and simulated annealing," *Proceeding of the SPIE*, Vol. 2958, 30–37, 1996.
4. Oliver, C. J. and S. Quegan, *Understanding of Synthetic Aperture Radar Images*, SciTech Publishing, 2004.
5. Baatz, M. and A. Schäpe, "Multiresolution segmentation: An optimization approach for high quality multi-scale image segmentation," *Angewandte Geographische Informationsverarbeitung*, Vol. XII, No. 12, 12–23, 2000.
6. Stewart, D., et al., "Ptimal approach to SAR image segmentation and classification," *IEEE Proceedings Radar, Sonar and Navigation*, Vol. 147, No. 3, 134–142, 2000.
7. Nock, R. and F. Nielsen, "Statistical region merging," *IEEE Transactions on Pattern Analysis and Machine Intelligence*, Vol. 26, No. 11, 1452–1458, 2004.
8. Redding, N. J., D. J. Crisp, and D. Tang, "An efficient algorithm for Mumford-Shah segmentation and its application to SAR imagery," *Digital Image Computing: Techniques & Applications*, 35–41, Australia, 1999.

New SAW Odor and Gas Sensor for Sensor Network Installed in Smart House

Mitsutaka Hikita and Jun Hosaka

Faculty of Global Engineering, Kogakuin University, Shinjuku-ku, Tokyo 163-8677, Japan

Abstract— Sensor network has been proposed with the development of mobile communications system such as cellular phone and wireless LAN. To detect CO, environmental gas and hydrogen leakage from future fuel-cell cars, we published the novel SAW sensor with self-temperature-compensated characteristics on the assumption of garage use at -40 to 80°C . However, the sensor network which operates under extreme low-power consumption requires small losses for delay-line-type sensors. We have developed a new low-loss sensor consisting of lattice-circuit type delay lines which have large spaces between IDTs and reflectors, where reactive films are formed.

1. INTRODUCTION

Mobile communications by means of the cellular-phone system have spread all over the world from the last half of the twentieth century to today. Recently, a sensor network has been investigated to control the environments at homes, offices and public places such as hospitals. In this system, small radio communications network is installed in a certain area to connect many distributed sensors by similar technology to that used in cellular-phone system. The sensor network is considered as the new concept which will have a big impact on our lives and will grow to a giant industry like the cellular-phone system. It will also contribute to future ecology, i.e., energy saving and environment preservation.

Recently HEMS (Home Energy Management Systems) have also been proposed to connect homes and offices seamlessly to the smart-grid systems. In these systems, the smart house will be achieved by the combination between energy-management devices, i.e., smart meters, and the sensor network. As shown in Fig. 1, many sensor nodes with various sensors including the smart meters will be installed within homes, offices and public places. These nodes can communicate one another via small radio network. Sensed signals from all nodes are gathered to a center node. The center node supervises all sensor nodes, processes collected data and sends control signals to other installations and devices.

In this paper, we propose a sensor-node structure which includes a novel SAW gas sensor taking hydrogen-gas leakage from future fuel-cell cars and odors from patients or in sickrooms as examples. SAW gas sensors are already under commerce. The zNose's provided by EST Corp. are the most successful SAW gas sensors, i.e., GC (gas chromatography) [1]. The odor sensors were also published by E. J. Staple et al. using the same technology [2]. However, use in a garage as sensor nodes must warrant large temperature range at -40 to 80°C , which requires the self-temperature-compensation characteristics as an essential feature. Moreover, the sensor nodes must operate more than couples of years under a single battery, which requires very low-power consumption and very low-loss characteristics for SAW sensors.

In general, the long propagation length is necessary to delay-line type SAW sensors because gas-particle density is measured by the phase shift between the signal to input IDT and that from output IDT. To increase the propagation length, ball SAW sensors use lap-type propagation paths along

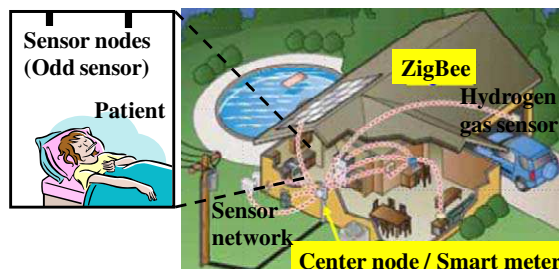


Figure 1: Sensor network involved in smart house. Sensors for hydrogen gas leakage from future fuel-cell cars and odor sensors for care environments, etc. are installed.

the equator of the quartz ball [3]. We investigated a new lattice-circuit type delay line consisting of SAW resonators. These resonators have large spaces between IDTs and reflectors to provide the long propagation length keeping the low-loss characteristics. We have also proposed a new sensor structure which uses three lattice-circuit delay lines. It has not only low-loss characteristics but also the self-temperature-compensation characteristics same as the previous one [4, 5]. Explanation about characteristics of the previous one, a new sensor configuration, a principle of the lattice-circuit type delay line with large-spaced SAW resonators, and simulation and experimental results will be presented in this paper.

2. CHARACTERISTICS OF TRANSVERSAL DELAY-LINE TYPE SENSOR

The previous sensor is shown in Fig. 2(a). Between input and output IDTs thin film reactive to specific gas/odor particles, e.g., palladium (Pd) thin film for the hydrogen gas, is formed. Small mass loading produced by sensing particles results in phase shift of the received SAW. The delay-line length for D-1 is L , while other lengths for D-2 and D-3 are $L + \lambda_o/8$ and $L - \lambda_o/8$, respectively. The D-1 is used as sensing delay lines. The D-2 and D-3 are isolated from air and provide standard phases determined by SAW propagation lengths between IDTs.

When the 1st-fundamental signal is supplied to all input IDTs, phase relations of three output signals from (1) to (3) shown in Fig. 2(b) are achieved. The (2) is assumed on X axis with 0 phase, then the (3) is located on Y axis due to $\lambda_o/4$ -propagation path difference. With no particle concentration the sensor output (1) is in-between. With increase of the concentration (1) only rotates in the constellation. With rise in temperature, all output (1), (2) and (3) rotate simultaneously in the constellation. The values of (1) projected to the rotated (2) and (3) axes can provide effects of concentrated particles without influence of temperature. Thus the self-temperature-compensated characteristics can be achieved, which is vitally important for sensor-network due to the requirement of extremely-wide temperature range from -40 to 80°C especially in a garage use. Almost same relation can be achieved at the 3rd-harmonic frequency as shown in Fig. 2(c).

Experimental results for temperature characteristics of phases of (1), (2), and (3) are shown in Figs. 2(d) and (e) for 1st-fundamental and 3rd-harmonic frequencies, respectively. Phase differences between (2) and (3) are exactly 90° . The phase shifts due to temperature changes are also same for all outputs, which can provide correct phase shift only due to the sensing-gas/odor effects at

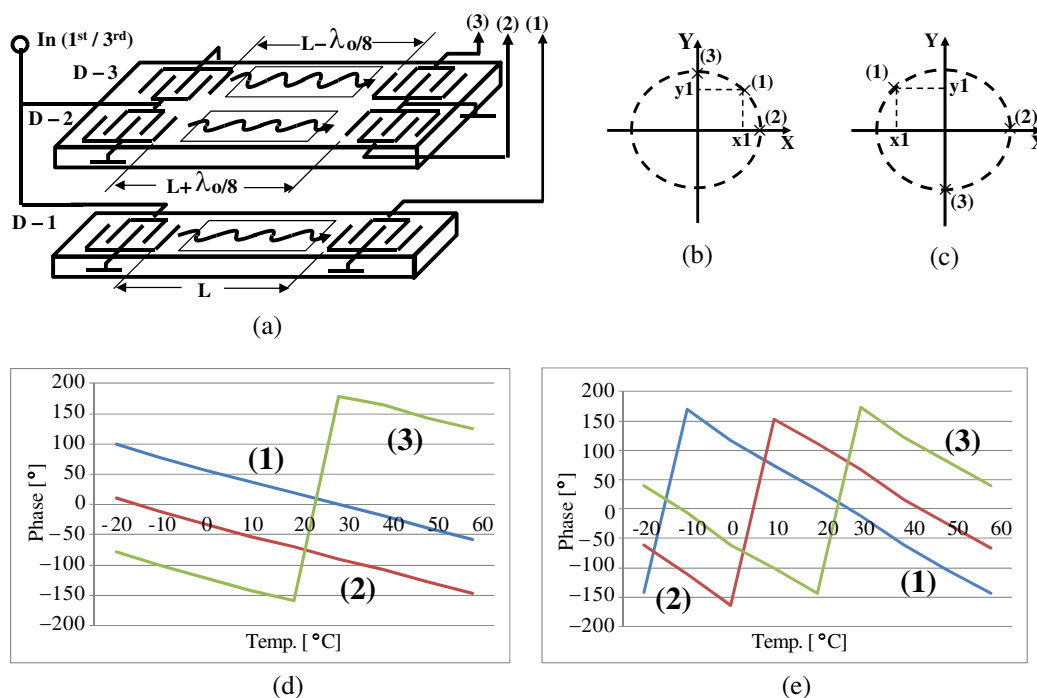


Figure 2: SAW sensor with self-temperature-compensation characteristic; (a) Basic configuration; (b) and (c) Phase constellations for 1st-fundamental and 3rd-harmonic signals respectively; (d) and (e) Temperature characteristics for 1st-fundamental and 3rd-harmonic signals respectively.

both frequencies.

3. NEW LOW-LOSS SAW SENSOR

3.1. Structure of Lattice-circuit Type Delay Line Sensor

One of the most promising radio communications media for the sensor network is 0.9–2.4-GHz ZigBee shown in Fig. 1, which has been regulated by IEEE802.15.4 [6]. As a block diagram is shown in Fig. 3, the ZigBee-based sensor node consists of 0.9–2.4-GHz VCO (Voltage-Controlled Oscillator) locked to TCXO (Temperature-Compensated Xtal Oscillator) and other circuit components. For the low-loss sensor, the sensing signal is also generated from 0.9–2.4-GHz VCO as shown in Fig. 3, which is the same procedure as used in the previous one. Only 1st-fundamental frequency signal is supplied to the sensor. It can be obtained from 0.9–2.4-GHz signal divided by N . Mixers are also used to obtain the projected components of the output (1) to the output (2) and (3), respectively.

Extreme low-loss performances are required for devices used in sensor nodes because the sensor nodes must operate for couples of years with a single battery. We have investigated a lattice-circuit type SAW delay line, which can also provide the self-temperature-compensation characteristics as well as low insertion losses. As shown in Fig. 4, the sensor consists of three kinds of lattice-circuit type delay lines, of which two delay lines, LC-2 and LC-3, are used to provide standard phases [7]. The LC-1 in Fig. 4 is used as a sensor delay line. Each lattice-circuit delay line has circuit elements of $Z1$ and $Z2$, or $Z1'$ and $Z2'$, or $Z1''$ and $Z2''$. The suffixes $i = 1$ and 2 mean impedance of SAW resonators with difference of $\pm\lambda_o/4$ in propagation lengths between IDTs and reflectors, which is one of the most essential features required for SAW resonators used in lattice-circuit type delay lines. The difference between $Z1'$ and $Z1''$, and between $Z2'$ and $Z2''$ is the difference of $\lambda_o/8$ in propagation lengths between IDTs and reflectors. $Z1'$ and $Z2'$, and $Z1''$ and $Z2''$ are used to construct lattice-circuit type delay lines which provide standard phases. The $\lambda_o/8$ difference in the propagation lengths between IDTs and reflectors corresponds to phase difference of 90° for the propagating SAW. Because SAW propagates twice along the paths between IDTs and reflectors, i.e., one is forward propagation to reflectors from IDTs and the other is backward propagation from the reflectors to IDTs.

The $Z1$ and $Z2$ construct a sensor delay line, of which phase shifts correspond to the concentration of sensing gas particles. Same procedures used in the previously transversal one can be applied to measure the phase shift. The projected values of (1) to (2) and (3) respectively provide the temperature-compensated phase components of (1). Balance output can be obtained from the delay lines. Double-balanced mixers (D. B. Mix.) are practical to obtain the projected phase components as shown in Fig. 4. The mixing procedures with balanced input and output can provide noise-reduction characteristics, which is very effective especially in case of these sensors using very subtle changes in output signals.

3.2. Principle of Lattice-circuit with Large-spaced SAW Resonators

When balanced signals with opposite signs, $\pm V_i/2$, are supplied to input terminals, balanced signals, $\pm V_o/2$, are obtained at output terminals as shown in Fig. 5(a). If taking the lattice-circuit type

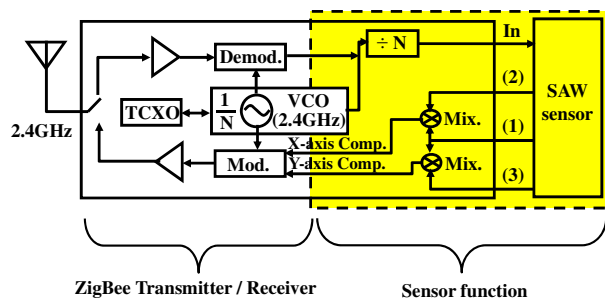


Figure 3: ZigBee-based sensor node including low-loss SAW sensor.

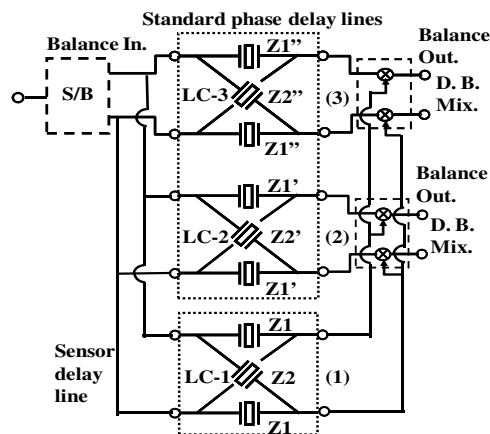


Figure 4: New low-loss SAW sensor constructed with lattice circuits.

delay line LC-1 in Fig. 4 as an example, schematic drawings of SAW resonators with large spaces between IDTs and reflectors are given in Figs. 5(b) and (c). The spaces, P and $P + \lambda_o/4$ for Z1 and Z2 respectively, are designed to be large to warrant enough interaction areas where specific gas particles concentrate in the reactive film. SAWs launched in both directions are reflected from the grating reflectors at both sides and enter the IDTs again. Thus small energy leakage from the resonators can be achieved within the reflection bandwidth of reflectors. The lattice-circuit type delay line shown in Fig. 5(a) with SAW resonators shown in Figs. 5(b) and (c) as lattice-arm elements can provide a pass band as wide as reflection bandwidth of reflectors regardless of many resonant frequencies within the band. Operation principle of the delay line is explained below.

If we treat the SAW resonator as a serial circuit-arm element, there are two kinds of currents which flow along two different paths from one terminal to the other. One is the current passing through capacitance between fingers of IDT as shown in Fig. 6(a). The other is the current which is converted to SAW once. The SAW is reflected from reflectors and reconverted to current again in IDT as shown in Fig. 7(a). Therefore, the former is direct coupling via capacitance and the latter is indirect coupling via SAW.

In the case of direct coupling, Z1 and Z2 can be expressed by simple capacitors shown in Fig. 6(b). When balanced signals with opposite signs, $\pm V_i/2$, are supplied to input terminals, they pass through the capacitors and come out at each output terminal as shown in Fig. 6(b). However, they have equal amplitude but opposite signs, i.e., + and - respectively, which results in naught outputs.

In the case of Fig. 7(a)'s indirect coupling via SAW, the current is converted to SAW, while the SAW is reflected from the reflectors to enter IDT again. However, Z1 and Z2 have spaces between IDTs and reflectors of which length difference is $\lambda_o/4$. Due to this difference, phase difference of π occurs between reflected SAWs of Z1 and Z2. So, when balanced signals with opposite signs, $\pm V_i/2$, are supplied to input terminals, they come out at each output terminal with equal amplitude and same sign as shown in Fig. 7(b). Thus the balanced output signal can be obtained between output

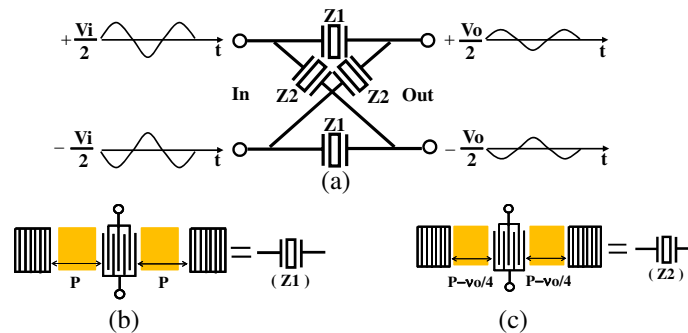


Figure 5: Lattice-circuit type delay line; (a) Basic configuration; (b) and (c) SAW resonators with large spaces between IDTs and reflectors. $\lambda_o/4$ difference exists between Z1 and Z2.

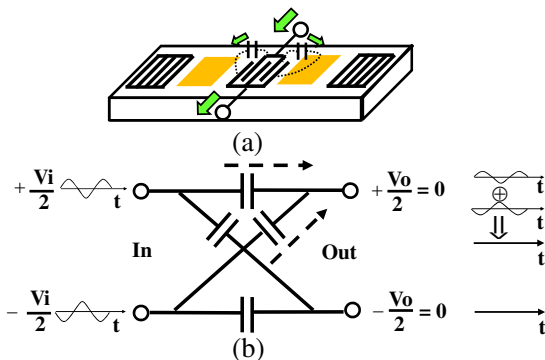


Figure 6: Direct coupling via capacitance between fingers of IDT; (a) Resonator acts as simple C; (b) Output currents with opposite signs cancel out to each other at output terminals.

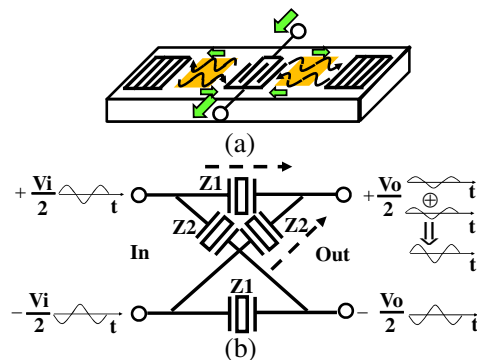


Figure 7: Indirect coupling via SAW; (a) Conversion from current to SAW and reconversion from SAW to current occur; (b) Output currents with same sign are added at output terminals.

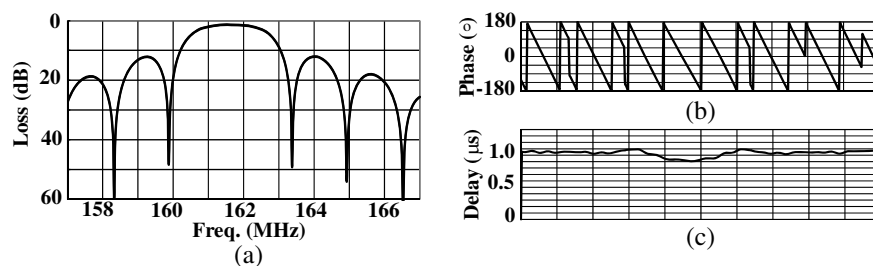


Figure 8: Simulation results for lattice-circuit type delay line; (a) Amplitude characteristics; (b) Phase characteristics; (c) Group delay characteristics.

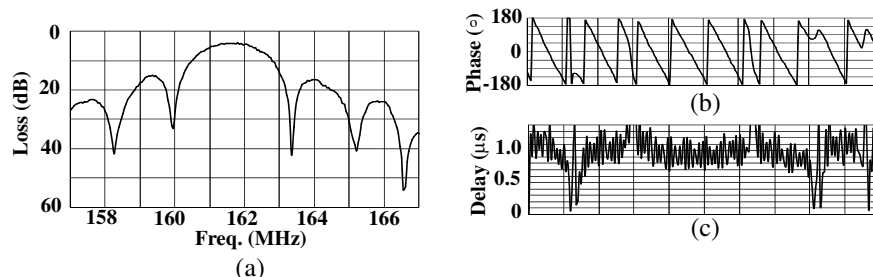


Figure 9: Experimental results for lattice-circuit type delay line; (a) Amplitude characteristics; (b) Phase characteristics; (c) Group delay characteristics.

terminals.

4. DESIGN AND EXPERIMENTAL RESULTS

We designed the lattice-circuit type delay line LC-1 shown in Fig. 4 as a typical example. The spaces between IDTs and reflectors, P and $P + \lambda_o/4$, are $50\lambda_o$ and $50.25\lambda_o$ for Z1 and Z2 respectively. A 128° Y-X LiNbO₃ was assumed as the substrate. Simulated amplitude characteristics are shown in Fig. 8(a). Frequency responses of almost same as reflection responses of the reflector can be achieved. Phase characteristics of the delay line are shown in Fig. 8(b). Group delay characteristics are shown in Fig. 8(c).

To verify our proposal, we carried out experiments based on the designed results. A 128° Y-X LiNbO₃ substrate was used. Experimental amplitude characteristics are shown in Fig. 9(a). Low-loss characteristics of about 4 dB were achieved. Good agreement between simulation and experimental frequency responses is attained, which is also similar to reflection responses of the reflector. Phase characteristics of the experimental delay line are shown in Fig. 9(b). Group delay characteristics of the experimental delay line are shown in Fig. 9(c). About 1- μ s delay time was achieved, which corresponds to the propagation length of about $160\lambda_o$. This value is larger than twice the length of $P = 50\lambda_o$ due to SAW penetration effect into IDTs and reflectors.

5. CONCLUSIONS

A new gas sensor configuration with self-temperature-compensation characteristics and wide-dynamic sensing range was illustrated. To overcome the biggest problem, i.e., large insertion losses for use in sensor network, we have invented a new sensor structure with low-loss delay lines, which also has self-temperature-compensation characteristics. The lattice circuit constructed with SAW resonators was used for the low-loss delay lines. Each resonator has large spaces between IDTs and reflectors to provide enough interaction areas to detect gases. Basic explanation about the lattice circuit, results of simulation design for lattice-circuit type delay line and experimental results were presented. These results showed the compatibility between self-temperature-compensation and low-loss characteristics.

REFERENCES

1. Home Page of Electronic Sensor Technology (EST) Corp., <http://www.estcal.com>.
2. Staples, E. J., "Odor chemistry of un-derivatized human body," http://www.estcal.com/TechPapers/Odor_of_Blood.doc.

3. Yamanaka, K., S. Ishikawa, N. Nakaso, N. Takeda, T. Mihara, and Y. Tsukahara, *IEEE Ultrason. Symp. Proc.*, 299–302, 2003.
4. Hikita, M., Y. Hiraizumi, H. Aoki, J. Matsuda, and T. Watanabe, *Electronics Letters*, 1101–1102, Vol. 45, Oct. 2009.
5. Hosaka, J. and M. Hikita, *IEEE Ultrason. Symp. Proc.*, 2285–2288, 2011.
6. IEEE Standard 802.15.4: Wireless Medium Access Control (MAC) and Physical Layer (PHY) Specifications for Low Rate Wireless Personal Area Networks (LR-WPANs), 2003.
7. Hikita, M., “Surface acoustic wave gas sensor,” Japanese Patent Pending, 2007-280020, Oct. 29, 2007.

Checking of Combustion Chamber of Liquid Rocket Using ECT with AMR Sensor

D. F. He¹, M. Shiwa¹, and S. Moriya²

¹National Institute for Materials Science, Sengen 1-2-1, Tsukuba 305-0047, Japan

²Japan Aerospace Exploration Agency, Kakuda, Miyagi, Japan

Abstract— Using the eddy current testing (ECT) system with AMR sensor developed by us, we tested a liquid rocket combustion chamber specimen. The signals produced by the cooling grooves reduced the signal-to-noise ratio and limited the smallest defect that can be detected. We developed an FFT (Fast Fourier Transform) method to reduce the influence of the coolant channel signals. We first made the FFT for the scanning result; and set the values of some frequencies and their harmonics to Zero (The frequencies are determined by the periodic cooling grooves signals); then made the inverse FFT (IFFT) of the spectrum. The results proved that this method was effective to reduce the influence of the cooling groove signals and the signal-to-noise ratio was improved.

1. INTRODUCTION

We have a research project to develop a high sensitive ECT (eddy current testing) system and use it to detect the small cracks in the copper alloy wall of combustion chamber of liquid rocket. A high sensitive AMR (anisotropic magneto resistive) sensor was developed and used ECT system [1]. With the AMR-based ECT system, we successfully detected the artificial defects in aluminum plate [2] copper alloy plate [3, 4], and copper alloy chamber type specimen [5] in which grooves and artificial defects were made to simulate the wall of the combustion chamber of liquid fuel rocket. The signals produced by the grooves reduced the signal-to-noise ratio and limited the smallest defect that can be detected. It is necessary to reduce it.

2. AMR-BASED ECT SYSTEM AND CHAMBER TYPE SPECIMEN

Figure 1 shows the schematic block diagram of dual frequency ECT system with AMR sensor [5]. AMR sensor of HMC1001 was used [6]. The coil was used to produce the AC magnetic field. Two lock-in amplifiers and two frequencies were used in this ECT system. For high frequency f_2 , the penetration depth is small, surface condition and lift off have big influence to the output of V2. For low frequency f_1 , the penetration depth is big. Both the inside and surface properties of the material can be detected. By subtracting the output of V1 and V2, the lift off related noise can be successfully reduced.

A chamber type specimen made of copper alloy was fabricated to simulate the combustion chamber of liquid rocket. Figure 2 shows it. Grooves were made on it to simulate the cooling grooves of the combustion chamber. From the bottom of the grooves, the wall thickness was about 1 mm. 12 artificial slits with different length and depth were made under the bottom of some grooves to simulate the defects. The width of the slits was about 0.2 mm. The lengths were 2 mm, 5 mm,

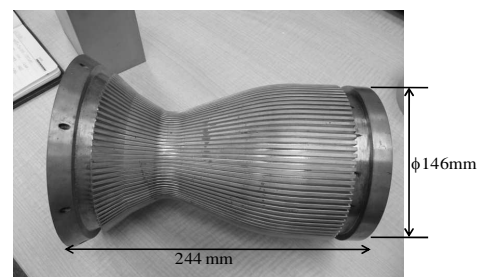
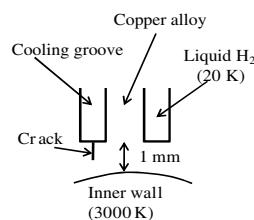
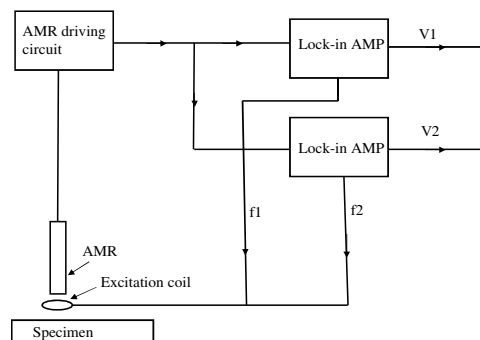


Figure 1: Schematic block diagram of ECT system with AMR sensor.

Figure 2: Chamber type specimen to simulate the combustion chamber of liquid rocket.

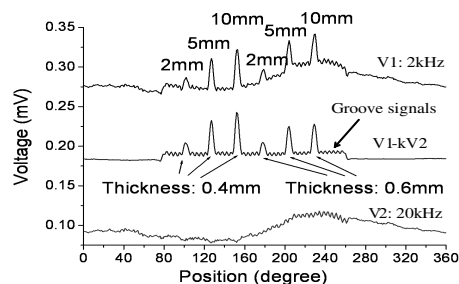


Figure 3: Scanning results for the slits with the left thickness of 0.4 mm and 0.6 mm.

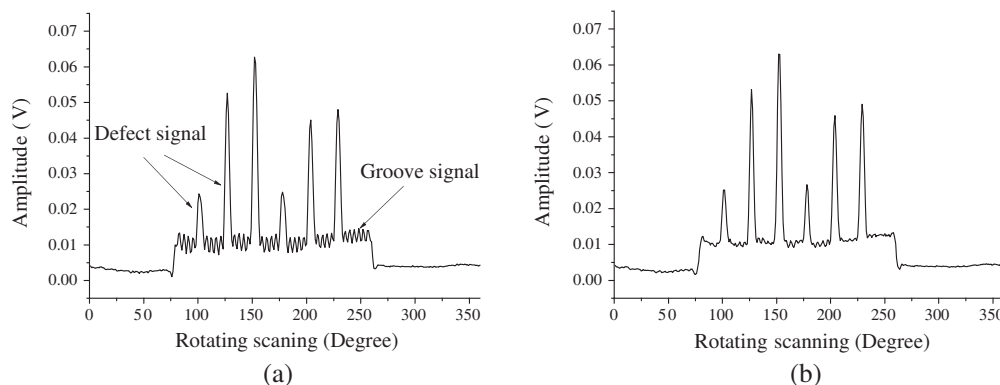


Figure 4: (a) ECT signals produced by the defects and the grooves. (b) ECT signals after FFT and inverse FFT. The groove signals were reduced and the signal-to-noise ratio was improved.

and 10 mm; and the left thickness of the wall at the positions of the slits were 0 mm (through), 0.2 mm, 0.4 mm, and 0.6 mm.

Figure 3 shows the scanning results for the slits with the left thickness of 0.4 mm and 0.6 mm. For the high excitation frequency of 20 kHz, due to the small penetration depth, no slit signals could be observed. For the low excitation frequency of 2 kHz, both the slit defect signals and the lift off related signals were observed. After the subtraction of the outputs of low frequency and high frequency, the line became flat. This proved that the dual frequency method was effective to reduce the influence of the variance of lift off. But the groove signals existed after subtraction, which reduced the signal-to-noise ratio and limited the smallest defect that can be detected.

3. FFT METHOD TO REDUCE THE GROOVE SIGNALS

We developed an FFT (Fast Fourier Transform) method to reduce the influence of the groove signals. The cooling grooves were periodic in space, so the signals produced by the grooves were also periodic signals. For the combustion chamber specimen, the periods of the grooves were about 4 degree, and the corresponding space frequency was about 0.25/degree.

We first made the FFT for the scanning result; and set the values of FFT spectrum to Zero at the special frequencies of 0.23/degree \sim 0.27/degree, 0.46/degree \sim 0.54/degree, and 0.69/degree \sim 0.81/degree; then made the inverse FFT (IFFT) of the spectrum. Figure 4(a) shows the ECT signals produced by the defects and the grooves. Figure 4(b) shows the results after FFT and IFFT. We can see that the groove signals were reduced and the signal-to-noise ratio was improved.

4. SUMMARY

Using FFT and inverse FFT method, the influence of the groove signals was reduced and the signal-to-noise ratio was improved. We will use this technology to small defect with size smaller than 1 mm.

REFERENCES

1. He, D. F., M. Tachiki, and H. Itozaki, "Highly sensitive anisotropic magnetoresistance magnetometer for Eddy-current nondestructive evaluation," *Rev. Sci. Instru.*, Vol. 80, 036102,

- 2009.
2. He, D. F., M. Shiwa, H. Yamawaki, M. Tachiki, H. Itozaki, S. Moria, T. Masuoka, and I. Uetake, “Basic examination for the defect detection of combustion chambers using ECT with an AMR sensor,” *Journal of JSNDI*, Vol. 59, No. 10, 510–514, 2010.
 3. He, D. F., M. Shiwa, J. P. Jia, et al., “Multi-frequency ECT with AMR sensor,” *NDT & E International*, Vol. 44, No. 5, 438–441, 2011.
 4. He, D. F., M. Shiwa, J. Takatsubo, and S. Moriya, “Checking of combustion chamber of rocket using ECT with AMR sensor,” *PIERS Proceedings*, 1620–1622, Kuala Lumpur, Malaysia, Mar. 27–30, 2012.
 5. He, D. F., Y. Z. Zhang, M. Shiwa, and S. Moriya, “Development of eddy current testing system for inspection of combustion,” *Rev. Sci. Instru.*, Vol. 84, 014701, 2013.
 6. Data sheet of HMC1001, Honeywell, <http://www.ssec.honeywell.com/magnetic/products.html>.

Prediction of Radar Reflectivity along Radio Link

Chrispin T. Mulangu¹, Senzo J. Malinga¹, and Thomas J. Afullo²

¹Department of Electrical Engineering, Mangosuthu University of Technology
Umlazi, KwaZulu-Natal 4031, South Africa

²School of Electrical, Electronic & Computer Engineering
University of KwaZulu-Natal, Durban 4041, South Africa

Abstract— Radiowave propagating through a rain zone, will be scattered, depolarized, absorbed and delayed in time. All these effects of rain on the wave propagation are related to the frequency at which the signal is transmitted and polarization of the wave as well as to the rain rate, which influences the form and size distribution of the raindrop. The average power received by the bistatic radar is proportional to the product of reflectivity and attenuation. These can be measured in practice but sometime there is need to determine them separately. In order to determine radar reflectivity, backscattering coefficient needs to be estimated. This study makes predictions about backscattering coefficient caused by hydro meters along terrestrial radio links, operated at wide bandwidth of 10–140 GHz frequencies. The scattering properties of the spherical raindrop are calculated for different sizes of raindrops. From the scattering properties, the back cross-sections for the spherical raindrops are determined for different frequencies. These are integrated over different established raindrop-size distribution models to formulate radar reflectivity and fitted to generate power-law models.

1. INTRODUCTION

Terrestrial links operating at frequencies higher than 10 GHz suffers degradation due to rain. Rain attenuation modeling on earth-space path has been conducted by many researchers and number of rain attenuation prediction models has been developed. Currently, ITU-R models are recommended models used to predict rain attenuation since, on average, they are simplified and have better accuracy [1]. However, to predict the signal degradation that will result from a rain event, the knowledge of the scattering cross section as well as the extinction properties are of importance [2]. Anumber of different techniques have been employed in seeking solutions to this problem. Spherical drops have been analysed by the use of the Mie Theory but other shapes may require a more complex analysis [2]. Among the methods which have been used in treating non-spherical raindrops are perturbation analysis [3–5], point matching techniques [5, 6] and integral equation formulations of the problem [7].

In this study, results for backscatter cross section and attenuation are calculated with a Mie scattering code for spherical drops at 19, 60 and 140 GHz. Result from the scattering algorithm is applied to the drop size distribution measured by Afullo in Durabn, South Africa [8], thereafter, the relationship between rainfall and radar reflectivity is derived.

2. RADAR REFLECTIVITY

2.1. Raindrop Distribution

The lognormal raindrop size distribution is expressed as:

$$N(D_i) = \frac{N_t}{\sigma\sqrt{2\pi}} \exp \frac{-(\ln(D_i) - \mu_i)^2}{2\sigma_i^2} \quad (1)$$

where N_t is the scattering point diameter density. The independent input, D_i the mean diameter of the scattering point which can be obtained directly from measurement. The input parameters N_t , μ , and σ are obtained by regression fitting procedurosto yield:

$$\begin{aligned} N_T &= a_o R^{b_o} \\ \mu_{\ln} &= A_\mu + B_\mu \ln R, \\ \sigma_{\ln}^2 &= A_\sigma + B_\sigma \ln R, \end{aligned} \quad (2)$$

where a_o , b_o , A_μ , B_μ , A_σ , and B_σ , all represent the regression coefficients of input parameters corresponding to the lognormal distribution, using the MoM. They were presented as [8];

$$\begin{aligned} N_T &= 544.4R^{0.1145} \\ \mu_{\ln} &= -0.6369 + 0.298 \ln R, \\ \sigma_{\ln}^2 &= 0.2887 - 0.041 \ln R, \end{aligned} \quad (3)$$

2.2. Reflectivity

Mie scattering is applied in this approach to determine the radar reflectivity. The backscattering coefficient Q_b is integrated over the drop size distribution $N(D)$ as suggested in [8], which leads to the radar reflectivity given by [9, 10]:

$$\eta = \int_0^{N_{\max}} Q_b(D)N(D)dD \quad (\text{mm}^2\text{mm}^{-3}) \quad (4)$$

The backscattering coefficient computations are performed under Mie theory. Fig. 1 shows the backscattering coefficient of spherical raindrops as function of raindrop diameter and signal incidences for 19.5, 60 and 140 GHz frequencies.

The exponential characteristic of the Q_b is observed for the entire raindrop range and the characteristic oscillations of resonance backscattering are also observe at for $D > 0.6$ mm at 140 GHz and $D > 1.5$ mm at 60 GHz.

The reflectivity in Equation (4) is calculated using Durban lognormal distribution and Mie theory as shows in Figs. 2–3 and compared with MP, JD, JT and LP drop size distributions. The results show that MP, JD, JT and LP drop size distributions underestimated the reflectivity at the frequencies below 15 GHz and overestimated the values of reflectivity at frequencies above 15 GHz.

Figure 4 shows reflectivity as a function of rainfall rate obtained using the lognormal drop size distribution (DSD) for 19, 60 and 140 GHz frequencies. The reflectivity at 19.5 GHz is greater than at 60 and 140 GHz for the entire rainfall rate range. This can be explained by observing the reflectivity as a function of frequencies (Fig. 2). For lognormal Durban distribution, after attaining a pick about 10 GHz, the reflectivity is decreasing while the frequency is increasing. As results, η at 19.5 GHz is greater than η at 60 and 140 GHz. It is can also be explain from Fig. 1. For the raindrop bigger that 1.5 mm Q_b at 60 GHz is greater than Q_b at 140 GHz, also, at $D > 3$ mm, Q_b at 19.5 GHz is greater than Q_b at 140 GHz. These observations mean that there are more contributions for radar reflectivity of bigger raindrops at lower frequencies.

2.3. Power Law Model

In order to estimate radar reflectivity (η), we employ an empirical scaling relationship expressed as:

$$\eta = \alpha R^\beta \quad (5)$$

where α and β are coefficients to bedetermined and R is the rainrate.

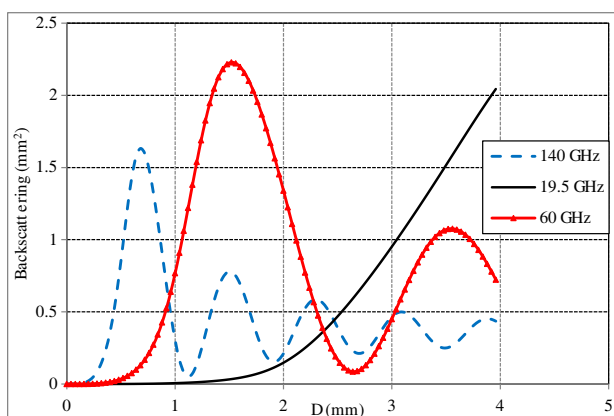


Figure 1: Backscattering coefficient of spherical raindrops as function of raindrop diameter.

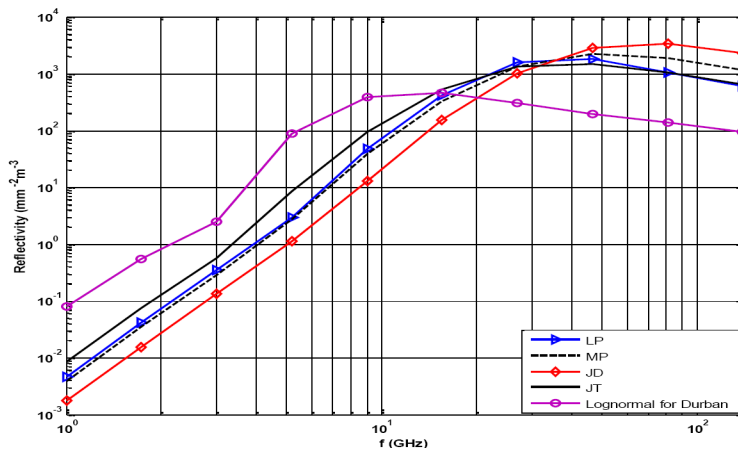


Figure 2: Reflectivity at rain rate 5 mm/h.

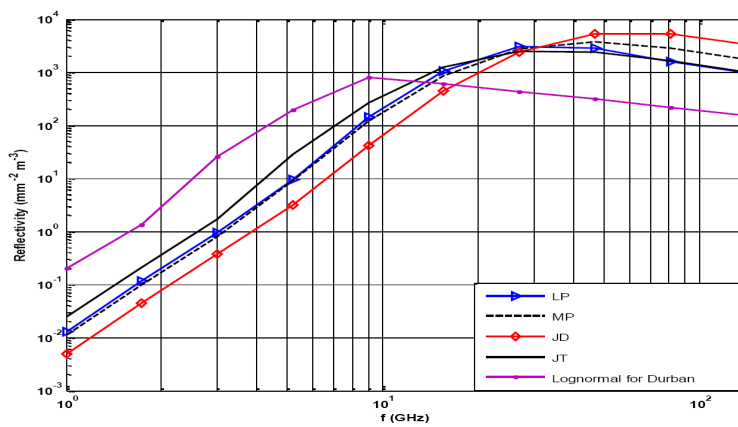


Figure 3: Reflectivity at rain rate 120 mm/h.

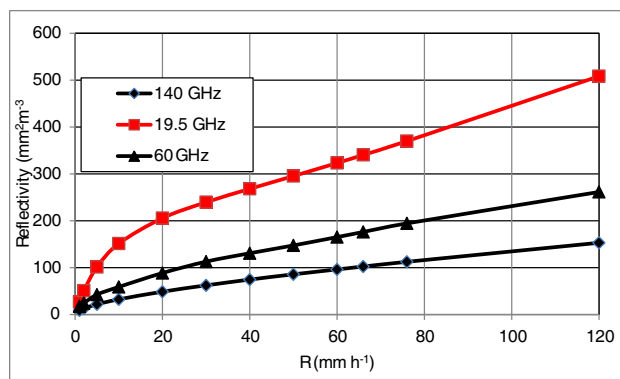


Figure 4: Radar reflectivity as a function of rainfall rate using the Durban lognormal drop size distribution.

Table 1: Power law relationship between radar reflectivity and rainrate obtained using Durban lognormal raindrop distribution for spherical model.

F (GHz)	α	β	R^2
19.5 GHz	33.802	0.5677	0.981
60 GHz	16.721	0.5624	0.9988
120 GHz	8.269	0.5624	0.999

The obtained results of the parameters α and β are shown in Table 1. It has been observed that the fitted model has a high coefficient of goodness (R^2) indicating a good fit to proposed model.

3. CONCLUSION

In this study, radar reflectivity is calculated using Durban lognormal distribution and Mie theory and compared with MP, JD, JT and LP drop size distributions. The results show that MP, JD, JT and LP drop size distributions underestimated the reflectivity at the frequencies below 15 GHz and overestimated the values of reflectivity at frequencies above 25 GHz. It was also observed that the reflectivity at 19.5 GHz is greater than at 60 and 140 GHz for the entire rainrate range. This can be explained by observing the reflectivity as a function of frequencies. For lognormal Durban distribution, after attaining a pick about 10 GHz, the reflectivity is decreasing while the frequency is increasing. As results, η at 19.5 GHz is greater than η at 60 and 140 GHz. Finally, the empirical scaling relationship has been employed for practical engineering application to estimate the parameters in order to predict radar reflectivity.

REFERENCES

1. Zhao, Z., L. Lin, and Y. Liu, "A prediction model of rain attenuation along Earth-space path," *2003 6th International Symposium on Antennas, Propagation and EM Theory*, China, 2003.
2. Klugmann, D. and O. Fiser, "Mie versus point matching algorithm for radar rain properties retrieval," *IEEE International Geoscience and Remote Sensing Symposium, (IGARSS)*, Vol. 4, 1002–1005, 2008.
3. Oguchi, T., "Attenuation of electromagnetic wave due to rain with distorted raindrops," *J. Radio Res. Labs.*, Vol. 7, 467–485, Japan, 1960.
4. Oguchi, T., "Attenuation of electromagnetic wave due to rain with distorted raindrops," *J. Radio Res. Labs.*, Vol. 11, 19–44, Japan, 1964.
5. Oguchi, T., "Attenuation and phase rotation of radio waves due to rain: Calculations at 19.3 and 34.8 GHz," *Radio Sci.*, Vol. 8, 31–38, 1973.
6. Morrison, J. A. and M. J. Cross, "Scattering of a plane electromagnetic wave by axisymmetric raindrops," *Bell Syst. Tech. J.*, Vol. 53, 995–1019, 1974.
7. Holt, A. R., N. K. Uzunoglu, and B. G. Evans, "An integral equation solution to the scattering of electromagnetic radiation by dielectric spheroids and ellipsoids," *IEEE Trans. Antennas Propag.*, Vol. 265, 706–712, 1978.
8. Afullo, T. J. O., "Raindrop size distribution modeling for radio link design along the eastern coast of South Africa," *Progress In Electromagnetics Research B*, Vol. 34, 345–366, 2011.
9. Aydin, K. and Y. Lure, "Millimeter wave scattering and propagation," *Radio Sci.*, Vol. 34, 1103–1124, 1991.
10. Mulangu, C. T., S. J. Malinga, and T. J. O. Afullo, "Impact of rain on microwave radars," *2012 International Conference on Electromagnetics in Advanced Applications (ICEAA)*, 1088–1091, Cape Town, South Africa, Sep. 2–7, 2012.

Time Domain Transient Analysis of Electromagnetic Field Radiation for Phased Periodic Array Antennas Applications

Shih-Chung Tuan¹ and Hsi-Tseng Chou²

¹Department of Communications Engineering, Oriental Institute of Technology, Pan-Chiao, Taiwan

²Department of Communications Engineering, Yuan Ze University, Chung-Li, Taiwan

Abstract— The increasing interest in the time domain (TD) analysis of ultra wideband or short pulse target identification and remote sensing applications has resulted in the development of new TD techniques to analyze the antenna radiation, which provides more physically appealing interpretation of wave phenomena. Most recently the applications have been extended to treat the problems arising in the near zone of electrically large antennas such as the vital life-detection systems and noncontact microwave detection systems, where the objects under detection may locate in the near zone of antenna. The potential applications of near-field antennas continue to grow dramatically and desire more exploration in the near future. A TD analytic solution to predict the transient radiation from a phased periodic array of elemental antennas is thus developed. This paper presents an analytical transient analysis of electromagnetic field radiation from a phased and finite periodic array of antennas for the near- and far-field focused applications.

1. INTRODUCTION

A TD analytic solution to predict the transient radiation from a phased periodic array of elemental antennas is thus developed. In this analysis, the array excitation phases were impressed to radiate electromagnetic (EM) fields focused in the near zone of array aperture [1–3]. Potential and practical antenna designs in the frequency domain (FD) have been investigated and found with feasible implementation strategies for the phased array antennas. The TD phenomena are investigated in this paper. The developed TD analytical solution is a response to the elemental antennas with a transient impulse input on its current moment. The response to a realistic astigmatic finite-energy pulse can be obtained by applying the ordinary convolution theorem to obtain the early-time transient radiation fields generated by the same antennas.

Due to the sophisticated complexity in the analytical analysis in TD, most of past TD EM analysis tends to employ TD numerical techniques, such as finite difference time domain (FDTD) and TD integral approaches, which provided exact solutions, but suffered from computational inefficiency to treat the radiations problems of electrically large antennas. Thus, it remains attractive to develop quasi-analytical TD solutions with simple and closed forms, which have the advantage of providing physical interpretations of wave behaviors. Examples include the developments of TD uniform geometrical theory of diffraction (TD-UTD), physical theory of diffraction (TD-PTD), physical optics (TD-PO) and TD aperture integration (TD-AI) techniques that were obtained by using either a direct inverse Laplace transform or an analytical time transform (ATT) of the corresponding FD formulations. These solutions are limited to the transient analysis of antenna radiation with scattering mechanisms such as the reflector antennas, and are not applicable to the current situation of direct antenna radiation from a phased array.

The past works most related to the current one are these in [4, 5] where the TD radiations of two-dimensional infinite or semi-infinite array of dipoles were analyzed. Sequentially linear phase impressions were assumed to produce far-field focused radiation of angularly offset beams. The TD phenomena of Floquet modes in the quantity of field potentials with a transient impulse excitation in the current moments were examined. The current work can be viewed as a generalization as it provides more complete and comprehensive analysis, and will reduce to previous solutions in [4, 5] when the focal point is moved into the far zone of array. In this generalized analysis, one first considers a two dimensional finite array of current moments with phases impressed to radiate fields focused in the near zone of array aperture, where the focal field point can be arbitrarily selected. Thus the presented analysis is valid for both near- and far-field focus applications. Also the assumption of near-field focusing for the array excitation exhibits many unique wave phenomena that were not revealed in the previous works [4, 5] since they appear to focus the array with a linear phase impression. These phenomena are very important for its application in the near-field communications.

2. FORMULATIONS OF THE TRANSIENT IMPULSE RESPONSE FOR A PLANAR AND RECTANGULAR ANTENNA ARRAY

2.1. Transient Phenomena of an Unit Current Moment

A planar, rectangular array of $(2N_x + 1) \times (2N_y + 1)$ elements of magnetic current moment, $d\bar{p}(\bar{r}', t)$, with periods, d_x and d_y , in the x - and y -axes, respectively, is illustrated in Figure 1. This current moment has a transient behavior by

$$d\bar{p}(\bar{r}', t) = d\bar{P}(\bar{r}') \cdot \delta(t - t') \quad (1)$$

where $\delta(\cdot)$ is the Dirac delta function. The nm th element of the array is located at $\bar{r}'_{nm} = (nd_x, md_y, 0)$ ($-N_x \leq n \leq N_x$, $-N_y \leq m \leq N_y$). The radiation exhibits a transient behavior of impulse in TD by

$$d\bar{F}_{nm}(\bar{r}, t) = \frac{1}{4\pi} d\bar{P}(\bar{r}') \frac{\delta(t - \frac{r_{nm}}{c})}{r_{nm}}, \quad (2)$$

where $\bar{r}_{nm} = \bar{r} - \bar{r}'_{nm}$ with $\bar{r} = (x, y, z)$ being the observer.

2.2. Transient Phenomena of an Array of Phased Unit Current Moments

The net potential of a NFA is given by

$$d\bar{F}(\bar{r}, s) = \sum_{m=-N_y}^{N_y} \sum_{n=-N_x}^{N_x} A(n, m) \frac{1}{r_{o,nm}} e^{j\phi(n,m)} d\bar{F}_{nm}(\bar{r}, s), \quad (3)$$

where $\bar{r}_{o,nm} = (x_o - nd_x, y_o - md_y, z_o)$ and $\phi(n, m) = r_{o,nm} - r_o$ with \bar{r}_o being the focus point. In (3), $A(n, m)$ is an amplitude taper to reduce the diffraction effects of a finite array. In TD, (3) becomes

$$d\bar{F}(\bar{r}, t) = \frac{1}{4\pi} \left[\sum_{m=-N_y}^{N_y} \sum_{n=-N_x}^{N_x} A(n, m) \cdot \frac{\delta\left(t - \frac{r_{nm} - \phi(n,m)}{c}\right)}{r_{o,nm} r_{nm}} \right] d\bar{P}(\bar{r}'). \quad (4)$$

Equation (4) can be expressed in terms of Floquet modes by using the Poisson sum formula, and becomes

$$d\bar{F}(r, t) = \frac{1}{4} \sum_{\ell=1}^4 \bar{C}_\ell(\bar{r}, t) + \frac{1}{2} \sum_{\alpha=1}^4 \bar{G}_\alpha(\bar{r}, t) + \sum_{q=-\infty}^{\infty} \sum_{p=-\infty}^{\infty} \bar{F}_{pq}^w(\bar{r}, t), \quad (5)$$

where each term is associated corner effects, edge effects and Floquet mode effects as illustrated in Figure 2. It is noted that each terms in (5) have been evaluated in a closed-form formulation, and will be presented in the conference.

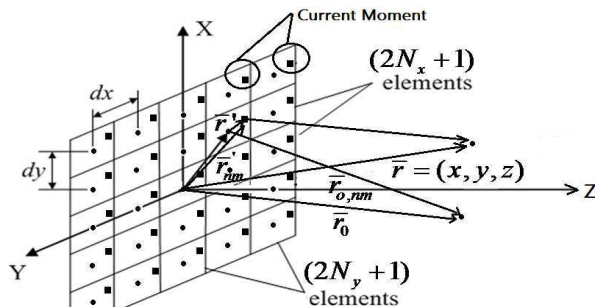


Figure 1: A two dimensional periodic array of current moments induced on the array antenna elements to radiate near-zone focused field at \bar{r}_o .

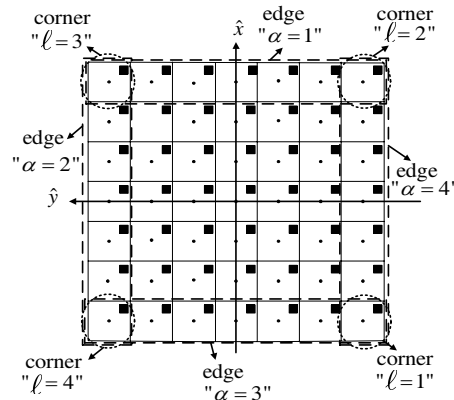


Figure 2: Illustration of edge column/row and corner elements used to compute $\bar{C}_\ell(\bar{r}, t)$ and $\bar{G}_\alpha(\bar{r}, t)$.

3. RADIATION CHARACTERISTICS

3.1. An Integration Contour and Its Characteristics

An equal time delay contour exists on the array aperture, which contributes to the radiation field at time, t as illustrated in Figure 3(a). This contour is either a hyperbolic or elliptical curve depending on the observation time and location. It is found that this contour, $C_t(t)$, is the intersection of a hyperbolic surface and $z = 0$ plane as illustrated in Figure 3(b) as an example, where the two focused points of the hyperbolic surface are located at $F_1 = (x, y, z)$ and $F_2 = (x_0, y_0, z_0)$, respectively. Thus the hyperbolic surface is formed by the two focuses at the focus and observer, which results in equal time delays. Detailed discussion of the integration contour will be presented in the conference.

3.2. Solution of $\bar{F}_{pq}^w(\bar{r}, t)$

The solution of $\bar{F}_{pq}^w(\bar{r}, t)$ can be formulated according to the integration contour. For an example of an elliptical contour, it can be expressed

$$\bar{F}_{pq}^w(\bar{r}, t) = -\frac{[U(t - t_1) - U(t - t_2)] cABL_t}{2d_x d_y (2N_x + 1)(2N_y + 1)} d\bar{P}(\bar{r}') e^{-j(p_d e_{1,d} + q_d e_{2,d})} \tilde{J}_0(\xi) \quad (6)$$

where $U(\cdot)$ is a step function, A and B are related to the radii of the elliptical contour with $(e_{1,d}, e_{2,d})$ being the location of center. In (6), $L_t = ct - \sqrt{x_0^2 + y_0^2 + z_0^2}$, (p_d, q_d) is related to the mode, and $\tilde{J}_0(\xi)$ is referred as the incomplete Bessel function. This formulation is presented here because it reduces to the case in the far-field focusing antenna array because the incomplete Bessel function will reduce to the ordinary Bessel Function as pointed. The formulations for the cases of linear and hyperbolic contours will be presented in the conference.

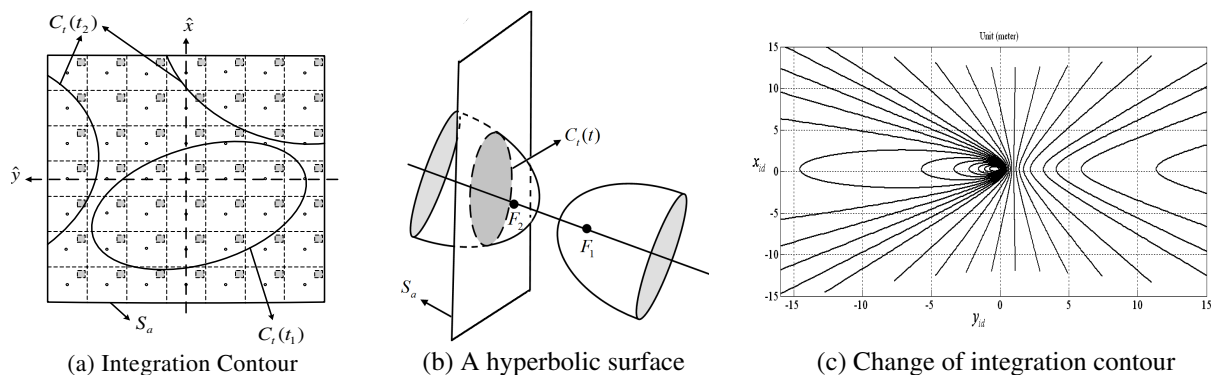


Figure 3: The variation of integration contour for phased array aperture, which is formed by the intersection between the aperture and a hyperbolic surface.

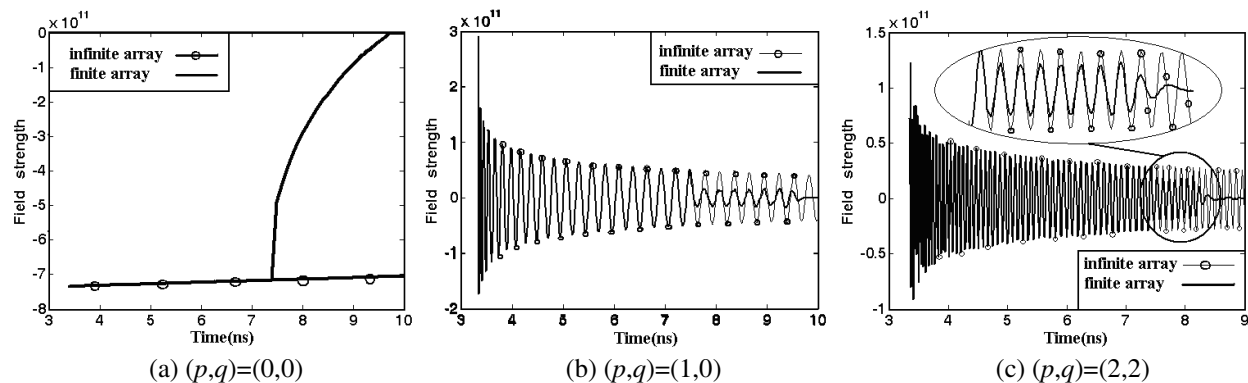


Figure 4: Transient responses of various Floquet modes for an infinite and a finite array of current sources with impulse excitations. The periods are 0.1 m in both x - and y -dimensions. The focus and observation points are at $(0, 0, 50 \text{ m})$ and $(0, 0, 1 \text{ m})$, respectively.

4. NUMERICAL EXAMPLES

The array of antennas has a period of 0.1 m in both x - and y -dimensions. The focus point is at $(x_o, y_o, z_o) = (0, 0, 50 \text{ m})$, which is relatively far away from the array aperture. The observation point is at $(0, 0, 1 \text{ m})$, and is in the near zone. In this examination, one considers the behaviors of $\bar{F}_{pq}(\bar{r}, t)$, which represents the dominating contributions in the array radiation for the impulse current distributions for every element.

One first considers the case of an infinite array, and examines the fundamental $(p, q) = (0, 0)$, $(1, 0)$ and $(2, 2)$ modes, whose results are shown in Figures 4(a)–(c).

5. CONCLUSIONS

This paper presents an analytical transient analysis of electromagnetic field radiation from a phased and finite periodic array of antennas for the near- and far-field focused applications. The elemental current moments of array are assumed with a transient impulse input for the excitations whose phases are impressed to radiate near-zone focused fields. The transient field phenomena for each of the Floquet mode expansion were analyzed. The solution reduces to the case of far-zone field radiation by moving the focus point to the far zone. The analysis shows that the radiation exhibits an impulse field at the focused point, and finite pulses at locations away from the focus point. Phenomena of partial cylindrical wave functions have been observed.

REFERENCES

1. Bogosanovic, M. and A. G. Williamson, "Antenna array with beam focused in near-field zone," *Electronics Letters*, Vol. 39, No. 9, 704–705, May 2003.
2. Bogosanovic, M. and A. G. Williamson, "Microstrip antenna array with a beam focused in the near-field zone for application in noncontact microwave industrial inspection," *IEEE Trans. Instrumentation Measurements*, Vol. 56, No. 6, 2186–2195, Dec. 2007.
3. Buffi, A., A. A. Serra, P. Nepa, H.-T. Chou, and G. Manara, "A focused planar microstrip array for 2.4 GHz RFID readers," *IEEE Trans. Antennas and Propagation*, Vol. 58, No. 5, 1536–1544, May 2010.
4. Capolino, G. and L. B. Felsen, "Time-domain Green's function for an infinite sequentially excited periodic planar array of dipoles," *IEEE Trans. Antennas Propag.*, Vol. 51, 160, 2003.
5. Capolino, F. and L. B. Felsen, "Short-pulse radiation by a sequentially excited semi-infinite periodic planar array of dipoles," *Radio Science*, Vol. 38, No. 2, 8023, 2003.

Multiphysics Analysis for Electromagnetic Radiation by Elastic Media

M. H. Wei, Y. Q. Zhang, Y. Q. Wang, and M. S. Tong

Department of Electronic Science and Technology, Tongji University
4800 Cao'an Road, Shanghai 201804, China

Abstract— Electromagnetic (EM) radiation by elastic media includes a multiplephysics process because the EM and mechanic processes exist simultaneously and are coupled together. To exactly describe the involved process, the coupled Maxwell's equations and elastic wave equations should be solved. Traditionally, these equations are in the original partial differential equation (PDE) form and they can only be solved with differential equation solvers in addition to analytical approaches for some simple problems. In this work, we develop an integral equation approach for the multiphysics process based on the Huygens' equivalence principle and extinction theorem and the resulting integral equations are solved using Nyström method. A numerical example for EM radiation from an elastic cube is presented to demonstrate the approach.

1. INTRODUCTION

Electromagnetic (EM) radiation is caused by electric oscillation in metallic devices like antennas. The fundamental mechanism of EM radiation is the acceleration or deceleration of free electric charges (electrons) when they move in metallic materials. Therefore, all devices with the acceleration or deceleration of free electric charges in movement will result in EM radiation through time-varying currents [1]. EM radiation could also be produced by mechanical approaches through the mechanical-to-electrical converters, such as piezoelectric or electrokinetic materials [2]. Mechanical oscillation or vibration in such materials can yield a motion of electric charges with varying velocity and generate time-varying currents leading to EM radiation. The EM radiation from piezoactive rocks under the influence of elastic oscillations triggered by shots or mechanical impacts was first observed and studied by former Soviet scientists in 1950's and the related techniques were widely applied to geophysical exploration for many valuable minerals [3]. To systematically study the EM radiation by mechanical approaches, one can exert controllable mechanical vibration on piezoelectric objects and measure radiated EM fields. The theoretical analysis and simulation for the phenomenon have been studied since 1950's based on coupled electrodynamic and elastodynamic equations [4]. However, the investigations were only based on the original partial differential equation (PDE) form of the equations and the solutions for the equations were obtained by PDE solvers or analytical approaches for some simple structures [5].

In this work, we develop an integral equation approach to study the EM radiation phenomenon from elastic objects in controllable mechanical vibration. The coupled governing integral equations are developed from the PDE counterparts by using Huygens' equivalence principle and extinction theorem [6]. In the derivation, it is recognized that the current source of EM radiation is generated by the varying displacement vector through strain tensors in the Maxwell's equations. By the developed integral equations, all integral equation solvers, such as method of moments (MoM), boundary element method (BEM) or Nyström method [7] can be used in the analysis and simulation, and their advantages can be enjoyed. Since the unknown functions are three-dimensional (3D) vectors on the object surface in elastic wave integral equations, we find that the Nyström method is more suitable to solve the coupled integral equations and we present a typical numerical example for EM radiation by an elastic cube to demonstrate the approach.

2. WAVE EQUATIONS

The EM radiation by elastic media can be described through the governing equations which are the coupled electrodynamic and elastodynamic equations. In a PDE form, they are [5]

$$\epsilon_{ijk} E_{k,j} = -\dot{B}_i, \quad \epsilon_{ijk} H_{k,j} = \dot{D}_i, \quad B_{i,i} = 0, \quad D_{i,i} = 0 \quad (1)$$

which are the Maxwell's equations and

$$T_{ji,j} + \rho f_i = \rho \ddot{u}_i \quad (2)$$

which is the elastic wave equation equivalent to the following widely-referred equation

$$(\lambda + \mu)\nabla\nabla \cdot \mathbf{u} + \mu\nabla^2\mathbf{u} + \omega^2\rho\mathbf{u} = -\mathbf{f}. \quad (3)$$

Note that one uses \mathbf{x} instead of \mathbf{r} to denote a position vector in space in elastodynamics so that indicial notation can be used conveniently (in the indicial notation, $x_1, x_2,$ and x_3 correspond to $x, y,$ and $z,$ respectively, and the components of a vector or tensor are denoted with indices). In the above, ϵ_{ijk} is the permutation tensor, B_i and D_i are the components of the magnetic induction (magnetic flux density) vector \mathbf{B} and electric displacement (electric flux density) vector $\mathbf{D},$ respectively, and T_{ij} are the components of stress tensor $\bar{\mathbf{T}}.$ A dot and two dots over a variable imply the first-order and second-order derivatives with respect to time, respectively, and a comma followed by an index denotes the partial differentiation with respect to the coordinate associated with the index. Also, \mathbf{u} is the displacement field vector, \mathbf{f} is the applied external force, ρ is the mass density, and λ and μ are the Lamé constants, respectively. The coupling between the two types of equations is reflected in the constitutive relations [5]

$$T_{ij} = c_{ijkl}S_{kl} - e_{kij}E_k \quad (4)$$

$$D_i = e_{ijk}S_{jk} + \epsilon_{ij}E_j \quad (5)$$

where ϵ_{ij} is the permittivity, e_{ijk} is the stress constant, and

$$S_{ij} = \frac{1}{2}(u_{j,i} + u_{i,j}) \quad (6)$$

$$c_{ijkl} = \lambda\delta_{ij}\delta_{kl} + \mu(\delta_{jk}\delta_{il} + \delta_{il}\delta_{jk}) \quad (7)$$

are the components of the strain tensor $\bar{\mathbf{S}}$ and the elastic stiffness, respectively. If we consider the symmetries in the strain and stress tensors which usually hold, and re-order the indices 11, 22, 33, 23 or 32, 31 or 13, and 12 or 21 in ij and kl as 1, 2, 3, 4, 5, and 6 in p and $q,$ respectively, then the components of those tensors can be re-indexed as

$$c_{ijkl} \rightarrow c_{pq}, \quad e_{ikl} \rightarrow e_{ip}, \quad T_{ij} \rightarrow T_p \quad (8)$$

$$S_1 = S_{11}, \quad S_2 = S_{22}, \quad S_3 = S_{33}, \quad S_4 = 2S_{23}, \quad S_5 = 2S_{31}, \quad S_6 = 2S_{12}. \quad (9)$$

With the new indices, the above constitutive relations can be written as

$$T_p = \sum_{q=1}^6 c_{pq}S_q - \sum_{q=1}^3 e_{qp}E_q, \quad p = 1, \dots, 6 \quad (10)$$

$$D_p = \sum_{q=1}^6 e_{pq}S_q + \sum_{q=1}^3 \epsilon_{pq}E_q, \quad p = 1, 2, 3. \quad (11)$$

The above coupled wave equations can be solved by any PDE solvers and may be solved analytically for certain simple problems.

3. INTEGRAL EQUATION APPROACH

Due to the well-known characteristics of PDE solvers, the integral equation approach is preferred for solving many wave problems. We can derive the coupled integral equations for the EM radiation by elastic media so that the merits of integral equation solvers can be enjoyed. To do so, we need to consider the EM wave part and elastic wave part separately and the corresponding integral equations can be derived from their PDE counterparts by using the Huygens' equivalence principle and extinction theorem [6]. For the EM wave part, we have the following electric field integral equations (EFIE) for the elastic object which is treated as a dielectric object in electrical property

$$\begin{aligned} & \hat{n} \times \int_S \left[i\omega\mu_1 g_1(\mathbf{r}, \mathbf{r}') \mathbf{J}(\mathbf{r}') - \frac{1}{i\omega\epsilon_1} \nabla g_1(\mathbf{r}, \mathbf{r}') \nabla' \cdot \mathbf{J}(\mathbf{r}') - \mathbf{M}(\mathbf{r}') \times \nabla g_1(\mathbf{r}, \mathbf{r}') \right] dS' \\ = & \hat{n} \times \mathbf{E}_1^{ex}(\mathbf{r}), \quad \mathbf{r} \in S \end{aligned} \quad (12)$$

$$\begin{aligned} & \hat{n} \times \int_S \left[i\omega\mu_2 g_2(\mathbf{r}, \mathbf{r}') \mathbf{J}(\mathbf{r}') - \frac{1}{i\omega\epsilon_2} \nabla g_2(\mathbf{r}, \mathbf{r}') \nabla' \cdot \mathbf{J}(\mathbf{r}') - \mathbf{M}(\mathbf{r}') \times \nabla g_2(\mathbf{r}, \mathbf{r}') \right] dS' \\ = & 0, \quad \mathbf{r} \in S \end{aligned} \quad (13)$$

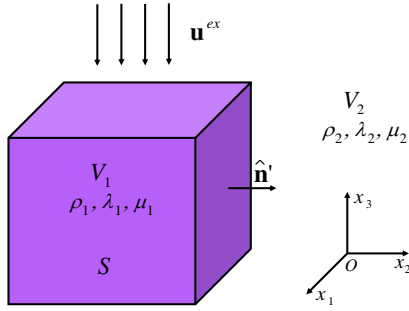


Figure 1: Geometry of an elastic object under a mechanical excitation.

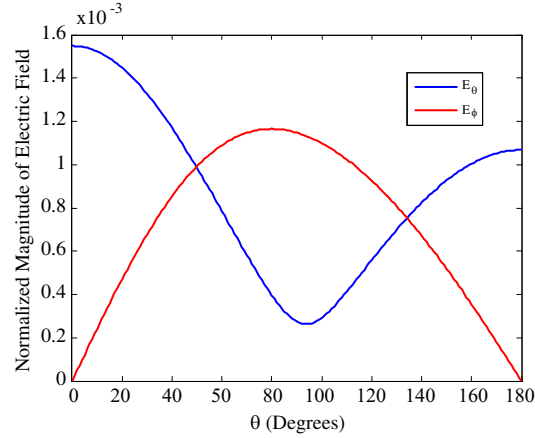


Figure 2: Radiated electric field by an elastic cube under a mechanical excitation. The cube has a side length $s = 0.2$ m, relative permittivity $\epsilon_r = 2.0$, mass density $\rho = 0.97$, and Lamé constants $\lambda = 0.51$ and $\mu = 0.23$, respectively.

where \hat{n} is the unit normal vector on the surface of the elastic object S as shown in Figure 1, $\mathbf{J}(\mathbf{r}')$ and $\mathbf{M}(\mathbf{r}')$ are the equivalent electric and magnetic current densities on S , $g_1(\mathbf{r}, \mathbf{r}')$ and $g_2(\mathbf{r}, \mathbf{r}')$ are the 3D scalar Green's function related to the object in Region 1 and surrounding medium in Region 2, respectively. Also, the indexed ϵ and μ are the permittivity and permeability in the corresponding regions and $\mathbf{E}_1^{ex}(\mathbf{r})$ represents the exciting electric field.

For the elastic wave part, the governing integral equations can be written as

$$\frac{1}{2}\mathbf{u}(\mathbf{r}) + \int_S \left[\bar{\mathbf{Q}}_1^T(\mathbf{r}, \mathbf{r}') \cdot \mathbf{u}(\mathbf{r}') - \bar{\mathbf{G}}_1^T(\mathbf{r}, \mathbf{r}') \cdot \mathbf{t}(\mathbf{r}') \right] dS' = \mathbf{u}_1^{ex}(\mathbf{r}), \quad \mathbf{r} \in S \quad (14)$$

$$\frac{1}{2}\mathbf{u}(\mathbf{r}) + \int_S \left[\bar{\mathbf{G}}_2^T(\mathbf{r}, \mathbf{r}') \cdot \mathbf{t}(\mathbf{r}') - \bar{\mathbf{Q}}_2^T(\mathbf{r}, \mathbf{r}') \cdot \mathbf{u}(\mathbf{r}') \right] dS' = 0, \quad \mathbf{r} \in S \quad (15)$$

where $\bar{\mathbf{Q}} = \hat{n}' \cdot \bar{\bar{\mathbf{W}}}(\mathbf{r}, \mathbf{r}')$ while $\bar{\bar{\mathbf{W}}}(\mathbf{r}, \mathbf{r}')$ is a third-rank Green's tensor, and \mathbf{u} and \mathbf{t} are the total displacement and traction vectors at the object surface S , which are the unknown vectors to be solved.

The above integral equations are coupled through the excitation, i.e., the excitation on the right-hand side of Eq. (12) should be from the contribution of the strain tensor. From the Maxwell's equations, we have

$$\epsilon_{ijk} H_{k,j} = \dot{D}_i = e_{ijk} \dot{S}_{jk} + \epsilon_{ij} \dot{E}_j. \quad (16)$$

We can treat the first term of the right-hand side of the above equation as an effective current which produces the exciting electric field $\mathbf{E}_1^{ex}(\mathbf{r})$ in Region 1, i.e.,

$$\mathbf{E}_1^{ex}(\mathbf{r}) = \int_{V_1} \bar{\mathbf{G}}_1(\mathbf{r}, \mathbf{r}') \cdot \mathbf{J}_1^u(\mathbf{r}') dV' \quad (17)$$

where $\mathbf{J}_1^u(\mathbf{r}')$ is the effective current in V_1 and the superscript u implies that it is related to the displacement field. From Eq. (11), the effective current has the following three components

$$J_p^u = -i\omega \sum_{q=1}^6 e_{pq} S_q, \quad p = 1, 2, 3 \quad (18)$$

for time-harmonic fields and S_q is determined by $S_{ij} = \frac{1}{2}(u_{j,i} + u_{i,j})$. Using the excitation in Eq. (17) as the excitation of the right-hand side in Eq. (12), we can solve the equivalent current densities $\mathbf{J}(\mathbf{r}')$ and $\mathbf{M}(\mathbf{r}')$ on the surface of the elastic object and then calculate the radiated EM fields by them in the surrounding medium. However, we have to solve Eqs. (14) and (15) to obtain the displacement field inside V_1 first and then calculate the effective current in V_1 through the strain tensor $S_{ij} = \frac{1}{2}(u_{j,i} + u_{i,j})$. Since the unknown vectors in Eqs. (14) and (15) are 3D vectors on the object surface, the Nyström method is more suitable than the MoM to solve them though treating the hypersingularity in the EFIE is required [8].

4. NUMERICAL EXAMPLE

We present one numerical example to illustrate the integral equation approach for analyzing the EM radiation by elastic objects. The selected elastic object is a cube with a side length $s = 0.2$ m and relative permittivity $\epsilon_r = 2.0$. Its elasticity is characterized with $\rho = 0.97$, $\lambda = 0.51$, $\mu = 0.23$, and

$$[e_{pq}] = \begin{bmatrix} 23.3 & -6.5 & -6.5 & 0 & 0 & 0 \\ 0 & 0 & 0 & 0 & 0 & 17.0 \\ 0 & 0 & 0 & 0 & 17.0 & 0 \end{bmatrix}, \quad (19)$$

respectively. Figure 2 shows the radiated electric field observed along the principal cut ($\phi = 0^\circ$ and $\theta = 0^\circ$ – 180°) at the spherical surface with a radius $r = 5.0$ m (its center is located at the center of the cube) when the exciting displacement field $\mathbf{u}_1^{ex}(\mathbf{r})$ is a plane wave.

5. CONCLUSION

Electromagnetic (EM) radiation by elastic object includes a multiple physics process, namely, the electrodynamic and elastodynamic processes exist simultaneously and are coupled together. Traditionally, the process is described with the coupled Maxwell's equations and elastic wave equation in their PDE form and only PDE solvers or analytical approach for certain simple cases can be used in the analysis. In this work, we develop an integral equation approach for governing the process and the coupled integral equations are derived from their PDE counterparts based on the Huygens' equivalence principle and extinction theorem. The coupling between the two kinds of integral equations is reflected in the effective current source produced from the strain tensor and the radiated EM fields can be calculated by the equivalent current densities on the object surface after solving the EFIE with the exciting electric field excited by the effective current source. With the coupled integral equations, the elegance of integral equation solvers like the Nyström method can be enjoyed as demonstrated in the numerical example.

ACKNOWLEDGMENT

This work was supported by the Program of Shanghai Pujiang Talents, Shanghai, China, with the Project No. 12PJ1408600.

REFERENCES

1. Balanis, C. A., *Advanced Engineering Electromagnetics*, John Wiley & Sons, New York, 1989.
2. Kyame, J. J., "Wave propagation in piezoelectric crystals," *J. Acoust. Soc. Amer.*, Vol. 21, No. 3, 159–167, 1949.
3. Kyame, J. J., "Conductivity and viscosity effects on wave propagation in piezoelectric crystals," *J. Acoust. Soc. Amer.*, Vol. 26, No. 6, 990–993, 1953.
4. Mindlin, R. D., "Electromagnetic radiation from a vibrating quartz plate," *Int. J. Solids Struct.*, Vol. 9, No. 6, 697–702, 1972.
5. Yang, J. S., *An Introduction to the Theory of Piezoelectricity*, Springer, New York, 2005.
6. Chew, W. C., M. S. Tong, and B. Hu, *Integral Equation Methods for Electromagnetic and Elastic Waves*, Morgan & Claypool, San Rafael, CA, 2008.
7. Tong, M. S. and W. C. Chew, "A higher-order Nyström scheme for electromagnetic scattering by arbitrarily shaped surfaces," *IEEE Antennas and Wireless Propagat. Lett.*, Vol. 4, 277–280, 2005.
8. Tong, M. S. and W. C. Chew, "Super-hyper singularity treatment for solving 3D electric field integral equations," *Microw. Opt. Technol. Lett.*, Vol. 49, No. 6, 1383–1388, 2007.

Input Impedance Measurement for Balanced Antenna by S-parameter Method

T. Sasamori, T. Tobana, and Y. Isota
Akita Prefectural University, Japan

Abstract— In this presentation, the S -parameter method that is a technique for measuring balanced impedance using a vector network analyzer is examined about the measurement that combines the SOLT calibration and the compensation by $ABCD$ -matrix, and measurement using the TRL calibration. A jig for measuring balanced loads is fabricated by the microstrip line on PCB to improve the fabrication accuracy and reproducibility. When the SOLT calibration is performed, three compensating methods using $ABCD$ -matrix, called open-correction, short-correction, and open-short-correction are applied to eliminate the influence of the jig. The wideband input impedance of a dipole antenna, which is one of typical balanced fed antennas, is measured using our proposed methods, and are compared with a calculated results using the moment method. The best measured result of the S -parameter method is in good agreement with calculated result.

1. INTRODUCTION

In recent years, many wireless telecommunication services have spread over the world. It is known that the characteristics of conventional antennas, such as monopole antennas, change considerably when the body of the handset is touched by the hand. This is caused by the variation of the current on the surface of the conducting box used for the handset due to human body influence. To decrease the influence of the human body, a balanced fed antenna is suggested [1]. The input impedance of the balanced antenna is measured conventionally by using a balun that forces opposite currents into each part of the radiation element. Generally, due to the narrow available bandwidth, balun is not suitable for the measurement of the wideband balanced antenna. Recently, the S -parameter method is proposed to measure the balanced impedance of the antenna using a jig instead of the balun, and two ports of a vector network analyzer (VNA) [2, 3]. We had examined the S -parameter method with calibration cables and a jig fabricated by semi-rigid cable [4].

In this presentation, to improve the measurement precision, a jig fabricated by microstrip line is examined. The microstrip line fabricated using a milling machine increases machining accuracy and reproducibility. The measured result of S -parameter method is examined about the SOLT calibration and the TRL calibration has been performed. In case of the SOLT calibration, accuracy of measurement can be improved by removing the influence of the jig for the measurement. Three compensating methods using $ABCD$ -matrix, called open-correction, short-correction, and open-short-correction are applied to eliminate the influence of the jig for the S -parameter method. The wideband input impedance of a dipole antenna, which is one of typical balanced fed antennas, is measured using our proposed methods, and are compared with a calculated results using the method of moment.

2. S-PARAMETER METHOD

Figure 1 shows the dipole antenna, which is one of the balanced fed antennas. Using the impedance matrix of the two-port network as shown in Fig. 2, the equation for the dipole antenna is given by

$$\left. \begin{aligned} V_1 &= Z_{11}I_1 + Z_{12}I_2 \\ V_2 &= Z_{21}I_1 + Z_{22}I_2 \end{aligned} \right\}. \quad (1)$$

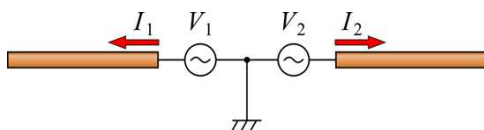


Figure 1: Dipole antenna.

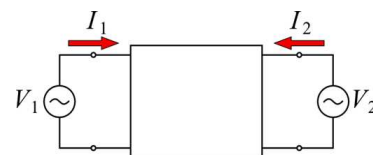


Figure 2: Two-port network.

When the dipole antenna is fed by a balanced source, the currents that flow on the two radiation elements are $I = I_1 = -I_2$. Because the differential voltage is $V_d = V_1 - V_2$, the input impedance Z_{in} is expressed as follows using the Z -parameter, in addition, it can be converted into S -parameter and $ABCD$ -parameter.

$$\begin{aligned} Z_{in} &= V_d/I = Z_{11} - Z_{12} - Z_{21} + Z_{22} = 2Z_0 \frac{(1 - S_{12})(1 - S_{21}) - S_{11}S_{22}}{(1 - S_{11})(1 - S_{22}) - S_{12}S_{21}} \\ &= \frac{1}{C} (A - D + AD + BC - 1) \end{aligned} \quad (2)$$

3. MEASUREMENT METHOD

Figures 3 and 4 show the geometry of jig for measurement and the fabricated jig. The jig is composed of two dielectric substrates with dimension of $40 \times 40 \times 0.8 \text{ mm}^3$, the dielectric constant of 2.15. A microstrip line with the characteristic impedance of 50Ω is printed on the dielectric substrate, and a SMA connector is soldered to one end of the microstrip line. Two dielectric substrates facing the ground each other are fixed with the six screws, as shown in Fig. 4. Then, the radiation element of the balanced antenna is soldered to the other end of the microstrip line. In this study, the jigs connected to port 1 and port 2 of VNA are called jig #1 and #2, respectively.

Figure 5 shows the circuit diagram with an antenna connected to the jig for measurement in a two-port network configuration. The $ABCD$ -matrix K' that is between the calibration planes can be determined by substituting the measured results of the S -parameter using the VNA in Eq. (3).

$$K' = \begin{bmatrix} \frac{(1+S_{11})(1-S_{22})+S_{12}S_{21}}{2S_{21}} & \frac{(1+S_{11})(1+S_{22})-S_{12}S_{21}}{2S_{21}} \\ \frac{(1-S_{11})(1-S_{22})-S_{12}S_{21}}{2S_{21}} & \frac{(1-S_{11})(1+S_{22})+S_{12}S_{21}}{2S_{21}} \end{bmatrix} \quad (3)$$

As shown in Fig. 5(a), the characteristic of jigs are included in the $ABCD$ -matrix K' when the SOLT calibration is performed. The $ABCD$ -matrix K of the antenna can be obtained by removing the $ABCD$ -matrices of jigs K_{J1} and K_{J2} , as given by

$$K = K_{J1}^{-1} K' K_{J2}^{-1} \quad (4)$$

As shown in Fig. 5(b), the $ABCD$ -matrix of the antenna can be measured directly when the TRL calibration is performed.

Finally, the input impedance of the balanced antenna can be obtained by substituting the $ABCD$ -parameter of the antenna for Eq. (2).

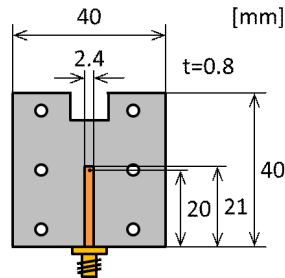


Figure 3: Geometry of jig.

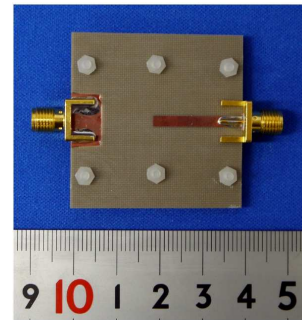


Figure 4: Fabricated jig.

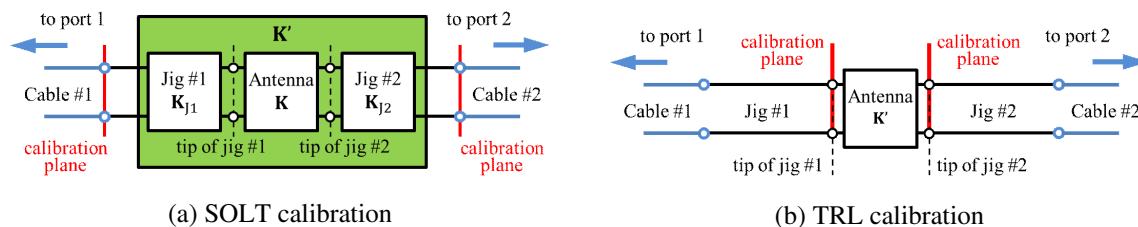


Figure 5: Equivalent circuit diagram of antenna with jig.

3.1. Open-correction and Short-correction

Open-correction and short-correction are the methods for determining the $ABCD$ -parameter of jig using the input impedance of the jig terminated in an open circuit and a short circuit, respectively, and the characteristic impedance of the jig. Thus the jig should be a transmission line. The input impedance of jig at calibration plane for both cases can be given by

$$\begin{cases} Z_O = Z_0/\tanh \gamma l: & \text{open-circuit} \\ Z_S = Z_0 \tanh \gamma l: & \text{short-circuit} \end{cases} \quad (5)$$

where Z_0 , γ and l are the characteristic impedance of the transmission line, the propagation constant and the length. The hyperbolic functions $\sinh \gamma l$ and $\cosh \gamma l$ can be given by Z_O or Z_S , and Z_0 using $\cosh^2 \gamma l - \sinh^2 \gamma l = 1$ and Eq. (5). Thus, the $ABCD$ -matrix of the jig can be written as Eq. (6).

$$\begin{cases} K_J = \frac{1}{\sqrt{Z_O^2 - Z_0^2}} \begin{bmatrix} Z_O & Z_0^2 \\ 1 & Z_O \end{bmatrix}: & \text{open-correction} \\ K_J = \frac{1}{\sqrt{Z_0^2 - Z_S^2}} \begin{bmatrix} Z_0 & Z_0 Z_S \\ Z_S/Z_0 & Z_0 \end{bmatrix}: & \text{short-correction} \end{cases} \quad (6)$$

3.2. Open-short-correction

Open-short-correction is a method for determining the $ABCD$ -matrix of jig using both input impedance of open-circuited and short-circuited line. When the jig is expressed by the $ABCD$ -matrix, the input impedance Z at calibration plane is given by

$$Z = \frac{V'_1}{I'_1} = \frac{AV'_2 + BI'_2}{CV'_2 + DI'_2} \quad (7)$$

Because $I'_2 = 0$, when the jig is terminated in an open circuit, the input impedance for open circuit is $Z_O = A/C$. On the other hand, because $V'_2 = 0$, when the jig is terminated in a short circuit, the input impedance for short circuit is $Z_S = B/D$. Because the jig is a symmetrical circuit ($A = D$) and a reciprocal circuit ($AD - BC = 1$), the $ABCD$ -matrix K_J is given by

$$K_J = \sqrt{\frac{Z_O}{Z_O - Z_S}} \begin{bmatrix} 1 & Z_S \\ 1/Z_O & 1 \end{bmatrix} \quad (8)$$

4. RESULTS AND DISCUSSION

Typical results for the S -parameter method are presented for a dipole antenna. Two pieces of copper wire with length of 50 mm and diameter of 1.0 mm are soldered onto the microstrip line of jig #1 and #2 for fabricating the dipole antenna to be measured. To discuss the accuracy of the measured result of the S -parameter method using the jig fabricated by microstrip line, the calculated result using the method of moments is also shown.

Figure 6 shows the measured input impedance of the dipole antenna after the SOLT calibration is performed. It is seen in Fig. 6(a) that the measured result of the S -parameter method calibrated by the open-correction agrees very well with the simulated result at about 6 GHz or less. The

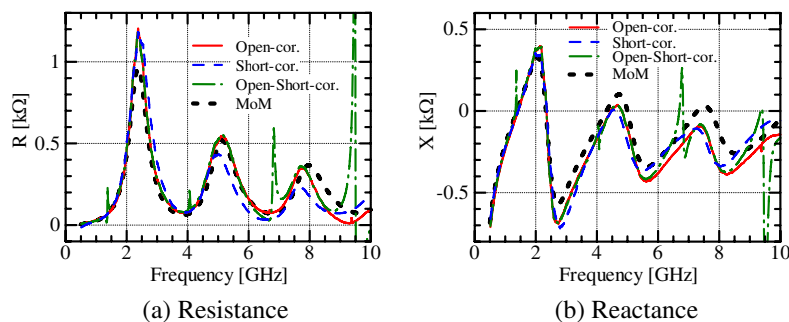


Figure 6: Measured input impedance after the SOLT calibration is performed.

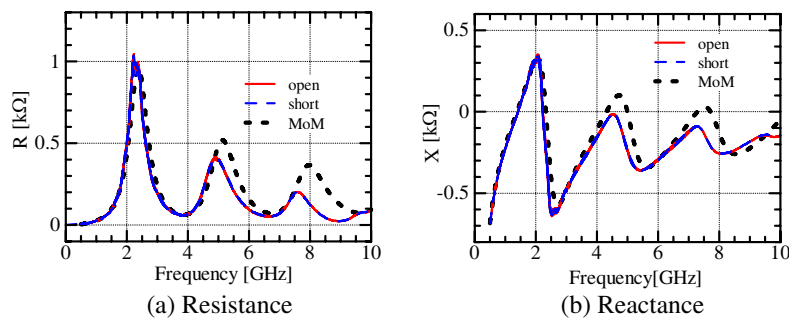


Figure 7: Measured input impedance after the TRL calibration is performed.

measured result of the open-short-correction also agrees with the simulated result at about 6 GHz or less, though some sharp peaks appear. Because the frequency of peak is the same as the resonant frequency of the jig, it can be said that and these error caused by the calculation of the compensation. Regarding the short-correction, it is understood that the measured result is worse than the other two compensation results. It seems that there is a problem in the short circuit load by via of microstrip line. As shown in Fig. 6(b), it is observed that the measured results of reactance are the same tendency as the resistance.

Figure 7 shows the measured input impedance after the TRL calibration is performed. In this figure, two kinds of measured results when the open-circuited jig and the short-circuited jig are used as a standard of reflect are shown. Because two measured results agree well, it is understood that both type of reflect can be used. Both measured results are corresponding to the calculated result quite well in the frequency of about 4.5 GHz or less.

5. CONCLUSIONS

In this presentation, to improve the measurement precision, a jig fabricated by microstrip line for the S -parameter method was examined. The measured result of S -parameter method was examined after the SOLT calibration and the TRL calibration had been performed. In case of the SOLT calibration, three compensating methods using $ABCD$ -matrix, called open-correction, short-correction, and open-short-correction were applied to eliminate the influence of the jig for the S -parameter method. The wideband input impedance of a dipole antenna, which is one of typical balanced fed antennas, was measured using our proposed methods, and were compared with a calculated results using the method of moment. Consequently, it was notable that the best measured result of the S -parameter method agreed very well with the simulated result in the frequency of about 6 GHz or less.

ACKNOWLEDGMENT

This study was partly supported by research grant from Japan Power Academy.

REFERENCES

1. Morishita, H., Y. Kim, and K. Fujimoto, "Design concept of antenna for small mobile terminals and the future perspective," *IEEE Antennas Propag. Mag.*, Vol. 44, No. 5, 30–42, Oct. 2002.
2. Meys, R. and F. Janssens, "Measuring the impedance of balanced antennas by an S -parameter method," *IEEE Antennas Propag. Mag.*, Vol. 40, No. 6, 62–65, Dec. 1998.
3. Palmer, K. D. and M. W. van Rooyen, "Simple broadband measurements of balanced loads using a network analyzer," *IEEE Trans. Instrum. Meas.*, Vol. 55, No. 1, 266–272, Feb. 2006.
4. Konya, S., T. Sasamori, T. Tobana, and Y. Isota, "Wideband impedance measurement of balanced antenna using the S -parameter method," *Proc. APMC 2011*, 717–720, Melbourne, Australia, Dec. 2011.

Near-field Magnetic Probe Method Predicting Far-field Measurements — Correlation of Dipole Boresight Measurements with Anechoic Range Model

Daniel Brooks, Stuart Nicol, Jesse Hones, and John Lee

Aprél Inc., Ottawa, Ontario, Canada

Abstract— Traditional methods for establishing EMC and field density can be predicted using a field approximation routine based on well documented principles. In the process of reducing spurious emissions or interference EMC engineers will use suppression techniques of shields, boxes and cages. These methods have been found to work in normal applications but as the frequency expands traditional methods of EMC suppression may not be as effective. The far field approximation technique presented in this paper allows an engineer to test a sub assembly in the near field and then have a value which can be extrapolated to the far field. Measurements taken using the broadband near field “magnetic probe method” used with an automated scanning system (EM-ISight) can be extrapolated to either a 3 m or 10 m range space. Such a technique can allow the design engineer to determine the effectiveness of their design prior to the final integration of an assembly thus understanding better the uncertainties of a previously developed reference design or suppression methods.

1. INTRODUCTION

Our interest is in pre-compliance measurements using the “magnetic probe method” [1, 2]. It is very useful for EMC design engineers to take the near-field behavior into account for predicting the far-field [3, 4]. The near-field to far-field transformation has been extensively studied since the plane-wave expansion method with probe correction proposed by Kerns in 1963 [5]. Several successful methods have been developed such as Fast Fourier Transformation (FFT) and equivalent source methods [6–14], and these activities have greatly enhanced the popularity of near-field measurement. In this paper, we use these techniques to demonstrate the degree of correlation that can be achieved translating actual near-field “*magnetic field*” measurements of elementary reference dipoles into equivalent far-field “*electric field*” numbers expected from range measurements. The theoretical, numerical and measurement techniques applied in our work are described in the methodology Section 2 of the report. Validation is provided in Section 3 using full 3D range propagation models of anechoic, semi-anechoic chambers and Open Area Test Site (OATS) ranges. Near-field measurements provided in Section 4 were taken in the Fresnel region near the reference dipole surface and compared with the results obtained using numerical methods. Further, these near-field measurements were performed in a normal lab environment rather than an OATS or anechoic chamber as required with far-field measurements, demonstrating that the magnetic probe coupling mechanism in close proximity with a reference dipole DUT can be sufficiently used to validate accurate measurements that are less affected by outside interactions and conditions. The standard far-field compliance test is not well suited for early stages of product development. Measured radiation patterns in the far-field can be regarded as a direct measurement [15], on the other hand near-field measurements can be used to obtain the electromagnetic fields from a DUT [16] as needed to provide source diagnostics of emissions in EMC studies of PCBs and ICs [17, 18]. Furthermore, performing a near-field scan provides knowledge added through visual interpretation of radiated emission signatures that can tell the EMC design engineer optimum placement of devices and the location of problems in PCB stacks and where to place shielding and other suppression methods necessary early in the design cycle. Near-field measurements have advantages in reliability and costs of applications [19], making it a highly feasible technique.

2. MEASUREMENT METHODOLOGY

Reference dipoles are used as the DUT for the work in this analysis. These devices are resonant balanced half-wave dipoles that are tuned and optimized for maximum free space radiation at the specified resonant frequency of 2.45 GHz and 5 GHz. Radial dimensions were obtained from actual reference dipoles used in calibration of traditional range measurements and are characterized using a vector network analyzer (VNA) with results shown in Figure 1 for both dipoles. The Finite

Frequency (MHz)	Z [ohms]	RL [dB]	VSWR	Gain (dBi)	D [mm]	R [mm]
2450.0	54.7+j4.9	-23.9	1.14	2.15	58.0	55.3
5000.0	47.3+j5.4	-24.2	1.13	2.16	29.0	28.2

Figure 1: Reference dipole.

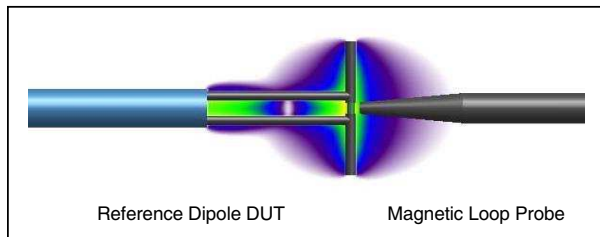


Figure 3: Magnetic field probe and DUT coupling.

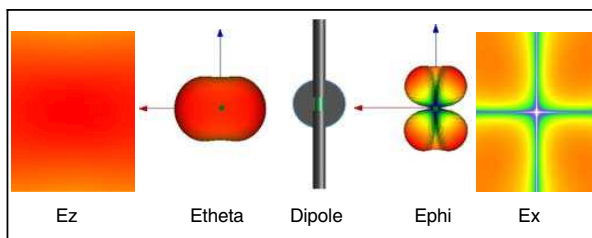


Figure 2: FFT numerical radiation pattern.

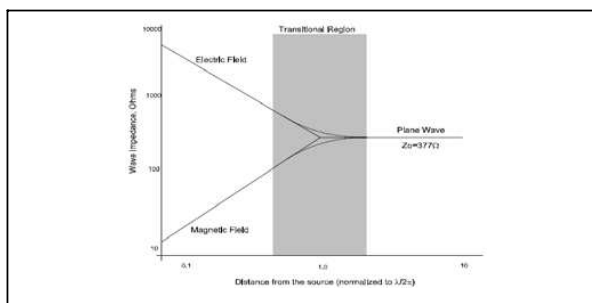


Figure 4: Theoretical wave impedance.

Difference Time Domain (FDTD) method is used to calculate the scatter parameter of each dipole model and for validation purposes are compared with the VNA measurements.

The FDTD numerical calculations were performed using complex models of the dipole geometry (radiating and balun elements) constructed and meshed into a rectangular Yee cell problem space of XYZ (60, 173, 353) with a 0.8 mm cubic cell dimension. Impedance matching using external devices was not needed excluding the $\lambda/4$ balun element incorporated into the dipole structure [20]. The temporal conditions for the center frequencies are reported in Figure 1 the respective impedance Z , return loss RL , VSWR, gain G , radial length D , and calculated far-field distance (R). Each dipole is excited and driven with a continuous wave sinusoid with (0 dBm) of power directly into the geometric center axis of symmetry.

Far-field radiation patterns are shown in Figure 2 are generated using the FFT method by forming a cuboid around the DUT shown in the center view of Figure 3 with the complex 3D radiation patterns adjacent to planer cuts in the outside views respectively. The direction of propagation (out of the page) is along the Y -axis. The standard spherical coordinate system is used to define vertical polarization attributes of elevation (page top down) as the Z -axis, and azimuth (page left to right) as the X -axis. These radiation patterns are used by the propagation model to calculate far-field “electric field” target numbers expected in a range measurement.

Magnetic field calculations and measurements of the H_x field vector are taken with the magnetic probe positioned at the reference point shown in Figure 3 and defined as separation distance (R_m) located in the dipole boresight moving away ranging R_m (0 to 156 mm) into the far-field.

Reference dipoles cover an important class of antenna as their electromagnetic characteristics; of radiation, wave impedance and power density are well understood and are frequently used for range calibration measurements. Similarly, calculations and measurements conducted in the near-field can be correlated to range calibration measurements. Equiphase properties [21, 22] in the radiation region of half wavelength dipoles are of particular interest in our paper. According to IEEE standard definitions [23], an equiphase aperture (determined on boresight) for which (D) is the dimension in the E or H plane that presents three different radiation regions. Each region has unique field characteristics that provide insight into the actual fields as a function of distance from the source DUT. The far-field (Fraunhofer Region) is the R distance greater than $2D^2/\lambda$ where the angular distribution is independent (22.6 degrees error) of distance from the source and where E and H fields are in-phase (orthogonal) and converge to 377 ohms free space wave impedance as shown Figure 4 [24]. The transition region is the soft boundary separating near-field (Fresnel Region).

The wave impedance of both reference dipoles are calculated with FDTD relative to the R_m probe separation distance. FDTD calculations in Figure 5 correlate with theoretical calculations

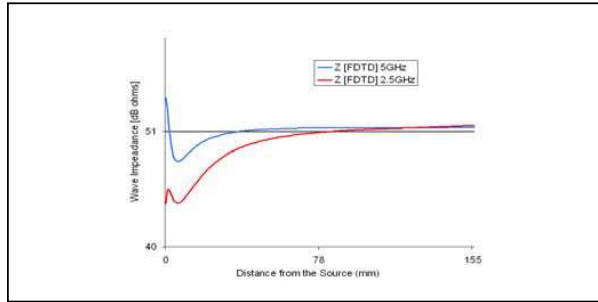


Figure 5: Numerical wave impedance.

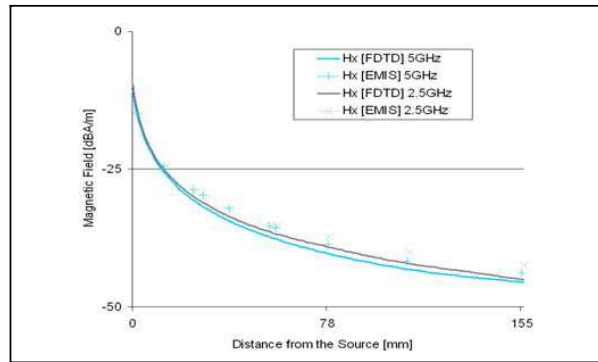


Figure 6: Magnetic field measurements vs: numerical calculations.

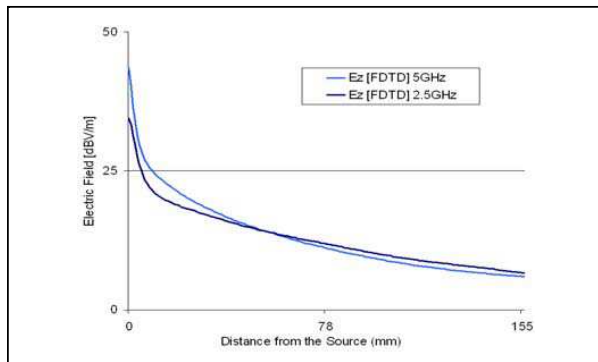


Figure 7: Electric field numerical calculations.

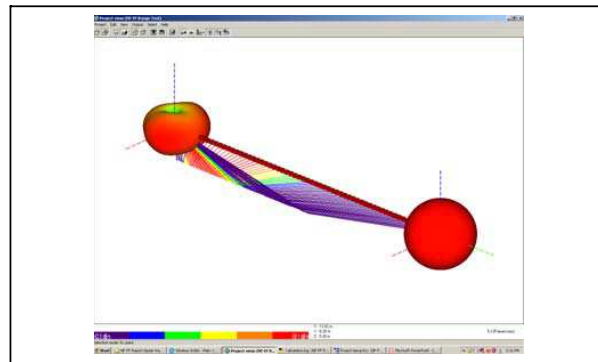


Figure 8: Range propagation model.

of Figure 4 as both converge to the free space impedance 377 ohms or 51.5 dBohms. The magnetic field measurements are converted into equivalent electric fields numbers using the 51.5 dBohm free space impedance.

Measurements of the reference dipole DUT are taken using the APREL robotic near-field scanning system EM-ISight (EMIS) to accurately place the probe at the reference position in-line of boresight. The probe is moved away from the DUT directly under robotic control along the Y -axis ranging outwards a distance R_m to 156 mm. The separation distance R_m is established from the top surface of the dipole to the nearest point on the probe element and 1.3 mm is added to the measurement distance to account for the magnetic probe loop aperture offset from the probe tip.

EMIS measurements of the magnetic H_x field vector (cross hatched) shown in Figure 6 are directly compared with FDTD calculations (solid lines). The electric field calculations in Figure 7 are included here for completeness and discussion purposes later on in the paper.

In testing the reference dipole DUT, the near-field EMIS measurements and the FDTD numerical calculation results can be translated to far-field numbers using Equation (1) [25].

$$\text{Amplitude}(10\text{ m}) = 20 \log(10\text{ m}/R_m) \quad (1)$$

Equation (1) provides the ability to translate measurements directly to any R_m distance of the far-field region, in our case 10 m (this is the distance used in standard procedures CISPR-22 for range measurements).

3. RANGE PROPAGATION MODEL

The OATS and anechoic chamber range model shown in Figure 8 is constructed as a full 3D propagation model for the far-field analysis of the reference dipole. The analysis method uses the Shooting Bouncing Ray Tracing (SBRT) algorithm with the Uniform Theory of Diffraction (UTD) [26,27]. Ray tracing is an effective way to evaluate complex antenna radiation patterns of electric fields and predicting their interactions of reflection and polarization in the spherical co-ordinate system.

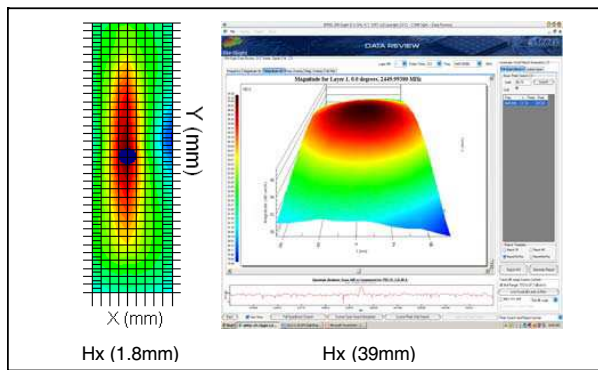


Figure 9: EMIS measured H_x field vector.

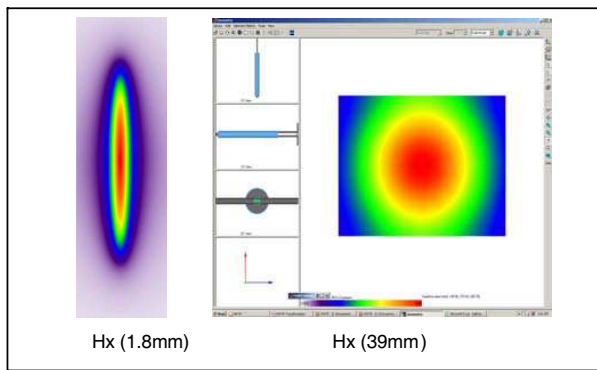


Figure 10: FDTD numerical H_x field vector.

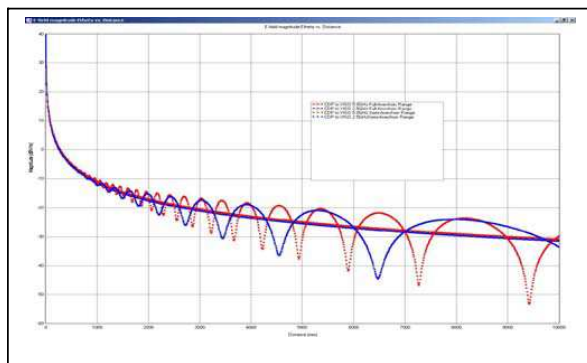


Figure 11: Propagation range SBRT predicted results.

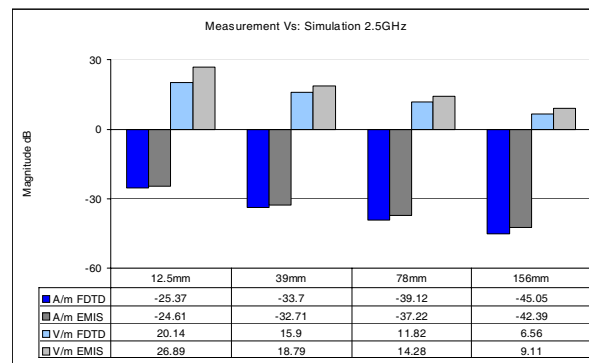


Figure 12: EMIS measured vs: FDTD numerical at 2.45 GHz.

Radiation patterns shown in Figure 2 were created using post processing FFT to transform the DUT electric fields into far-field 3D radiation patterns. These complex patterns capture all attributes of gain directivity and are imported into the SBRT ray tracing model as vertically polarized transmitting antennas. Within the range model the DUT is located at point (0) one meter in elevation above ground level and driven with 0 dBm of input power at the respective operating frequency. Further, (1000) receiver antennas are placed in-line with boresight ranging outwards 10 meters at the same elevation above ground. These antennas are defined as vertically polarized isotropic radiator receivers with 0 dB gain were used to map ground reflections.

The entire propagation model as viewed in Figure 8 shows the real radiation pattern (total electric field) of the transmitting dipole DUT located in the top left pointing in the boresight direction ($\theta=90^\circ$, $\phi=90^\circ$) inline with isotropic range receiving antennas.

4. MEASUREMENT AND NUMERICAL ANALYSIS

The magnetic field measurements shown in Figure 9 are taken in the Fresnel region in boresight of the 2.45 GHz reference dipole. EMIS provides important visual interpretations of the H_x field vector distribution very near to the surface of the dipole and also at distance R_m of 39 mm where a volumetric 4D view is displayed. The FDTD calculations displayed in Figure 10 are in fine agreement.

The numerical range propagation model SBRT analysis in Figure 11 displays the predicted electric field target numbers. The full-anechoic response has a smooth continuous free space path loss (FSPL), whereas semi-anechoic or OATS range shows multipath interference reflection from the metallic ground plane. These are consistent with what can be expected in a large range and must be taken into account. Indications show approximately a 6 dB electric field variation at 10 m due to multipath bounce, not considered when testing in near-field or full anechoic chambers.

The EMIS magnetic field measurements in Figures 12–13 are directly compared with FDTD calculations and are found to be in fine agreement moving towards the source. The opposite is true of the electric field as the numbers tend toward agreement moving farther away from the source. This is evident in Figure 14 where equivalent electric fields defined as *translation* numbers are

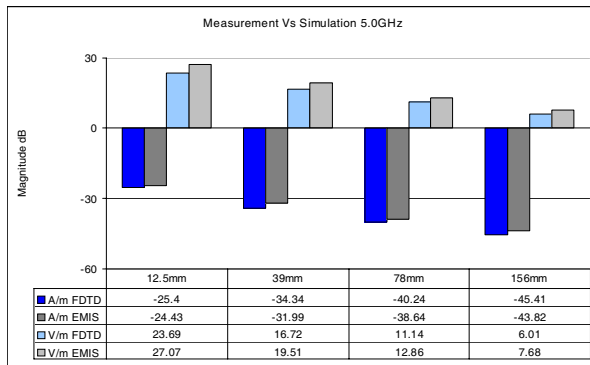


Figure 13: EMIS measured vs: FDTD numerical at 5.0 GHz.

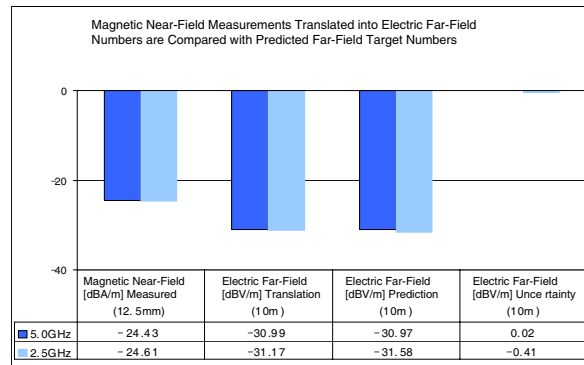


Figure 14: EMIS vs: SBRT 10 m prediction delta.

found to be in very fine agreement with the *prediction* target numbers calculated by the SBRT range propagation model.

5. DISCUSSION AND CONCLUSION

The results presented in Section 4 of this paper clearly demonstrate that a significant degree of correlation exists between magnetic probe near-field measurements and electric far-field range calculations. The EMIS system magnetic field measurements shown in Figure 14 taken at Rm 12.5 mm convert and translate to equivalent electric field strength numbers at 10 meters with an uncertainty delta of less than 0.5 dBV/m are in very fine agreement with electric field strength numbers predicted by the SBRT range propagation model. Magnetic field calculations and measurements in Figure 6 demonstrate a smooth continuous function beginning at the surface of the dipole that continues unabated well into the far-field region. This is not the case with the electric field as calculations in Figure 7 demonstrate significant fluctuation moving towards the source. Observations of the data in Figures 12–13 show that magnetic field uncertainty decreases moving closer to the source, whereas electric field uncertainty increases moving closer to the source. The magnetic probe field coupling mechanism in close proximity with the reference dipole can be sufficiently used to validate accurate measurements that are less affected by interactions and conditions expected from semi-anechoic or OATS test ranges [28]. This study has demonstrated the advantages of working in the near-field using the EM-ISight system and the automated volumetric averaging method early in the design stage to mitigate risks which may occur further in the design process due to changes in reference design or components such as shielding mechanisms or final assembly packaging. When extrapolating fields outside of a measurement volume it is possible to choose an appropriate spatial step size dependent on a maximum tolerated error and minimum size of scanned elements, this is a subject for future work.

ACKNOWLEDGMENT

Many thanks to Tektronix worldwide for their support.

REFERENCES

1. IEC, International Standard, 61967-6, "Measurement of conducted emissions, magnetic probe method," 11, 2002.
2. IEC, International Standard, 61967-6-amd1, "Measurement of conducted emissions, magnetic probe method," 2002.
3. Aunchaleevarapan, K., K. Paithoonwatanakij, W. Khan-Ngern, and S. Nitta, "Novel method for predicting PCB configurations for near-field and far-field radiated EMI using a neural network," *IEICE Trans. Commun.*, Vol. E86-B, No. 4, 1368–1369, Apr. 2003.
4. Ludwig, A. C., "Near-field far-field transformations using spherical wave expansions," *IEEE Transactions Antennas and Propagation*, Vol. 15, No. 2, 214–220, Mar. 1971.
5. Kerns, D. M., "Analytical techniques for the correction of near-field antenna measurements made with an arbitrary but known measuring antenna," *Abstracts of URSI-IRE Meeting*, 6–7, Washington, DC, Apr.–May 1963.

6. Leach, Jr., W. M. and D. T. Paris, "Probe-compensated near-field measurements on a cylinder," *IEEE Transactions Antennas and Propagation*, Vol. 21, 435–445, Jul. 1973.
7. Wacker, P. F., "Non-planar near-field measurements: Spherical scanning," NBSJR 75-809, Jun. 1975.
8. Jensen, F., "On the probe compensation for near-field measurements on a sphere," *AEU*, Vol. 29, 305–308, Jul.–Aug. 1975.
9. Petre, P. and T. K. Sarkar, "Planar near-field to far-field transformation using an equivalent magnetic current approach," *IEEE Transactions Antennas and Propagation*, Vol. 40, No. 11, 1348–1356, Nov. 1992.
10. Sarkar, T. K. and A. Taaghola, "Near-field to near/far-field transformation for arbitrary near-field geometry utilizing an equivalent electric current and MoM," *IEEE Transactions Antennas and Propagation*, Vol. 47, No. 3, 566–573, Mar. 1999.
11. Laurin, J. J., J. F. Zürcher, and F. E. Gardiol, "Near-field diagnostics of small printed antennas using the equivalent magnetic current approach," *IEEE Transactions Antennas and Propagation*, Vol. 49, No. 5, 814–828, May 2001.
12. Barrière, P. A., J. J. Laurin, and Y. Goussard, "Mapping of equivalent currents on high speed digital printed circuit boards based on near-field measurements," 649–658, 2009.
13. Reguè, J. R., M. Ribo, J. M. Garrell, and A. Martin, "A genetic algorithm based method for source identification and far-field radiated emissions prediction from near-field measurements for PCB characterization," *IEEE Trans. Electromagn. Compat.*, Vol. 43, No. 4, 520–530, Nov. 2001.
14. Vives-Gilabert, Y., C. Arcambal, A. Louis, F. de Daran, P. Eudeline, and B. Mazari, "Modelling magnetic radiations of electronic circuits using near-field scanning method," *IEEE Trans. Electromagn. Compat.*, Vol. 49, No. 2, 391–400, 2007.
15. Balanis, C. A., *Antenna Theory: Analysis and Design*, Wiley, New York, 2005.
16. Johnson, C., H. A. Ecker, and J. S. Hollis, "Determination of far-field antenna patterns from near-field measurements," *Procedures IEEE*, Vol. 61, No. 12, 1668–1694, Dec. 1973.
17. Thomas, D. W. P., K. Biwojno, X. Tong, A. Nothofer, P. Sewell, and C. Christopoulos, "Measurement and simulation of the near-field emissions from microstrip lines," *Proc. EMC Europe 2008*, 1–6, Sep. 2008.
18. Sugawara, K., C. P. Chen, Z. Ma, T. Anada, and D. W. P. Thomas, "Non-contacting electric and magnetic field probe for measuring EM fields on microwave planar circuits," *Proc. Asia-Pacific Microwave Conference*, 1441–1444, 2007.
19. Slater, D., *Near-field Antenna Measurements*, Artech House, Norwood, MA, 1991.
20. Brooks, D., S. Nicol, and J. Wojcik, "Wideband complex dipole antenna design for reference measurements in the human body from frequencies in 5–6 GHz band," *EMC*, 97–101, Zurich, Feb. 2005.
21. Laybros, S. and P. F. Combes, "On radiating zone boundaries of short, dipoles," *IEEE Antennas and Propagation Magazine*, Vol. 45, No. 5, 53–64, Oct. 2004.
22. Laybros, S., P. F. Combes, and H. J. Mametsa, "'The very-near-field' region of equiphase radiating apertures," *IEEE Antennas and Propagation Magazine*, Vol. 47, No. 4, 50–51, Aug. 2005.
23. "IEEE standard definitions of terms for antennas," *IEEE Transactions on Antennas and Propagation*, Vol. 17, No. 3, 252–259, May 1969; and Vol. 22, No. 1, Jan. 1974.
24. Kraz, V., "Near-field methods of locating EMI sources," *Compliance Engineering Magazine*, 6–7, May–Jun. 1995.
25. Rocznik, A., E. M. Petriu, and G. I. Costache, "3D electromagnetic field modeling based on near-field measurements," *IEEE Instrumentation and Measurement Technology Conference*, 890–896, Brussels, Belgium, Jun. 1996.
26. Keller, J. B., "Geometric theory of diffraction," *J. Opt. Soc. America*, Vol. 52, No. 2, 116–130, Feb. 1962.
27. Balanis, C., *Advanced Engineering Electromagnetics*, John Wiley and Sons Inc, 1989.
28. Yaghjian, A. D., "An overview of near-field antenna measurements," *IEEE Transactions on Antennas and Propagation*, Vol. 34, No. 1, January 1986.

Effects of Residual Stress on Assembled SAW Strain Sensors

J. Hempel¹, J. Wilde², and L. M. Reindl¹

¹Laboratory for Electrical Instrumentation
Department of Microsystems Engineering, IMTEK
University of Freiburg, Germany

²Laboratory for Assembly and Packaging Technology
Department of Microsystem Engineering, IMTEK
University of Freiburg, Germany

Abstract— In this paper, the effects of residual stress on SAW strain sensors due to the assembly process are analyzed. SAW strain sensors are mounted with different adhesives and the sensors response is evaluated with the measured scattering parameters S_{11} . Sensors deformation is investigated using a “With-Light-Interferometry” approach, and compared with the simulations. Additionally, the temperature dependency of the SAW strain sensors is analyzed before and after the assembly. Finally, a thermal aging step is performed and the sensor response and its deformation are evaluated.

1. INTRODUCTION

State of the art SAW strain sensors have a vast range of applications as passive wireless sensing devices [1–6]. However, the room of improvement in assembly and packaging of SAW sensors for structural integration in measurement applications still exists [7, 8]. Depending on the assembly technologies and materials, the sensors performance is affected tremendously. A mismatch in the *CTE* of the carrier material, the glue, and the α -quartz substrate of the SAW resonator causes an offset in the sensor signal [9, 10]. Moreover, the material properties and the bond layer thickness influences the sensor offset as well as the sensor sensitivity [11, 12]. Selecting adapted bond components will fully utilize the performance of SAW strain sensors. Analyzing the bond process, utilized materials, and the corresponding thermo-mechanical stress, the existing weak points in the assembly and packaging of the SAW technology for industrial applications can be solved. This paper is organized as follows. Used materials, processes, and experimental setup are summarized in Section 2. In Section 3, experiments and results are presented. Section 4 elaborates the simulation approach of the residual stress problem and Section 5 gives a conclusion of the presented work.

2. MATERIALS, PROCESSES, AND EXPERIMENTAL SETUP

Experiments within this work have been carried out using industrial SAW strain sensors [13]. These sensors provide reproducible and reliable sensor signals, which are mandatory for convincing stress investigations. Commonly used heat-treatable steel has been selected as carrier material for the SAW strain sensors. The *CTE* of the steel carrier is in the range of the α -quartz sensor substrate [14]. Two polymer adhesives were chosen, which were already investigated and particularly suitable for SAW strain sensor application [12]. The adhesives and the bare SAW strain sensors were deposited with a dispensing system, respectively, applied with a pick and place tool. Therefore, a high process quality and repeatability is achieved. Bare sensor chips without electrical connectors were selected, for minimizing the sensor signal distortion. Material parameters are summarized in Table 1, whereby *CTE* is representing the coefficient of thermal expansion, E the Young’s modulus, T_g the glass transition temperature, and T_P the process temperature. Figure 1 depicts the experimental setup, used for residual stress investigations.

3. EXPERIMENTS

For the experiments three sensors were assembled in each case with the selected adhesives (Table 1). A probe station has been used for interconnection of the SAW strain sensor with a network analyzer [15]. Therefore a well reproducible and reliable electrical connection has been achieved for the sensor response analysis. The sensors were characterized before and after their assembly. The temperature dependency of the sensors was analyzed up to 125°C. The sensor deformation due to the thermo mechanical stress of the assembly process was measured using “With-Light-Interferometry” approach. These measurements were directly compared with the results of the implemented 3 D FEM simulations. In conclusion, the whole setup was aged at 150°C for a time span of 100 h and the sensor performance and its deformation were analyzed.

Table 1: Material data of the setup, consisting of SAW strain sensor, polymer adhesives, and heat treatable steel carrier at 25°C.

Material		CTE in ppm/K	E in GPa	T_g in °C	T_p in °C
Steel carrier		12	210	-	-
Polymer adhesive	1	42*/147**	5.5*/0.3**	134	150
	2	24*	9.0*	179	150
α -quartz***		7.1–20.91	78–103	-	-

*Below the glass transition temperature T_g .

**Above the glass transition temperature T_g .

***Strong anisotropy parallel and perpendicular to the optical axis of the quartz in combination with a high temperature dependency of the CTE.

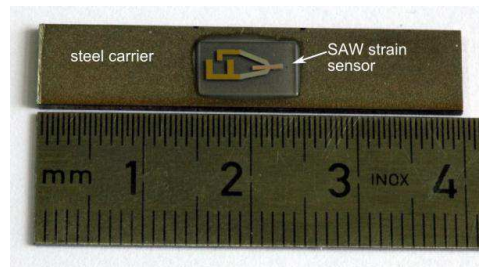


Figure 1: Assembled SAW strain sensor for residual stress investigations, fixed with polymer adhesive 1.

3.1. SAW Strain Sensor Response

Sensors relative resonance frequency shift $\Delta f/f_0$ were calculated from the measured S_{11} parameters. The term $\Delta f/f_0$ is independent from the unloaded sensors resonance frequency f_0 . Due to the thermo mechanical stress, induced by the bond process with the polymer adhesive 1, a sensor offset of 94.5 ± 17.7 ppm was measured at room temperature. Attached sensors with polymer adhesive 2 had an offset of 159.3 ± 28.4 ppm at room temperature. Figures 2 and 3 exhibits the temperature responses of the SAW strain sensors, assembled with polymer adhesive 1 and 2, respectively. Furthermore, the temperature response of the sensors after an aging time span of 100 h at 150°C is also depicted in Figures 2 and 3.

The constraint free measurement (before gluing) of the SAW strain sensors response, by varying the temperature up to 125°C in 20°C steps shows an unexpected high deviation of the sensor signal between the heating and cooling cycle. Reference measurements with a resistive temperature sensor proved an inhomogeneous temperature distribution on the thermo chuck of the probe station. The thermo chuck has a limited accuracy in temperature distribution. Therefore, small thermal contact area of the sensor leads to the depicted sensor response deviation. With an increasing thermal interconnection the sensor signal deviation decreases.

For both sets of experiments, the parabolic temperature response of the sensors has been changed due to their fixation on the steel carrier. In case of the attachment with polymer adhesive 1 (Figure 2), the sensor response converges for increasing temperatures to the sensor response without any constrains in displacement. At temperatures above 100°C the SAW strain sensors temperature response of the fixed sensors is approximately equal to the constraint free sensor response. This is due to the fact, that the operating temperature is in the range of the stress free temperature T_g (134°C) of the polymer adhesive 1. In case of polymer adhesive 2 fixed sensors, the sensor signal also converges to the constraint free sensor response. However at 125°C operating temperature, there is an offset between the associated sensor signals, which indicates an existing residual stress at this temperature. This behavior corresponds to a higher stress free temperature T_g (179°C) of the polymer adhesive 2. No significant sensor signal change has been observed between the measurement directly after the gluing process and the measurements performed after the aging time span of 100 h at 150°C. Only in case of polymer adhesive 1 fixed sensors (Figure 2), a non-significant sensor signal shift was detected.

Figure 4 shows an assembled SAW strain sensor using polymer adhesive 1 after the aging time span of 100 h at 150°C. The bond material demonstrates a color change after the aging step, which indicates a degradation of the adhesive. However, the bond strength did not decrease after the aging step, which was measured with a shear test as described in [12]. The change in color of polymer adhesive 1 is originated in the aging temperature of 150°C, which is above the glass transition temperature T_g (134°C) of the glue. The bond layers consisting of polymer adhesive 2 did not evince any change after the aging, due to the high glass transition temperature T_g (179°C) of the glue.

3.2. SAW Strain Sensor Deformation Measurement

The SAW strain sensor deformation perpendicular to the sensor surface (z -direction) before (bare chip deformation) and after the bond process were measured. The deformation is anisotropic,

relating to the α -quartz sensor substrate cut orientation. The maximum deformation in z -direction occurs at diagonally opposite corners of the sensor, as depicted in Figure 5. The bare sensor chips demonstrate a deflection of $0.53 \pm 0.03 \mu\text{m}$, which indicates the existence of residually inner stress in the α -quartz sensor substrate. After the assembly of the sensors, their deformation due to the residual stress is $1.82 \pm 0.13 \mu\text{m}$ for polymer adhesive 1 fixed sensors (Figure 5), and $2.41 \pm 0.06 \mu\text{m}$ for polymer adhesive 2 mounted sensors (Figure 6). This deformation is consequently a superposition of the residual inner stress caused sensor deflection and the thermo mechanical stress induced deflection from the bond process. The difference between the bare sensor chip measurement and the assembled sensor deformation is $1.29 \pm 0.13 \mu\text{m}$ for polymer adhesive 1 and $1.88 \pm 0.07 \mu\text{m}$ for polymer adhesive 2 fixed sensors. As the process temperature T_P is equal (150°C) for both bond materials, the different chip deformations are obtained by the difference in the Young's modulus E , the glass transition temperature T_g , the CTE , and the bond layer thickness (polymer adhesive 1, $117 \pm 18 \mu\text{m}$, polymer adhesive 2, $62 \pm 6 \mu\text{m}$). The different chip deformations correspond to the measured sensor response, which verifies a higher chip deformation and a higher offset in the sensor

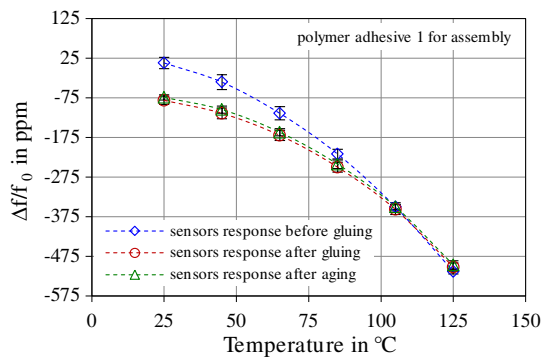


Figure 2: Temperature response of SAW strain sensors, bare and assembled sensor chips with polymer adhesive 1.

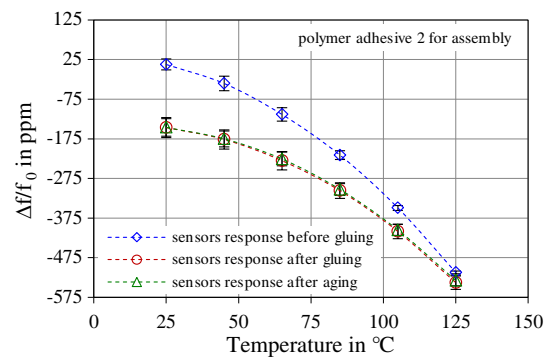


Figure 3: Temperature response of SAW strain sensors, bare and assembled sensor chips with polymer adhesive 2.

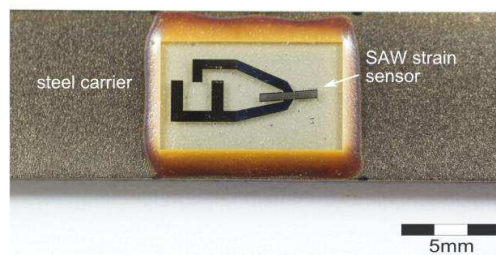


Figure 4: Assembled SAW strain sensor after aging time span of 100 h at 150°C , fixed with polymer adhesive 1.

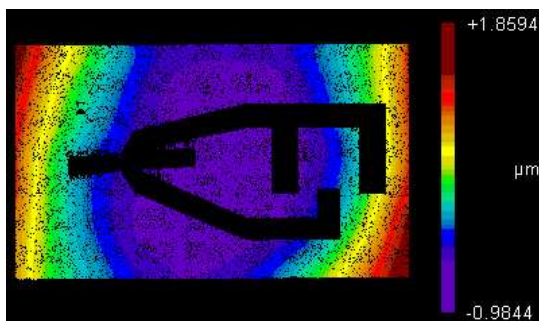


Figure 5: Measured SAW strain sensor deformation perpendicular to the sensor surface after the bonding onto a steel carrier with polymer adhesive 1.

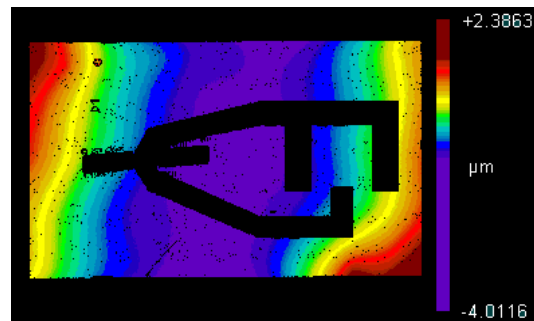


Figure 6: Measured SAW strain sensor deformation perpendicular to the sensor surface after the bonding onto a steel carrier with polymer adhesive 2.

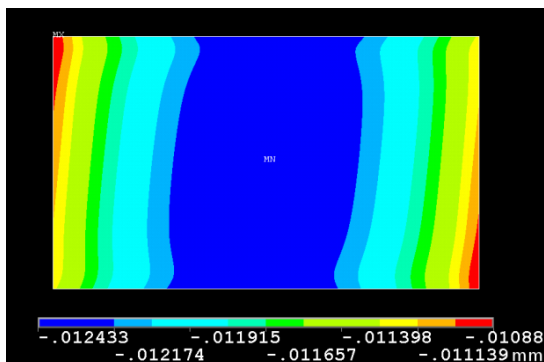


Figure 7: Simulated SAW strain sensor chip deformation perpendicular to the sensor surface after the bonding onto a steel carrier with polymer adhesive 1.

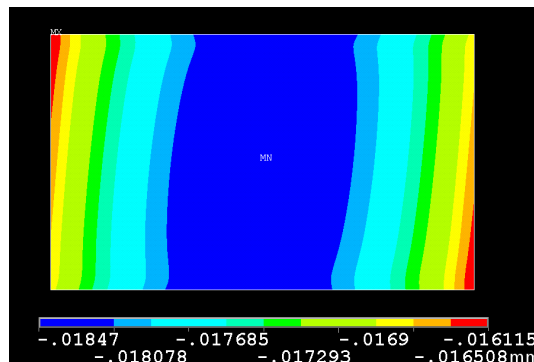


Figure 8: Simulated SAW strain sensor chip deformation perpendicular to the sensor surface after the bonding onto a steel carrier with polymer adhesive 2.

signal at room temperature. After the aging time span of 100 h at 150°C, for both bond materials no change in sensor chip deformation was observed.

4. SIMULATION OF SENSOR DEFORMATION

For the thermo mechanical simulation a 3D FEM model has been implemented using *ANSYS*. The residual stress in the SAW sensor chip and its deformation was computed by cooling down from the process temperature T_P to room temperature. The measured mean bond layer thickness of polymer adhesive 1 and 2 was used for the modeling. Sensor chip and steel carrier thickness of 350 μm and 1.2 mm were defined, respectively. The anisotropy of the α -quartz sensor substrate has been modeled as described by Zukowski [16].

Figures 7 and 8 show the simulated sensor chip deformation due to the residual stress induced by the bond process with polymer adhesive 1 and 2, respectively. The simulated sensor chip deformation in z -direction (perpendicular to the sensor surface) for polymer adhesive 1 and 2 fixed sensors is 1.55 μm and 2.35 μm , respectively. Simulation and measurements are deviating 20% for polymer adhesive 1 and 25% for polymer adhesive 2. This deviation between the simulation results and the measured sensor chip deformation originates mainly from not well known bond material properties. Therefore, extensive investigations in material properties are required. With more precise modeling of the material parameters, the simulation can converge to measurement results.

5. CONCLUSIONS

The experimental and simulation results obtained within this work contribute to a better understanding of SAW strain sensor assembly and the effects of residual stress on the sensor performance. The sensor offset and its performance depend on the *CTE*, the Young's modulus E , the glass transition temperature T_g , the process temperature T_P , and the bond layer thickness of the used bond materials and the carrier material properties, respectively. Depending on the cut orientation of the α -quartz sensor substrate, the sensor has a maximum offset at room temperature. In case of sensor operation within the range of the glass transition temperature, the influencing residual stress decreases and the sensor response converges to the constraint free sensor response. It has been demonstrated, with a well-controlled bond process and skillful selection of bond materials, the sensor performance is reliable, reproducible, and predictable. These characteristics are mandatory for a successful establishment of SAW strain sensors in industrial applications.

ACKNOWLEDGMENT

The authors would like to thank the Federal Ministry of Education and Research BMBF for funding (FKZ 16SV5192) and express their gratitude for the fruitful cooperation with the project partners SANDNER Messtechnik GmbH and SENSEOR GmbH.

REFERENCES

1. Dixon, B., V. Kalinin, J. Beckley, and R. Lohr, "A second generation in-car tire pressure monitoring system based on wireless passive SAW sensors," *IEEE International Frequency Control Symposium and Exposition*, 374–380, Miami, FL, Jun. 2006.

2. Hribšek, M. F., D. V. Tošić, and M. R. Radosavljević, “Surface acoustic wave sensors in mechanical engineering,” *FME Transaction*, Vol. 38, No. 1, 11–18, 2010.
3. Kalinin, V., R. Lohr, A. Leigh, and G. Bown, “Application of passive SAW Resonant sensors to contactless measurement of the output engine torque in passenger cars,” *IEEE International Frequency Control Symposium, Joint with the 21st European Frequency and Time Forum*, 499–504, Geneva, Switzerland, Jun. 2007.
4. Pohl, A. and F. Seifert, “Wirelessly interrogable SAW-sensors for vehicular applications,” *IEEE Instrumentation and Measurement Technology Conference*, Vol. 2, 1465–1468, Brussels, Belgium, Jun. 1996.
5. Hermelin, D., W. Daniaux, S. Ballandras, and B. Belgacem, “Fabrication of surface acoustic wave wireless pressure sensor,” *IEEE International Frequency Control Symposium, 2009 Joint with the 22nd European Frequency and Time Forum*, 96–99, Besancon, France, Apr. 2009.
6. Stoney, R., B. Donohoe, D. Geraghty, and G. E. O’Donnell, “The development of surface acoustic wave sensors (SAWs) for process monitoring,” *Procedia CIRP*, Vol. 1, 569–574, 2012.
7. Wilde, J., T. Fellner, E. Zukowski, and M. Berndt, “Assembling mechanical sensors into engineering structures,” *Smart Systems Integration, International Conference and Exhibition*, Zurich, Switzerland, Mar. 2012.
8. Grossman, R., J. Michel, T. Sachs, and E. Schrüfer, “Measurement of mechanical quantities using quartz sensors,” *European Frequency and Time Forum, 1996. EFTF 96, Tenth (IEE Conf. Publ. 418)*, 376–381, Brighton, UK, Mar. 1996.
9. Donohoe, B., D. Geraghty, G. E. O’Donnell, and R. Stoney, “Packaging considerations for a surface acoustic wave strain sensor,” *IEEE Sensors Journal*, Vol. 12, No. 5, 922–925, 2012.
10. Stoney, R., B. Donohoe, G. E. O’Donnell, and D. Geraghty, “Initial results on the characterization and application of packaged surface acoustic wave strain sensors,” *Proceedings of IMC 28, DCU*, Dublin, Ireland, Sep. 2011.
11. Donohoe, B., D. Geraghty, and G. E. O’Donnell, “Wireless calibration of a surface acoustic wave resonator as a strain sensor,” *IEEE Sensors Journal*, Vol. 11, No. 4, 1026–1032, 2011.
12. Hempel, J., E. Zukowski, M. Berndt, J. Wilde, and L. M. Reindl, “Assembly of α -quartz for surface acoustic wave (SAW) strain gauges application,” *4th Electronic Systems Integration Technologies Conference, IEEE/CPMT*, Amsterdam, Netherlands, Sep. 2012.
13. http://www.sensor.com/images/stories/download/Brochures/SENSeOR_SSEE015.pdf, Dec. 27, 2012.
14. Sosman, R. B., “Properties of Silica,” *American Chemical Society Monograph Series*, Chemical Catalog Co. Inc., New York, 1927.
15. <http://www.home.agilent.com/en/pd-1000004587%3Aeps%3Apro/ena-rf-network-analyzer>, Dec. 27, 2012.
16. Zukowski, E., T. Fellner, J. Wilde, and M. Berndt, “Parameter optimization of torque wireless sensors based on surface acoustic waves (SAW),” *13th International Conference on Thermal, Mechanical and Multi-physics Simulation and Experiments in Microelectronics and Microsystems (EuroSimE)*, 219–225, Lisbon, Portugal, Apr. 2012.

Design of Second-order Inductive-coupled Resonator-based Bandpass Filter with Controllable Multiple Transmission Zeros

H.-H. Huang and T.-S. Horng

Department of Electrical Engineering, National Sun Yat-Sen University, Kaohsiung 804, Taiwan

Abstract— This study proposes synthetic design for a compact LTCC bandpass filter with high rejection over a wide stopband for use in 2.4–2.5 GHz WLAN application. The presented design derives formulas for synthesizing a filter to meet the specification requirement in the passband insertion and return losses as well as the stopband attenuation. The presented bandpass filter has feedback paths for a coupling capacitor and a grounding inductor to provide controllable multiple transmission zeros at 5.0 GHz and 3.3 GHz stopband, resulting in high stopband rejection in 4.8 to 5.0 GHz range and 3.2 to 4.8 GHz range, which suppresses the second harmonic band and Ultra-wideband (UWB) signals. Experiment results are very agreement with the full-wave simulation results.

1. INTRODUCTION

The most favored bandpass filters, which are microwave devices that are used in wireless communication systems, have a miniature architecture, low insertion loss, sharp transition edge and excellent stopband rejection. Therefore, much of the relevant literature is concerned with designs in which sharp-transition edge and large stopband high rejection. Most of the conventional microstrip filters developed to date are based mainly on transmission-line structures [1]. These filters require too much area because each resonator needs quarter- or half-wavelength to get resonance. Although some studies have proposed stepped impedance resonators [2, 3] to reduce filter size, the proposed designs are still not size-competitive with LTCC filters. For device miniaturization, many filters are designed on an LTCC substrate. For a second-order lumped-element bandpass filter topology, a grounding capacitor can be used to generate transmission zeros in the stopband [4] to enhance the rejection, or a capacitive input/output configuration [5] can be used so that the attenuation pole is sufficiently close to the passband to realize a sharp-transition edge. Normally, these filters [4, 5] are not sufficiently rejection-competitive over a wide stopband because they only have two transmission zeros. Although, the third-order designs in [6] can achieve high rejection effectively. Normally, the area of a bandpass filters design of greater than second-order is large.

The synthesis method proposed in this study can be used to design a LTCC bandpass filter that is both miniaturized and has superior stopband rejection in WLAN application. Fig. 1 shows that, by controlling the grounding inductor and coupling capacitor, the filter creates multiple transmission zeros at the desired frequency and generates a rejection band sufficient for suppressing 4.8–5.0 GHz second harmonic band, 0.82–0.96 GHz GSM band and 3.2–4.8 GHz UWB signals.

2. BANDPASS FILTER ANALYSIS

Figure 1 shows a bandpass filter with a coupling capacitor (C_c) installed between the Input/Output terminals of the second-order filter and a grounding inductor (L_g) installed between the second-order filter and the ground plane. The proposed filter can be regarded as three two-port networks connected in parallel-serial with first, second and third parts. The first network can be regarded as a second-order filter with infinite a transmission zero, as shown in Fig. 2(a). The second network is a simple grounding inductor (L_g) (Fig. 2(b)). The third network is a simple coupling capacitor (C_c) (Fig. 2(c)).

The impedance matrix (Z^L) for the lower network of the proposed filter can formulate as the sum of the first (Z^a) and second network (Z^b) as follows:

$$Z^L = Z^a + Z^b = \begin{bmatrix} Z_{11}^a & Z_{12}^a \\ Z_{21}^a & Z_{22}^a \end{bmatrix} + \begin{bmatrix} sL_g & sL_g \\ sL_g & sL_g \end{bmatrix} \quad (1)$$

Since these matrices assume a lossless filter, the admittance matrix (Y) of the proposed filter that can be constructed by summing the third (Y^c) and lower network (Y^L) as follows:

$$Y = Y^c + Y^L = \begin{bmatrix} sC_c & -sC_c \\ -sC_c & sC_c \end{bmatrix} + \begin{bmatrix} Z_{11}^L & Z_{12}^L \\ Z_{21}^L & Z_{22}^L \end{bmatrix}^{-1} \quad (2)$$

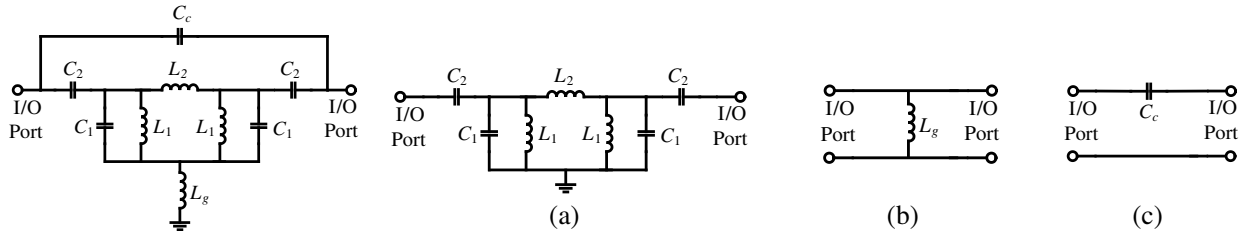


Figure 1: Scheme of proposed bandpass filter with a grounding inductor and a coupling capacitor.

Figure 2: (a) The first network without the feedback coupling capacitor and the grounding inductor. (b) The second network of a grounding inductor. (c) The third network of a coupling capacitor.

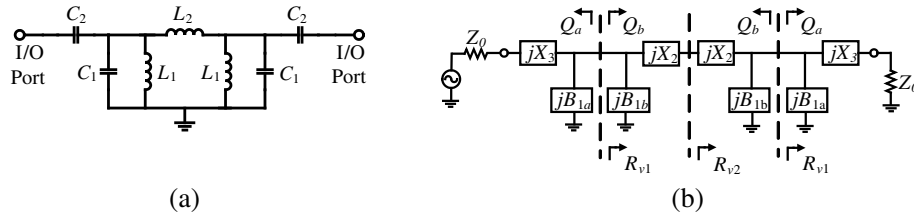


Figure 3: The proposed second-order bandpass filter with inductive-coupled resonator. (a) Schematic. (b) Its equivalence to a cascade of four L -shape matching networks.

Therefore, the Y_{21} can be expressed as

$$Y_{21} = sC_c + \frac{s^3 C_2^2}{[L_2 + L_1(2 + s^2 C_1 L_2 + s^2 C_2 L_2)]} \times \left[\frac{L_2 L_g + 2L_1 L_g(1 + s^2 C_1 L_2) + L_1^2(1 + 2s^2 C_1 L_g + s^4 C_1^2 L_2 L_g)}{1 + s^2 C_2(L_1 + 2L_g) + s^2 C_1 L_1(1 + 2s^2 C_2 L_g)} \right] \quad (3)$$

The transmission zero is produced when $Y_{21}(s) = 0$. Where each side of the passband has one transmission zero, let $Y_{21}(s) = 0$ after separately substituting (3). Finally, based on these quantities (L_2, C_2, L_1, C_1), the values for the L_g and C_c can be obtained by combining $Y_{21}(s = j\omega_{t1}) = 0$ and $Y_{21}(s = j\omega_{t2}) = 0$.

3. SECOND-ORDER INDUCTIVE-COUPLED FILTER SYNTHESIS

Figure 3(a) shows the architecture of a second-order bandpass filter with two LC resonators linked in parallel by inductive coupling and a capacitor (C_2) in series between the inductor (L_2) and the front and back stage of the filter. The two resonators generate two poles that support the passband of the filter. Capacitor (C_2) functions not only as an inverter for matching resonators to the external impedance, but also as a dc-decoupling capacitor for blocking the dc signal from both the front and back stage of the filter. This filter can be equivalent to a cascade of four symmetric L -shaped matching networks as shown in Fig. 3(b) with two interstage matching resistances denoted by R_{v1} and R_{v2} . For $R_{v2} < R_{v1}$ and $Z_0 < R_{v1}$, the solutions of C_2 , L_2 , L_1 and C_1 at the reflection zero angular frequencies of ω_{r1} and ω_{r2} ($\omega_{r1} > \omega_{r2}$) must satisfy these equations below

$$C_2 = \frac{1}{\omega_{r1} Z_0 Q_{a1}} = \frac{1}{\omega_{r2} Z_0 Q_{a2}} \quad (4)$$

$$L_2 = \frac{2Z_0 Q_{b1}}{\omega_{r1}} \cdot \frac{(Q_{a1}^2 + 1)}{(Q_{b1}^2 + 1)} = \frac{2Z_0 Q_{b2}}{\omega_{r2}} \cdot \frac{(Q_{a2}^2 + 1)}{(Q_{b2}^2 + 1)} \quad (5)$$

$$L_1 = \frac{(Q_{a1}^2 + 1) Z_0}{\omega_{r1} (Q_{a1} - Q_{b1})} \left(1 - \frac{\omega_{r1}^2}{\omega_{r,LC}^2} \right) = \frac{(Q_{a2}^2 + 1) Z_0}{\omega_{r2} (Q_{a2} - Q_{b2})} \left(1 - \frac{\omega_{r2}^2}{\omega_{r,LC}^2} \right) \quad (6)$$

$$C_1 = \frac{1}{\omega_{r,LC}^2 L_1} \quad (7)$$

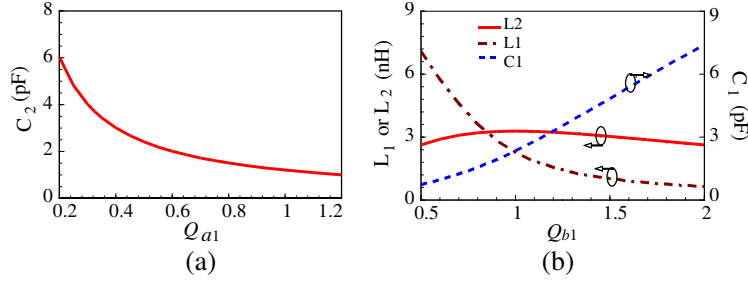


Figure 4: Second-order bandpass filter design. (a) C_2 for various design values of Q_{a1} . (b) L_2 , C_1 and L_1 for various design values of Q_{b1} when $Q_{a1} = 0.3$.

where $\omega_{r,LC}$ represents the resonant angular frequency of the L_1C_1 resonator. System impedance Z_0 is $50\ \Omega$. The $Q_{a1,2} = [(R_{v1}(\omega_{r1,2})/Z_0) - 1]^{1/2}$ and $Q_{b1,2} = [(R_{v1}(\omega_{r1,2})/R_{v2}(\omega_{r1,2})) - 1]^{1/2}$ represent the quality factors of the L -shaped matching network operating at $\omega_{r1,2}$ [7]. Equations (4)–(6) can then be used to obtain Q_{a2} , Q_{b2} and $\omega_{r,LC}$, respectively. It can be expressed as

$$Q_{a2} = \frac{\omega_{r1}Q_{a1}}{\omega_{r2}} \quad (8)$$

$$Q_{b2} = \frac{1}{2} \left[\frac{\omega_{r1} (Q_{a2}^2 + 1) (Q_{b1}^2 + 1)}{\omega_{r2} Q_{b1} (Q_{a1}^2 + 1)} \right] - \frac{1}{2} \sqrt{\left[\frac{\omega_{r1} (Q_{a2}^2 + 1) (Q_{b1}^2 + 1)}{\omega_{r2} Q_{b1} (Q_{a1}^2 + 1)} \right]^2 - 4} \quad (9)$$

$$\omega_{r,LC} = \sqrt{\omega_{r1}\omega_{r2}} \times \sqrt{\frac{\omega_{r1} (Q_{a1}^2 + 1) (Q_{a2} - Q_{b2}) - \omega_{r2} (Q_{a2}^2 + 1) (Q_{a1} - Q_{b1})}{\omega_{r2} (Q_{a1}^2 + 1) (Q_{a2} - Q_{b2}) - \omega_{r1} (Q_{a2}^2 + 1) (Q_{a1} - Q_{b1})}} \quad (10)$$

The synthesis steps for all elements are complete. After setting two reflection zeros (ω_{r1}, ω_{r2}) and their matching quality factors (Q_{a1}, Q_{b1}), the values for Q_{a2}, Q_{b2} and $\omega_{r,LC}$ can be determined by substituting (8)–(10), respectively. Finally, all elements of the second-order filter can be calculated by substituting the above parameters in (4)–(7).

The proposed second-order bandpass filter design has a center frequency of 245 GHz, a passband bandwidth of $BW = 100$ MHz a passband insertion loss of $IL \leq 1.5$ dB, and a passband return loss of $RL \geq 15$ dB. First, considering the possibility of center frequency shift due to the fabrication tolerance, we set a wide passband by choosing that $\omega_{r1} = 2\pi \times 229$ GHz and $\omega_{r2} = 2\pi \times 64$ GHz. Second, quality factors (Q_{a1}, Q_{b1}) are set for the L -shaped matching network. Figs. 4(a)–(b) show the relations between synthetic elements and quality factors (Q_{a1}, Q_{b1}). We hypothesized that the value of the capacitor is smaller than 5 pF and that the value of the inductor is smaller than 3.5 nH considering the area of the filter and the limits of the process. The experiments showed that the C_2 value decreases and the Q_{a1} value increases, which causes the extra transmission zero (ω_{t3}) to move toward the ω_{t2} . Therefore, a C_2 value larger than 3 pF was chosen to avoid a ω_{t3} that was too close to the ω_{t2} . Given the above considerations, the values selected for Q_{a1} and Q_{b1} were 0.3 and 1.5, respectively. The values calculated for Q_{a2}, Q_{b2} , and $\omega_{r,LC}$ by (8)–(10) were 0.346, 0.479 and 14.141 GHz, respectively. Finally, after substituting the above parameters in (4)–(7), the values obtained for C_2, L_2, L_1 and C_1 were 4.02 pF, 3.03 nH, 1.03 nH, 4.86 pF, respectively.

4. FILTER IMPLEMENTATION AND MEASURED RESULTS

A bandpass filter is designed with the center frequency of 2.45 GHz and a passband bandwidth of $BW = 100$ MHz for WLAN applications. The passband insertion loss is $IL \leq 1.5$ dB, and the passband return loss is $RL \geq 15$ dB. The required stopband attenuation levels are set to values greater than 30 dB at 4.8–5.0 GHz and 0.82–0.96 GHz to suppress the second harmonic band and GSM band. However, considering the possibility of transmission zeros being shifted by fabrication tolerance, the frequency was heightened by setting $\omega_{t1} = 2\pi \times 1.07$ GHz and $\omega_{t2} = 2\pi \times 5.05$ GHz. With these quantities (L_2, C_2, L_1, C_1), the values of L_g and C_c obtained by uniting $Y_{21}(s = j\omega_{t1}) = 0$ and $Y_{21}(s = j\omega_{t2}) = 0$ were $L_g = 0.06$ nH and $C_c = 0.43$ pF, respectively.

Figure 5(a) shows the LTCC bandpass filter implemented in a Heraus ceramic (dielectric constant, 7.8; loss tangent, 0.003) and silver metal. The bandpass filter surface-mounted onto an FR4

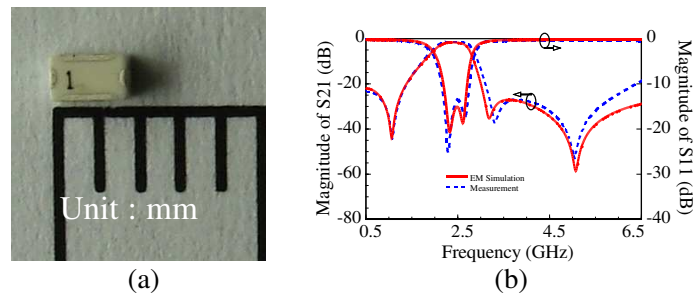


Figure 5: Implemented LTCC bandpass filter. (a) Photograph. (b) Comparison of EM-simulated and measured magnitudes of S_{21} and S_{11} .

printed-circuit board for measuring its S parameters. The designed bandpass filter has an area of $2.0 \text{ mm} \times 1.25 \text{ mm}$. Fig. 5(b) compares the simulated and measured magnitudes of S_{21} and S_{11} of the proposed bandpass filter design. The agreement is good over the frequency range from 0.1 to 6 GHz. The EM simulation is based on a full-wave analysis by Ansoft HFSS. The measured passband insertion loss approximates 1.47 dB, which approaches the predicted value of $IL \leq 1.5 \text{ dB}$, and the measured passband return loss is better than 13.3 dB. The measured stopband attenuation level at 1.07 GHz reaches 44 dB, and the resulting 26 dB stopband rejection in the 0.82 to 0.96 GHz range suppresses the GSM band. The measurement stopband level at 5.05 GHz reaches 53 dB, resulting in a 38 dB stopband rejection in the 4.8 to 5.0 GHz range, which suppresses the second harmonic band. The extra transmission zero at 3.3 GHz also reaches an attenuation level of 37 dB, and the resulting 26.5 dB stopband rejection in the 3.2 to 4.8 GHz range suppresses the UWB signals.

5. CONCLUSIONS

This work proposed synthesis method for a bandpass filter design with three transmission zeros over a large stopband operating in the 2.4–2.5 GHz WLAN band. Two transmission zero frequencies (ω_{t1} , ω_{t2}) are arbitrarily controlled. Another transmission zero frequency (ω_{t3}) is conditional controlled. This method quickly yields a design solution that minimizes the required area of filter and provides excellent rejection over a large stopband.

REFERENCES

1. Chu, Q. X. and H. Wang, "A compact open-loop filter with mixed electric and magnetic coupling," *IEEE Trans. Microwave Theory Tech.*, Vol. 56, No. 2, 431–439, Feb. 2008.
2. Djaiz, A. and T. A. Denidni, "A new compact microstrip two-layer bandpass filter using aperture-coupled SIR-hairpin resonators with transmission zeros," *IEEE Trans. Microwave Theory Tech.*, Vol. 54, No. 5, 1929–1936, May 2006.
3. Xiao, J.-K., S.-W. Ma, and S.-L. Zhang, "Novel compact split ring stepped-impedance resonator (SIR) bandpass filters with transmission zeros," *Progress In Electromagnetics Research*, Vol. 21, 329–339, 2007.
4. Chang, C. F. and S. J. Chung, "Bandpass filter of serial configuration with two transmission zeros using LTCC technology," *IEEE Trans. Microwave Theory Tech.*, Vol. 53, 2383–2388, Jul. 2005.
5. Dai, Y. S., H. S. Zhang, G. P. Qi, D. L. Lu, Z. L. Tao, G. X. Qian, and H. Wang, "LTCC bandpass filter for bluetooth application with dual transmission zeros," *IEEE MTT Int. International Conference on Microwave and Millimeter Wave Technology*, 284–286, 2008.
6. Tang, C. W., "Harmonic-suppression LTCC filter with the step-impedance quarter-wavelength open stub," *IEEE Trans. Microwave Theory Tech.*, Vol. 52, 617–624, Feb. 2004.
7. Bowick, C., *RF Circuit Design*, Newnes, Newton, MA, 1982.

Design of Dual-band Coupling Matrix-based Matching Network

Chieh-Sen Lee and Chin-Lung Yang

National Cheng Kung University, Taiwan

Abstract— This study developed a novel dual-band matching technique based on a coupling matrix transformer that matches complex load impedances at two frequencies simultaneously. Matching performance can be significantly improved by the dual-band filter-based matching network at operation dual-bands. Especially, excellent selectivity at the operation frequencies and rejection capability in undesired bands can be achieved. A general design principle is analyzed, and the results of numerical examples demonstrated that complex impedances can be successfully matched at two arbitrary frequencies simultaneously with excellent performance rates.

1. INTRODUCTION

In modern wireless systems or communication devices, dual-band matching networks are necessary to enable the full potential performance of these complex and compact systems. For example, GSM systems demand dual-standard transceivers that may contain dual-band microwave amplifiers requiring a well-designed dual-band matching network. Moreover, some dual-band systems can be applied for wireless power transmission to improve the efficiency [1].

To design a dual-band matching network, new matching techniques have considered the necessity for matching complex impedance at dual-bands [2–5]. The analytical method of a dual-frequency transformer was introduced for two arbitrary real impedances [2]. In 2009, a complex impedance transformer in dual frequencies connected was proposed by two or three unequal transmission line sections and extended to match two complex impedances [3]. However, the [3] methodology and the design equations require a higher order of numerical optimizations that find convergence for selected frequency ratios and complex input impedances [4]. In [5], a general technique for synthesis of matching networks is expanded to quad-band applications. However, these techniques encounter that dual-frequency transformers may accompany the harmonic of the matching operation bands.

This paper presents an alternative methodology, which is a systematic approach to the design of a dual-band matching network and overcome the previous out-of-band problem. This methodology can suppress unnecessary matching bands without the harmonic issues. The band-pass filter coupling matrix characteristics of poles and zeros allowed for the determination of impedance transformation [6]. To obtain band-pass performance, an equivalent lumped element network was previously introduced [6, 7]. However, the optimization requirement for finding roots or inability to achieve equal ripple caused problems when applying these equivalent lumped networks [8]. The coupling matrix technique has advantages for hardware implementation and optimization methods and generates analytical synthesis through proper cost functions. The frequency selectivity, impedance transformation, and response of the network can be compromised and predicted [9]; therefore, a coupling matrix-based matching network is proposed with numerical examples to aid understanding.

2. ANALYSIS OF INPUT IMPEDANCE AND DESIGN PRINCIPLES FOR COUPLING PROTOTYPE NETWORK

The methodology is to synthesize a matching network that presents two different complex impedances based on a coupling matrix-based 2-order filter with inverters. Such a network is shown in Fig. 1, and the coupling matrix is expressed as follows:

$$M = \begin{bmatrix} 0 & M_{S,1} & 0 & 0 \\ M_{S,1} & 0 & M_{1,2} & 0 \\ 0 & M_{1,2} & 0 & M_{2,L} \\ 0 & 0 & M_{2,L} & 0 \end{bmatrix} \quad (1)$$

Figure 1 shows an impedance transformer for a coupling circuit with a series resonator and impedance inverter of complex impedances (Z_L and Z_{in}). The matrix subscripts S and L correspond to source and load, respectively, which can be corresponding to the subscript indices 0 and 3, respectively, and subscripts 1 and 2 correspond to the first and second resonators, respectively.

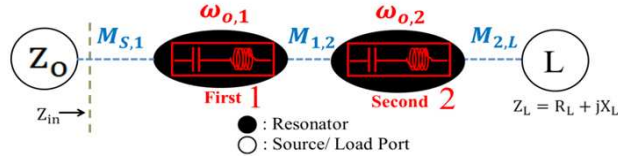


Figure 1: The coupling routing diagram of a conventional second-order filter model with resonators and coupling coefficients. Z_{in} is the input impedance from the front-end of the filter circuit; Z_L corresponds to the load impedance.

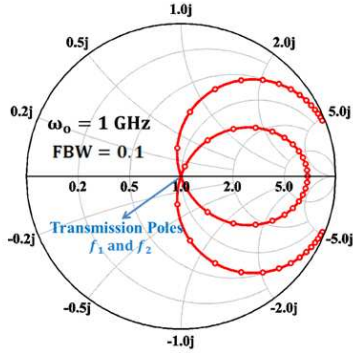


Figure 2: Trace of typical 2-Pole Chebyshev filter input impedance with $M_{S,1} = 1.2247$, $M_{1,2} = 4.753$, and $M_{2,L} = 1.2247$ in frequency from 0 to 2 GHz.

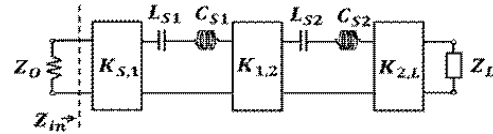


Figure 3: Generalized bandpass filters (including distributed elements) using impedance inverters.

Coupling matrix (M -matrix) methods [9] are applied to calculate the coupling matrix values for a typical second-order Butterworth or Chebyshev band-pass. A trace of the reflection coefficient at the input based on Chebyshev filters is shown on a Smith chart in Fig. 2. The trace passes through the center of the chart twice, indicating a potential match at two frequencies.

2.1. Impedance Transfer Function

The coupling matrix value can correspond to the synthesis of prototype filter circuits with inverters [7]. A conventional second-order filter with resonators and mutual coupling (Fig. 1) can be converted into an equivalent circuit model as shown in Fig. 2. In the case of an impedance inverter realization, the input impedance of the transformer is expressed by the fraction expansion:

$$Z_{in} = \frac{K_{0,1}^2}{R_1 + \frac{K_{1,2}^2}{R_2 + \frac{K_{2,3}^2}{Z_L}}} \quad (2)$$

The resonator composed of the lumped L_{si} and C_{si} series type resonance, where jR_1 and jR_2 are the impedance of the first and second series resonators. K represents the corresponding coupling matrix inverters of the series type. Therefore, K inverter value can be obtained as follows:

$$R_1 = \omega L_{s1} - 1/(\omega C_{s1}) \quad (3)$$

$$R_2 = \omega L_{s2} - 1/(\omega C_{s2}) \quad (4)$$

$$K_{S,1} = M_{1,S} \sqrt{\frac{Z_O \omega O L_{S1} FBW}{\Omega_c}} \quad (5)$$

$$K_{2,L} = M_{2,L} \sqrt{\frac{Z_O \omega O L_{S2} FBW}{\Omega_c}} \quad (6)$$

$$K_{1,2} = \frac{(FBW) M_{1,2} \omega O}{\Omega_c} \sqrt{L_{s1} L_{s2}} \quad (7)$$

$$C_{si} = 1/(\omega_{o,i})^2 L_{si} \quad (8)$$

where FBW is the fractional bandwidth. Equations (7) and (5) (6) represent the internal coupling ($M_{1,2}$) and the external coupling ($M_{1,s}$ and $M_{2,L}$) of the K impedance inverter, respectively. In

this paper, Ω represents a radian frequency variable of a band pass prototype filter with the cutoff frequency (Ω_c) at 1 (rad/s). Finally, ω_O is the original prototype network operation resonance frequency, and ω'_o is the modified one after impedance matching; The corresponding series capacitor C'_{si} can be calculated from (8).

2.2. Coupling Coefficients for Matching Load Impedance

For this impedance transfer network, the $M_{2,L}$ and $\omega'_{o,2}$ parameters can be determined by the matching impedance. To match the source impedance Z_O , we let $Z_{in}=50\Omega$ temporarily. The coupling coefficients related to impedance transfer on frequency response can be obtained after applying $Z_L(=R_L+jX_L)$ to rearrange (2) and separating real and imaginary portions. After algebraic substitutions (9)–(11), the simplified Equations (12) and (13) can be expressed as follows:

$$\Delta = Z_O R_1 \left(Z_O R_1 R_L + X_L (K_{01})^2 \right) - (K_{01})^2 (Z_O R_1 X_L - R_L (K_{01})^2) \quad (9)$$

$$\Delta m = Z_O X_L (K_{12})^2 \left(Z_O R_1 R_L + X_L (K_{01})^2 \right) - Z_O R_L (K_{12})^2 \left(Z_O R_1 X_L - R_L (K_{01})^2 \right) \quad (10)$$

$$\Delta n = R_1 R_L Z_O^2 (K_{12})^2 - (K_{01})^2 Z_O R_L (K_{12})^2 \quad (11)$$

$$M_{2,L} = \frac{\Delta m}{\Delta} \left(\sqrt{\Omega_c} / \sqrt{(Z_O \omega_O L_2 (FBW))} \right) \quad (12)$$

$$\omega'_{o,2} = \sqrt{\left(\left(\omega_O L_2 - \frac{\Delta n}{\Delta} \right) \omega_O \right) L_2} \quad (13)$$

where $\omega'_{o,2} = 2\pi f'_{o,2}$ is the resonance frequency of the second resonator, which should be modified to differ from the original ω_o . In this paper, the L_{si} is fixed, and C_{si} is variable to present the modified $\omega'_{o,2}$. Equation (8) shows the relationship between L_{si} and C_{si} at the operation frequency. Therefore, the L_2 value in (12) and (13) can be decided from the L value original LC resonance in the filter at ω_O . The complex impedance Z_L can be the arbitrary to match system characteristic impedance Z_o with proper coupling coefficients. From the original band-pass filter design case, we designed the required coupling coefficients for desired transmission response to obtain the transmission pole frequency at original f_1 and f_2 locations. Our proposed concept of a dual matching network for complex impedance used two parameters $M_{2,L}$ and $\omega'_{o,2}$ to design matched complex impedance at original f_1 and f_2 . Subsequently, the matching band can be modified by appropriate internal coupling $M_{1,2}$.

2.3. Matching Dual-band Frequency

For desired matching frequency, (2) describes the input impedance depending on frequency response. Because of the band-pass characteristic, as shown in Fig. 2, equal input impedance occurs in dual-frequency. The matching impedance is determined after the coupling coefficients $M_{2,L}$ and $\omega'_{o,2}$ have been chosen in (12), (13), and the frequencies f_1 and f_2 can be modified as f'_1 and f'_2 when $M_{1,2}$ is modified as $M'_{1,2}$. The first step is to determine the prototype of the band-pass circuit at operation center frequency $\omega_0 = 2\pi\sqrt{f'_1 f'_2}$. The $M_{2,L}$ and $\omega'_{o,2}$ can be obtained. Therefore, the task to finish the design is to solve for the values of $M'_{1,2}$. From (2), we can obtain the following:

$$M'_{1,2} = \sqrt{\frac{(Z_O R_1 K_{23}^2 + (Z_O R_1 X_L - R_L K_{01}^2) R_2)(\Omega_c)}{Z_O X_L L_1 L_2 (\omega_o FBW)^2}} \quad (14)$$

If one of the matching dual frequencies f'_1 is known, $M_{1,2}$ can be obtained by applying the coupling condition to (14). The other matching frequency f'_2 is symmetric for f'_1 with the center frequency at ω_0 .

3. DESIGN PROCEDURE

A number of numerical examples are presented in this section to verify design methods. The main design procedures are shown in Fig. 4 with the detailed numerical explanations as follows. First, for matching complex impedance, coupling matrix methods [9] demonstrate that the coupling coefficients for a typical two-pole Chebyshev response filter are $M_{S,1} = 1.2247$, $M_{1,2} = 1.6583$, $M_{2,L} = 1.2247$, FBW is 0.1. We start designing based on these conditions. In these cases, we

first designed $M_{1,2} = 4.753$, and fixed this $M_{1,2}$. The chosen load impedances, including four different cases and the calculated results, are listed in Table 1. From the prototype filter response, the operation central frequency was $\omega_0 = 1$ GHz, and we obtained the transmission poles with $M_{1,2} = 4.753$ at 0.815 GHz and 1.25 GHz. *FBW* for filter design is the ratio of operation frequency bandwidth with central frequency. For this matching design theorem, the *FBW* determines the initial matching frequency location from original filter; the locations poles of frequency response can be determined the required bandwidth. Based on the *FBW*, the coupling coefficients for matching can be designed.

Following (12) and (13), Fig. 5 shows the simulation result using the ADS (Advanced Design System). The desired matching load impedance of the four cases can be matched to Z_O in a narrow band at the dual frequencies. Another methodology using dual-frequency transformer based on two unequal microstrip line [3] is also calculated (matching to 200 Ω) to compare the matching performance. As shown in Fig. 4, the proposed method has a high selectivity and a superior reflection response, especially on the undesired harmonic operation frequencies such as 2 GHz and 3 GHz. Furthermore, at the middle band between 0.815 GHz and 1.25 GHz, our proposed method provides more than 5 dB improvement of in S_{11} at 1 GHz than the design performance of two microstrip line dual-frequency transformer in [3]. The required coupling coefficients and resonance frequencies are listed in Table 1.

Second, the arbitrary dual-band frequencies were also determined through our proposed model, and the result is shown in Fig. 6. The proposed dual-frequency impedance matching transformer between complex impedances $400-j200 \Omega$ and system impedance Z_O can be designed at several arbitrary frequencies. One of the matching characteristic frequency is fixed at f'_1 1.8 GHz, and f'_2 can be tuned at different frequencies, such as 2.4 GHz, 3.5 GHz, 4 GHz, and 5.2 GHz. The results are summarized in Table 2. The tunable dual-band frequencies f'_1 and f'_2 ($\omega_0 = 2\pi\sqrt{f'_1 f'_2}$) will

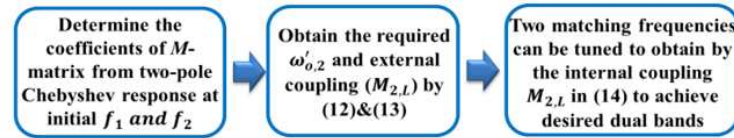


Figure 4: Design flow of the proposed filter-based dual-band matching network.

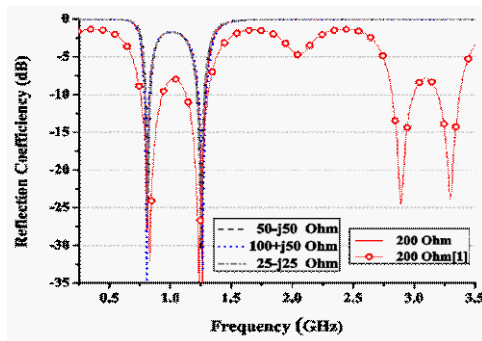


Figure 5: Comparison of dual-band complex impedance matching performance and unmatched band (out-band) rejection capability.

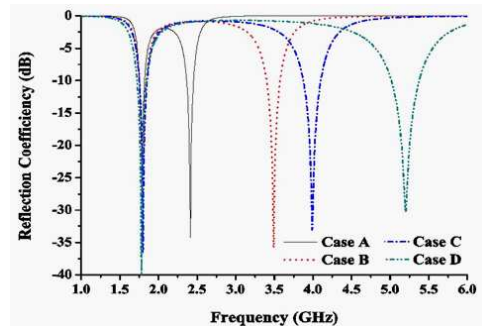


Figure 6: Dual-band complex impedance with different matching frequencies.

Table 1: Parameters of the dual-frequency impedance matching ($M_{S,1} = 1.2247$, $M_{1,2} = 4.753$, $f_o = 1$ GHz).

$R_L(\Omega)$	$X_L(\Omega)$	$M_{2,L}$	$f'_{o,2}$ (GHz)
200	0	2.4396	1.0065
50	-50	1.725	1.081
100	50	1.9286	0.9672
25	-25	1.2198	1.081

Table 2: Parameters of the dual-frequency impedance matching ($Z_L = 400-j200\ \Omega$, $M_{S,1} = 1.2247$, $M_{2,L} = 3.874$, $f_1 = 1.8\ \text{GHz}$).

Type	f'_1 (GHz)	f'_2 (GHz)	f_o (GHz)	$M'_{1,2}$
Case A	1.8	2.4	2.0785	4.537
Case B	1.8	3.5	2.5100	6.737
Case C	1.8	4	2.6825	7.068
Case D	1.8	5.2	3.0594	8.953

vary because the ω_0 center frequency is reconfigurable. As shown in the table, the larger frequency separation between f'_1 and f'_2 , the larger coupling $M'_{1,2}$ should be, which also agrees with the filter theories. The central operation ω_0 frequency is decided at the first step in band-pass filter synthesizing. $M_{2,L}$, $\omega'_{o,2}$, and $M'_{1,2}$ are designed from (12) to (14); however, $\omega_{0,1} = \omega_0$ is kept the same in each case.

4. CONCLUSIONS

The analytic nonlinear characteristics for dual-frequency matching between complex impedances and system Z_O impedance based-on band-pass filter were obtained by a thorough derivation. By combining coupling matrix filter characteristics to fulfill this network, matching performance can be improved at operation dual-bands, and excellent undesired band rejection capability can be achieved. The designed schemes are easy to implement. By extending the proposed concepts, the multi-band matching networks based on filter design can be realized and verified.

REFERENCES

1. Yang, C.-L., C.-L. Tsai, Y.-L. Yang, and C.-S. Lee, "Enhancement of wireless power transmission by using novel multitone approaches for wireless recharging," *IEEE Antennas Wireless Propag. Lett.*, Vol. 10, 1353–1357, 2011.
2. Monzon, C., "A small dual-frequency transformer in two sections," *IEEE Trans. Microw. Theory Tech.*, Vol. 51, No. 4, 1157–1161, Apr. 2003.
3. Wu, Y., Y. Liu, and S. Li, "A dual-frequency transformer for complex impedances with two unequal sections," *IEEE Microw. Wireless Compon. Lett.*, Vol. 19, 77–79, 2009.
4. Rawat, K. and F. M. Ghannouchi, "Dual-band matching technique based on dual-characteristic impedance transformers for dual-band power amplifiers design," *IET Microw, Antennas & Propag.*, Vol. 5, 1720–1729, 2011.
5. Nallam, N. and S. Chatterjee, "Design of concurrent multi-band matching networks," *2011 IEEE International Symposium on Circuits and Systems (ISCAS)*, 201–204, Rio de Janeiro, Brazil, 2011.
6. Naglich, E. J., J. Lee, D. Peroulis, and W. J. Chappell, "A tunable bandpass-to-bandstop reconfigurable filter with independent bandwidths and tunable response shape," *IEEE Trans. Microw. Theory Tech.*, Vol. 58, 3770–3779, 2010.
7. Bell, H. C., "The coupling matrix in low-pass prototype filters," *IEEE Microwave Magazine*, Vol. 8, 70–76, 2007.
8. Kuo, Y.-T., J.-C. Lu, C.-K. Liao, and C.-Y. Chang, "New multiband coupling matrix synthesis technique and its microstrip implementation," *IEEE Trans. Microw. Theory Tech.*, Vol. 58, 1840–1850, 2010.
9. Lee, J. and K. Sarabandi, "Synthesizing microwave resonator filters," *IEEE Microwave Magazine*, Vol. 10, 57–65, 2009.

Design and Characterization of Cryogenic Wideband LNA Using WIN 0.15 μm GaAs pHEMT Process

Ying Chen¹, Bin Li¹, Kun-Long Wu², and Robert Hu²

¹SHAO, Chinese Academy of Sciences, China

²College of Electrical and Computer Engineering, NCTU, Taiwan

Abstract— This manuscript describes our progress in the development of cryogenic wideband LNA for radio-astronomical applications. With technology maturity and fabrication cost taken into account, the WIN 0.15 μm GaAs pHEMT process is used for the 5–10 GHz and 8–20 GHz LNA design. Room-temperature S -parameters and noise temperature are measured first with gain larger than 20 dB, input and output reflection coefficients below -10 dB within the intended bandwidth. As for the cryogenic noise measurement, the 6 dB cold-attenuator method is used to obtain the corresponding T_n at different ambient temperatures. A noise improvement factor of 3 is observed for cryogenic LNA designed with this 0.15 μm GaAs process.

1. INTRODUCTION

Cryogenic wideband LNA is among the most critical components used in the microwave and millimeter-wave radio-astronomical receivers. The LNA designed using TRW (now NGST) and HRL 0.1 μm InP processes have both shown superb cryogenic noise performance [1, 2]; however, these processes are difficult to obtain outside the US due to the export permit and security issues. The Asia-based semiconductor foundry WIN, on the other hand, is focusing on commercial markets with its 0.15 μm GaAs process which is available in most regions. Since very little is revealed about the cryogenic performance of this WIN 0.15 μm GaAs process, we are curious whether an improvement factor of around 10 in noise temperature T_n , as in the cases of TRW and HRL, will be observed when the amplifier is cooled down from room temperature to below 20 K? If the answer is yes, it is worth using this cryogenic GaAs LNA as second-stage, or even first-stage amplifier since its impact on the receiver system's noise may now be more tolerable. This paper intends to report our progress in developing the 5–10 GHz and 8–20 GHz LNA's using WIN 0.15 μm GaAs pHEMT process; their S -parameters and noise temperature will then be measured on-wafer at room temperature. Once packaged, the 5–10 GHz LNA will then be cooled down to allow cryogenic characterization.

2. THE 5–10 GHz AND 8–20 GHz LNA DESIGN AND THEIR CHARACTERIZATION

Figures 1 and 2 are the photographs of the 5–10 GHz and 8–20 GHz LNA's, where the common-source transistors are used to achieve low noise and good input and output matching [3]. Fig. 3 displays the S -parameters and noise temperature measured on-wafer at room temperature; small S_{11} and S_{22} , and large S_{21} , all are achieved for these two amplifiers and the measured noise temperature is reasonably good. Fig. 4 records the measured gain versus input power at 8 GHz, which can be used to derive the input-referred 1 dB compression point (P1 dB) at that specific frequency point; the 5–10 GHz and 8–20 GHz P1 dB of these two LNA's are obtained in similar way. The use of smaller transistors and more amplification stages in the LNA₀₈₂ causes its P1dB to be smaller than that of LNA₀₅₁₀.

Figure 5 shows the cryogenic noise measurement setup. Inside the cryostat, the long input and output coaxial cables act as thermal buffers, thus the temperature of both the attenuator and the

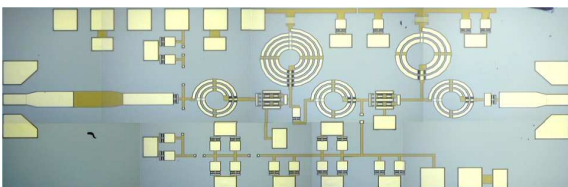


Figure 1: Photograph of the 5–10 GHz low-noise amplifier, i.e., LNA₀₅₁₀.

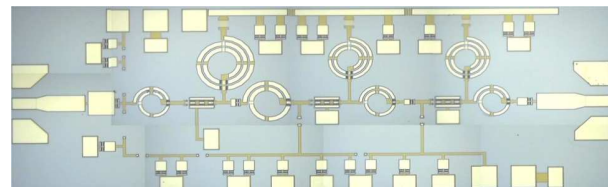


Figure 2: Photograph of the 8–20 GHz low-noise amplifier, i.e., LNA₀₈₂₀.

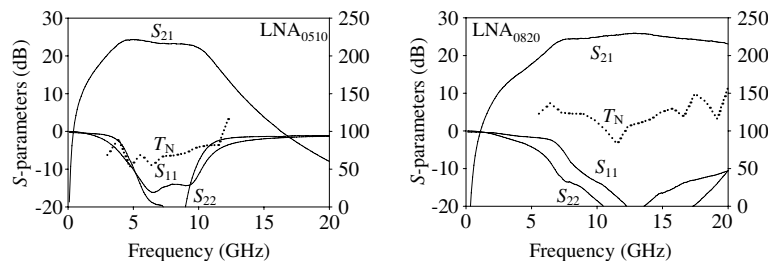


Figure 3: S -parameters and T_n (right Y -axis) of the 5–10 GHz and 8–20 GHz LNA's measured on-wafer at room temperature.

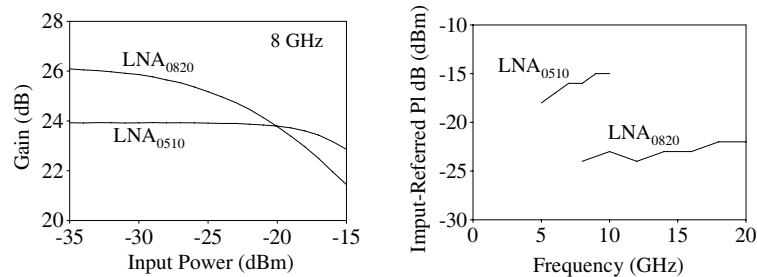


Figure 4: Gain versus input power as measured at 8 GHz of the LNA's, and their input-referred P1 dB curves.

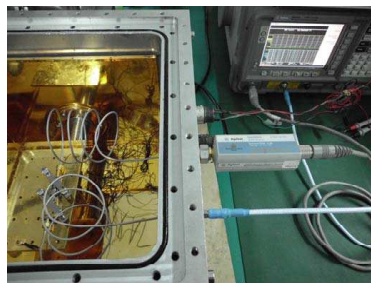


Figure 5: Noise measurement setup with input and output stainless-steel cables used as thermal buffers.

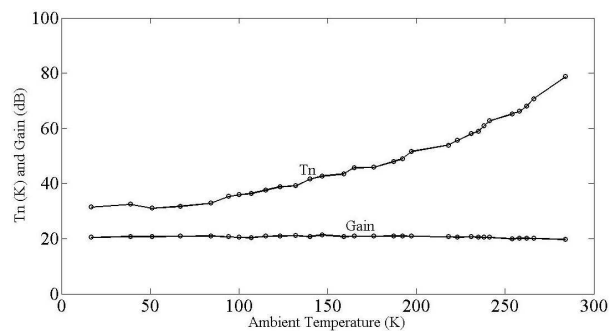


Figure 6: 5–10 GHz averaged T_n (in K) and gain (in dB) versus ambient temperature of LNA₀₅₁₀.

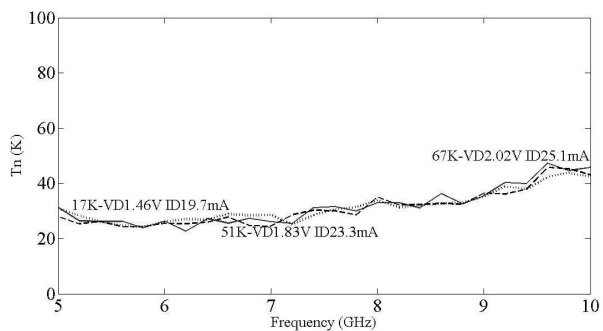


Figure 7: Measure T_n of the LNA₀₅₁₀ at 67 K (solid), 51 K (dashed) and 17 K (dotted).

LNA can be assumed to be that of the cold plate. With prior knowledge of the cable loss at different temperatures, proper noise de-embedding can thus be carried out during the T_n measurement [4]. For the noise measurement at very low temperature, a 20 dB cold attenuator has to be inserted in front of the LNA so that the equivalent hot/cold noise will be more comparable to T_n of the LNA. As ambient temperature rises, the noise contribution of this 20 dB attenuator will also increase and, at certain point, becomes very large as compared with the noise source itself which in turn makes accurate noise measurement to be difficult. To obtain T_n of the LNA over wide-range ambient

temperatures, the 6 dB cold attenuator is used as a compromise between 20 dB cold attenuator (preferable for low temperature) and no attenuation (suitable for high temperature) at all. Fig. 6 displays the 5–10 GHz averaged T_n and gain of the LNA₀₅₁₀ measured at different temperatures. Fig. 7 is the measured T_n versus frequency of this LNA₀₅₁₀ where the cold-plate temperature is gradually lowered from 67 K to 17 K. It becomes clear that little noise improvement can be obtained once the ambient temperature is below 80 K, and a noise improvement factor of 3 is the best that can be obtained for cryogenic LNA designed using WIN 0.15 μm GaAs pHEMT process.

3. CONCLUSIONS

In this paper, the 5–10 GHz and 8–20 GHz low-noise amplifiers have been designed using WIN 0.15 μm GaAs pHEMT process and characterized at different temperatures. Using 6 dB cold attenuator method, it is found that the LNA's noise performance can be improved by lowering the ambient temperature but once it is below 80 K, no discernible T_n improvement is observed. Exploring possible solutions for further lowering T_n will be our next research topics.

ACKNOWLEDGMENT

The authors Y. Chen and B. Li wish to thank Z.-Q. Shen, S.-K. Liang, and J.-J. Cao for discussions and encouragements; their research work is supported under contracts NSFC 11078003, Special Foundation of The Chinese Academy of Sciences 173018, and 863-Program 2012AA-121603. The authors K.-L. Wu and R. Hu would like to thank K.-T. Ly, H.-T. Tsai and the Chip Implementation Center for assistance on the measurement; their research work is supported in part under contract NSC 101-2221-E-009-170.

REFERENCES

1. Hu, R., "An 8–20-GHz wide-band LNA design and the analysis of its input matching mechanism," *IEEE Microwave Wireless Comps. Letts.*, Vol. 14, No. 11, 528–530, 2004.
2. Hu, R. and S. Weinreb, "A novel wide-band noise parameter measurement method and its cryogenic application," *IEEE Trans. Microwave Theory Tech.*, Vol. 52, No. 5, 1498–1507, 2004.
3. Liao, C.-H., C.-H. Hsieh, R. Hu, D.-C. Niu, and Y.-S. Shiao, "W-band 90 nm CMOS LNA design," *Asia Pacific Microwave Conference (APMC)*, Kaohsiung, Taiwan, Dec. 2012.
4. Hu, R., "Analysis of the input noise contribution in the noise temperature measurements," *IEEE Microwave Wireless Comps. Letts.*, Vol. 15, No. 3, 141–143, 2005.

Evaluation of Nonlinear Effect Impact on Optical Signal Transmission over Combined WDM System

V. Bobrovs, A. Udalcovs, R. Parts, and I. Trifonovs
Institute of Telecommunications, Riga Technical University, Latvia

Abstract— The authors have investigated the impact of nonlinear distortions to optical signal transmission over proposed configuration of combined wavelength division multiplexed (WDM) fiber-optic transmission system (FOTS). In chosen model of ultra-dense combined WDM system optical signals are transmitted with two different per channel bitrates (i.e., 10 and 40 Gbit/s) and three different optical signal modulation formats are used for the encoding of transmitted data body (i.e., non-return to zero encoded on-off keying or NRZ-OOK, orthogonal polarization shift keying or 2-POLSK and NRZ encoded differential phase shift keying or NRZ-DPSK) and in addition “non ITU-T” defined minimum and equal frequency intervals are used for the channels separation.

1. INTRODUCTION

The transmission throughput over the existing wavelength division multiplexed (WDM) fiber-optic transmission systems (FOTS) can be increased in the following manner: using higher per channel bitrates, narrower channel spacing or wider amplifier bandwidth [1–3]. So, the increase of “for WDM-suitable” band utilization (or increase of spectral efficiency) allows to reduce the number of channel required for the transmission of the same data body as compared with relatively spectrally inefficient WDM systems (i.e., $SE < 0.2$ bit/s/Hz) [4]. As well as allows postpone the shortage of “for WDM-suitable” band and avoid the deployment of new optical fibers [7]. That is why the method of increase of transmissions SE has some characteristics that are adequate for future needs and requirements of continuous traffic growth.

Obviously, it is necessary to evaluate the impact of all fiber nonlinearities to optical signal transmission over the purposed model of combined-WDM system designed for the future optical transport networks. Hence, two different nonlinear impacts are analyzed in this paper: optical signal self-phase modulation (SPM) and cross-phase modulation (XPM), while four waves mixing (FWM) and scattering process are planned for further research efforts.

This impact occurs from the increased power levels coupled to the optical fiber as well as due to variations of fiber’s dispersion coefficient [8, 9]. Note that data in investigated combined-WDM systems are encoding by manipulation with optical signal’s freedom degrees such as intensity, phase and state of polarization. In accordance with each freedom degree and respecting previous researches (e.g., [4, 10]) the most applicable modulation format has been chosen: non-return to zero encoded on-off keying (NRZ-OOK), NRZ encoded differential phase shift keying (NRZ-DPSK) and orthogonal binary polarization shift keying (2-POLSK). The similar combined or hybrid WDM systems currently are starting to appear as the result of upgrade of existing transport infrastructure [2, 5].

2. NUMERICAL ANALYSIS AND MATHEMATICAL MODEL

In this paper, the impact of nonlinear optical effects (NOE, SPM and XPM particularly) on optical signal transmission have been mainly analyzed for the 9-channel combined-WDM systems that complies with the following scheme of configuration: [1st ($f_c = 193.025$ THz), 4th and 7th channels: NRZ-OOK, $R = 10$ Gbit/s] — [2nd ($f_c = 193.100$ THz), 5th and 8th channels: 2-POLSK, $R = 40$ Gbit/s] — [3rd ($f_c = 193.175$ THz), 5th and 9th channels: $R = 40$ Gbit/s].

The detailed configuration and the main blocks of simulation model in RSoft Design Group, Inc. software OptSim 5.2 is shown on Fig. 1. The basic system’s configuration such as the modulation format distribution among the channel as well as the basic parameters of transmitting and receiving units such as optical filter type, bandwidth and order have been obtained in [10] but the minimum and equal channel spacing value acceptable for signal detection on the other fiber end with appropriate error probability below the maximum permissible threshold have been obtained in [4]. The investigated configuration represents the “worst case scenario” since have a higher average BER value for signals detected as compared with the rest of possible configurations [4, 10]. Optical signal booster and pre-amplifier have been placed after the multiplexer and before the demultiplexer, respectively, for achieving the expressions of the fiber nonlinearities. The part of

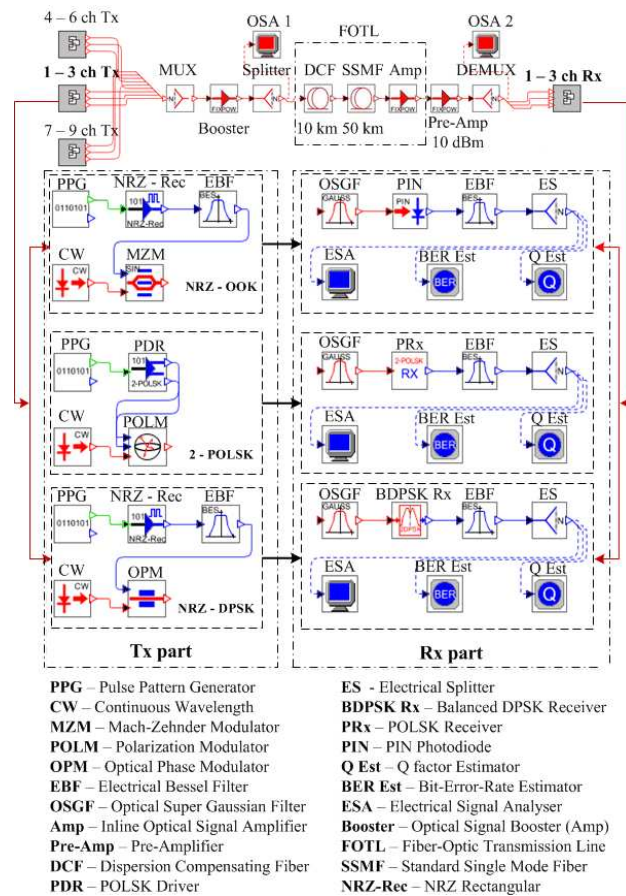


Figure 1: The configuration of simulation scheme in OptSim 5.2 used for the evaluation of self-phase modulation impact on optical signal transmission over the ultra-dense WDM system with combined data rates and signal formats; the blocks of transmitting and receiving units for NRZ-OOK, 2-POLSK and NRZ-DPSK signal formats.

fiber-optic transmission line consists of chromatic dispersion (CD) compensation module (DCM) based on DCF, standard single mode fiber (SSMF, ITU-T Recommendation G. 652) and inline fixed output power EDFA. The fixed output power level was changed exactly for the booster and inline amplifier, whereas it remained unchanged and equal to 10 dBm for pre-amplifier. During the simulations we have analyzed the NOE while others impacts such as amplified spontaneous emission (ASE) noise and other fibers nonlinearities (e.g., FWM, Brillouin scattering and Raman crosstalk) are being ignored. The 10 km of DCF (dispersion coefficient at 1550 nm is -80 ps/nm/km, its core effective area is $20 \cdot 10^{-12}$ m² and fiber non-linearity coefficient is 5.071/W/km) compensates CD that optical signal will accumulated during the transmission over 50 km of SSMF (dispersion coefficient at 1550 nm is 16 ps/nm/km, its core effective area is $80 \cdot 10^{-12}$ m² and fiber non-linearity coefficient is 1.271/W/km). In further researches the number of such FOTL can be increased for the evaluation of system performance after the transmission over several such sectors (using the principle of iteration loops already described in [10]).

3. RESULTS AND DISCUSSIONS

This research revealed the maximum output power level of EDFA at which the BER values for the single channel as well as multichannel FOTS are still fulfill the requirements addressed to the maximum permissible error probability for signal detection. As well as it is analyzed the influence of fiber's first order dispersion coefficient variations to optical signal distortions (and increment of detected signals BER value) rose due to SPM and XPM. Before the analyze such impact to signal transmission over the spectrally efficient multichannel WDM FOTS with combined data rates and signal formats, let is evaluate their impact on single channel FOTS performance.

WDM system detailed described in previous section, the NRZ-OOK modulated optical signals with 10 Gbit/s per channel bitrate are transmitted in the first system's channel. If such signals

are transmitted in single channel FOTS, the BER value of detected signals exceed the maximum permissible threshold of 10^{-12} if the booster and inline optical amplifier's fixed output power level is larger than 18 dBm. Note that the central wavelength value of each channel in single channel FOTS are as similar as in 3-channel combined-WDM FOTS and the configuration of FOTL units remains unchanged. The similar effect of BER value improvement in combined-WDM system in comparison with traditional systems with one modulation format has been described in [11]. FOTL structure was modified as compared with depicted in Fig. 1 in order to analyze the influence of SSMF first order dispersion coefficient variations to the changes of signals' BER values due to XPM. In addition, 10 Gbit/s NRZ-OOK, 40 Gbit/s 2-POLSK and 40 Gbit/s NRZ-DPSK modulated signals were transmitted not over one span of SMF but two in order to become more evident changes on detected signal spectrum.

Instead of dealing with one channel FOTS as it was for SPM, here we placed two channels. One of them is so-called pump channel but the second one is the probe channel containing informative signal. For 10 Gbit/s NRZ-OOK signal, channel spacing between pump and signal channel is 25 GHz, 100 GHz for 40 Gbit/s 2-POLSK and 200 GHz for 40 Gbit/s NRZ-DPSK (see Fig. 2). 10 Gbit/s NRZ-OOK signal spectrum sufficiently changes and its left part broadens if SMF dispersion coefficient is close to 0 ps/nm/km (see Fig. 2(a)). As for the 40 Gbit/s 2-POLSK and NRZ-DPSK signals, the spectrum distortions are almost no noticeable (see Figs. 2 (b)–(c)). 40 Gbit/s 2-POLSK channel power increases but by less than 0.1 dBm if dispersion coefficient is around 0 ps/nm/km as compared with the power levels at $D = 16$ ps/nm/km. Whereas, for 40 Gbit/s NRZ-DPSK channel, it is almost constant (see Fig. 3). Such power level variations of filtered channel lead to some evidence changes in detected informative signals Q -factor values (see Fig. 4). For 40 Gbit/s 2-POLSK channel, it decreases by 0.8 dB whereas, 40 Gbit/s NRZ-DPSK channels experiences some Q -factor increase, if a value of dispersion coefficient is close to 0 ps/nm/km. In contrast, power level of filtered informative 10 Gbit/s NRZ-OOK channel increases sufficiently (by more than 1 dB), if dispersion coefficient changes from 16 to 0 ps/nm/km. Q -factor value decreases as it is shown in Fig. 4. The gradual increase of the fixed output power levels of booster and inline optical amplifiers allows obtaining in system's channel detected signal BER correlation diagram for each channel. As can be seen in Fig. 5, the first channel's BER value is sufficiently below the 10^{-12} even if power levels of optical amplifiers are larger than 25 dBm. In this case, the 1st channel's BER = $5 \cdot 10^{-23}$ and the detected eye diagram evidences only about small amount of "1" amplitude jitter. The third channel's BER exceeds the maximum acceptable error probability of 10^{-16} only at 19 dBm. At 18 dBm the BER for this channel is equal to $1 \cdot 10^{-19}$ and the detected eye diagram evidences about some noticeable timing jitter that reduces the eye opening. As for the second system's channel where 2-POLSK modulated signals are transmitted with 40 Gbit/s per channel bitrate, then its BER values obtained for such power level range of booster and inline optical amplifier are exceeding the maximum permissible threshold of 10^{-16} . At 4 dBm its value is equal to $3 \cdot 10^{-7}$. As can be seen from the eye diagram obtained for this channel, it is very noisy with lot of an amount of amplitude jitter. The eye opening width is not enough for securing of signal detection with appropriate error probability below the maximum acceptable threshold. Variations of BER values of 40 Gbit/s 2-POLSK channel is non-essential depending on fiber's dispersion coefficient (see green

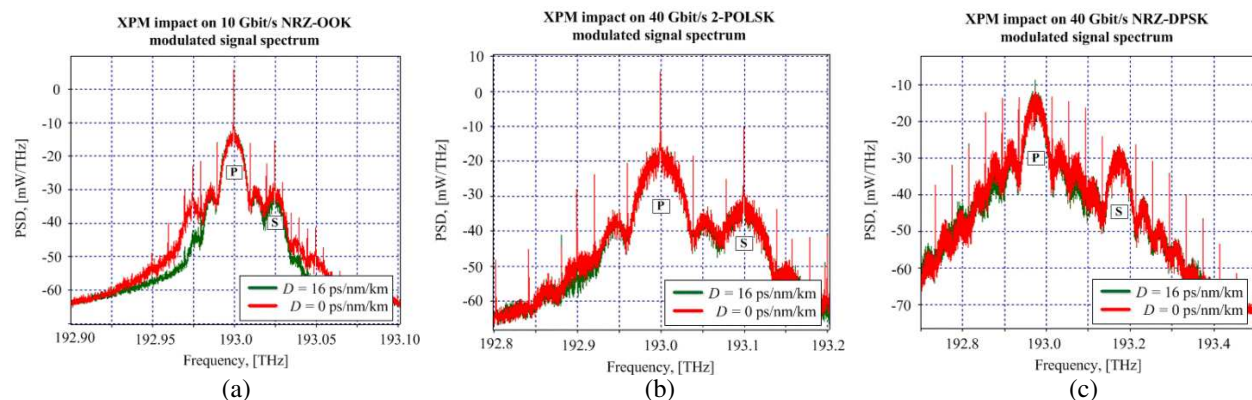


Figure 2: XSPM and XPM impact on modulated signal spectrum: (a) 10 Gbit/s NRZ-OOK; (b) 40 Gbit/s 2-POLSK; (c) 40 Gbit/s NRZ-DPSK, where P is the pump signal and S is probe or informative signal.

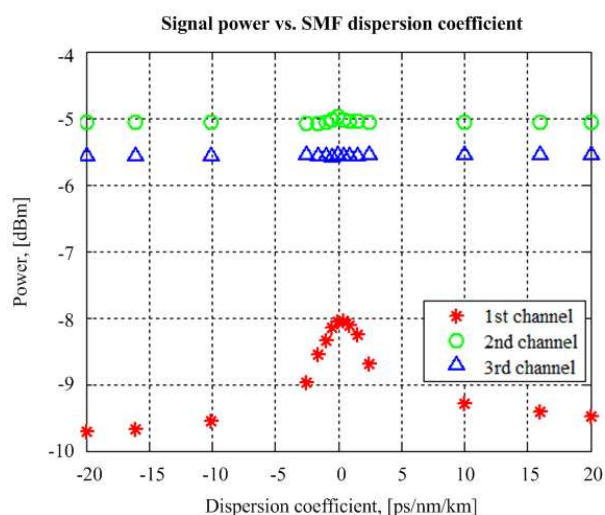


Figure 3: Filtered informative signal power in function of SMF dispersion coefficient.

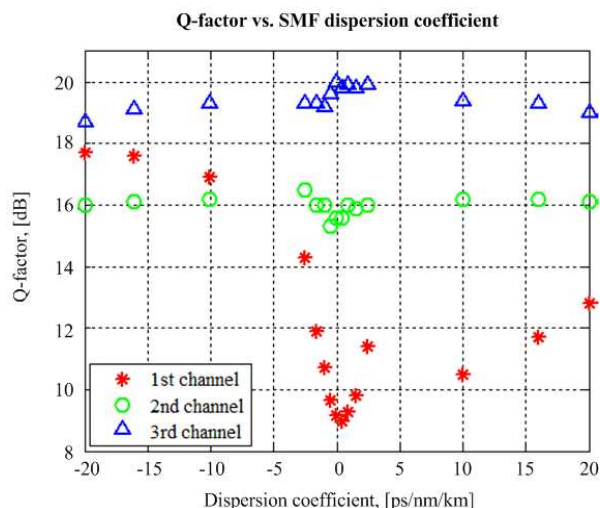


Figure 4: Detected informative signal Q -factor value in function of SMF dispersion coefficient.

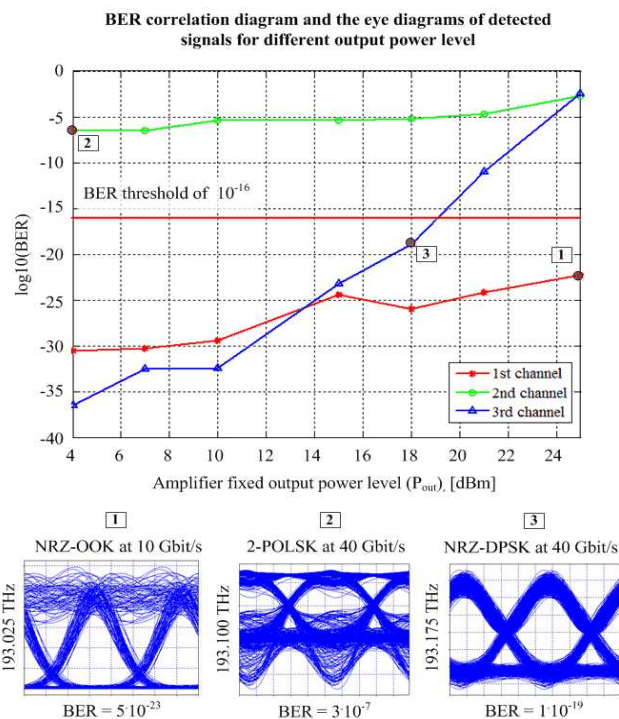


Figure 5: BER correlation diagram for the central systems channels (i.e., those with number 1–3) that represents BER as a function on the output power level of optical signal amplifiers (booster and inline amplifier) and the eye diagrams of each channel for the maximum tolerable amplifiers' output power levels.

curve in Fig. 5) and these values in all investigated range sufficiently exceed defined threshold. They vary around the value of 10^{-6} , so in such spectrally efficient combined-WDM system some FEC technique must be used.

4. CONCLUSIONS

As for the spectrally efficient combined-WDM system in which 75 GHz non ITU-T defined but equal frequency intervals are used for channel separation, then transmission in the first channel (10 Gbit/s NRZ-OOK) does not fail even at 25 dBm of amplifiers output power levels. In the third channel (40 Gbit/s NRZ-DPSK) it fails only at 18 dBm, whereas in the second channel (40 Gbit/s 2-POLSK) fails already at 4 dBm and in this channel detected signals cannot be performed with ap-

appropriate error probability below 10^{-16} . Similar “bad” performance of 40 Gbit/s 2-POLSK channel is observed after the evaluation of dispersion coefficient influence to the detected BER values. To sum up, comparing the performance of two 40 Gbit/s channels we have to conclude that 2-POLSK modulated signals are more susceptible to the impact of fiber nonlinearities (i.e., SPM particularly) in such ultra-dense combined transmission mode than NRZ-DPSK signals. As result, transmission fails in this 2-POLSK channel and some FEC technique must be used to secure signal detection with appropriately low BER.

ACKNOWLEDGMENT

The travel costs and participation fee to conference was supported by the European Regional Development Fund project “Development of international cooperation projects and capacity in science and technology Riga Technical University”, Nr. 2DP/2.1.1.2.0/10/APIA/VIAA/003.

REFERENCES

1. Cisco Systems, “Cisco visual networking index — Forecast and methodology 2010–2015,” *White Paper*, Jun. 1, 2011.
2. Wellbrock, G. and T. J. Xia, “The road to 100G deployment,” *IEEE Communication Magazine*, Vol. 48, No. 3, 14–18, 2010.
3. Dutta, A. K., N. K. Dutta, and M. Fujiwara, *WDM Technologies: Optical Networks*, Elsevier Inc., USA, 2004.
4. Udalcovs, A. and V. Bobrovs, “Investigation of spectrally efficient transmission for differently modulated optical signals in mixed data rates WDM systems,” *Proceedings of 2011 IEEE Swedish Communication Technologies Workshop, SWE-CTW 2011*, 7–12, Stockholm, Sweden, Oct. 2011.
5. Birks, M. and B. Mikkelsen, “40 Gbit/s upgrades on existing 10 Gbit/s transport infrastructure,” *Proc. of SPIE*, Vol. 6012, 60120D, 2005.
6. Bobrovs, V., A. Udalcovs, S. Spolitis, O. Ozolins, and G. Ivanovs, “Mixed chromatic dispersion compensation methods for combined HDWDM systems,” *Proceedings of 2011 International Conference on Broadband and Wireless Computing, Communication and Applications, BWCCA 2011*, 313–319, Barcelona, Spain, Oct. 2011.
7. Elluis, A. D. and F. C. G. Gunning, “Coherent WDM, towards > 1 bit/s/Hz information spectral density,” *Proc. of SPIE*, Vol. 5828, 482–490, 2005.
8. Bertaina, A. and S. Biga, “Impact of residual dispersion on SPM-related power margins in 10 Gbit/s-based systems using standard SMF,” *Proceedings of 24th European Conference on Optical Communications (ECOC)*, Vol. 1, 681–682, 1998.
9. Dewanjee, A., M. S. Islam, M. S. Monjur, and S. P. Majumder, “Impact of cross-phase and self-phase modulation on the performance of a multispan WDM system,” *Proceedings of IEEE 9th Malaysia International Conference on Communications (MICC)*, 285–289, 2009.
10. Bobrovs, V., A. Udalcovs, and I. Trifonovs, “Investigation of maximum distance reach for spectrally efficient combined WDM systems,” *Proceedings of 2nd Baltic Congress of Future Internet Communications (BCFIC)*, 52–55, Vilnius, Lithuania, Apr. 2012.
11. Udalcovs, A., V. Bobrovs, and G. Ivanovs, “Investigation of allowed channel spacing for differently modulated optical signals in combined HDWDM systems,” *Elektronikair Electrotehnika*, No. 6, 19–24, 2011.

Performance Improvement of Spectrum-sliced Passive Optical Network

G. Ivanovs, S. Spolitis, R. Parts, and V. Bobrovs

Institute of Telecommunications, Riga Technical University, Latvia

Abstract— Spectrum-sliced dense wavelength-division-multiplexed passive optical network (SS-DWDM PON) is an attractive and cost effective solution to satisfy the growing worldwide demand for transmission capacity in the next generation fiber optical access networks. The strength of SS-DWDM PON technology is use of one common broadband seed light source and its ability to place electronics and optical elements in one central office (CO), in that way simplifying the architecture of fiber optical network. The authors have successfully demonstrated the optical link reach improvement by implementation of chromatic dispersion compensation for cost effective SS-DWDM PON system.

1. INTRODUCTION

Traditional WDM systems have multiple transmitter lasers operating at different wavelengths, which need to be wavelength selected for each individual channel operated at a specific wavelength. It increases complexity of network architecture, cost and wavelength (channel) management. The strength and benefit of SS-DWDM PON optical systems from the same advantages as WDM, while employing low cost incoherent light sources like amplified spontaneous emission (ASE) source or light-emitting diode (LED). This spectral slicing method is a promising cost-efficient solution for a transmitter in an optical line terminal (OLT) of WDM-PON architecture. SS-WDM PON system is more energy efficient than traditional WDM PON because there is employed a single common broadband light source for transmission on a large number of wavelength channels, not a one source per user as it is in the traditional WDM-PON [1–3].

The optical bandwidth per channel of SS-WDM PON system is large compared to the bit rate. Therefore, dispersion considerably degrades the performance of this system more than it is observed in conventional laser-based systems. The influence of dispersion needs to be studied in order to understand the characteristic of a SS-WDM PON system employing a standard single mode optical fiber. In traditional time-division multiplexed passive optical network (TDM-PON), the number of ONTs (users) is limited by the attenuation of optical splitter in a single wavelength, but using WDM PON technology we can provide up to 64 or even more wavelengths in an optical access network [4]. Therefore WDM-PON becomes the strongest competitor because of its upgradeability and high capacity. In case of large number of end users the WDM-PON system can be assumed as an effective way to solve the bottleneck problem because each user receives its own wavelength [5].

It is very important to build a new type optical system based on widely used frequency grid, recommended by international standards because of such a system potentially is much more compatible with other already existing WDM-PON optical systems. The main benefit includes the reduction of network architecture complexity as well as cost per one user. It is possible by replacing the classic WDM-PON system (where one laser source is used for each user) with our proposed spectrum-sliced dense WDM PON system with CD compensation (where one seed broadband ASE source is spectrally sliced and used for multiple users) [6, 7].

2. SIMULATION MODEL AND NUMERICAL ANALYSIS

Our accepted research method is a mathematical simulation using newest OptSim 5.2 simulation software, where complex differential equation systems are solved using Split-Step algorithm. In order to study the nonlinear effects in optical fiber the nonlinear Schrödinger equation (NLS) is used. Except certain cases this equation cannot be solved analytically. Therefore, OptSim software is used for simulation of fiber optical transmission systems where it solves complex differential equations using Time Domain Split-Step (TDSS) method [3]. The performance of simulated scheme was evaluated by the obtained bit error ratio (BER) value of each WDM channel in the end of the fiber optical link. Basis on ITU recommendation G.984.2 it should be noticed that BER value for fiber optical transmission systems with data rate 2.5 Gbit/s per channel is specified less than 10^{-10} [8].

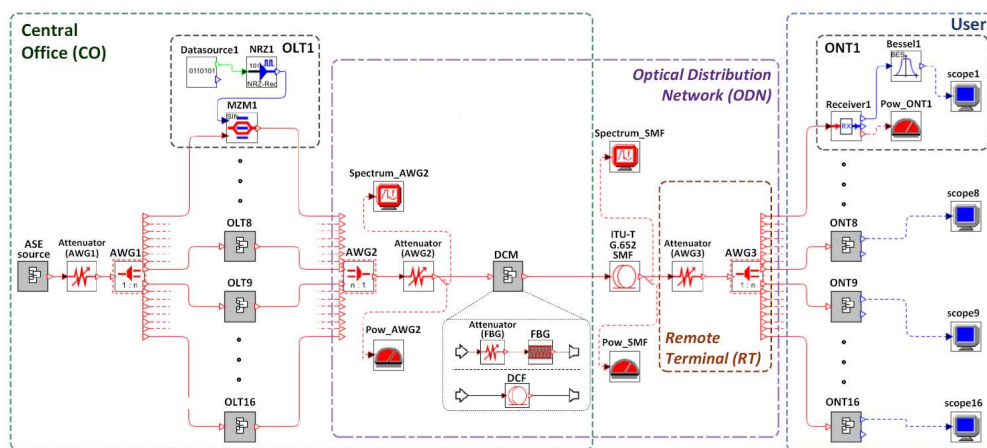


Figure 1: Experimental model of proposed high-speed 16-channel AWG filtered ASE seeded SS-DWDM PON system with DCM module.

In order to investigate the performance of incoherent broadband ASE light source as seed light for usage in spectrum sliced WDM passive optical networks we created a simulation scheme of high-speed 16 channel SS-DWDM PON system in OptSim 5.2 software, see Fig. 1. The design of high performance broadband flat spectrum ASE source on the output of cascaded EDFAs in details is described in next chapter. This chapter describes the simulation model and parameters of proposed SS-DWDM PON system with flat ASE seed source. As one can see in Fig. 1, SS-WDM PON simulation scheme consists of 16 channels. The frequency grid is anchored to 193.1 THz and channel spacing is chosen equal to 100 GHz frequency interval. This frequency grid and interval is defined in ITU-T recommendation G.694.1.

Broadband ASE light source is spectrally sliced using 16-channel AWG filter (AWG1) with channel spacing equal to 100 GHz (0.8 nm in wavelength). Using this AWG unit we can obtain spectrally sliced optical channels (slices) with dense channel interval 100 GHz. Insertion losses of AWG units are simulated using attenuation blocks (attenuators).

Simulated athermal high-performance AWG multiplexers and demultiplexers are absolutely passive optical components (no need for thermal regulation and monitoring electronics) with insertion loss up to 3 dB each [1]. After spectrum slicing by AWG1 optical slices are transmitted to the optical line terminals (OLTs). OLTs are located at central office (CO). Each OLT consists of data source, NRZ driver, and external Mach-Zehnder modulator (MZM). Generated bit sequence from data source is sent to NRZ driver where electrical NRZ pulses are formed. Afterwards formed electrical NRZ pulses are sent to MZM modulator. MZM modulates the optical slices from AWG1 and forms optical pulses according to electrical drive signal. These formed optical pulses from all OLTs are coupled by AWG multiplexer (AWG2) and sent into standard optical single mode fiber (SMF) defined in ITU-T recommendation G.652. Information from OLT is transmitted to an optical network terminal (ONT) or user over the fiber optical transmission link called optical distribution network (ODN). In the end of fiber optical link optical channels are split using AWG demultiplexer (AWG3) located in remote terminal (RT). Receiver section includes ONT units. Each ONT consists of sensitivity receiver with PIN photodiode (sensitivity $S = -25$ dBm at sensitivity reference error probability $BER = 1 \cdot 10^{-10}$), Bessel electrical filter (3-dB electrical bandwidth $B_E = 1.6$ GHz), optical power meter and electrical probe to evaluate the quality of received optical data signal. Optical signal is converted to electrical signal using PIN photodiode and filtered by Bessel electrical filter to reduce noise [9]. In simulation setup we used real parameters of standard DCF fiber and tunable FBG.

3. RESULTS AND DISCUSSIONS

Flat-top type AWG units were chosen for spectral slicing of ASE light source in our optical system because of good filtering performance, excellent WDM channel separation and bandwidth allow passing sufficient high optical power [2]. To reduce the negative impact of intensity noise as well as cross phase modulation the correct choice of filter's shape and 3-dB pass bandwidth is very important [10, 11]. In Fig. 2, are compared two SS-DWDM PON channels (central frequencies

193.1 and 193.2 THz) which are filtered by Gaussian and flat-top type AWGs with identical 50 GHz 3-dB pass bandwidth.

It is shown that flat-top AWG has narrower spectral filter shape than Gaussian type AWG. Wider filter shape leads to larger slice width, higher resultant slice's power and optical signal dispersion [6]. In OptSim software we simulated flat-top type AWG filter shape using Raised Cosine optical filter's transfer function but using Super-Gaussian transfer function we approximate Gaussian AWG filter shape [10].

As one can see in Fig. 2, in the case of Gaussian filter the crosstalk between channels will be much higher than employing flat-top type filter. Based on this we can make a conclusion that AWG with flat-top filter spectral shape has higher optical signal to noise ratio (OSNR) than AWG with Gaussian type filter shape at identical bandwidth (3-dB bandwidth is 50 GHz). Based on above mentioned facts we chose flat-top AWGs for our investigated SS-DWDM PON simulation scheme. In Fig. 2, it is shown optical spectrum on the output of ASE source and spectra after each flat-top AWG unit.

We found that optimal 3-dB bandwidth value of flat-top type AWG unit for maximal system performance must be about 90 GHz. By slicing the spectrum of proposed ASE source with first AWG demultiplexer we obtain 16 separate WDM channels with channel output power variation less than 0.42 dB. As one can see in Fig. 3, the performance of investigated SS-DWDM PON system was completely sufficient to provide data transmission with $BER < 1 \cdot 10^{-10}$ over the fiber optical span of 12 km in length without CD compensation.

The first realized chromatic dispersion compensation method includes the implementation of DCF in central office. It was found that the optimal required DCF fiber length for maximum improvement of our SS-DWDM PON system's performance is 5.1 km. This length of DCF fiber can compensate about 410 ps/nm of accumulated CD. Using DCF fiber with such a length we can achieve the maximal 16-channel SS-DWDM PON system's link length of 24 km, see Fig. 3(a).

By using FBG we achieve better results than using DCF for accumulated CD compensation. Implementation of FBG for CD compensation extends the total reach of SS-DWDM PON system

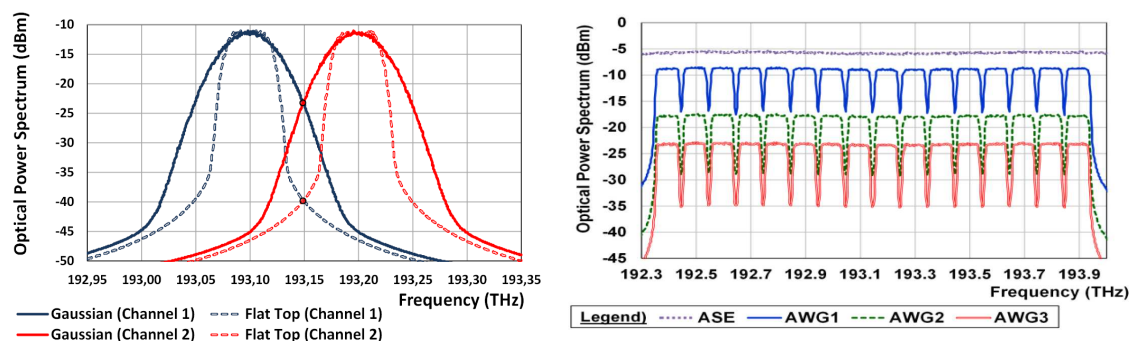


Figure 2: Optical output power spectrum of ASE source and 16-channel SS-DWDM PON system after each stage of flat-top type AWG unit. Comparison of Gaussian and flat-top type AWGs with 50 GHz 3-dB bandwidth in case of two adjacent WDM.

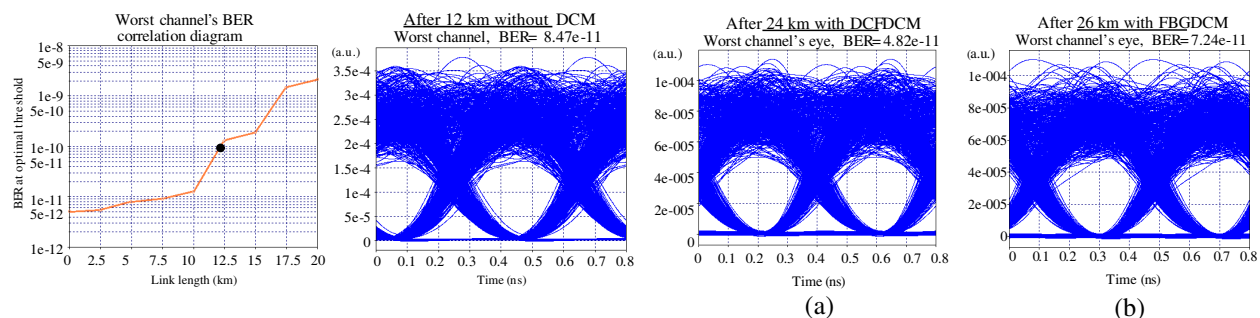


Figure 3: BER correlation diagram and output eye diagram of worst spectrally sliced dense WDM PON system's channel after 12 km SMF link length without CD compensation module. SS-DWDM PON system's eye diagrams and BER values of the received signal from worst channels employing, (a) DCF fiber and (b) FBG for accumulated CD compensation in DCM unit.

up to 26 km, see Fig. 3(b). This result can be explained by the fact that FBG has relatively small insertion loss (< 4 dB) and instead of DCF fiber it can be used at higher optical powers without inducing nonlinear optical effects, which can reduce the system's performance. Optimal CD compensation amount that must be compensated by FBG is -420 ps/nm and this amount is equivalent to full CD compensation.

4. CONCLUSIONS

In this work, using we have realized and investigated an experimental high-speed SS-DWDM PON system where DCF and FBG are used for accumulated chromatic dispersion (CD) compensation to improve the maximal link reach from OLT to ONT at the same time providing high system performance with $BER < 1 \cdot 10^{-10}$. It is shown design of broadband ASE source with $+23$ dBm output power and flat spectrum in system's operating wavelength range (C-band) using two EDFAs connected in cascade mode. We demonstrate that using DCF for CD compensation SS-DWDM PON reach can be improved by 100% or extra 12 km in length — from 12 km to 24 km. But using FBG unit network reach can be improved by 117% or extra 14 km — from 12 km to 26 km. Basis on these results authors recommend to use FBG DCM units for CD compensation in future high-speed 16-channel dense SS-WDM PON systems for maximal system's performance and network reach.

ACKNOWLEDGMENT

The travel costs and participation fee to conference was supported by the European Regional Development Fund project "Development of international cooperation projects and capacity in science and technology Riga Technical University", Nr. 2DP/2.1.1.2.0/10/APIA/VIAA/003.

REFERENCES

1. Spolitis, S. and G. Ivanovs, "Extending the reach of DWDM-PON access network using chromatic dispersion compensation," *Proceedings of 2011 IEEE Swedish Communication Technologies Workshop, SWE-CTW 2011*, 29–33, Stockholm, Sweden, Oct. 2011.
2. El-Sahn Z. A., W. Mathlouthi, H. Fathallah, S. La Rochelle, and L. A. Rusch, "Dense SS-WDM over legacy PONs: Smooth upgrade of existing FTTH networks," *Journal of Lightwave Technology*, Vol. 28, No. 10, 1485–1495, May 15, 2010.
3. Spolitis, S., V. Bobrovs, and G. Ivanovs, "Realization of combined chromatic dispersion compensation methods in high speed WDM optical transmission systems," *Electronics and Electrical Engineering*, Vol. 10, No. 116, 33–38, 2011.
4. Choi, B. H. and S. S. Lee, "The effect of AWG-filtering on a bidirectional WDM-PON link with spectrum-sliced signals and wavelength-reused signals," *Optics Communications*, Vol. 284, No. 24, 5692–5696, 2011.
5. Bobrovs, V., A. Udalcovs, S. Spolitis, O. Ozolins, and G. Ivanovs, "Mixed chromatic dispersion compensation methods for combined HDWDM systems," *Proceedings of 2011 International Conference on Broadband and Wireless Computing, Communication and Applications, BWCCA 2011*, 313–319, Barcelona, Spain, Oct. 2011.
6. ITU-T Recommendation G.984.2, "Gigabit-capable passive optical networks (GPON): Physical media depend (PMD) layer specification," 2003.
7. Spolitis, S., V. Bobrovs, and G. Ivanovs, "Investigation of high-speed AWG filtered spectrum-sliced WDM PON system," *Proceedings of 2012 8th International Symposium on Communication Systems, Network and Digital Signal Processing, CSNDSP 2012*, Poznan, Poland, Jul. 2012.
8. Lee, K., D. S. Lim, M. Y. Jhon, H. C. Kim, P. Ghelfi, T. Nguyen, et al., "Broadcasting in colorless WDM-PON using spectrum-sliced wavelength conversion," *Optical Fiber Technology*, Vol. 18, No. 2, 112–116, 2012.
9. Keiser, G., *Optical Communications Essentials*, McGraw-Hill, 2007.
10. Ozolins, O., V. Bobrovs, and G. Ivanovs, "Efficient wavelength filters for DWDM systems," *Latvian Journal of Physics and Technical Sciences*, Vol. 47, No. 6, 47–58, 2010.
11. Ivanovs, G., V. Bobrovs, O. Ozolins, and J. Porins, "Realization of HDWDM transmission system," *International Journal of Physical Sciences*, Vol. 5, No. 5, 452–458, 2010.

Design of an Optimal Benes WEX Architecture Based on Sufficient Permutations

J.-C. Wu¹ and M. H. Wei^{2,3}

¹Department of Computer and Communication Engineering
National Kaohsiung First University of Science and Technology, Kaohsiung, Taiwan

²Institute of Engineering Science and Technology
National Kaohsiung First University of Science and Technology, Kaohsiung, Taiwan

³Center of General Education, Kao Yuan University, Kaohsiung, Taiwan

Abstract— In order to achieve nonblocking connection, all the switching networks are designed to provide connections of full permutations. To reduce the hardware complexity, we propose designing wavelength-exchanging cross connect (WEX) to support sufficient permutations instead of full permutations. In this paper, we propose an algorithm to construct an optimal Benes WEX architecture with sufficient permutations. The idea is to select a minimal number of switching elements in a Benes WEX so that all connections of sufficient permutations can be provided. Our case study results show that the architectures of our proposed WEX based on sufficient permutations in the cases of 2 and 4 wavelengths in each fiber can save up to half switching elements compared with that of the existing Benes WEXs based on full permutations.

1. INTRODUCTION

Wavelength cross-connect (WXC) [1–3] is a wavelength division multiplexing (WDM) device with switching capability. Basically, a WXC consists of two types of main elements: space switching elements (SSEs) and wavelength converters (WCs). SSEs are capable of connecting input ports to the required output ports without performing any wavelength conversion on input signals. WCs are usually employed to relax the wavelength continuity constraint and hence improve the blocking performance of the networks [4].

A new type of WXC, namely wavelength-exchanging cross connect (WEX), was proposed whose architecture consists of SSEs and wavelength-exchange optical crossbars (WOCs) [5–9]. WOC is a switching element with 2 inputs and 2 outputs and can perform a single-step space switching and wavelength conversion between two wavelengths. Consequently, the WEX architecture does not require the stages of separated WCs.

To reduce the hardware complexity of switch, Waksman [10] observed that some elementary cells (switches) of a switch are left in the bar state and can be eliminated. Similarly, a 4×4 wavelength-exchangeable permutation switching network was proposed, in which there exists a WOC always left in the bar state so that it can be reduced. Such a switching network was employed to build a large-scale Benes WEX network [9].

The design of all the existing switching networks is based on full-permutation to achieve non-blocking connections [1–9]. However, this results in a huge amount of hardware complexity in the switching networks.

We observed that the permutations correspond to mutually exchange wavelengths within an output fiber may not be necessary and can be regarded to perform the same switching job. Based on the idea, we classified all of the permutations into several equivalent sets, each performing a particular switching job. From each equivalent set, any one permutation could be selected as a representative, and all of the representative permutations were grouped together to form a set called *sufficient permutations* [11].

We applied the concept of sufficient permutations to simplify the Benes WEX architecture shown in [11]. However, it was to run all the control states of all the switching elements. This leads complex computing. In order to design a compact WEX architecture, we select the minimal number of the switching elements in Benes WEX such that all the sufficient permutations can be provided.

2. SUFFICIENT PERMUTATIONS

We consider the $N \times N$ wavelength-exchanging cross connect with F input fibers, F output fibers, and W wavelengths in each fiber, where $N = WF$. In this paper, we will focus on the WEX architecture with $F = 2$.

Let $W^\lambda(F \times F)$ switch denote such a WEX. The set of fibers and the set of wavelengths are denoted as $\{f_1, f_2, \dots, f_F\}$ and $\{\lambda_1, \lambda_2, \dots, \lambda_W\}$, respectively. Let $X = [1, 2, 3, 4, \dots, N]^t$ be the input vector of a $W^\lambda(F \times F)$ switch, where k is the input signal S_k on wavelength λ_j in fiber f_i and $k = i + 2 \cdot (j - 1)$, $k = 1, 2, \dots, N$. Such an arrangement is known as the connection pattern of fiber-based type [7].

Let $Y = [\pi_1, \pi_2, \dots, \pi_N]^t$ be a permutation vector at the switch output for input vector X , where $\pi_y = k \in \{1, 2, \dots, N\}$ denotes that signal S_k is routed to output port y . For example, the permutation vector $[3, 4, 1, 2]^t$ in a $2^\lambda(2 \times 2)$ switch (shown in Figure 1(d)) stands for that signals 1, 2, 3, and 4 will be routed to output port 3, 4, 1, and 2, respectively. Suppose that we examine the destination fibers instead of the destination ports of the input signals, we find that the permutation vector $[3, 4, 1, 2]^t$ in a $2^\lambda(2 \times 2)$ switch implies that signals 1, 2, 3, and 4 will be routed to output fiber $f_1, f_2, f_1,$ and f_2 , respectively. Since signals 1, 2, 3, and 4 also come from $f_1, f_2, f_1,$ and f_2 , respectively, we say that all of these input signals *stay* at the fiber, where they come from. We find that the permutation vectors $[1, 2, 3, 4]^t$, $[3, 2, 1, 4]^t$, and $[1, 4, 3, 2]^t$ (shown in Figures 1(a), 1(b), and 1(c), respectively) have also the same phenomenon. All of the permutation vectors $[3, 4, 1, 2]^t$, $[1, 2, 3, 4]^t$, $[3, 2, 1, 4]^t$, and $[1, 4, 3, 2]^t$ correspond to mutually exchange wavelengths within an output fiber, we say that these four permutation vectors in a $2^\lambda(2 \times 2)$ switch do the same switching job, which routes input signals so that all of them stay at the fiber where they come from. Therefore, any one of these four permutations can to provide this switching job. These four permutations are shown in Figure 1.

Assume that a signal arriving at a particular input port of a WEX has two states: *stay* and *jump*. The *stay* state indicates that the arriving signal intends to stay at the same fiber, and the *jump* state indicates that the arriving signal intends to jump into the other fiber. To design the WEX with nonblocking connections, the number of signals with jump state in two fibers f_1 and f_2 should be the same.

Let $\{a_1, a_2, \dots, a_m\}$ and $\{A_1, A_2, \dots, A_m\}$ denote the set of m different signals with jump state in fiber f_1 and f_2 , respectively, where $a_k \in \{1, 3, \dots, 2W - 1\}$ corresponds to index k of signal S_k from fiber f_1 and $A_k \in \{2, 4, \dots, 2W\}$ corresponds to index k of signal S_k from fiber f_2 . Since the mutual exchange between $\{a_1, a_2, \dots, a_m\}$ and $\{A_1, A_2, \dots, A_m\}$ performs a switching job for a particular nonzero number of m , we use the notation: $\{a_1, a_2, \dots, a_m\} \leftrightarrow \{A_1, A_2, \dots, A_m\}$ to represent such a switching job. For $m = 0$ which indicates the all input signals have *stay* state, we denote it as: $\Phi \leftrightarrow \Phi$. The permutations that perform all switching jobs are defined by the *sufficient permutations*. This implies that sufficient permutations perform both $\Phi \leftrightarrow \Phi$ and any combination of $\{a_1, a_2, \dots, a_m\} \leftrightarrow \{A_1, A_2, \dots, A_m\}$ for $m = 1, 2, \dots, W$. For example, the sufficient permutations of a $2^\lambda(2 \times 2)$ switch perform the following switching jobs: $\Phi \leftrightarrow \Phi$, $\{1\} \leftrightarrow \{3\}$, $\{2\} \leftrightarrow \{4\}$, $\{2\} \leftrightarrow \{3\}$, $\{1\} \leftrightarrow \{4\}$, and $\{1, 2\} \leftrightarrow \{3, 4\}$.

For a $W^\lambda(2 \times 2)$ WEX, we observe that there are combinations in the switching job of $\{a_1, a_2, \dots, a_m\} \leftrightarrow \{A_1, A_2, \dots, A_m\}$, where C_m^W denotes the number of ways to choose m different signals from W ones. Consequently, the number of switching jobs is $(C_m^W)^2$ or a particular number of m , and the total number of switching jobs is $\sum_{m=0}^W (C_m^W)^2 = C_W^{2W}$ for sufficient permutations.

3. DESIGN ALGORITHM

In this section, we will propose an algorithm to design an optimal Benes WEX architecture, which is based on sufficient permutations. Then, we will give two examples of case study. The reason why our design focuses on the Benes architecture is because Benes architecture is known as one of most efficient switch architectures in terms of the numbers of 2×2 switches it uses to build larger switches [12].

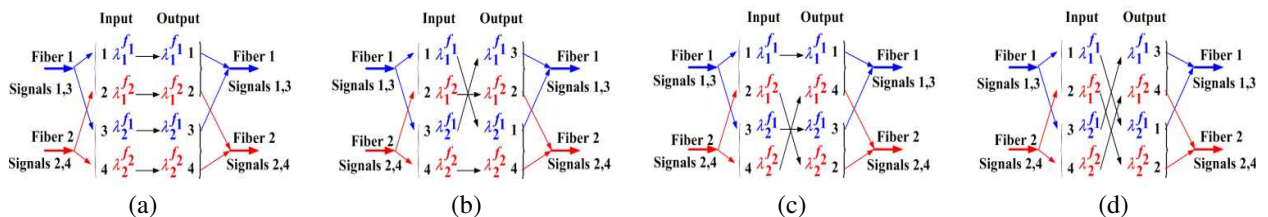


Figure 1: Four permutation vectors do the same switching job in a $2^\lambda(2 \times 2)$ switch.

A WEX architecture consisting of SSEs and WOCs as the switching elements is said to be *optimal*, if it has the minimal number of switching elements and it can to perform all the sufficient permutations.

To find the minimal number of switching elements in a WEX architecture, we observe that (a) each switching element performs either the bar or the cross state; (b) the states of switching elements determine the permutation output; (c) a particular permutation output may result from one or more than one combination of the states of all switching elements. This implies that if the number of switching elements in a WEX is n , the number of different permutation outputs is not greater than 2^n . Therefore, a $W^\lambda(2 \times 2)$ WEX with sufficient permutations, whose number of switching job is C_W^{2W} , must have at least n switching elements, where $2^n \geq C_W^{2W}$.

The idea of our proposed algorithm is to (i) select a candidate architecture by removing some of switching elements in the original Benes WEX, where the candidate architecture has minimal number switching elements, (ii) verify if this candidate can perform all switching jobs, and (iii) modify the candidate architecture by increasing total number of switching elements by one and repeat the procedure (ii), if this candidate cannot perform all switching jobs.

In the following, we show the algorithm for designing an optimal $W^\lambda(2 \times 2)$ Benes WEX architecture, based on sufficient permutations. The algorithm takes the parameters W as inputs, and it outputs an optimal Benes WEX architecture.

- (1) Construct a $W^\lambda(2 \times 2)$ Benes WEX.
- (2) Find n , where n is the minimal number of 2×2 switching elements and n satisfies $2^n \geq C_W^{2W}$.
- (3) Select a sub-WEX architecture of the Benes WEX, which has n switching elements.
- (4) Verify if the sub-WEX can perform all of the switching jobs for sufficient permutations.
- (5) If the sub-WEX can provide all switching jobs, then this sub-WEX is optimal. Otherwise, we increase n by one, and go to step (3).

Next, we apply the algorithm given above to construct $2^\lambda(2 \times 2)$ and $4^\lambda(2 \times 2)$ Benes WEX. And, the results of the optimal $2^\lambda(2 \times 2)$ and $4^\lambda(2 \times 2)$ Benes WEXs are shown in Figure 2(b) and Figure 3(b), respectively.

4. COMPARISON OF ARCHITECTURES

We will compare our optimal Benes WEXs with the original Benes WEXs in [5, 9] and simplified Benes WEXs in [11] with respect to hardware complexity for the cases of $2^\lambda(2 \times 2)$ and $4^\lambda(2 \times 2)$. Notice that the design of the original Benes WEXs in [5, 9] is based on full permutations; while the simplified Benes WEXs in [11] and our optimal Benes WEXs are based on sufficient permutations.

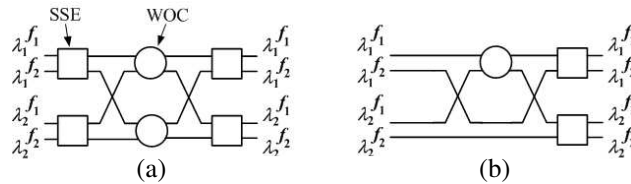


Figure 2: (a) The $2^\lambda(2 \times 2)$ Benes WEX. (b) The optimal $2^\lambda(2 \times 2)$ Benes WEX.

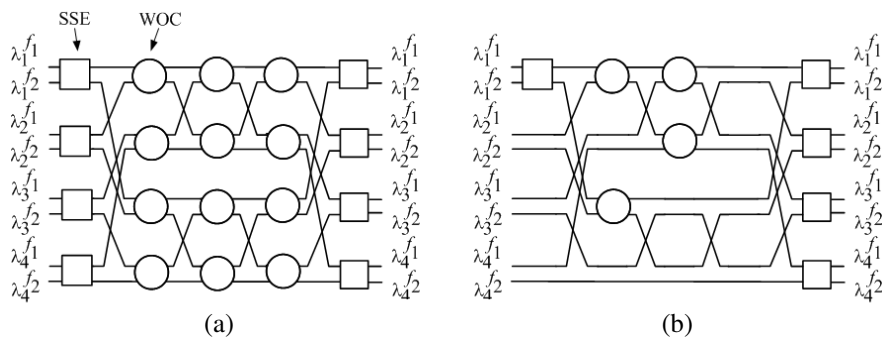


Figure 3: (a) The $4^\lambda(2 \times 2)$ Benes WEX. (b) The optimal $4^\lambda(2 \times 2)$ Benes WEX.

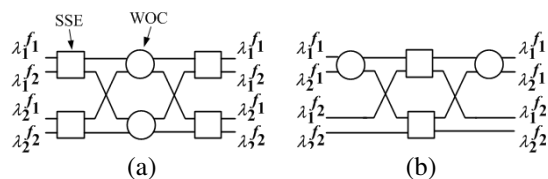


Figure 4: (a) The original $2^\lambda(2 \times 2)$ Benes WEX [5]. (b) The simplified $2^\lambda(2 \times 2)$ Benes WEX [11].

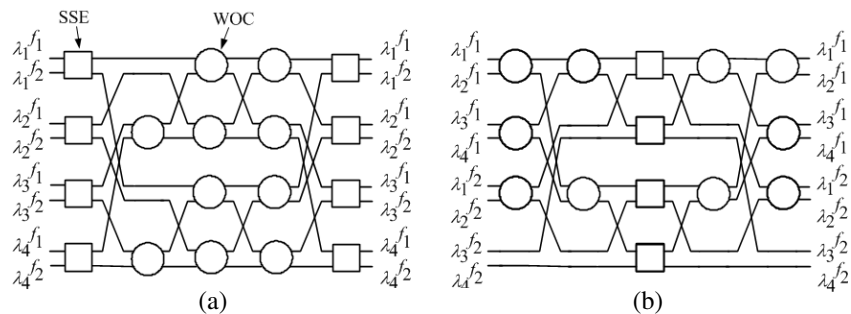


Figure 5: (a) The original $4^\lambda(2 \times 2)$ Benes WEX [9]. (b) The simplified $4^\lambda(2 \times 2)$ Benes WEX [11].

Table 1: The hardware complexity comparison.

Architectures	original WEX	simplified WEX [11]	optimal WEX
$2^\lambda(2 \times 2)$	$4 + 2$ [5]	$2 + 2$	$2 + 1$
$4^\lambda(2 \times 2)$	$8 + 10$ [9]	$4 + 10$	$5 + 4$

Note: $x + y$ stands for x SSEs and y WOCs.

In the case of $2^\lambda(2 \times 2)$ Benes WEX switch, the original Benes WEX uses 6 switching elements [5], as shown in Figure 4(a); while the simplified Benes WEX uses 4 switching elements [11], as shown in Figure 4(b). Recall that our optimal Benes WEX only uses 3 switching elements, as shown in Figure 2(b).

In the case of $4^\lambda(2 \times 2)$ Benes WEX switch, the original Benes WEX uses 18 switching elements [9], as shown in Figure 5(a); while the simplified Benes WEX uses 14 switching elements [11], as shown in Figure 5(b). Recall that our optimal Benes WEX uses 9 switching elements, as shown in Figure 3(b).

Table 1 shows the number of SSEs and the number of WOCs (denoted by a number x plus a number y) used in these WEXs that we have compared.

5. CONCLUSIONS

In this paper, we propose an algorithm to design an optimal $W^\lambda(2 \times 2)$ Benes WEX architecture based on sufficient permutations, where sufficient permutations perform the switching operations of routing input signals to destination fibers instead of destination ports. To achieve an optimal design, we propose using minimal number of switching elements. Our study results show that the proposed Benes WEX architecture in both $2^\lambda(2 \times 2)$ and $4^\lambda(2 \times 2)$ cases can cut the hardware complexity by half in comparison with the original WEX architectures.

ACKNOWLEDGMENT

This work was supported by the National Science Council of Taiwan under the Grant NSC 100-2221-E-327-030.

REFERENCES

1. Brackett, C. A., "Forward: Is there an emerging consensus on WDMnetworking?," *J. Lightwave Technol.*, Vol. 14, 936–941, Jun. 1996.
2. Zhong, W. D., J. P. R. Lacey, and R. S. Tucker, "Multiwavelength crossconnects for optical transport networks," *J. Lightwave Technol.*, Vol. 14, 1613–1620, Jul. 1996.

3. Chen, Y. K. and C. C. Lee, “Fiber Bragg grating-based large nonblocking multiwavelength cross-connects,” *J. Lightw. Technol.*, Vol. 16, No. 10, 1746–1756, Oct. 1998.
4. Lee, K. C. and V. O. K. Li, “A wavelength-convertible optical network,” *J. Lightwave Technol.*, Vol. 11, 962–97, May/June. 1993.
5. Hamza, H. S. and J. S. Deogun, “Architectures for WDM Benes interconnection network with simultaneous space-wavelength switching capability,” *2nd IEEE Int. Conf. on Broadband Networks*, Oct. 2005.
6. Hamza, H. S. and J. S. Deogun, “Wavelength-exchanging cross-connect (WEX) — A new class of photonic cross-connect architectures,” *J. Lightw. Technol.*, Vol. 24, No. 3, 1101–1111, Mar. 2006.
7. Hamza, H. S. and J. S. Deogun, “Designing full-connectivity WDM photonic interconnects with reduced switching and conversion complexity,” *14th IEEE Symposium on High-performance Interconnects*, Aug. 2006.
8. Hamza, H. S. and J. S. Deogun, “WDM photonic interconnects: A balance design approach,” *IEEE/ACM Trans. Netw.*, Vol. 15, No. 6, 1565–1578, Dec. 2007.
9. Hamza, H. S., “Optimizing complexity in Benes-type WDM switching networks,” *Journal of Photonic Network Communications*, Vol. 17, No. 3, 277–291, 2009.
10. Waksman, A., “A Permutation network,” *J. of the ACM*, Vol. 15, No. 1, 159–163, Jan. 1968.
11. Wu, J.-C. and M. H. Wei, “A design methodology to simplify WDM Benes photonic switches,” *2009 IEEE 9th Malaysia International Conference on Communications (MICC 2009)*, 381–386, Dec. 2009.
12. Ramaswami, R., K. N. Sivarajan, and G. H. Sasaki, *Optical Networks: A Practical Perspective*, 3rd Edition, Morgan Kaufmann, San Francisco, 2010.

Analysis of Anisotropic Diffraction in Volume Gratings Using Liquid Crystal Composites

A. Ogiwara¹, H. Shichi¹, H. Kakiuchida², A. Emoto³, and H. Ono⁴

¹Department of Electronic Engineering, Kobe City College of Technology, Japan

²Materials Research Institute for Sustainable Development
National Institute of Advanced Industrial Science and Technology (AIST), Japan

³Electronics and Photonics Research Institute
National Institute of Advanced Industrial Science and Technology (AIST), Japan

⁴Department of Electrical Engineering, Nagaoka University of Technology, Japan

Abstract— A micro-periodic structure composed of polymer and liquid crystal (LC) phases is called holographic polymer dispersed liquid crystal (HPDLC) grating. The HPDLC grating has been applied for grating formation to obtain both high optical efficiency and electric switching function. Moreover, HPDLC grating shows polarization dependence in diffraction efficiencies against the incident polarization state of laser light. The anisotropic diffraction is modulated by the distribution of submicrometer-scale liquid crystal (LC) droplet in a polymer matrix using interferometric laser exposure. The refractive-index modulations (n_{1x}, n_{1y}, n_{1z}) in grating medium corresponding to the three dimensional directions are obtained by applying theoretical calculation based on the anisotropy for the experimental results of angular dependence of diffraction efficiencies in various grating structures. Our analysis shows that the diffraction efficiency and the characteristic ratio of diffraction efficiency in polarization parallel to the grating vector to that in polarization perpendicular to the grating vector are markedly affected by the refractive-index modulations.

1. INTRODUCTION

The development of holographic and diffractive optical technologies is of considerable interest for integrated optics, sensor systems, displays, optical interconnects, and optical data storage devices. In many applications, it is desirable to have control over the diffraction efficiency of a device by applying electric field. A useful approach is to employ a liquid-crystal (LC) phase, which can consider the change in birefringence induced by electric field as refractive index modulation in the device. Such a device has been realized using a polymer-dispersed liquid crystal (PDLC) consisting of LC droplets embedded in a polymer matrix. Since the LC molecules in the droplets can be aligned by applying electric field, the change in refractive index by LC orientation in the polymer matrix is usable for electric switching application. The refractive index modulation in PDLC systems is realized by spatial density or concentration variation in the resulting polymer, or spatially distributed voids. Thus, when a mixture of LC and monomer materials containing a photo initiator is irradiated using a spatially periodic intensity, the formation of polymer networks is induced in the bright regions of fringes. At the same time as the reaction, LC molecules are separated in the dark regions of fringes. As a result, a periodic structure consisting of polymerized and LC concentration regions is produced in the PDLC systems using the obtained irradiation pattern. If a holographic optical system with a laser source is applied to the PDLC systems, fine periodic structures produced by cured-polymer and separated LC phases, that is, holographic polymer-dispersed liquid crystal (HPDLC) gratings, can be realized using the optical system [1–8].

Diffusion and phase-separation processes during grating formation, which are induced by photo polymerization, are considered to dominate the diffraction properties of the fabricated HPDLC gratings. The high polarization dependence of the diffraction property developed in the HPDLC gratings is expected to provide novel polarization-controllable optical devices, such as thin polarized beam splitting films with a microscopic holographic structure [9, 10]. Therefore, the anisotropic diffraction properties in the HPDLC gratings are theoretically and experimentally important issues to be studied for the development of novel optical devices. We report in this article the anisotropic diffraction of HPDLC gratings based on the refractive-index modulations (n_{1x}, n_{1y}, n_{1z}) in grating medium affecting the behaviors of LC molecules in the grating structure.

2. THEORETICAL TREATMENT FOR GRATING STRUCTURE

Figure 1 shows the grating structure for theoretical treatment. The amplitudes of refractive-index modulation (n_{1x}, n_{1y}, n_{1z}) in grating medium corresponding to the three dimensional directions are

estimated by expanding the Kogelnik's coupled-wave theory using the incident angle dependence in anisotropic diffraction against the p and s -polarizations [6, 11]. The estimation procedure is described as follows. The difference in the amplitude of refractive-index modulation in the grating between P - and S -polarizations is regarded as an indicator of the order of LC orientation. The amplitude of refractive-index modulation in the grating is related to diffraction efficiency ($\eta(\theta_\rho)$) for incident light angle (θ_ρ) in grating medium through Kogelnik's coupled-wave theory as expressed by [11]

$$\eta(\theta_\rho) = \frac{\sin^2 \sqrt{\nu^2 + \xi^2}}{1 + \frac{\xi^2}{\nu^2}} \quad (1)$$

where $\nu = \kappa d$ (κ_p and κ_s) for p - and s -polarizations as follows,

$$\kappa_p = \frac{\pi (n_{1x} \cos^2 \theta_\rho - n_{1z} \sin^2 \theta_\rho)}{\lambda \cos \theta_\rho} \quad (2)$$

$$\kappa_s = \frac{\pi n_{1y}}{\lambda \cos \theta_\rho}, \quad (3)$$

and $\xi = \Gamma d / 2C_s$ is expressed by following parameters:

$$\Gamma = \Delta\theta K \sin(\phi - \theta_0) \quad (4)$$

$$C_s = \cos(\theta_\rho) - \left(\frac{K}{\beta}\right) \cos(\phi) \quad (5)$$

The parameters described above are expressed as $K = 2\pi/\Lambda$ and $\beta = 2\pi n_o/\lambda$. Here, d is the thickness of the grating, $\Delta\theta$ is the deviation between incidence angle (θ_ρ) and Bragg angle (θ_0) in the grating medium, ϕ is the slanted angle, n_o is the average refractive index, Λ is the grating spacing, and in the present case, λ , d , and Λ correspond to 0.532 μm , 10 μm , and 1 μm respectively. n_o is estimated to be 1.532 from the mixture ratio of LC and polymer molecules. d , ϕ , and Λ are confirmed by SEM observation, as detailed in later section. The amplitude of refractive-index modulation values of the present samples are estimated from the measurement of the incident angle dependence in anisotropic diffraction against the p and s -polarizations using Eq. (1).

3. EXPERIMENT

3.1. Sample Preparation

LC composite for an HPDLC grating was prepared using isotropic monomers (Kyoetisha Chemical) such as 2-hydroxy-3-phenoxy-propyl acrylate, 2-hydroxyethyl methacrylate, and dimethylol tricyclo decane diacrylate mixed with LC materials. The ratios of the isotropic monomers mixtures were 80, 5, and 15 wt.%, respectively, and two kinds of nematic LC materials K-15 and BL024 (Merck) was added to the prepolymer mixture at content ratio of 25 and 35 wt.% based on the fraction of all ingredients. N-phenylglycine and xanthene dye (dibromofluorescein) as a coinitiator and photoinitiator were introduced to the LC composites composed of isotropic and anisotropic monomers, respectively. The refractive index of the cured composition for isotropic monomers was found to be 1.520 by ellipsometric analysis. The physical properties (n_o/n_e , clearing point) of nematic LC supplied by Merck as follows: K-15 (1.5331/1.7288, 35.1°C), and BL024 (1.5132/1.7174, 81°C).

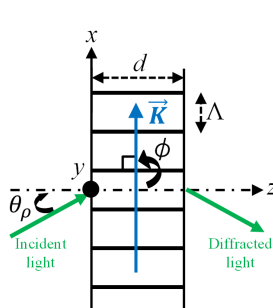


Figure 1: Grating structure for theoretical treatment.

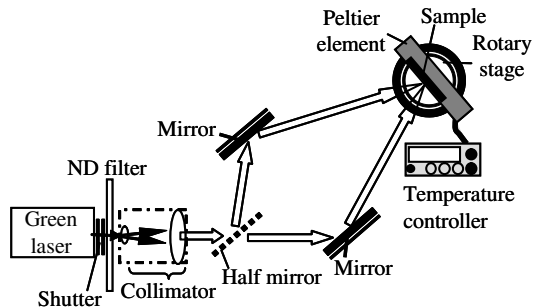


Figure 2: Optical setup for fabricating an HPDLC grating at controlled temperature using laser interferometer.

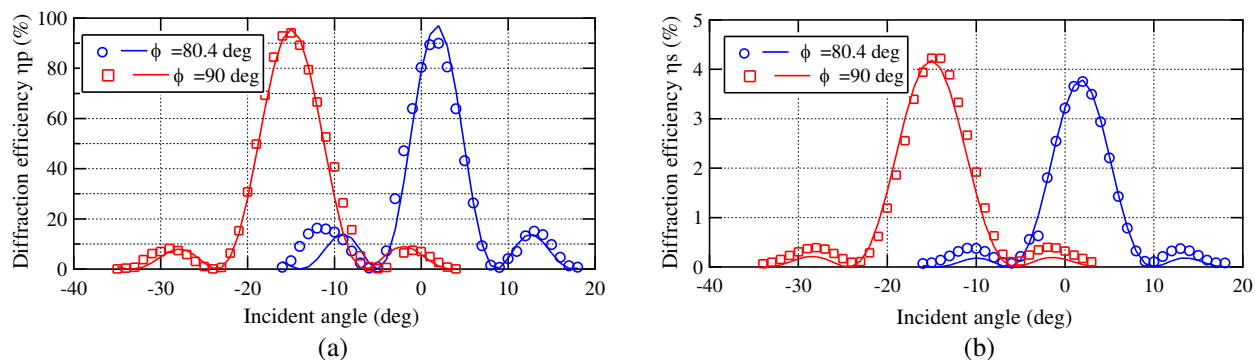


Figure 3: Incidence angle dependences of diffraction efficiencies for an unslanted HPDLC grating (square) at $\phi = 90$ and a slanted grating (circle) at $\phi = 80.4$ formed by LC (K15): (a) p - and (b) s -polarizations.

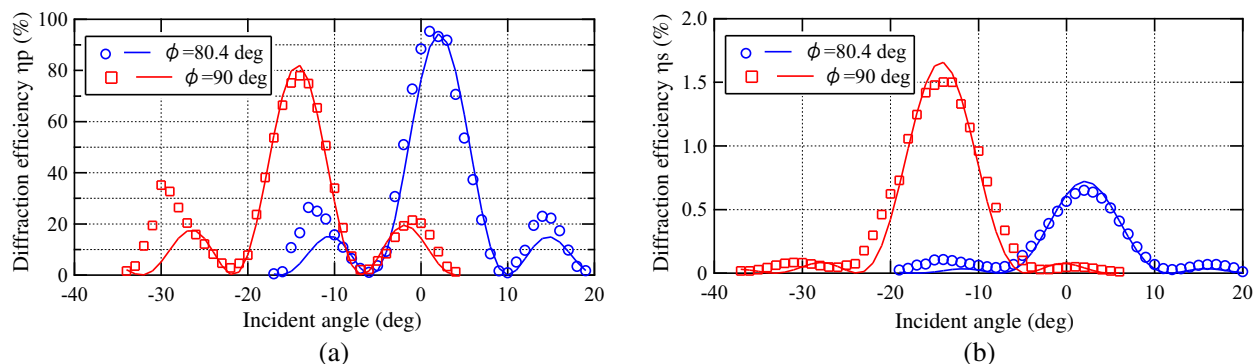


Figure 4: Incidence angle dependences of diffraction efficiencies for an unslanted HPDLC grating (square) at $\phi = 90$ and a slanted grating (circle) at $\phi = 80.4$ formed by LC (BL024): (a) p - and (b) s -polarizations.

3.2. Optical Setup for Device Fabrication

Figure 2 shows the optical setup for the formation of optical gratings. Interferometric exposure using a green laser (Nd:YVO₄, $\lambda = 532$ nm) induces spatially periodic modulation in the refractive index at various spacings as the angle of the laser beam crossing the samples is adjusted. Using the rotary stage under the sample, the direction of grating formation can be adjusted to yield unslanted and slanted gratings. The temperature for the device fabrication was adjusted to 50°C using the temperature controller with the Peltier element in this setup. The laser source for photopolymerization was collimated and linearly polarized perpendicularly to the grating vector, and the intensity on the samples was fixed at 5 mW/cm². The polarization directions parallel and perpendicular to the grating vector are called P - and S -polarizations, respectively.

4. RESULTS AND DISCUSSION

Figure 3 shows incidence angle dependences of diffraction efficiencies for an unslanted HPDLC grating (square marks) at $\phi = 90$ and a slanted grating (circle marks) at $\phi = 80.4$ formed by the nematic LC (K15). The solid lines show the theoretical predictions obtained using Eq. (1). The diffraction efficiency was obtained as the ratio of diffracted first order intensity to the total of 0th and first order diffracted intensity. Figs. 3(a) and 3(b) show the diffraction efficiencies (η_p and η_s) for incident p - and s -polarization lights. On the other side, Figure 4 shows incidence angle dependences of diffraction efficiencies for an unslanted HPDLC grating (square marks) at $\phi = 90$ and a slanted grating (circle marks) at $\phi = 80.4$ formed by the nematic LC (BL024). The theoretical predictions are well coincident with the experimental results. The obtained gratings show highly anisotropic diffraction properties since the diffraction efficiencies of η_p are much larger than η_s in both unslanted and slanted gratings. The resultant diffraction anisotropy, that is, the distinctive ratio (η_p/η_s), is larger observed in the gratings formed by the nematic LC (BL024) than that of the nematic LC (K-15).

Figure 5 shows anisotropic refractive indices obtained based on the theoretical and experimental treatments in various HPDLC gratings. We can observe that the anisotropic refractive index (n_{1x})

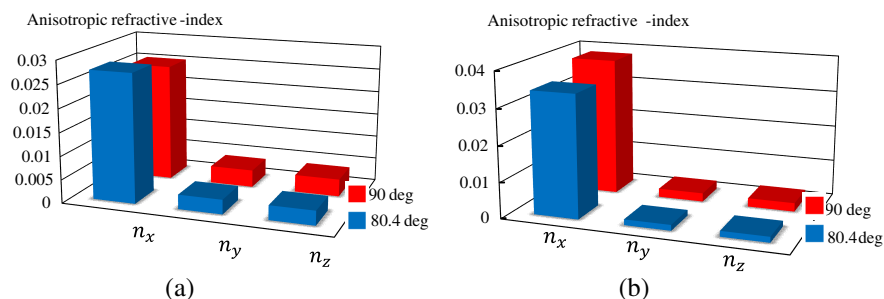


Figure 5: Anisotropic refractive indices estimated by the theoretical analysis in the HPDLC gratings formed by LC composites composed of isotropic monomers and different LC materials: (a) K-15 and (b) BL024.

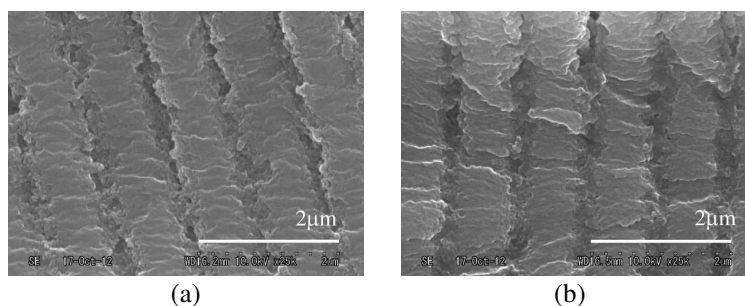


Figure 6: SEM cross-sectional views of the HPDLC gratings formed by LC composites: (a) K-15 and (b) BL024.

is much larger than other refractive indices (n_{1y} , and n_{1z}), and that the ratio is dominant at amplitude of n_{1x} in Fig. 5(b) by the LC (BL024) compared with that in Fig. 5(a) by the LC (K-15). The amplitude of n_{1x} corresponds to the direction of p -polarization which is parallel to the grating vector. Figure 6 shows the SEM cross-sectional views of the HPDLC gratings formed by LC composites composed of isotropic monomers and different LC materials at (a) K-15 and (b) BL024. The SEM images show the cured polymer and the trace of LC droplets distributed to form a periodic structure. The periodic structure separated by the LC layer composed of the coalesced fine droplets is clearly observed.

5. CONCLUSIONS

Anisotropic volume holographic gratings were produced from a polymer-dispersed liquid crystal by different LC composites. The angular dependence of diffraction efficiencies were experimentally investigated for various gratings formed by different grating structures and LC contents. The theoretical predictions obtained by the equation based on the anisotropic diffractions were well coincident with the experimental results. The refractive-index modulations (n_x , n_y , n_z) in grating medium corresponding to the three dimensional directions were estimated by applying theoretical calculation for the incidence angle dependence of the diffraction efficiencies. The SEM observations show the separated phase morphology of LC-rich and polymer-rich regions. The results of refractive-index modulation in the grating indicate that the anisotropic refractive index (n_{1x}) is much larger than other refractive indices (n_{1y} and n_{1z}) and that the LC orientation in a small droplet is highly ordered along the grating vector.

ACKNOWLEDGMENT

This work was supported in part by a JSPS Grant-in-Aid for Scientific Research C (23560427).

REFERENCES

1. Butler, J. J. and M. S. Malcuit, "Diffraction properties of highly birefringent liquid-crystal composite gratings," *Opt. Lett.*, Vol. 25, 420–422, 2000.
2. Bunning, T. J., L. V. Natarajan, V. P. Tondiglia, and R. L. Sutherland, "Holographic polymer-dispersed liquid crystals (H-PDLCs)," *Annu. Rev. Mater. Sci.*, Vol. 30, 83–115, 2000.

3. Bowley, C. C. and G. P. Crawford, “Diffusion kinetics of formation of holographic polymer-dispersed liquid crystal display materials,” *Appl. Phys. Lett.*, Vol. 76, 2235–2237, 2000.
4. Sutherland, R. L., V. P. Tondiglia, L. V. Natarajan, and T. J. Bunning, “Evolution of anisotropic reflection gratings formed in holographic polymer-dispersed liquid crystals,” *Appl. Phys. Lett.*, Vol. 79, 1420–1422, 2001.
5. Butler, J. J., M. S. Malcuit, and M. A. Rodriguez, “Diffractive properties of highly birefringent volume gratings: Investigation,” *J. Opt. Soc. Am. B*, Vol. 19, 183–189, 2002.
6. Sutherland, R. L., “Polarization and switching properties of holographic polymer-dispersed liquid-crystal gratings. I. Theoretical model,” *J. Opt. Soc. Am. B*, Vol. 19, 2995–3003, 2002.
7. Holmes, M. E. and M. S. Malcuit, “Controlling the anisotropy of holographic polymer-dispersed liquid-crystal gratings,” *Phys. Rev. E*, Vol. 65, 066603-1–066603-4, 2002.
8. Drevenšek-Olenik, I., M. Jazbinšek, M. E. Sousa, A. K. Fontecchio, G. P. Crawford, and M. Èopiè, “Structural transitions in holographic polymer-dispersed liquid crystals,” *Phys. Rev. E*, Vol. 69, 051703-1–051703-10, 2004.
9. Ogiwara A., H. Kakiuchida, M. Tazawa, and H. Ono, “Analysis of anisotropic diffraction gratings using holographic polymer-dispersed liquid crystal,” *Jpn. J. Appl. Phys.*, Vol. 46, 7341–7346, 2007.
10. Ogiwara, A., S. Horiguchi, H. Kakiuchida, M. Tazawa, K. Yoshimura, and H. Ono, “Control of anisotropic diffraction in liquid-crystal composite volume gratings,” *Opt. Lett.*, Vol. 33, 1521–1523, 2008.
11. Kogelnik, H., “Coupled wave theory for thick hologram gratings,” *Bell Syst. Tech.*, Vol. 48, 2909–2947, 1969.

Temperature Dependable Holographic Memory Using Holographic Polymer-dispersed Liquid Crystal

A. Ogiwara¹, M. Watanabe², and R. Moriwaki²

¹Department of Electronic Engineering, Kobe City College of Technology, Japan

²Department of Electrical and Electronic Engineering
Faculty of Engineering, Shizuoka University, Japan

Abstract— Grating devices using photosensitive organic materials play an important role in the development of optical and optoelectronic systems. High diffraction efficiency and polarization dependence achieved in a holographic polymer-dispersed liquid crystal (HPDLC) grating are expected to provide novel polarization controllable optical devices, such as the holographic memory for optically reconfigurable gate arrays (ORGAs). However, the optical property is affected by the temperature change under environments where the HPDLC devices are applied. The temperature dependence of the diffraction efficiency in holographic memory is investigated for various LC composite materials. The anisotropic diffraction induced by the alignment of LC in periodic structure in the HPDLC memory is confirmed to be maintained at high temperature over 100°C by adjusting the combination of refractive index of LC and polymer materials.

1. INTRODUCTION

In recent years, the holographic memory for optically reconfigurable gate arrays (ORGAs) have been worthy of notice as a multi-context field programmable gate array (FPGA) to realize fast and numerous reconfiguration contexts using optical information processing technique [1–6]. As presented in Fig. 1, the ORGAs consist of laser sources, an optical holographic memory, and a programmable gate-array VLSI. A configuration procedure is executed by writing the reconstructed light patterns depending on the logical circuit to the photodiode array in gate-array VLSI using the optical reconfiguration system. Thus the optical connections based on the holographic memory can propose parallel programmability and fast reconfiguration. Moreover, holographic memories are well known to have high defect-tolerance because each bit of a reconfiguration context can be generated from the entire holographic memory [4]. For that reason, the damage to some fraction of the component rarely affects its diffraction pattern or a reconfiguration context. Therefore, the ORGAs are extremely robust against the components defects such as laser arrays, gate arrays, and holographic memories, and are particularly useful for space applications, which require high reliability [3]. Therefore the optical performance to store numerous contexts and to reconstruct them with high quality is needed for holographic memory in the ORGAs system. The HPDLC memory is suitable for ORGAs system because the configuration context pattern embedded in the polymer matrix is stored based on the parallel light reaction induced by the laser light exposure as fine periodic structures produced by cured-polymer and separated LC droplets phases, and it can be reconstructed with high diffraction efficiency and transparency [7–10].

However, the optical property is affected by the temperature change under environments where the HPDLC devices are applied. In this paper, we propose the temperature dependable holographic

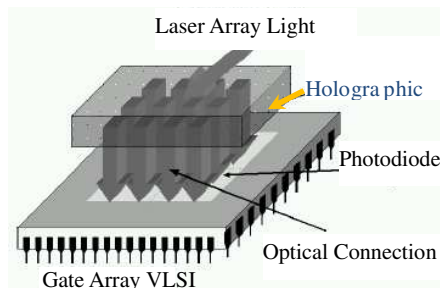


Figure 1: Overview of an ORGA comprising a gate-array VLSI, a holographic memory, and a laser array.

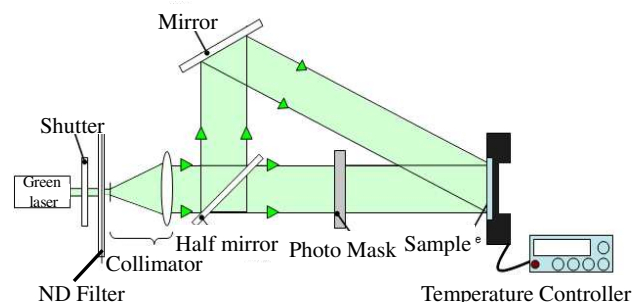


Figure 2: The optical setup for fabricating HPDLC memory using a laser interferometer with a photo mask.

memory using the combination of nematic LC and LC diacrylate monomer materials. The HPDLC memory is fabricated by a photo-induced phase separation technique using laser light interference exposures for the LC and polymer composites with different physical properties, such as refractive indices and the temperature at clearing point. The temperature dependence of the diffraction efficiency in holographic memory is investigated for various LC composites materials. The anisotropic diffraction induced by the alignment of LC in periodic structure in the HPDLC memory is confirmed to be maintained at high temperature over 100°C by adjusting the combination of refractive index of LC and polymer materials.

2. EXPERIMENT

2.1. Sample Preparation

LC composite for an HPDLC grating was prepared using isotropic monomers (Kyoisha Chemical) such as 2-hydroxy-3-phenoxy-propyl acrylate, 2-hydroxyethyl methacrylate, and dimethylol tricyclo decane diacrylate mixed with LC materials [9]. The ratios of the isotropic monomers mixtures were 80, 5, and 15 wt.%, respectively, and nematic LC material (Merck BL024) was added to the prepolymer mixture at content ratio of 25 wt.% based on the fraction of all ingredients. Another LC composite was prepared using the LC diacrylate monomer (Merck RM257) and the nematic LC material (Merck MLC7023). The wt.% of LC and monomer were 25 and 75 wt.%, respectively. N-phenylglycine and xanthene dye (dibromofluorescein) as a cointiator and photoinitiator were introduced to the LC composites composed of isotropic and anisotropic monomers, respectively.

The refractive index of the cured composition for isotropic monomers was found to be 1.520 by ellipsometric analysis. The physical properties of LC diacrylate monomer (RM257) given by the Material supplier indicate that their refractive indices for ordinary and extraordinary light are ($n_o = 1.508$, $n_e = 1.687$) and the melting and clearing points are 66 and 127°C, respectively. The physical properties (n_o/n_e , clearing point) of nematic LC supplied by Merck as follows: BL024 (1.5132/1.7174, 81°C), and MLC7023 (1.465/1.525, 79.5°C).

2.2. Optical Setup for Device Fabrication

Figure 2 shows an optical setup used to record a holographic memory. The light source is a green laser (Nd:YVO4) of 100 mW with 532 nm wavelength. The laser source for photopolymerization was collimated and linearly polarized perpendicularly to the grating vector. The laser light was divided into two parallel beams: a reference beam and an object beam. The object beam is incident to a photo mask including configuration contexts for a logical circuit. Interferometric exposure induces spatially periodic modulation of refractive index at the grating spacing of 1 μm by the laser beam angle crossed at 30° on the samples. The temperature condition in the device fabrication was adjusted at 50°C and 100°C for isotropic and LC diacrylate monomers, respectively in this setup using the temperature controller with a Peltier element. A photo mask was located at one pass of the laser beam in the laser interferometer to record the information of mask pattern as a grating structure.

3. RESULTS AND DISCUSSION

3.1. Temperature Dependence of Diffraction Efficiencies of Holographic Memory

Figure 3 show the temperature dependence of diffraction efficiencies of HPDLC gratings formed in the different LC composites: (a) isotropic monomers mixtures with LC (BL024) and (b) LC diacrylate monomer (RM257) with LC (MLC7023). The closed and opened marks such as η_p and η_s correspond to the diffraction efficiencies for incident p - and s -polarization laser lights which are coincident with the wavelength in device fabrication. The grating in Fig. 3(a) is formed on the bare glass plate while the grating in Fig. 3(b) is formed on the glass plate with the polyimide layer rubbed direction of 0°.

In Fig. 3(a), the diffraction efficiency of P -polarization component (η_p) starts to decrease around 70°C near the clearing point (81°C), while S -polarization (η_s) starts to increase around the temperature. At the temperature above 80°C, the diffraction efficiencies of P - and S -polarization components (η_p and η_s) are coincident and the polarization dependence of diffraction efficiencies has disappeared. On the other side, in Fig. 3(b), the diffraction efficiencies of η_p and η_s show approximately 80% and 40% in the temperature region which ranges from room temperature (25°C) to 110°C above clearing point of LC (79.5°C). The resultant HPDLC grating shows that the temperature dependence of anisotropic diffractions is improved by the design of refractive indices of LC composites.

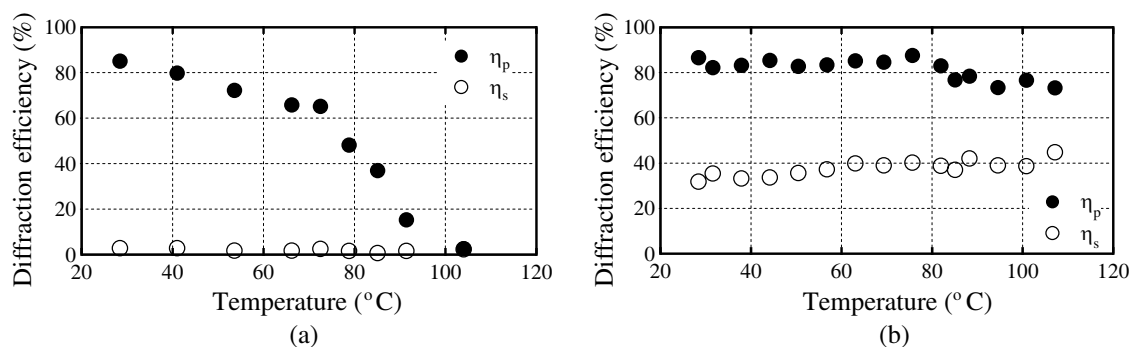


Figure 3: Temperature dependence of diffraction efficiencies of HPDLC gratings fabricated by (a) the nematic LC (BL024) and isotropic monomers, and (b) the nematic LC (MLC7023) and LC diacrylate monomer at rubbed direction of 0° .

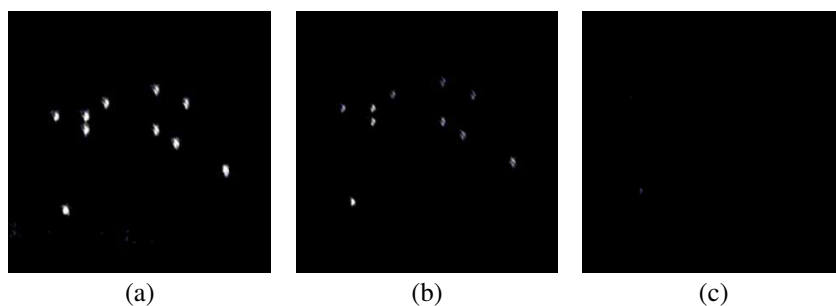


Figure 4: Effects of thermal modulation on the context images for AND circuit reconstructed under various temperatures at (a) 25°C , (b) 50°C , and (c) 100°C in the HPDLC grating formed by the nematic LC (BL024) and isotropic monomers.

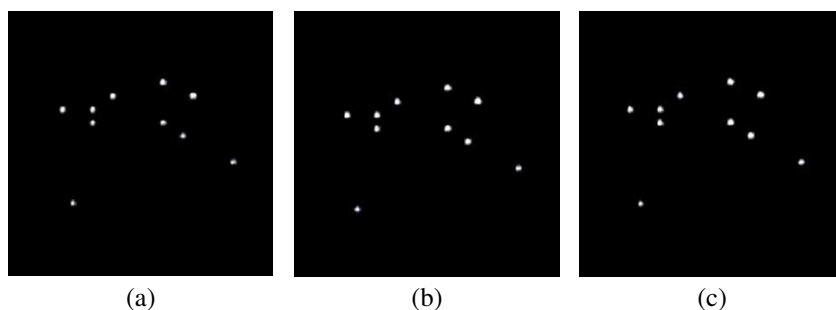


Figure 5: Effects of thermal modulation on the context images for AND circuit reconstructed under various temperatures at (a) 25°C , (b) 50°C , and (c) 100°C in the HPDLC grating formed by the nematic LC (MLC7023) and LC diacrylate monomers.

3.2. Effect of Thermal Modulation on Holographic Memory

Figures 4 and 5 show the effects of thermal modulation on the context image of AND circuit reconstructed from the HPDLC memory by the green laser irradiation of 532 nm. In Figs. 4(a) and 5(a), we can clearly observe the white and dark points in the image respectively which signify the binary states H and L for programming elements composed of the photodiodes array in the ORGA-VLSI [6]. At the temperature of 50°C , the intensity of white spots in Fig. 4(b) show lower level than those of Fig. 5(b). At the temperature of 100°C , white spots in Fig. 4(c) are almost vanished while the context image of AND circuit clearly appears in Fig. 5(c). Thus the temperature dependence of diffraction efficiency of HPDLC memory above N-I transition temperature can be improved by the design based on the refractive indices for LC composites materials. Therefore, the temperature dependable holographic memory which can maintain reconstruction performance at high temperature region over 100°C are realized.

4. CONCLUSIONS

Formation of HPDLC gratings were studied by the LC composite materials composed of isotropic and anisotropic monomers. The anisotropic diffractions of HPDLC gratings were influenced by the LC composites composed of nematic LC and monomers which have different clearing points and refractive indices. The diffraction efficiency of HPDLC memory above N-I transition temperature were improved by the design based on the refractive indices for LC composites materials. The experimental results demonstrate that the holographic memory fabricated by the LC diacrylate monomer (Merck RM257) and the nematic LC (Merck MLC7023) of low refractive index between extra-ordinary and ordinary indices (n_e and n_o) can reconstruct the configuration contexts to implement optical reconfiguration under harsh environmental condition in the high temperature over 100°C.

ACKNOWLEDGMENT

This research is supported by the Ministry of Internal Affairs and Communications of Japan under the Strategic Information and Communications R & D Promotion Programme (SCOPE: 121806016).

REFERENCES

1. Mumburu, J., G. Zhou, X. An, W. Liu, G. Panotopoulos, F. Mok, and D. Psaltis, "Optical memory for computing and information processing," *Proc. SPIE*, Vol. 3804, 14–24, 1999.
2. Mumburu, J., G. Panotopoulos, D. Psaltis, X. An, F. Mok, S. Ay, S. Barna, and E. Fossum, "Optically programmable gate array," *Proc. SPIE*, Vol. 4089, 763–771, 2000.
3. Nakajima, M. and M. Watanabe, "Optical buffering technique under a space radiation environment," *Opt. Lett.*, Vol. 34, 3719–3721, 2009.
4. Ogiwara, A., M. Watanabe, T. Mabuchi, and F. Kobayashi, "Formation of holographic memory for defect tolerance in optically reconfigurable gate arrays," *Appl. Opt.*, Vol. 49, 4255–4261, 2010.
5. Ogiwara, A., M. Watanabe, T. Mabuchi, and F. Kobayashi, "Holographic polymer-dispersed liquid crystal memory for optically reconfigurable gate array using subwavelength grating mask," *Appl. Opt.*, Vol. 50, 6369–6376, 2011.
6. Ogiwara, A. and M. Watanabe, "Optical reconfiguration by anisotropic diffraction in holographic polymer-dispersed liquid crystal memory," *Appl. Opt.*, Vol. 51, 5168–5177, 2012.
7. Sutherland, R. L., "Polarization and switching properties of holographic polymer-dispersed liquid-crystal gratings. I. Theoretical model," *J. Opt. Soc. Am. B*, Vol. 19, 2995–3003, 2002.
8. Sutherland, R. L., L. V. Natarajan, V. P. Tondiglia, S. Chandra, C. K. Shepherd, D. M. Brandelik, and S. A. Siwecki, "Polarization and switching properties of holographic polymer-dispersed liquid-crystal gratings. II. Experimental investigations," *J. Opt. Soc. Am. B*, Vol. 19, 3004–3012, 2002.
9. Ogiwara, A., H. Kakiuchida, K. Yoshimura, M. Tazawa, A. Emoto, and H. Ono, "Effects of thermal modulation on diffraction in liquid crystal composite gratings," *Appl. Opt.*, Vol. 49, 4633–4640, 2010.
10. Ogiwara, A., "Effects of anisotropic diffractions on holographic polymer-dispersed liquid-crystal gratings," *Appl. Opt.*, Vol. 50, 594–603, 2011.